DOE/NASA CONTRACTOR REPORT

DOE/NASA CR-161329

AUTOMATED LONGWALL GUIDANCE AND CONTROL SYSTEMS
Phase I Report

Prepared by

The Bendix Corporation
Energy, Environment, and Technology Office
2582 South Tejon Street
Englewood, Colorado 80110

Under Contract NAS8-32921 with

The National Aeronautics and Space Administration
George C. Marshall Space Flight Center, Alabama 35812

September 6, 1978

For the U. S. Department of Energy

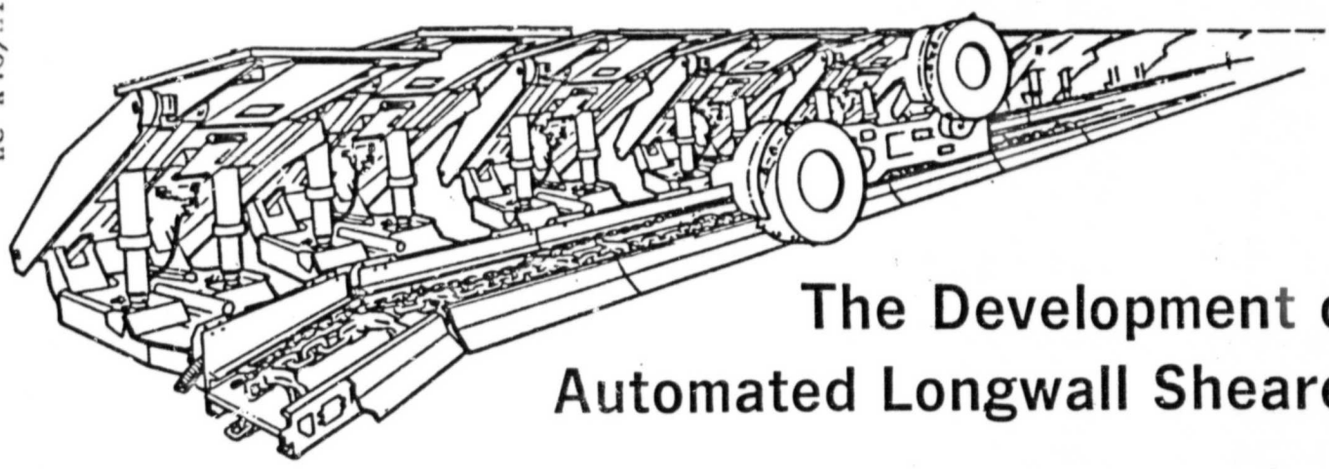

The Development of Automated Longwall Shearer

George C. Marshall Space Flight Center
Marshall Space Flight Center, Alabama 35812

Prepared for
U. S. Department of Energy
and
National Aeronautics Administration

161329

THE
BENDIX
CORPORATION

ENERGY, ENVIRONMENT
AND TECHNOLOGY OFFICE

PHASE I REPORT

CONTRACT NAS8-32921

AUTOMATED LONGWALL GUIDANCE AND CONTROL SYSTEMS

SEPTEMBER 6, 1978

PREPARED FOR:

NATIONAL AERONAUTICS
AND SPACE
ADMINISTRATION
GEORGE C. MARSHALL
SPACE FLIGHT CENTER
MARSHALL SPACE FLIGHT
CENTER, ALABAMA
35812

Prepared by:

S. C. Rybak
Program Manager

V. R. Karanam
Project Engineer

William H. Gelbach
Staff Engineer

G. A. Cornell
Principal Engineer

Approved by:

S. C. Rybak
Program Manager

Milton Brown
Technical Director

FOREWORD

This report is submitted in accordance with NASA Contract No. NAS8-32921, Automated Longwall Guidance and Control System, DRL Line Item MA03, Phase I Report.

CONTENTS

CONTENTS (Continued)

CONTENTS (Continued)

CONTENTS (Continued)

Figure

CONTENTS (Continued)

CONTENTS (Continued)

CONTENTS (Continued)

CONTENTS (Continued)

CONTENTS (Continued)

1. INTRODUCTION

Dwindling domestic and world oil and gas supplies with the inevitable rise in the price of these fuels have generated deep concern within government, industry, and the general public as to how the energy needs of the country can reasonably and economically be met in the future. The increased use of coal, our most abundant fossil fuel reserve, during the next quarter century will necessitate increasing the efficiency of underground coal extraction. Longwall mining techniques have tne potential of greatly increasing the coal yield per acre and coal production per man per shift since it is essentially a continuous mining process. In addition, since longwall is a continuous mining process employing continuous haulage, it is extremely well suited for automation which is the subject of the present study. Automating longwall coal extraction will not only increase production but also minimize the amount of foreign material taken along with the coal thus reducing sorting time and cutter bit wear. In addition, automating or remoting the longwall mining process will increase operator health and safety by removing the miner from the shearer and thus the hazards encountered in the immediate cutting area.

The present study has been divided into two phases. Phase I was primarily concerned with the analyses and simulation of candidate Vertical Control Systems (VCS) and Face Advancement Systems (FAS) required to satisfactorily automate the longwall system. The purpose of these studies were to specify the desired overall longwall system configuration for preliminary design which will be performed during Phase II of the study. This report outlines the analyses, and simulations that were performed during Phase I of the subject study which has led to the satisfactory specification of the overall longwall system on which a preliminary design will be performed during Phase II.

2. SUMMARY AND CONCLUSIONS

In the paragraphs that follow, a summary of the results obtained and the conclusions drawn during the Phase I portion of the study will be outlined by major longwall subsystem. These major subsystems are the Vertical Control System (VCS), and the Face Advance System (FAS) which consists of the yaw and roll control subsystems.

In a study of this nature, a procedure is needed by which the performance of various control system configurations could be compared in order to determine which one is "best" for a particular application. In order to accomplish this end, "baseline" system configurations for all of the control subsystems required for longwall automation were defined. The baseline definitions used the work performed by MSFC as a starting point and were the "simplest" (and hence least expensive and probably most reliable) subsystem configuration that would satisfactorily perform a particular control function. It was against the performance achieved by the "baseline" systems that various other control system configurations/additions/modifications were compared.

Proposed modifications/additions to the baseline system definition were evaluated by considering the improved performance realized vs. the additional complexity and relative cost introduced by incorporation of the modification, and only those modifications/additions to the baseline systems that were cost effective were incorporated. Following this procedure, a highly reliable and economically advantageous longwall system design emerged.

2.1 Vertical Control System (VCS)

The function of the VCS is to control the two cutting drums of the double ended ranging arm shearer so that they remain within the coal seam. The VCS should be capable of taking all the coal on the roof and floor, or if desired, leave a given amount (i.e., bias) of head and/or

floor coal while taking a minimum amount of rock. In addition, the distance between two successive cuts would have to remain within given limits in order that the roof supports advance satisfactorily.

In order to analyze and design the VCS, a typical longwall shearer had to be chosen for computer simulation. The longwall shearer chosen was the Joy LW 300 and all control system studies involving the shearer were performed with this model. In addition, a reasonable representation of the coal/shale interface that would be encountered during in-mine operations had to be simulated. It became apparent early in the study that using artificial "worst case" profiles would not be very satisfactory from two viewpoints:

a. It is very difficult if not impossible to define a "worst case" coal shale interface without having access to the actual interface profiles in most or possibly all of the operational longwall faces and those being projected for longwall mining.

b. Even if a "worst case" profile could be defined, it would place extreme requirements on the required longwall system resulting in an unrealistic and costly system design.

It was, therefore, decided to model typical coal/shale interface profiles that one would commonly encounter during longwall mining operations. To accomplish this end, use was made of a survey performed by A. D. Little, Inc., the results of which were given in a report titled, "Last Cut Survey," published in June 1977, in which the coal/shale interface profiles for six mines representing a variety of geologic conditions and seam heights were given. Statistical analyses were performed on the twelve profiles (i.e., top and bottom) given and it was determined that all of the mine profiles were statistically similar. This result certainly gives credence

to the hypothesis that coal/shale interface profiles are more similar than different when going from mine to mine. Therefore, the York Canyon profiles were chosen from the given data set as representing typical (i.e., mean) coal/shale interface profiles that would be encountered during in-mine operations and most performance runs were made with these profiles. Performance evaluations made with other mine profiles had little effect on overall performance as will be discussed in Section 3.

In order to evaluate VCS performance and compare various configurations with respect to each other, a measure of performance had to be defined. There are numerous performance measures that one can define for the VCS, no single one of which will be an adequate measure of performance for all operational conditions. The most commonly used to characterize the performance of a control system is the RMS of the error between the desired and actual control achieved which, in our case, is the RMS of the difference between the desired and actual cuts achieved, or the cut error. Although this is generally an excellent measure of VCS performance, it does not totally specify all aspects of VCS performance. Other performance characteristics that are of interest are the amount of time spent cutting rock, the volume of rock taken, the volume of coal erroneously left, and the volume of coal erroneously taken. Therefore, in order to augment the RMS cut error, a number of other performance parameters were also determined which are: a) percent of time spent in rock; b) volume of rock taken; c) volume of excess coal taken; d) volume of coal erroneously left; and e) the average of the absolute value of the cut error. These performance parameters, in conjunction with the RMS cut error completely specify VCS performance over its designated range of operation.

A block diagram of the VCS computer simulation is shown in Figure 3-1. The major features of the simulation are listed below:

a. Detailed modeling of the mine geometry including actual interface profiles and techniques for generating statistically similar coal/shale interface profiles from a given initial profile which is used to give realistic results when multiple passes are made.

b. Detailed geometrical model of the shearer including its location along, and orientation with respect to, the face.

c. Technique for determining the actual track that would result when laying five foot conveyor sections along a roughly cut bottom.

d. Detailed non-linear representation of shearer actuator dynamics including the hydraulic coupling between the two ranging arms.

e. Detailed representation of the nucleonic and natural radiation coal interface detectors including the nonlinear calibration curves, Poisson distributed sensor noise, and air gaps.

f. Complete representation of coal/shale presence sensors including a probabilistic representation of their correctness.

g. Complete representation of last and present cut followers.

h. Modular hierarchical control law algorithm that is able to accommodate a variety of sensor complements and control law implementations.

i. The effect of drum filtering on the cut obtained.

For a more detailed discussion of the VCS simulation see sections 3.2 and 3.3

The "baseline" system configuration for the VCS consisted of the following:

a. An active nucleonic coal interface detector (CID) for measuring coal thickness on the roof.

b. Sensitized picks incorporated into each of the two cutting drums in order to detect the presence of coal or rock.

c. A last cut follower mechanism in order to measure the present cut relative to the last one made.

d. The bottom cutting drum is slaved to the top one if a given amount of floor coal is to be left. The reason for not using a CID for proportional floor cutting drum control is that it is not feasible to mount such a detector on the floor given all the debris and water found there.

e. Use presently obtained CID data in a measure and cut algorithm as opposed to optimal filtering/prediction algorithms which can be used to compensate for CID noise and that the measurement point is some 2.5 feet behind the actual drum cutting point.

f. Use of the nonlinear hydraulic actuation system commonly found on longwall shearers.

Modifications/additions to the defined VCS "baseline" considered are listed below.

1. Use of optimal filtering/predictive control algorithms for cutting drum control.

2. Use of a natural radiation CID.

3. Use of an impact penetrometer/reflectometer for a coal/shale presence sensor.

A number of techniques for bottom drum slaving were considered. They are:

1. Maintaining constant height between both cutting drums.

2. Using CID measurements instantaneously and in a delayed mode.

3. Use of the last cut follower.

4. Use of a last cut follower located in the middle of the shearer.

5. Use of a separate present cut follower located above the rear drum.

Figure 3-86 shows the shearer slaving geometry and the various slaving techniques listed above.

2.1.1 Baseline System Parameter Determination - For the baseline VCS defined, system parameters (i.e., gains, sensor locations, sampling and averaging times, etc.) had to be determined in order to

obtain optimum performance for this configuration. One of the first parameters to be determined was the loop gain/compensation to be used for the position loop closed around the actuators which control cutting drum height. Various loop gains were investigated and it was determined that a gain of 170 (see Figure 3-21) yielded best overall performance even though the actuator did have a limit cycle at this gain value. The only problem that can occur if the actuator is operated in the limit cycle region is that it may heat excessively. Should that be the case, a heat exchanger could easily be designed which will maintain temperatures within acceptable limits. Therefore, a loop gain of 170 was specified and used for the gain of the actuator loop in all of the control studies subsequently performed.

Another parameter to be determined was the mounting location of CID sensors. It was clearly shown (see Table 3-3) that system performance improves as the CID is moved closer to the cutting drum (and hence the cutting point) since this minimizes the distance between the point measured and the point being controlled. The closer the CID can be moved to the cutting point the better is the probability that the CID measurement reflects the coal/shale interface at the cutting location, hence improving the measurement. Therefore, the CID's were located 2.5 feet behind the cutting drum which was as close to the cutting drum as the CID could be mounted without interference.

Another critical parameter to be determined was the CID output interval or averaging time. Again, it was clearly shown (see Table 3-4) that in the absence of CID measurement noise, increasing the CID output interval degraded system performance. The reason for this is that as the output interval is increased, greater measurement lags are introduced into the system degrading its performance. However, the longer the output interval or averaging time, the smaller the effect of CID measurement noise and hence the more accurate the measurements obtained. Therefore, there should be an output interval which will

balance the detrimental effect of increased output interval due to added lag against the benefit gained by reducing the effect on CID measurement noise, thus yielding optimum system performance. Such an output interval was indeed found (see Table 3-5), and was 0.25 second for the active nucleonic CID. When a natural radiation CID was employed the optimum output intervals were 1 and 2 seconds for 5 and 3 inch detection crystals respectively.

2.1.2 Baseline VCS Performance Characteristics

2.1.2.1 Effect of Nonlinear CID Calibration Curve

The active nucleonic or passive natural radiation CID's have calibration curves that are nonlinear (see Figures 3-11 and 3-12) and saturate as the thickness of coal increases. Therefore, for the same CID measurement noise, the error in the sensor measurement would increase as the desired thickness of coal to be left approaches the saturation characteristics of the sensor thus giving degraded system performance. Such an effect has been found and is outlined in Table 3-7 for the active nucleonic CID. Examination of this table indicates that for a one second output interval the RMS cutting error went from 1.61 inch to 2.39 inch, an increases of 48.45 percent, when the coal thickness to be left increased from 4 to 6 inches. However, it should be noted that cut error will remain invariant as the desired coal to be left is 5 inches or less since in this range the CID calibration curve is essentially linear.

2.1.2.2 Effect of Adding Sensitized Pick and Last Cut Follower (LCF) to CID

The effect of adding a sensitized pick and using it in conjunction with the CID in a hierarchical manner is to improve cutting performance. The technique that is used is to command the cutting drums on the basis of CID information and when the pick indicates that rock is being mined to override the CID command and depress the cutting

head a given amount. The improvement realized by the addition of the sensitized pick is most pronounced when attempting to leave a small coal thickness (i.e., between zero and 2 inches), since it is during this mode of operation that using CID information only has a high probability of commanding the drum to cut the roof due to CID measurement errors. Once the drum has cut into the roof the CID cannot say how far into the roof the drum has cut and gives an indication of zero coal thickness regardless of the depth the cutting drum has penetrated the rock. Therefore, once the roof is penetrated the cutting drum would only be commanded to depress the coal bias amount even if the roof were penetrated considerably more than this value, hence degrading cutting performance. The addition of a sensitized pick does not allow the cutting drum to appreciably penetrate the roof, thereby keeping the CID in its linear range, thus improving cutting performance. The addition of a last cut follower to the CID and sensitized pick and employing this sensor configuration in a hierarchical manner where the last cut follower is given highest priority, the sensitized pick next, with the CID having lowest priority, further improves cutting performance. The reason for the improved performance when introducing a last cut follower is that it filters even further errors in the CID measurements since the present cut cannot deviate more than a prescribed amount (i.e., $\pm$ 2 inches) from the previous cut.

It should also be noted that the cutting accuracy achieved when using a sensitized pick in conjunction with the CID or CID and last cut follower, is not appreciably affected as the accuracy of the pick information degrades to 80 percent. The reason for this is that the pick is one of two or three sensors controlling the VCS and hence a wrong piece of information from it does not have a one-to-one effect on system performance. The results discussed above are outlined in Tables 3-8 and 3-9.

2.1.2.3 VCS Performance with Sensitized Pick Only

When attempting to take all of the coal the VCS will be controlled by the sensitized pick only, or possibly acting in conjunction with a last cut follower. In this mode of operation error in the sensitized pick information does have a marked effect on system cutting performance. When the pick information is 100 percent correct an RMS cut error of 0.68 in. is achieved. However, if the pick information is 90 percent correct the RMS cut error is 1.24 in., when it is only 80 percent correct the RMS cut error grows to 2.33 in. The reason for this sensitivity is that when the VCS is under pick control, errors in the pick information cause an immediate error in the cutting drum command, hence directly affecting system performance. It is, therefore, concluded that the sensitized pick should be between 80 to 90 percent accurate to enable taking all of the coal, while maintaining the rock taken to a minimum. These results are given in Table 3-10.

2.1.2.4 Effects of Actuator Dynamics of VCS Performance

Inserting the nonlinear actuator dynamics into the VCS control system had little effect on system performance when a given amount of coal is to be left, and hence a CID is employed. However, if all of the coal is to be taken, and the VCS is under pick control, then the insertion of actuator dynamics has a more marked effect on the performance achieved with the RMS cut error going from 0.68 inches without actuators to 2.06 inches when the effect of actuator dynamics are considered. The reason for this sensitivity is that when the sensitized pick is employed it actually measures the presence of coal or shale at the cutting point. Therefore, if the actuators respond quickly, a very small RMS cut error is realized (i.e., 0.68 inch RMS). Adding the actuator dynamics has the effect of introducing lag into the system and hence performance degrades. When the VCS is under CID control the errors introduced by CID noise and its being mounted behind the cutting drum overshadow the effect of the actuator dynamics thus minimizing its effect on overall system performance. These results are outlined in Table 3-11.

2.1.2.5 Effects of Varying VCS Traverse Speed Across the Face

The nominal traverse speed at which the baseline system was designed and its performance evaluated was 30 ft/min. Increasing this speed to 50 ft/min or decreasing it to 20 ft/min had no effect on system performance. The reason for this result is that a 0.25 second output interval is being used for the CID which is quite fast and within the speed range of 20-50 ft/min the shearer does not travel an appreciable distance between CID information updates. This would imply that if the CID output interval were increased one should see an effect of varying shearer traverse speed on overall system performance with performance degrading the faster the shearer traverses the face. This effect was observed when the CID output interval was increased to one second and the results are tabulated in Table 3-12.

2.2 VCS Performance with Optimum Filtering/Predictive Algorithms

Since the CID is mounted behind the cutting drum it is not measuring the coal/shale interface at the cutting point. Using the measured depth of the coal/shale interface at the CID location and saying that this is the depth at the cutting drum location obviously is in error since the coal/shale interface changes as one proceeds down the face. Therefore, one would suspect that using some form of filtering/predictive algorithm system performance could be improved, since a more accurate estimate of the coal/shale interface both at the point of measurement and at the cutting drum could be determined. There are many types of filtering/predictive algorithms one can formulate, all of which to varying degrees make use of past as well as the present CID measurements in the determination of the coal/shale interface. At first glance one would be tempted to make use of all or many past CID measurements in order to obtain a "best estimate" of the coal/shale interface at the present measurement location and cutting point. Implied in such a scheme

would be a method by which all of the CID measurements could be referenced with respect to each other through some common reference frame. However, no such frame exists in the longwall system and there doesn't appear to be any reasonable way by which such a frame could be obtained. Therefore, if an algorithm were formulated that used many past CID measurements to aid in the determination of the coal/shale interface at the present measurement point and the cutting drum, any contribution in these measurements due to the floating reference frame in which the measurements are taken would go undetected. The frame, with respect to which the height of the coal/shale interface is measured could be considered the shearer skid plane. Therefore, measurement changes due to floor undulations could not be differentiated from changes due to actual variations in the coal/shale interface height above the skid plane. Therefore, the contribution due to floor undulations in the measurement obtained would be attributed to coal/shale interface variations and the filtering and predicive alogorithms would yield answers that would be in error by appreciable amounts. Optimum filtering and predictive algorithms that have extremely good potential of determining and predicting the coal/shale interface by using many past CID measurements are generally quite sensitive to unmodeled processes that were not considered in their formulation which in this case would be a floor undulation. In such a case, performance degrades rapidly to where it is actually worse than that which would be obtained if these algorithms were not employed. Given this situation the filtering/predictive algorithms that will be considered for the longwall are those which employ CID measurements in the immediate vicinity of the present measurement and cutting points. These types of algorithms would require a priori knowledge of the coal/shale interface statistics in terms of correlation function, mean and variance as well as a description of the sensor noise in terms of its mean and variance. The reason for this a priori knowledge requirement is that the statistics of the coal/shale interface could not be derived from past CID measurements due to the lack of a common reference frame.

Two types of optimal filtering/predictive algorithms employing CID measurements in the immediate vicinity of the present measurement and cutting points were formulated. One algorithm (Scheme 2) uses the present CID measurements in conjunction with CID data in the immediate vicinity of the present measurement to estimate and predict the coal/shale interface at the measurement point and cutting drum respectively. The other technique (Scheme 1) uses the present CID measurement in conjunction with estimates of the coal/shale interface in the immediate vicinity of the present measurement point for estimation and prediction. These two types of algorithms were formulated in a one-dimensional sense using present cut CID data/estimates, and in a two-dimensional sense using present and past cut CID data/estimates yielding four different optimal filtering algorithms for possible use in the VCS control system.

Analyses performed on these algorithms indicated that both should give appreciable performance improvement if the floor didn't undulate, with Scheme 1 being better than Scheme 2. In addition, it was shown that the algorithm employing CID measurements only would be less sensitive to the unmodeled floor undulations than the scheme employing CID data in conjunction with coal/shale interface estimates. These results were verified by simulation for the two one-dimensional algorithms, and the data indicated that cutting performance degraded due to floor undulations to the point where it wasn't any better, and in most cases, worse than that obtained with the baseline measure and cut algorithm (see Table 3-15). The degradation in performance due to floor undulations would be even worse for the two-dimensional version of these algorithms and hence were not simulated. Therefore, the conclusion of this investigation was that there is no advantage to be gained by using optimal filtering and predictive algorithms for VCS control. Thus, the simple measure and cut control algorithm defined in the baseline system should be used for cutting drum control.

2.3 Use of Impact Penetrometer/Reflectometer for VCS Control

Investigations were conducted into the use of an impact penetrometer/reflectometer as the coal/shale presence sensor, i.e., to replace the sensitized pick. The prime difference between the two types of coal presence sensors from an overall systems viewpoint is the manner in which they are integrated into the VCS. The sensitized pick, which is mounted on the cutting drum measures whether the drum is presently cutting coal or rock, while the impact penetrometer/reflectometer is mounted at the approximate CID location, and hence can only measure whether the drum has cut coal or rock. This difference is basic in determining the VCS performance obtained when using these two coal presence sensors. The sensitized pick yielded excellent cutting performance (0.68 inch RMS) and VCS seam following capability when used by itself since it does measure what the drum is cutting virtually instantaneously. However, the impact penetrometer/reflectometer being mounted some 2.5 feet behind the cutting drum cannot measure whether the drum is cutting rock or coal until the shearer has traversed 2.5 feet to the present drum location, which at 30 ft/min shearer traverse speed takes 5 seconds. During this total time, if the impact penetrometer/reflectometer is measuring rock, it is continuously depressing the cutting drum or if it is measuring coal it is continuously commanding the cutting drum to rise, thus giving rise to severe system limit cycles and an RMS cut error of 21.7 inches. When the impact penetrometer/reflectometer is augmented by a last cut follower, system limit cycles are limited by the deviation allowed between the present and previous cuts. If, as in our case, this value is set at ± 2 inches the ensuing RMS cut error is 1.83 inches which is essentially the RMS of a limit cycle ranging between $\pm$ 2 inches. These results are outlined in Table 3-10 with the actual system cutting performance shown in Figures 3-65 and 3-66. Therefore, the conclusion of these studies are that the impact penetrometer/reflectometer is not a very

satisfactory coal presence sensor for our longwall application, particularly when all the coal is to be taken, and hence is not presently recommended.

2.4 Use of Natural Radiation CID for VCS Control

The use of a natural radiation CID instead of an active nucleonic one was investigated. The prime difference between these two sensors that affects system performance is the number of counts per unit time for a given coal thickness. The active nucleonic CID has many more counts per second (approximately a factor of 20) for a given coal thickness than a reasonably sized (i.e., 3 to 5 inch detection crystal) natural radiation ICD. The counts per unit time as a function of coal depth for both types of CIDs are shown in Figures 3-11 and 3-12. Therefore, the noise and hence the coal depth measurement uncertainty is worse with the natural radiation than with the active nucleonic CID and degraded system performance when using the natural radiation CID should be expected. This indeed has been verified by simulation with RMS cutting error increasing from 1.64 inches to 2.25 inches when the active nucleonic CID was replaced by the natural radiation sensor. These results are documented in Tables 3-5 and 3-11. Therefore, from a performance viewpoint the active nucleonic CID is recommended for system implementation. However, there are drawbacks to the active nucleonic sensor ranging from sociological, (i.e., active radiation source) to technical (i.e., sensitivity to air gaps) to potentially severe integration problems (i.e., sophisticated suspension that must keep the sensor against roof with a minimum of air gaps, deployment and stowage mechanisms, etc.) that the natural radiation CID does not have. During preliminary design (i.e., Phase II) these problems will be addressed in detail. Should these investigations indicate that the problems related to the active nucleonic CID precludes its use or detracts significantly from the merits of its use, the natural radiation CID would be used instead. Although, as

pointed out above, system cutting performance degrades to a degree by its use, however, the performance achieved is still quite good when compared to what is presently being obtained manually. In addition, all of the benefits with respect to the health and safety that one gains by longwall automation would remain intact when using a natural radiation CID.

2.5 Slaving of Bottom Drum

Since it became clear early in the study that it would not be feasible to mount a CID on the floor for controlling the drum cutting the bottom due to debris and water that will be there, an alternate technique of control for the bottom drum had to be devised for the condition where a given amount of coal is to be left on the bottom. (When all the coal is to be taken the bottom cutting drum can be controlled by a sensitized pick in the same manner that roof cutting drum control is achieved.) The technique used was to slave the bottom cutting drum to the top one by maintaining the instantaneous height of the cut constant. A number of ways of accomplishing drum slaving were investigated. The first of these was to maintain the height between the two cutting drums constant by using the readouts of the linear actuators controlling both drums. This implementation was quite sensitive to floor undulations and did not yield satisfactory system performance. Another implementation that was investigated was to use CID measurements to determine the height of the roof and command the bottom drum to maintain the instantaneous cut height constant. This implementation, although better than maintaining the instantaneous height between the cutting drums constant, still yielded performance that wasn't any better than locking the drum for a flat floor, and degraded when the actual floor undulations were introduced. Examination of Table 3-2 indicates that four of the six mines surveyed exhibited a high degree of correlation between the top and bottom coal/shale interface profiles. This phenomenon suggested that if the CID measurements were delayed until the bottom cutting drum was

directly below the CID measurement point and then used to control the bottom drum, better slaving performance should be realized. This was indeed the case (for a flat floor) with the improvement being quite apparent when the top and bottom interfaces were highly correlated such as in the Robinson Run Mine. It was also true to a lesser degree in a mine that did not have a high degree of correlation between top and bottom such as in York Canyon. However, when the floor undulations were introduced, significant performance degradation resulted and better system performance would be achieved by locking the bottom cutting drum. The results discussed above are tabulated in Table 3-16.

One basic problem (besides performance) that the slaving implementations discussed above have in common is that they do not tend to maintain the difference between two successive bottom cuts within a prescribed value. Slaving implementations that would tend to maintain two successive bottom cuts within specified limits would be to slave the bottom drum to the last cut follower or to a present top cut following mechanism. Slaving the bottom drum to the last cut follower mechanism was tried and it was found that the system performance was sensitive to floor undulations. An attempt was made to slave the bottom drum to a last cut following mechanism located in the middle of the shearer in order to minimize the effect of floor undulations. This implementation did indeed improve slaving performance to acceptable levels; however, roof cutting performance degraded appreciably. Slaving the bottom drum to a separate present top cut following mechanism was tried and the performance obtained was the "best" of all of the implementations evaluated. Having a separate present top cut following mechanism above the floor cutting drum essentially eliminates the problems due to floor undulations and is presently the recommended technique for bottom drum slaving. These results are outlined in Table 3-17.

2.6 Recommended VCS System

As a result of the studies performed, the recommended VCS implementation is outlined below as a function of the mining capabilities desired.

a. Leaving a prescribed amount of coal on top and bottom.

1) Top Drum Control

Active Nucleonic CID

Two sensitized picks mounted 180 degrees apart on cutting drum

Last Cut Follower

2) Bottom Drum Control

Present Top Cut Follower

Two Sensitized Picks Mounted in the Cutting Drum 180 Degrees Apart

b) Leaving a Prescribed Amount of Coal on Top Taking all Coal on Bottom.

1) Top Drum Control

Active Nucleonic CID
Two Sensitized Picks
Last Cut follower

2) Bottom Drum Control

Two Sensitized Picks

c) Taking all of the Coal on Top and Leaving a Prescribed Amount of Coal on Bottom

1) Top Drum Control

Two Sensitized Picks
Last Cut Follower

2) Bottom Drum control

Two Sensitized Picks
Present Top Cut Follower Mechanism

d) Taking all of the Coal on Top and Bottom

1) Top Drum Control

Two Sensitized Picks
Last cut Follower

2) Bottom Drum Control

Two Sensitized Picks

The recommended systems for VCS control are shown in tabular form in Table 3-20.

2.7 Performance of Recommended System

The average performance of the recommended VCS configuration is shown in Table 2-1. Examination of this table indicates that the recommended VCS configuration will outperform a human operator by at least a factor of two at a shearer speed as high as 50 ft/min. While

Table 2-1. VCS Performance Summary

	AVERAGE RMS ROOF CUT ERROR (IN)	AVERAGE RMS FLOOR CUT ERROR (IN)	AVERAGE RMS CUT ERROR (IN)
AUTOMATED VERTICAL CONTROL NUCLEONIC CID	1.36	2.84	2.1
AUTOMATED VERTICAL CONTROL NATURAL RADIATION CID 5 IN. CRYSTAL	2.25	4.63	3.44
* MANUALLY OPERATED VERTICAL CONTROL SYSTEM	N/A	N/A	** 5.5

* AVERAGE OF ALL MEASURED PERFORMANCE
12 FACES IN 10 DIFFERENT MINES
A.D. LITTLE SURVEY (DEC. 1976-JUNE 1977)

** 3.1 IN. MEAN ERROR

SHEARER VELOCITY = 30 FT/MIN
RESULTS ESSENTIALLY UNCHANGED AT 50 FT/MIN

under manual control the shearer can only move approximately 10 to 12 ft/min. These results indicate the increased productivity and hence economic potential of automating the longwall, in addition to the health and safety gains.

2.8 Roll Control System

The function of the roll control system is to maintain the attitude of the longwall shearer about its longitudinal (roll) axis at a specific value regardless of the twists that may be in the conveyor track on which the shearer is riding. This mode of control is necessary if the shearer is to be maintained perpendicular to the longwall panel being mined and hence within the coal seam as repeated passes are made.

Two control loop implementations were investigated. One has the control loop closed around the inclinometer, i.e., the inclinometer is within the closed loop. The advantage of this implementation is that there is no need to instrument the hydraulic ram. However, since the inclinometer is within the closed loop any filtering that might be added to eliminate the effects of cross-axis acceleration will affect overall control loop stability and hence is an added constraint on the filter design. The other implementation closes the control loop around the hydraulic actuator with the inclinometer being external to this loop and furnishing what essentially can be looked at as an update signal. This implementation has the advantage of eliminating the dependence of control loop stability on the filter characteristics that may be used to eliminate the effects of cross-axis accelerations, thus enabling the filter design to proceed from these considerations only. However, this implementation requires that the linear hydraulic actuator be instrumented.

A computer simulation for the roll control system was developed and consisted of the following:

a. Full nonlinear model of the linear hydraulic actuation system.

b. Second order inclinometer dynamics

c. Cross axis accelerations due to the cutting forces and torques as the shearer proceeds along the face.

This simulation was used to evaluate the performance characteristics of the two roll control system implementations described.

2.8.1 Roll Control Loop Bandwidth Determination

In order to choose the parameters for both control loop implementations the desired loop bandwidth had to be determined. This was done by estimating the maximum input frequency that the roll control loop would have to respond to. Assuming that two adjacent 5 foot conveyor sections are twisted in opposite directions, an input frequency of 0.05 Hz results for a shearer traverse speed of 30 ft/min. Hence the desired roll control loop bandwidth was set at 0.05 Hz.

In order to choose system parameters so that the desired 0.05 Hz control loop bandwidth would be realized, system frequency responses were taken at various amplitude inputs ranging from the maximum commanded roll angle of $\pm$ 5 degree to one quarter this maximum. The reason for taking frequency responses at different input amplitudes is due to system nonlinearities which make system response characteristics a function of input amplitude. The gains that were finally chosen for both control loop implementations were such that a control loop bandwidth of 0.05

Hz would be realized at a 2.5 degree input, or one-half the maximum possible command. This was judged to be adequate since it is highly unlikely that the roll control loop would be required to command a larger value than 2.5 degree. In addition, the loop bandwidth also falls off due to flow constraints and attempting to achieve the desired loop bandwidth at 5 degree inputs would probably require a hydraulic modification which isn't desirable.

Frequency responses for the two control loop implementations considered are given in Figures 5-4 through 5-6 and 5-8 through 5-10.

2.8.2 Roll Control Loop Performance Characteristics

Both control loop implementations perform well (i.e., RMS errors between 0.05 to 0.1 degree) in the absence of cross-axis accelerations, with the implementation that closes a control loop around the actuator being slightly more accurate. However, system performance for both implementations degrade significantly even when relatively small values of cross-axis accelerations are introduced, as outlined in Table 5-1. The reason for this sensitivity becomes clear when one examines the value of RMS g represented by a 10 percent error in tracking a 1.77 degree (i.e., $\pm$ 2.5 degree peak) input signal. This value is approximately 3×10^{-3} g RMS which means that if the sensed accelerations are in error by approximately 3 milli g's a ten percent tracking error should be expected. Or alternately, if the cross-axis acceleration sensed by the inclinometer mounted on the shearer has an RMS level of approximately 3 milli g's within the control loop bandwidth at least a ten percent tracking error will result. In addition, it should be noted that if the cross axis RMS g levels within the control loop bandwidth are in the order of three milli g's or greater, filtering of the inclinometer

output will not yield appreciably better performance if the control loop bandwidth is to be maintained at 0.05 Hz. This result was verified by simulation when the inclinometer bandwidth was reduced from 2.4 to 0.24 Hz to simulate the effect of filtering. These results are also outlined in Table 5-1.

The conclusion of this portion of the study is that since both of the control loop implementations yield almost identical performance for all operational conditions, the open-loop actuator implementation (i.e., the inclinometer within the feedback loop) is recommended since it eliminates the requirement for instrumenting the hydraulic ram. However, due to the sensitivity of roll control system performance to cross-axis accelerations, it is recommended that measurements be taken of the cross-axis acceleration levels on a longwall shearer while mining coal, particularly within and around the expected roll control loop bandwidth. It is possible that when these measurements become available that it might be more economical to remove the inclinometer from the feedback loop and implement a position loop around the actuator in order to better filter the inclinometer output.

2.9 Yaw Alignment Systems

The function of the yaw alignment system is to automatically advance the conveyor and roof supports in such a manner that the face "straightness" remains within acceptable limits. The "baseline" system defined to accomplish this control function consists of an angle cart, diagrammatically shown in Figure 4-5, which is integrated with the shearer and measures the angles between respective conveyor sections as the shearer proceeds along the face. (The conveyor geometry and the angles measured by the angle cart are shown diagrammatically in Figure 4-6.) Once a set of measurements are taken the present conveyor profile is computed. A set of conveyor advance commands are then computed and sent

to each roof support, such that if perfectly implemented, would result in a totally straight conveyor. This procedure is followed (i.e., angle cart measurements taken, conveyor profile computed, and appropriate conveyor advance commands computed) on every advance.

Various algorithms for computing the conveyor profile from the angle cart measurements were investigated. These algorithms were a basic angle cart measurement scheme and an optimal weighting scheme. In addition the effect of not being able to measure the angle between a number of conveyor sections on either end due to the inability of moving the shearer far enough into the headgate and tailgate was also investigated.

An alternate system implementation to the baseline defined was also investigated. This implementation consisted of a directional gyro mounted on the shearer which measures the orientation of each conveyor section with respect to a defined reference. These measurements are then used to compute the present conveyor profile and a set of conveyor advance commands are subsequently generated that if implemented perfectly would straighten the conveyor in much the same manner as in the angle cart implementation.

Two computer simulations were developed in order to evaluate the performance of the yaw alignment system. The first was a Monte-Carlo simulation which evaluated the accuracy with which the conveyor profile could be computed in the presence of measurement error. This was accomplished by performing 500 measurement runs using particular values of measurement errors and computing the conveyor profile for each run. The RMS error between the computed and actual conveyor profiles was then computed and the average RMS error was determined for the 500 runs made.

The average of the RMS error for the 500 runs made, called the "mode of RMS", was used as the performance measure of the measurement scheme being evaluated in the presence of measurement error. A block diagram of this simulation is shown in Figure 4-7.

The other simulation developed was the Yaw Advance Simulation. This simulation actually made repeated advances of the conveyor in the presence of system measurement, conveyor placement, and roof support pull-up errors, and yaw advancement stability evaluated. In order to evaluate whether yaw advancement is proceeding stably, twenty advancements of the conveyor were made in the presence of a particular set of system errors. System instability was defined when a particular roof support was commanded to move the conveyor backwards, which is impossible, within the twenty advances made. If this condition resulted for a particular set of system errors, the system error vector was perturbated slightly and two more sets of twenty advances made. The average value of the error vector for the set of three twenty advances were then used to define the stability boundary. The yaw advancement simulation block diagram is shown in Figure 4-12.

2.9.1 Angle Cart Performance Characteristics

The basic angle cart measurement system uses two sets of measurements made by the angle cart. One set of measurements are taken when the angle cart is totally in a single conveyor section. These measurements are used to estimate the bias or constant error in the resolvers, and are used in correcting the second set of measurements which are the angles between contiguous conveyor sections. The angle that the first conveyor section makes with the desired reference (i.e., line perpendicular to headgate and tailgates) is computed via the relative angle measurements between the conveyor sections in conjunction with the

knowledge where the ends of the conveyor are with respect to each other. This is obtained by measuring the distance on both ends of the conveyor with respect to surveyed points within the headgate and tailgate.

The results with the basic measurement scheme indicate that the mode of RMS increases linearly with increased measurement error as shown in Figure 4-8. From a stability viewpoint the maximum allowable one sigma measurement error that can be tolerated in the presence of a 0.1 ft (i.e., 1.2 in.) one sigma roof support pullup error and a one sigma conveyor placement error of 0.02 ft is 0.03 degree. These results remain unchanged even if the angle between one conveyor section on either end cannot be measured and hence assumed to be zero. These results are outlined in Figures 4-14 through 4-17. It should be noted that the angle cart employs eight speed resolvers to make the angular measurements. The accuracy of an eight speed resolver is in the order of two arc minutes (0.033 degree). Since 200 measurements are taken for each angle between the conveyor sections and averaged, and two resolvers are used to determine those angles, the basic resolver measurement accuracy needed to achieve a 0.03 degree one sigma measurement accuracy on the angle between the conveyors is 20 arc minutes (0.33 degree). This is approximately an order of magnitude greater than the two arc minute accuracy of the eight speed resolver. Hence, a considerable amount of degradation could be accommodated by the angle cart sysem due to vibrational errors as the shearer is traversing the face, while still meeting the required measurement accuracies for the angles between the conveyor sections.

Conversations with mining personnel at Old Ben Mining Company where they are presently operating longwall faces indicated that the roof support pullback error does not exceed one inch. In addition, a ram placement error of 0.02 ft (0.24 inch) represents approximately one part in 100 for a 30 inch advance which can easily be achieved with state-of-the-art instrumentation. Therefore, it is seen that the expected

system errors are within those allowable for stable face advancement as determined via computer simulation, making the basic angle cart system a viable way of implementing yaw face alignment.

The weighting and bias estimation algorithm for determining the conveyor profile using the angle cart measurements requires that the angle between the conveyor sections on both ends be known with respect to a line perpendicular to the headgate and tailgate. Once these values are known the algorithm makes use of the fact that the conveyor profile could be computed with the same set of measurements proceeding from either end. Therefore, two coordinates could be determined for each joint of the conveyor which then could be combined to obtain a minimum variance estimate of the conveyor profile. This technique yields better results than the basic angle cart measurement scheme by allowing larger measurement errors, or, for the same measurement errors yielding a more accurate determination of the conveyor profile. However, in order to obtain any benefit from the bias and estimation algorithm the angle of the end conveyor sections with respect to the desired reference must be known to 0.2 degrees or better as shown in Figures 4-18 and 4-19. This would require that specialized instrumentation to be located in the headgate and tailgate to determine these angles to the required accuracy. Therefore, the basic angle cart measurement scheme is the technique recommended if the angle cart implementation is used for yaw alignment.

2.9.2 Directional Gyro Performance Characteristics

In order to evaluate the performance of a directional gyro implementation for yaw alignment and to specify the required gyro for satisfactory system performance a directional gyro error model had to be formulated. This model is shown diagrammatically in Figure 4-23 where the errors considered are:

1) Low frequency random walk error (white noise through the integrator)

2) Constant drift error (ϵ_b)

3) High frequency error (white noise through first order filter)

4) Gyro reference error (ϵ_R)

Various types of algorithms for processing the directional gyro data in order to determine the conveyor profile were investigated and are discussed in section 4.5. The results of these investigations indicated that the best algorithm for processing the directional gyro data is one that uses a single measurement as soon as the gyro is aligned in a particular conveyor section. The measurements thus obtained are then put through an optimum filtering scheme such that a minimum variance estimate of the conveyor profile is obtained.

Investigations into the allowable system errors using the above algorithm with a shearer traverse speed of 30 ft/min, indicated that a spectral noise intensity of approximately $1 \times 10^{-7} \frac{(\text{rad/sec})^2}{\text{rad/sec}}$ could be tolerated in the presence of a gyro reference error of 0.2 degrees and a roof support pullup error of 0.1 ft (1.2 inch), for stable yaw advancement (see Figure 4-33). This value of spectral noise intensity corresponds to a random drift error of approximately 0.6 deg/hr which is considered to be a good and relatively expensive gyro. In order to increase the allowable random drift error that can be tolerated the gyro would have to be towed along the conveyor at a greater speed than 30 ft/min. This implies that the gyro would have to be mounted on a separate cart which would either have its own motive power or possibly be towed by the conveyor. In either case, the money saved by allowing the use

of a cheaper gyro would have to go into the cost of manufacturing a separate gyro cart. In addition, the use of a separate gyro cart would introduce operational problems with respect to integrating the measurement with standard longwall operations requiring additional time to make the required measurements, and would almost certainly preclude the measurement of the angles of the end conveyor sections due to interference with the shearer. Therefore, the recommended system implementation for yaw face alignment is the angle cart system employing the basic measurement scheme described above.

3. VERTICAL CONTROL SYSTEM

3.1 FUNCTIONAL DESCRIPTION

The function of the vertical control system (VCS) is to control the position of the shearing drums so that their cut follows the coal/shale interface (CSI) on the top and the bottom of the mine and leaves a prescribed amount of top and bottom coal. The VCS must also maintain the present cut within a prescribed amount of the last cut made. The shearing drums are positioned by raising and lowering the ranging arms on which they are mounted, using hydraulic actuators. The drums are controlled independently and are coupled only through the hydraulic system, where the pump flow is shared between the two ranging arm actuators.

Commands to the hydraulic actuators are generated from a complement of coal interfaces and drum position sensors. These sensors include proportional coal interface detectors (CIDs) which measure the coal depth remaining, and discrete CIDs which indicate the presence of coal or rock. The position sensors include a last cut follower (LCF) which indicates the shearing drum's position relative to the last cut made, and an actuator position sensor which allows the position of the ranging arms relative to the shearer body to be determined. The proportional CIDs are radiation detectors, either sensing natural background radiation or backscatter from a radiation source. The discrete or coal presence sensors use the optical and hardness properties of coal and rock to detect the difference between them, hence the presence of either.

The sensors are combined in a hierarchical manner to develop actuator commands. The LCF has the highest priority and will never allow the present cut to differ by more than a prescribed amount from the last cut. The coal presence CID has the next priority and will move the shearing drum away from the interface if rock is detected. The proportional CID is the lowest priority and will provide the control for the cutting drum when it is within the coal beam and the commands are within the prescribed limits relative to the last cut.

Since the shearer operates in either direction, both drums must be capable of cutting either the top or the bottom. The lead drum cuts the top while the trailing drum cuts the bottom, and the individual drum control laws are therefore changed appropriately, depending on whether the drum is leading or trailing. The control laws also change, depending on the desired coal depth to be maintained. If it is desired to take all the coal, only the coal presence sensors are used for control.

It appears impractical to use proportional CID sensors on the bottom, due to loose coal, rock, and water which collect there. The discrete coal sensors provide the capability of taking all the bottom coal, but when it is desired to leave the bottom coal, an alternative control scheme is used. The rear drum is slaved to the top drum, thus providing the capability of maintaining a constant cut height. This leaves a prescribed amount of bottom coal. In addition, slaving of the bottom drum will render the system relatively insensitive to undulations in the conveyer, thus maintaining the shearer in the coal seam.

3.2 DETAILED MATHEMATICAL MODEL OF THE VCS

3.2.1 Overall System Description

The VCS simulation model, shown in Figure 3-1, includes the control system, sensors, actuators, and shearer dynamics as well as the mine geometry. Asterisks indicate those portions of the figure which are part of the simulation, but are not part of the actual shearer or control system. Each portion of the diagram will be discussed in detail in Sections 3.2.2 through 3.2.7.

The chassis location module represents those calculations necessary to determine the position and orientation of the shearer chassis relative to the mine. This includes keeping track of the chassis position along the face and the chassis pitch angle α. The mine model is that portion of this simulation which represents the mine geometry. Actual coal seam profiles were digitized and used to realistically simulate the conditions in which the shearer operates.

The ranging arm geometry calculations use the pitch angle α and the arm angular position relative to the chassis β to calculate the shearing drum position in the mine. The quantities computed are the coal depth presently being cut, the drum height relative to the CID, P, and the drum height relative to this last cut, Q. The CID module processes the coal depth measurements, introducing the appropriate errors to simulate the various CID sensors. The coal depth output measurement is designated ϵ.

The baseline control compares the measured coal depth with the desired coal depth bias C_B. This difference is summed with the drum position relative to the CID sensor, resulting in a command Δz, the

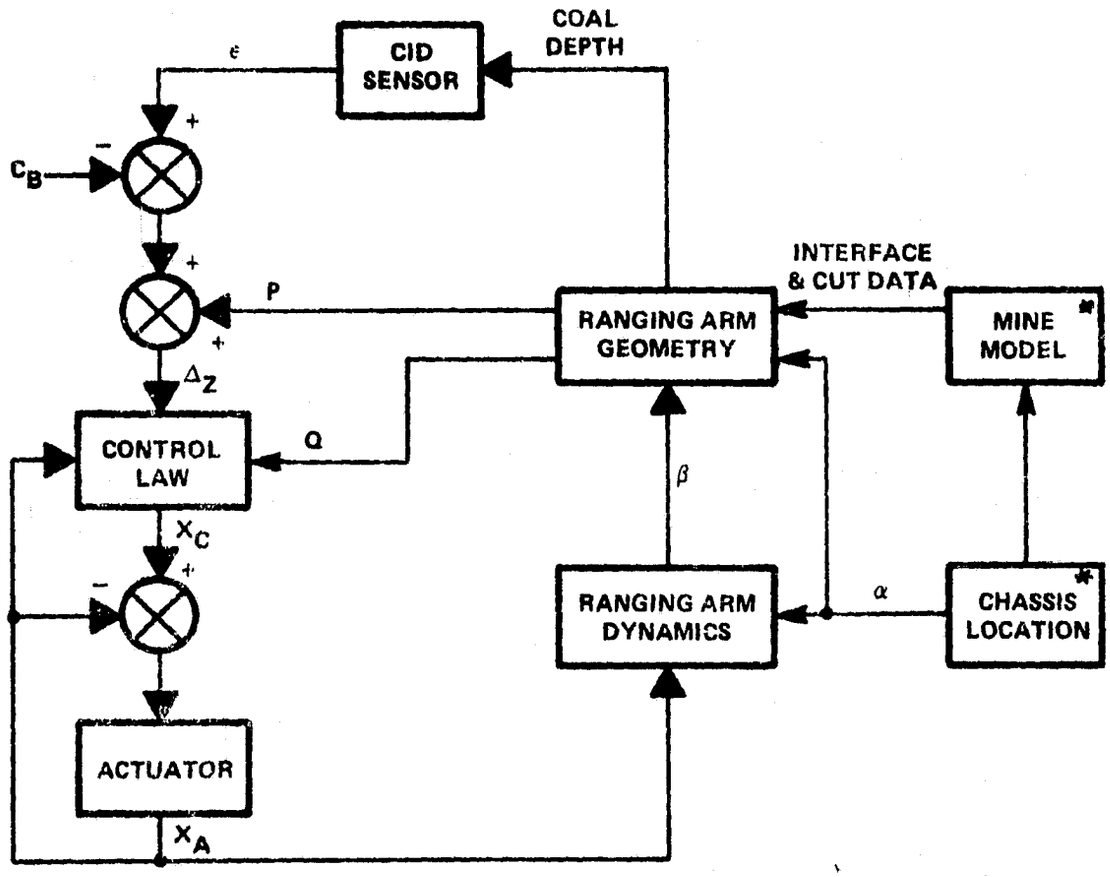

Figure 3-1. VCS Simulation Model Block Diagram

desired change in height of the cutting drum. This information, along with the last cut data and present actuator ram displacement X_A, is used in the control law computations. The result is X_C, the desired displacement of the hydraulic ram.

Actuator dynamics and the ranging arm dynamics are modeled in some detail. The actuator model includes the control valve with input thresholds, check valves, and pump flow rates. Ranging arm dynamics are coupled with the actuator and develop the ranging arm angle β. The actuator is instrumented with a position sensor and used in a closed loop so it can be position commanded.

3.2.2 Chassis Location Model

Figure 3-2 shows the mine coordinate system and defines major components of the chassis and mine simulation. The shearer position along the face is taken to be the +X direction, positive to the right as viewed from the gob side. The seam height is the Z direction, positive upward, and the cut is in the y direction positive into the face (into the plane of the y figure).

The six profiles shown in Figure 3-2 will be discussed in Section 3.2.7, which deals with the mine model. These are the interface or CSI, the present cut, and the last cut for both the top and bottom. The right drum is designated as drum 1 and the left drum as drum 2. Drum hub coordinates are designated as X_{Di} and Z_{Di} for i = 1, 2. The CID sensors are located a distance K_R behind the drum hub. The sensor coordinates are X_{Si} and Z_{Si}. Present cut locations are given by (X_{CC}, Z_{CC}) and (X_{FC}, Z_{FC}).

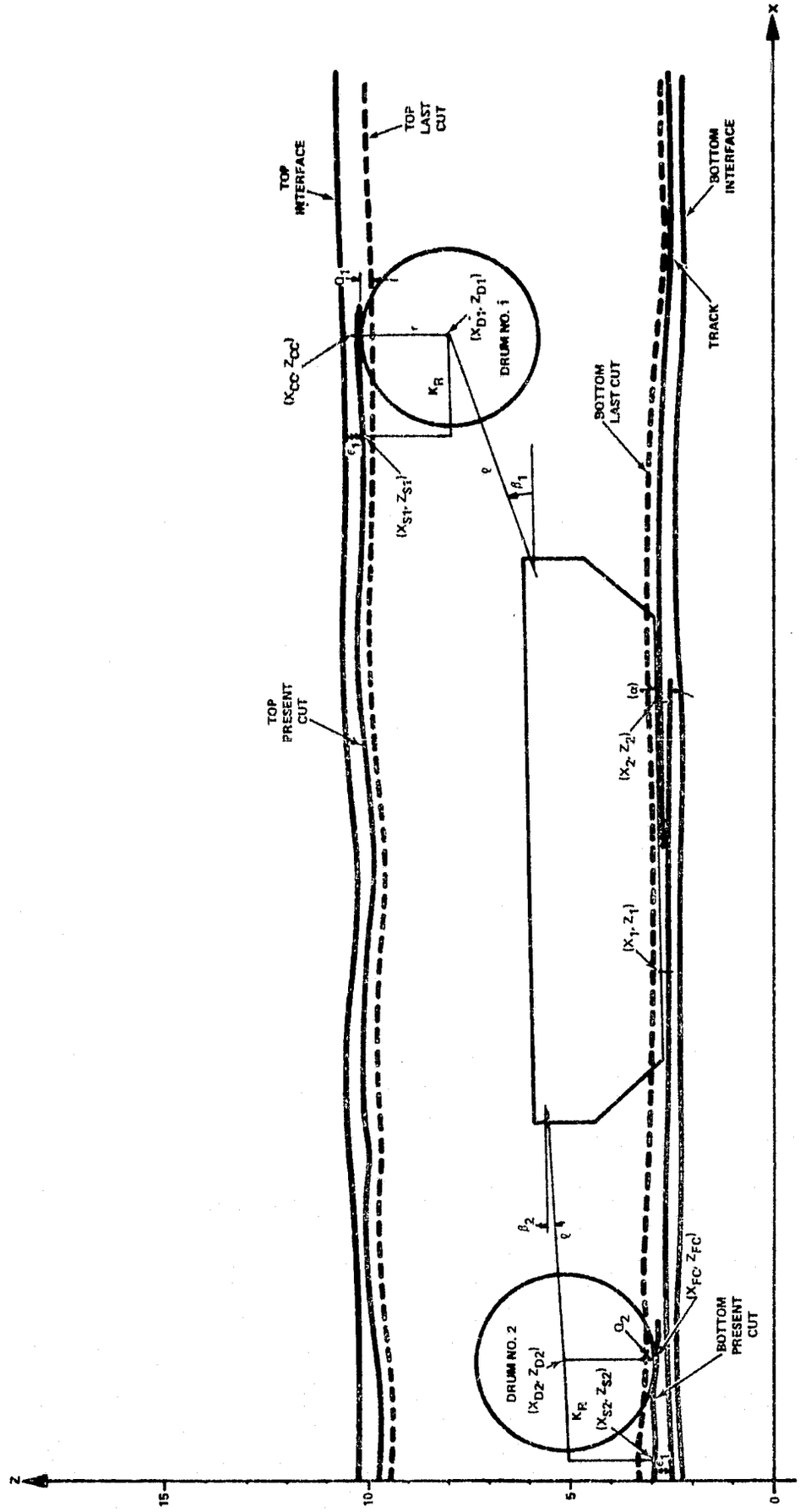

Figure 3-2. Mine and Shearer Coordinate System and Parameter Definition

The shearer chassis contacts the conveyer track at points (X_1, Z_1) and (X_2, Z_2). The motion of the shearer is computed assuming a constant velocity in the X direction. That is

$$X_1 = VT + X_{1I}$$

where T is the integration interval of 0.05 s, and X_{1I} is the initial value of X_1, and V is the chassis velocity given by the profile in Figure 3-3. In the figure,

$$T_N = L_F/V_m$$

$$T_F = T_N + T_m$$

L_F = length of face to be cut (ft)

V_M = maximum velocity

The quantity T_m is the time to accelerate to the maximum velocity V_m, which in most cases was 0.5 ft/s (30 ft/min). The value of T_m used was 6 s, and the deceleration time $T_F - T_N$ is equal to T_m. The time T_F is the total cutting time of a given simulation run.

The chassis pitch angle α is computed from the difference in z coordinates at the chassis contact points. The shearer chassis is illustrated in more detail in Figure 3-4. Alpha is computed as

$$X_2 = X_1 + C \cos \alpha$$

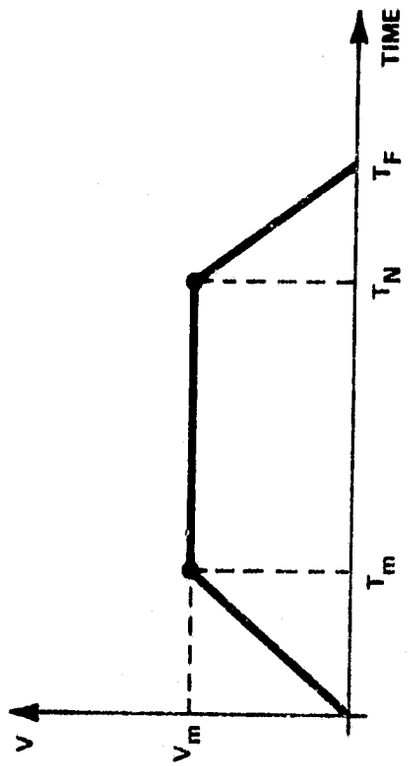

Figure 3-3. Shearer Velocity Profile

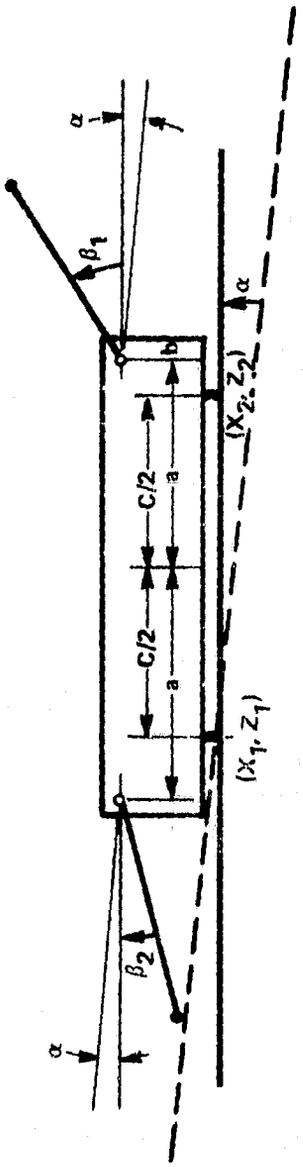

Figure 3-4. Shearer Chassis Geometry

Z_1, Z_2 = Z coordinate at X_1 and X_2

$$\alpha = \sin^{-1}\left(\frac{Z_2 - Z_1}{C}\right)$$

Finally, Z coordinates of the shearer contact points are computed from the track. The track simulates the effect of placing the 5 ft conveyer sections on the bottom just cut. This is necessary because the 5 ft conveyer section effectively filters the bottom cut and provides a smoother surface than the cut itself. The procedure for determining the track is recursive, placing the sections one at a time on the bottom cut. The procedure is as follows:

Let

X_S, Z_s = coordinates of start of a conveyer section
X_F, Z_F = coordinates of the end of the section

The above points may or may not be on the bottom cut. An initial value for X_F and Z_F is found by searching the bottom cut profile until

$$(X_S - X_F)^2 + (Z_S - Z_F)^2 \geq 25$$

Once the probable conveyer endpoint is found, it is necessary to determine if any point on the cut is higher than the endpoint (X_F, Z_F). The highest point on the cut between (X_S, Z_S) and (X_F, Z_F) is found and designated (X_H, Z_H). The following logic is then used:

(1) If $Z_H \leq Z_F$, then (X_F, Z_F) is the actual conveyer endpoint

(2) If $Z_H > Z_F$

$$\gamma = \tan^{-1} [(Z_H - Z_S)/(X_H - X_S)]$$

and $X_F = X_S + 5 \cos \gamma$

$$Z_F = Z_S + 5 \sin \gamma$$

The above procedure computes the conveyer coordinates. If the point (X_H, Z_H) is higher than (X_F, Z_F), then it must determine the slope γ and new endpoint of the conveyer. The procedure repeats with $(X_S = X_F)$ and $(Z_S = Z_F)$ until all sections have been placed.

3.2.3 Ranging Arm Geometry

Orientation of the ranging arms relative to the shearer chassis is shown in Figure 3-4. Pivot points of the arms are located a distance 2a (163 in.) apart and a distance b (35.25 in.) above the conveyer pan. The ranging arm angles relative to the shearer are β_1 and β_2. Note that β_1 is positive in a counterclockwise sense, while β_2 is positive clockwise. Chassis and ranging arm parameter values are given in Table 3-1.

Figure 3-5 illustrates details of the right ranging arm. The shearing drum hub is located ℓ (74.5 in.) from the arm pivot point, at an angle θ_H (4.04 deg) from the horizontal. The nominal actuator displacement X_o is 23.25 in. The actuator requires an additional displacement of 3.255 in. to raise the arm 4.04 deg and set β to zero.

Table 3-1. VCS Parameter Values

$W = 28.324$ in.

$D = 81.0$ in.

$c = 35.25$ in.

$a = 81.5$ in.

$\ell = 74.5$ in.

$X_o = 23.25$ in.

$r = 27.0$ in.

$\phi = 69.3256$ deg

$\theta_H = 4.041$ deg

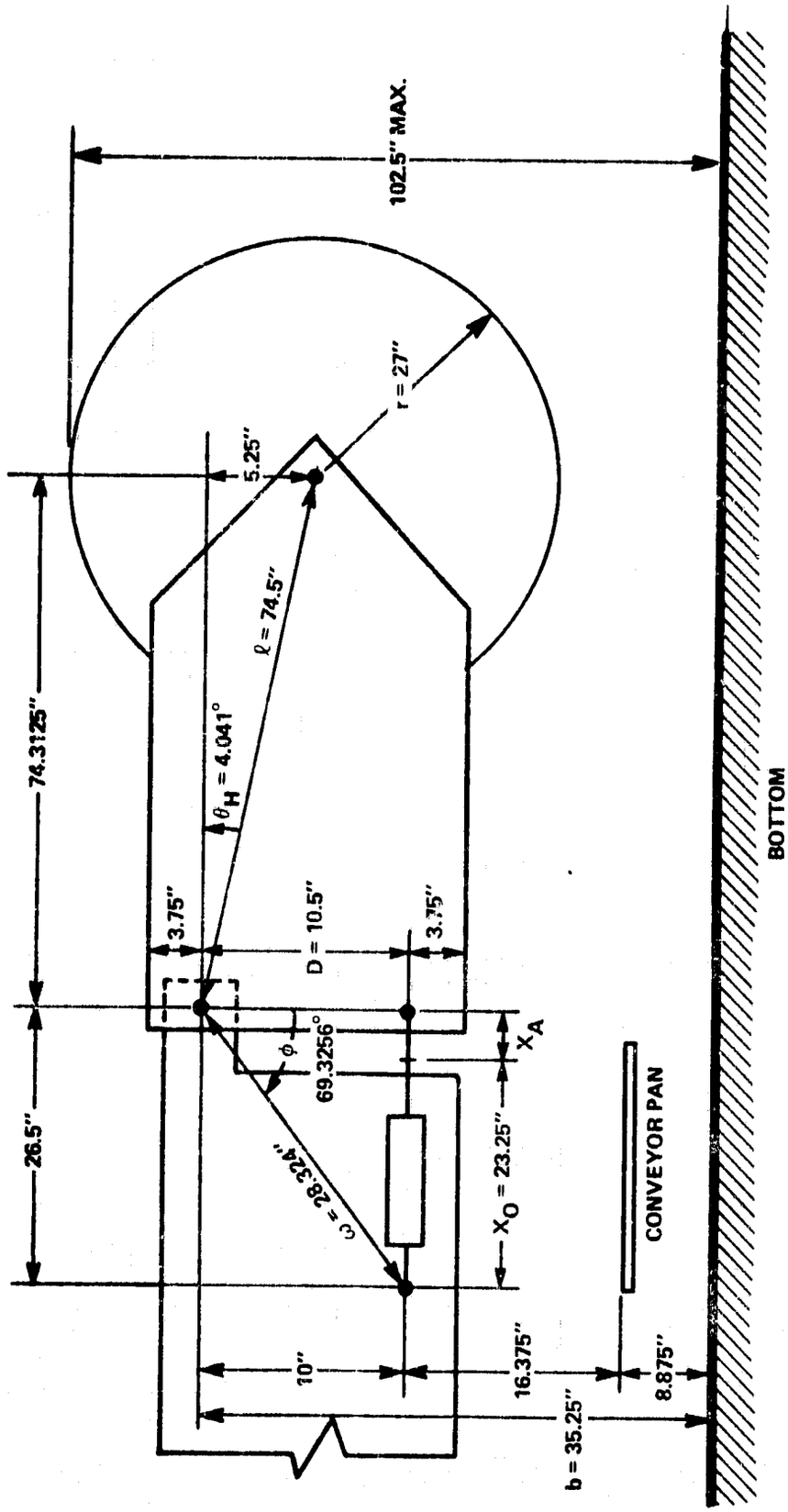

Figure 3-5. Ranging Arm Diagram

Figure 3-6 shows the geometry of arm elevation. The triangle of interest is formed by W, D and $X_o + X_A$. From the law of cosines

$$(X_o + X_A)^2 = W^2 + D^2 - 2WD \cos (\phi + \theta_H + \theta)$$

This relationship can be solved for the ranging arm rigid position. Thus,

$$\theta = \cos^{-1} \left(\frac{W^2 + D^2 - (X_o - X_A)^2}{2WD} \right) - (\phi + \theta_H)$$

and

$$X_A = \sqrt{W^2 + D^2 - 2WD \cos (\phi + \theta_H + \theta)} - X_o$$

when the arm is horizontal

$\theta = -4.041$ deg

$X_A = 3.2547$ in.

The range of X_A is between 1.32 and 9.5 in. for

$X_A = 1.32$ in. $\theta = -14.6442$ deg

$X_A = 9.5$ in. $\theta = 32.2444$ deg

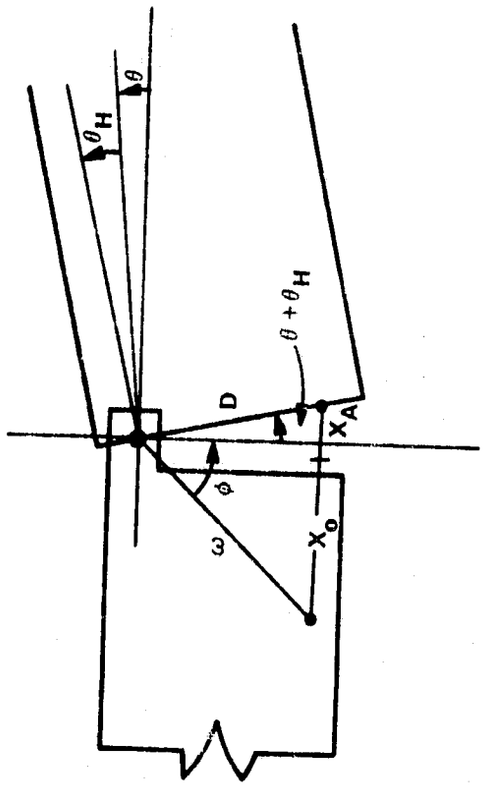

Figure 3-6. Ranging Arm Elevation Geometry

Once the angles β_1 and β_2 are known, it is possible to compute the coordinates of the hubs of the shearing drums (X_{D1}, Z_{D1}) and (X_{D2}, Z_{D2}). When the shearer chassis rotates an angle α in pitch, it does so by rotating about the track contact which is lowest if about the point with the smallest Z value. The coordinate equations are as follows.

$$X_{D1} = X_T + A_1 \cos \alpha - b \sin \alpha + \ell \cos (\beta_1 + \alpha)$$

$$Z_{D1} = Z_T + A_1 \sin \alpha + b \cos \alpha + \ell \sin (\beta_1 + \alpha)$$

$$X_{D2} = X_T - A_2 \cos \alpha - b \sin \alpha - \ell \cos (\alpha - \beta_2)$$

$$Z_{D2} = Z_T - A_2 \sin \alpha + b \cos \alpha - \ell \sin (\alpha - \beta_2)$$

The parameters X_T, Z_T, A_1, and A_2 vary, depending on which contact point is acting as the pivot. This is determined by the algebraic sign of α. If

$\alpha \geq 0$

$$A_1 = a + C/2$$

$$A_2 = a - C/2$$

$$X_T = X_1$$

$$Z_T = Z_1$$

and for any $\alpha < o$, $A_1 = a - C/2$

$$A_2 = a + C/2$$

$$X_T = X_2$$

$$Z_T = Z_2$$

There are several sensors associated with the shearing drum and the CID. These sensors indicate the elevation of the shearing drum relative to the CID and to the last cut made. The geometry of the CID sensor mounted on drum 1 is shown in Figure 3-7. The CID is mounted on an arm extending from (X_{D1}, Z_{D1}) to (X_{P1}, Z_{P1}), a distance K_R from the drum hub. This arm is maintained parallel to the chassis, so that any pitching is reflected in the orientation of the arm relative to the seam. The distance P_1 is measured by a displacement sensor. Ideally, it is desirable to measure the drum height relative to the CID in the vertical direction indicated by (X_{P1}, Z_{P1}) and (X_{B1}, Z_{B1}). However, when α is nonzero, the distance is measured in the direction (X_{P1}, Z_{P1}) to (X_{S1}, Z_{S1}). P_1 is therefore

$$P_1 = \sqrt{(X_{S1} - X_{P1})^2 + (Z_{S1} - Z_{P1})^2} - r$$

The coal depth at any instant is ϵ_1 which is measured vertically and is

$$\epsilon_1 = \sqrt{(X_{S1} - X_{C1})^2 + (Z_{S1} - Z_{C1})^2}$$

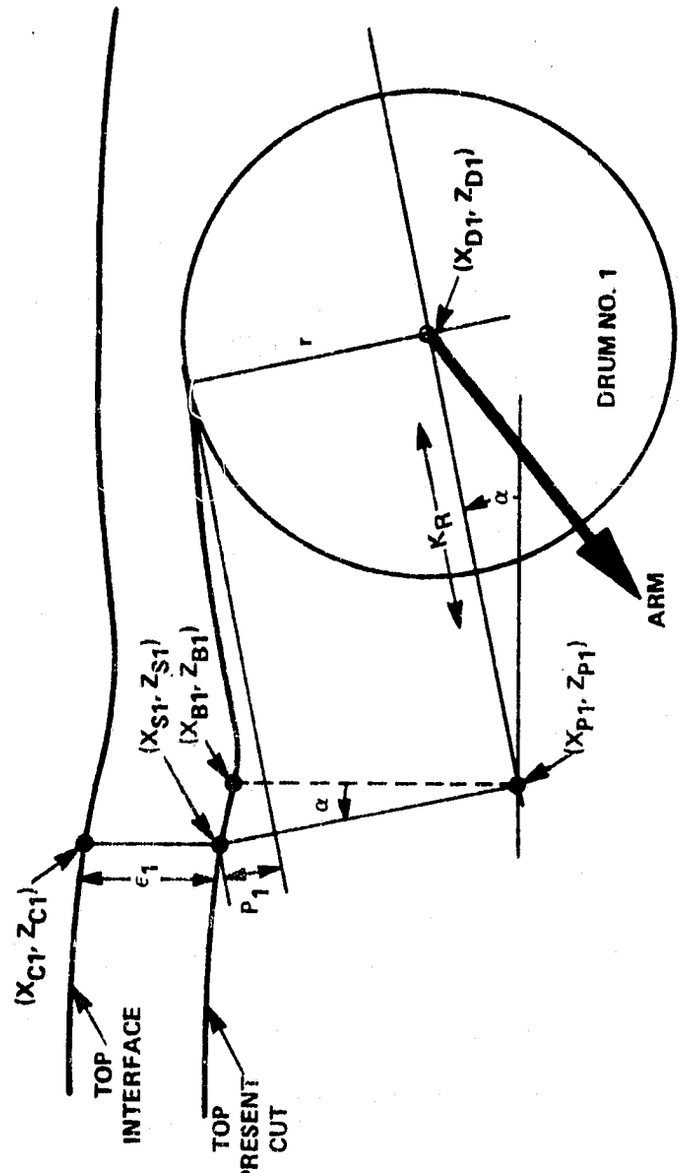

Figure 3-7. CID Sensor Geometry for Top Drum

where $X_{C1} = X_{S1}$. Figure 3-8 shows the geometry of the last cut follower for drum 1. The distance Q_1 is the height of drum 1 relative to the last cut. This measurement is also effected by pitching and is given by

$$Q_1 = \sqrt{(X_{D1} - X_{LC1})^2 + (Z_{D1} - Z_{LC1})^2} - r$$

Figures 3-9 and 3-10 show the sensor geometry for drum 2. The equations for the measurements are the same.

3.2.4 CID Sensors

The coal interface detectors or CIDs are of two basic types: proportional sensors which measure coal depth, and discrete sensors which indicate the presence of coal or rock. The proportional sensors are the nucleonic sensor which measures depth by counting backscattered γ radiation from a cesium source, and a natural radiation sensor which measures depth by counting natural background radiation transmitted through the coal. Both of these sensors are mounted behind the shearing drum. The descrete sensors are a sensitized pick and a combination impact penetrometer-reflectometer. The sensitized pick measures forces exerted on instrumented cutting picks to determine rock presence, while the penetrometer-reflectometer measures surface hardness and reflectance to sense rock. The pick is of course mounted on the shearing drum while the penetrometer-reflectometer is mounted behind the drum.

3.2.4.1 Nucleonic CID Model

The calibration curve for a 20 in. CID sensor is shown in Figure 3-11. There is a cesium source emitting gamma radia-

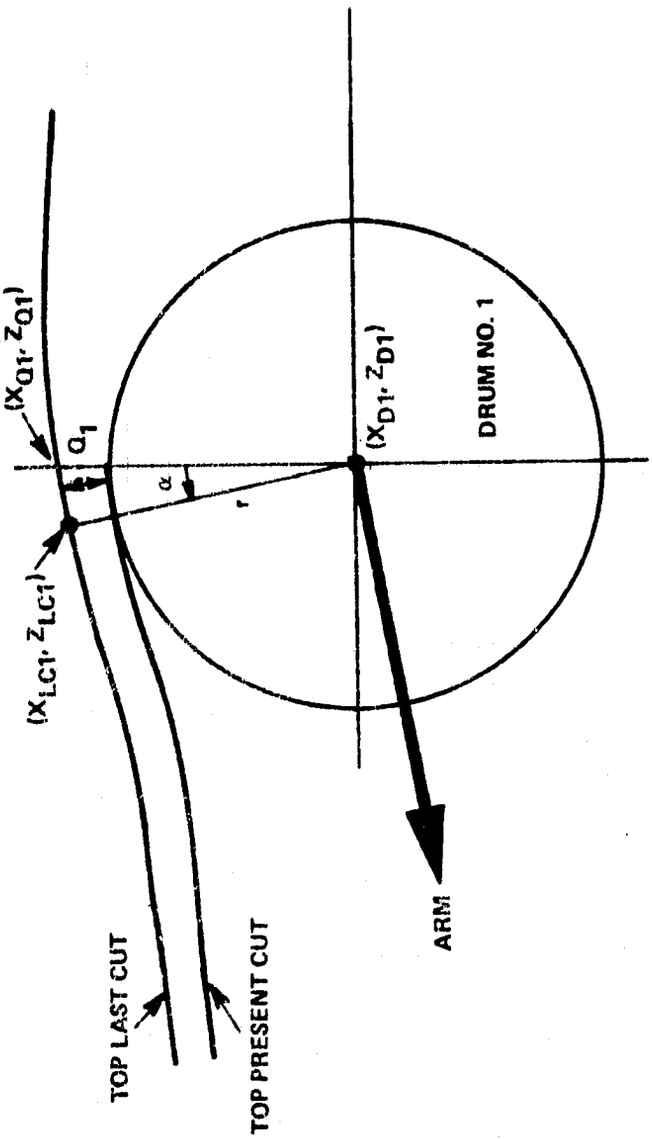

Figure 3-8. Last Cut Follower Geometry for Top Drum

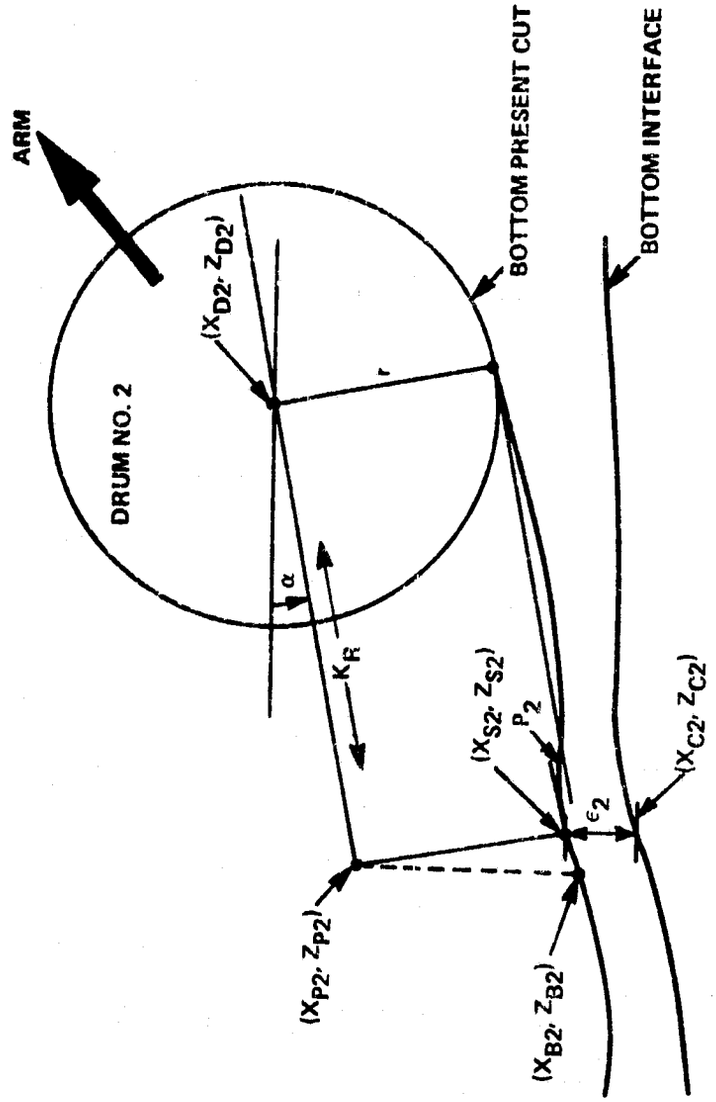

Figure 3-9. CID Sensor Geometry for Bottom Drum

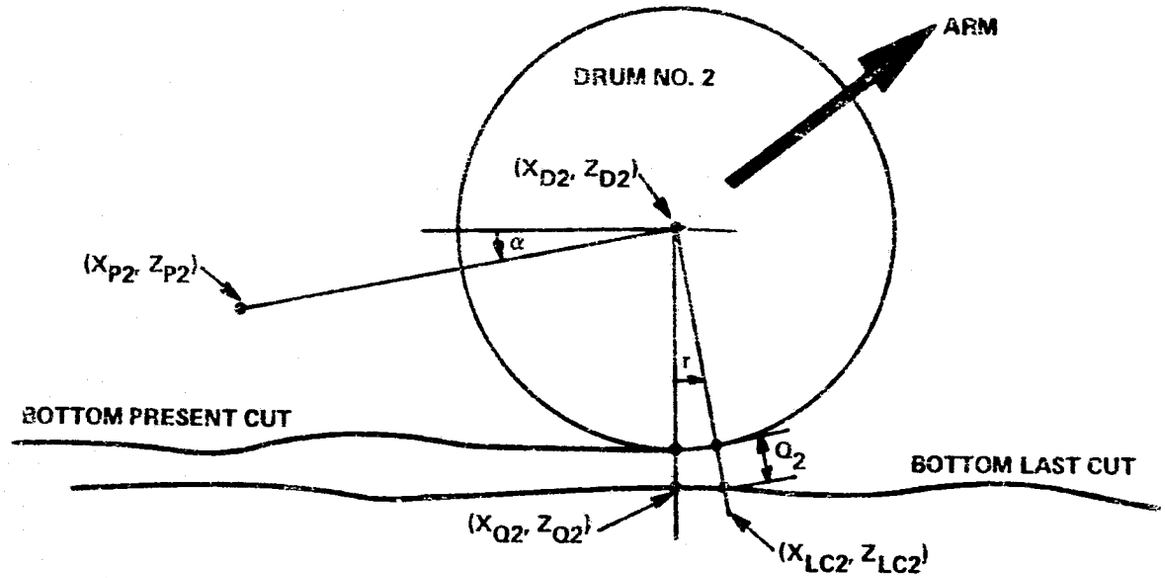

Figure 3-10. Last Cut Follower Geometry for Bottom Drum

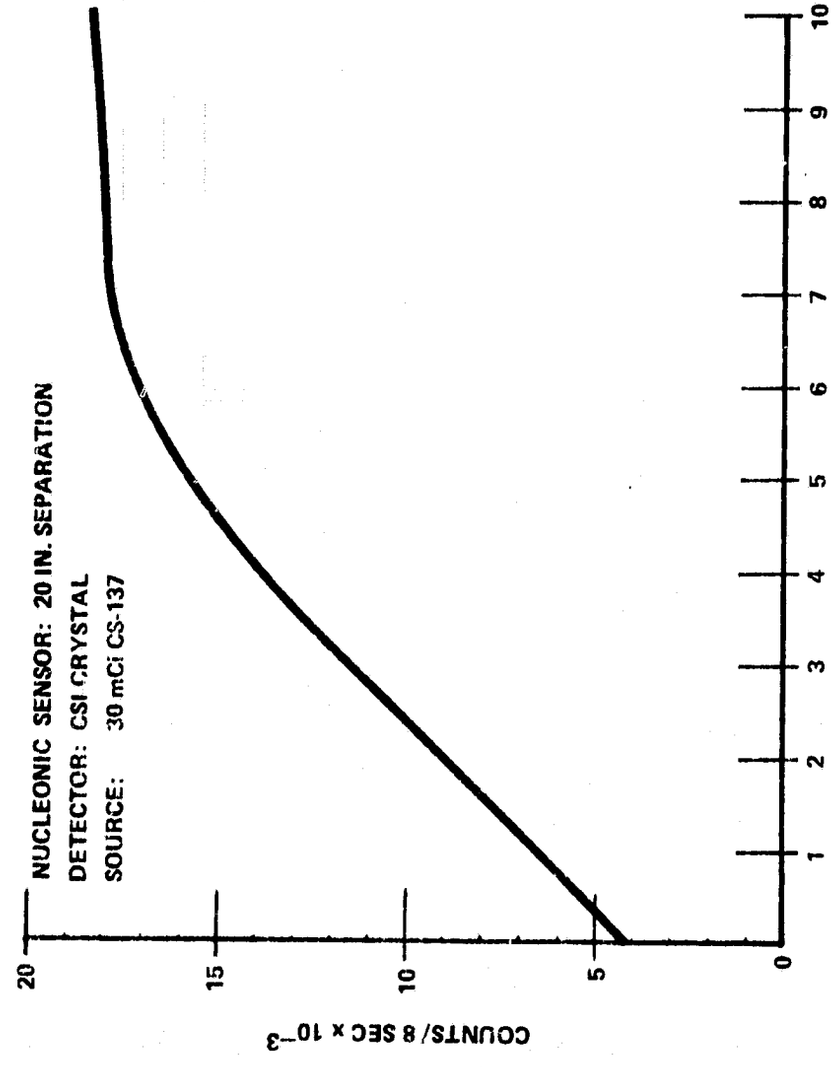

Figure 3-11. Nucleonic CID Calibration Curve

tion, which is backscattered by the coal. Therefore, the thicker the coal, the more backscatter. Thus, the number of counts per second increase with the coal depth. Two basic sources of error are modeled for this sensor: a variation in the number of counts received in a given inteval, and the effect of air gap.

The curve in Figure 3-11 illustrates the relation between coal depth and the number of counts acquired in 8 s. The counts represent the average number of counts received in this interval. The number of events occurring in a given interval is Poisson distributed, with density function

$$f(\lambda) = \frac{(\lambda\tau)^i e^{-\lambda\tau}}{i!} \qquad i = 0, 1, 2, \ldots$$

where λ is the parameter of the distribution - in this case, the average number of counts per unit time. For a given time interval τ, the mean and variance of the Poisson distribution are

$$\mu = \lambda\tau$$

$$\sigma^2 = \lambda\tau$$

thus, as the interval τ is reduced, the average number of counts decreases as well as the variance. The measurements become noisier, however, because the ratio of standard deviation to mean becomes larger as τ decreases.

The air gap error occurs whenever the source or detector is not in complete contact with the coal surface. In this case, radiation short-circuits the coal and is picked up by the sensor

directly, thereby resulting in a larger number than would normally be expected for a given depth of coal. When the calibration curve shown in Figure 3-11 is used to interpret this data, the coal depth indicated by the sensor is larger than that actually present.

The simulation of this sensor was as follows:

(1) Coal depth is computed every 0.05 s and averaged for t seconds.

$$n = \tau/0.05$$

$$\varepsilon_A = \frac{1}{n} \sum_{i=1}^{n} \varepsilon_i$$

(2) Calibration curve f_{CAL} (X) is used to determine the number of counts/second for ε_A inches of coal

$$C = f_{CAL}\ (\varepsilon_A)/8$$

$$C_{ACT} = C\tau$$

(3) Poisson distributed noise is added to C_{ACT} with mean and variance of $C\tau$

$$C_N = C_{ACT} + P(C\tau)$$

(4) Uniformally distributed noise on the interval (0 - 250) counts/second is added to simulate an air gap of 0 - 0.5 in.

$$C_N = C_N + U(0 - 250)$$

(5) The calibration curve is again used to interpret C_N as inches of coal

$$\varepsilon_N = f_{CAL}^{-1}(8C_N)$$

The resultant value of ε_N is treated as the CID output, available every τ second.

3.2.4.2 Natural Radiation CID Model

The natural radiation sensor measures background radiation transmitted through the coal, from the naturally radioactive overburden. Figure 3-12 shows the calibration curve for a 3 in. crystal detector without shielding. Since the radiation is transmitted rather than backscattered, the number of counts decreases as coal depth increases. The number of counts is considerably lower than that with the nucleonic sensor and, as a result, the natural radiation sensor is inherently noisy. Since there is no radiation source, air gaps have little effect on the sensor performance. The simulation is the same as with the nucleonic sensor, except that the natural radiation calibration curve is used, and air gap noise is omitted.

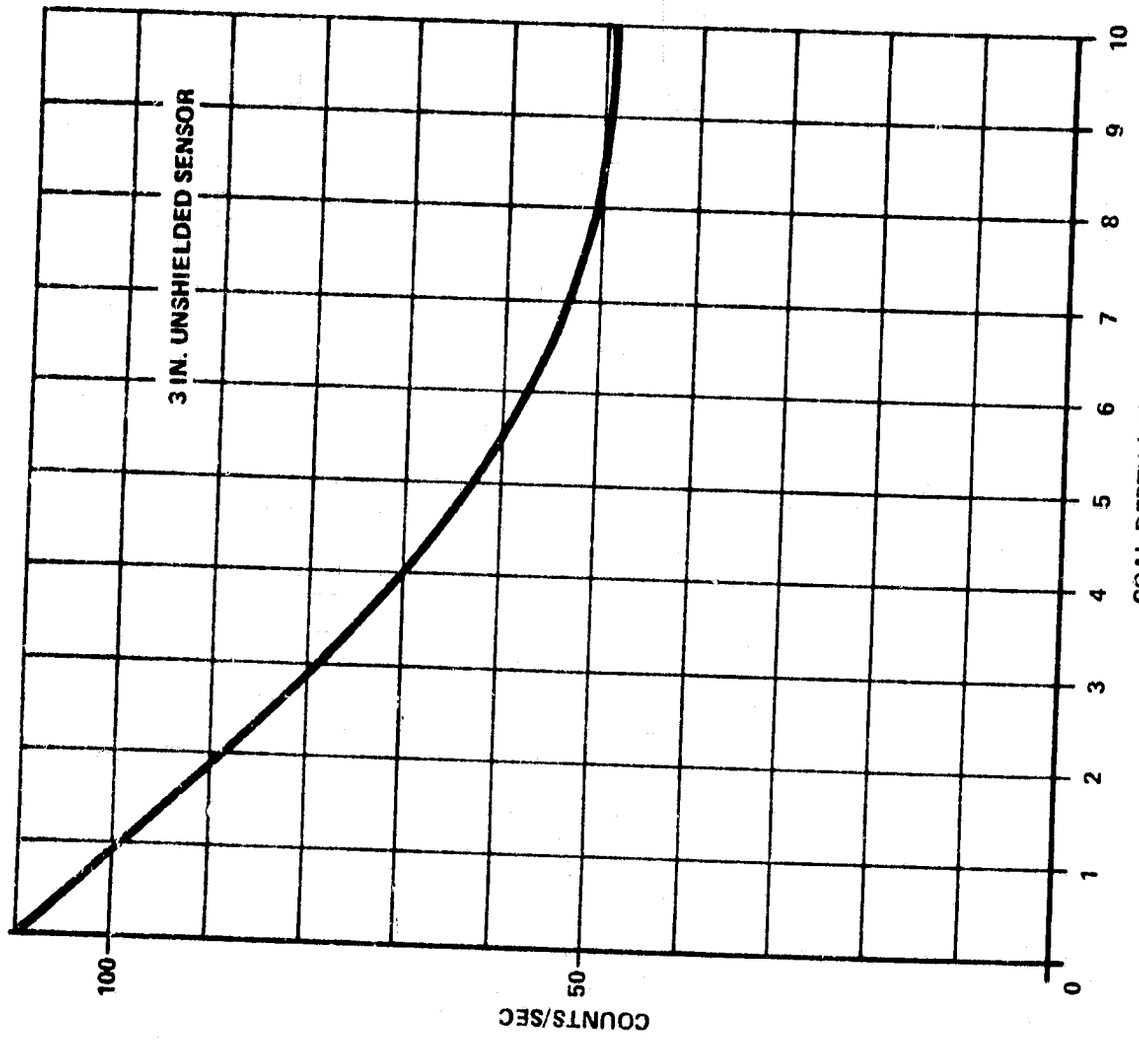

Figure 3-12. Natural Radiation CID Calibration Curve

3.2.4.3 Sensitized Pick Sensor

The sensitized pick sensor is implemented by instrumenting picks on the cutting drum. The picks are instrumented with force transducers whose outputs are analyzed to detect the signature of coal, rock, or air. A minimum of two picks is used, spaced 180 deg apart. Thus, there is a pick latency of 0.66 s based on a nominal drum opening of 45 rpm. That is, new data is available only every 0.66 s. Since it is desirable to measure rock presence, it is necessary to interrogate the picks only when they are in a region near the interface.

The simulation model determines the presence of rock, coal, or nothing, under the pick in an approximately 15 deg region near the top of its rotation. Figure 3-13 shows the point examined on the top drum. These points are vertical from the drum hub, 3 and 6 in. in front of the hub. That is

X_{D1}, Z_{D1} + 27 in.

X_{D1} + 3 in., Z_{D1} + 26.833 in.

X_{D1} + 6 in., Z_{D1} + 26.325 in.

Each of these points is examined to determine if they are in rock or coal. It is also possible that this area may have been previously cut and the picks are therefore in air.

The sensitized pick sensor model assumes that a fixed force threshold would be established and any output above that level would be rock. Also, the lower forces resulting from cutting coal or air yield the same output. The simulation model outputs a 0 or 1

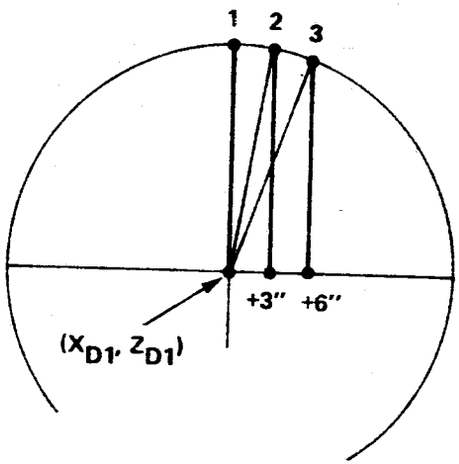

Figure 3-13. Sensitized Pick Geometry

every 0.66 s, depending on whether rock or coal/air is sensed, respectively. A 0 is outputted if any of the 3 test points indicate rock. The output of the sensor is assumed to be a 2 when it is interrogated and the data is not fresh. To simulate errors in detection of coal or rock, the 0 or 1 output which is modified to be correct a percent of the time is, 90 and 80 percent.

3.2.4.4 Impact Penetrometer-Reflectometer Sensor

The impact penetrometer-reflectometer detects the presence of coal or rock by sensing the optical and hardness properties of the present cut surface. The penetrometer is really not a penetration device, but rather taps the cut surface. The deceleration of the impact device can be interpreted to indicate the hardness of the surface. Since rock is harder than coal, it can be detected by this device. The reflectometer measures light return from the cut surface, and since there is a reasonable difference in color and reflectance between coal and rock, the two materials can be detected optically. The sensor, illustrated in Figure 3-14, contains a penetrometer and two reflectometer which are voted to determine the sensor output.

This sensor was simulated by determining the presence of rock or coal at the CID location, i.e., behind the shearing drum. The simulation model would output a 0 for rock and a 1 for coal. It was assumed that the sensor could provide data as often as required. The percent correctness could also be varied to simulate sensor errors.

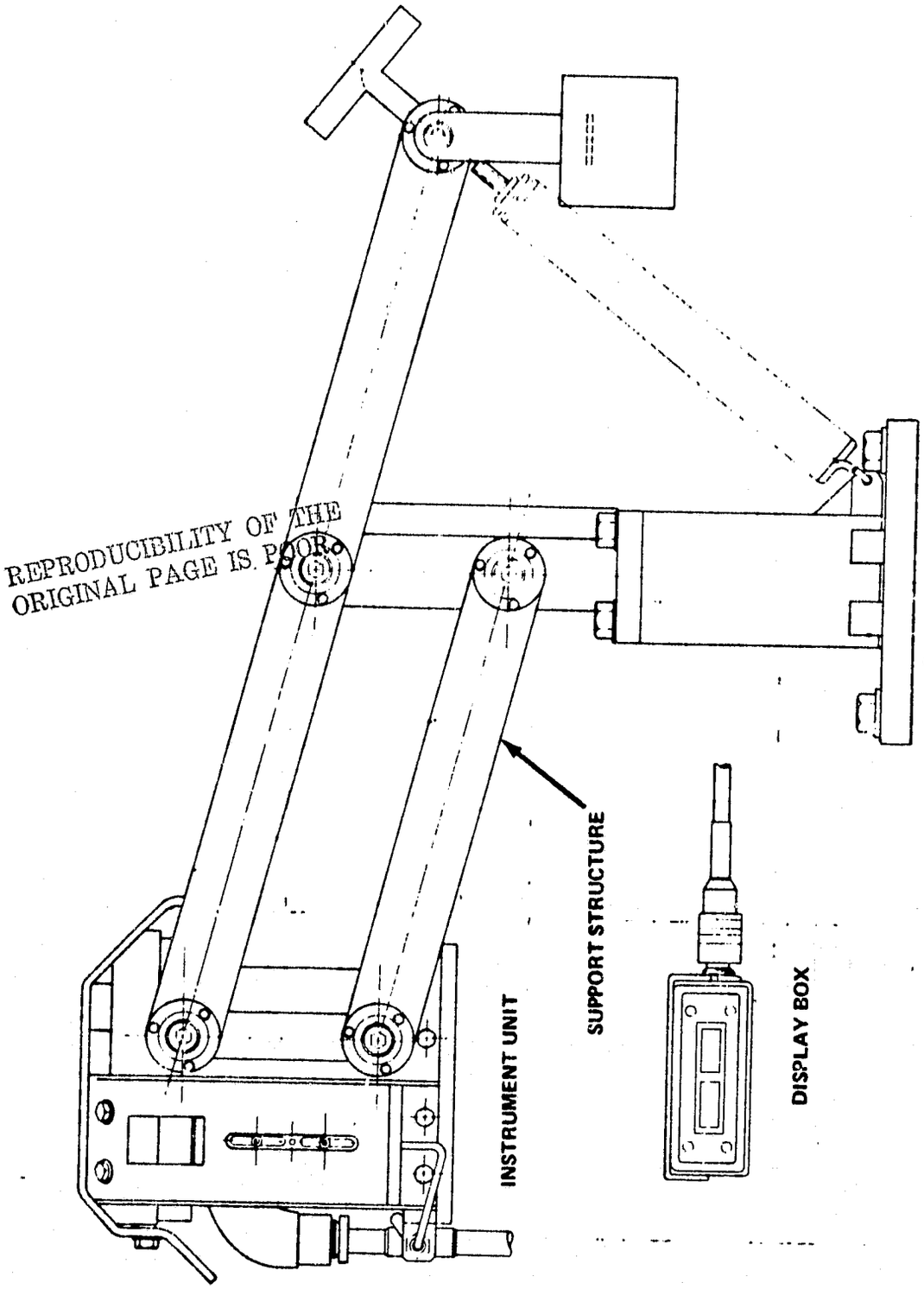

Figure 3-14. Penetrometer - Reflectometer Sensor

3.2.5 Actuator System

A diagram of the VCS hydraulic system is shown in Figure 3-15. A single hydraulic pump, regulated to 2200 psi, supplies all the hydraulics on the shearer. Each ranging arm is actuated by a hydraulic cylinder, which is controlled by a control valve through a dual pilot check valve and a needle and check valve. The basic system is a rate command system where a control valve displacement causes the cylinder to move at a constant rate, determined by the amount of valve displacement. In manual operation, the ranging arm height is adjusted via the control valve, and held in place by the dual check valves, when control is stopped. The needle and check valve are used to compensate the system when lowering the arm. The cylinder piston has different areas on each side because the actuator ram is attached to one side. This causes the rate at which the cylinder retracts to be greater than the rate at which it extends. The needle valve is adjusted to restrict the flow on retraction and equalize the two rates. The needle valve also prevents chattering when the arm is lowered.

Figure 3-16 illustrates the simulation model of the hydraulic actuator and ranging arm dynamics. The input deadband represents an electrical threshold of the control valve, whose input can range from ±8 V, with 2.4 V required to produce any valve motion. The control valve is modeled by a 6 Hz second order loop with a 0.9 damping ratio. This second order loop is also rate and position limited. The rate limit is adjusted so that the valve reaches its maximum travel in 0.25 s. The maximum valve travel is limited to ±1, with the valve being fully open at ±1 and closed at zero. The maximum flow rate available is 8 gallons per minute (GPM), while the control valve capacity is 10 GPM.

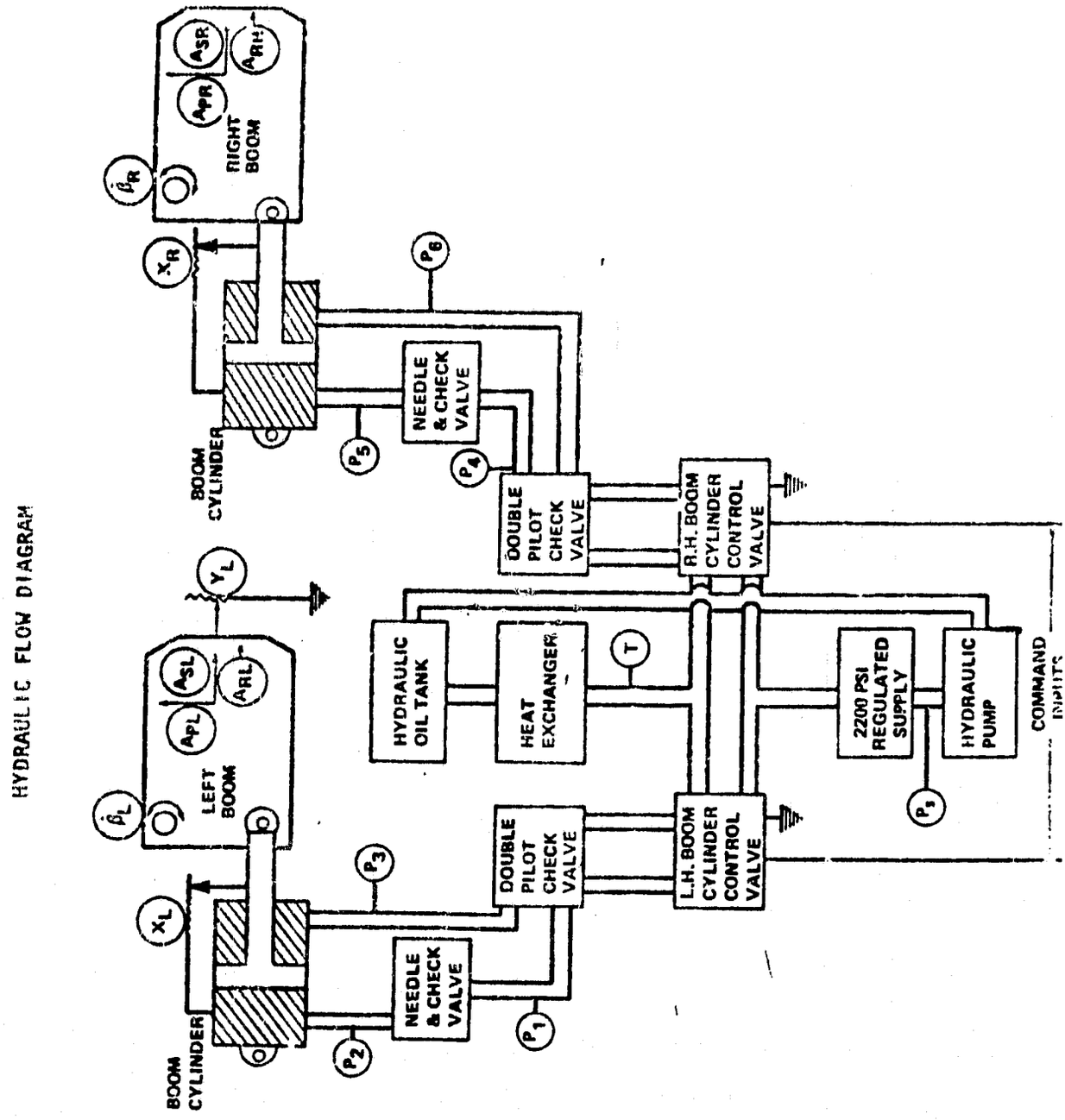

Figure 3-15. VCS Hydraulic System

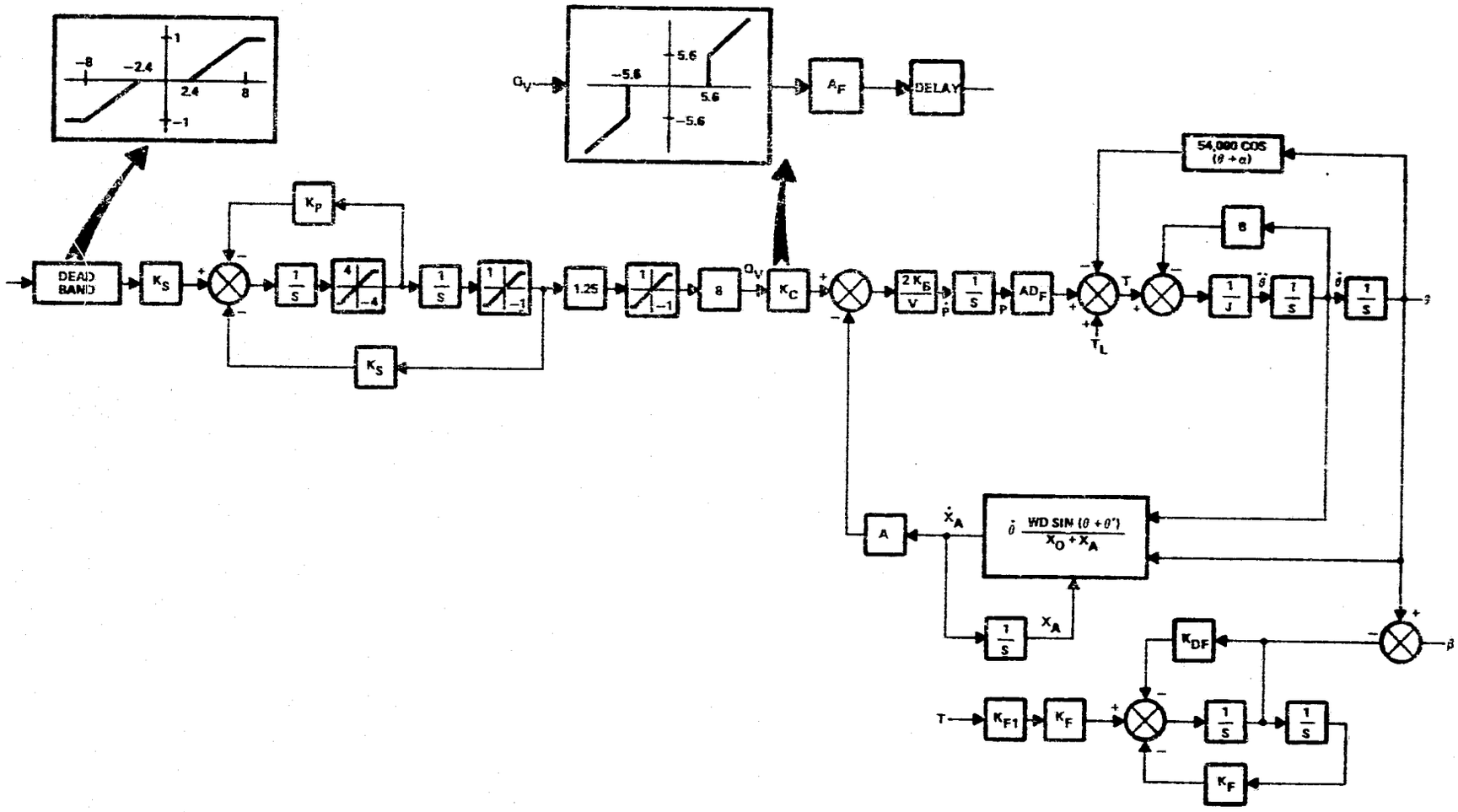

Figure 3-16. Actuator and Ranging Arm Simulation Model

Thus, the 1.25 gain, limit, and 8 gain simulate this effect. When the valve displacement is 0.8, the flow Q_V is 8 GPM and limits at that valve.

The gain K_C consists of three parts, which simulate the dual pilot check valve, a flow split between ranging arms, and a supply regulator delay. The dual pilot check valve is simulated by a deadband, where no flow is experienced until the flow rate reaches 5.6 GPM. At this time, the valve opens and flow jumps to 5.6 GPM and is proportional from there to 8 GPM. This check valve represents the principal non-linearity in the system, and in conjunction with the control valve rate limit, creates an effective delay. It takes 0.8 s for the control valve to open in response to an 8 V command, such that 5.6 GPM flow is achieved, resulting in a delayed response to an input. There is an additional delay due to the supply regulator. If no flow is required, the pump output is diverted by the regulator, and when a flow demand occurs, the regulator must respond, and restore flow to the system. This procedure takes 0.33 s. If one cylinder is in use or has been in use in the last 0.5 s, this delay does not occur because the pump is already on line. The flow split logic simulates the effect caused by simultaneous operation of both ranging arms, when the pump flow must be shared between the two cylinders. This sharing of flow reduces the ram extension rate by a factor of two. However, the retraction rate remains constant since the arm weight aids in this direction. Figure 3-17 shows a diagram of the gain A_F which varies as a function of load torque to simulate flow split.

The remaining portion of Figure 3-16 comprises the actuator cylinder and ranging arm dynamics. The actuator model is a simplified linearized hydraulic model assuming constant supply pressure, and a rigid coupling between the actuator and ranging arm. Defining the following:

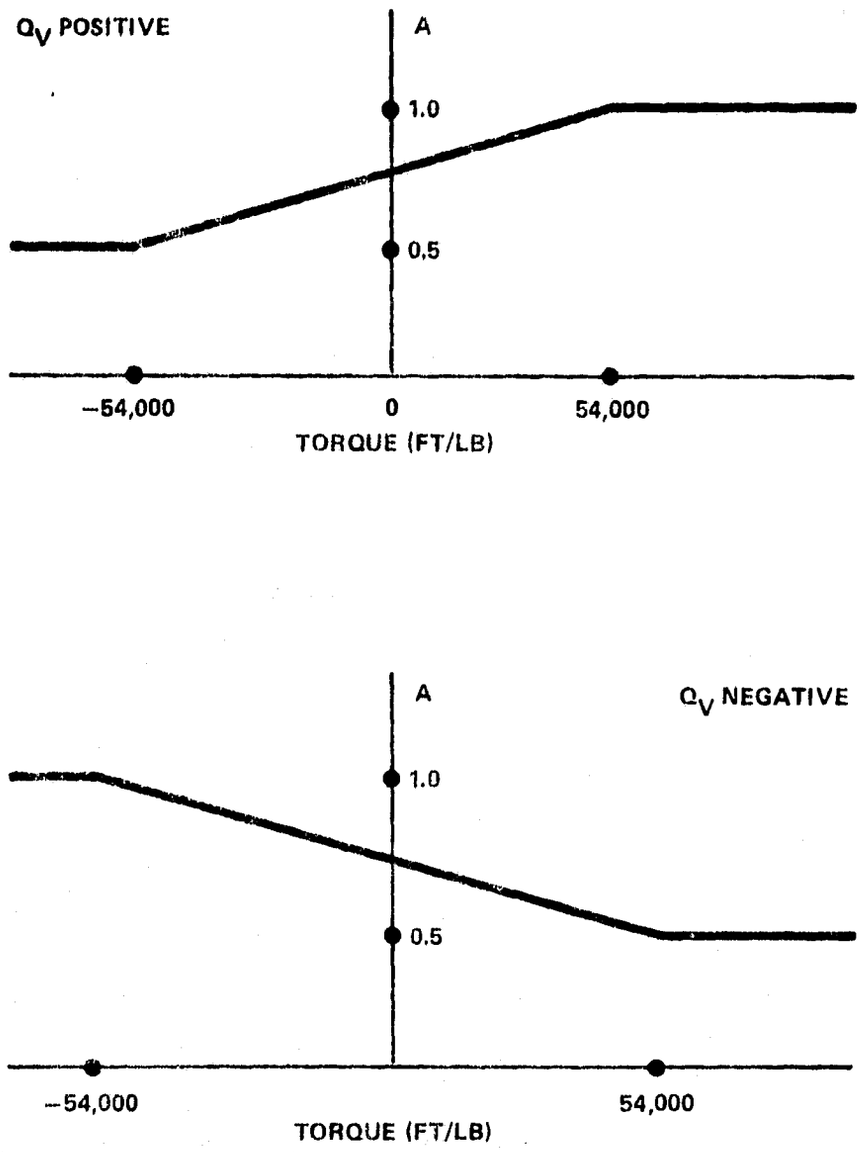

Figure 3-17. Flow Split Gains

$C_x = \frac{\partial q}{\partial x}$

$C_{P_L} = \frac{\partial q}{\partial P_L}$

K_B = fluid bulk modulus

X = valve position

X_A = ram position

q = flow rate

P = load pressure

A = piston area

V = volume of fluid

D_F = ranging arm lever arm

ℓ_1 = leakage coefficient

T_L = load torque

The actuator equation of motion is given as follows:

$$A \dot{X}_A = C_x X - \frac{V}{2K_B} \dot{P} - (C_p + \ell_1) P$$

The load equation (ranging arm) is:

$$T = AD_F P = J\ddot{\theta} + B\dot{\theta} + T_L$$

Rearranging:

$$\frac{V}{2K_B}\dot{P} = C_x X - (C_p + \ell_1) P - A \dot{X}_A$$

$$J\ddot{\theta} = -B\dot{\theta} + AD_F P - T_L$$

To find the relation between $\dot{X}_A$ and $\dot{\theta}$, the expression from Section 3.2.3 is used here:

$$X_A = \sqrt{W^2 + D^2 - 2WD\cos(\phi + \theta_H + \theta)} \quad -X_o$$

or

$$(X_A + X_o)^2 = W^2 + D^2 - 2WD\cos(\phi + \theta_H + \theta)$$

Differentiating with respect to time yields

$$X_A = \frac{WD\sin(\phi + \theta_H + \theta)}{(X_A + X_o)} \dot{\theta}$$

If the leakage terms are neglected, the resulting equations can be diagrammed as shown in Figure 3-16. There is an additional second order loop shown in this figure, whose output is subtracted from θ to yield the ranging arm elevation angle β. This loop is a 4.7 Hz 0.05 damped second order loop used to simulate arm flexibility. The amplitude of this added term was chosen so that the simulation output agreed with actual test data.

Figures 3-18 through 3-20 show the open loop response of the actuator to step inputs. The input was an 8 V positive step for

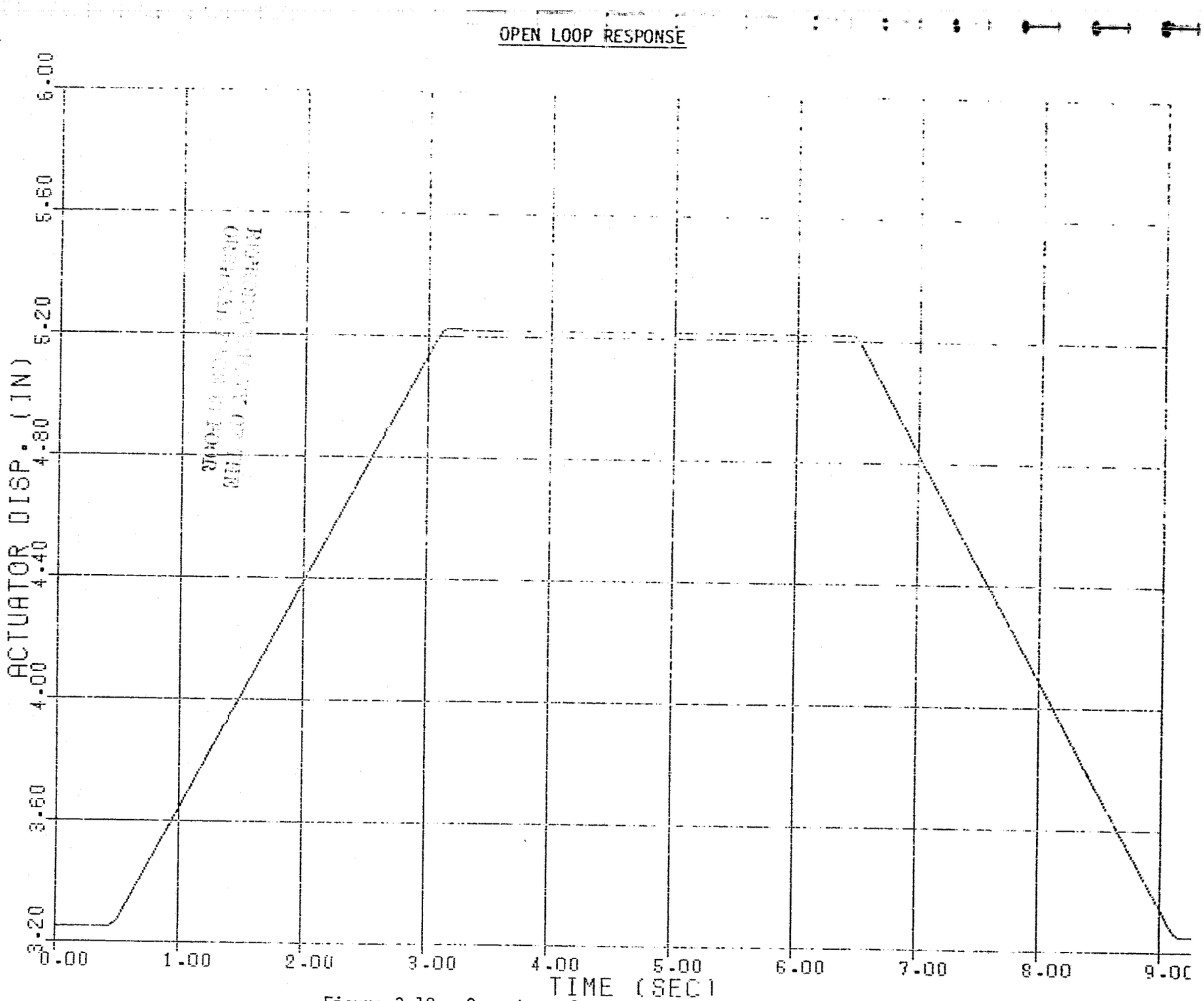

Figure 3-18. Open Loop Actuator Displacement Response

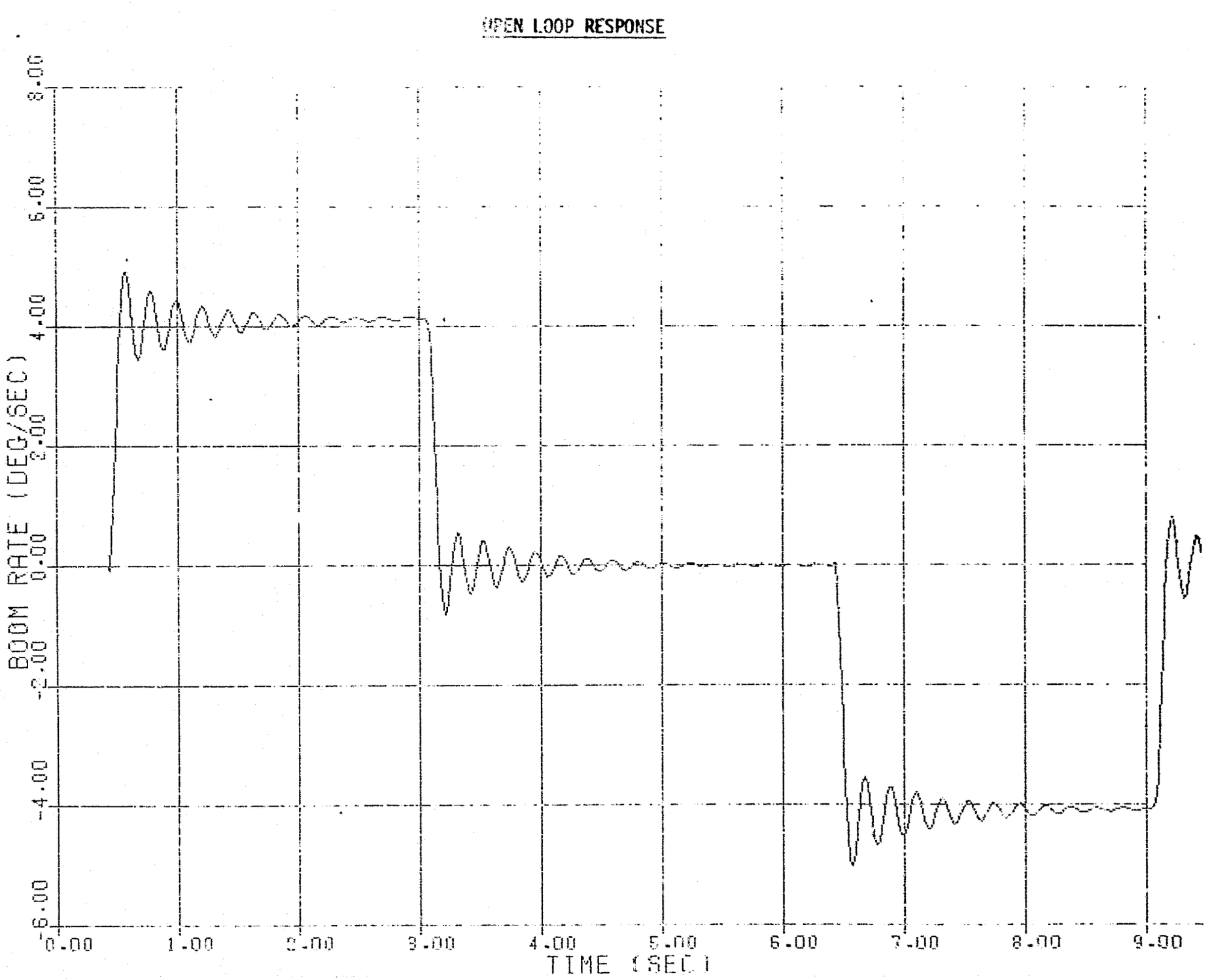

Figure 3-19. Open Loop Ranging Arm Rate Response

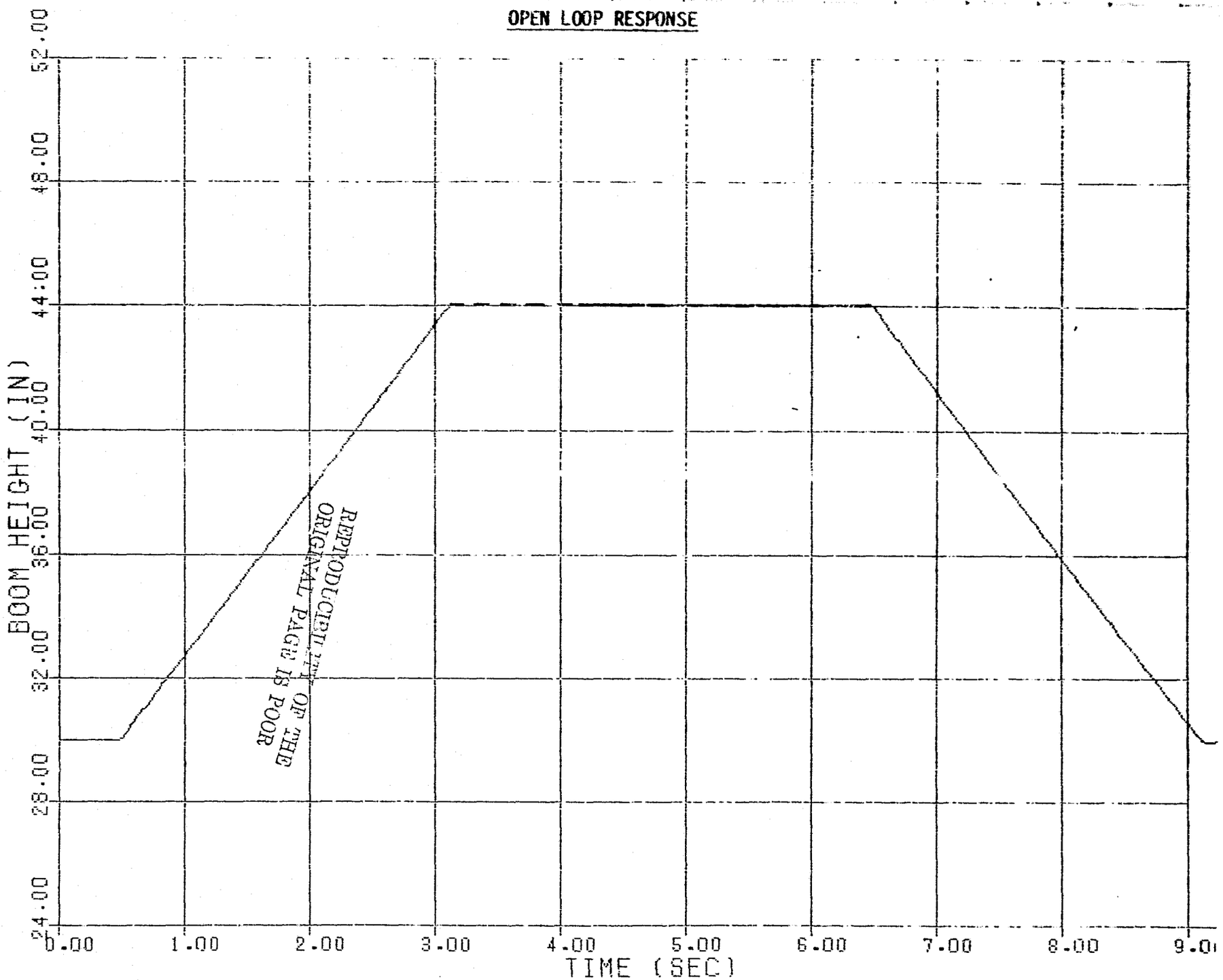

Figure 3-20. Open Loop Drum Height Response

3 s, zero V for 3 s, a -8 V step for 3 s, then zero again. This is the response of a single actuator so the supply regular delay is very evident. The total of this and the effective check valve delay is approximately 0.5 s as shown in the figures. The rate oscillations shown in Figure 3-19 are due to the flexibility model described above.

The actuator is used in a closed loop configuration in the VCS, such that its displacement can be commanded. The ram is instrumented with a position sensor and a loop closed around it with a gain of 170 as shown in Figure 3-21. This gain is such that a 0.15 in ram error will generate 2.4 V and thus exceed the control valve threshold. Figures 3-22 through 3-24 show the actuator response to a step command to extend to 7.5 in. It is important to note the pronounced limit cycle behavior present in this response, which is clearly seen in the rate time history. Lowering the loop gain will eliminate this behavior at the expense of positioning accuracy. Despite this limit cycle behavior, the loop was operated as shown in the figures because studies showed better mining performance than with lower gains.

3.2.6 VCS Control Laws

The basic VCS control laws, shown in Figures 3-25 through 3-29, include various combinations of CID and position sensors. Throughout these control laws, a sensor hierarchy was employed. The discrete or rock detecting CIDs were given the highest priority of the CID sensors, and the shearing drum would be moved away from the CSI whenever rock was detected. The proportional CIDs had the lowest priority and provided the control for the drum when it is in the seam and within prescribed limits of the last cut. The highest priority sensor of all was the last cut follower, which maintained the present cut to within ± 2 in. of the last cut. If either the discrete or proportional CID data generated drum commands which would cause the cut to deviate more than ± 2 in., the drum displacement was limited to ± 2 in. until CID data again commanded the cut within these limits.

CLOSED LOOP ACTUATOR MODEL

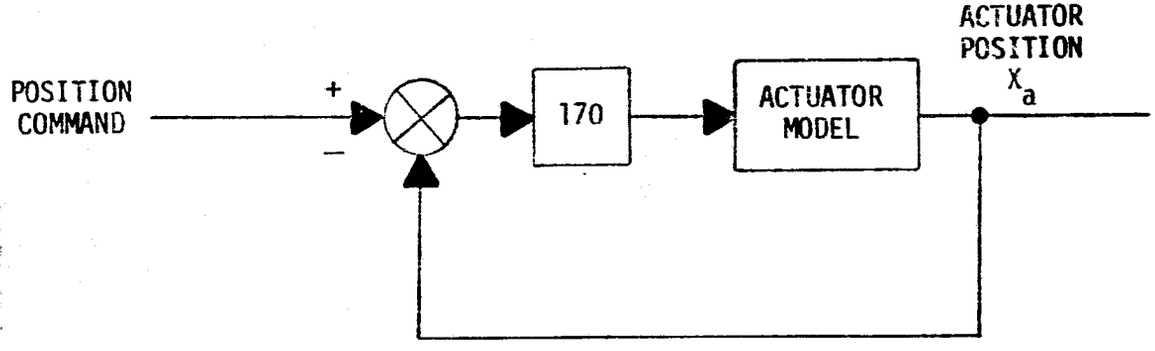

Figure 3-21. Closed Loop Actuator System

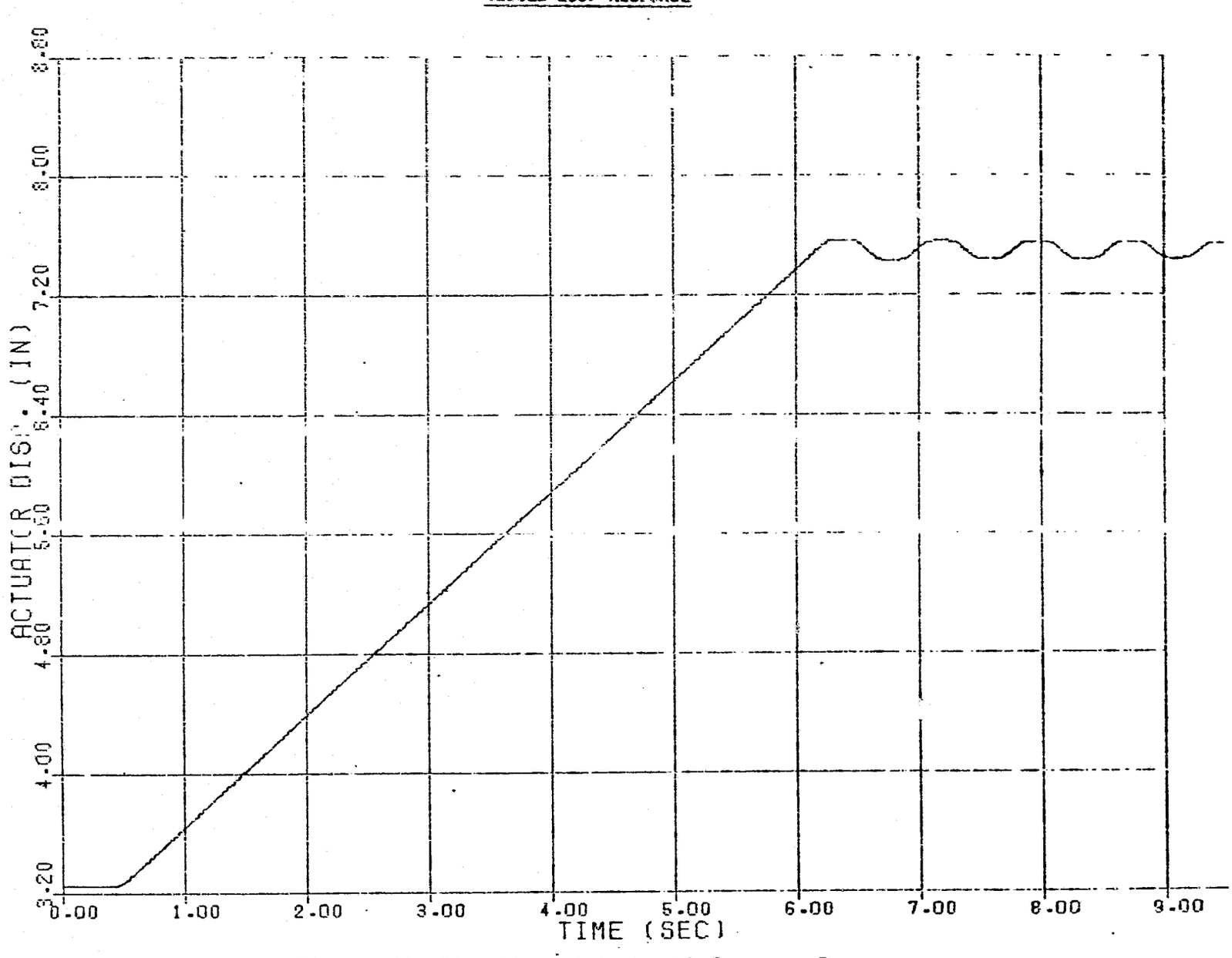

Figure 3-22. Closed Loop Actuator Displacement Response

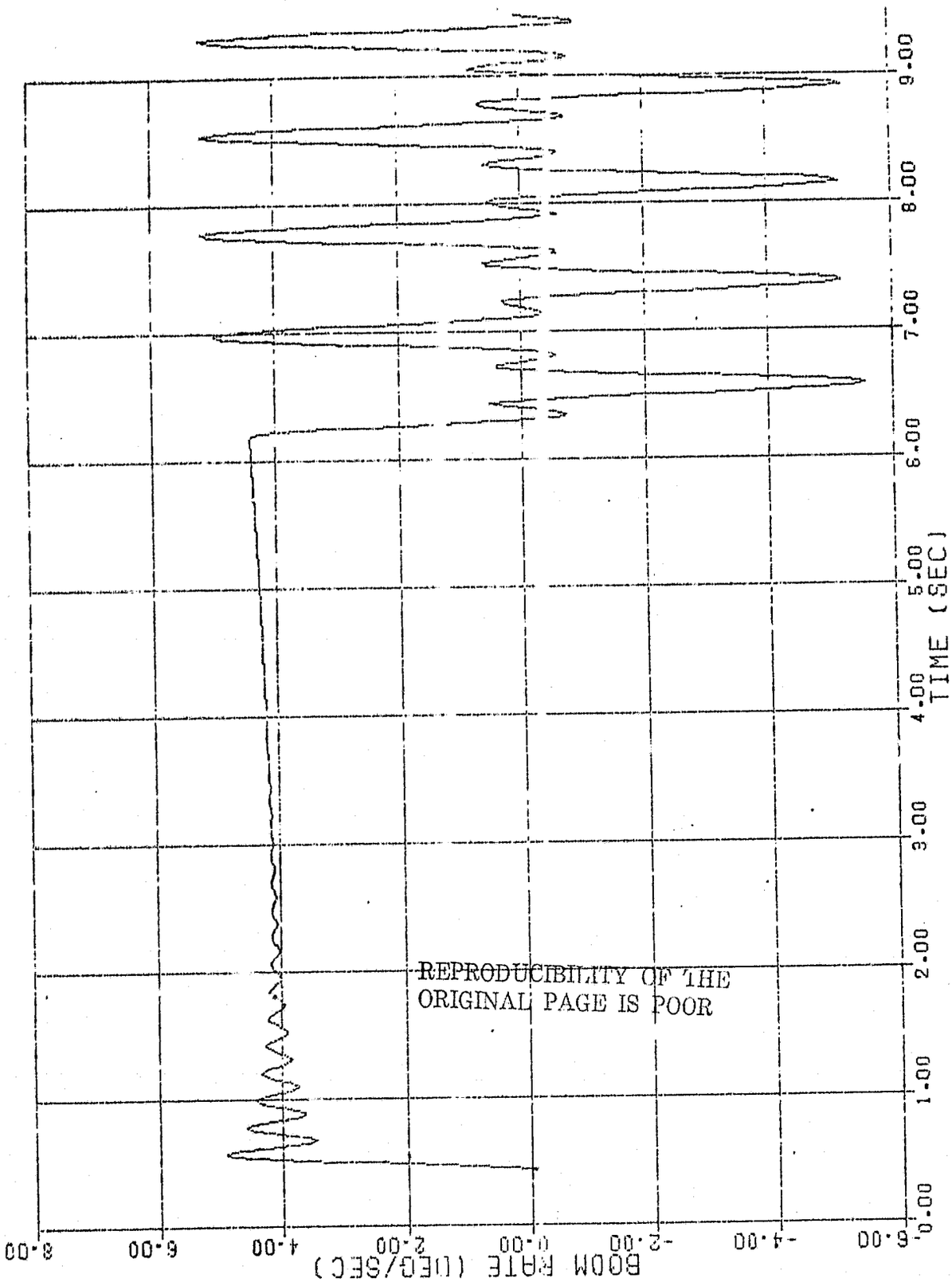

Figure 3-23. Closed Loop Ranging Arm Rate Response

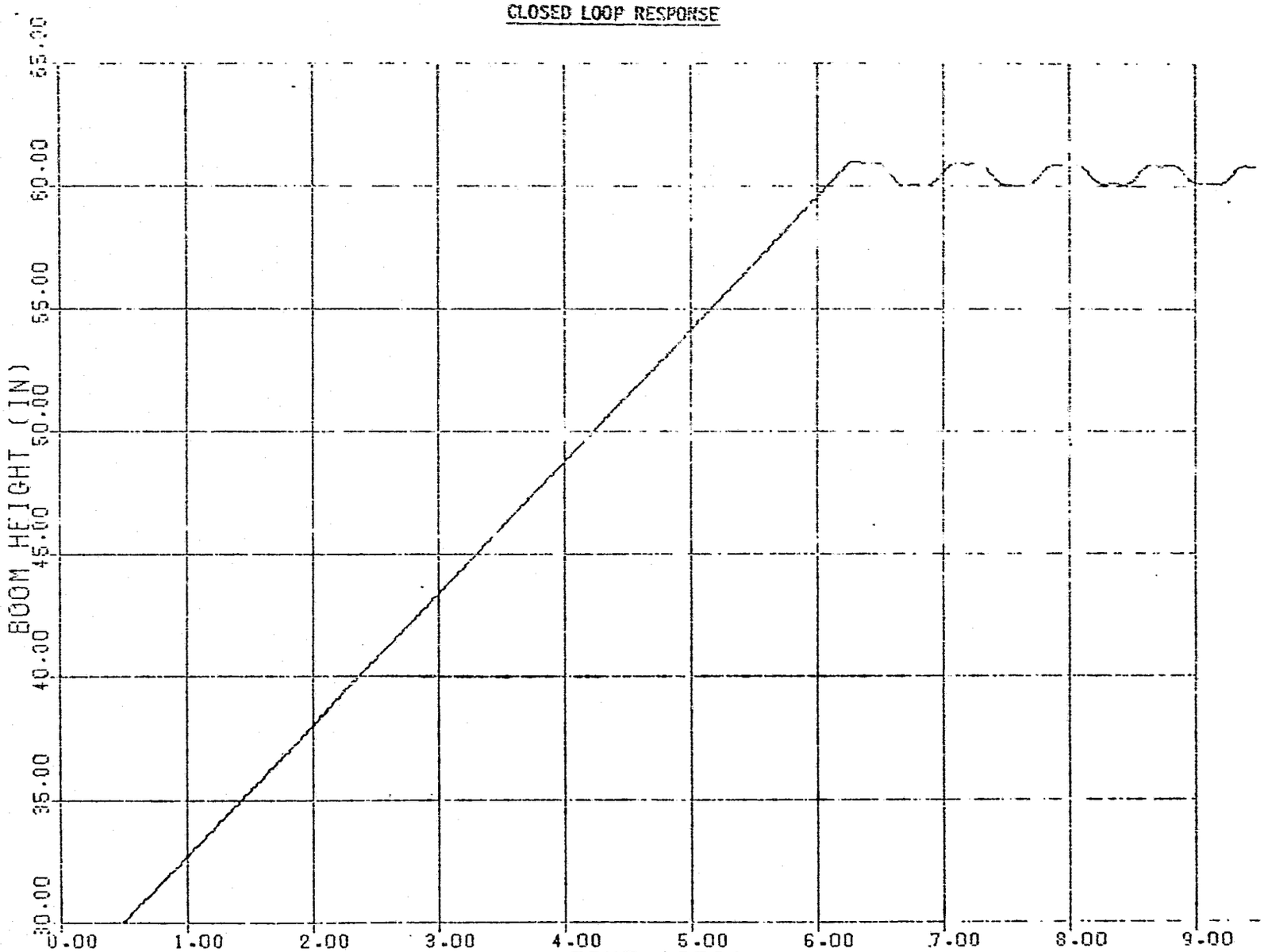

Figure 3-24. Closed Loop Drum Height Response

CID

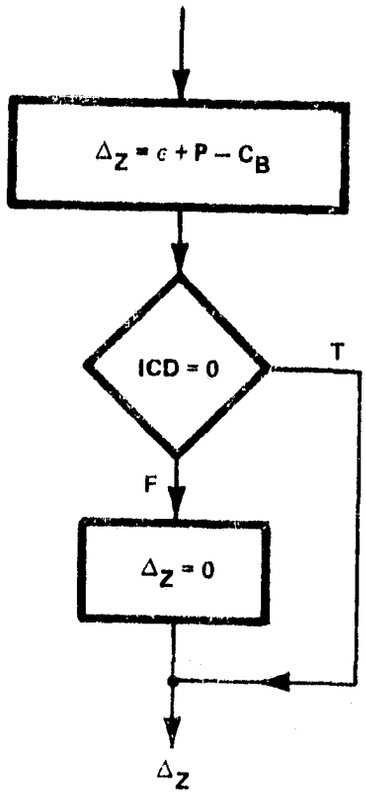

Figure 3-25. CID Control Law

CID, LCF

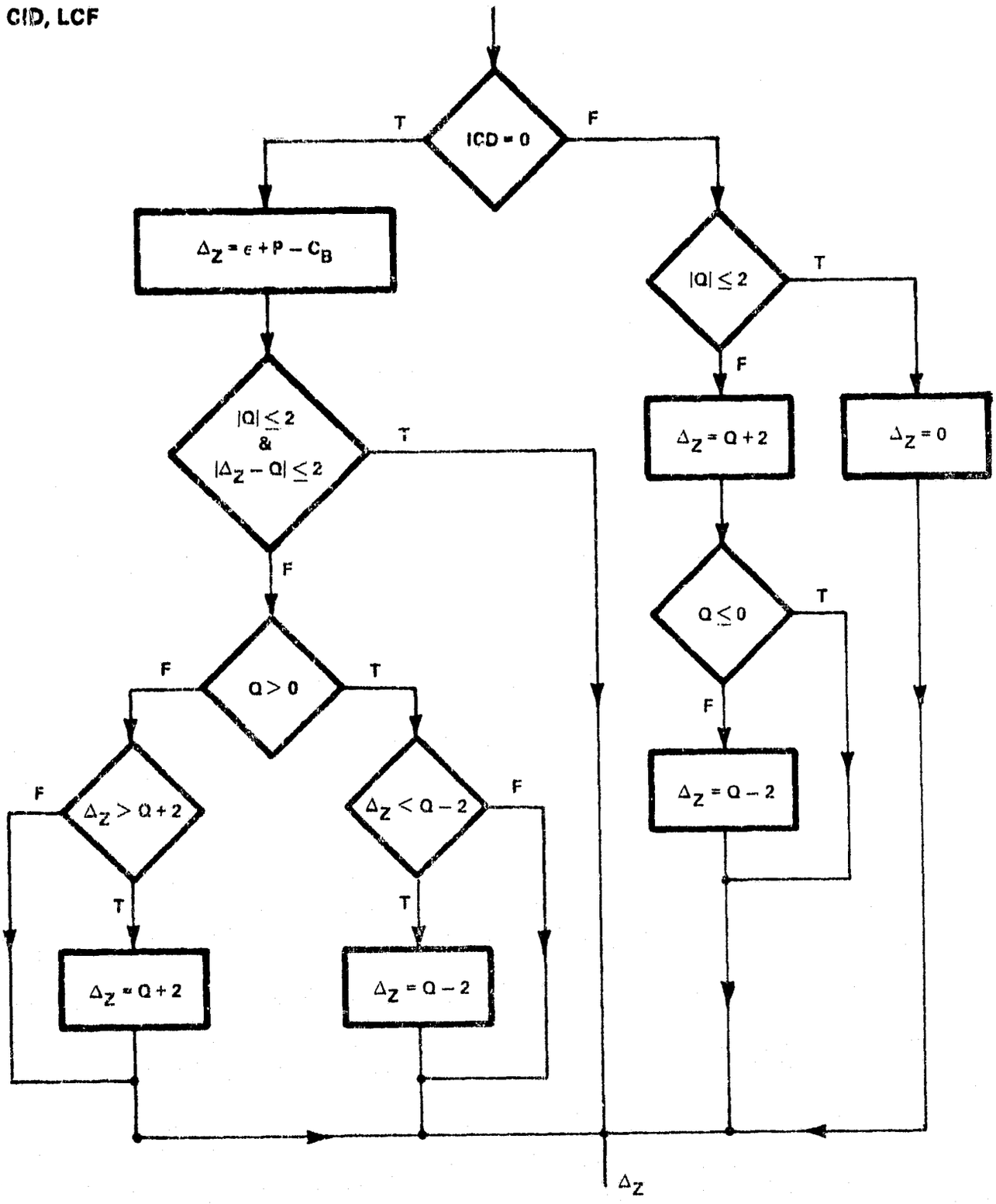

Figure 3-26. CID and LCF Control Law

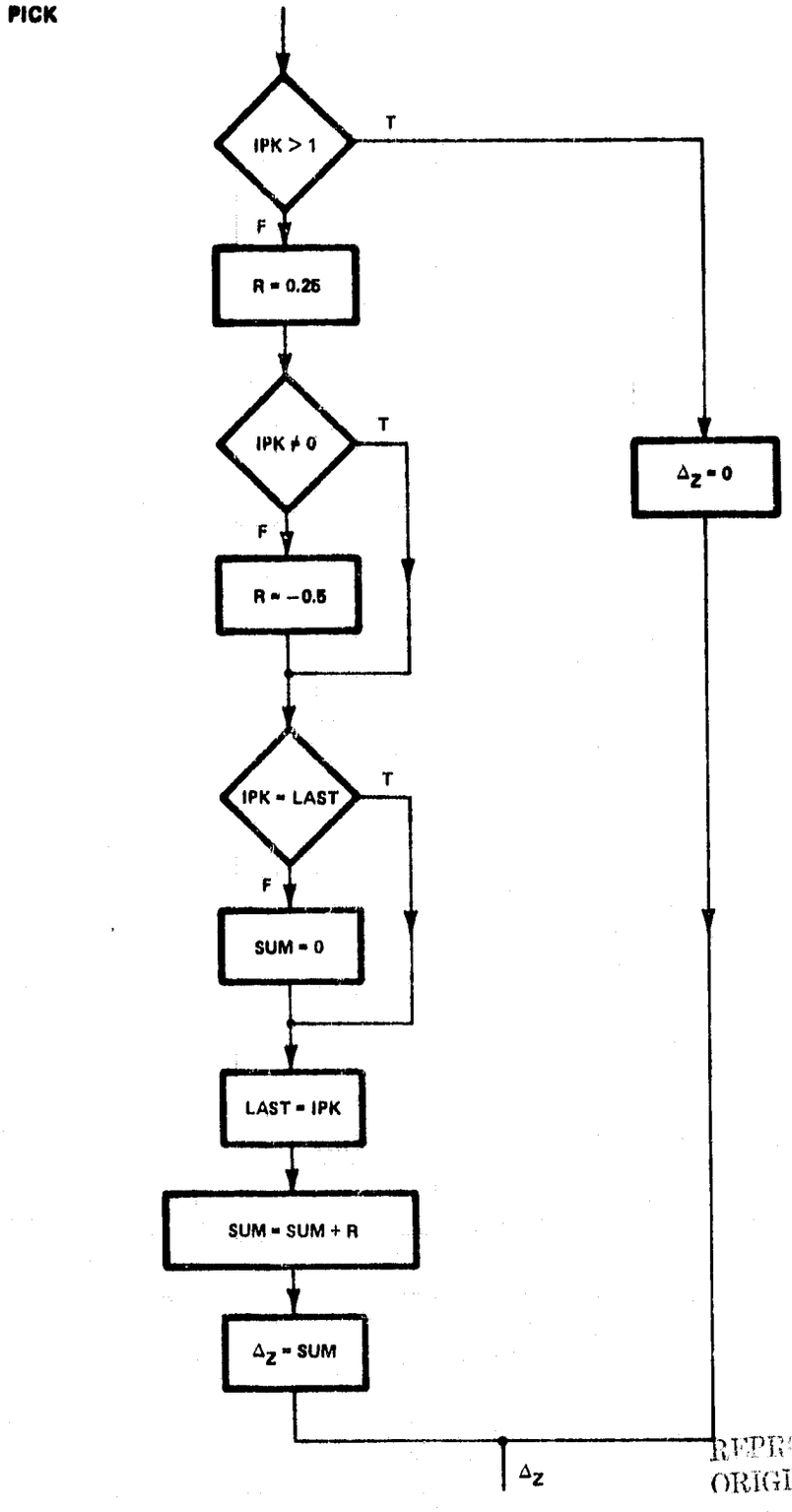

Figure 3-27. Pick Control Law

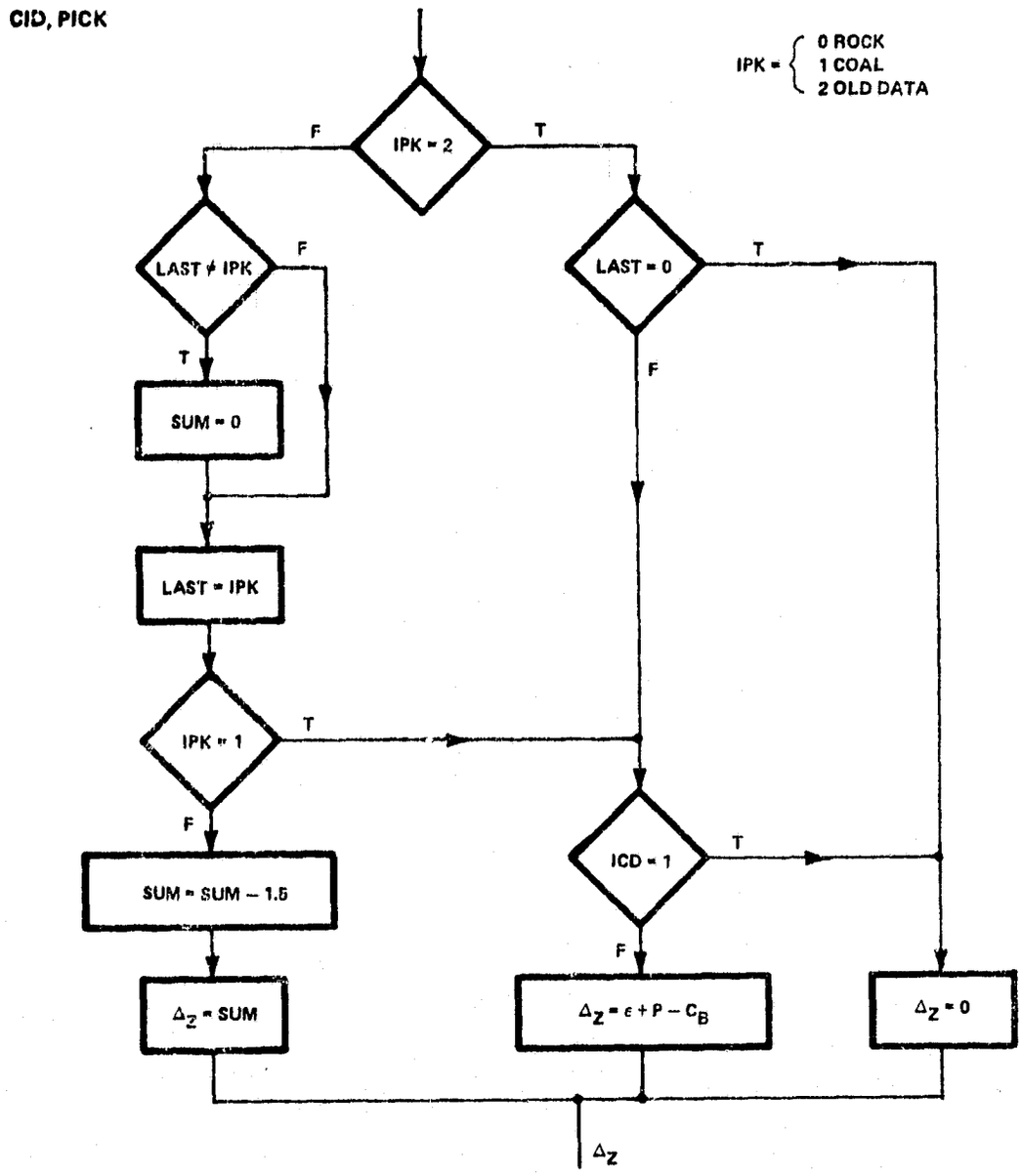

Figure 3-28. CID and Pick Control Law

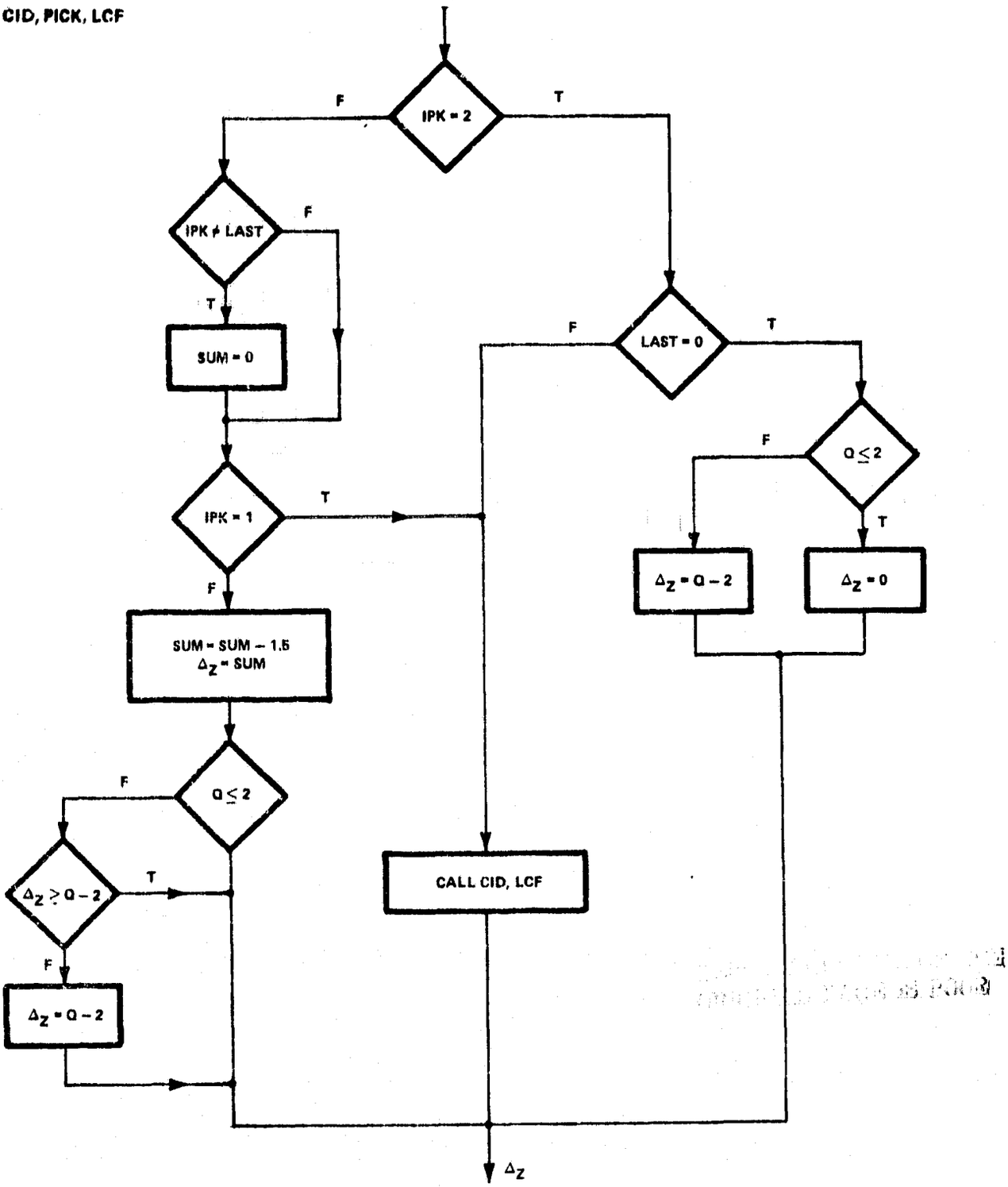

Figure 3-29. CID, Pick and LCF Control Law

The control law for the proportional CID alone, shown in Figure 3-25, is used for both the nucleonic and natural radiation CIDs. The desired drum height change command Δ_z is simply the sum of the measured coal depth ϵ and the drum position relative to the CID P minus the desired bias C_B. The P sensor maintains the drum at the same distance from the skid plane as the CID, and the coal depth minus bias provides the cut error. Δ_z is computed only when there is current CID data available.

Figure 3-26 is a flow chart of the proportion CID and LCF control law. The LCF measurement Q is assumed to be available as often as necessary; in this case, every 0.05 s, the iteration rate of the simulation. If CID data were not current, the LCF was checked for $\pm$2 in. and the drum commanded, if necessary, to maintain this limit. If CID data were available, a Δ_z was computed and used if $|Q|$ was not greater than 2 in., and would not be greater than 2 in. if Δ_z was used. If Q exceeded limits, the Δ_z was modified to maintain the 2 in. limit in the direction determined by CID.

Figure 3-27 shows the control law for the pick sensor only. To use this sensor, the drum is raised until rock is detected, withdrawn, and alternately raised until rock is encountered again and the cycle is repeated. Controlling in this limit cycle manner allows the shearing drum to follow the CSI. The rate of drum rise and withdrawal were adjusted to yield a good cutting performance. The control scheme used a nominal depression of 0.25 in. and a nominal withdrawal of 0.5 in. If current pick data is available, a Δ_z is computed, depending on whether coal or rock is sensed. If the same sensor indication occurs several times in a row, the depression command is integrated until the sensor indication changes. That is, if the pick indicates rock the drum is withdrawn 0.5 in. If the next reading is a rock indication, Δ_z is then set to 1 in., then 1.5 in., etc., until the sensor indication changes state.

The control laws for proportional CID and pick, and CID, pick, and LCF are shown in Figures 3-28 and 3-29 respectively. These are essentially combinations of the previous control laws. When the pick is used with other sensors, it determines only the withdrawal of the drum; the depression is controlled by the proportional CID. The last cut follower, when used with other sensors, has the highest priority and overrides the other commands.

These basic control laws were used with other sensors as well. The same CID schemes were used with the natural radiation CID providing proportional information. The pick control law was also used with a penetrometer, and the penetrometer with an LCF. Drum slaving control, which will be discussed later, uses a control law essentially like the CID and pick law with the slaving sensor providing the proportional data.

3.2.7 Mine Model

For the purpose of simulation, it was necessary to develop a mine model in which to evaluate the VCS control schemes. To achieve this, several 1 pass mine surveys were digitized and analyzed to provide an information base with which to generate subsequent simulated mine data. The statistical data obtained from these mines, including seam slopes, CSI variances, and seam heights, are presented in Table 3-2. An auto-correlation analysis of the top and bottom of each mine was performed, along with the corresponding power spectral density. The auto-correlation and power spectral densities of the York Canyon and Robinson Run mines are illustrated in Figures 3-30 through 3-33. A cross-correlation analysis was also performed between the top and bottom of the mines. The maximum cross-correlations of the six mines are also shown in Table 3-2. Figures 3-34 and 3-35 show the cross-correlations of the York Canyon and Robinson Run mines, respectively. It can be seen from these data

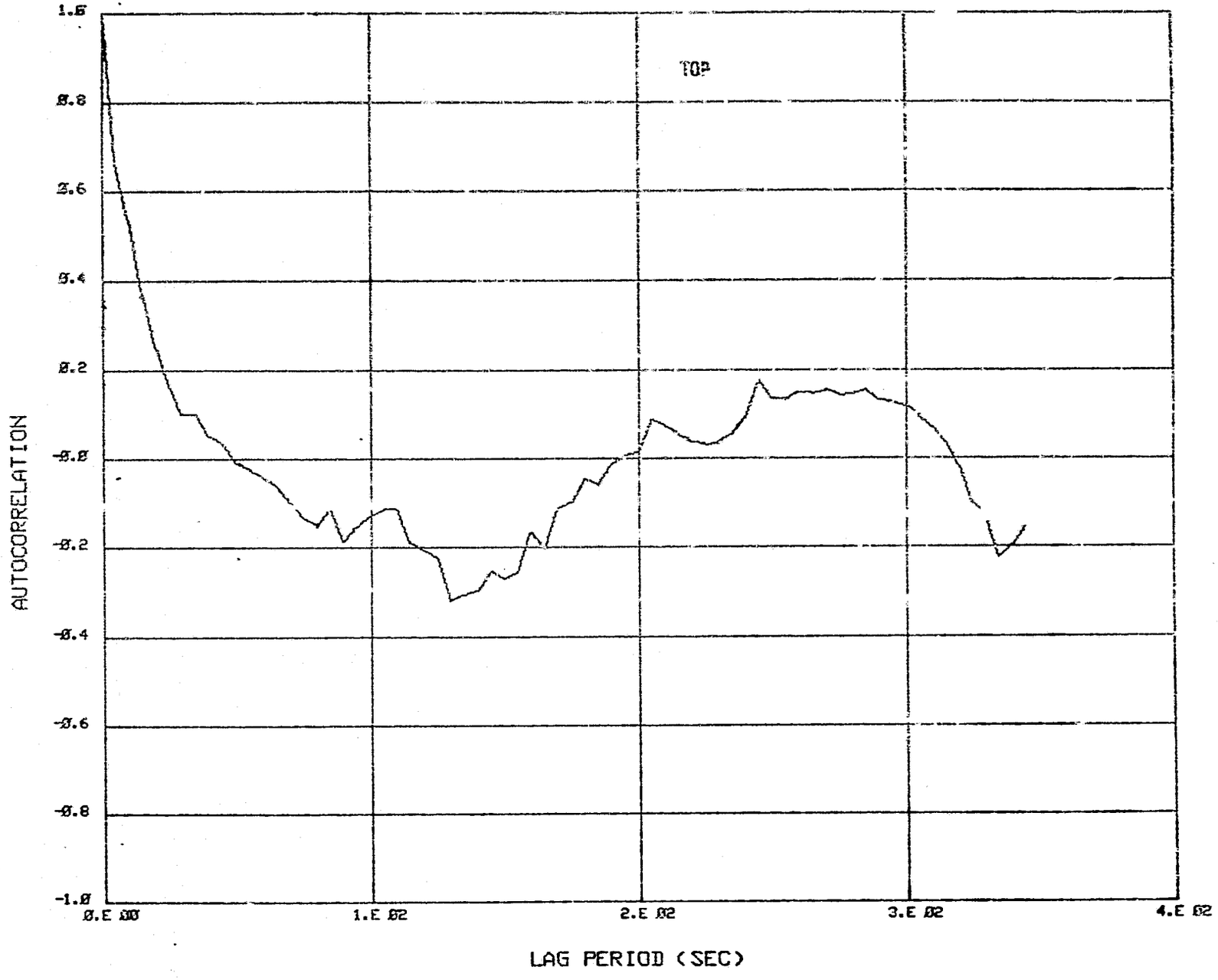

Figure 3-30. Autocorrelation of York Canyon Mine

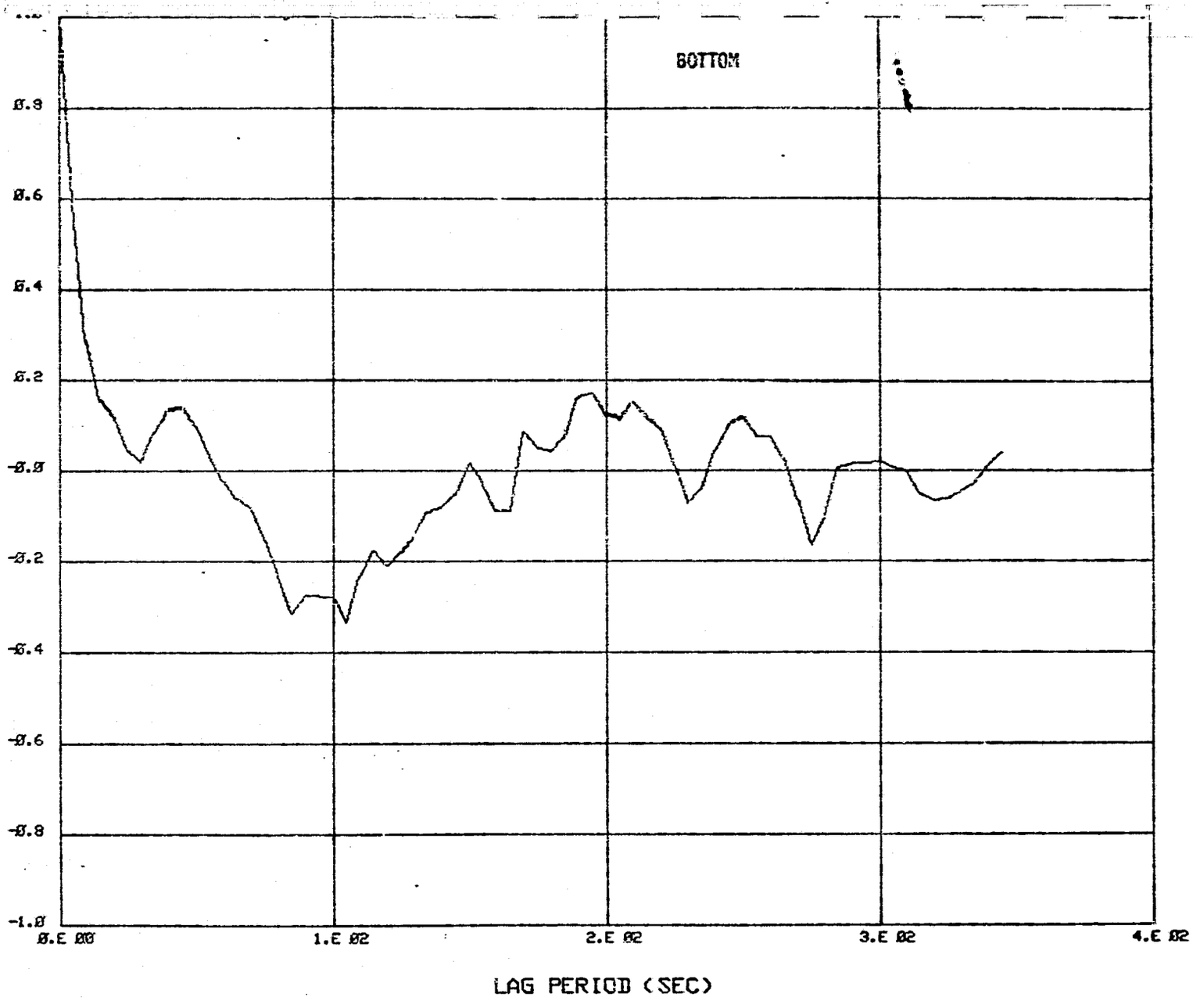

Figure 3-30. Autocorrelation of York Canyon Mine (Concluded)

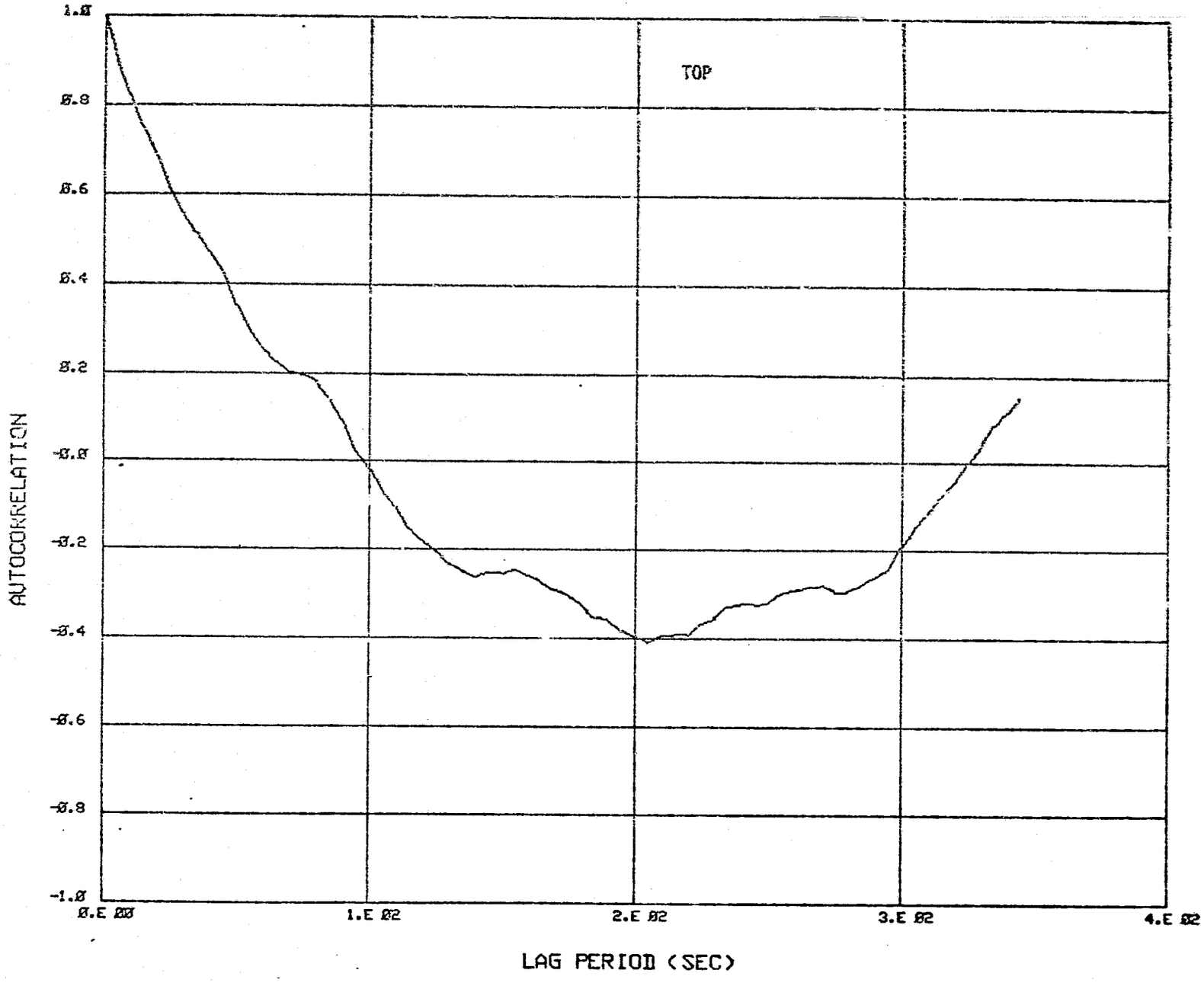

Figure 3-31. Autocorrelation of Robinson Run Mine

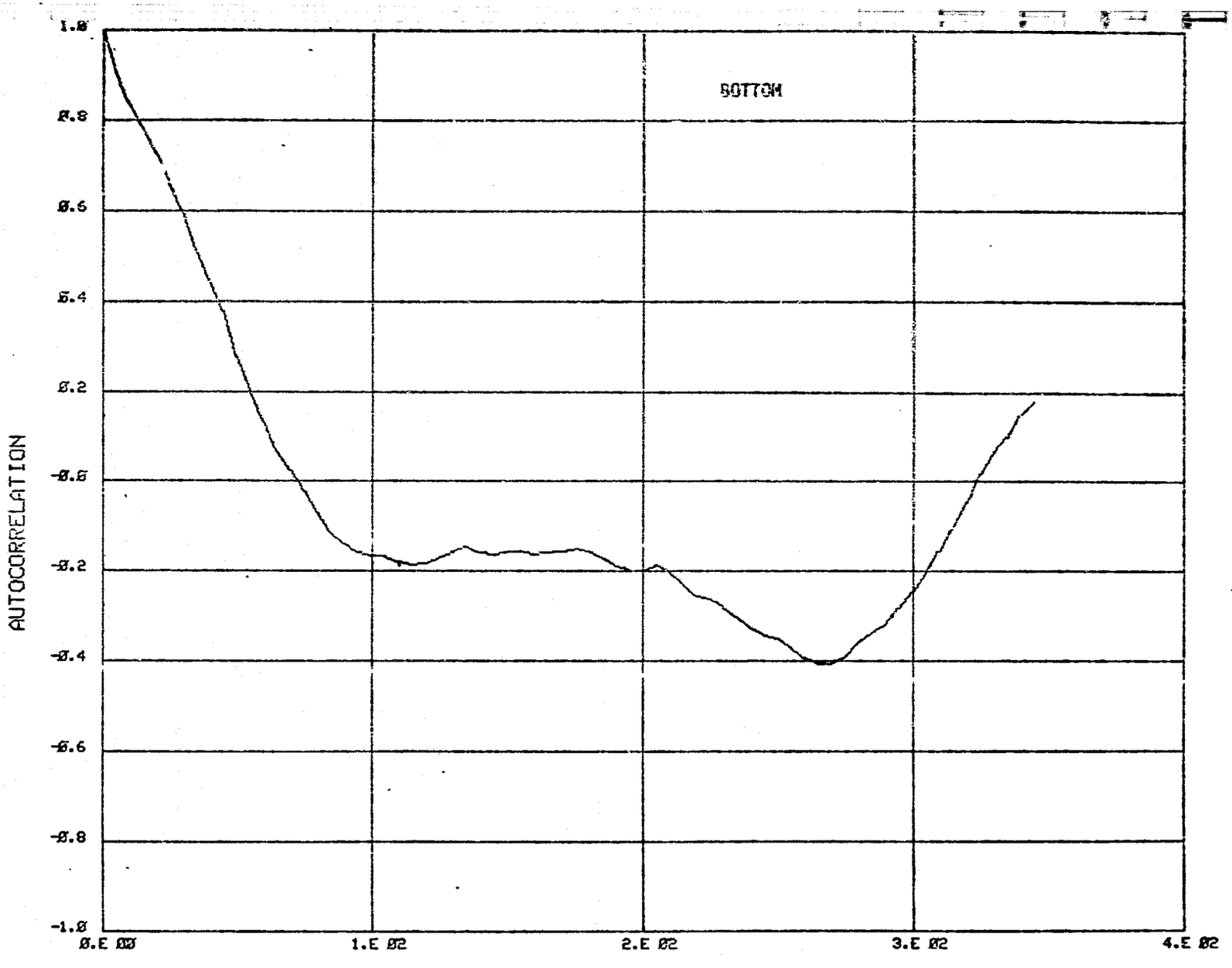

Figure 3-31. Autocorrelation of Robinson Run Mine (Concluded)

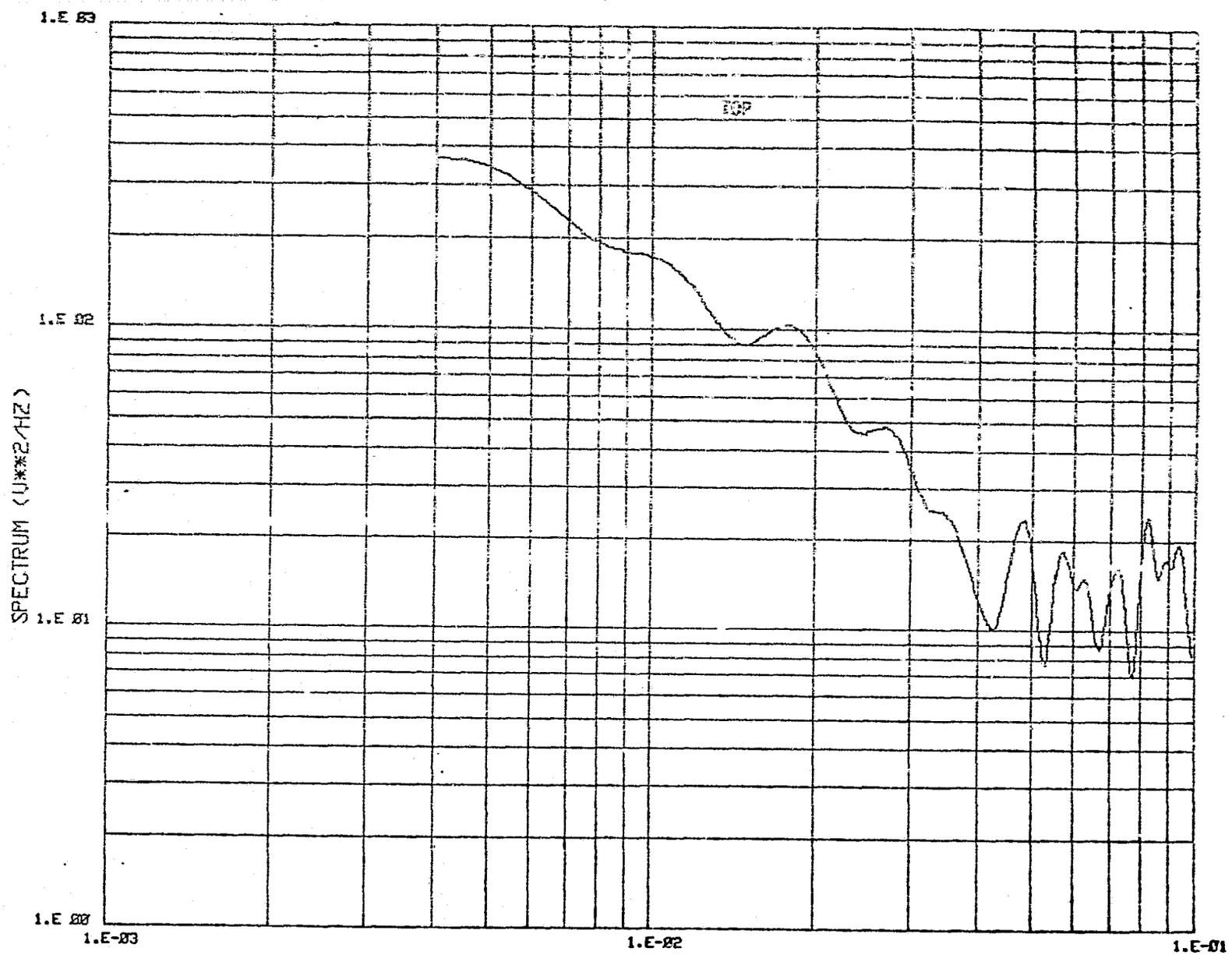

Figure 3-32. Power Spectral Density of York Canyon Mine

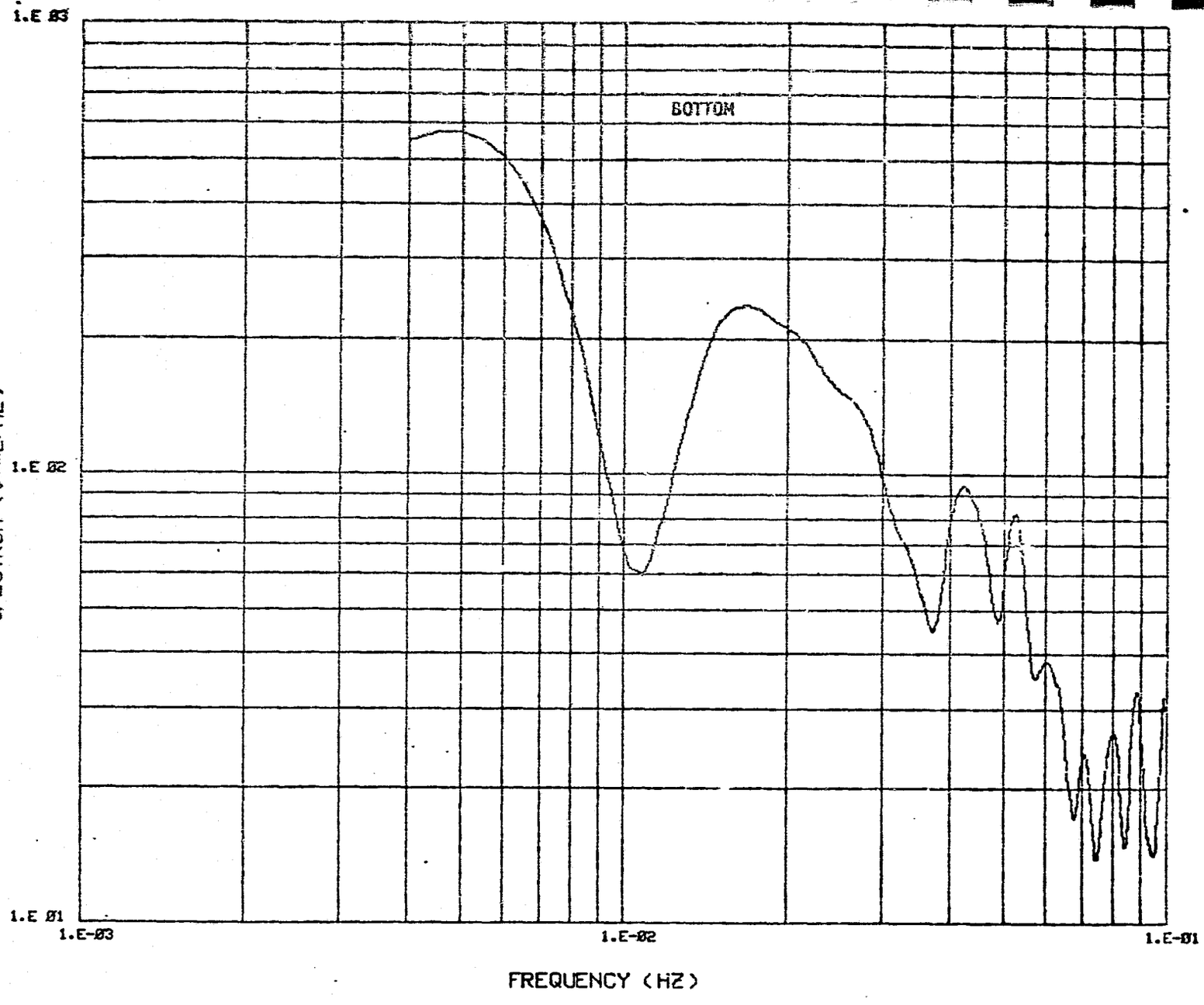

Figure 3-32. Power Spectral Density of York Canyon Mine (Concluded)

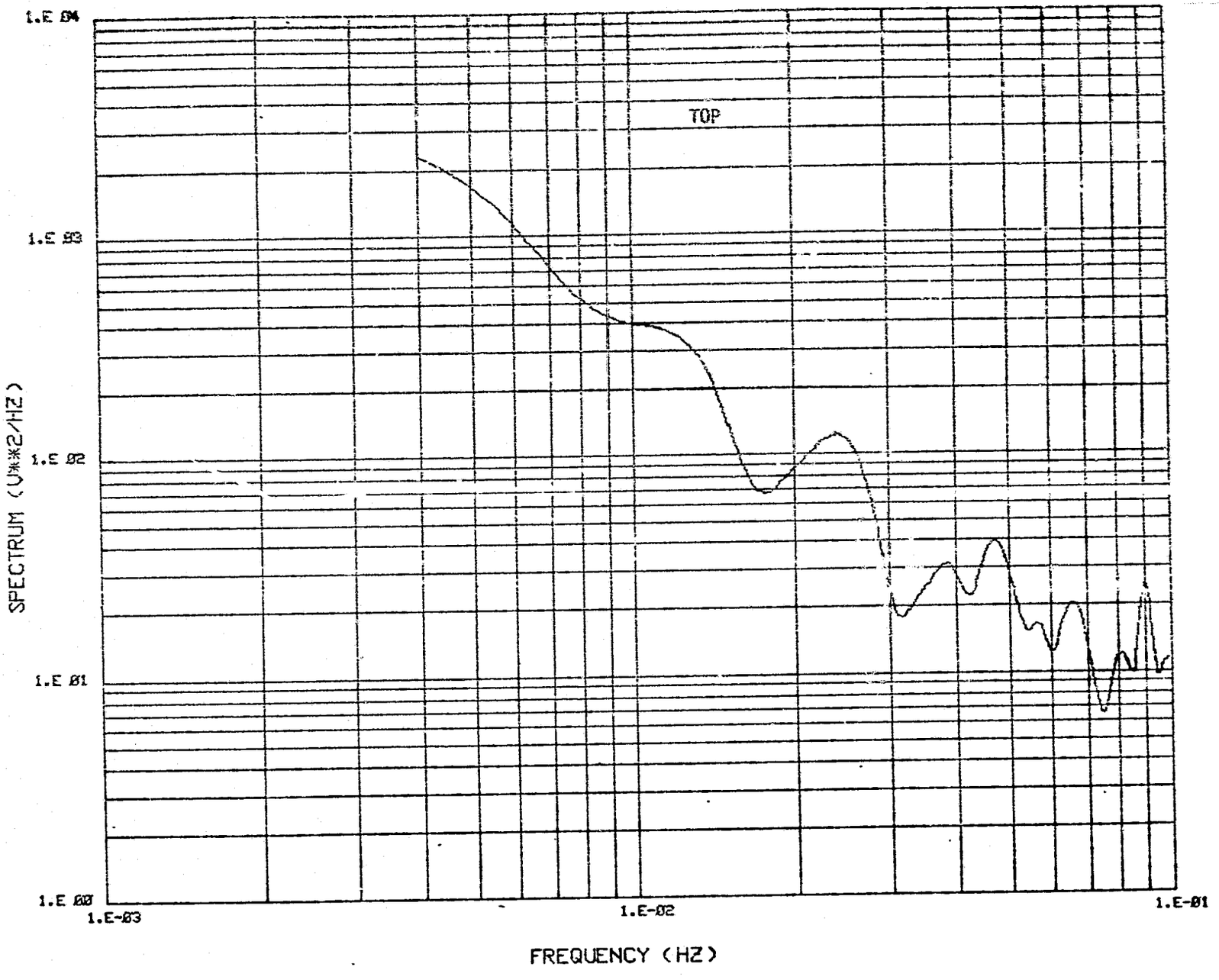

Figure 3-33. Power Spectral Density of Robinson Run Mine

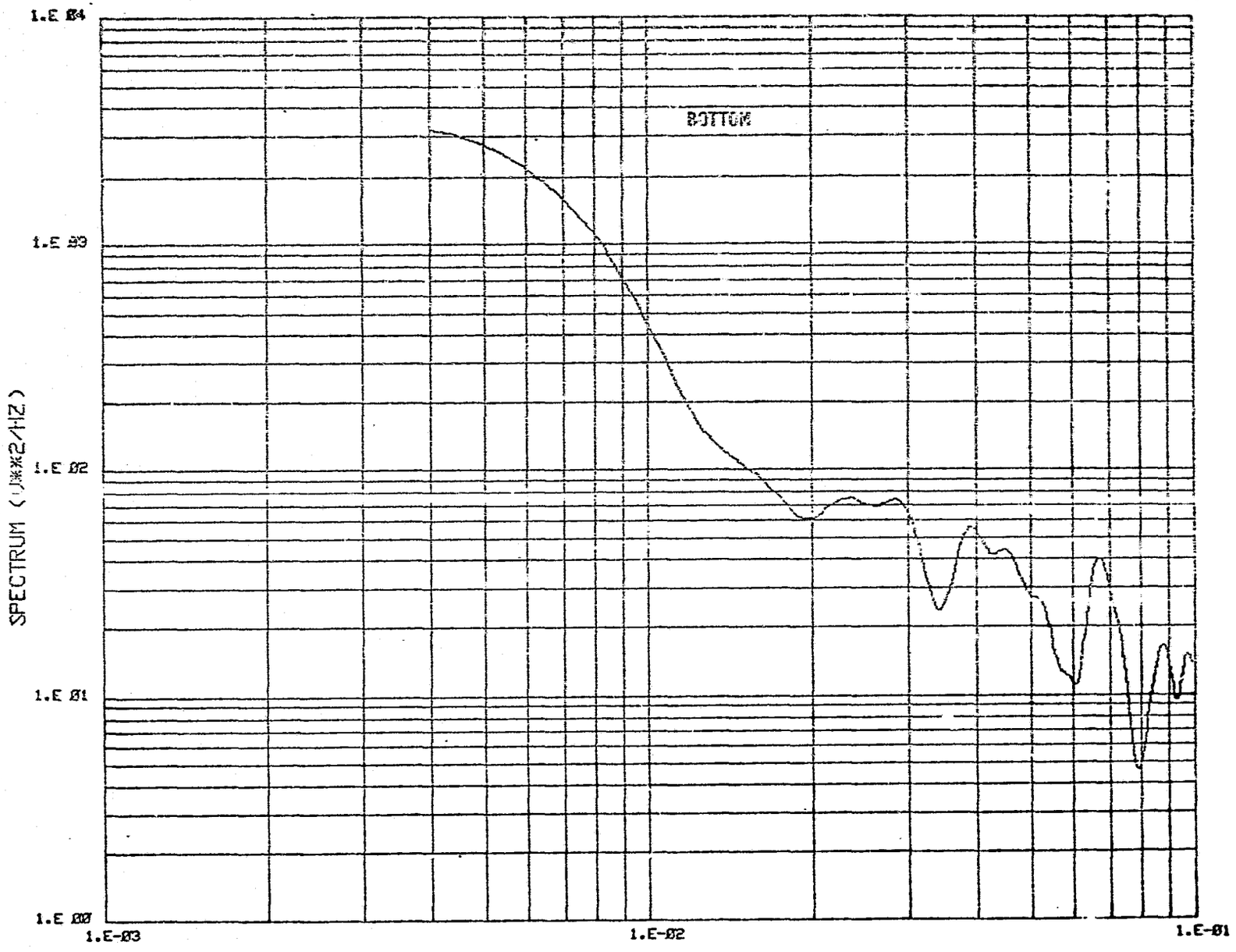

Figure 3-33. Power Spectral Density of Robinson Run Mine (Concluded)

Table 3-2. Mine Statistics

MINE	SLOPE (IN/5 FT)	BIAS (IN)	STANDARD DEVIATION (IN)	CROSS CORRELATION BETWEEN TOP AND BOTTOM
SHOEMAKER BOTTOM	-.0204	50.01	4.63	.91
SHOEMAKER TOP	-.0214	117.7	4.88	
FEDERAL #1 BOTTOM	-.0314	17.24	2.69	.75
FEDERAL #1 TOP	-.0349	116.0	3.81	
ROBINSON RUN BOTTOM	0.243	-1.5	5.18	.85
ROBINSON RUN TOP	0.236	96.06	4.57	
MARTINKA BOTTOM	0.0527	30.8	10.84	.98
MARTINKA TOP	0.057	86.01	10.49	
FEDERAL #2 BOTTOM	-.0397	51.74	4.86	.27
FEDERAL #2 TOP	-.0218	136.41	2.27	
YORK CANYON BOTTOM	0.513	38.6	3.07	.24
YORK CANYON TOP	.486	113.7	2.283	

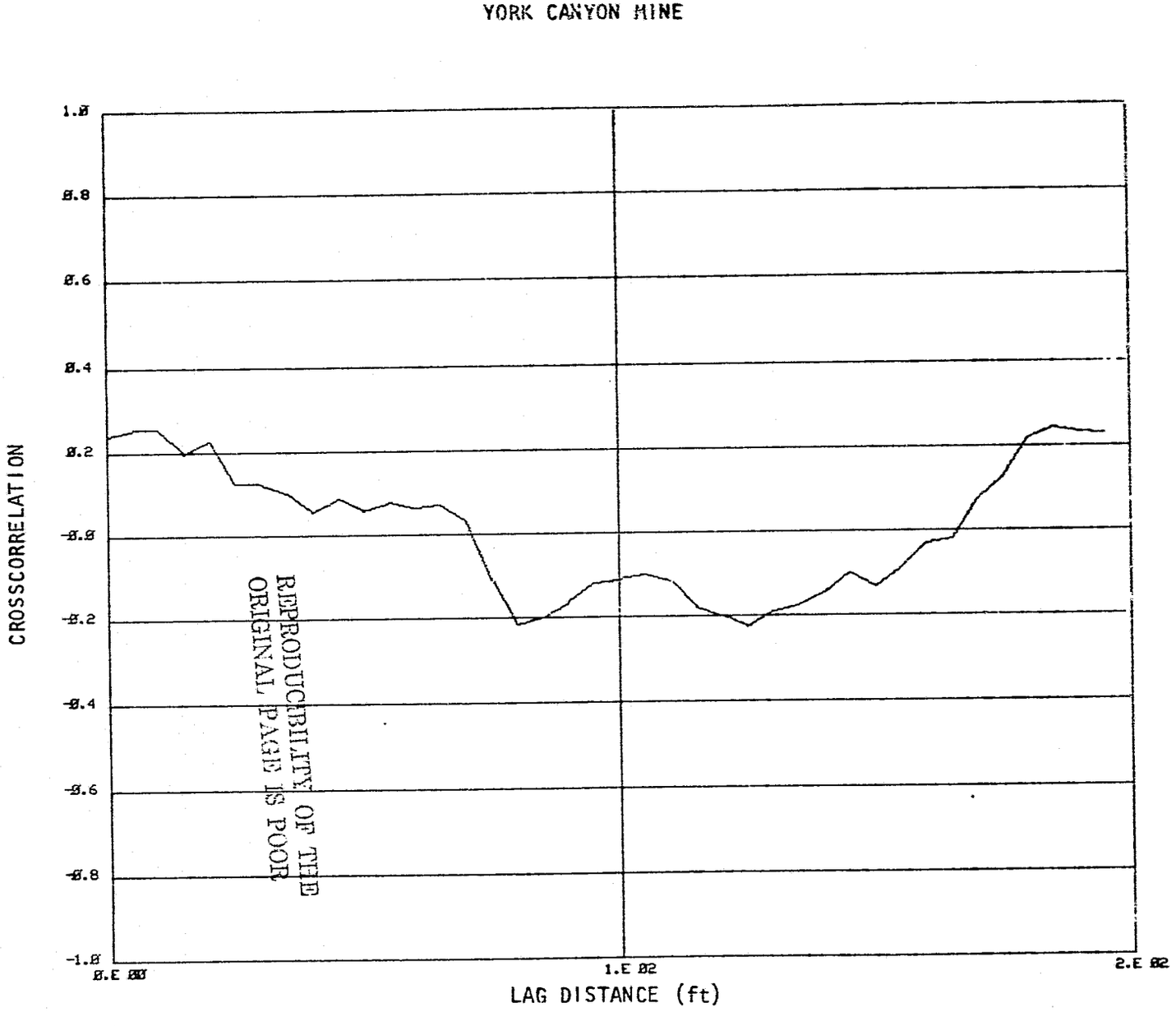

Figure 3-34. Cross Correlation Between Top and Bottom of York Canyon Mine

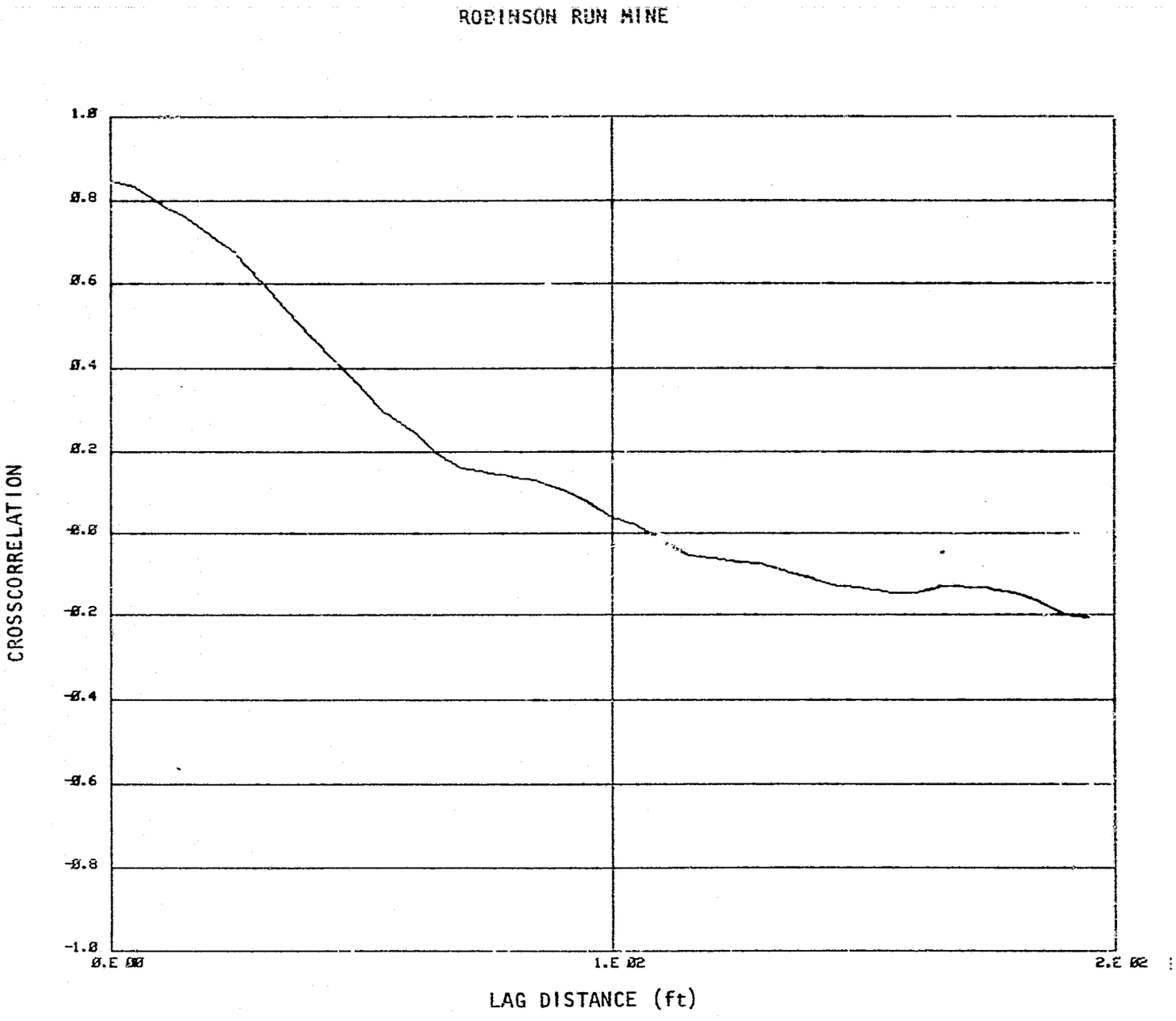

Figure 3-35. Cross Correlation Between Top and Bottom of Robinson Run Mine

that, statistically, there is a great deal of similarity between the mines considered. The CSI variances and correlation data are quite similar. In addition, except for the York Canyon and Federal #2 mines there was a significant degree of correlation between the top and bottom which will be of some importance when drum slaving is considered.

For the simulation, it was necessary to have more than the single CSI profile for a given mine. To do this, a procedure was developed to generate random data with the same statistical and spatial correlations as the original surveyed data. The profile generation scheme is based on the following theorem of conditional distributions with multiple correlations:

Given: a. $\overline{X} = (X_1, X_2, \ldots, X_N)^T$ a vector formed from realizations of a set of N jointly normally distributed random variables $(X_1, X_2, \ldots, X_N)$ which are all N(0,1).

b. $A = (\rho_{ij})$ an NxN correlation matrix of the N sequence elements.

c. $\overline{B} = (\rho_{N+1,1}, \rho_{N+1,2}, \cdots, \rho_{N+1,N})^T$ a vector (Nx1) of desired correlations of the (N+1)'th point and the previous N.

The theorem states that the density of the (N+1)'th point given $\overline{X}$, is $N(X_{N+1} | \overline{B}^T A^{-1} \overline{X}, 1-\overline{B}^T A^{-1} \overline{B})$ or normal with mean $\overline{B}^T A^{-1} \overline{X}$ and variance $1 - \overline{B}^T A^{-1} \overline{B}$.

The following procedure was used to generate multiple profiles from the original data:

1. The original data were detrended by fitting a regression line and subtracting it off. This results in essentially a zero mean process. The standard deviation was then estimated and divided out.

2. Correlation analysis showed that the mine profiles are approximately exponentially correlated.

$$\rho_{ij} = e^{-\frac{d}{D}}$$

where d is the distance between points i and j and D is the correlation distance. D was found to be between 25 and 50 ft for the mines analyzed.

3. To generate a new point on a mine profile, all points original or generated within D ft of the new point are found, and become the elements of $\bar{X}$.

4. The matrix A and vector $\bar{B}$ are formed using the spatial relationships of the selected points and the above correlation function.

5. A is inverted, the mean and variance found, and a new point generated using a random number generator.

Figures 3-36 and 3-37 show the top and bottom profiles for the Robinson Run mine. Five profiles were generated along with the original data shown. These are not 3 dimensional plots but rather the 6 profiles biased apart for plotting purposes. It can be seen that the generated profiles show similar characteristics to the original data. Figure 3-38 presents a 3 dimensional view of a 12.5 by 50 ft section of this simulated Robinson Run bottom. It can be seen that the randomly generated profiles form a realistic surface.

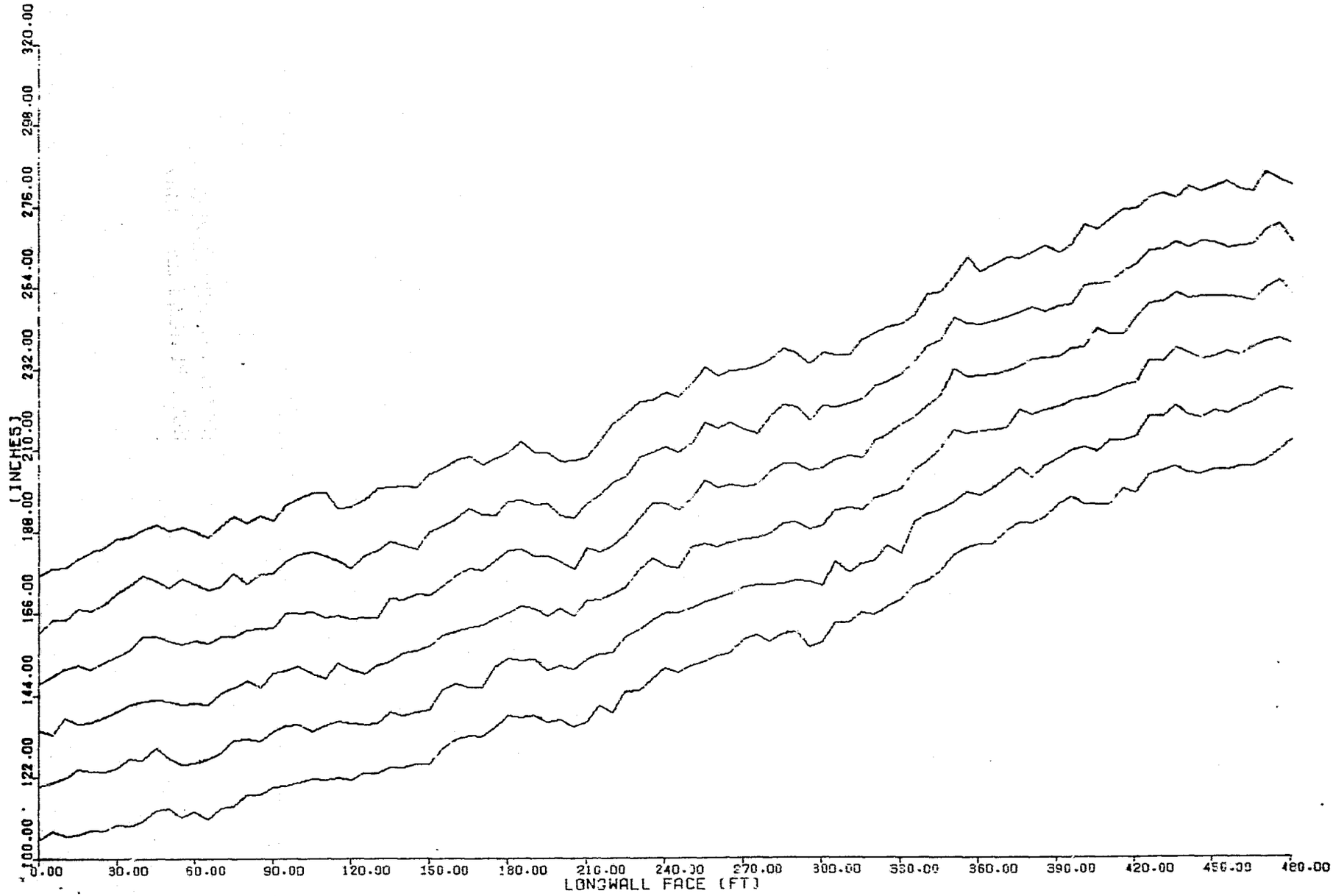

Figure 3-36. Generated Profiles for the Robinson Run Top

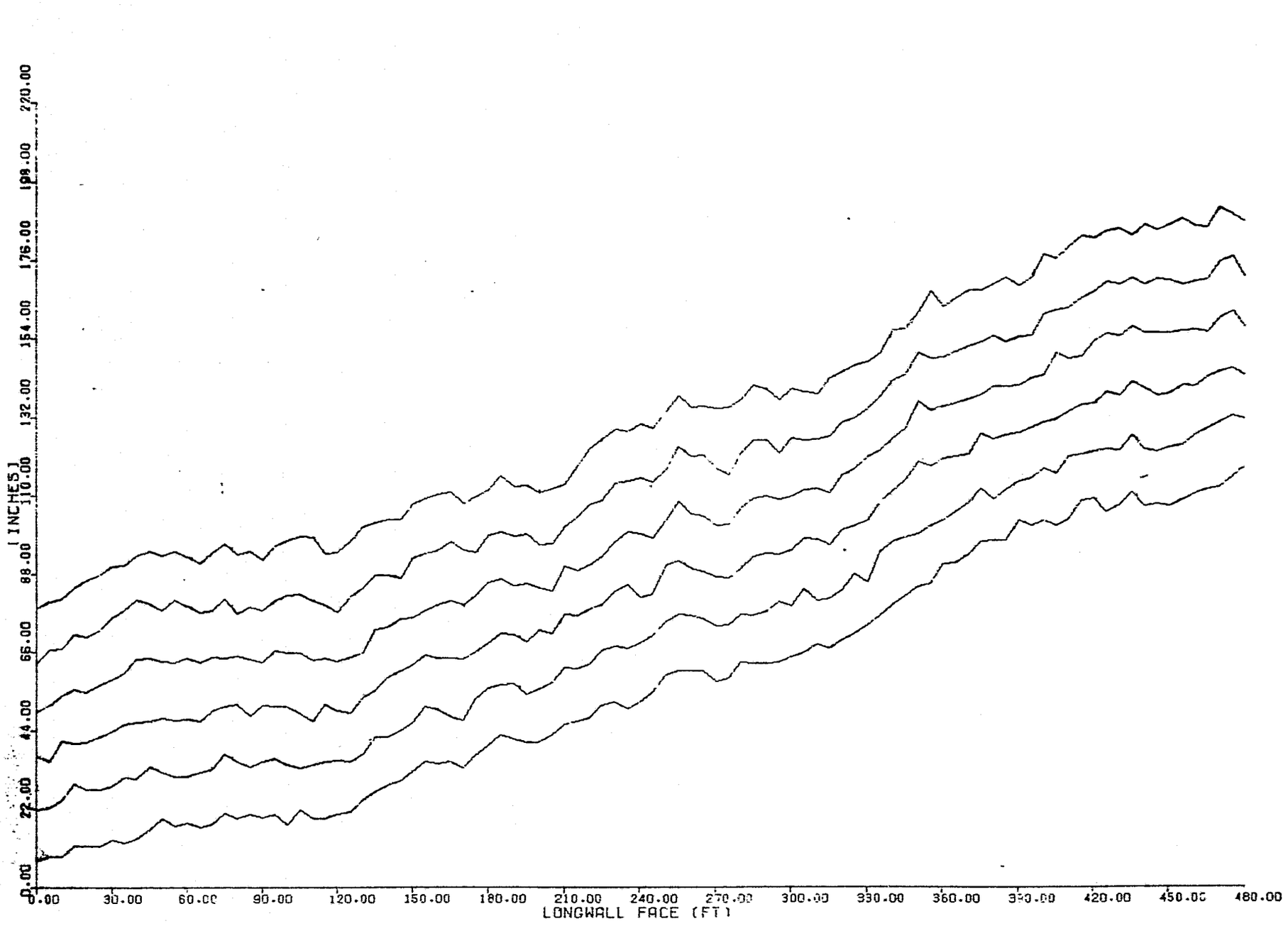

Figure 3-37. Generated Profiles for the Robinson Run Bottom

Figure 3-38. 3D View of the Generated Bottom for the Robinson Run Mine

The mine data were used in the simulation to provide current CID measurements and initial conditions. For a simulation run, the first or the original mine profile was used for initial conditions, providing the last cut data; and to form the conveyor track. The last cut, taken as the CSI on the top minus the desired bias, and the CSI on the bottom plus the desired bias, therefore represented a perfect cut. The track on which the shearer moved was formed from this perfect last cut. On subsequent mining passes within the same simulation run, the last cut was that actually cut, and the track formed from the actual cut surface.

3.3 SIMULATION DETAILS

3.3.1 Initialization

The simulation structure follows the diagram shown in Figure 3-1. The basic iteration cycle of the simulation was 0.05 s, and the actuator dynamics were integrated at a 0.01 s rate. All the simulation runs were made using the same initial conditions. The shearer was positioned such that drum No. 1 was cutting the top, with the cut height initially set to a perfect cut, that is, the interface height minus the bias. Each mine interface profile was modified so that the first 30 ft were level. This allowed easy initialization, since α was zero in this level section.

Fixing the front drum with $\alpha = 0$, fixes the position of the shearer chassis and the rear drum in the mine. The initial values of X_1 and (X_2, Z_2) are then computed as follows:

Given initial X_{D1}, Z_{D1} and Z_1,

$$B_1 = \sin^{-1}\left(\frac{Z_{D1} - Z_1 - b}{L}\right)$$

thus

$$X_1 = X_{D1} - a + c/2 - L \cos \beta_1$$

$$X_2 = X_1 + C$$

$$Z_2 = Z_1$$

The rear drum is then set to a perfect cut position, given Z_{D2}

$$\beta_2 = - \sin^{-1} \left(\frac{Z_1 + b + Z_{D2}}{L}\right)$$

The initial values of Z_{D1}, Z_1, and Z_{D2} are obtained from the mine profile data.

The cut surfaces were initialized as discussed in Section 3.2.7. The last cuts were assumed to be perfect, and the track formed from this perfect cut. The interface data is stored at 5 ft intervals and therefore the initial last cuts and track replicate the interface and this data spacing. Present cut data are stored at 3 in. intervals uniformly across the face. Therefor on repeated passes, the last cut data has this resolution.

3.3.2 Cut Surface Determination

The determination of the cut surface, the surface which remains after the shearing drum has passed, is critical to the simulation of VCS operation and performance evaluation. Since CID sensors ride on this surface, and measure the coal thickness from the cut surface to the interface, the cut surface simulation affects CID, and, therefore, VCS performance. Evaluation of cutting performance, i.e., rms errors, coal taken and left in error, is also affected by the correctness of the cut surface representation.

The cut surface algorithm starts by storing the Z drum coordinates at 3 in. intervals along the face. To find the cut height at some location x, the drum positions on either side are checked.

Figure 3-39 shows this procedure. The cut at point x resulting from drum position N is the point where the drum radius r intersects the line X = x. The N'th point is determined by the nearest 3 in. interval to x, and all the points in the range N - 7 to N + 7 are checked for their contribution at x. The cut at x is taken to be the highest radius intersection at that point. In Figure 3-39, this would be the cut from N + 1. The cut Z coordinate is given by

$$Z = Z_D(N + 1) + \sqrt{r^2 - (x - X_D(N + 1))^2}$$

3.3.3 Performance Evaluation

A number of quantities are computed for the performance evaluation of the VCS. Figure 3-49 presents an example of the performance evaluation computer output. The basic measure used is the rms of the deviation of the actual cut from the desired bias thickness. The average of the absolute value of this error is also computed, along with volumetric coal errors. The excess coal left is that volume of coal which is thicker than the desired bias, and the excess coal taken is the volume of coal which is thinner than desired. The volume of rock taken is also computed. The percentages shown after each of these quantities represent the percent of the total volume of material taken, shown at the top of the printout. The percent time in rock is the percentage of the total cutting time that the drum was in rock.

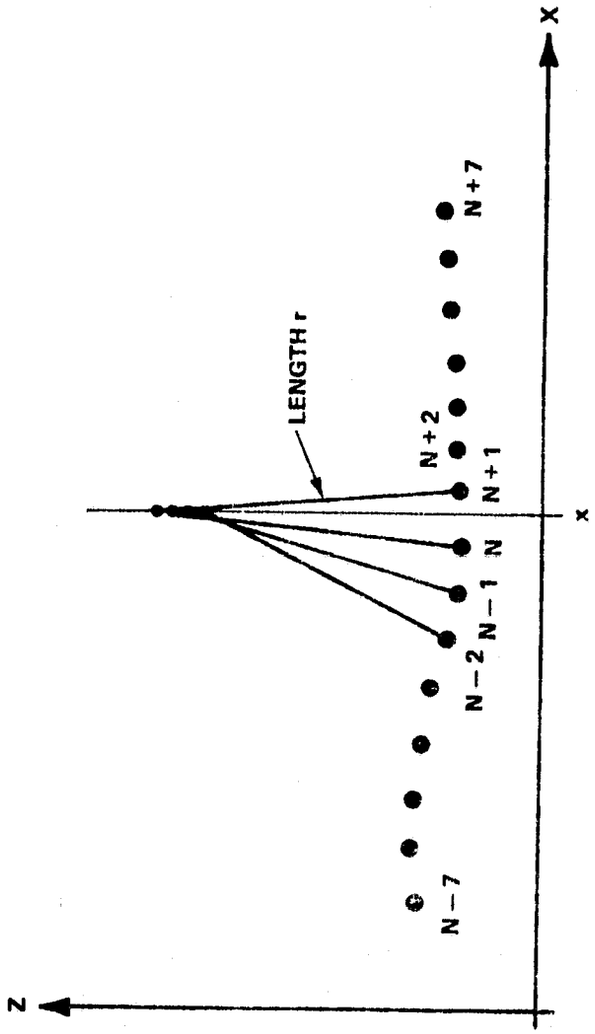

Figure 3-39. Drum Cut Geometry

3.4 BASELINE SYSTEM PERFORMANCE

3.4.1 Philosophy and Specification of Baseline System

The baseline system involves specifying a system concept which will solve the required problem and provide a baseline or standard against which to compare the results of parameterization studies and performance of other system concepts. The baseline is generally the simplest system which will solve the problem. To this end, a baseline concept was specified for the VCS. The baseline sensors include a nucleonic CID for a proportional measurement and a sensitized pick for a rock presence sensor. The last cut follower is included to maintain the cut within a given distance of the last cut. For these studies, this distance was chosen to be ± 2 in. Finally, to cut bottom coal, drum slaving is used on the bottom drum.

3.4.2 Performance of Baseline System

3.4.2.1 Performance as a Function of Sensor Location

Figure 3-7 shows the geometry of the CID location. The CID is located at distance K_R behind the shearing drum. Table 3-3 shows the effect of varying the CID location. It can be seen that locating the CID closer to the drum results in better cutting performance. As K_R is increased, the delay is larger and performance degrades. Figures 3-40 through 3-42 show that computer runs were for the 0.75, 1.5, and 2.5 ft displacements. It is therefore desirable to locate the CID as close as possible to the cutting drum, and with current designs, the minimum K_R is 2.5 ft.

Table 3-3. Effects of CID Location

CID DISPLACEMENT (FT)	RMS TOP ERROR (IN.)	RMS BOTTOM ERROR (IN.)
0.75	0.33	0.38
1.5	0.63	0.75
2.5	1.0	1.23

(A) NO NOISE

(B) 4 IN. BIAS

(C) YORK CANYON MINE

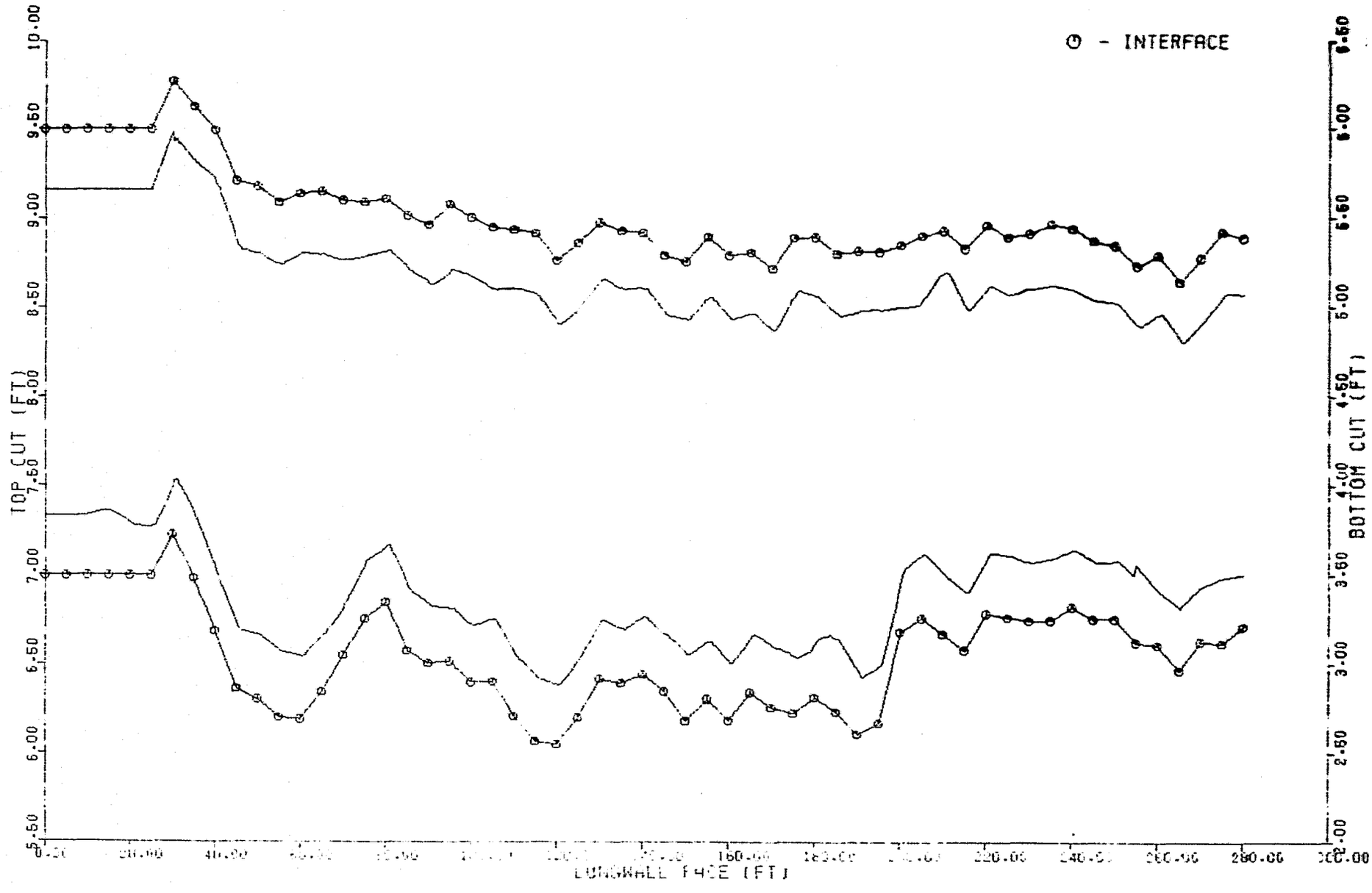

Figure 3-40. VCS Performance with 0.75 Feet CID Displacement

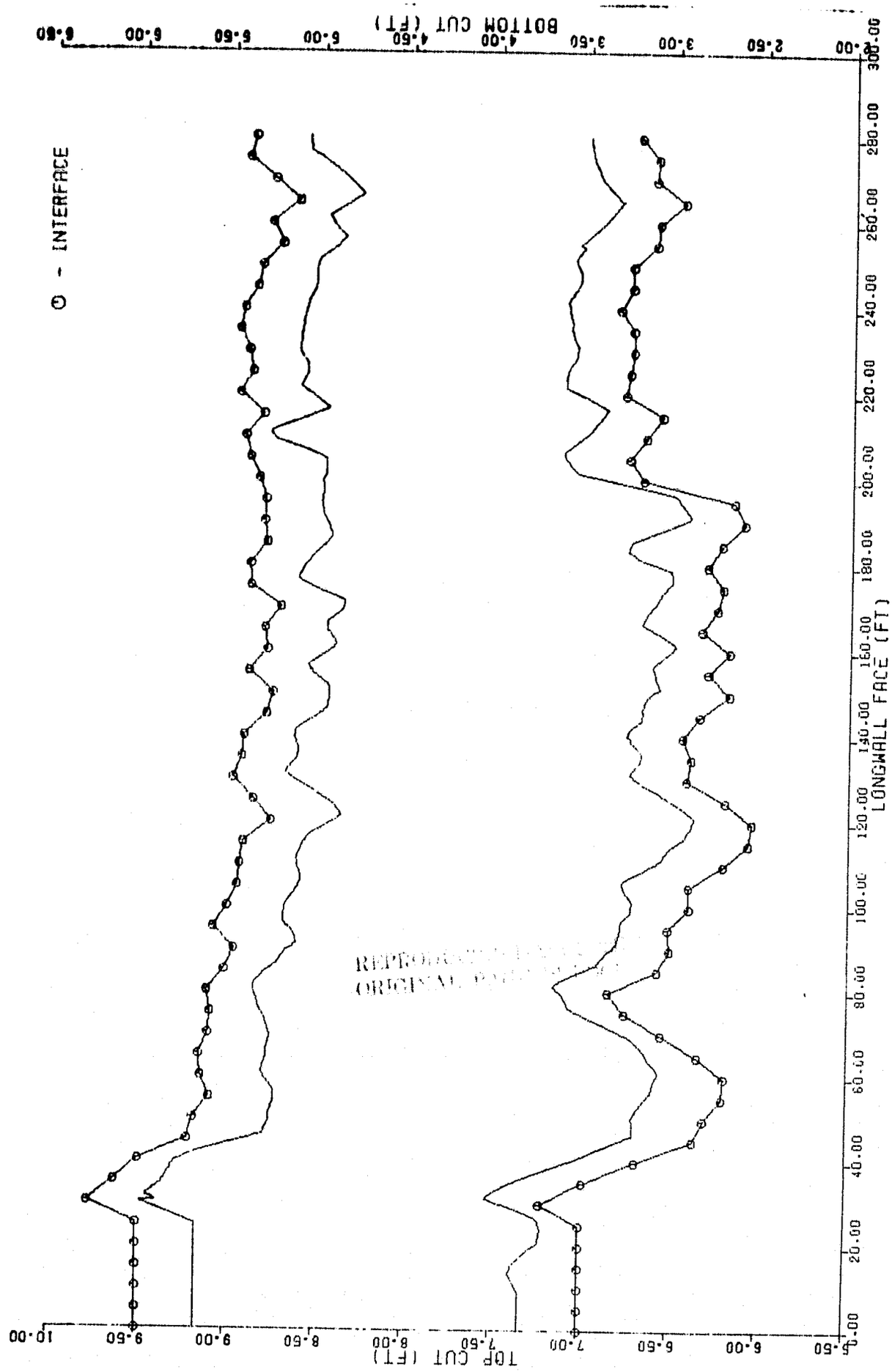

Figure 3-41. VCS Performance with 1.5 Feet CID Displacement

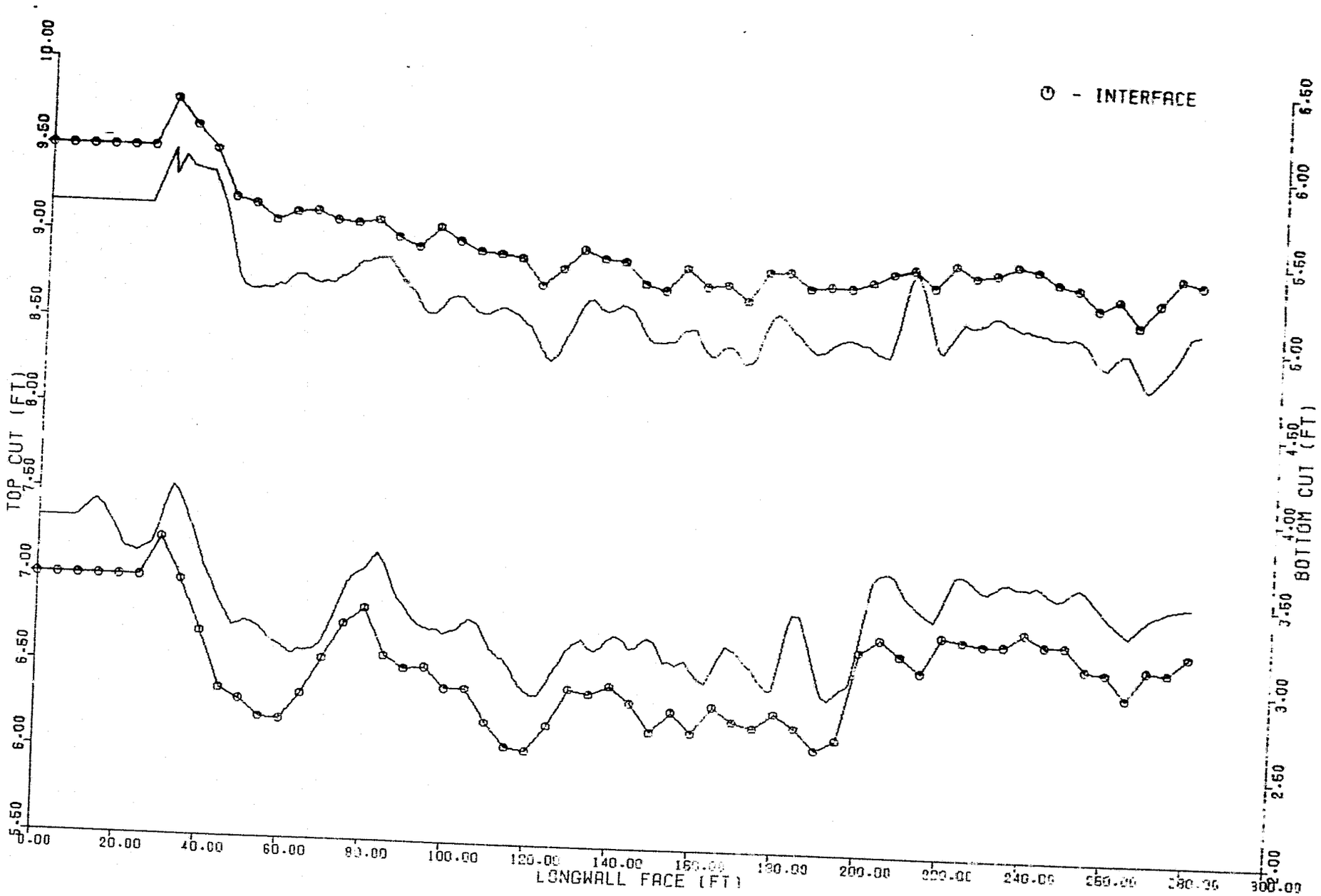

Figure 3-42. VCS Performance with 2.5 Feet CID Displacement

3.4.2.2 Performance as a Function of Sensor Output Interval Without Noise

The effects of varying the sensor output interval, in this case, for the nucleonic CID, are shown in Table 3-4. A measurement is outputted only at the intervals shown in the table. Increasing this interval increases the delay from measurement to measurement and also gives a more smoothed measurement, in that the coal depth is averaged for a longer distance. It can be seen from Table 3-4 that performance degrades significantly as the output interval is increased, showing that additional delay and smoothing adversely affects performance. System cutting performance with a 1, 5, and 10 s delay is illustrated in Figures 3-43 through 3-45, respectively.

3.4.2.3 Performance as a Function of Sensor Output Interval With Noise

Two effects are evident when the sensor output interval is varied with sensor noise. As seen in Section 3.4.2.2, the VCS system performance improves with reduction in the sensor output interval. However, the sensor noise will increase as the output interval is shortened. This is due to the smaller number of counts obtained in each interval thus resulting in greater dispersion of these counts. Since the two effects are in opposition, a clearly defined performance maximum should exist as a function of output interval.

Table 3-5 shows this effect for the nucleonic CID, and for a 3 and 5 in. natural radiation sensor. The 5 in. sensor was simulated by scaling up the 3 in. sensor calibration curve (Figure 3-12) by the ratio of the sensor areas. It can be seen in Table 3-5 that the nucleonic CID exhibits the best performance at 0.25 s output

Table 3-4. Effects of CID Output Interval

CID OUTPUT INTERVAL (SEC)	RMS TOP ERROR (IN.)	RMS BOTTOM ERROR (IN.)
1	1.20	1.43
2	1.72	1.83
5	3.30	3.70
10	4.43	5.06

(A) NO NOISE

(B) 4 IN. BIAS

(C) 2.5 FT CID DISPLACEMENT

(D) YORK CANYON MINE

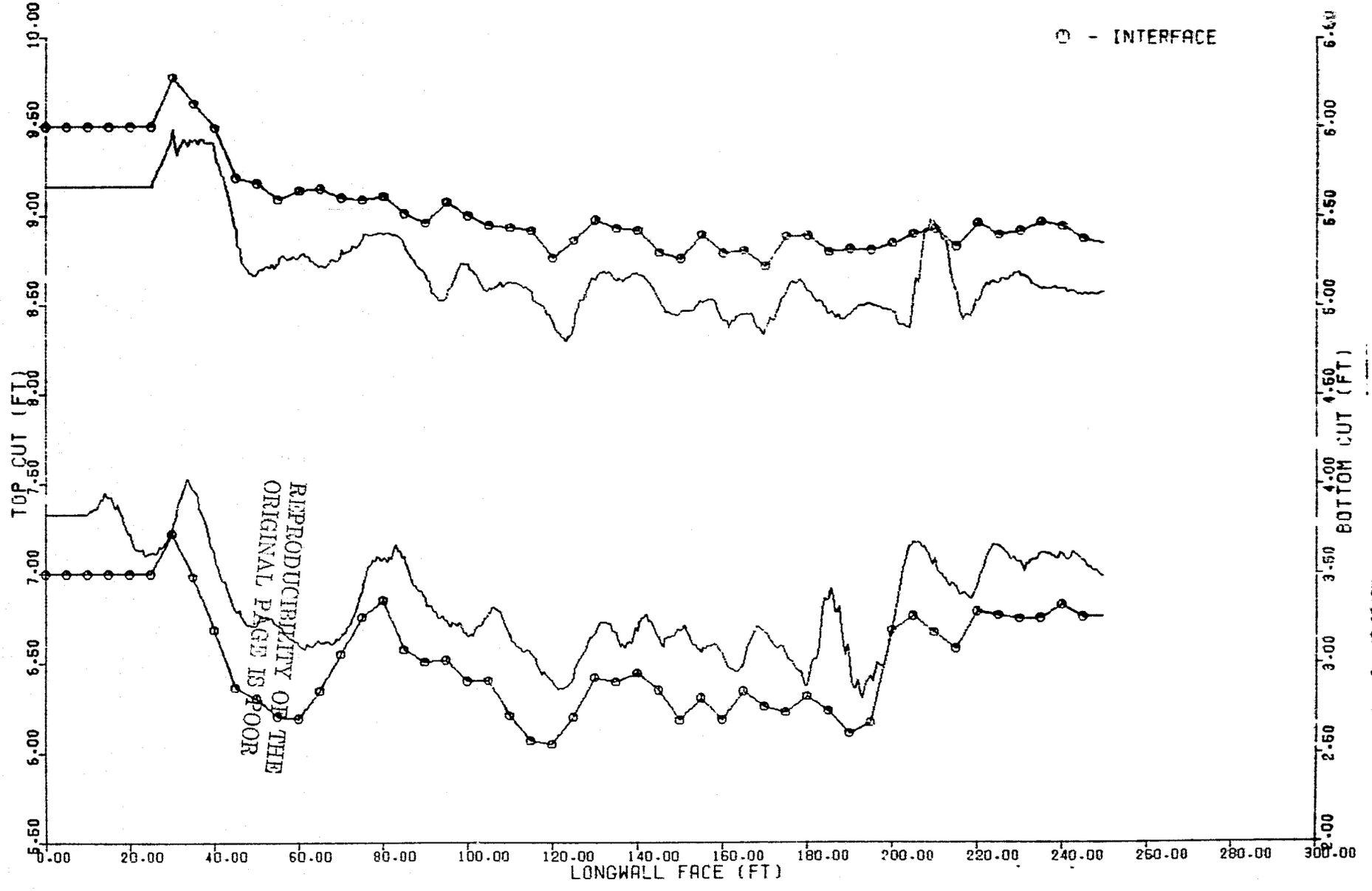

Figure 3-43. VCS Performance with 1 Sec. CID Output Interval

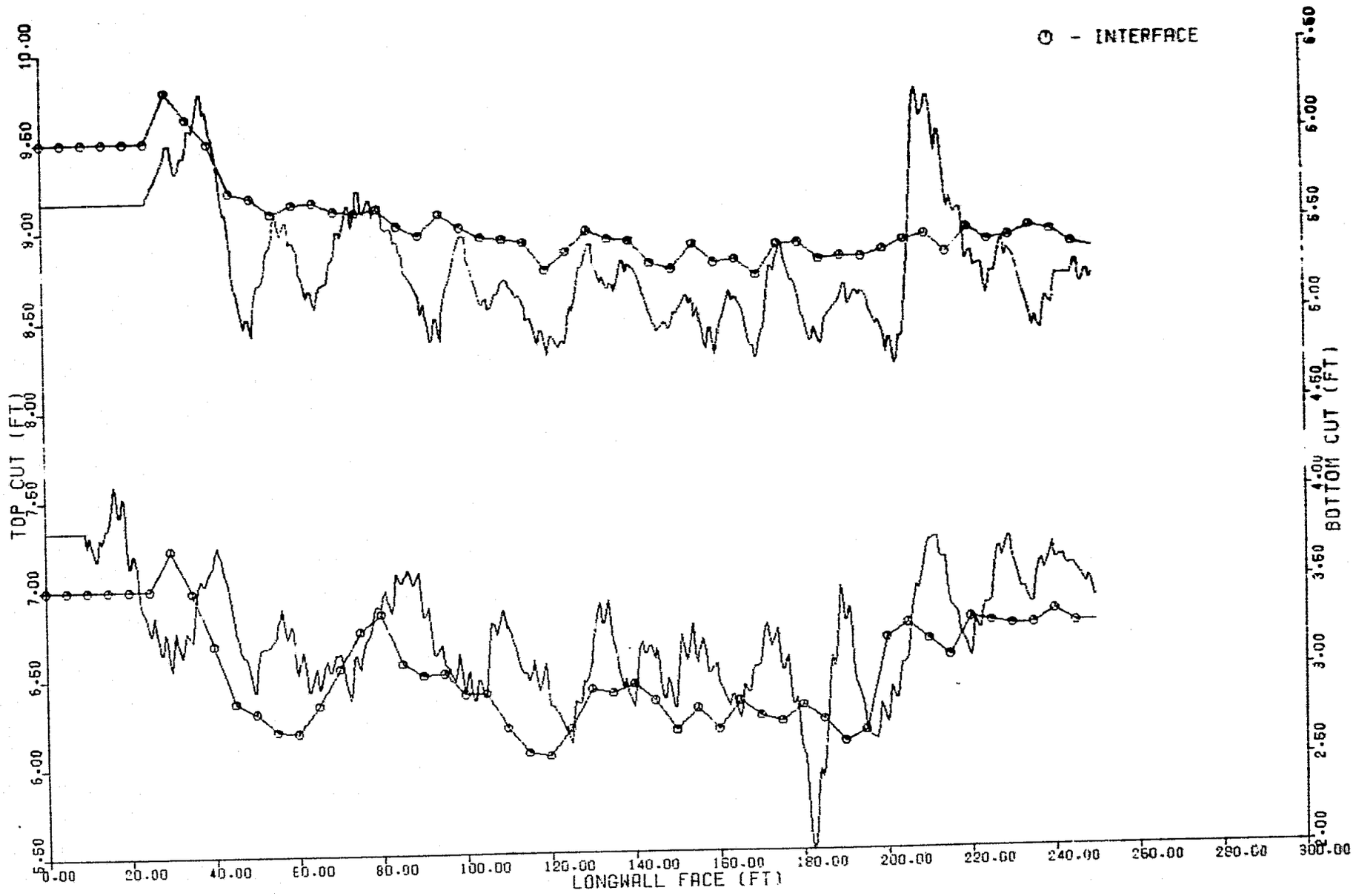

Figure 3-44. VCS Performance with 5 Sec. CID Output Interval

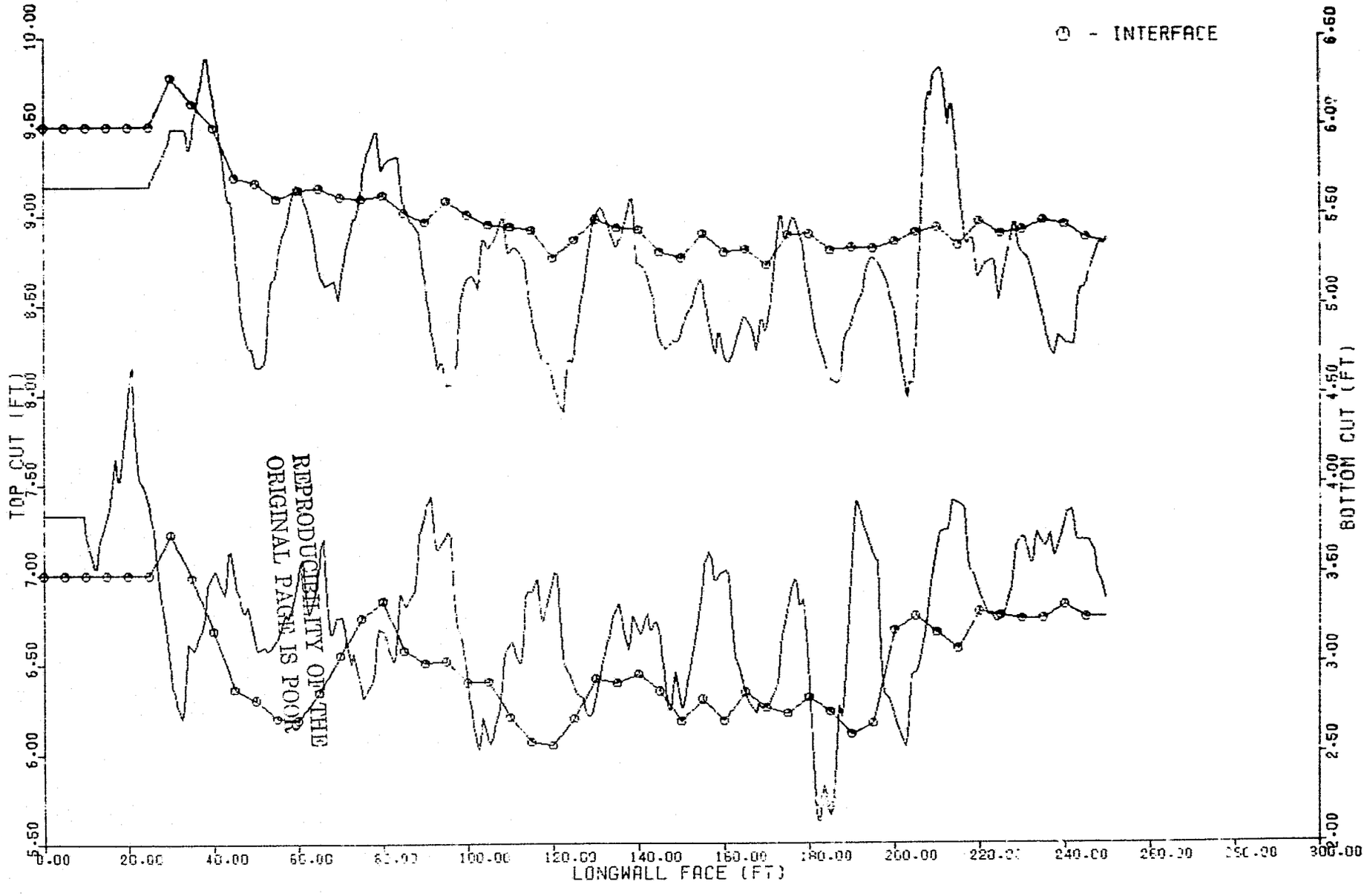

Figure 3-45. VCS Performance with 10 Sec. CID Output Interval

Table 3-5. Effects of CID Noise

CID OUTPUT INTERVAL (SEC)	NUCLEONIC CID		NATURAL RADIATION CID (3")		NATURAL RADIATION CID (5")	
	RMS (IN.)	% TIR	RMS (IN.)	% TIR	RMS (IN.)	% TIR
0.1	1.61	2.3	6.32	67.1	5.90	59.6
0.25	1.33	0.9	6.31	66.2	5.75	49.2
0.5	1.36	2.0	5.66	54.2	3.23	12.2
1.0	1.53	2.5	3.44	18.8	2.09	5.4
2.0	2.34	5.7	2.28	6.6	2.76	5.9
5.0	3.96	23.1	3.44	14.3	3.17	12.0

(1) 4 IN. BIAS

(2) NO ACTUATOR

interval. The natural radiation sensors have their best performance at 2 and 1 s for the 3 and 5 in. sensors, respectively. The nucleonic CID is better over all, having an rms error of 1.33 in. as opposed to an rms error of 2.09 in. for the 5 in. natural radiation sensor. Figures 3-46 through 3-50 show the nucleonic sensor at 0.25, 1, and 2 s output interval, and the 3 and 5 in. natural radiation sensors at their maximum performance points.

3.4.2.4 VCS Performance in Different Mines

The statistical data shown in Table 3-2 and discussed in Section 3.2.7 show that, statistically, the mines surveyed are quite similar. Several of the previous runs were made on both the Robinson Run and York Canyon mines. A comparison of results between the two mines is shown in Table 3-6. It can be seen that the VCS performance in the cases shown is very similar. The differences are due, essentially, to the differences between the mines, as shown in Table 3-7. The conclusion is therefore that VCS performance is affected very little by the mine in which it operates. However, mines which are statistically rougher will show a slightly worse performance than will smoother mines. Figures 3-51 and 3-52 show VCS performance with a 2.5 ft CID displacement and a 1 s output interval for the York Canyon and Robinson Run mines, respectively.

3.4.2.5 Effects of Nonlinear CID Calibration Curve

The calibration curves for both types of proportional CIDs are not linear in their relationship between coal depth and number of counts received. For both sensors, the curves flatten out at larger coal depths. Variation in the number of counts received in a given interval at the larger depths has a greater effect and produces larger depth errors than does the same variation at smaller coal depths. This effect is shown in Table 3-7. It can be seen that at a 1 s output

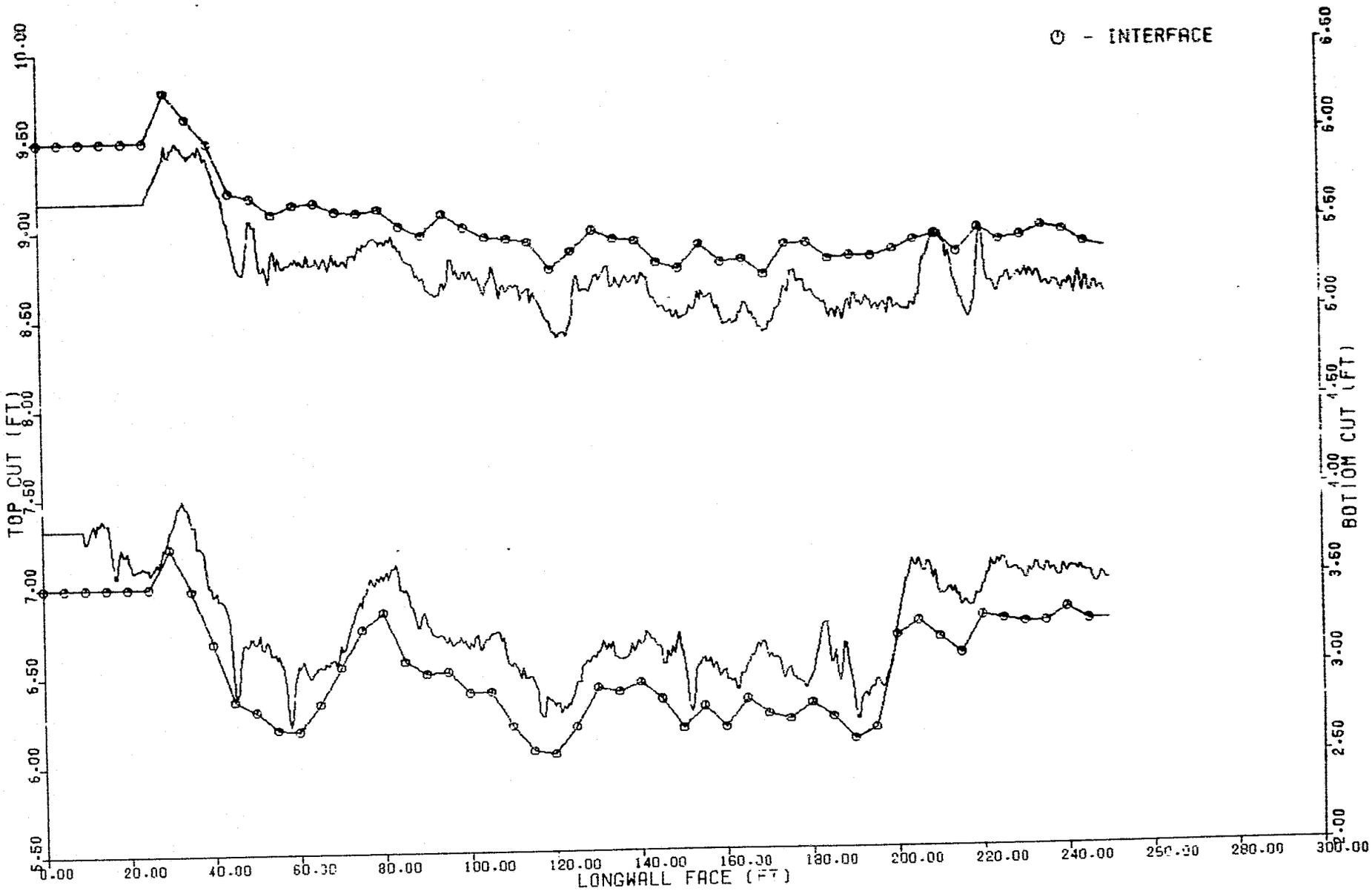

Figure 3-46. Performance with Nucleonic Sensor at 0.25 Sec. Output Interval with Noise

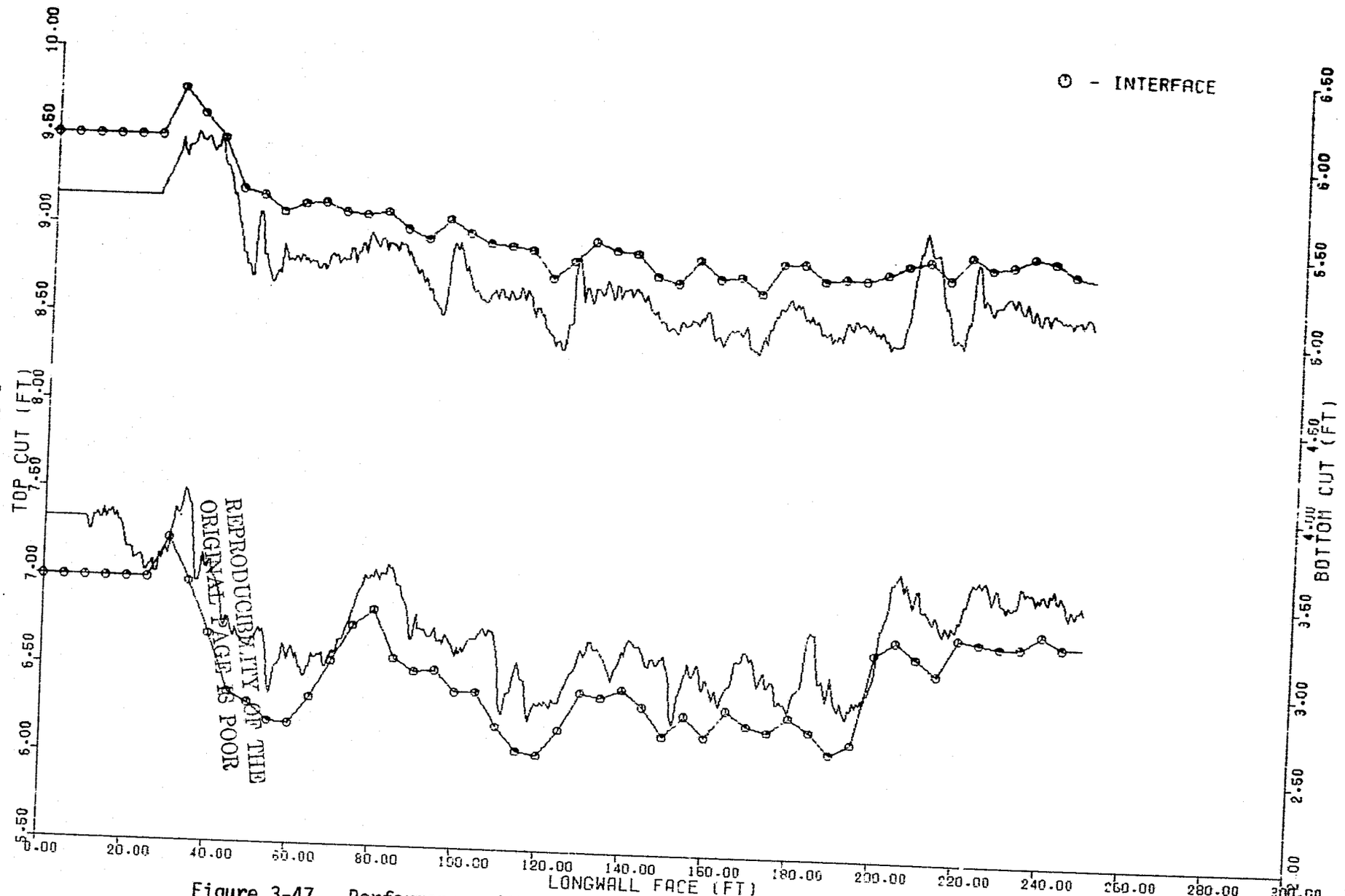

Figure 3-47. Performance with Nucleonic Sensor at 1.0 Sec. Output Interval with Noise

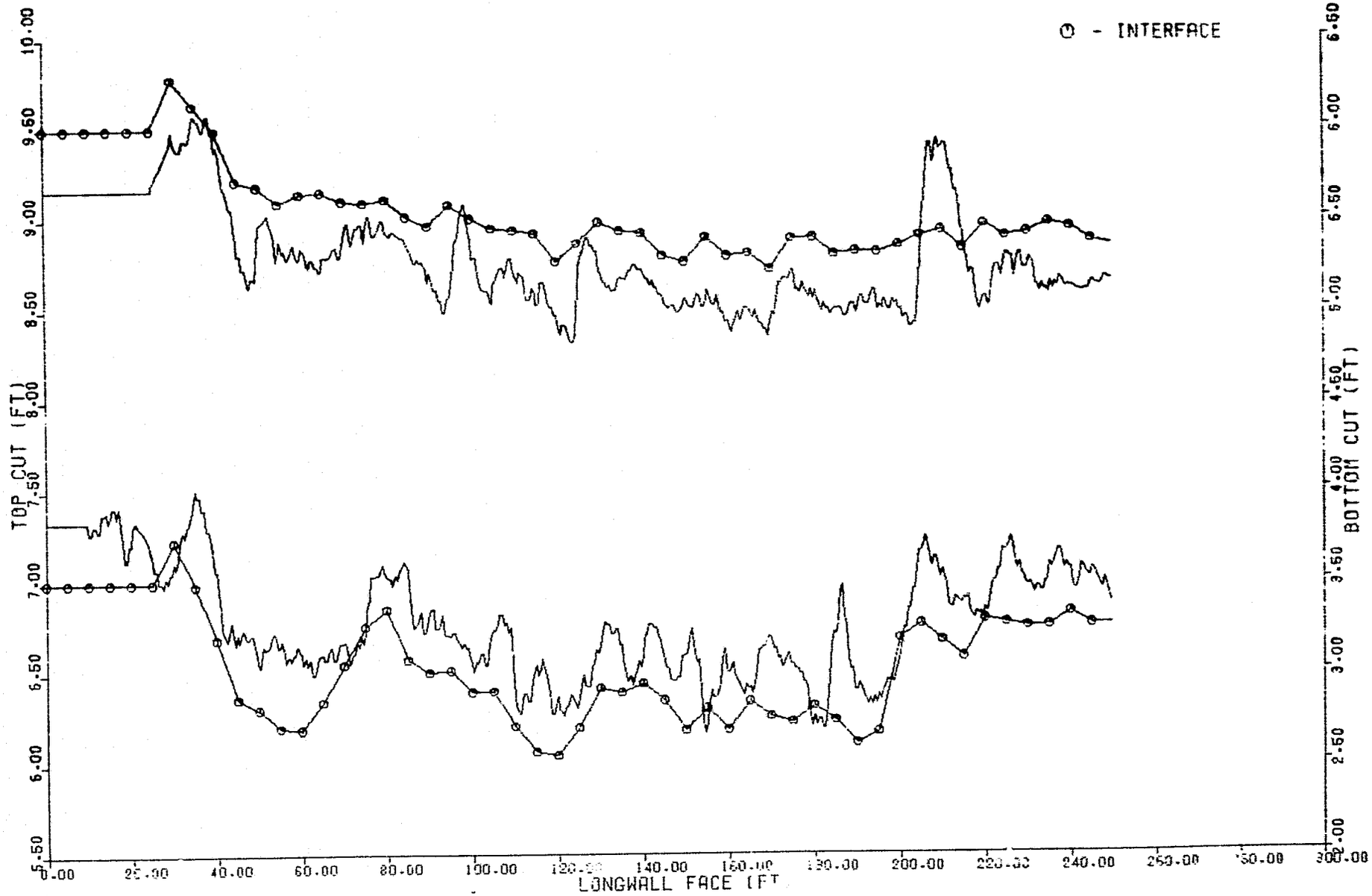

Figure 3-48. Performance with Nucleonic Sensor at 2.0 Sec. Output Interval with Noise

PERFORMANCE EVALUATION PASS 1

TOTAL COAL TAKEN = 3024.286 CU. FT.

AVERAGE CUT HIGHT = 5.486 FT.

CUT STANDARD DEVIATION = 0.294 FT.

FLOOR

RMS ERROR = 2.592 IN.

AVERAGE ABSOLUTE ERROR = 1.939 IN.

VOLUME EXCESS COAL LEFT = 24.535 CU. FT. (0.81%)

VOLUME EXCESS COAL TAKEN = 56.827 CU. FT. (1.88%)

VOLUME ROCK TAKEN = 7.693 CU. FT. (0.25%)

TIME IN ROCK = 9.98%

ROOF

RMS ERROR = 2.283 IN.

AVERAGE ABSOLUTE ERROR = 1.559 IN.

VOLUME EXCESS COAL LEFT = 15.569 CU. FT. (0.51%)

VOLUME EXCESS COAL TAKEN = 47.851 CU. FT. (1.58%)

VOLUME ROCK TAKEN = 8.175 CU. FT. (0.27%)

TIME IN ROCK = 6.58%

Figure 3-49. Performance with 3 In. Natural Radiation Sensor at a 2 Sec. Output Interval with Noise

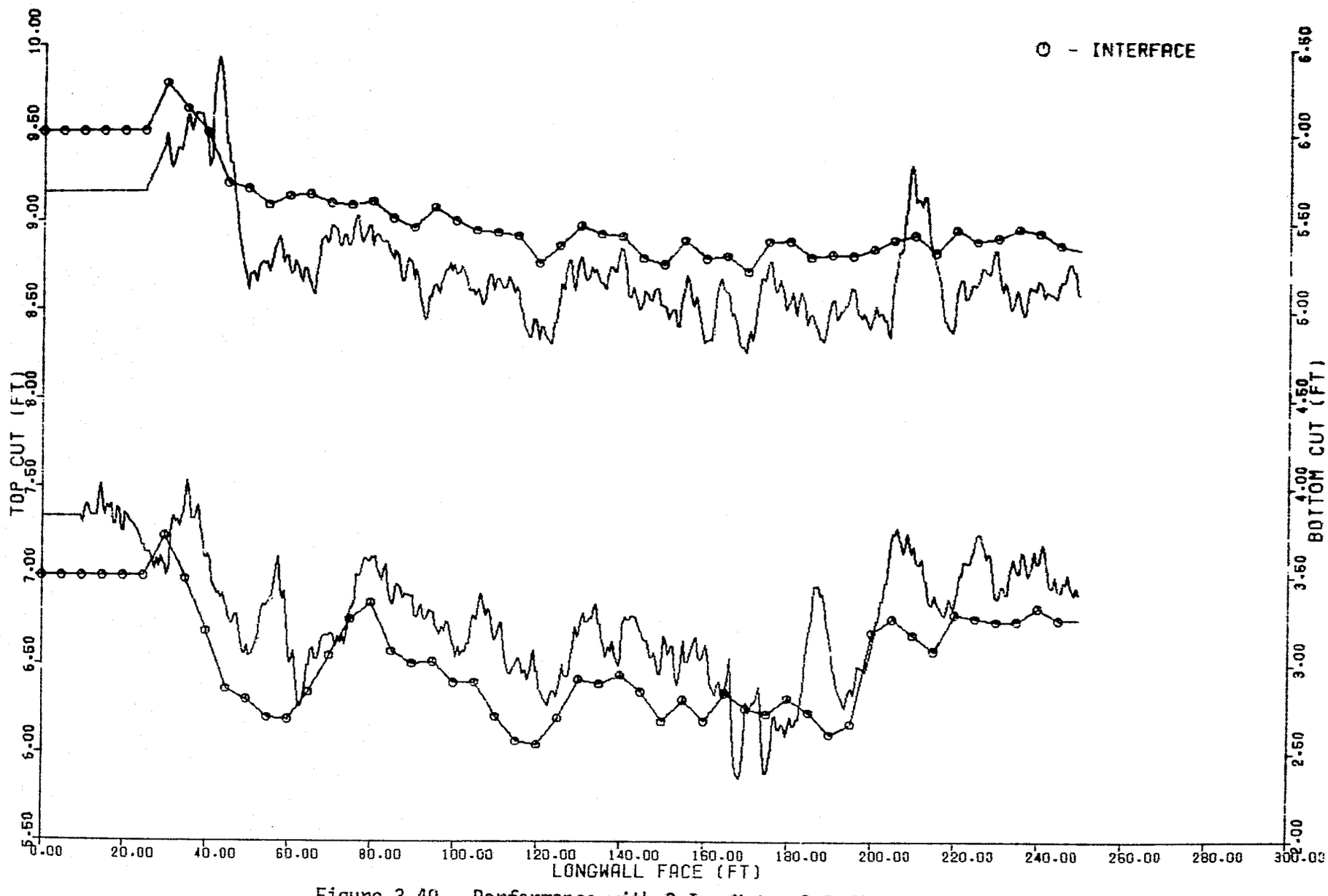

Figure 3-49. Performance with 3 In. Natural Radiation Sensor at a 2 Sec. Output Interval with Noise (Concluded)

PERFORMANCE EVALUATION

PASS 1

TOTAL COAL TAKEN = 3030.354 CU. FT.

AVERAGE CUT HIGHT = 5.497 FT.

CUT STANDARD DEVIATION = 0.289 FT.

FLOOR

RMS ERROR = 2.333 IN.

AVERAGE ABSOLUTE ERROR = 1.558 IN.

VOLUME EXCESS COAL LEFT = 13.022 CU. FT. (0.43%)

VOLUME EXCESS COAL TAKEN = 49.568 CU. FT. (1.64%)

VOLUME ROCK TAKEN = 8.999 CU. FT. (0.30%)

TIME IN ROCK = 6.58%

ROOF

RMS ERROR = 2.085 IN.

AVERAGE ABSOLUTE ERROR = 1.379 IN.

VOLUME EXCESS COAL LEFT = 11.192 CU. FT. (0.37%)

VOLUME EXCESS COAL TAKEN = 45.735 CU. FT. (1.51%)

VOLUME ROCK TAKEN = 6.424 CU. FT. (0.21%)

TIME IN ROCK = 5.44%

Figure 3-50. Performance with 5 In. Natural Radiation Sensor at a 1 Sec. Output Interval with Noise

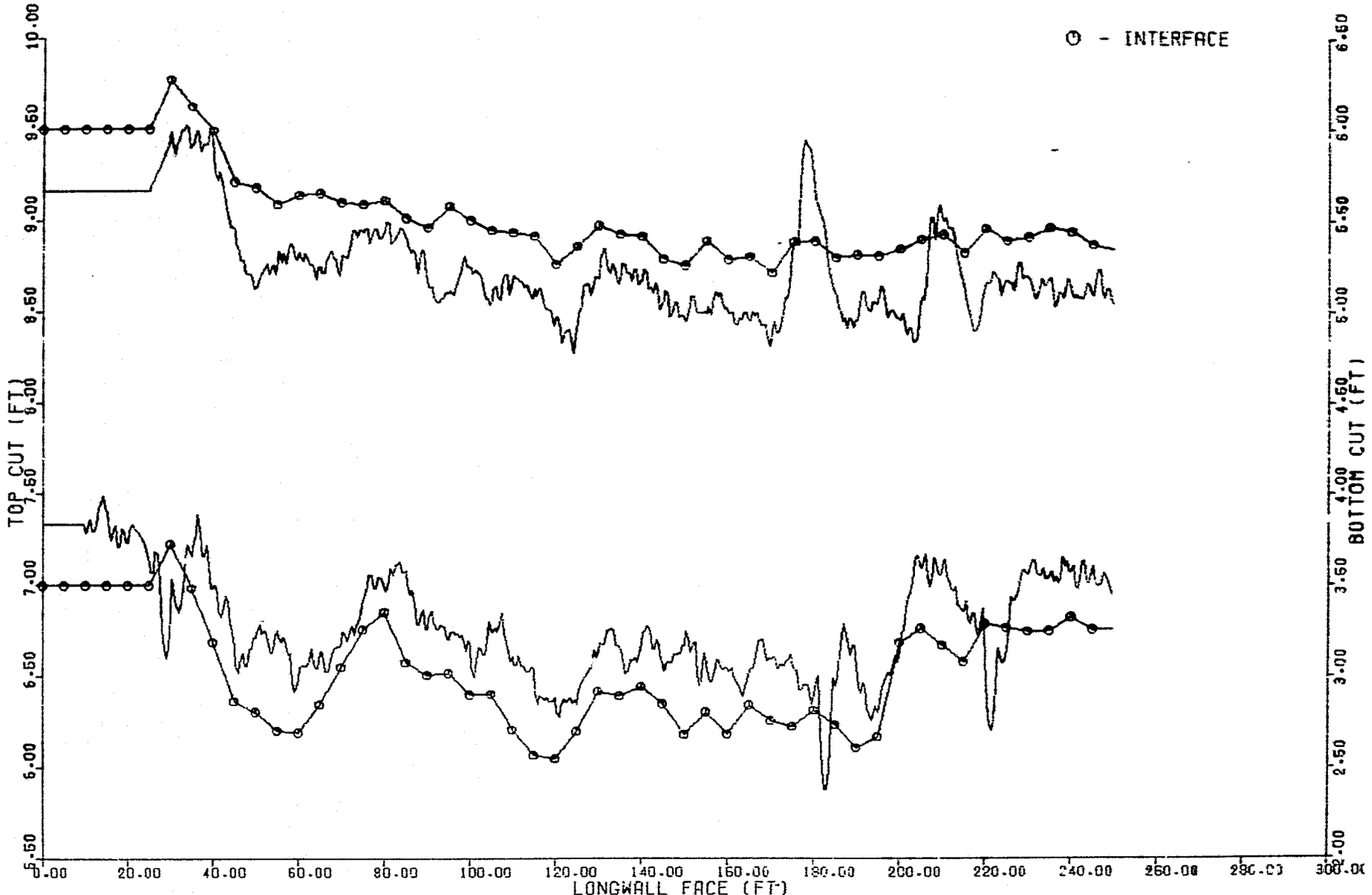

Figure 3-50. Performance with 5 In. Natural Radiation Sensor at a 1 Sec. Output Interval with Noise (Concluded)

Table 3-6. Comparison of Performance on Different Mines

CONDITIONS		YORK CANYON RMS TOP ERROR (IN.)	ROBINSON RUN RMS TOP ERROR (IN.)
CID DISPLACEMENT (FT)	0.75	0.33	0.37
	1.5	0.63	0.71
	2.5	1.00	1.16
(C) CID OUTPUT INTERVAL (SEC)	1	1.20	1.65
	2	1.72	2.26
	5	3.30	3.56

(A) NO NOISE

(B) 4 IN. BIAS

(C) 2.5 FT CID DISPLACEMENT

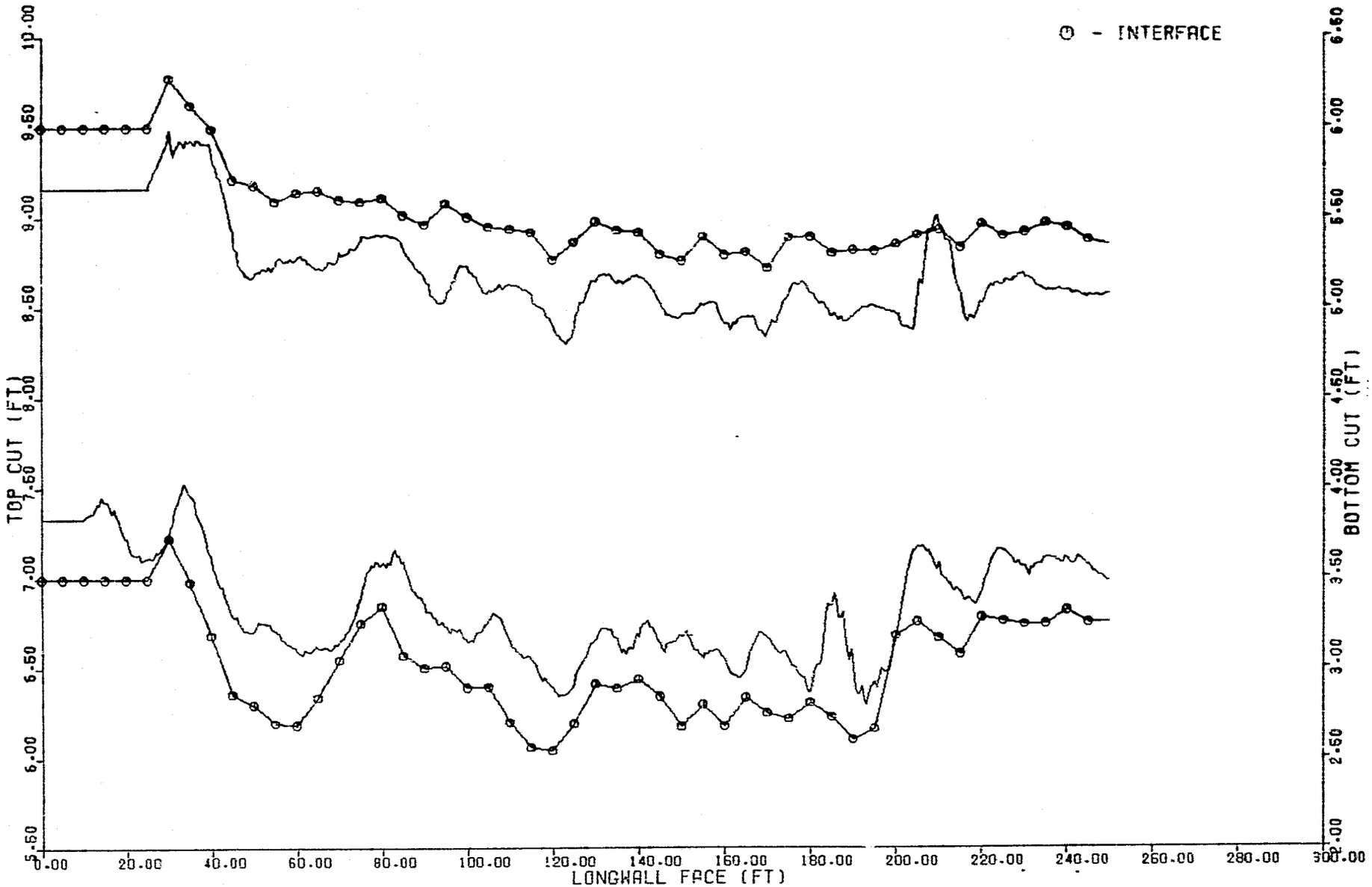

Figure 3-51. VCS Performance in the York Canyon Mine

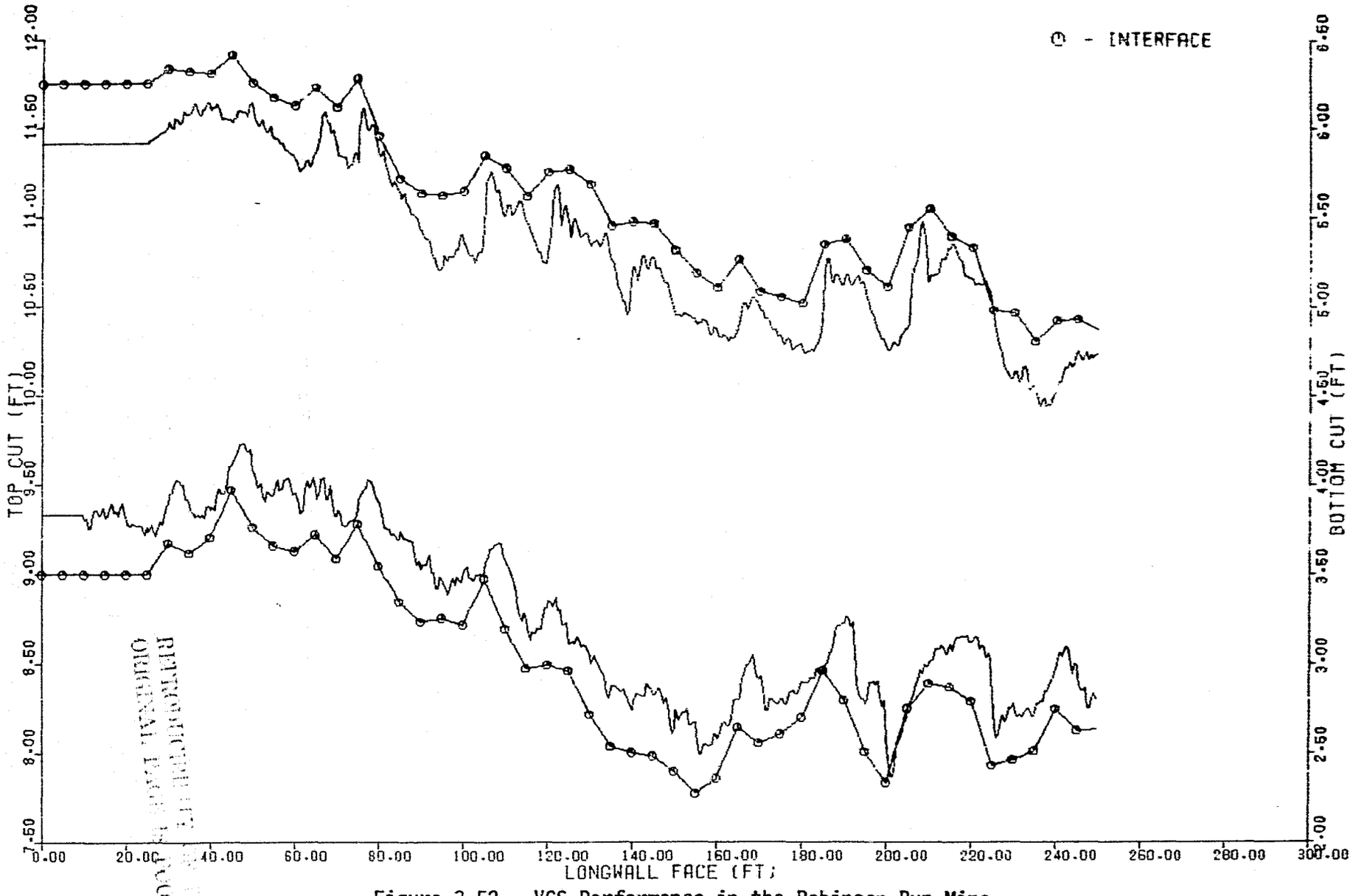

Figure 3-52. VCS Performance in the Robinson Run Mine

Table 3-7. Effects of Nonlinear CID Calibration Curve

CID OUTPUT INTERVAL (SEC)	RMS TOP ERROR (IN.)	RMS BOTTOM ERROR (IN.)	BIAS
1	1.53	1.61	4 IN.
2	2.34	2.18	
5	3.96	4.22	
1	2.46	2.39	6 IN.
2	2.59	2.84	
5	3.9	4.40	

(A) YORK CANYON MINE

(B) WITH NOISE

(C) 2.5 FT CID DISPLACEMENT

interval, there is a 61% increase in rms error by going from a 4 to a 6 in. bias. The increase in error is not so evident at larger output intervals since the dominant effect there is the delay between outputs.

These results show that reasonable performance is obtained up to a 4 to 5 in. bias. Results for larger biases will be worse because of the sensor nonlinearities. Figure 3-53 shows the VCS performance with a 6 in. bias.

3.4.2.6 Performance With Various Control Laws

The performance of various VCS control configurations is shown in Table 3-8. These control laws were discussed in detail in Section 3.2.6. Table 3-8 indicates the rms errors and the percent time in rock. Comparisons of the data show that the CID, pick, and LCF offer the best performance, showing a significant improvement over the CID sensor only. The sensor used here was the nucleonic CID. The penetrometer performance appears satisfactory, but is made to look better because of the limiting effects of the LCF. The CID and LCF offer similar performance to the CID, pick, and LCF at 2 and 4 in. biases, but at 0 and 1 in. biases, they have a larger rms error and spend more time in rock without the pick sensor. Figures 3-54 through 3-58 illustrate the results of the five control laws for a 2 in. bias.

Table 3-9 demonstrates the effect on performance of introducing errors in the pick sensor data. The CID and pick combination is affected somewhat more than the CID, pick and LCF, with the latter essentially unaffected by pick errors. It can also be seen in Table 3-9 that there is little difference between the performance with

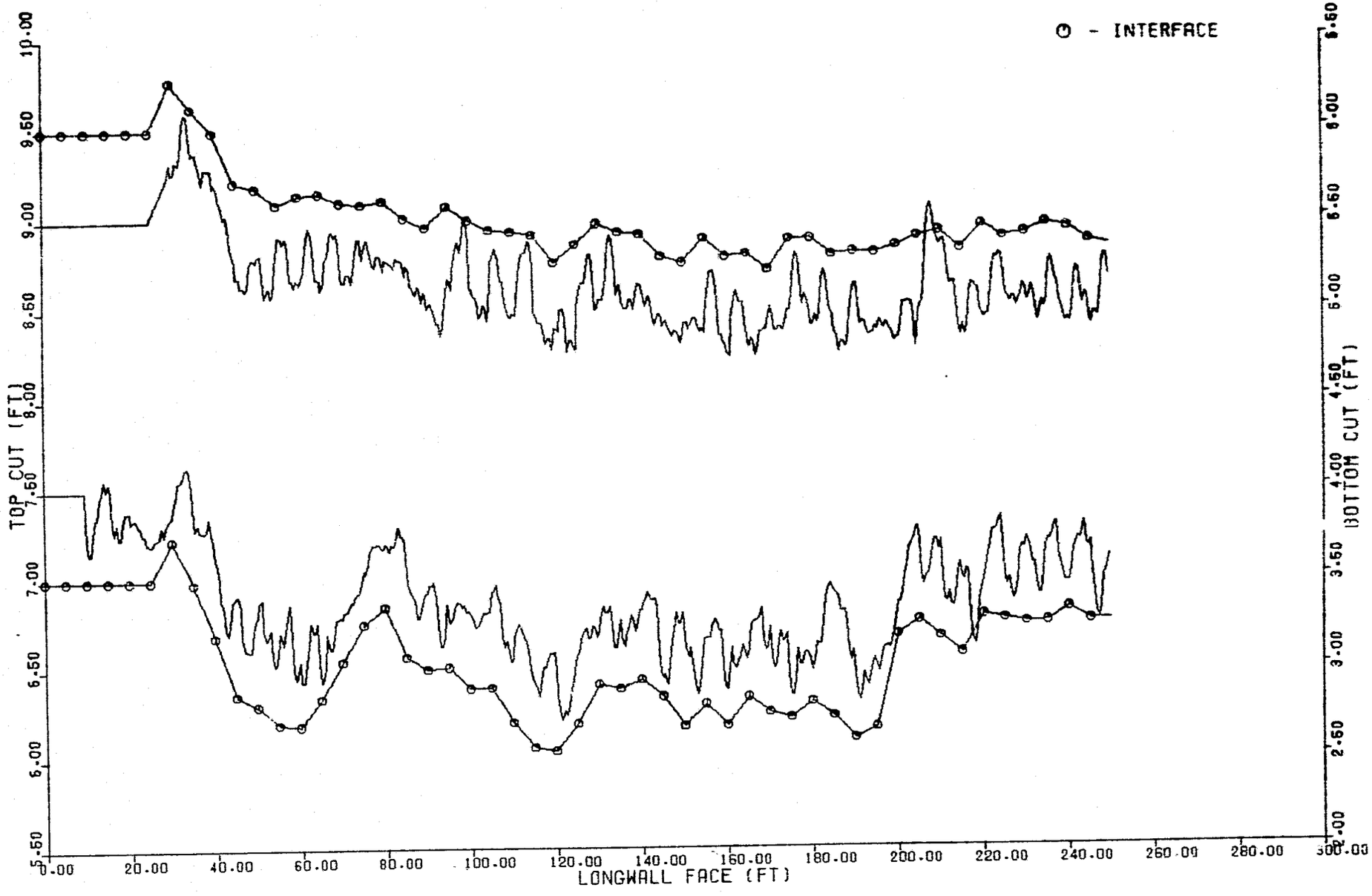

Figure 3-53. VCS Performance with a 6 In. Bias

Table 3-8. VCS Control Law Comparison

BIAS (IN.)	CID		CID, LCF		CID, PICK		CID, PICK, LCF		CID, PENETROMETER, LCF	
	RMS (IN.)	% TIR	RMS (IN.)	% TIR	RMS (IN.)	% TIR	RMS (IN.)	% TIR	RMS (IN.)	% TIR
0	9.25	99.8	1.37	83.9	2.05	64.9	1.07	61.2	1.26	49.6
1	2.30	41.0	1.09	35.2	1.24	29.5	0.96	25.6	1.03	27.5
2	1.67	14.3	1.07	3.0	1.29	8.6	1.05	1.6	1.05	2.3
4	1.53	2.5	1.12	0.0	1.40	1.4	1.12	0.0	1.13	0.0

(1) NOISE ON CID

(2) PICK AND PENETROMETER 100% CORRECT

(3) PENETROMETER AT CID LOCATION

(4) TIR = TIME IN ROCK

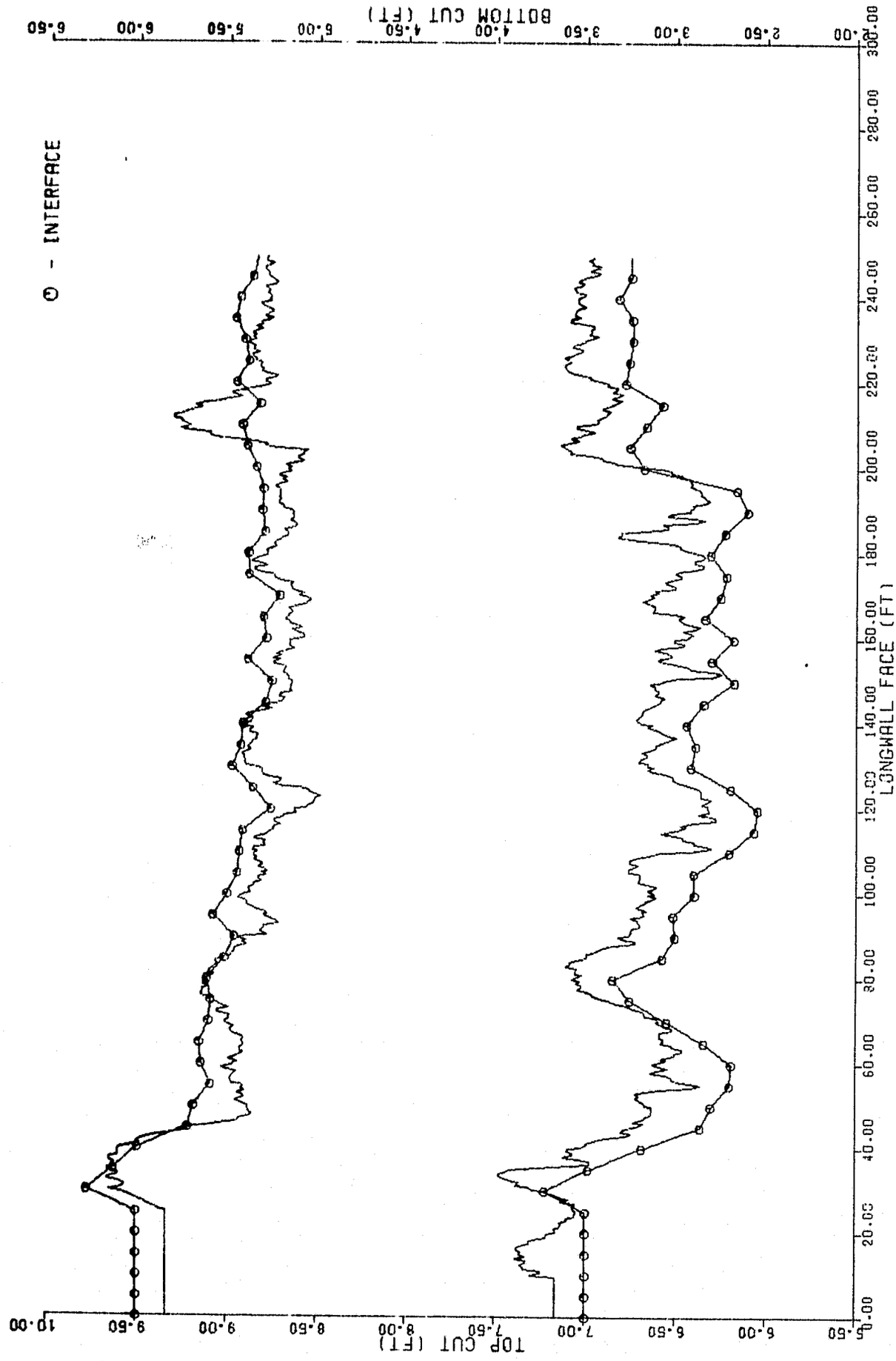

Figure 3-54. VCS Performance with CID Control Law Leaving a 2 In. Bias

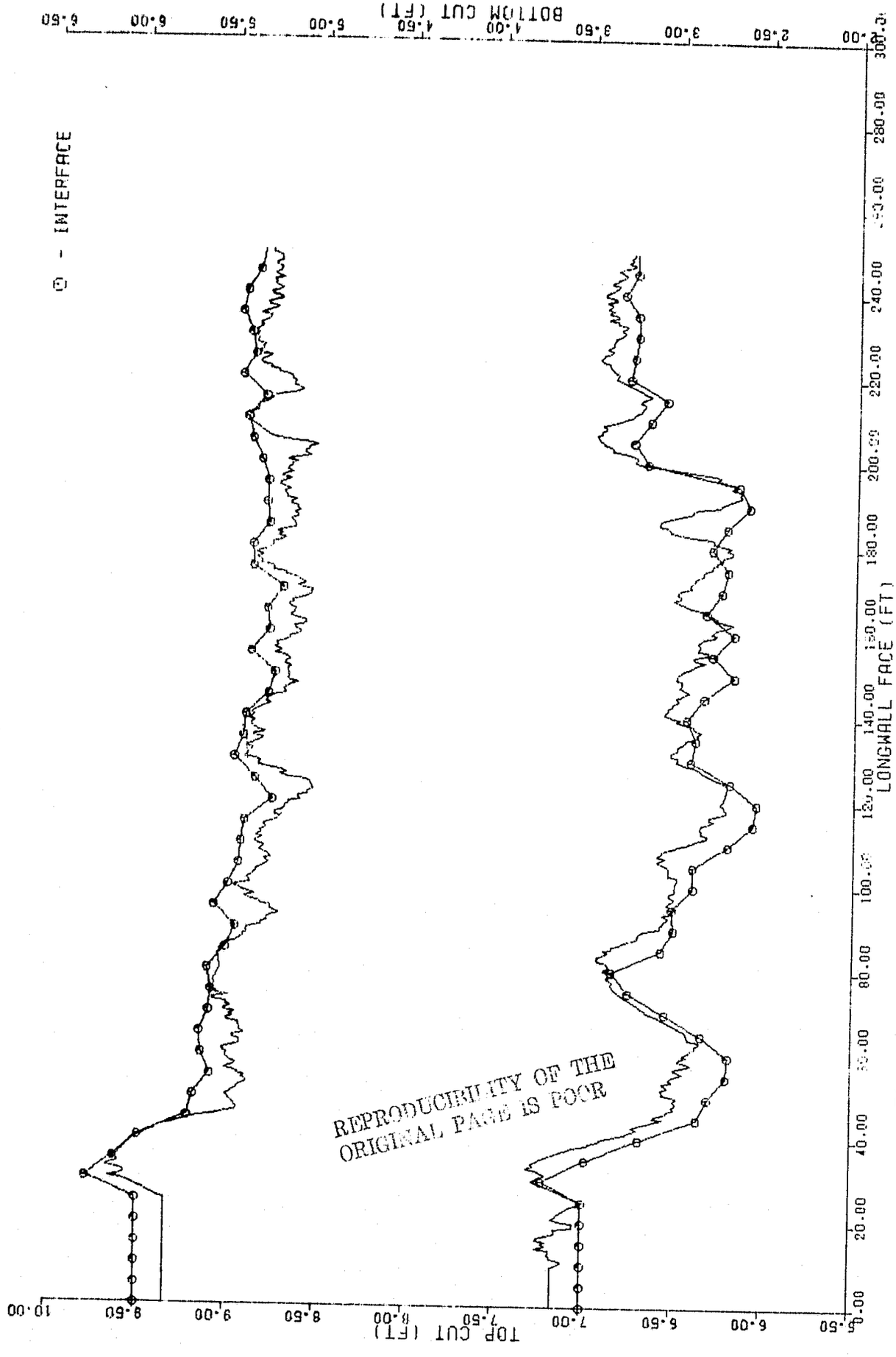

Figure 3-55. VCS Performance with CID & LCF Control Law Leaving a 2 In. Bias

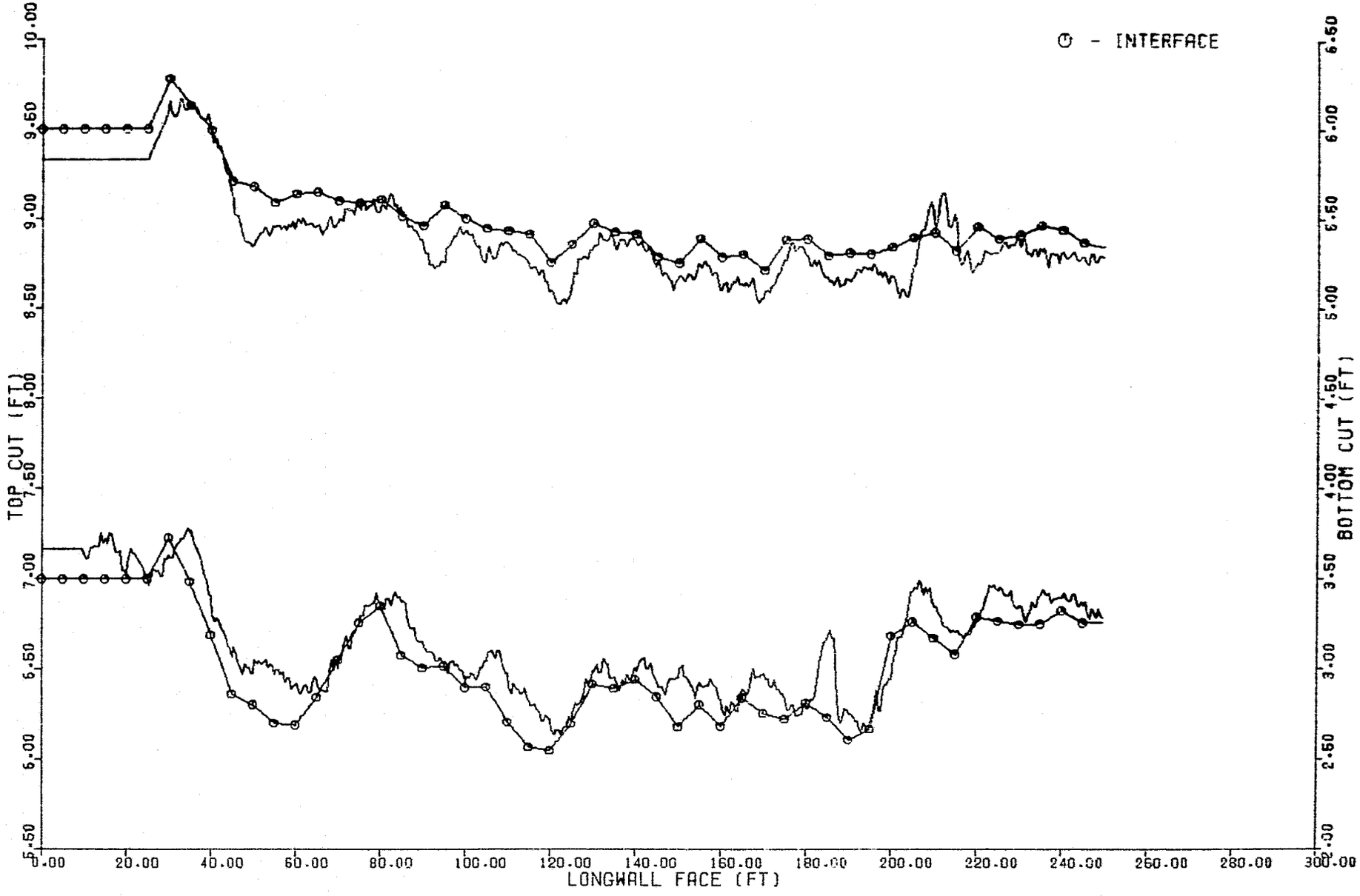

Figure 3-56. VCS Performance with CID & Pick Control Law Leaving a 2 In. Bias

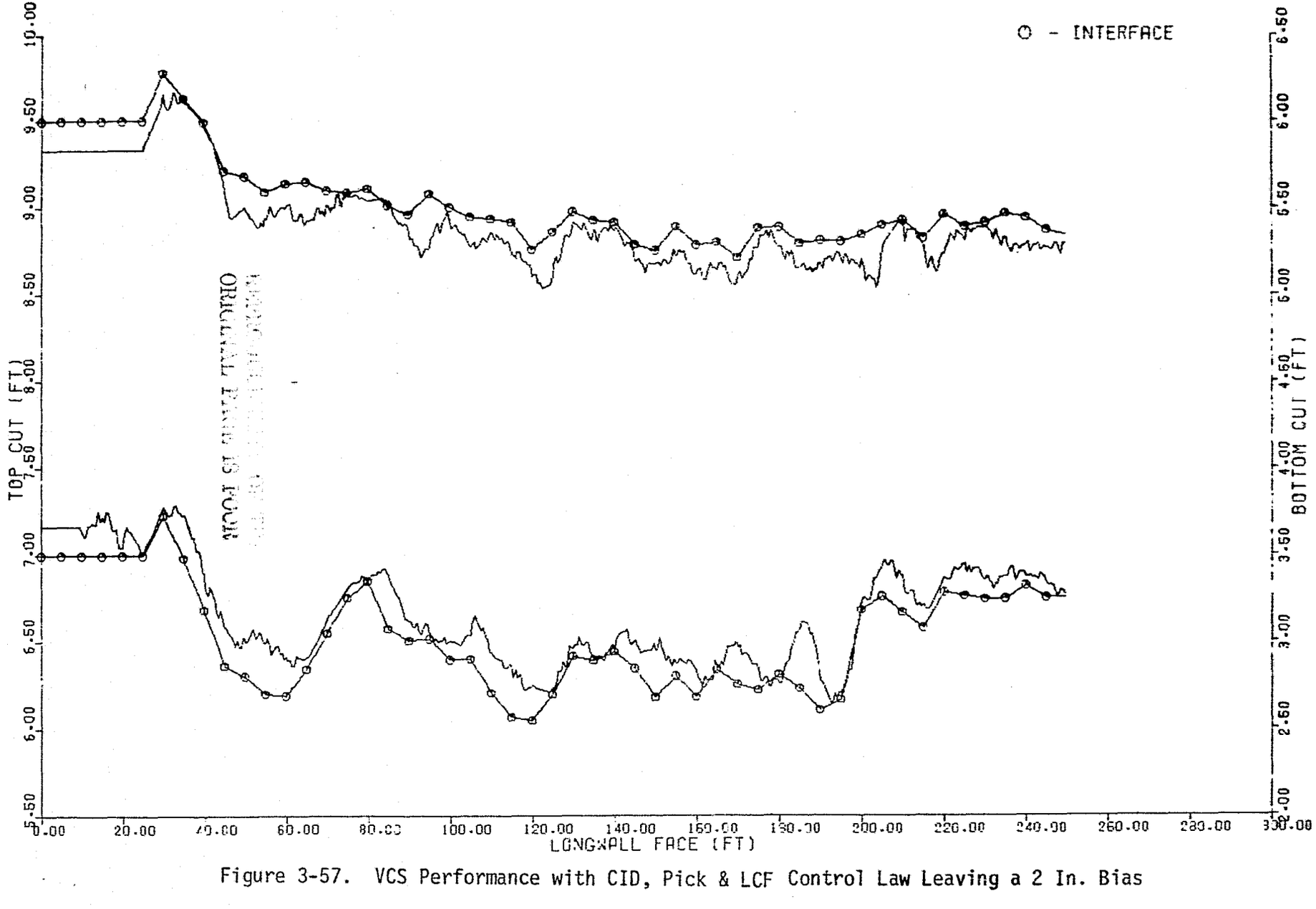

Figure 3-57. VCS Performance with CID, Pick & LCF Control Law Leaving a 2 In. Bias

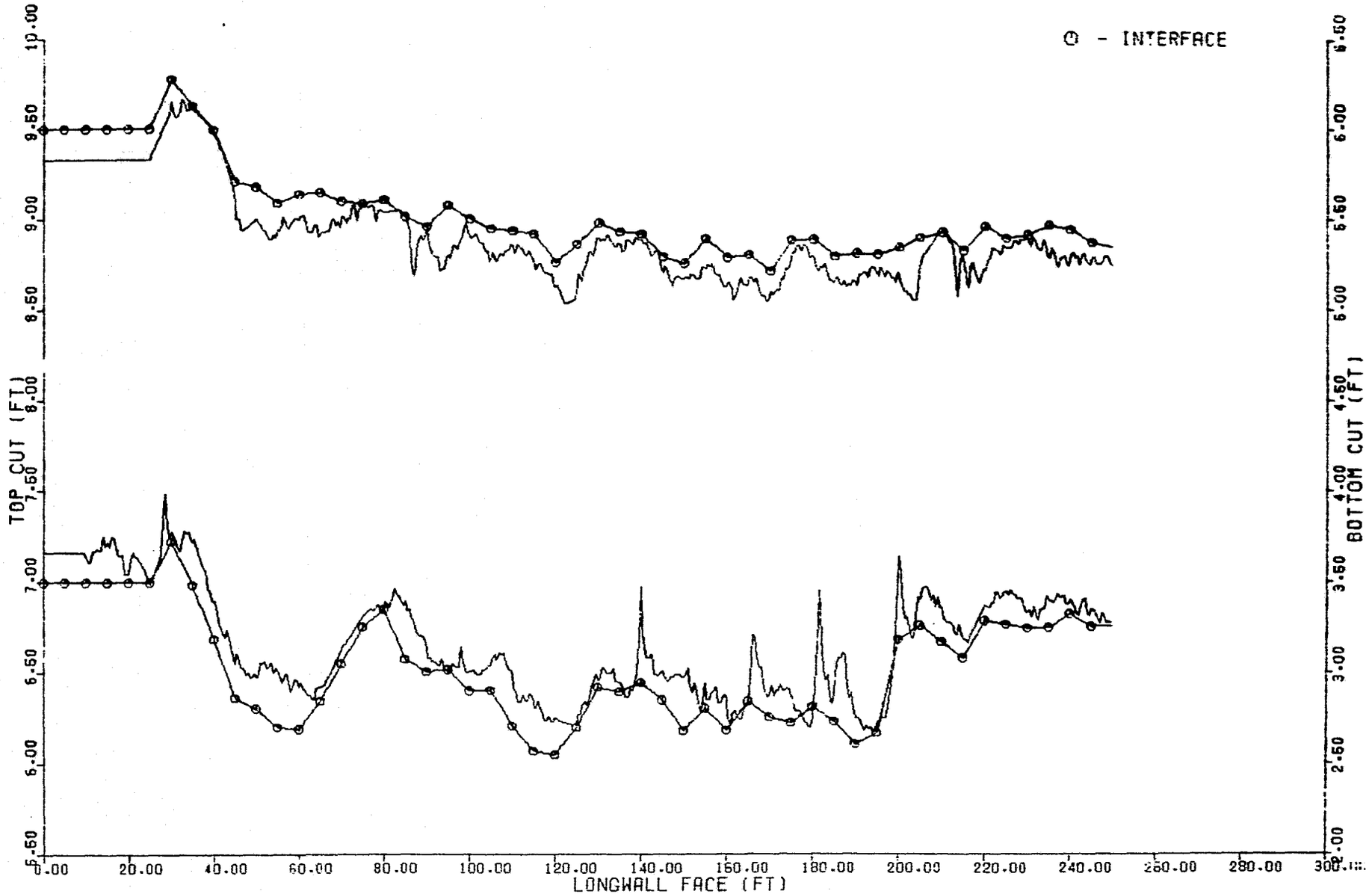

Figure 3-58. VCS Performance with CID, Penetrometer & LCF Control Law Leaving a 2 In. Bias

Table 3-9. Effects of Sensitized Pick Errors

BIAS (IN.)	CID, PICK (90%)		CID, PICK (80%)		CID, LCF, PICK (90%)		CID, LCF, PICK (80%)	
	RMS (IN.)	% TIR	RMS (IN.)	% TIR	RMS (IN.)	% TIR	RMS (IN.)	% TIR
1	1.47	30.6	1.85	31.1	0.99	25.4	0.99	26.1
2	1.47	10.7	1.46	9.5	1.05	1.2	1.08	1.6
4	1.44	1.6	1.44	1.6	1.12	0.0	1.12	0.0

80 and 90% correct pick data. Figures 3-59 through 3-62 show the CID, pick, and the CID, pick, and LCF performance at a 2 in. bias with 90 and 80% pick errors, respectively.

3.4.2.7 Performance With Discrete CID Control

The discrete sensors, when used alone, provide a means of taking all the coal and cutting to the CSI. The control law used for the pick or penetrometer-reflectometer was discussed in Section 3.2.6. Results of simulation studies using picks only or a penetrometer-reflectometer and an LCF are given in Table 3-10. Performance with the pick control shows that excellent results are obtained with 100% correct picks. Performance degrades as the percent correctness decreases, but is still acceptable for values between 80 and 90 percent. The percent TIR appears very large for this control configuration, but the percent rock, also shown in Table 3-10, indicates that only a small volume of rock was actually taken. The pick sensors must contact rock to produce a change in their output state, and thus be able to control. As a result, the pick sensors are in contact with the rock a large percentage of the time, but take very little rock.

The penetrometer-reflectometer control was implemented in the same manner as the picks. While the cutting error does not appear excessive, the performance is unacceptable. Because the sensor is mounted behind the drum, and only outputs a discrete measurement, the VCS operates in a severe limit cycle. The LCF limits this behavior, producing what appears to be acceptable performance. However, when the penetrometer-reflectometer is used alone, as is also shown in Table 3-10, the resulting errors are very large. Figures 3-63 and 3-64 illustrate the pick control performance for 100 and 90% correctness while Figures 3-65 and 3-66 show corresponding runs with the penetrometer-reflectometer and LCF combination.

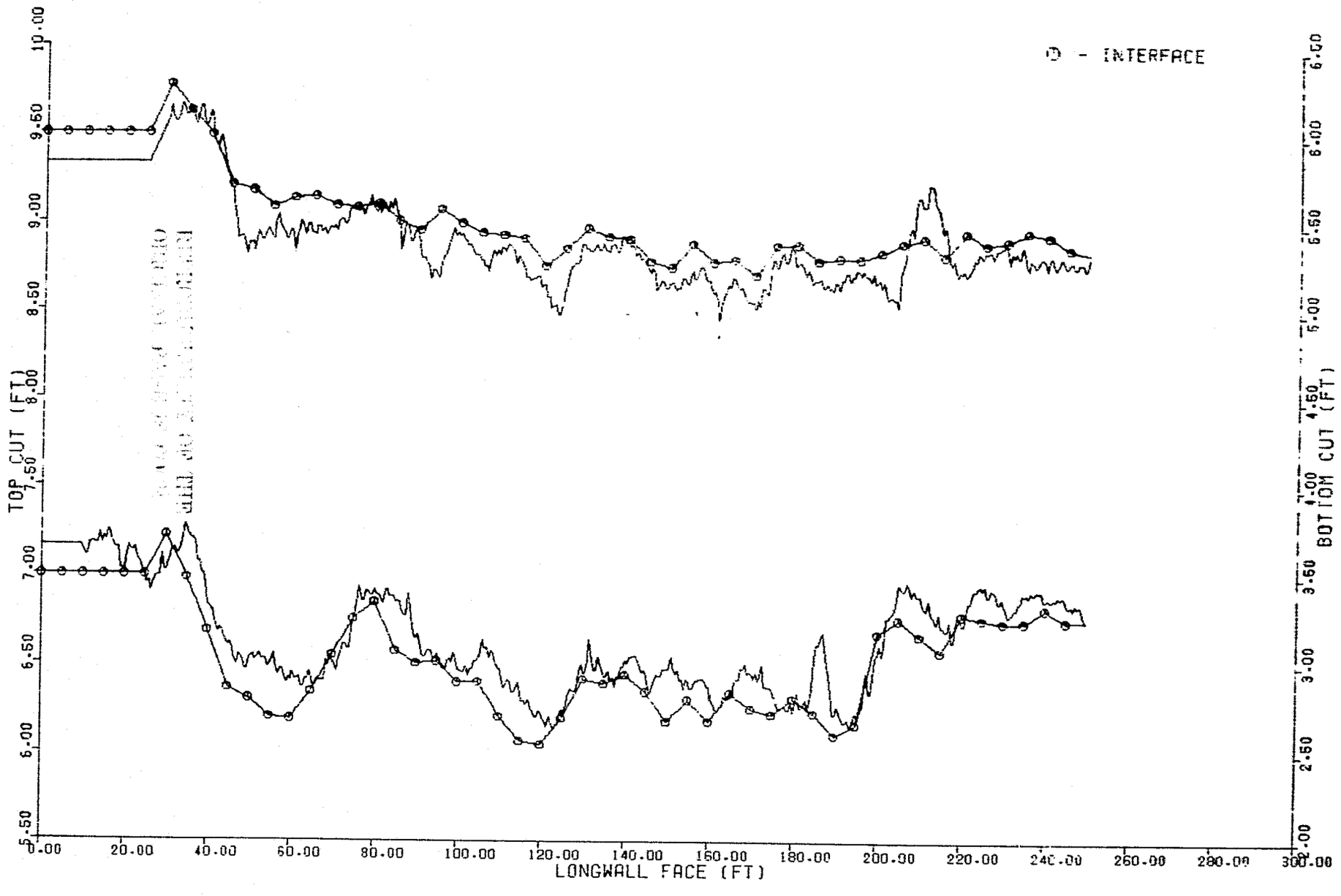

Figure 3-59. VCS Performance for CID, Pick Control Law with 90% Pick Errors for a 2 In. Bias

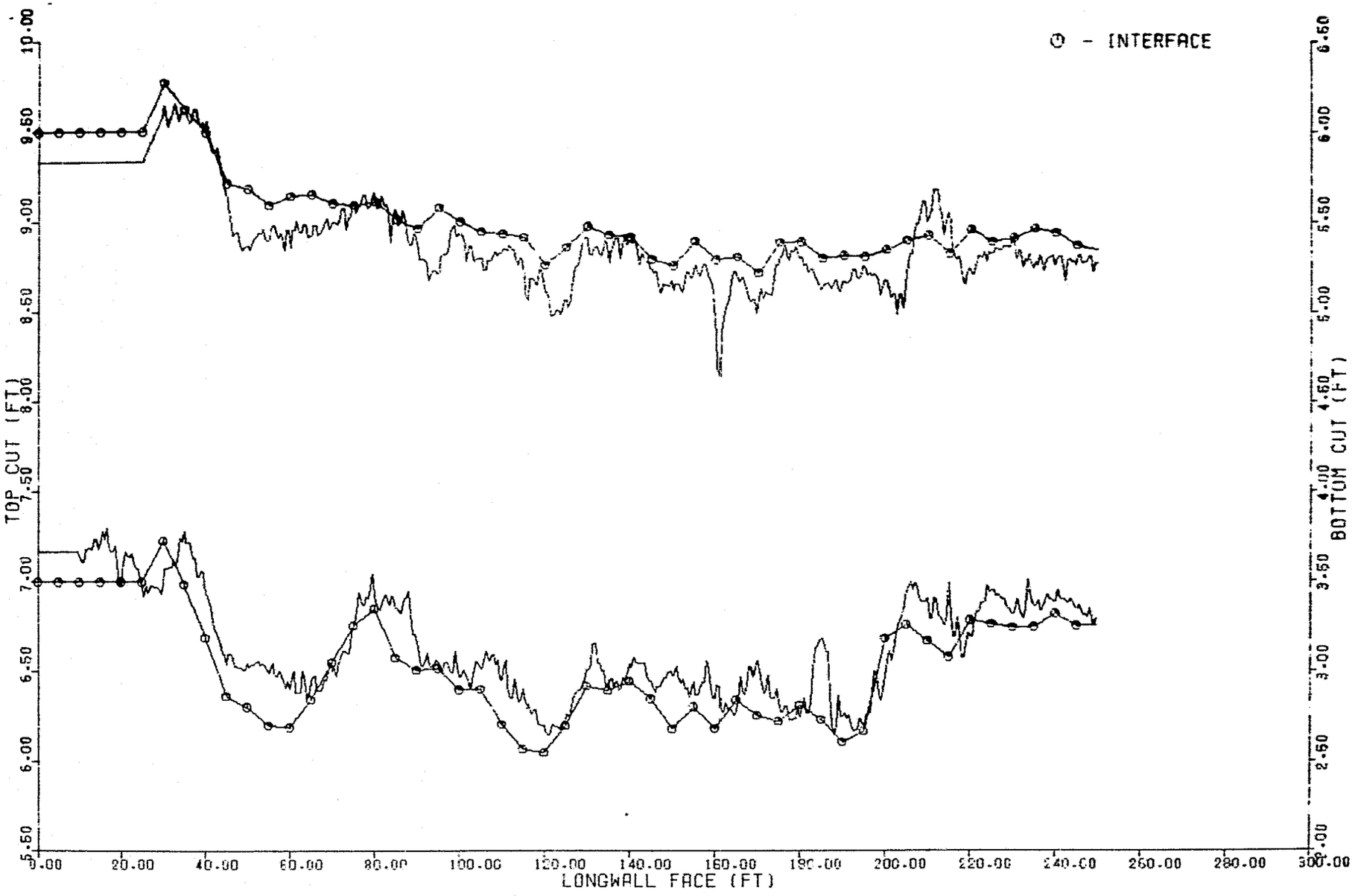

Figure 3-60. VCS Performance for CID, Pick Control Law with 80% Pick Errors for a 2 In. Bias

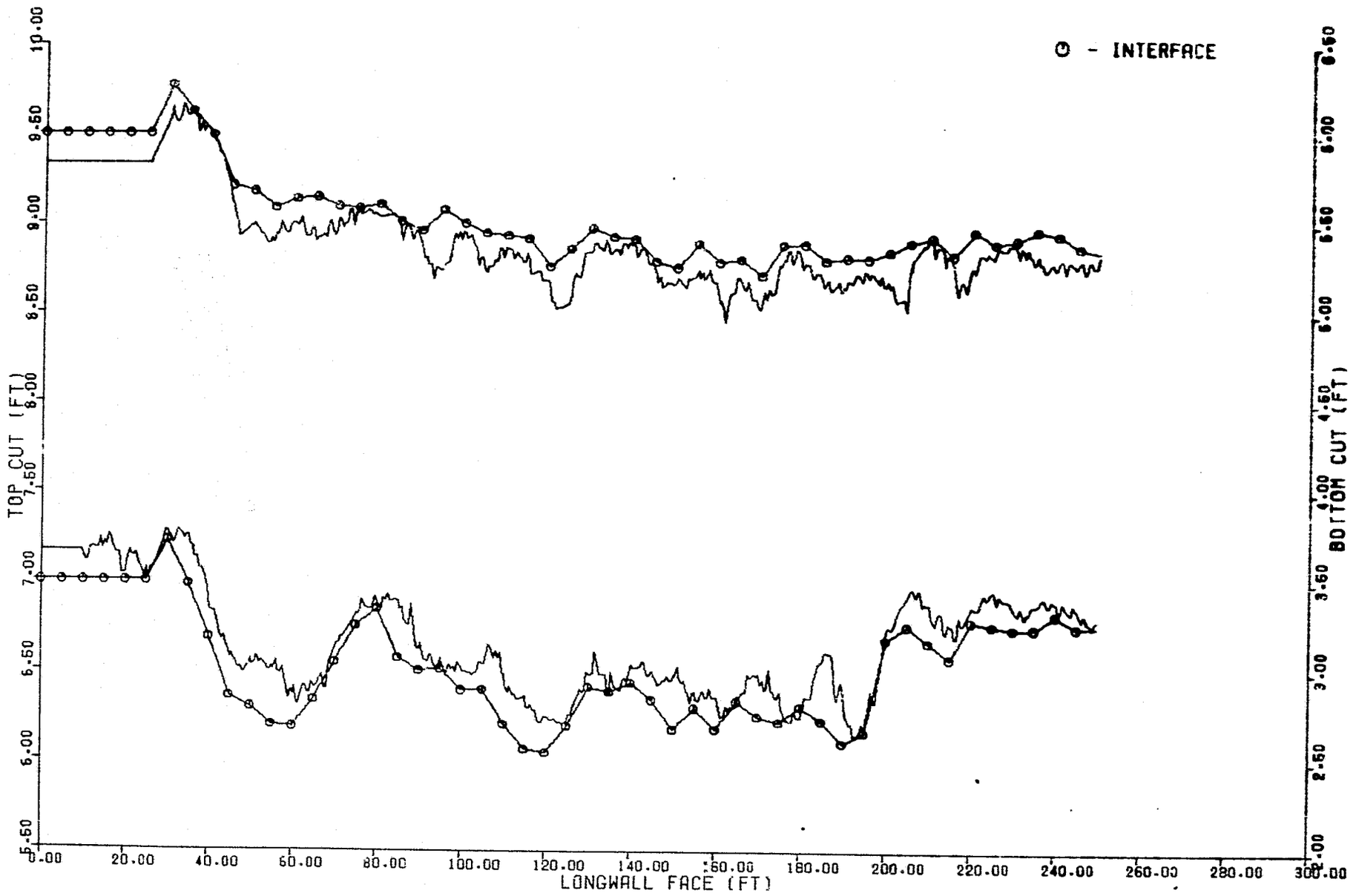

Figure 3-61. VCS Performance for CID, Pick and LCF Control Law with 90% Pick Error for a 2 In. Bias

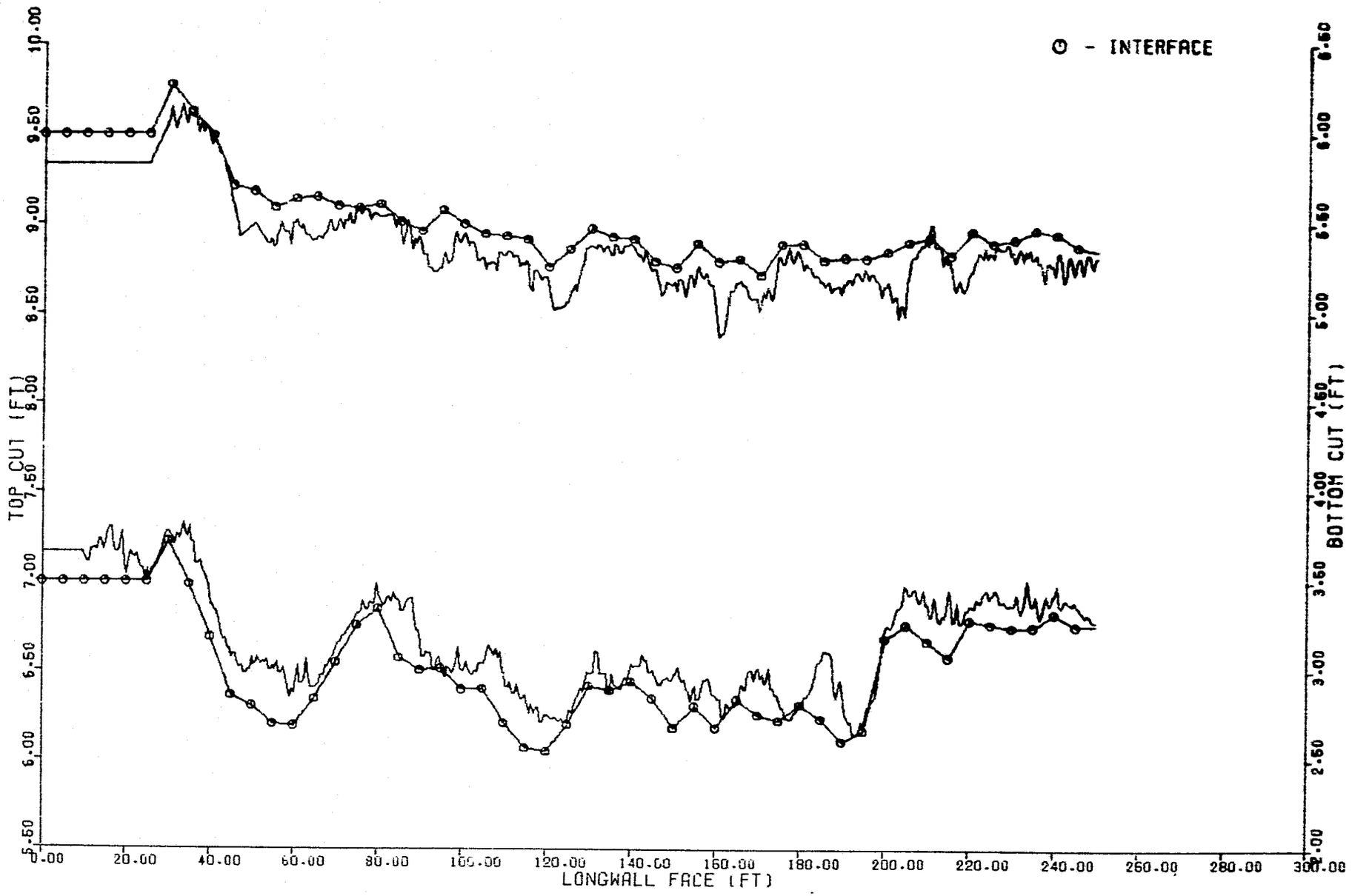

Figure 3-62. VCS Performance for CID Pick and LCF Control Law with 80% Pick Errors for a 2 In. Bias

Table 3-10. VCS Performance of Rock Presence Sensors Only

% CORRECT	PICKS			PENETROMETER & LCF	
	RMS (IN.)	% TIR	% ROCK	RMS (IN.)	% TIR
100	0.68	74.4	0.48	1.83 21.7*	63.5 70.5*
90	1.24	64.0	0.6	1.81	63.7
80	2.33	59.2	0.98	1.74	61.2

*PENETROMTER ONLY

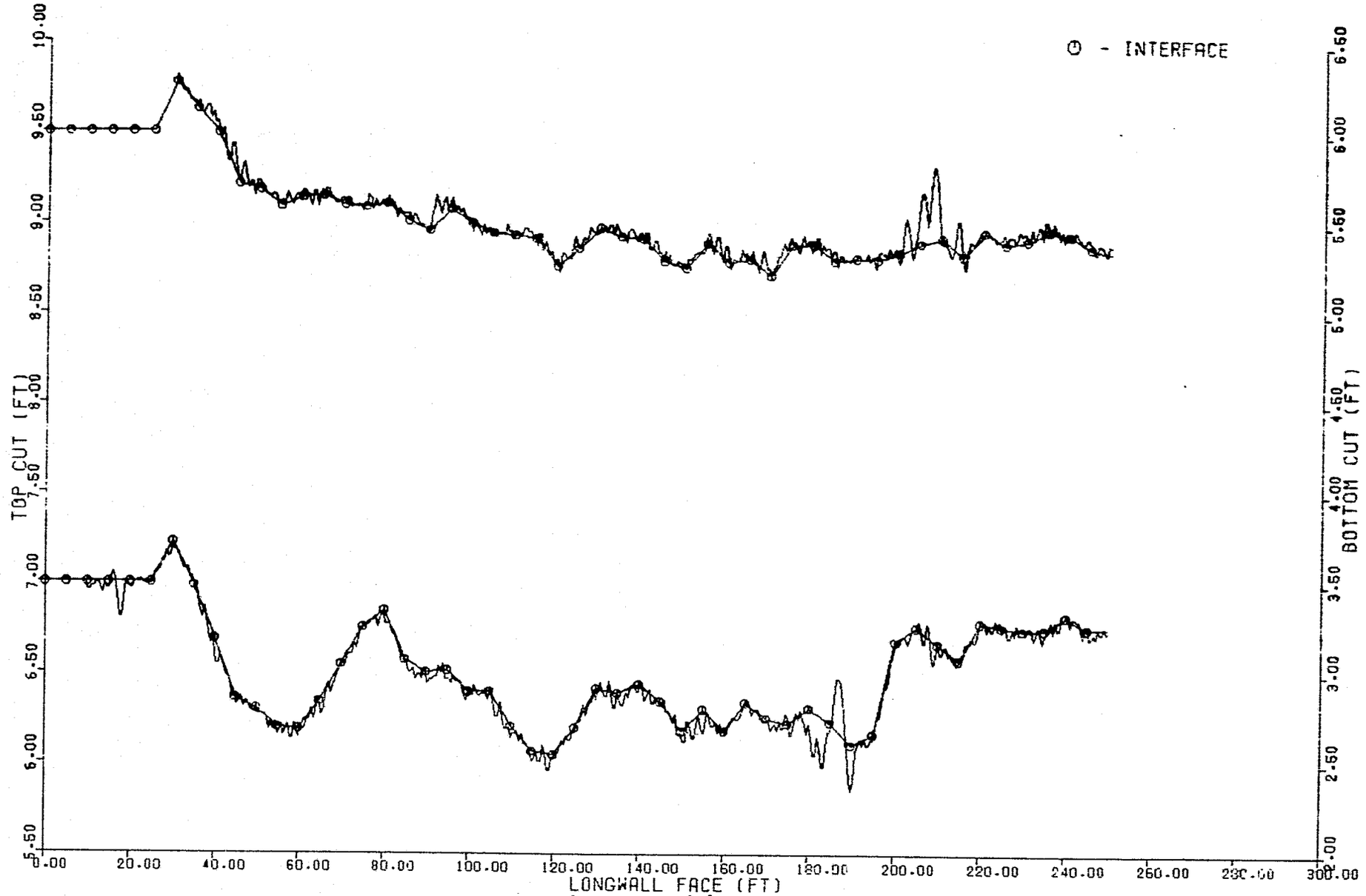

Figure 3-63. VCS Performance with 100% Correct Pick Control

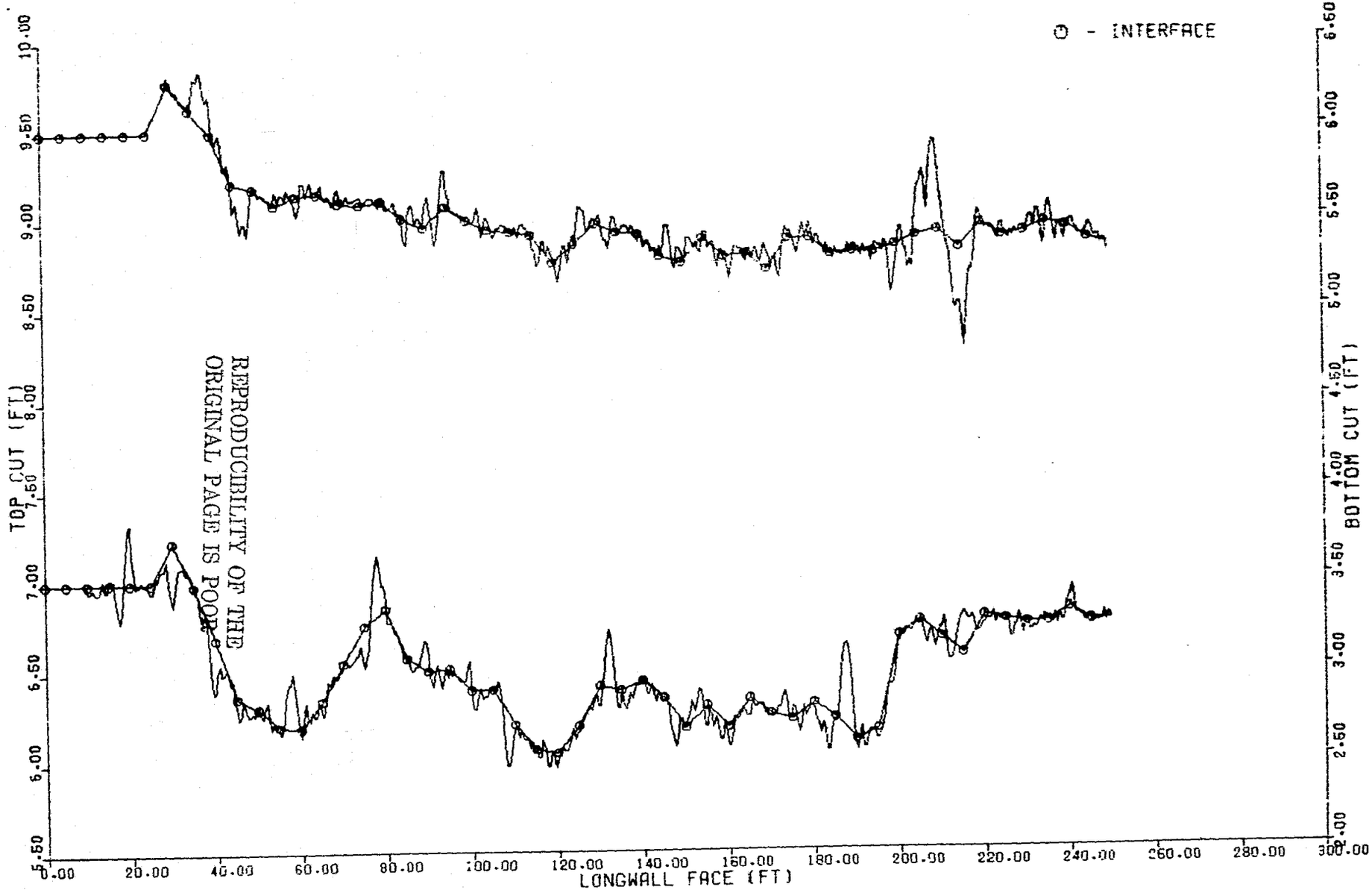

Figure 3-64. VCS Performance with 90% Correct Pick Control

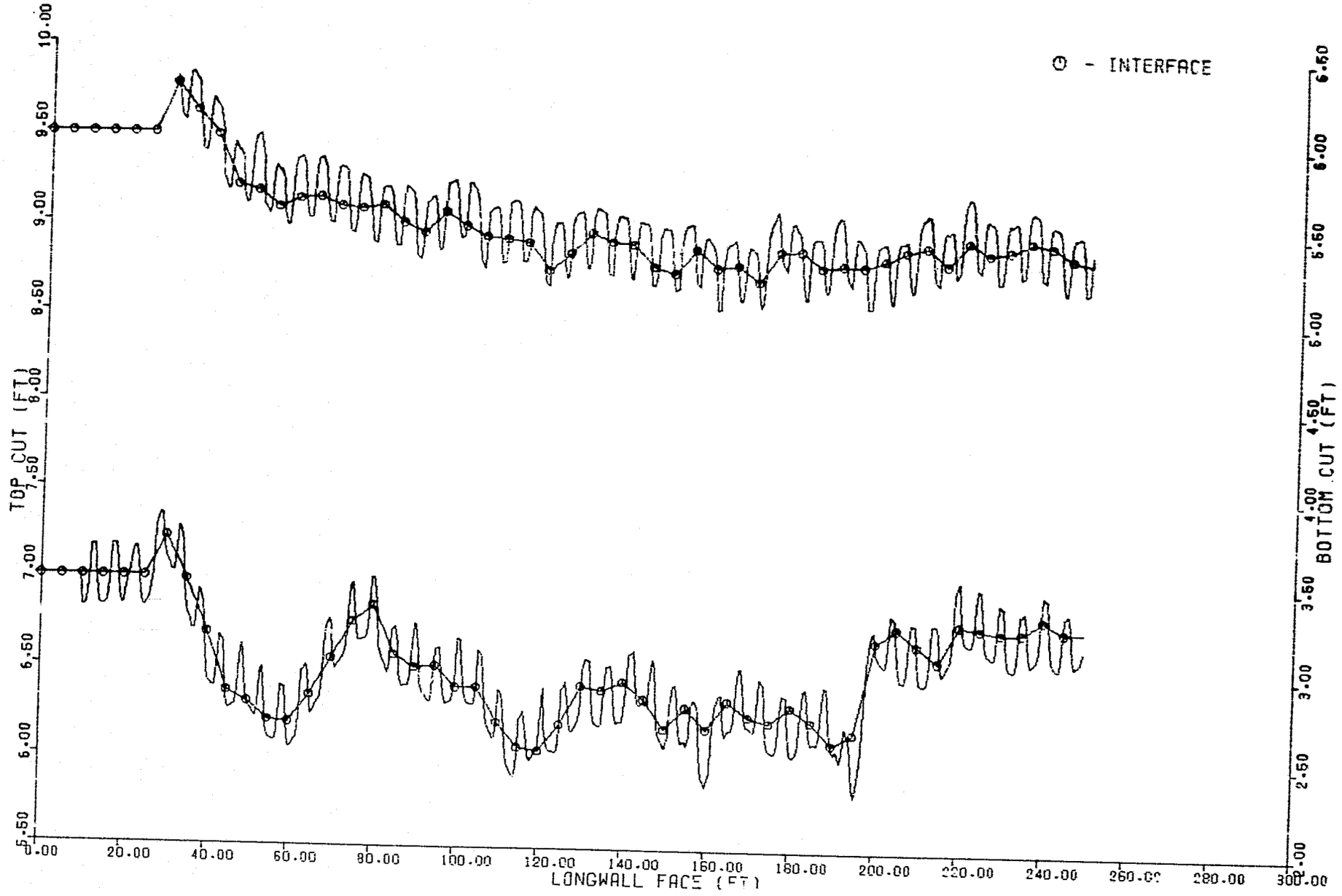

Figure 3-65. VCS Performance with 100% Correct Penetrometer-Reflectometer , LCF Control

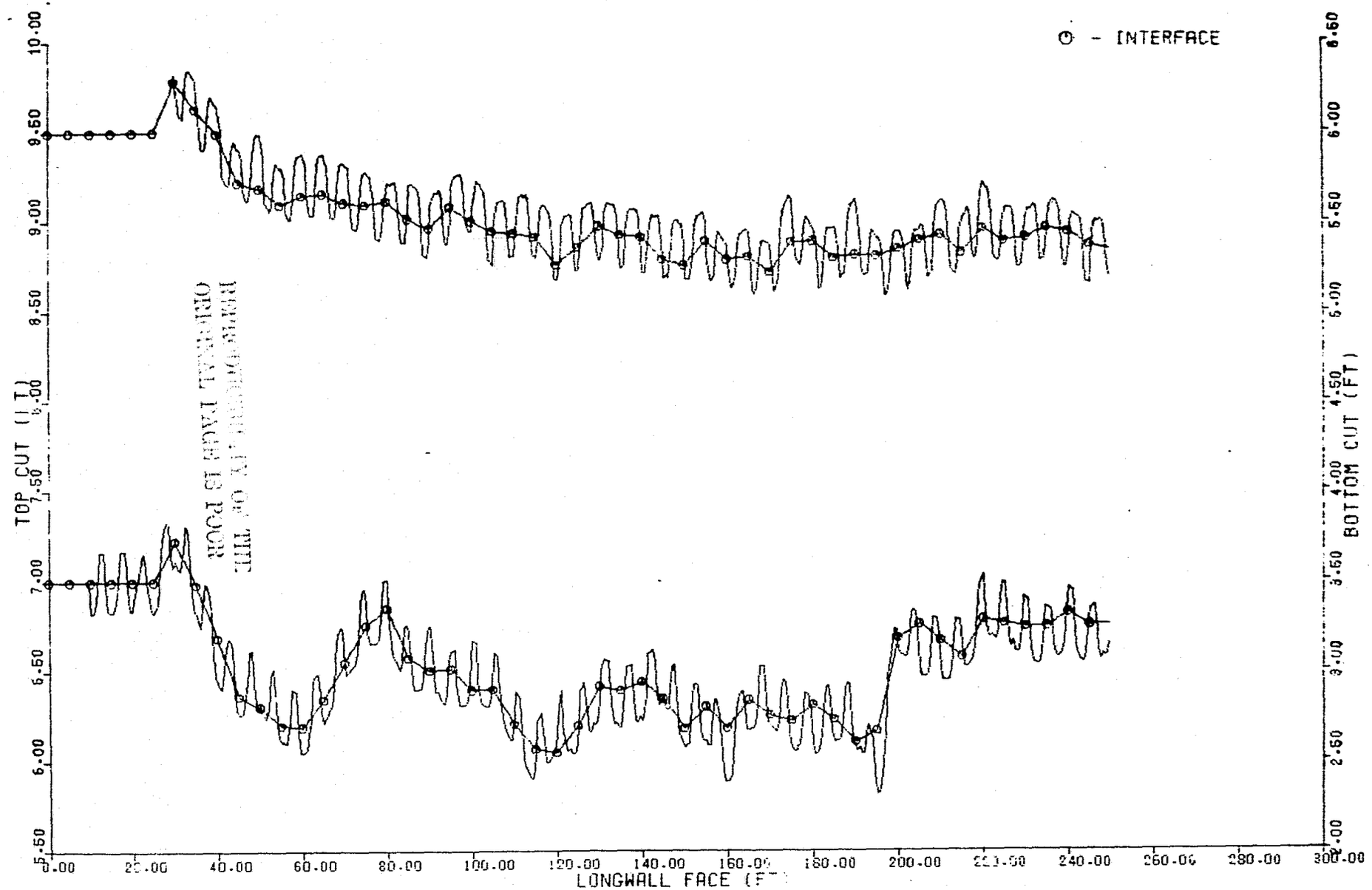

Figure 3-66. VCS Performance with 90% Correct Penetrometer-Reflectometer , LCF Control

3.4.2.8 Effects of Actuator Dynamics

Table 3-11 shows a comparison between simulation runs made with and without actuator dynamics, to access the effects of these dynamics. It can be seen that the control configurations involving proportional CIDs are not significantly affected by the actuator dynamics The rms errors increase from 7 to 16% with proportional sensors. It should be remembered that the VCS actuators are operated in a position loop which exhibited limit cycle behavior. Therefore, it is seen that despite this actuator loop response, the VCS performance is still acceptable.

The only control configuration which was significantly affected by actuator dynamics was the pick control. This is due to the lag introduced by the rate limited hydraulic system. While on a percentage basis, the performance is significantly affected by the actuator dynamics, the resulting error of 2.06 in. rms is not excessive. It may also be possible to achieve some improvement in this error by modifying the pick control law gains. These gains were selected to yield good performance with no actuator dynamics and may therefore require adjustment when used with the actuator.

3.4.2.9 Effect of Variations in Chassis Speeds

All of the preceding results were obtained by cutting with a chassis speed of 30 ft/min down the face. Results of varying the cutting speed for different nucleonic CID output intervals are shown in Table 3-12. It can be seen that at a 0.25 s output interval, cutting performance is unaffected by cutting speed. However, at a 1 s output interval, the effect of cutting speed is more noticeable. Cutting speed has a more pronounced effect at the longer output interval because the system is more sensitive to the distance traveled between measurements.

Table 3-11. Effect of Actuator Dynamics on VCS Performance

CONDITION	WITH ACTUATOR		WITHOUT ACTUATOR	
	RMS (IN.)	% TIR	RMS (IN.)	% TIR
(A) CID	1.64	3.17	1.53	2.5
(A) 5 IN. NATURAL RADIATION SENSOR	2.25	6.9	2.09	5.4
100% PICKS	2.06	79.1	0.68	74.4
(B) CID AND 100% PICKS	1.49	11.1	1.29	8.6
(B) CID, LCF & 100% PICK	1.22	7.7	1.05	1.6

(A) 4 IN. BIAS

(B) 2 IN. BIAS

Table 3-12. VCS Performance When Varying Cutting Speeds

SPEED (FT/MIN) / CID OUTPUT INTERVAL	YORK CANYON MINE BOTTOM ERROR			
	0.25 sec.		1.0 sec.	
	RMS (IN.)	% TIR	RMS (IN.)	% TIR
20	1.23	0.0	1.15	0.0
30	1.22	0.0	1.31	0.0
40	1.23	0.0	1.30	0.0
50	1.23	0.0	1.50	0.68

(A) WITH NOISE

(B) CID, LCF, PICK (90%)

(C) 4 IN. BIAS

(D) NO ACTUATOR

3.5 FILTERING AND PREDICTIVE ALGORITHMS FOR VCS

The CID trails the drum and thus does not measure coal seam thickness at the point the drum is cutting. Hence, it is necessary to develop techniques to predict the depth of coal at the drum so that the drum can be commanded to the required height so as to achieve a desired coal bias. In this section, four filtering and predictive algorithms for VCS control, using present cut CID data only and using both present and past cut CID data, are developed.

3.5.1 Philosophy Behind the Developed Algorithms - The philosophy behind the formulated schemes is to use CID measurements or estimates of the coal-shale interface (CSI) only in the immediate vicinity of the prediction point which is at the cutting drum. This is motivated by the fact that there is no common reference frame with respect to which the CID measurements of the CSI could be referenced with respect to each other over an appreciable distance due to the undulations in the present cut surface (PCS) on which the CID is riding and due to the floor undulations. If the VCS is doing its job then the CID measurements tend to converge to a constant value equal to the amount of coal (i.e., bias, B") to be left and the cut surface profile will be the same as the actual CSI. Since the CID rides on this cut surface,it will tend to measure a constant coal thickness regardless of how the CSI profile varies. Using measurements or estimates in the immediate area of the prediction point minimizes the effect of a floating reference frame at the expense of not being able to make an optimum use of all the CID measurements in the prediction of the CSI at the cutting drum.

The developed algorithms require a priori knowledge of the coal-shale interface statistics in terms of the correlation function and the variance as well as a description of the sensor noise in terms of its mean and variance. The question of any adaptive scheme to estimate the required statistics of the coal-shale interface from the CID measurements is ruled out due to the fact that there is no common reference frame, as discussed above.

3.5.2 Schemes Using Present Cut Data - The two schemes presented here use only the present cut CID measurements. The first scheme uses the present measurement to obtain an estimate of the CSI at the present point. Coupled with the CSI profile characteristics, this estimate is used to predict the CSI at the next measurement point and at the cutting drum. The estimate of the CSI at the next point is then combined with the CID measurement at that point to obtain an optimum estimate of the CSI at that point. Once this is obtained the CSI at the following measurement point and at the cutting drum is made and the process is repeated as

the shearer proceeds down the longwall face. The second scheme uses the present measurement and the immediate previous measurement to obtain an optimum estimate of the CSI at the present point and this estimate is used to predict the CSI at the cutting drum. In both schemes the estimates are optimal in the sense that the variance of the estimation error is a minimum.

Before outlining the two schemes, the assumptions and the notation involved are stated as follows.

3.5.2.1 Assumptions and Notation - The output of the CID is defined as the average coal depth taken over the sensor output period. Since noise is inherent in any measuring device, the CID output at the k^{th} measurement (z_k) is assumed to be the sum of the average coal depth (x_k) and the CID error in the k^{th} measurement (n_k), i.e.,

$$z_k = x_k + n_k \tag{3.1}$$

The measurement errors are assumed to be uncorrelated since the k^{th} measurement error is in no way influenced by the previous or future measurements. Further, it is assumed that the error is a zero mean process with a variance σ_n^2. The k^{th} measurement point on the coal-shale interface (CSI) is assumed to be distributed with a mean μ (same for all k) and a variance $\sigma^2_{x_k}$. It is also assumed that the correlation function for the CSI profiles is known. For a perfect cut the final cut surface should have the same profile as the CSI but B" (bias-the amount of coal to be left) apart from the latter. Thus the mean μ is nothing but B and during the final pass, the CID measurements would be B" if the control system is doing a perfect job. The above assumptions are summarized for convenience:

$$\text{mean of } x_k = E\{x_k\} = \mu = B$$

$$\text{var}\{x_k\} = E\{(x_k-\mu)^2\} = \sigma^2_{x_k}$$

correlation coefficient of x_i and $x_j = \rho_{ij}$

$$E\{n_k\} = 0$$

$$E\{n_i n_j\} = \begin{cases} 0 & , \ i \neq j \\ \text{var}\{n_i\} = \sigma_n^2 & , \ i = j \end{cases}$$

$$E\{x_i n_j\} = 0 \quad \text{for all i and j} \tag{3.1a}$$

It is to be noted that neither the CSI nor the CID measurement error is assumed to be necessarily gaussian distributed.

The following notation is adopted: $\hat{x}(k+j/k)$ denotes the predicted value of the coal-shale interface at $(k+j)^{th}$ point ($j = 1,2,3,\ldots$), i.e., of x_{k+j}, using the best estimate of the CSI at the k^{th} measurement point, i.e., $\hat{x}_k$.

$\sigma_{x_i x_j}$ is a measure of the correlation of x_i and x_j and is defined as

$$\sigma_{x_i x_j} = E\{(x_i - \mu)(x_j - \mu)\}$$

where μ is the mean of x_i and x_j. It can be written in terms of the correlation coefficient ρ_{ij} of x_i and x_j as

$$\sigma_{x_i x_j} = \rho_{ij} \sigma_{x_i} \sigma_{x_j}$$

where σ_{x_i} and σ_{x_j} are the standard deviations of x_i and x_j respectively. Thus, once the variance and the correlation function of the profiles are known, $\sigma_{x_i x_j}$ is known for all x_i and x_j.

The prediction and estimation errors are defined as

$$\tilde{x}(k+j/k) = x_{k+j} - \hat{x}(k+j/k)$$

$$\tilde{x}_k = x_k - \hat{x}_k$$

3.5.2.2 Scheme I - Predictor-Corrector Approach - The estimate of x_k, the actual coal depth at the k^{th} measurement point, is obtained by using the predicted value of x_k based on the previous CID measurement and then correcting the prediction with the new information in the current (k^{th}) CID measurement, i.e., with the difference between the actual current observation and the best estimate of the current observation, $z_k - \hat{x}(k/k-1)$. Thus the algorithm is developed in terms of this predictor-corrector approach and the estimator $\hat{x}_k$ is of the form

$$\hat{x}_k = \hat{x}(k/k-1) + g_k(z_k - \hat{x}(k/k-1)) \qquad (3.2)$$

where g_k is a weighting factor to be determined such that the variance of the estimation error, $E\{(x_k - \hat{x}_k)^2\}$, is minimized. Similarly, the coal depth at $(k+j)^{th}$ point ($j = 1,2,\ldots$) is predicted around μ, the mean of the coal-shale interface using $\hat{x}_k$, the current best estimate:

$$\hat{x}(k+j/k) = \mu + \alpha_k^{(j)} (\hat{x}_k - \mu) \qquad (3.3)$$

where $\alpha_k^{(j)}$ is to be determined such that the variance of the prediction error, $E\{(x_{k+j} - \hat{x}(k+j/k))^2\}$, is minimized. The estimator and the predictor are developed such that they are unbiased, that is

$$E(\hat{x}_k) = \mu$$

$$E(\hat{x}(k+j/k)) = \mu$$

Thus we have an unbiased minimum variance estimator. The estimation scheme outlined above is illustrated in Figure 3-67.

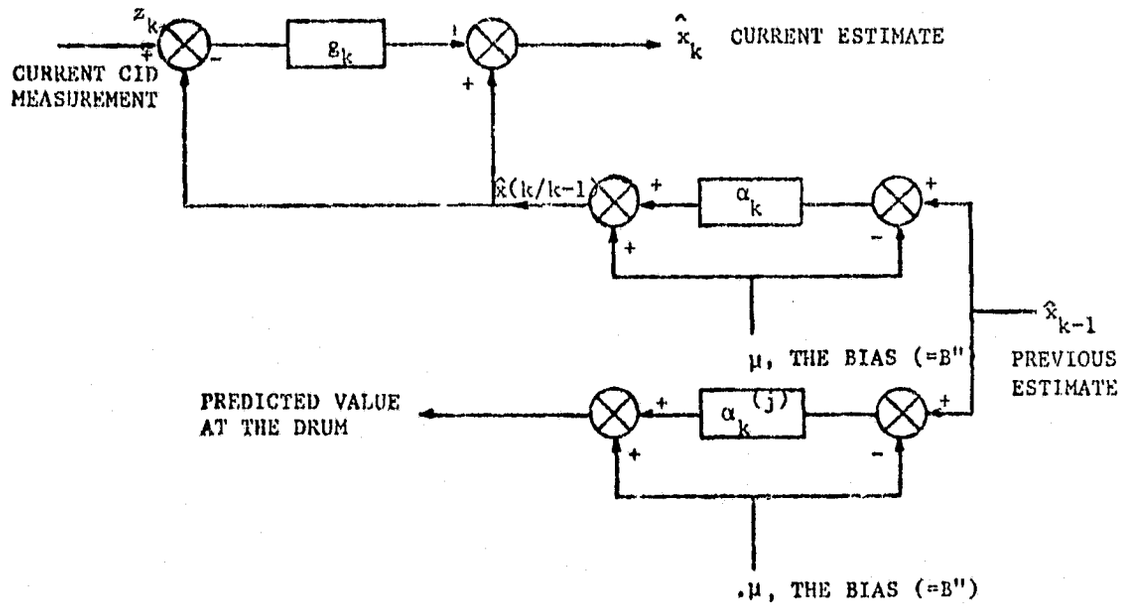

Figure 3-67. Block Diagram of Scheme 1

The optimal value of g_k, that is, the one that minimizes the cost function which is the error variance, $V = E\{(x_k-\hat{x}_k)^2\}$, is found using variational calculus approach. Let

$$g_k = g_k^* + \epsilon\Delta g_k \tag{3.4}$$

where g_k^* is the optimal value of g_k and then set

$$\left.\frac{\partial V}{\partial \epsilon}\right|_{\epsilon=0} = 0$$

and make this result independent of Δg_k. Using (3.2) and (3.4),

$$V = E\{(x_k - \hat{x}(k/k-1) - (g_k^* + \epsilon\Delta g_k)(z_k - \hat{x}(k/k-1)))^2\}$$

$$\left.\frac{\partial V}{\partial \epsilon}\right|_{\epsilon=0} = 0 = E\{\Delta g_k(z_k-\hat{x}(k/k-1))(x_k-\hat{x}(k/k-1)-g_k^*(z_k-\hat{x}(k/k-1)))\}$$

which results in the optimal value of g_k of (3.2) as

$$g_k^* = \frac{E\{(z_k - \hat{x}(k/k-1))(x_k-\hat{x}(k/k-1))\}}{E\{(z_k-\hat{x}(k/k-1))^2\}} \tag{3.5}$$

Using (3.1) and (3.1a), (3.5) may be written as

$$g_k^* = \frac{\text{var}\{\tilde{x}(k/k-1)\}}{\text{var}\{\tilde{x}(k/k-1)\} + \sigma_n^2} \tag{3.6}$$

where

$$\text{var}\{\tilde{x}(k/k-1)\} = E\{(x_k - \hat{x}(k/k-1))^2\}$$

is the error variance in prediction.

In order to determine the error variance, var{$\tilde{x}(k/k-1)$}, it is required to find $\alpha_{k-1}^{(j)}$ of

$$\hat{x}(k+j/k-1) = \mu + \alpha_{k-1}^{(j)} (\hat{x}_{k-1} - \mu) \qquad j = 0,1,2,... \tag{3.7}$$

Again, using the variational calculus approach, $\alpha_{k-1}^{(j)}$ is found such that it minimizes the prediction error variance $V_1 = E\{(x_{k+j} - \hat{x}(k+j/k-1))^2\}$.

Let

$$\alpha_{k-1}^{(j)} = \alpha_{k-1}^{(j)*} + \epsilon\Delta\alpha_{k-1} \tag{3.8}$$

where $\alpha_{k-1}^{(j)*}$ is the optimal value of $\alpha_{k-1}^{(j)}$ and then set

$$\left.\frac{\partial V_1}{\partial \epsilon}\right|_{\epsilon=0} = 0$$

Using (3.7) and (3.8)

$$V_1 = E\{(x_{k+j} - \mu - (\alpha_{k-1}^{(j)*} + \epsilon\Delta\alpha_{k-1})(\hat{x}_{k-1} - \mu))^2\}$$

$$\left.\frac{\partial V_1}{\partial \epsilon}\right|_{\epsilon=0} = 0 = E\{\Delta\alpha_{k-1}(\hat{x}_{k-1}-\mu)(x_{k+j}-\mu-\alpha_{k-1}^{(j)*}(\hat{x}_{k-1}-\mu))\}$$

which results in the optimal value of $\alpha_{k-1}^{(j)}$ of (3.7) as

$$\alpha_{k-1}^{(j)} = \frac{E\{(\hat{x}_{k-1}-\mu)(x_{k+j}-\mu)\}}{E\{(\hat{x}_{k-1}-\mu)^2\}} \triangleq \frac{\sigma_{\hat{x}_{k-1}x_{k+j}}}{\sigma_{\hat{x}_{k-1}}^2} \tag{3.9}$$

For j = 0, define

$$\alpha_{k-1} = \alpha_{k-1}^{(o)} = \frac{\sigma_{\hat{x}_{k-1}x_k}}{\sigma_{\hat{x}_{k-1}}^2} \tag{3.10}$$

Now expressions for the numerator and denominator of (3.9) are obtained as follows:

$$\sigma_{\hat{x}_{k-1}x_{k+j}} = E\{(x_{k+j}-\mu)(\hat{x}_{k-1}-\mu)\}$$

$$= E\{(x_{k+j}-\mu)(\hat{x}(k-1/k-2)-\mu+g_{k-1}(z_{k-1}-\hat{x}(k-1/k-2)))\} \quad \text{using (3.2)}$$

$$= E\{(x_{k+j}-\mu)(\alpha_{k-2}(\hat{x}_{k-2}-\mu)+g_{k-1}(z_{k-1}-\mu-\alpha_{k-2}(\hat{x}_{k-2}-\mu)))\} \quad \text{using (3.3)}$$

$$= \alpha_{k-2}(1-g_{k-1})\,\sigma_{\hat{x}_{k-2}x_{k+j}} + g_{k-1}\,\sigma_{x_{k-1}x_{k+j}}$$

Similarly,

$$\sigma_{\hat{x}_{k-2}x_{k+j}} = \alpha_{k-3}(1-g_{k-2})\,\sigma_{\hat{x}_{k-3}x_{k+j}} + g_{k-2}\,\sigma_{x_{k-2}x_{k+j}}$$

and, in general,

$$\sigma_{\hat{x}_i x_{k+j}} = \alpha_{i-1}(1-g_i)\,\sigma_{\hat{x}_{i-1}x_{k+j}} + g_i\,\sigma_{x_i x_{k+j}} \qquad (3.11)$$

$$\text{for } i = 1,2,\ldots,(k-1)$$
$$j = 0,1,2,\ldots$$

Thus the numerator of (3.9) is computed recursively using (3.11). It may be pointed out that (3.11) need be computed only for x_i and x_{k+j} within the correlation distance and hence the number of α_i's and g_i's that are to be stored for evaluating (3.11) are less than or equal to 2(k-1).

The denominator of (3.9) can be evaluated as follows:

$$\sigma^2_{\hat{x}_k} = E\{(\hat{x}_k - \mu)^2\}$$

$$= E\{((\hat{x}(k/k-1) - \mu) + g_k(z_k - \hat{x}(k/k-1)))^2\} \qquad \text{using (3.2)}$$

$$= E\{(\alpha_{k-1}(\hat{x}_{k-1} - \mu) + g_k(z_k - \mu) - g_k\alpha_{k-1}(\hat{x}_{k-1} - \mu))^2\} \quad \text{using (3.3)}$$

$$= \alpha^2_{k-1}\sigma^2_{\hat{x}_{k-1}} + g_k^2\,(\sigma^2_{x_k} - \alpha_{k-1}\sigma_{\hat{x}_{k-1}x_k} + \sigma^2_n) +$$

$$\{g_k^2\alpha^2_{k-1}\sigma^2_{\hat{x}_{k-1}} - g_k^2\alpha_{k-1}\sigma_{\hat{x}_{k-1}x_k} + 2\alpha_{k-1}g_k\sigma_{\hat{x}_{k-1}x_k} - 2g_k\alpha^2_{k-1}\sigma^2_{\hat{x}_{k-1}}\}$$

Using (3.10) it can be seen that the terms in the braces cancel out, resulting in

$$\sigma^2_{\hat{x}_k} = \alpha^2_{k-1}\sigma^2_{\hat{x}_{k-1}} + g_k^2(\sigma^2_{x_k} - \alpha_{k-1}\sigma_{\hat{x}_{k-1}x_k} + \sigma^2_n) \qquad (3.12)$$

The variance of the prediction error may be computed as follows:

$$\text{var}\{\tilde{x}(k/k-1)\} = E\{(x_k - \hat{x}(k/k-1))^2\}$$

$$= E\{((x_k - \mu) - \alpha_{k-1}(\hat{x}_{k-1} - \mu))^2\} \quad \text{using (3.3)}$$

$$= \sigma^2_{x_k} - 2\alpha_{k-1}\sigma_{\hat{x}_{k-1}x_k} + \alpha^2_{k-1}\sigma^2_{\hat{x}_{k-1}}$$

$$= \sigma^2_{x_k} - \alpha_{k-1}\sigma_{\hat{x}_{k-1}x_k} \qquad \text{using (3.10)} \qquad (3.13)$$

Thus (3.12), using (3.6) and (3.13) becomes

$$\sigma^2_{\hat{x}_k} = \alpha^2_{k-1}\sigma^2_{\hat{x}_{k-1}} + g_k \text{ var } \{\tilde{x}(k/k-1)\} \qquad (3.14)$$

The algorithm developed above is summarized as follows:

ALGORITHM I $\qquad k \geq 1$

Filtering:

$$\hat{x}_k = \hat{x}(k/k-1) + g_k(z_k - \hat{x}(k/k-1))$$

Prediction:

$$\hat{x}(k+j/k-1) = \mu + \alpha^{(j)}_{k-1}\,(\hat{x}_{k-1} - \mu) \qquad j = 0,1,2,\ldots$$

$$g_k = \frac{\text{var}\{\tilde{x}(k/k-1)\}}{\text{var}\{\tilde{x}(k/k-1)\} + \sigma^2_n}$$

$$\text{var}\{\tilde{x}(k/k-1)\} = \sigma^2_{x_k} - \alpha_{k-1}\sigma_{\hat{x}_{k-1}x_k}$$

$$\alpha^{(j)}_{k-1} = \frac{\sigma_{\hat{x}_{k-1}x_{k+j}}}{\sigma^2_{\hat{x}_{k-1}}} \qquad j = 0,1,2,\ldots$$

$$\alpha_{k-1} = \alpha^{(0)}_{k-1}$$

$$\sigma_{\hat{x}_i x_{k+j}} = \alpha_{i-1}(1-g_i)\sigma_{\hat{x}_{i-1}x_{k+j}} + g_i\sigma_{x_i x_{k+j}} \qquad \begin{matrix} j = 0,1,2\ldots \\ i = 1,2,\ldots,(k-1) \end{matrix}$$

$$\sigma^2_{\hat{x}_k} = \alpha_{k-1}\sigma_{\hat{x}_{k-1}x_k} + g_k \text{ var}\{\tilde{x}(k/k-1)\}$$

A few remarks are in order.

a. If x_{k-1} and x_{k+j} are farther apart than the correlation distance of the coal-shale interface then $\sigma_{x_{k-1}x_{k+j}} \to 0$ since $\rho_{k-1,k+j} \to 0$ and hence $\sigma_{\hat{x}_{k-1}x_{k+j}} \to 0$, $\alpha_{k-1} \to 0$ and $\hat{x}(k+j/k-1)$, the predicted value of x_{k+j}, becomes μ, which is as expected.

b. If the noise variance, $\sigma_n^2 \to 0$, then $g_k \to 1$ and hence $\hat{x}_k = z_k$ which is as it should be.

c. If the noise variance, $\sigma_n^2 \to \infty$, then $g_k \to 1$ and hence $\hat{x}_k = \hat{x}(k/k-1)$ which is true, since a highly noise corrupted observation contains practically no new information.

d. If the variance of the coal-shale interface is large i.e., if $\sigma_{x_k}^2 \to \infty$ then $g_k \to 1$ and hence $\hat{x}_k = z_k$

e. If the variance of the CSI is very small, i.e., $\sigma_{x_k}^2 \to 0$ then $\sigma_{x_i x_k} \to 0$ and hence $g_k \to 0$ and $\alpha_k \to 0$ and the predicted value of x_{k+j} is the mean of CSI profile, μ and $\hat{x}_k = \mu$.

A few sample calculations are given illustrating the developed algorithm.

Sample Calculations:

Initial measurement: z_0

Initial estimate $\hat{x}_o = x_o = z_0; \sigma_{\hat{x}_0}^2 = \sigma_{x_0}^2 + \sigma_n^2$

<u>k = 1</u>

$$\alpha_0^{(j)} = \frac{\sigma_{\hat{x}_0 x_{j+1}}}{\sigma_{\hat{x}_0}^2} = \frac{\sigma_{x_0 x_{j+1}}}{\sigma_{x_0}^2} = \rho_{0\,(j+1)} \frac{\sigma_{x_0}\sigma_{x_{j+1}}}{\sigma_{x_0}^2}$$

$$\alpha_0 = \alpha_0^{(0)} = \frac{\sigma_{x_0 x_1}}{\sigma_{x_0}^2} \; ; \; \alpha_0^{(1)} = \frac{\sigma_{x_0 x_2}}{\sigma_{x_0}^2} \text{, etc.}$$

Prediction:

$$\hat{x}(j+1/0) = \mu + \alpha_0^{(j)} (\hat{x}_0 - \mu)$$

e.g. $j = 0$: $\hat{x}(1/0) = \mu + \alpha_0(\hat{x}_0 - \mu)$

$j = 1$: $\hat{x}(2/0) = \mu + \alpha_0^{(1)}(\hat{x}_0 - \mu)$, etc.

$$\text{var}\{\tilde{x}(1/0)\} = \sigma^2_{x_1} - \alpha_0 \sigma_{x_0 x_1}$$

$$g_1 = \frac{\text{var}\{\hat{x}(1/0)\}}{\text{var}\{\tilde{x}(1/0)\} + \sigma_n^2}$$

$$\hat{x}_1 = \hat{x}(1/0) + g_1(z_1 - \hat{x}(1/0))$$

$$\sigma^2_{\hat{x}_1} = \alpha_0 \sigma_{x_0 x_1} + g_1 \text{var}\{\tilde{x}(1/0)\}$$

<u>k = 2</u>

$$\sigma_{\hat{x}_1 x_{2+j}} = \alpha_0(1-g_1)\sigma_{x_0 x_{2+j}} + g_1 \sigma_{x_1 x_{2+j}}$$

$$\alpha_1^{(j)} = \sigma_{\hat{x}_1 x_{2+j}} / \sigma^2_{\hat{x}_1}$$

$$\alpha_1 = \alpha_1^{(0)} = \frac{\sigma_{\hat{x}_1 x_2}}{\sigma^2_{\hat{x}_1}}$$

Prediction:

$$\hat{x}(j+2/1) = \mu + \alpha_1^{(j)}(\hat{x}_1 - \mu)$$

e.g. $\hat{x}(2/1) = \mu + \alpha_1(\hat{x}_1 - \mu)$

$\hat{x}(3/1) = \mu + \alpha_1^{(1)}(\hat{x}_1 - \mu)$ where $\alpha_1^{(1)} = \dfrac{\sigma_{\hat{x}_1 x_3}}{\sigma^2_{\hat{x}_1}}$

and $\sigma_{\hat{x}_1 x_3} = \alpha_0(1-g_1)\sigma_{x_0 x_3} + g_1\sigma_{x_1 x_3}$

$$\text{var}\{\tilde{x}(2/1)\} = \sigma^2_{x_2} - \alpha_1 \sigma_{\hat{x}_1 x_2}$$

$$g_2 = \frac{\text{var}\{\tilde{x}(2/1)\}}{\text{var}\{\tilde{x}(2/1)\} + \sigma_n^2}$$

$$\hat{x}_2 = \hat{x}(2/1) + g_2(z_2 - \hat{x}(2/1))$$

$$\sigma^2_{\hat{x}_2} = \alpha_1\sigma_{\hat{x}_1 x_2} + g_2 \text{ var}\{\tilde{x}(2/1)\}$$

<u>k = 3</u>

$$\sigma_{\hat{x}_2 x_{3+j}} = \alpha_1(1-g_2)\sigma_{\hat{x}_1 x_{3+j}} + g_2 \sigma_{x_2 x_{3+j}}$$

where

$$\sigma_{\hat{x}_1 x_{3+j}} = \alpha_0(1-g_1)\sigma_{x_0 x_{3+j}} + g_1 \sigma_{x_1 x_{3+j}}$$

$$\alpha_2^{(j)} = \frac{\sigma_{\hat{x}_2 x_{3+j}}}{\sigma^2_{\hat{x}_2}}$$

$$\alpha_2 = \alpha_2^{(0)} = \frac{\sigma_{\hat{x}_2 x_3}}{\sigma^2_{\hat{x}_2}}$$

Prediction:

$$\hat{x}(3+j/2) = \mu + \alpha_2^{(j)}(\hat{x}_2 - \mu)$$

e.g. $\hat{x}(3/2) = \mu + \alpha_2(\hat{x}_2 - \mu)$,

$\hat{x}(4/2) = \mu + \alpha_2^{(1)}(\hat{x}_2 - \mu)$, etc.

where $\alpha_2^{(1)} = \frac{\sigma_{\hat{x}_2 x_4}}{\sigma^2_{\hat{x}_2}}$

and so on.

For an example of prediction at the cutting drum assume that the chassis velocity is 15 ft/min and that the CID output period is 10 seconds. Then $j = 0$ and the prediction at the drum is given by, say for $k=3$, $\hat{x}(3/2)$.

3.5.2.3 Scheme II - Approach Using Present and Immediate Previous Measurements - In scheme II the best estimate of x_k is obtained as a linear combination of the present measurement z_k and the immediate previous measurement z_{k-1}. That is, the best estimate $\hat{x}_k$ is sought in the form

$$\hat{x}_k = \mu + g_1(z_{k-1} - \mu) + g_2(z_k - \mu)$$

where g_1 and g_2 are to be determined such that the error variance

$$V_2 = E\{(x_k - \hat{x}_k)^2\}$$

is minimized. Again using the variational calculus approach, let

$$g_1 = g_1^* + \epsilon_1 \Delta g_1$$

$$g_2 = g_2^* + \epsilon_2 \Delta g_2$$

where g_1^* and g_2^* are the optimal value of g_1 and g_2 and then set

$$\left.\frac{\partial V_2}{\partial \epsilon_1}\right|_{\epsilon_1=\epsilon_2=0} = \left.\frac{\partial V_2}{\partial \epsilon_2}\right|_{\epsilon_1=\epsilon_2=0} = 0$$

$$V_2 = E\{(x_k-\mu-g_1^*(z_{k-1}-\mu)-g_2^*(z_k-\mu)-\epsilon_1\Delta g_1(z_{k-1}-\mu)-\epsilon_2\Delta g_2(z_k-\mu))^2\}$$

$$\left.\frac{\partial V_2}{\partial \epsilon_1}\right|_{\epsilon_1=\epsilon_2=0} = 0 = E\{\Delta g_1(z_{k-1}-\mu)(x_k-\mu-g_1^*(z_{k-1}-\mu)-g_2^*(z_k-\mu))\}$$

$$\left.\frac{\partial V_2}{\partial \epsilon_2}\right|_{\epsilon_1=\epsilon_2=0} = 0 = E\{\Delta g_2(z_k-\mu)(x_k-\mu-g_1^*(z_{k-1}-\mu)-g_2^*(z_k-\mu))\}$$

which result in

$$g_1^*(\sigma^2_{x_{k-1}} + \sigma_n^2) + g_2^*\sigma_{x_k x_{k-1}} = \sigma_{x_k x_{k-1}}$$

$$g_1^*\sigma_{x_k x_{k-1}} + g_2^*(\sigma^2_{x_k} + \sigma_n^2) = \sigma^2_{x_k}$$

Solving for g_1^* and g_2^*,

$$g_1^* = \frac{1}{D_k}\sigma_n^2\sigma_{x_k x_{k-1}}$$

$$g_2^* = \frac{1}{D_k} g_k$$

where $D_k = g_k + \sigma_n^2\sigma^2_{x_{k-1}} + \sigma_n^4$

and $g_k = \sigma^2_{x_{k-1}}\sigma^2_{x_k} - \sigma^2_{x_{k-1}x_k} + \sigma_n^2\sigma^2_{x_k}$

Thus

$$\hat{x}_k = \mu + \frac{1}{D_k}\{\sigma_n^2 \sigma_{x_k x_{k-1}} (z_{k-1}-\mu) + g_k(z_k-\mu)\} \qquad (3.15)$$

The CID coal depth measurement at $(k+j)^{th}$ point ($j = 1,2,\ldots$) is again predicted around the mean of the coal-shale interface and using $\hat{x}_k$, the current best estimate:

$$\hat{x}(k+j/k) = \mu + \gamma_k^{(j)}(\hat{x}_k - \mu) \quad j = 1,2,3,\ldots$$

where $\gamma_k^{(j)}$ is to be determined so that the prediction error variance $V_3 = E\{(x_{k+j}-\hat{x}(k+j/k))^2\}$ is minimized. Again using the variational calculus approach, let

$$\gamma_k^{(j)} = \gamma_k^{(j)*} + \varepsilon\Delta\gamma_k$$

then

$$V_3 = E\{(x_{k+j}-\mu-\gamma_k^{(j)*}(\hat{x}_k-\mu) - \varepsilon\Delta\gamma_k (\hat{x}_k-\mu))^2\}$$

$$\left.\frac{\partial V_3}{\partial \varepsilon}\right|_{\varepsilon=0} = 0 = E\{\Delta\gamma_k(\hat{x}_k-\mu)(x_{k+j}-\mu-\gamma_k^{(j)*}(\hat{x}_k-\mu))\}$$

which results in $\gamma_k^{(j)} = \dfrac{E\{(\hat{x}_k-\mu)(x_{k+j}-\mu)\}}{E\{(\hat{x}_k-\mu)^2\}} = \dfrac{\sigma_{\hat{x}_k x_{k+j}}}{\sigma^2_{\hat{x}_k}}$

The numerator and denominator are evaluated as follows:

$$\sigma_{\hat{x}_k x_{k+j}} = E\{(\hat{x}_k-\mu)(x_{k+j}-\mu)\}$$

$$= E\{\frac{1}{D_k}\sigma_n^2\sigma_{x_k x_{k-1}}(z_{k-1}-\mu)(x_{k+j}-\mu) + \frac{1}{D_k} g_k(z_k-\mu)(x_{k+j}-\mu)^2\}$$

using (3.15)

$$= \frac{1}{D_k}\sigma_n^2\sigma_{x_k x_{k-1}}\sigma_{x_{k-1}x_{k+j}} + \frac{1}{D_k} g_k \sigma_{x_k x_{k+j}}$$

$$\sigma^2_{\hat{x}_k} = E\{(\hat{x}_k-\mu)^2\}$$

$$= \frac{1}{D_k^2} E\{(\sigma_n^2\sigma_{x_k x_{k-1}}(z_{k-1}-\mu) + g_k(z_k-\mu))^2\} \text{ using (3.15)}$$

$$\text{or } \sigma^2_{\hat{x}_k} = \frac{1}{D_k}\sigma^2_{x_k x_{k-1}}\sigma_n^2 + \frac{1}{D_k^2} g_k\{\sigma^2_{x_k x_{k-1}}\sigma_n^2 + (\sigma^2_{x_k} + \sigma_n^2)g_k\}$$

The variance of the prediction error can be computed to be

$$\text{var}\{\tilde{x}(k+j/k)\} = \sigma^2_{x_{k+j}} - \gamma_k^{(j)}\sigma_{\hat{x}_k x_{k+j}}$$

A summary of the algorithm developed above is given below.

ALGORITHM II

Estimation:

$$\hat{x}_k = \mu + \frac{1}{D_k}\{\sigma_{x_{k-1}x_k}\sigma_n^2(z_{k-1}-\mu) + g_k(z_k-\mu)\}$$

where

$$D_k = g_k + \sigma_n^2\sigma^2_{x_{k-1}} + \sigma_n^4$$

and $$g_k = \sigma^2_{x_{k-1}}\sigma^2_{x_k} - \sigma^2_{x_{k-1}x_k} + \sigma_n^2\sigma^2_{x_k}$$

Prediction:

$$\hat{x}(k+j/k) = \mu + \gamma_k^{(j)}(\hat{x}_k - \mu) \qquad j = 1,2,3\ldots$$

where

$$\gamma_k^{(j)} = \frac{\sigma_{\hat{x}_k x_{k+j}}}{\sigma^2_{\hat{x}_k}}$$

$$\sigma_{\hat{x}_k x_{k+j}} = \frac{1}{D_k}\{\sigma_{x_{k-1}x_k}\sigma_{x_{k-1}x_{k+j}}\sigma_n^2 + g_k\sigma_{x_k x_{k+j}}\}$$

$$\sigma^2_{\hat{x}_k} = \frac{1}{D_k}\sigma^2_{x_{k-1}x_k}\sigma_n^2 + \frac{g_k}{D_k^2}\{\sigma^2_{x_{k-1}x_k}\sigma_n^2 + (\sigma^2_{x_k} + \sigma_n^2)g_k\}$$

Note that:

a. as $\sigma_n^2 \to 0$, $\hat{x}_k \to z_k$

b. as $\sigma_n^2 \to \infty$, $\hat{x}_k \to \mu$

c. as $\sigma^2_{x_k} \to 0$, $\hat{x}_k \to \mu$

d. as $\sigma^2_{x_k} \to \infty$, $\hat{x}_k \to z_k$

which are as expected.

Sample Calculations:

Initial measurement: z_0

Initial Estimate: $\hat{x}_0 = x_0 = z_0$; $\sigma^2_{\hat{x}_0} = \sigma^2_{x_0} + \sigma_n^2$

a. Prediction:

$$\hat{x}(j/0) = \mu + \gamma_0^{(j)}(\hat{x}_0 - \mu) \qquad j = 1,2,3,\ldots$$

where

$$\gamma_0^{(j)} = \frac{\sigma_{x_0 x_j}}{\sigma^2_{\hat{x}_0}}$$

<u>k = 1</u>

$$\hat{x}_1 = \mu + \frac{1}{D_k}\{\sigma_{x_0 x_1}\sigma_n^2(z_0 - \mu) + g_1(z_1 - \mu)\}$$

$$D_1 = g_1 + \sigma_n^2\sigma^2_{x_0} + \sigma_n^4$$

$$g_1 = \sigma^2_{x_0}\sigma^2_{x_1} - \sigma^2_{x_0 x_1} + \sigma_n^2\sigma^2_{x_1}$$

b. Prediction:

$$\hat{x}(j+1/1) = \mu + \gamma_1^{(j)}(\hat{x}_1 - \mu) \qquad j = 1,2,3...$$

where $$\gamma_1^{(j)} = \frac{\sigma_{\hat{x}_1 x_{j+1}}}{\sigma^2_{\hat{x}_1}}$$

$$\sigma_{\hat{x}_1 x_{j+1}} = \frac{1}{D_j}\{\sigma_{x_0 x_1}\sigma_{x_0 x_{j+1}}\sigma_n^2 + g_1\sigma_{x_1 x_{j+1}}\}$$

$$\sigma^2_{\hat{x}_1} = \frac{1}{D_1}\{\sigma^2_{x_0 x_1}\sigma_n^2\} + \frac{g_1}{D_1^2}\{\sigma^2_{x_0 x_1}\sigma_n^2 + (\sigma^2_{x_1} + \sigma_n^2)g_1\}$$

and so on.

3.5.2.4 Comparison of the Two Schemes - The first scheme is intuitively appealing in the sense that it is similar to Kalman filter of modern control theory. Any error due to PCS undulations is minimized by this scheme and it can be shown for some special cases that it results in less prediction error variance compared to scheme II and it is fair to assume that this is true in general cases. However, since it is so vitally dependent on all the correlations within the correlation distance it is to be expected that any errors in the correlation function of the CSI profiles result in an increased prediction error variance. Scheme II does not suffer from this drawback as much as scheme I since it is dependent on only the correlations of points which are close together. Further, it is computationally simpler and so is easier to implement. However, it is more sensitive to PCS undulations as the algorithm depends on a previous measurement.

It may be pointed out that when any of the measurements is zero, say due to cutting the rock, then the drum should be lowered by B" and the control algorithms are started afresh (i.e., set k = 0) from the point where the measurement is found to be zero.

It is instructive to compare the developed schemes with the baseline scheme known as the measure and cut scheme wherein the present CID measurement at x_k is taken as the depth of coal at the drum (which is at x_d). The prediction error variance in the measure and cut scheme is equal to $2(1-\rho_{kd})\sigma^2_{x_k x_d} + \sigma_n^2$. Table 3-13 illustrates that the prediction error variances of schemes I and II are less than the measure and cut scheme. It can easily be shown for both schemes I and II that

Table 3-13. Comparison of Prediction Error Variances

ASSUMED VALUES:

τ_{CID} = 5 SEC

CHASSIS VELOCITY = 30'/MIN

D = CORRELATION DIST. = 50'

CORRELATION FUNCTION = $e^{-\frac{d}{D}}$

ρ = 0.9512

$\sigma^2_{x_i x_j} = \sigma^2_{CSI}$

	ERROR VARIANCE	
CID NOISE VARIANCE	$\sigma^2_n = 1$	
COAL SHALE INTERFACE VARIANCE	$\sigma^2_{CSI} = 1$	$\sigma^2_{CSI} = 5$
MEASURE AND CUT SCHEME	1.1	1.49
SCHEME I	<.33	<.95
SCHEME II	.415	.975

(A)

	ERROR VARIANCE	
CSI VARIANCE	$\sigma^2_{CSI} = 1$	
CID NOISE VARIANCE	$\sigma^2_n = 1$	$\sigma^2_n = 3$
MEASURE AND CUT SCHEME	1.1	3.19
SCHEME II	.415	.652

(B)

ev (prediction) $\leq$ ev (estimate and cut) $\leq$ ev (measure and cut)

where ev (.) denotes the error variance for (.) and estimate and cut refers to taking the optimum estimate of CSI at CID (i.e., $\hat{x}_k$) as the depth of coal at the drum.

3.5.3 Schemes Using Present and Past Cut Data - In scheme III all the available (present or past cut) CID measurements that fall within a semicircle of specified radius (say, two measurement distance) with the present CID measurement point as the center, are employed to obtain an optimum estimate of the CSI at the present measurement point. The estimate thus computed is then used to predict the coal depth at the drum. Scheme IV uses estimates obtained during the present and the immediate previous passes, zeroing in on coal thickness at the drum from two directions - one in the direction of the cut and one into the coal seam face. The present measurement is coupled with the predicted value at the present point to get an optimum estimate of the CSI at that point. This estimate, which is along the present cut, together with the immediate previous estimate of the CSI along the seam face (and which is along the immediate previous cut) is used to predict the CSI at the next CID measurement point as well as at the drum. This two-dimensional version of predictor-corrector approach is continued as the shearer proceeds down the longwall face as well as for subsequent passes. In both the schemes, the estimates are optimal in the sense that the variance of the estimation/prediction error is a minimum.

Before outlining the two developed schemes, the assumptions and the notation involved are stated:

3.5.3.1 Assumptions and Notation - The CID output at the k^{th} measurement during the r^{th} pass, denoted by $z(k,r)$, is assumed to be the sum of the average coal depth, $x(k,r)$, and the error in the k^{th} measurement, $n(k,r)$, i.e.,

$$z(k,r) = x(k,r) + n(k,r) \qquad (3.16)$$

The assumptions made are summarized as follows:

mean of $x(k,r) = E\{x(k,r)\} = \mu$

variance of $x(k,r) = E\{(x(k,r)-\mu)^2\} = \sigma^2_{x(k,r)}$

mean of $n(k,r) = 0$

variance of $n(k,r) = \sigma^2_n$

It is further assumed that the correlation function of the CSI profiles $x(k_1,r_1)$ and $x(k_2,r_2)$ is known. It is also assumed that the measurement errors are uncorrelated and that the actual CSI is uncorrelated with the CID measurement error, that is,

$$E\{x(k_1,r_1)n(k_2,r_2)\} = 0 \quad \text{for all } k_1,\ k_2,\ r_1, \text{ and } r_2$$

The following notation is adopted: $\hat{x}(k,r)$ and $\hat{x}_p(k,r)$ denote, respectively, the best estimate and the predicted value of the CSI at the k^{th} measurement point during the r^{th} pass of the shearer down the longwall face. $\hat{x}_d(k,r)$ represents the predicted value of $x_d(k,r)$, the coal depth at the drum from the k^{th} measurement point during the r^{th} pass (henceforth referred to as the (k,r) measurement point).

$\sigma_{x(k_1,r_1)x(k_2,r_2)}$ is a measure of the correlation of the CSI $x(k_1,r_1)$ and $x(k_2,r_2)$ and is defined as

$$\sigma_{x(k_1,r_1)x(k_2,r_2)} = E\{(x(k_1,r_1)-\mu)(x(k_2,r_2)-\mu)\}$$

It can be rewritten in terms of the correlation coefficient $\rho_{(k_1,r_1)(k_2,r_2)}$ of $x(k_1,r_1)$ and $x(k_2,r_2)$ as

$$\sigma_{x(k_1,r_1)x(k_2,r_2)} = \rho_{(k_1,r_1)(k_2,r_2)}\sigma_{x(k_1,r_1)}\sigma_{x(k_2,r_2)}$$

The estimation and prediction errors are respectively defined as

$$\tilde{x}(k,r) = x(k,r) - \hat{x}(k,r)$$

$$\tilde{x}_p(k,r) = x(k,r) - \hat{x}_p(k,r)$$

3.5.3.2 Scheme III - Two-Dimensional Version of Scheme II - The best estimate of x(k,r) is obtained from all the CID measurements within a radius of m measurements (z_i) from the (k,r) point. This is illustrated in Figure 3-68 for m = 2.

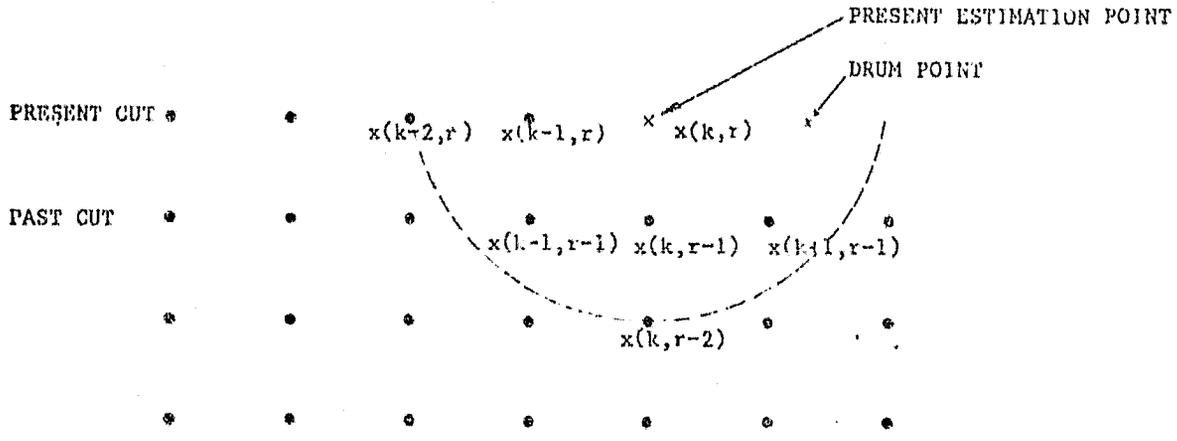

Figure 3-68. Scheme III

The estimate $\hat{x}(k,r)$ is sought as a linear combination of the measurements z_i and the estimator is of the form

$$\hat{x}(k,r) = \mu + \sum_{i=1}^{m_1} g_i(z_i - \mu)$$

or in vector form

$$\hat{x}(k,r) = \mu + \underline{g}^T(k,r)(\underline{z}(k,r) - \underline{\mu}) \qquad (3.17)$$

where the vector $\underline{g}(k,r)$ is determined so that the estimation error variance, $V_1 = E\{(x(k,r)-\hat{x}(k,r))^2\}$, is minimized. For the case $m = 2$ (see Figure 3-68) the vector $\underline{z}(k,r)$ consists of all the measurements within the dotted semicircle. The vector $\underline{\mu}$ has μ as its components.

The coal depth at the drum is predicted around μ, the mean of the CSI, using the current best estimate at (k,r) point obtained from (3.17)

$$\hat{x}_d(k,r) = \mu + \gamma_d(k,r)(\hat{x}(k,r) - \mu) \tag{3.18}$$

where $\gamma_d(k,r)$ is found so that the prediction error variance, $V_2 = E\{(x_d(k,r)-\hat{x}_d(k,r))^2\}$, is minimized.

The optimal value of $\underline{g}$ of (3.17) is found using variational calculus approach. Let

$$\underline{g}(k,r) = \underline{g}^*(k,r) + \varepsilon\Delta\underline{g}$$

where $\underline{g}^*(k,r)$ is the optimal value of $\underline{g}(k,r)$ and then set

$$\left.\frac{\partial V_1}{\partial \varepsilon}\right|_{\varepsilon=0} = 0$$

and make this result independent of $\Delta\underline{g}$. Thus

$$\left.\frac{\partial V_1}{\partial \varepsilon}\right|_{\varepsilon=0} = 0 = E\{\Delta\underline{g}^T(\underline{z}(k,r)-\underline{\mu})(x(k,r)-\mu-\underline{g}^{*T}(k,r)(\underline{z}(k,r)-\underline{\mu}))\}$$

which results in the optimal $\underline{g}(k,r)$ of (3.17) as

$$\underline{g}(k,r) = \left[E\{(\underline{z}(k,r)-\underline{\mu})(\underline{z}(k,r)-\underline{\mu})^T\}\right]^{-1} E\{(\underline{z}-\underline{\mu})(x(k,r)-\mu)\} \tag{3.19}$$

Again, using the variational calculus approach, let

$$\gamma_d(k,r) = \gamma_d^*(k,r) + \varepsilon\Delta\gamma_d$$

where $\gamma_d^*(k,r)$ is the value of $\gamma_d(k,r)$ that minimizes V_2. Thus

$$\left.\frac{\partial V_2}{\partial \epsilon}\right|_{\epsilon=0} = 0 = E\{\Delta\gamma_d(\hat{x}(k,r)-\mu)(x_d(k,r)-\mu-\gamma_d^*(k,r)(\hat{x}(k,r)-\mu))\}$$

so that

$$\gamma_d^*(k,r) = \frac{E\{(\hat{x}(k,r)-\mu)(x_d(k,r)-\mu)\}}{E\{(\hat{x}(k,r)-\mu)^2\}} \triangleq \frac{\sigma_{\hat{x}(k,r)x_d(k,r)}}{\sigma^2_{\hat{x}(k,r)}} \qquad (3.20)$$

The numerator and denominator of (3.20) can be computed as follows:

$$\sigma_{\hat{x}(k,r)x_d(k,r)} = E\{(\hat{x}(k,r)-\mu)(x_d(k,r)-\mu)\}$$

$$= \underline{g}^T(k,r)\, E\{(\underline{z}(k,r)-\underline{\mu})(x_d(k,r)-\mu)\} \text{ using (3.17)} \qquad (3.21)$$

$$\sigma^2_{\hat{x}(k,r)} = E\{(\hat{x}(k,r)-\mu)^2\}$$

$$= \underline{g}^T(k,r)\, E\{(\underline{z}(k,r)-\mu)(x(k,r)-\mu)\} \text{ using (3.17) and (3.19)} \qquad (3.22)$$

The variance of the prediction error can be found to be

$$\text{var}\{\tilde{x}_d(k,r)\} = E\{(x_d(k,r)-\hat{x}_d(k,r))^2\}$$

$$= \sigma^2_{x_d(k,r)} - \gamma_d(k,r)\sigma_{\hat{x}(k,r)x_d(k,r)} \qquad (3.23)$$

using (3.18) and (3.20)

The developed algorithm is summarized for convenience:

ALGORITHM III

Estimation:

$$\hat{x}(k,r) = \mu + \underline{g}^T(k,r)(\underline{z}(k,r)-\underline{\mu})$$

Prediction: (at the drum from (k,r) point)

$$\hat{x}_d(k,r) = \mu + \gamma_d(k,r)(\hat{x}(k,r)-\mu)$$

$$\gamma_d(k,r) = \sigma_{\hat{x}(k,r)x_d(k,r)} \Big/ \sigma^2_{\hat{x}(k,r)}$$

$$\sigma_{\hat{x}(k,r)x_d(k,r)} = \underline{g}^T(k,r)\ E\{(\underline{z}(k,r)-\underline{\mu})(x_d(k,r)-\mu)\}$$

$$\sigma^2_{\hat{x}(k,r)} = \underline{g}^T(k,r)\ E\{(\underline{z}(k,r)-\underline{\mu})(x(k,r)-\mu)\}$$

$$\underline{g}(k,r) = \left[E\{(\underline{z}(k,r)-\underline{\mu})(\underline{z}(k,r)-\underline{\mu})^T\}\right]^{-1} E\{(\underline{z}(k,r)-\underline{\mu})(x(k,r)-\mu)\}$$

Note that during the first pass, as well as at the first measurement of each pass, scheme II is used for estimation and prediction. During the subsequent passes one can resort to the cases m = 1 or m = 2.

For the case m = 1, with $\underline{z}(k,r) = (z(k-1,r),\ z(k,r),\ z(k,r-1))^T$, the (noninverted) symmetric matrix that appears in the expression for $\underline{g}(k,r)$ can be explicitly written as follows:

$$E\{(\underline{z}(k,r)-\underline{\mu})(\underline{z}(k,r)-\underline{\mu})^T\} = \begin{bmatrix} \sigma^2_{x(k-1,r)}+\sigma^2_n & \sigma_{x(k-1,r)x(k,r)} & \sigma_{x(k-1,r)x(k,r-1)} \\ \sigma_{x(k-1,r)x(k,r)} & \sigma^2_{x(k,r)}+\sigma^2_n & \sigma_{x(k,r)x(k,r-1)} \\ \sigma_{x(k,r-1)x(k-1,r)} & \sigma_{x(k,r-1)x(k,r)} & \sigma^2_{x(k,r-1)}+\sigma^2_n \end{bmatrix}$$

Also

$$E\{(\underline{z}(k,r)-\underline{\mu})(x(k,r)-\mu))\} = \begin{bmatrix} \sigma_{x(k-1,r)x(k,r)} \\ \sigma^2_{x(k,r)} \\ \sigma_{x(k,r-1)x(k,r)} \end{bmatrix}$$

The above two expressions determine $g(k,r)$. Explicit expressions for (3.21) and (3.22) can be obtained in a similar manner.

3.5.3.3 Scheme IV - Two-Dimensional Predictor-Corrector Approach - The optimum estimate of $x(k,r)$ is obtained from the present CID measurement $z(k,r)$ in conjunction with the predicted value at (k,r) point, i.e., $\hat{x}_p(k,r)$, which is based on $\hat{x}(k-1,r)$, the best estimate of the previous measurement point along the cut, and $\hat{x}(k,r-1)$, the best estimate of $(k,r-1)$ point out the seam face from the (k,r) point. This is illustrated in Figure 3-69.

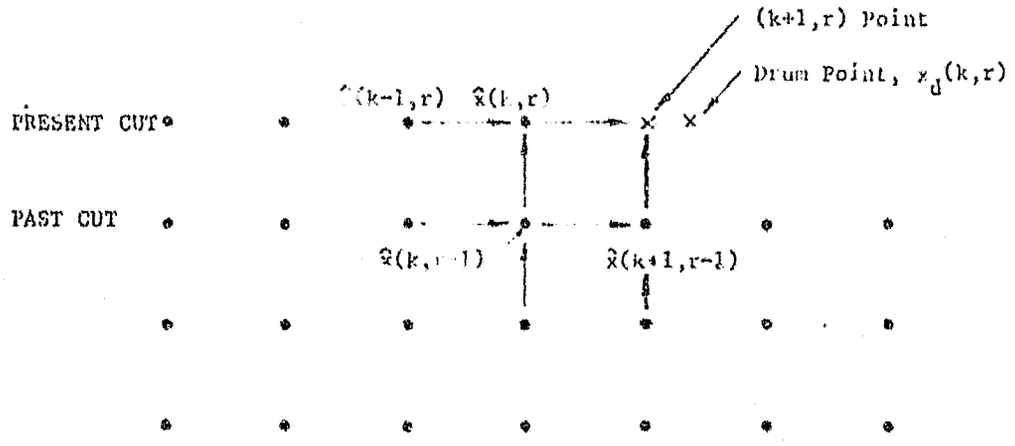

Figure 3-69. Scheme IV

The estimator is of the form

$$\hat{x}(k,r) = \hat{x}_p(k,r)+g(k,r)(z(k,r)-\hat{x}_p(k,r)) \qquad (3.24)$$

where the weighting factor $g(k,r)$ is determined so that the variance of the estimation error, $V_3 = E\{(x(k,r)-\hat{x}(k,r))^2\}$, is minimized. The coal depth at the next CID measurement point (3.25) and at the drum (3.26) are predicted around μ, the mean of the CSI, using the current best estimate along the cut, $x(k,r)$, and the immediate previous best estimate along the seam face, $\hat{x}(k+1,r-1)$:

$$\hat{x}_p(k+1,r) = \mu+\alpha(k,r)(\hat{x}(k,r)-\mu)+\beta(k+1,r-1)(\hat{x}(k+1,r-1)-\mu) \qquad (3.25)$$

$$\hat{x}_d(k,r) = \mu+\alpha_d(k,r)(\hat{x}(k,r)-\mu)+\beta_d(k+1,r-1)(\hat{x}(k+1,r-1)-\mu) \qquad (3.26)$$

Here $\alpha(k,r)$ and $\beta(k+1,r-1)$ are weighting constants to be determined so that the prediction error variance, $V_4 = E\{(x(k+1,r) - \hat{x}_p(k+1,r))^2\}$, is minimized. Similarly, $\alpha_d(k,r)$ and $\beta_d(k+1,r-1)$ are found such that the prediction error variance at the drum, $V_5 = E\{(x_d(k,r)-\hat{x}_d(k,r))^2\}$, is minimized.

The optimal value of $g(k,r)$ of (3.24) is found using variational calculus approach.

Let $\quad g(k,r) = g^*(k,r)+\epsilon\Delta g$

where $g^*(k,r)$ is the value of $g(k,r)$ that minimizes V_3. Thus

$$\left.\frac{\partial V_3}{\partial \epsilon}\right|_{\epsilon=0} = 0 = E\{\Delta g(z(k,r)-\hat{x}_p(k,r))(x(k,r)-\hat{x}_p(k,r)-g^*(k,r)(z(k,r)-\hat{x}_p(k,r))\}$$

which results in the optimal value of $g(k,r)$ of (3.24) as

$$g(k,r) = \frac{\text{var}\{\tilde{x}_p(k,r)\}}{\text{var}\{\tilde{x}_p(k,r)\} + \sigma_n^2} \tag{3.27}$$

where $\text{var}\{\tilde{x}_p(k,r)\} = E\{(x(k,r)-\hat{x}_p(k,r))^2\}$ is the variance of the prediction error.

Equation (3.25) can be written in a form similar to (3.17) and, hence, the weighting factors $\alpha(k,r)$ and $\beta(k+1,r-1)$ can be computed in a manner similar to $\underline{g}(k,r)$ of (3.17) (see (3.19)) and can be found to be

$$\begin{bmatrix} \alpha(k,r) \\ \beta(k+1,r-1) \end{bmatrix} = \begin{bmatrix} \sigma^2_{\hat{x}(k,r)} & \sigma_{\hat{x}(k,r)\hat{x}(k+1,r-1)} \\ \sigma_{\hat{x}(k,r)\hat{x}(k+1,r-1)} & \sigma^2_{\hat{x}(k+1,r-1)} \end{bmatrix}^{-1} \begin{bmatrix} \sigma_{\hat{x}(k,r)x(k+1,r)} \\ \sigma_{\hat{x}(k+1,r-1)x(k+1,r)} \end{bmatrix}$$

which results in

$$\alpha(k,r) = \frac{1}{D_{kr}}\left(\sigma^2_{\hat{x}(k+1,r-1)}\sigma_{\hat{x}(k,r)x(k+1,r)} - \sigma_{\hat{x}(k,r)\hat{x}(k+1,r-1)}\sigma_{\hat{x}(k+1,r-1)x(k+1,r)}\right) \tag{3.28}$$

and

$$\beta(k+1,r-1) = \frac{1}{D_{kr}}(\sigma^2_{\hat{x}(k,r)}\sigma_{\hat{x}(k+1,r-1)x(k+1,r)} - \sigma_{\hat{x}(k,r)\hat{x}(k+1,r-1)}\sigma_{\hat{x}(k,r)x(k+1,r)}) \tag{3.29}$$

where

$$D_{kr} = \sigma^2_{\hat{x}(k,r)}\sigma^2_{\hat{x}(k+1,r-1)} - \sigma^2_{\hat{x}(k,r)\hat{x}(k+1,r-1)} \tag{3.30}$$

Expressions for all the correlations that appear in the right hand side of equations (3.28) thru (3.30) can easily be obtained by using (3.24) and (3.25). These expressions are included in the summary of the developed algorithm below.

It may be pointed out that during the first pass Scheme I should be used. Also, the same scheme is used (laterally) at the first measurement point during each pass. This is explicitly given in the algorithm below.

ALGORITHM IV

$k \geq 1,\ r \geq 2,\ i \geq 1,\ j \geq 1$

Estimation at the present measurement point, (k,r):

$$\hat{x}(k,r) = \hat{x}_p(k,r) + g(k,r)(z(k,r) - \hat{x}_p(k,r))$$

Prediction at the next measurement point, (k+1,r):

$$\hat{x}_p(k+1,r) = \mu + \alpha(k,r)(\hat{x}(k,r)-\mu) + \beta(k+1,r-1)(\hat{x}(k+1,r-1)-\mu)$$

Prediction at the drum from (k,r) point:

$$\hat{x}_d(k,r) = \mu + \alpha_d(k,r)(\hat{x}(k,r)-\mu) + \beta_d(k+1,r-1)(\hat{x}(k+1,r-1)-\mu)$$

$$g(k,r) = \frac{\text{var}\{\tilde{x}_p(k,r)\}}{\text{var}\{\tilde{x}_p(k,r)\} + \sigma_n^2}$$

$$\alpha(k,r) = \frac{1}{D_{kr}}(\sigma^2_{\hat{x}(k+1,r-1)}\sigma_{\hat{x}(k,r)x(k+1,r)} - \sigma_{\hat{x}(k,r)\hat{x}(k+1,r-1)}\sigma_{\hat{x}(k+1,r-1)x(k+1,r)})$$

$$\beta(k+1,r-1) = \frac{1}{D_{kr}}(\sigma^2_{\hat{x}(k,r)}\sigma_{\hat{x}(k+1,r-1)x(k+1,r)} - \sigma_{\hat{x}(k,r)\hat{x}(k+1,r-1)}\sigma_{\hat{x}(k,r)x(k+1,r)})$$

$$D_{kr} = \sigma^2_{\hat{x}(k,r)}\sigma^2_{\hat{x}(k+1,r-1)} - \sigma^2_{\hat{x}(k,r)\hat{x}(k+1,r-1)}$$

$$\sigma^2_{\hat{x}(k+1,r)} = (1-g(k+1,r))^2\{\alpha^2(k,r)\sigma^2_{\hat{x}(k,r)}+\beta^2(k+1,r-1)\sigma^2_{\hat{x}(k+1,r-1)}$$

$$+2\alpha(k,r)\beta(k+1,r-1)\sigma_{\hat{x}(k,r)\hat{x}(k+1,r-1)}\}$$

$$+2g(k+1,r)(1-g(k+1,r))\{\alpha(k,r)\sigma_{\hat{x}(k,r)x(k+1,r)}$$

$$+\beta(k+1,r-1)\sigma_{\hat{x}(k+1,r-1)x(k+1,r)}\}$$

$$+g^2(k+1,r)\sigma^2_{x(k+1,r)}+g^2(k+1,r)\sigma^2_n$$

$$\sigma_{\hat{x}(k+1,r)x(j,i)} = (1-g(k+1,r))\alpha(k,r)\sigma_{\hat{x}(k,r)x(j,i)}$$

$$+(1-g(k+1,r))\beta(k+1,r-1)\sigma_{\hat{x}(k+1,r-1)x(j,i)}$$

$$+g(k+1,r)\sigma_{x(k+1,r)x(j,i)}$$

$$\sigma_{\hat{x}(k+1,r)\hat{x}(j,i)} = (1-g(k+1,r))(1-g(j,i))\{\alpha(k,r)\alpha(j-1,i)\sigma_{\hat{x}(k,r)\hat{x}(j-1,i)}$$

$$+\alpha(k,r)\beta(j,i-1)\sigma_{\hat{x}(k,r)\hat{x}(j,i-1)}+\alpha(j-1,i)\beta(k+1,r-1)\sigma_{\hat{x}(k+1,r-1)\hat{x}(j-1,i)}$$

$$+\beta(k+1,r-1)\beta(j,i-1)\sigma_{\hat{x}(k+1,r-1)\hat{x}(j,i-1)}\}$$

$$+g(k+1,r)(1-g(j,i))\{\alpha(j-1,i)\sigma_{\hat{x}(j-1,i)x(k+1,r)}+\beta(j,i-1)\sigma_{\hat{x}(j,i-1)x(k+1,r)}\}$$

$$+g(j,i)(1-g(k+1,r))\{\alpha(k,r)\sigma_{\hat{x}(k,r)x(j,i)}+\beta(k+1,r-1)\sigma_{\hat{x}(k+1,r-1)x(j,i)}\}$$

$$+g(k+1,r)g(j,i)\sigma_{x(k+1,r)x(j,i)}$$

$$(k+1 \neq j \text{ when } r = i \text{ and vice versa})$$

$$\text{var}\{\tilde{x}_p(k+1,r)\} = \sigma^2_{x(k+1,r)}+\alpha^2(k,r)\sigma^2_{\hat{x}(k,r)}-2\alpha(k,r)\sigma_{\hat{x}(k,r)x(k+1,r)}$$

$$+2\alpha(k,r)\beta(k+1,r-1)\sigma_{\hat{x}(k,r)\hat{x}(k+1,r-1)}$$

$$-2\beta(k+1,r-1)\sigma_{\hat{x}(k+1,r-1)x(k+1,r)}+\beta^2(k+1,r-1)\sigma^2_{\hat{x}(k+1,r-1)}$$

The expressions for $\alpha_d(k,r)$ and $\beta_d(k+1,r-1)$ are similar to those of $\alpha(k,r)$ and $\beta(k+1,r-1)$ appropriately modified.

During the first pass (r=1): $k \geq 1$

$$\hat{x}(k+1,1) = \hat{x}_p(k+1,1)+g(k+1,1)(z(k+1,1)-\hat{x}_p(k+1,1))$$

$$\hat{x}_p(k+1,1) = \mu+\alpha(k,1)(\hat{x}(k,1)-\mu)$$

$$\hat{x}_d(k,1) = \mu+\alpha_d(k,1)(\hat{x}(k,1)-\mu)$$

$$g(k+1,1) = \frac{\text{var}\{\hat{x}_p(k+1,1)\}}{\text{var}\{\hat{x}_p(k+1,1)\}+\sigma_n^2}$$

$$\text{var}\{\hat{x}_p(k+1,1)\} = \sigma^2_{x(k+1,1)}-\alpha(k,1)\sigma_{\hat{x}(k,1)x(k+1,1)}$$

$$\alpha(k,1) = \frac{\sigma_{\hat{x}(k,1)x(k+1,1)}}{\sigma^2_{\hat{x}(k,1)}}$$

$$\alpha_d(k,1) = \frac{\sigma_{\hat{x}(k,1)x_d(k,1)}}{\sigma^2_{\hat{x}(k,1)}}$$

$$\sigma_{\hat{x}(j+1,1)x(k+2,1)} = \alpha(j,1)(1-g(j+1,1))\sigma_{\hat{x}(j,1)x(k+2,1)}+g(j+1,1)\sigma_{x(j+1,1)x(k+2,1)}$$

$$j = 1, 2, \ldots, k$$

$$\sigma_{\hat{x}(j+1,1)x_d(k,1)} = \alpha(j,1)(1-g(j+1,1))\sigma_{\hat{x}(j,1)x_d(k,1)}+g(j+1,1)\sigma_{x(j+1,1)x_d(k,1)}$$

$$j = 1, 2, \ldots, k$$

$$\sigma^2_{\hat{x}(k+1,1)} = \alpha(k,1)\sigma_{\hat{x}(k,1)x(k+1,1)}+g(k+1,1)\ \ \text{var}\{\tilde{x}_p(k+1,1)\}$$

Initial conditions:

$$\hat{x}(1,1) = x(1,1) = z(1,1)$$

$$\sigma^2_{\hat{x}(1,1)} = \sigma^2_{x(1,1)}+\sigma^2_n$$

At the first measurement point of each pass (k = 1): $r \geq 1$

$$\hat{x}(1,r+1) = \hat{x}_p(1,r+1)+g(1,r+1)(z(1,r+1)-\hat{x}_p(1,r+1))$$

$$\hat{x}_p(1,r+1) = \mu+\beta(1,r)(\hat{x}(1,r)-\mu)$$

$$\hat{x}_d(1,r) = \mu+\beta_d(1,r)(\hat{x}(1,r)-\mu)$$

$$g(1,r+1) = \frac{\text{var}\{\tilde{x}_p(1,r+1)\}}{\text{var}\{\tilde{x}_p(1,r+1)\}+\sigma_n^2}$$

$$\text{var}\{\tilde{x}_p(1,r+1)\} = \sigma^2_{x(1,r+1)}-\beta(1,r)\sigma_{\hat{x}(1,r)x(1,r+1)}$$

$$\beta(1,r) = \frac{\sigma_{\tilde{x}(1,r)x(1,r+1)}}{\sigma^2_{\tilde{x}(1,r)}}$$

$$\beta_d(1,r) = \frac{\sigma_{\tilde{x}(1,r)x_d(1,r)}}{\sigma^2_{\tilde{x}(1,r)}}$$

$$\sigma_{\tilde{x}(1,i+1)x(1,r+2)} = \beta(1,i)(1-g(1,i+1)\sigma_{\tilde{x}(1,i)x(1,r+2)}+g(1,i+1)\sigma_{x(1,i+1)x(1,r+2)}$$

$$i = 1, 2, \ldots, r$$

$$\sigma_{\tilde{x}(1,i+1)x_d(1,r)} = \beta(1,i)(1-g(1,i+1))\sigma_{\hat{x}(1,i)x_d(1,r)}+g(1,i+1)\sigma_{x(1,i+1)x_d(1,r)}$$

$$i = 1, 2, \ldots, r$$

$$\sigma^2_{\tilde{x}(1,i+1)} = \beta(1,r)\sigma_{\hat{x}(1,r)x(1,r+1)}+g(1,r+1)\text{var}\{\tilde{x}_p(1,r+1)\}$$

Initial conditions same as for the first pass.

It is seen from Sections 3.5.3.2 and 3.5.3.3 that the basic differences between the two developed algorithms is that one employs estimates in the immediate vicinity of the present measurement to obtain an optimum estimate of the coal/shale interface at the present measurement point (algorithm IV), while the other uses CID measurements to accomplish the same goal (algorithm III). Moreover, algorithm III uses past cut data that is ahead of the present measurement point (but obtained during the previous passes) whereas the framework of scheme IV does not permit such usage.

Analytical comparison of all the developed schemes is difficult due to the complexity of scheme IV. However, it is expected that scheme IV results in the least prediction error variance and is most sensitive to unmodeled errors.

3.6 VCS PERFORMANCE WITH PREDICTIVE ALGORITHMS

3.6.1 Predictive Algorithm Simulation

Two simulations were used to study the performance of the predictive algorithms: the VCS simulation previously described, and a simplified simulation by which parameter studies could be made.

In the simplified simulation, a random process was generated with known variance and correlation properties. The mine correlation studies showed that an exponential correlation model could be used to approximate the correlation of the actual mines. Therefore, such a first order process was generated and inputted to the predictive algorithms. White noise of known variance was added to the correlated noise input, to simulate CID measurement noise. The output of the algorithms was then compared with the input to determine both estimation and prediction performance. This was determined by computing the RMS errors. The RMS of the input was computed and used as a measure of unaided system performance. The prediction refers to the performance obtained by projecting the estimated CID measurement ahead to the cutting point. Estimation refers to the results obtained by processing the CID measurement to remove measurement noise, and using this estimate as the raw CID data would be used.

C-3

3.6.2 Predictive Algorithm Performance With Simplified Simulation

3.6.2.1 Effect of Errors in Correlation Distance

Table 3-14 shows the simulation results for a number of parameter studies intended to determine the sensitivity of the algorithm to unknown statistics. The subscripts ACT and f refer, respectively, to the actual value and the value used in the filtering process. σ^2_{CSI} denotes the variance of the coal-shale interface. The entries in the table denote the RMS error in inches. The nominal run used the nominal conditions listed in the table. For this run, it was assumed that the filter had complete knowledge of the process and measurement noise statistics. The nominal run is in agreement with the analysis of Section 3.5 where it was determined that prediction has better performance than estimation, and that both are better than the measure and cut.

The correlation distance in the filter was varied holding the other parameters fixed. The actual process correlation distance was a constant 25 ft, while the correlation parameter in the filter was set to 13.2, 25, and 50 ft. The results shown in Table 3-14 indicate that the algorithms are relatively insensitive to uncertainty in knowledge of the correlation distances.

3.6.2.2 Effects of Errors in CSI Variance

Filter knowledge of the CSI variance was also studied. The filter CSI variance was set to half and twice the nominal

Table 3-14. Predictive Algorithms - Effects of Parameter Variations Simplified Simulation

CONDITIONS	SCHEME #1		SCHEME #2		MEASURE & CUT
	ESTIMATION	PREDICTION	ESTIMATION	PREDICTION	
NOMINAL	0.72	0.67	0.73	0.68	0.81
D_{ACT} = 25 FT D_f = 13.2 FT	0.58	0.55	0.59	0.56	0.68
D_{ACT} = 25 FT D_f = 25 FT	0.56	0.54	0.58	0.56	0.68
D_{ACT} = 25 FT D_f = 50 FT	0.55	0.54	0.58	0.57	0.68
σ^2_{CSI} = 3.469 σ^2_{CSIf} = 1.735	0.71	0.68	0.71	0.68	0.81
σ^2_{CSI} = 3.469 σ^2_{CSIf} = 6.938	0.74	0.69	0.74	0.70	0.81

NOMINAL CONDITIONS

V = 0.5 FT/S $\quad\quad$ σ^2_{CSI} = 3.469 IN^2

τ = 1 S $\quad\quad$ σ^2_{CSIf} = 3.469 IN^2

σ_N^2 = 0.25 IN^2 $\quad\quad$ D_{ACT} = 13.2 FT

D_f = 13.2 FT

ALL ENTRIES IN THE TABLE ARE RMS CUT ERROR IN INCHES.

value. Again, there is little effect, except that slightly worse performance was obtained where the filter variance was higher than the nominal value. In all cases, the prediction and estimation results were better than measure and cut results.

3.6.2.3 Comparison of Schemes

Parameter variation results for schemes 1 and 2 are shown in Table 3-14. It can be seen that scheme 2 is slightly worse than scheme 1 in both estimation and prediction. Scheme 2, however, is still better than the measure and cut results. Parameter variations yield the same conclusion as with scheme 1 namely, that the algorithm is essentially insensitive to parameter variations, and performs as predicted analytically.

3.6.3 Predictive Algorithm Performance With VCS Simulation

3.6.3.1 Effects of Measurement Type

Two possible procedures can be used to derive the measurement to be inputted to the predictive algorithms. One procedure is to simply input the CID data directly. However, such a procedure introduces a modeling error because the filters assume that the only randomness in the measurements is the CSI and measurement noise. The CID measurement also has randomness due to the roughness of the cut surface. A quantity called the total measurement is computed as the sum of the CID measurement plus the CID relative position sensor. This has the effect of referencing

the measurement to the shearer chassis and eliminating the cut roughness error. The total measurement and CID measurement results, shown in rows 2 and 3 of Table 3-15, are essentially the same as the nominal run with the simplified simulation. These results show that the total measurement yields better performance than the CID measurements. It should be noted that the mine bottom was artificially flattened to remove the effects of chassis undulation. The relationship between schemes 1 and 2 is the same as previously, in that scheme 1 performs better than scheme 2. Figures 3-70 and 3-71 show the performance of scheme 1 when total measurements are employed for both estimation and prediction. Figures 3-72 and 3-73 indicate VCS performance with scheme 2 using total measurements for both estimation and prediction.

3.6.3.2 Effects of Bottom Undulation

Another source of modeling errors is the undulation of the mine bottom which introduces an additional source of randomness which affects algorithm performance. Runs with the actual bottom, i.e., with bottom undulations, are shown in rows 4 and 5 of Table 3-15. It can be seen that under these conditions, the CID measurements yield better performance than the total measurements because the undulation causes larger errors in the total computation from the skid plane than it does in the CID measurement.

The effect of undulation has changed the performance of the algorithms relative to each other and relative to the measure and cut. It can be seen that estimation now performs better

Table 3-15. Prediction Algorithms - Effects of Modeling Errors VCS Simulation

CONDITIONS	SCHEME #1		SCHEME #2		CUT WITH CID DATA
	ESTIMATION	PREDICTION	ESTIMATION	PREDICTION	
FLAT FLOOR: NO NOISE	--	--	--	--	0.61
FLAT FLOOR: TOTAL MEASUREMENT: NORMAL NOISE	0.71	0.66	0.71	0.66	0.82
FLAT FLOOR: CID MEASUREMENT: NORMAL NOISE	0.75	0.75	0.77	0.77	0.82
ACTUAL FLOOR: TOTAL MEASUREMENT: NORMAL NOISE	1.47	2.22	1.41	1.96	1.27
ACTUAL FLOOR: CID MEASUREMENT: NORMAL NOISE	1.32	1.59	1.30	1.41	1.27
ACTUAL FLOOR: TOTAL MEASUREMENT: TREND IN TOP:	1.53	2.48	1.47	2.28	1.29
ACTUAL FLOOR: CID MEASUREMENT: TREND IN TOP: NORMAL NOISE	1.35	1.63	1.33	1.43	1.29
ACTUAL FLOOR: TOTAL MEASUREMENT: TREND IN TOP: ACTUAL NOISE	1.81	2.60	1.70	2.43	1.53
ACTUAL FLOOR: CID MEASUREMENT: TREND IN TOP: ACTUAL NOISE	1.56	2.03	1.53	1.68	1.53

ALL ENTRIES IN THIS TABLE ARE RMS CUT ERROR IN INCHES.

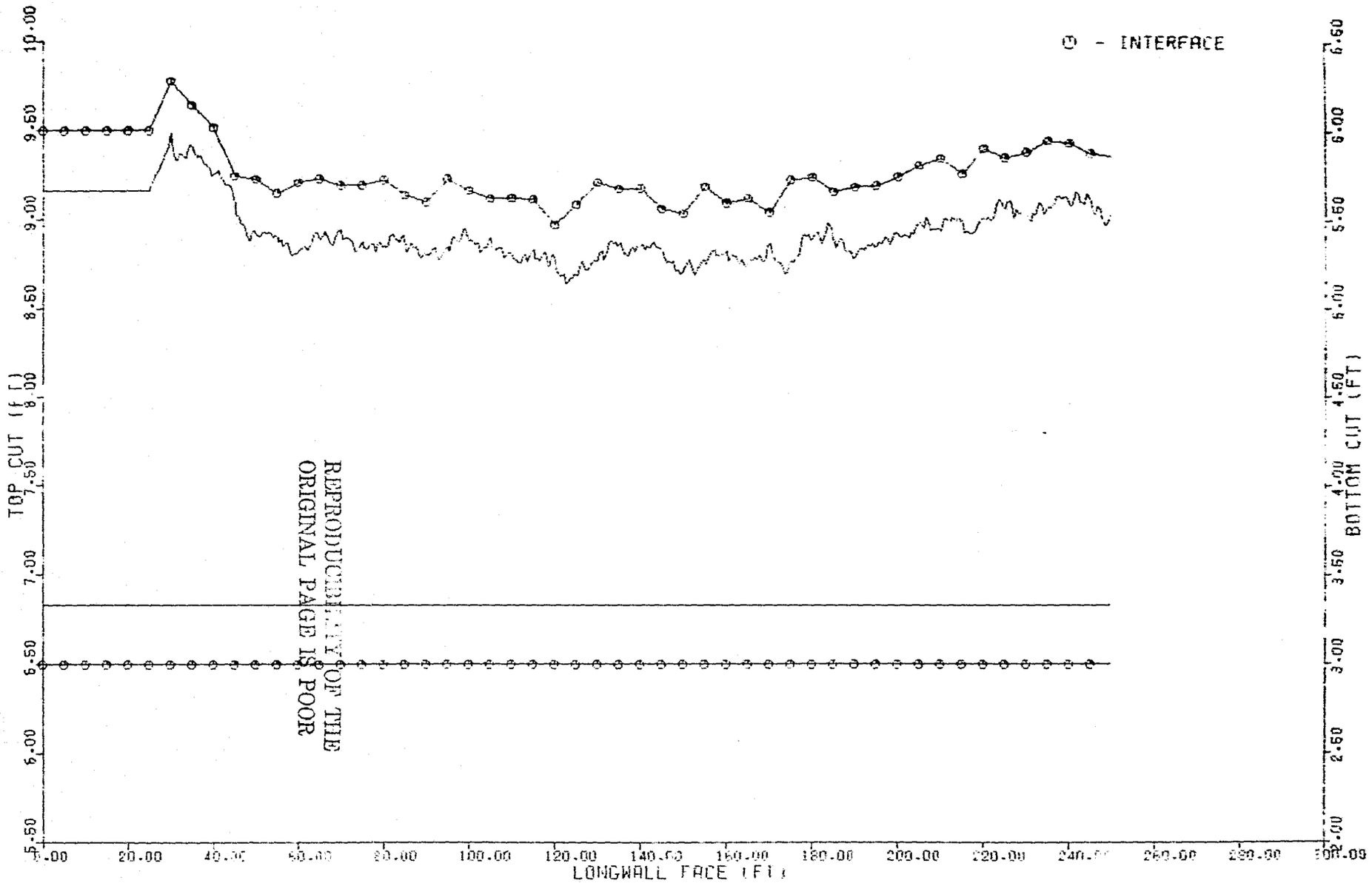

Figure 3-70. VCS Performance with Scheme 1 Estimation Using Total Measurements and Flat Bottom

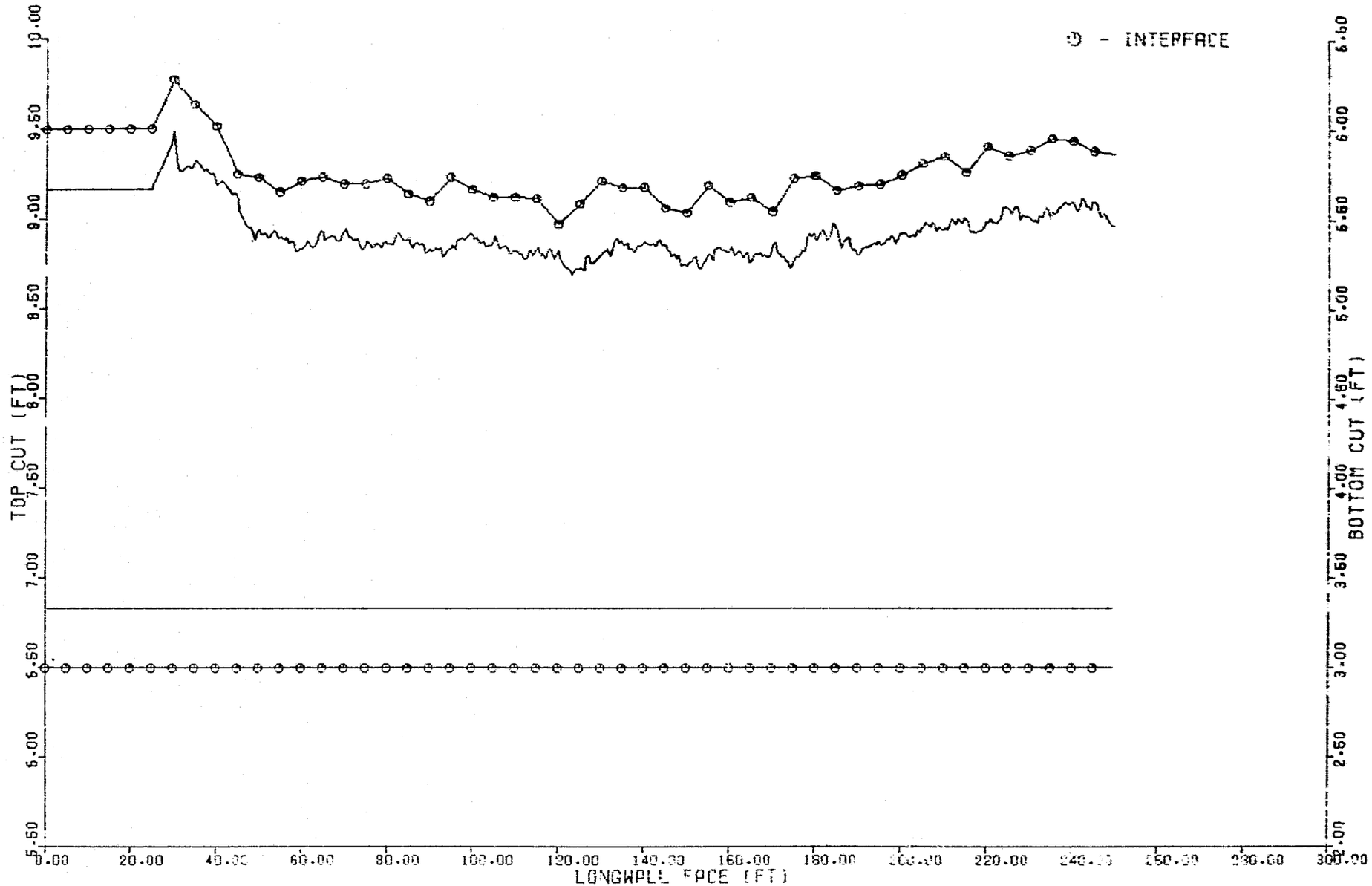

Figure 3-71. VCS Performance with Scheme 1 Prediction Using Total Measurements and Flat Bottom

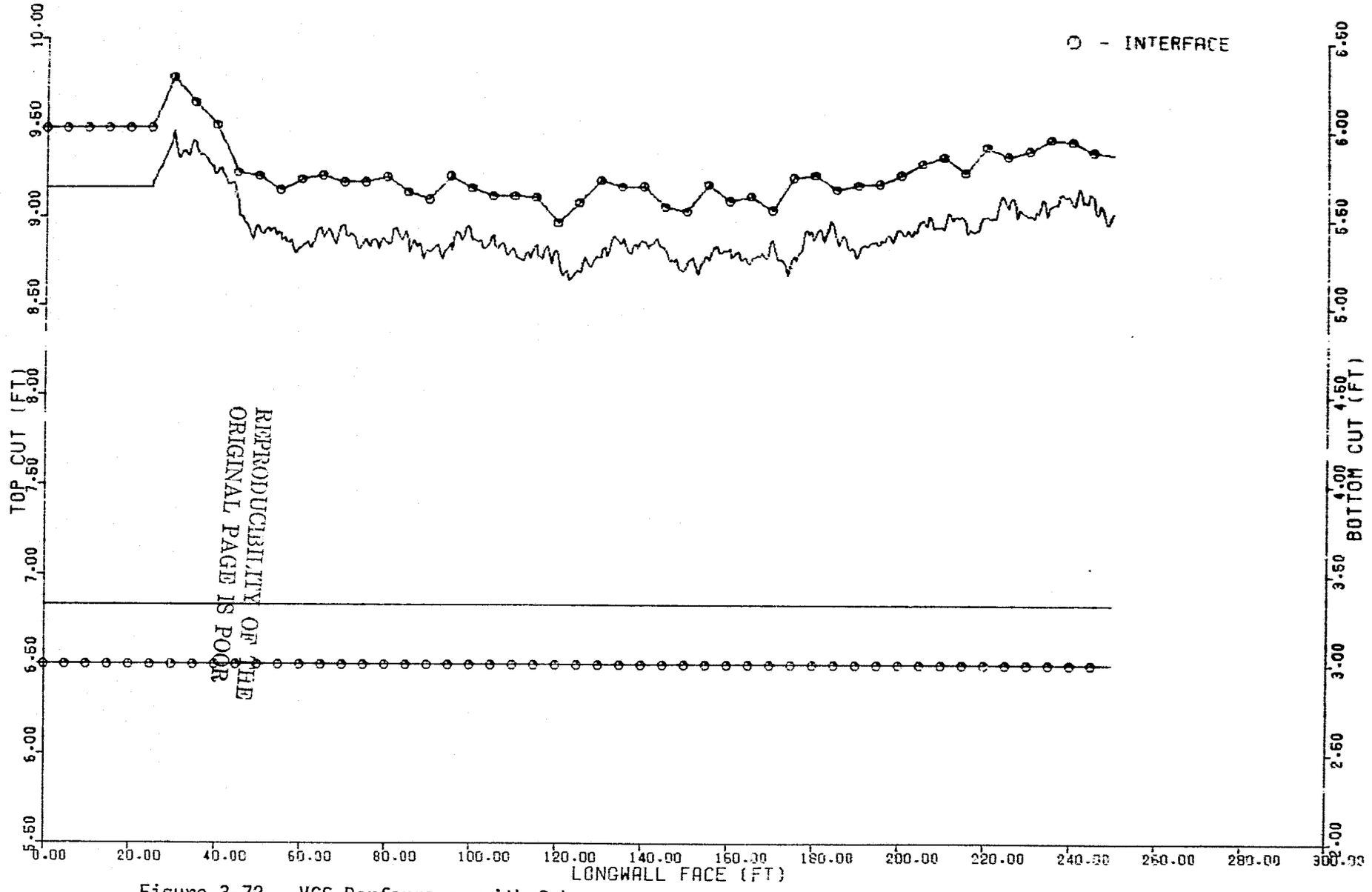

Figure 3-72. VCS Performance with Scheme 2 Estimation Using Total Measurements and Flat Bottom

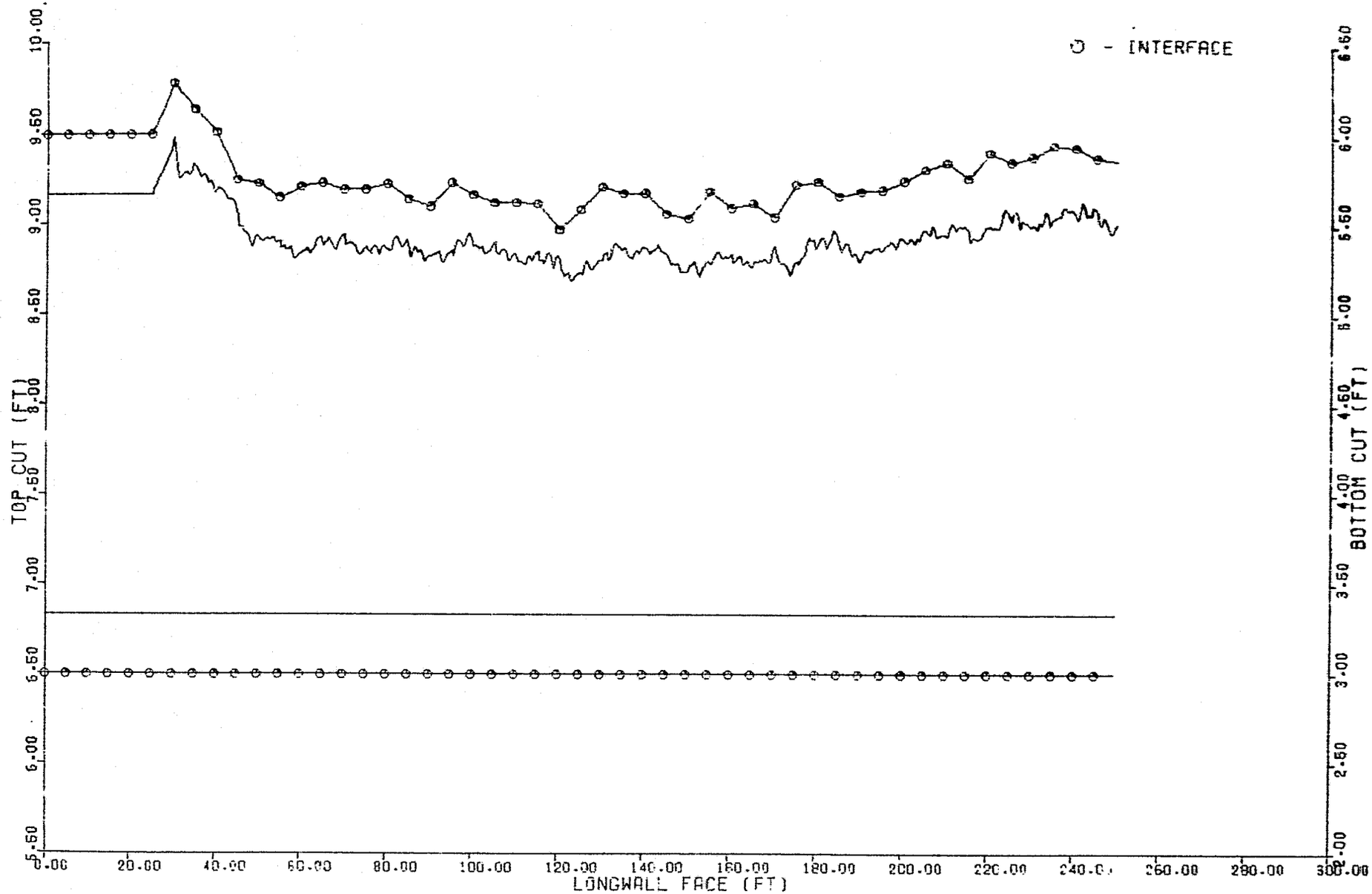

Figure 3-73. VCS Performance with Scheme 2 Prediction Using Total Measurements and Flat Bottom

than prediction for both schemes, and scheme 2 now performs somewhat better than scheme 1. A larger error is made in attempting prediction than in not attempting prediction because of the unmodeled error due to bottom undulation. Scheme 2 performs better than scheme 1 because the latter is more sensitive to unmodeled errors. Finally, it should be noted that both schemes perform worse than measure and cut in the presence of bottom undulations. Figures 3-74 through 3-81 present times histories of the prediction algorithms runs shown in rows 4 and 5 of Table 3-15.

3.6.3.3 Effects of Relative Slope Between Top and Bottom

The prediction algorithms assume that they are operating on the sum of zero mean, stationary random processes. If the mine top is not parallel to the bottom, that is, if it has a trend or slope relative to the bottom, the measurements appear nonstationary, and this affects performance. Rows 6 and 7 of Table 3-15 show this effect with total and CID measurements. The CID measurements are better than the total measurements and, again, scheme 2 performs better than scheme 1. Both schemes remain worse than measure and cut, and larger errors are made in prediction than in estimation.

3.6.3.4 Effects of Measurement Noise Model

The simulation results presented in rows 1 through 7 of Table 3-15 were obtained using normally distributed measurement noise. In fact, the measurement is not normal, but involves the nonlinear CID calibration curve discussed in Section 3.2.4.1. Rows

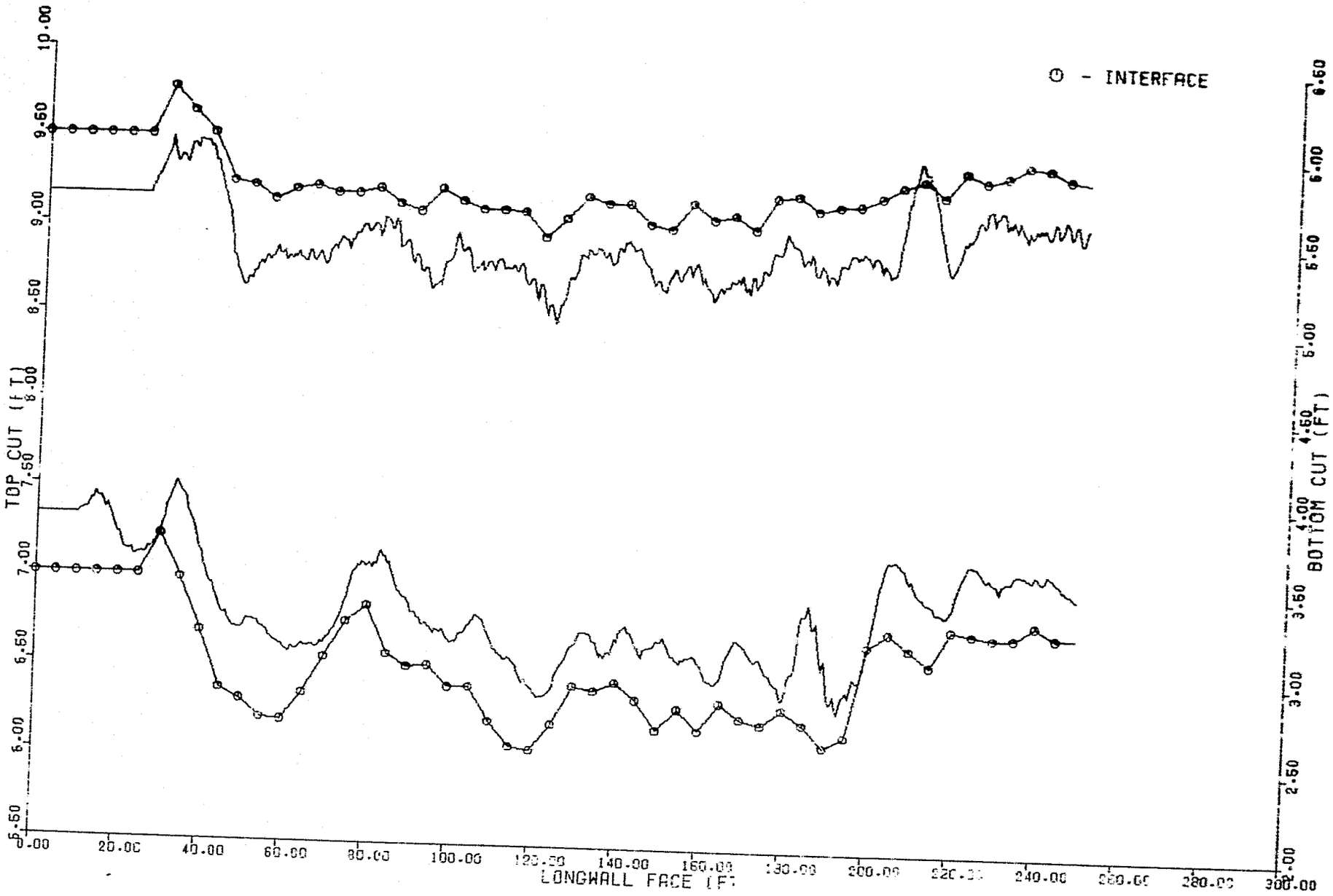

Figure 3-74. VCS Performance with Scheme 1 Estimation, with CID Measurements and Bottom Undulations

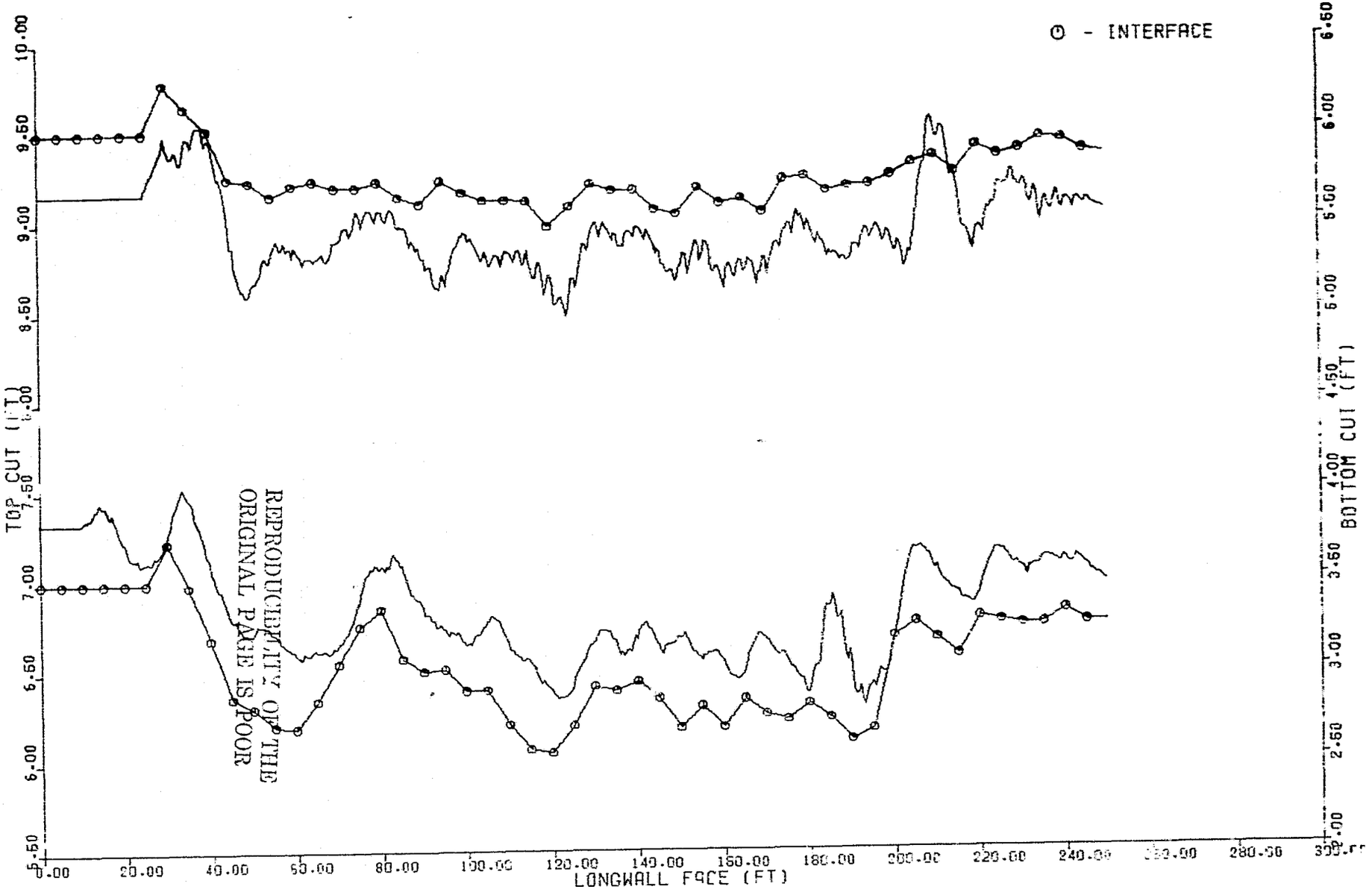

Figure 3-75. VCS Performance with Scheme 1 Prediction, with CID Measurements and Bottom Undulations

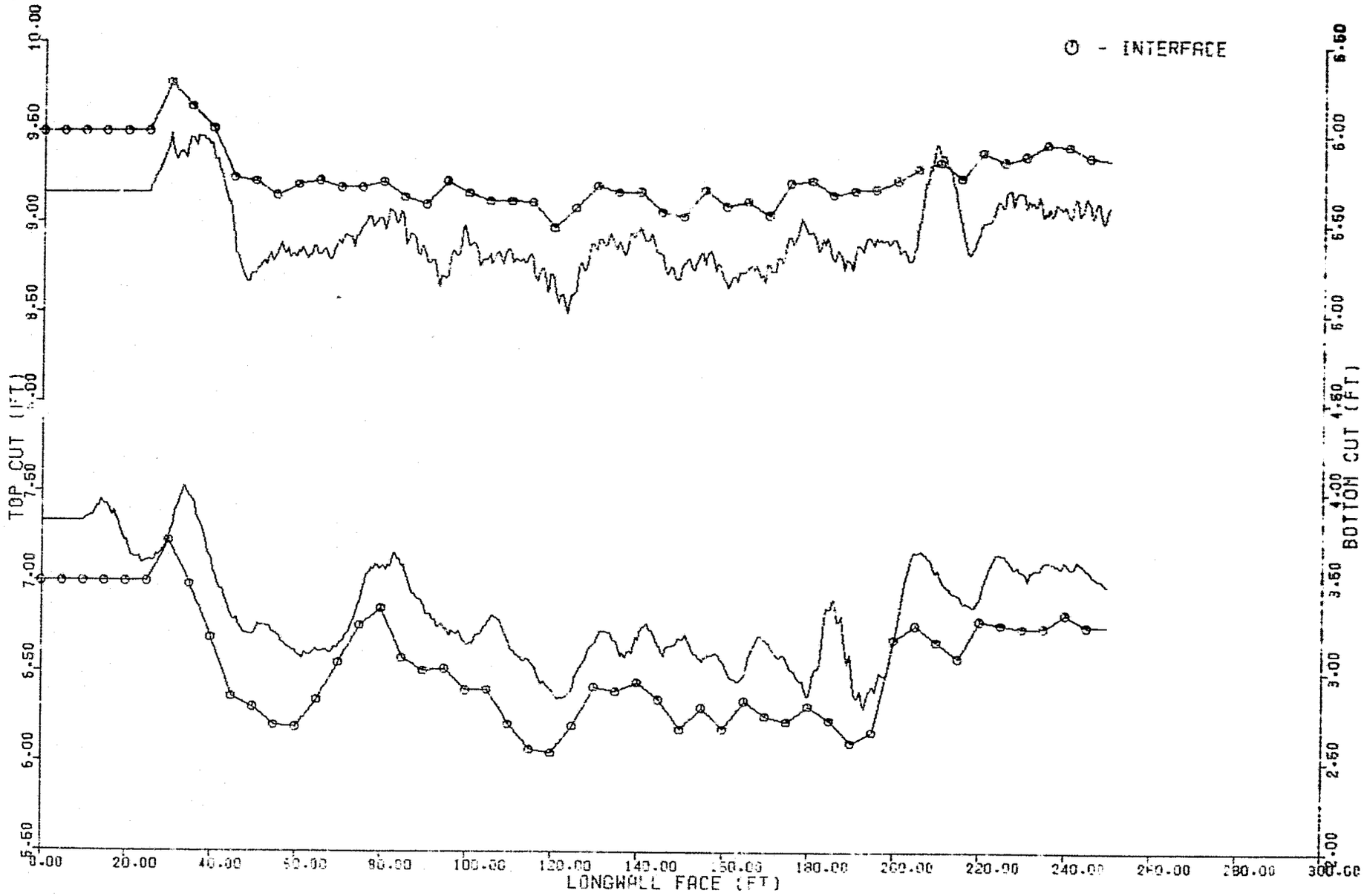

Figure 3-76. VCS Performance with Scheme 2 Estimation, with CID Measurements and Bottom Undulations

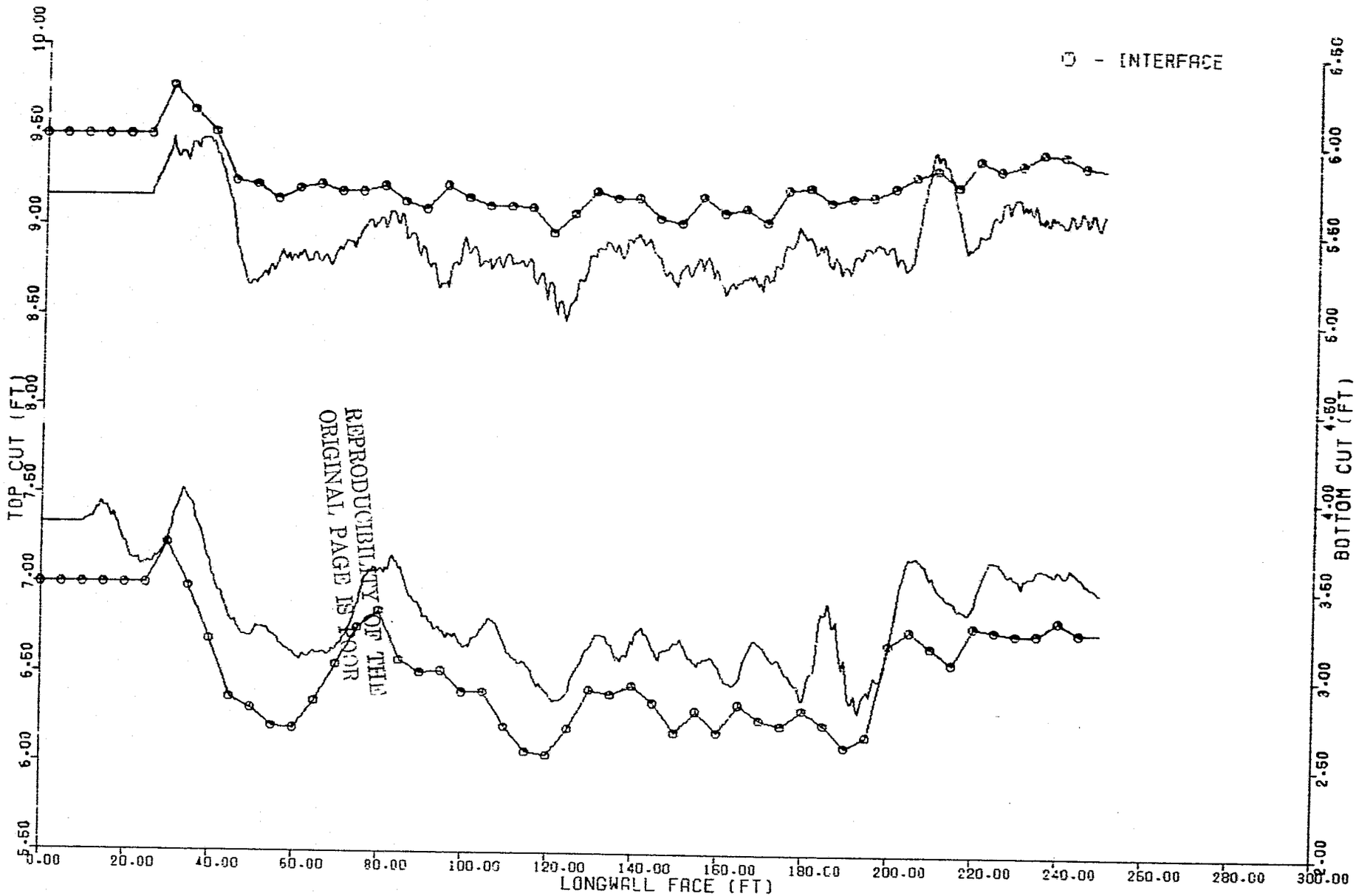

Figure 3-77. VCS Performance with Scheme 2 Prediction, with CID Measurements and Bottom Undulations

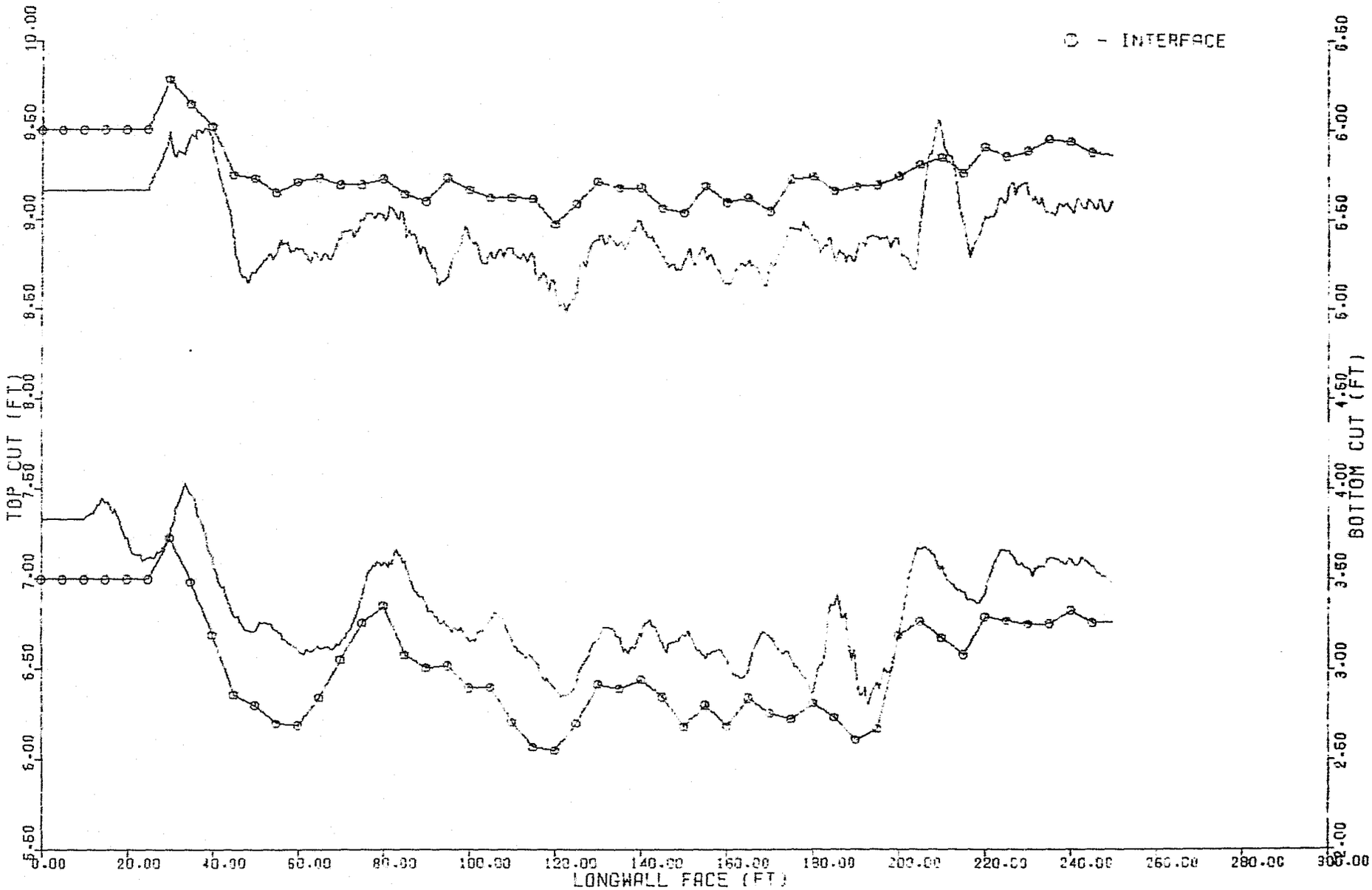

Figure 3-78. LCS Performance with Scheme 1 Estimation with Total Measurements and Bottom Undulations

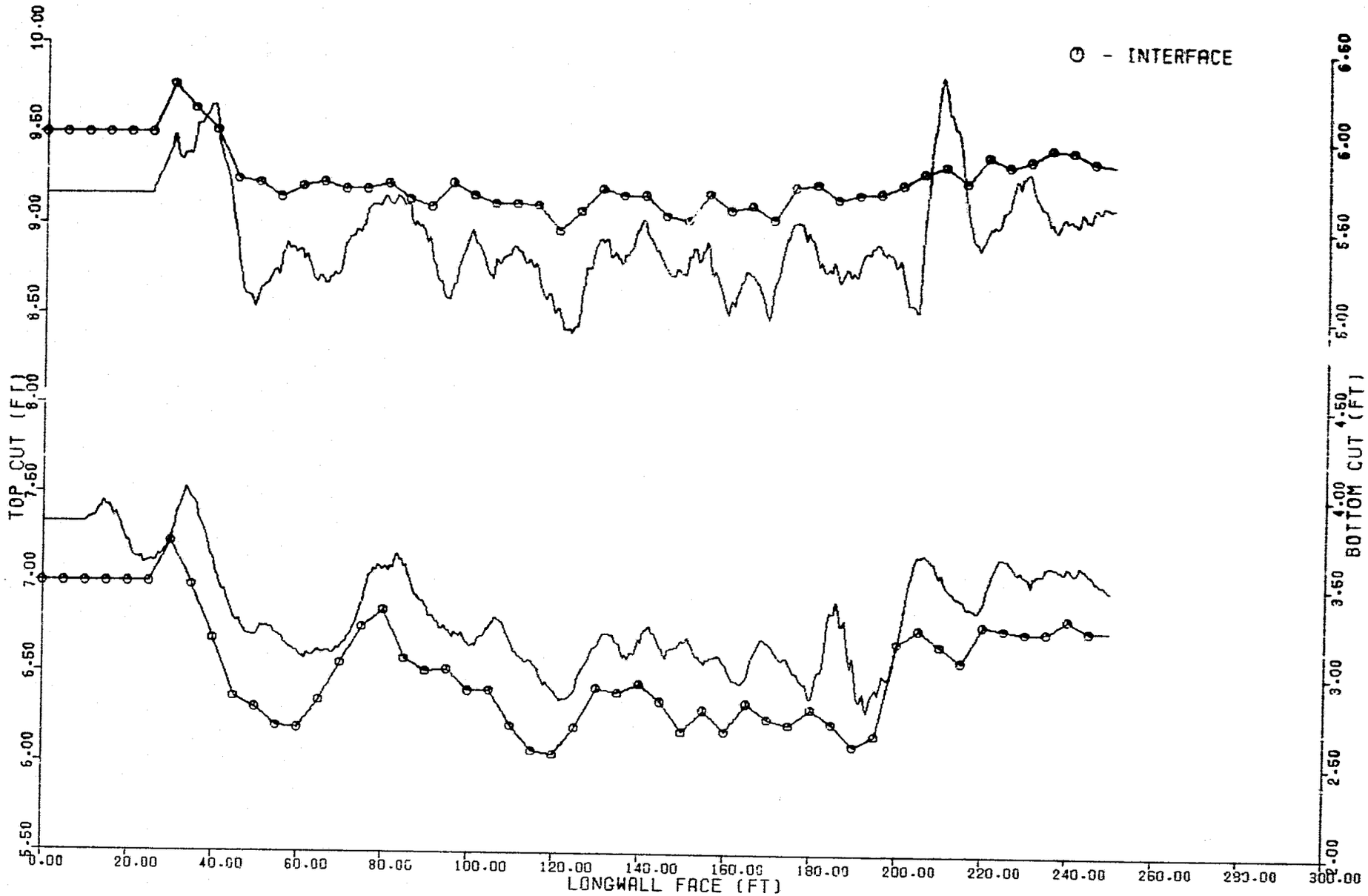

Figure 3-79. VCS Performance with Scheme 1 Prediction with Total Measurements and Bottom Undulations

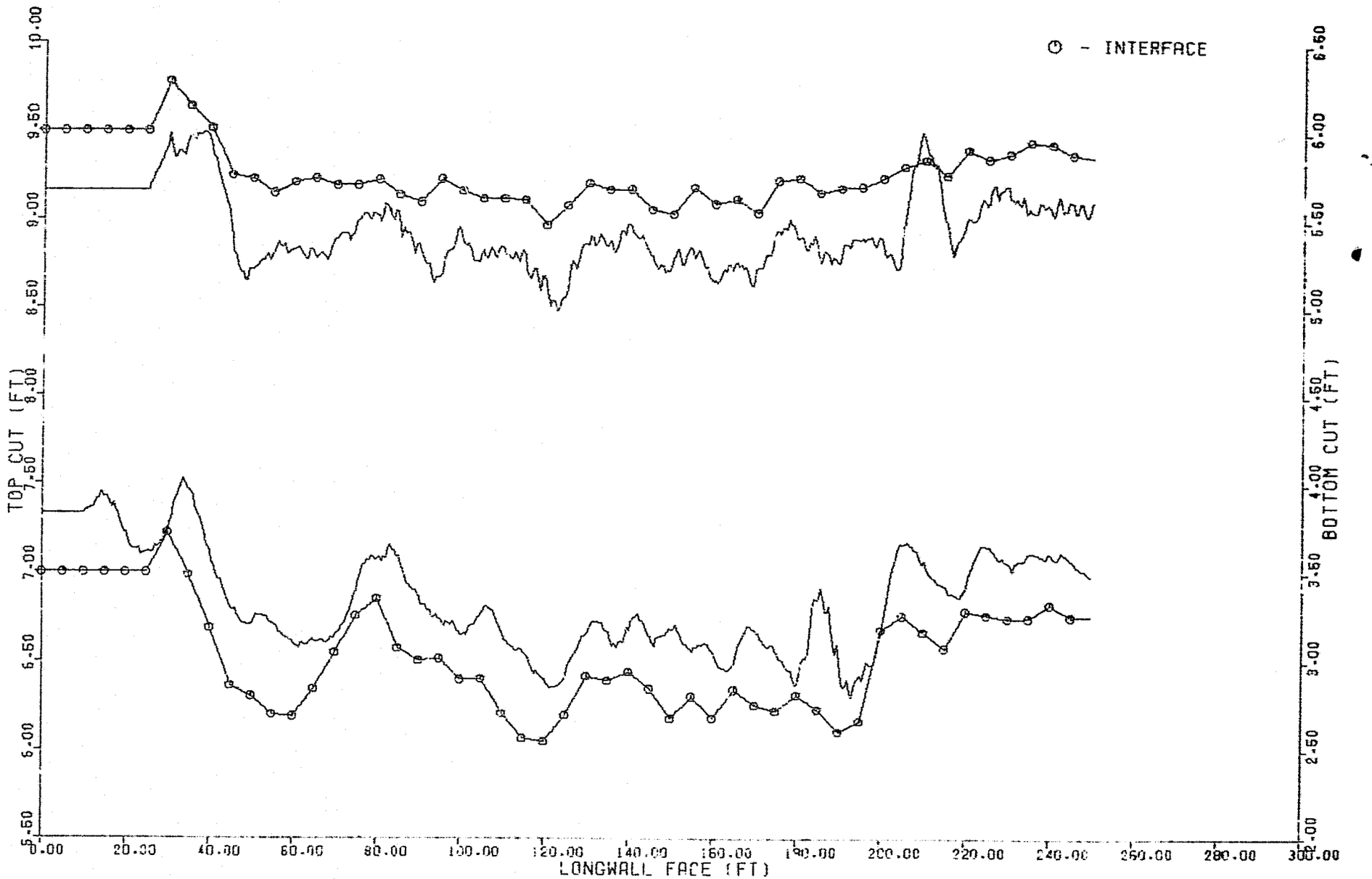

Figure 3-80. VCS Performance with Scheme 2 Estimation with Total Measurements and Bottom Undulations

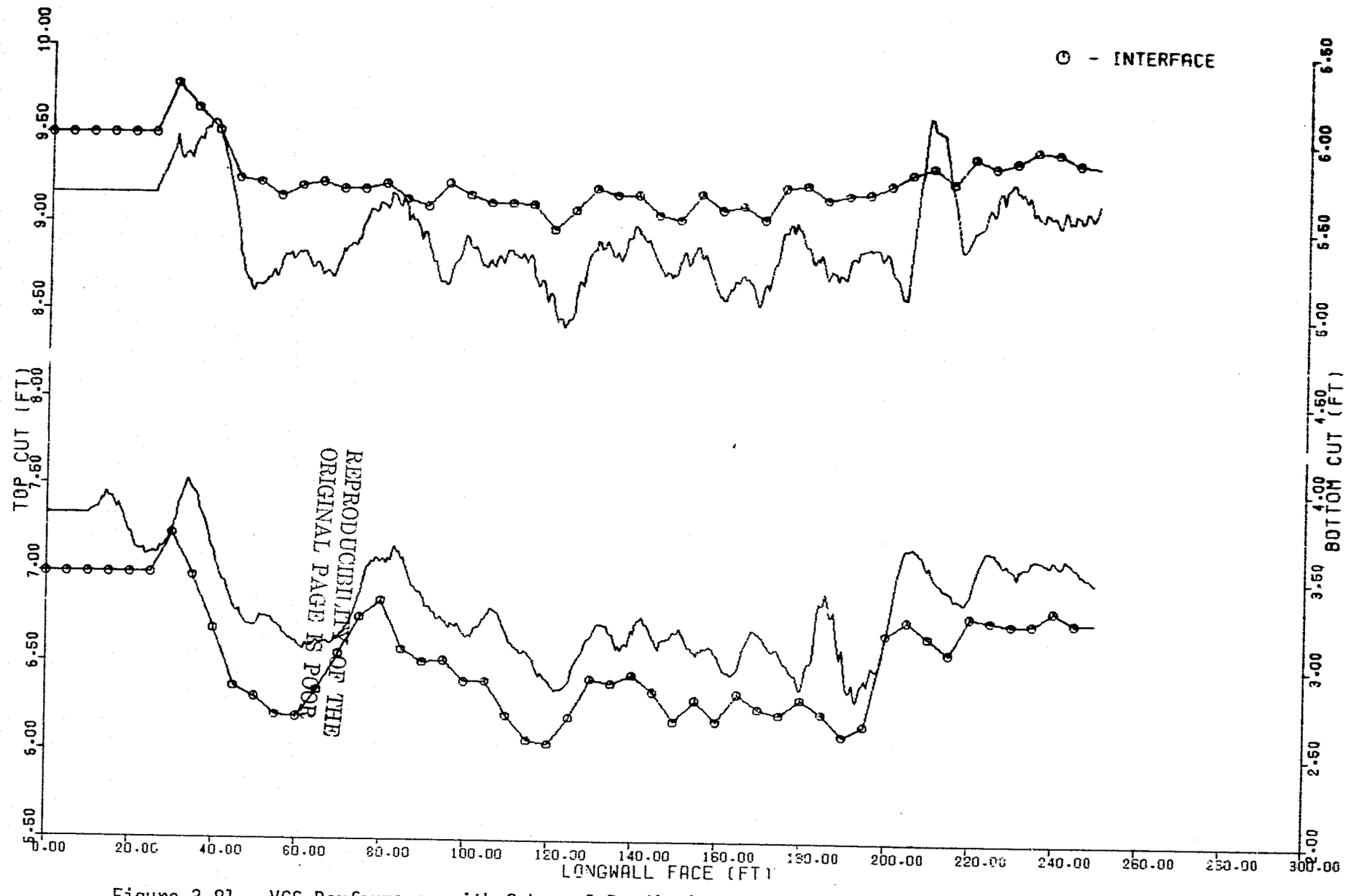

Figure 3-81. VCS Performance with Scheme 2 Prediction with Total Measurements and Bottom Undulations

8 and 9 of Table 3-15 show the impact on performance of the actual CID measurement noise. The relationships between the schemes remains the same, but the errors are approximately 15% larger. Row 9 therefore represents the performance that might be expected in an actual mine. Figures 3-82 through 3-85 show estimation and prediction results for schemes 1 and 2, respectively.

3.6.3.5 Conclusions and Recommendations

Under ideal conditions, where the measurement processes are exactly as modeled, the prediction algorithms can achieve a 21% improvement over the use of unfiltered CID data. The simplified simulation also showed that precise knowledge of mine statistics was not essential to performance. However, when the algorithms are used in a realistic environment, with realistic measurement noise, their performance is worse than that obtained with unfiltered CID data. This is due to the presence of unmodeled noise processes in the measurements to be filtered. The schemes using present and past cut data (algorithms III & IV) are not simulated because of the degradation in performance by using schemes I and II with realistic mine conditions.

Also under ideal conditions, scheme 1 performs better than scheme 2, but this is reversed in the presence of modeling errors. Prediction was also found to be detrimental to performance under these conditions because of lack of knowledge of the measurements structure. It must therefore be concluded that in an actual mine, prediction algorithms do not appear to be a viable means of improving system performance and hence are not recommended.

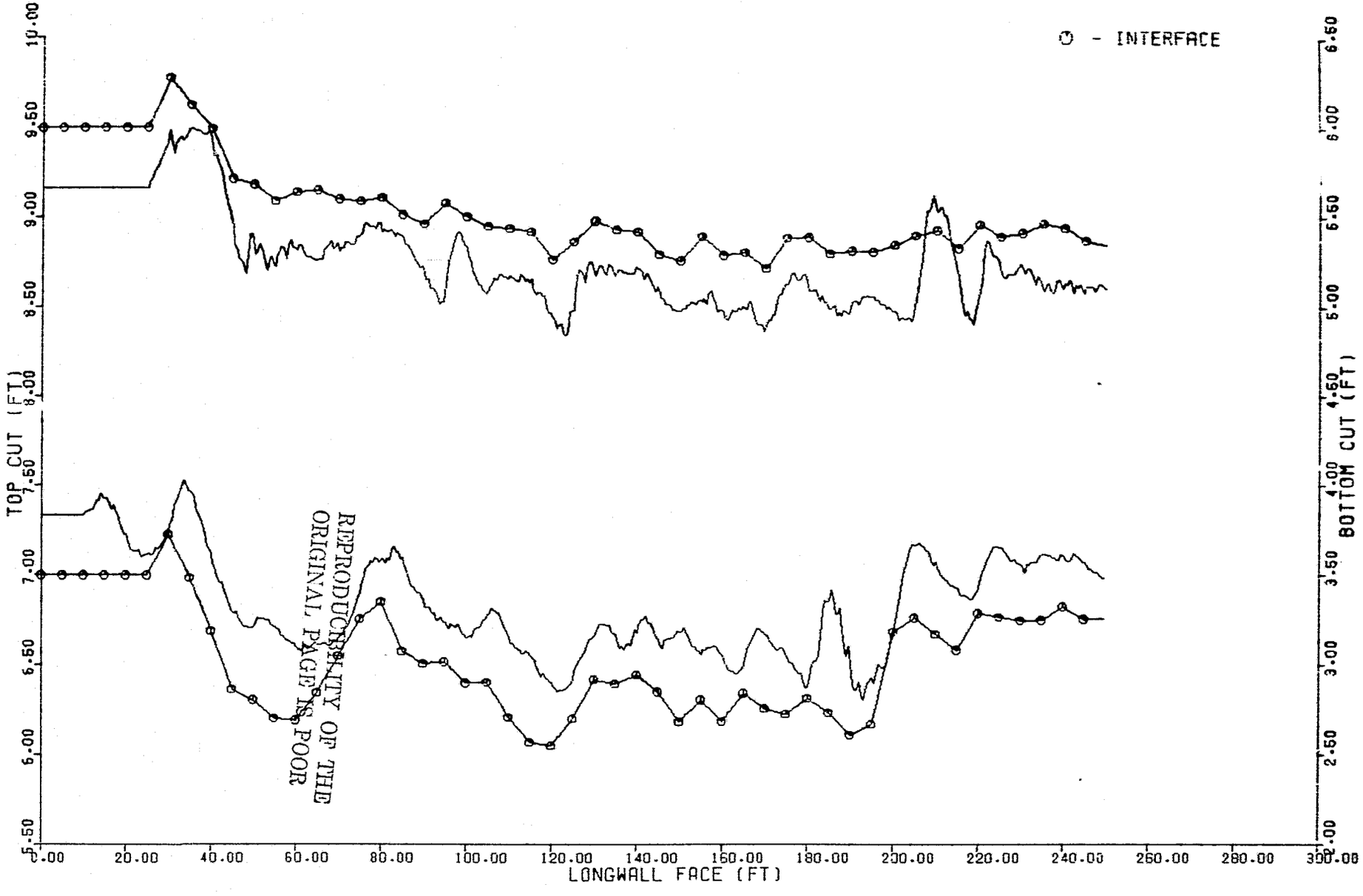

Figure 3-82. VCS Performance with Scheme 1 Estimation Under Actual Conditions

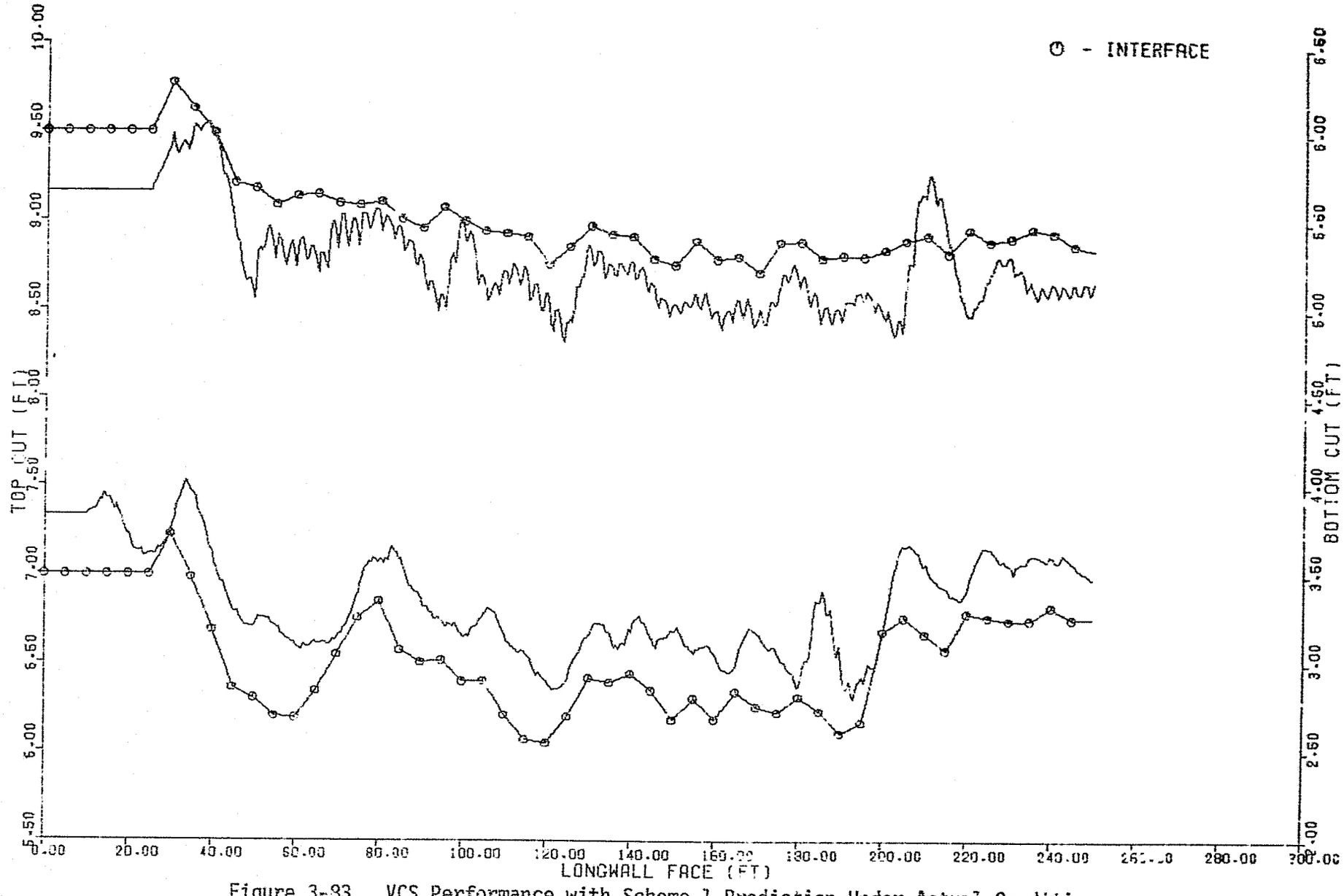

Figure 3-33. VCS Performance with Scheme 1 Prediction Under Actual Conditions

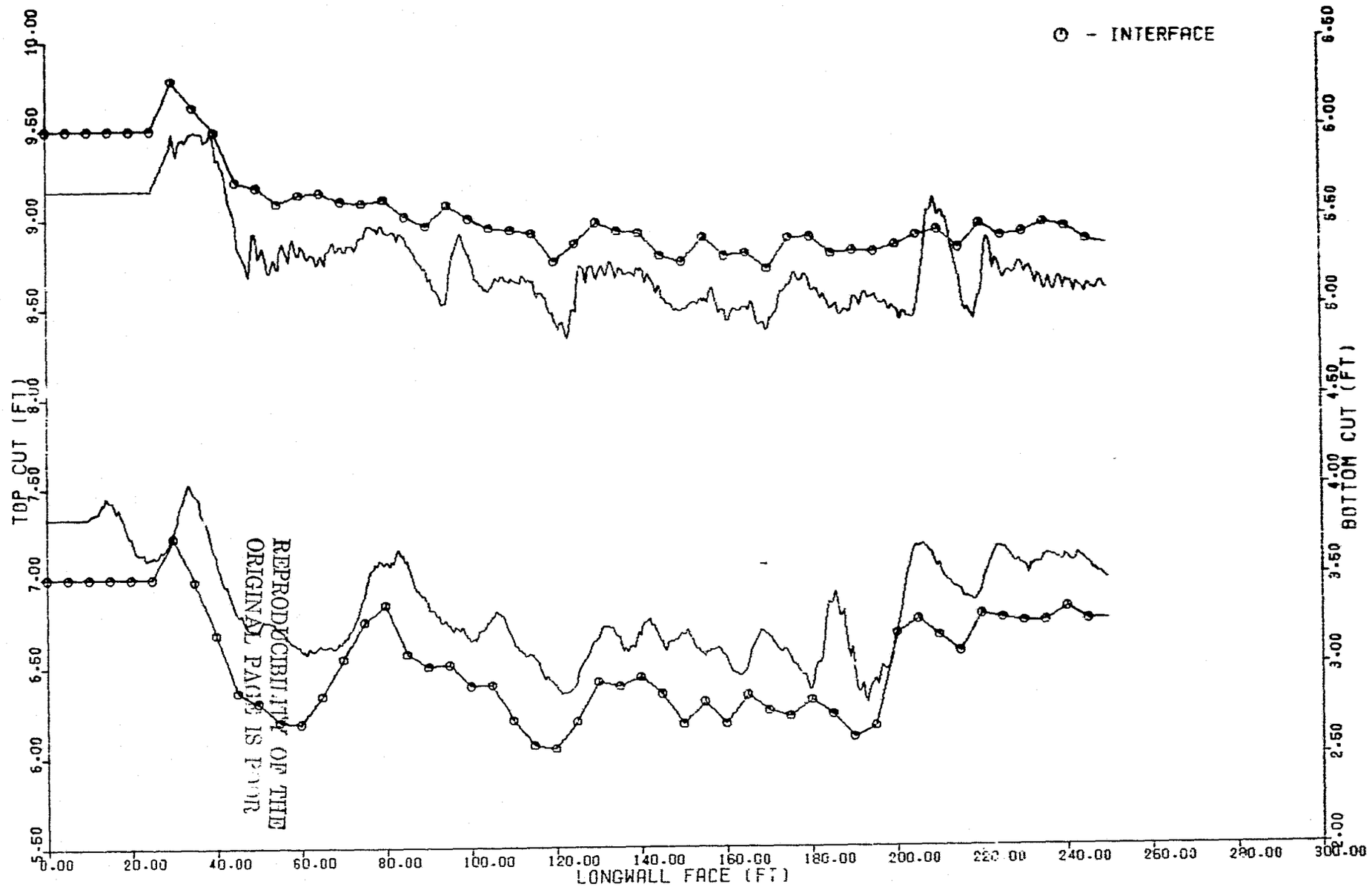

Figure 3-84. VCS Performance with Scheme 2 Estimation Under Actual Conditions

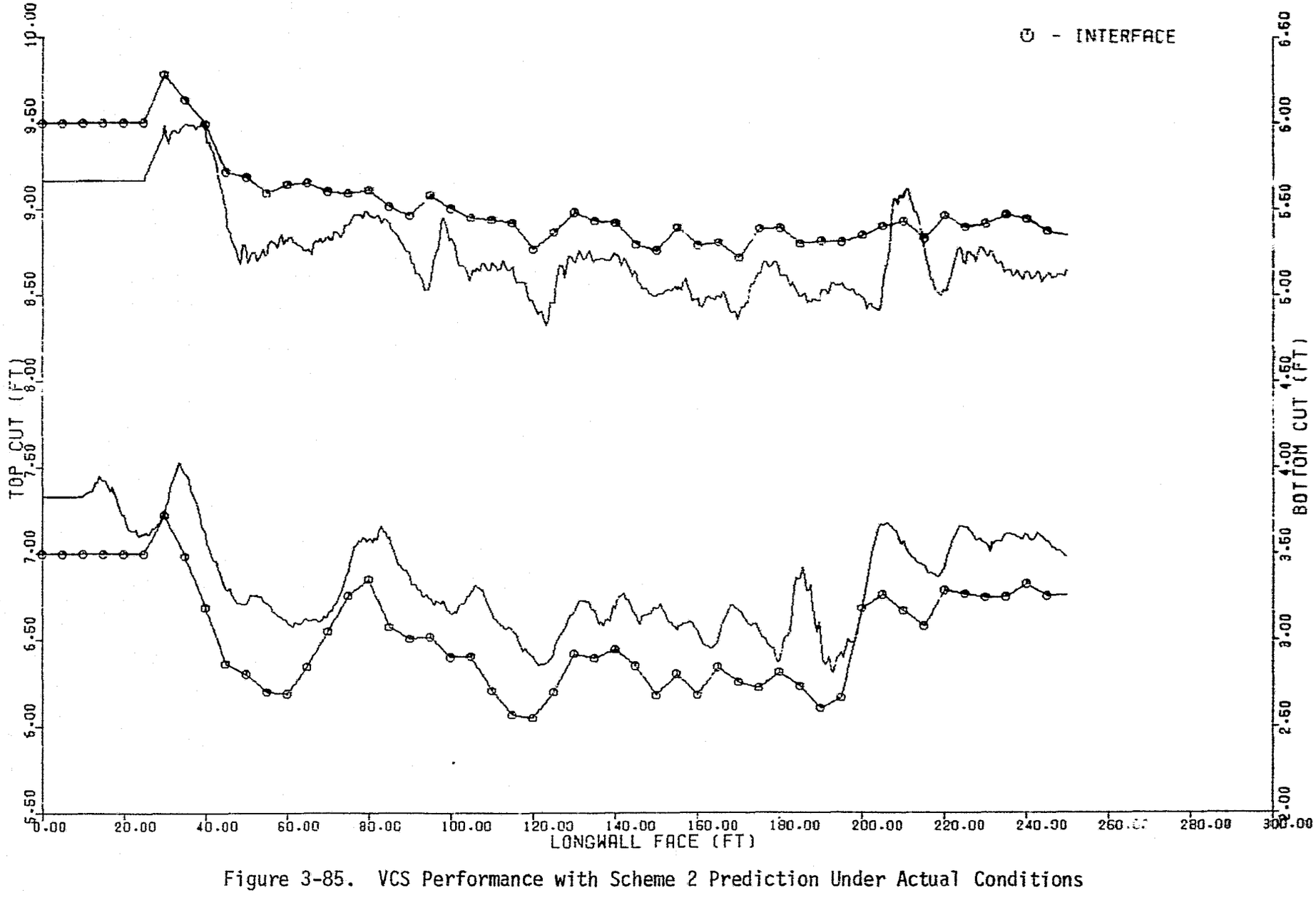

Figure 3-85. VCS Performance with Scheme 2 Prediction Under Actual Conditions

3.7 CONTROL OF BOTTOM DRUM FOR BASELINE SYSTEM

3.7.1 Drum Control Procedures

When it is desired to take all the coal on the bottom, the discrete CIDs provide a means by which this can be accomplished. Performance with these sensors is discussed in Section 3.4.2.7, where it was shown that the sensitized pick can successfully control cutting at the CSI. When it is desired to leave bottom coal, an alternate control procedure must be used. Since it is impractical to mount a proportional CID on the bottom drum, locking and drum slaving procedures were developed and investigated.

The drum locking consists of simply setting the drum at a desired location and applying no further control. The drum slaving procedures actively control the rear drum to cut a constant seam height or a constant distance from the top last cut. The sensor configurations used in this study are shown in Figure 3-86. Drum slaving was done by computing the distance h indicated, where

$$h = \varepsilon_1 + P_1 + \ell \sin \beta_1 + r$$

This represents the interface height above the front ranging arm pivot. If the desired seam height is H, the ranging arm angle of the trailing drum is given by

$$\beta_2 = \sin^{-1} \frac{h + r + C_B - H}{\ell}$$

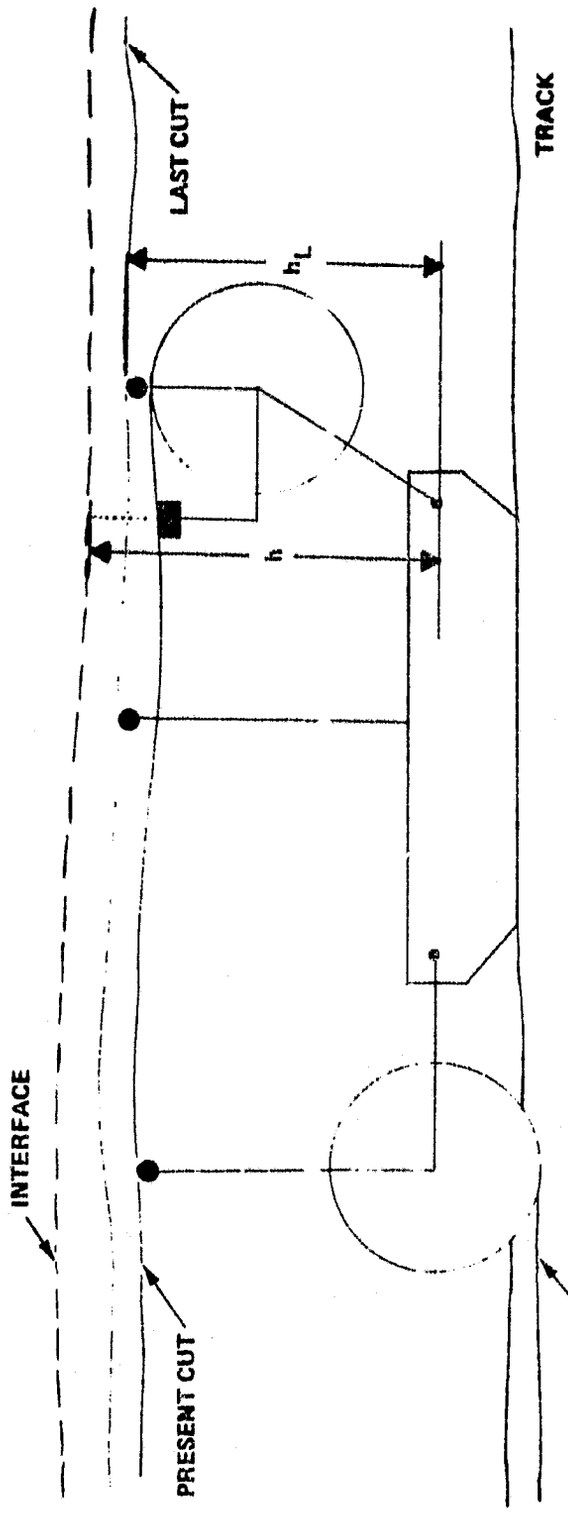

Figure 3-86. Slaving Sensor Geometry

where C_B is the desired coal bias on the bottom. A delayed slaving procedure was also used, where a measurement h was taken and saved until the trailing drum reached the measurement point. This delayed data was then used to control the drum.

To control the rear drum to the top last cut, the height h_L (Figure 3-86) was computed as

$$h_L = Q_1 + \ell \sin \beta_1 + r$$

and

$$\beta_2 = \sin^{-1} \frac{h_L + r + C_B - H}{\ell}$$

These measurements were used in the delayed mode as described above. This same LCF procedure was used without the delaying, using an LCF mounted in the middle of the shearer. Finally, a rear drum top follower was used, which provided a direct measurement of the bottom drum location relative to the top present cut.

3.7.2 Performance with Bottom Drum Locked

The results of drum slaving and locking studies are presented in Table 3-16. Rows 1 and 4 show the locking results with a flat mine bottom and a regular or undulating bottom. These studies were performed on the York Canyon mine where the top and bottom are uncorrelated, and the Robinson Run mine where the top and bottom are highly correlated. The correlation of top and bottom has a significant effect on the performance of slaving.

Table 3-16. VCS Performance with Rear Drum Slaving

CONDITION	YORK CANYON MINE				ROBINSON RUN MINE			
	RMS (IN.)	% TIR	MEAN HEIGHT (FT)	σ (FT)	RMS (IN.)	% TIR	MEAN HEIGHT (FT)	σ (FT)
FLAT TRACK DRUM LOCKED	3.07	4.54	5.37	0.22	3.19	11.6	7.47	0.18
FLAT TRACK DRUM SLAVED	3.19	15.9	5.41	0.16	3.00	11.3	7.41	0.29
FLAT TRACK DELAYED SLAVED	3.08	4.5	5.33	0.03	2.67	6.4	7.45	0.05
REGULAR TRACK DRUM LOCKED	4.25	15.4	5.42	0.43	3.20	12.5	7.47	0.36
REGULAR TRACK DRUM SLAVED	7.04	25.9	5.45	0.58	5.35	25.6	7.49	0.51
REGULAR TRACK DELAYED SLAVED	5.61	23.1	5.37	0.46	4.69	20.2	7.46	0.40
REGULAR TRACK REAR DRUM TOP FOLLOWER	3.03	3.4	5.31	0.02	2.69	4.1	7.42	0.02

(A) σ IS CUT HEIGHT STANDARD DEVIATION.

When the bottom is flat, the RMS error with the drum locked is the RMS of the CSI. The desired seam cut height is 5.27 and 7.41 ft in the York Canyon and Robinson Run mines respectively. The results show that with the drum locked, the mean seam heights are approximately 1 in. in error, with a standard deviation of approximately 2 in. The cutting performance is similar for the two mines. When tne mine bottom is undulating, locking performs worse in the uncorrelated mine than in the correlated mine. Performance in the Robinson Run mine is essentially the same with undulating or flat floor except that with undulation, the height standard deviation is larger. Performance in the York Canyon mine is worse with undulation than with the flat track. Mean seam height and standard deviation are also worse. Figures 3-87 through 3-90 are simulation runs with both mines, with the flat and undulating bottom.

3.7.3 Performance with Bottom Drum Slaved

The system results with drum slaving are shown in rows 2 and 5 of Table 3-16. In the York Canyon mine, slaving produces worse results than with locking. The differences between locking and slaving are much more apparent with the regular mine bottom. In the Robinson Run or correlated mine, slaving yields similar results to locking with a flat bottom, but worse results with regular bottom. Slaving performs better when the top and bottom are correlated, but in any case, all results are worse than when the drum is locked.

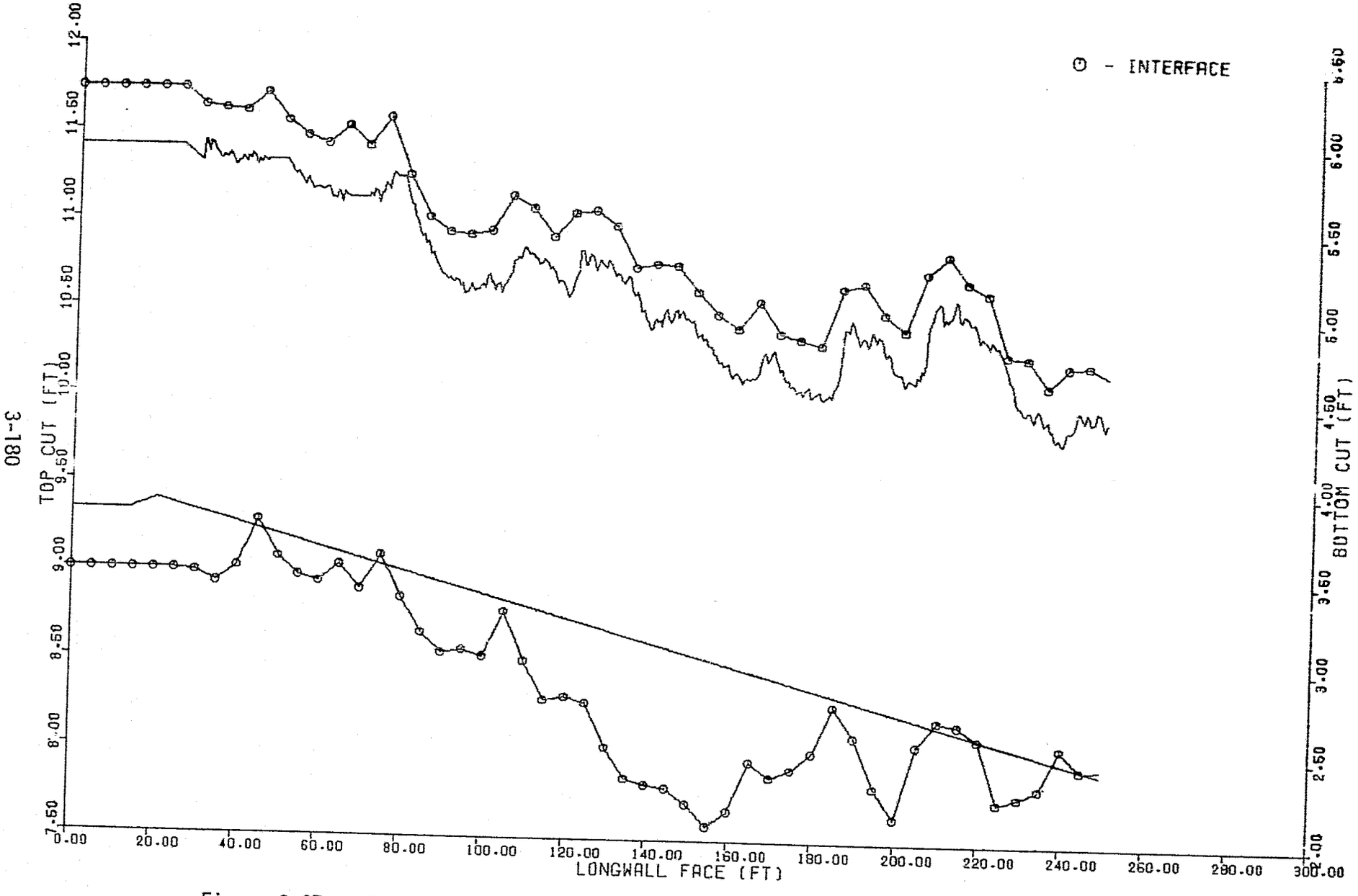

Figure 3-87. VCS Performance in Robinson Run Mine with Flat Bottom and Rear Drum Locked

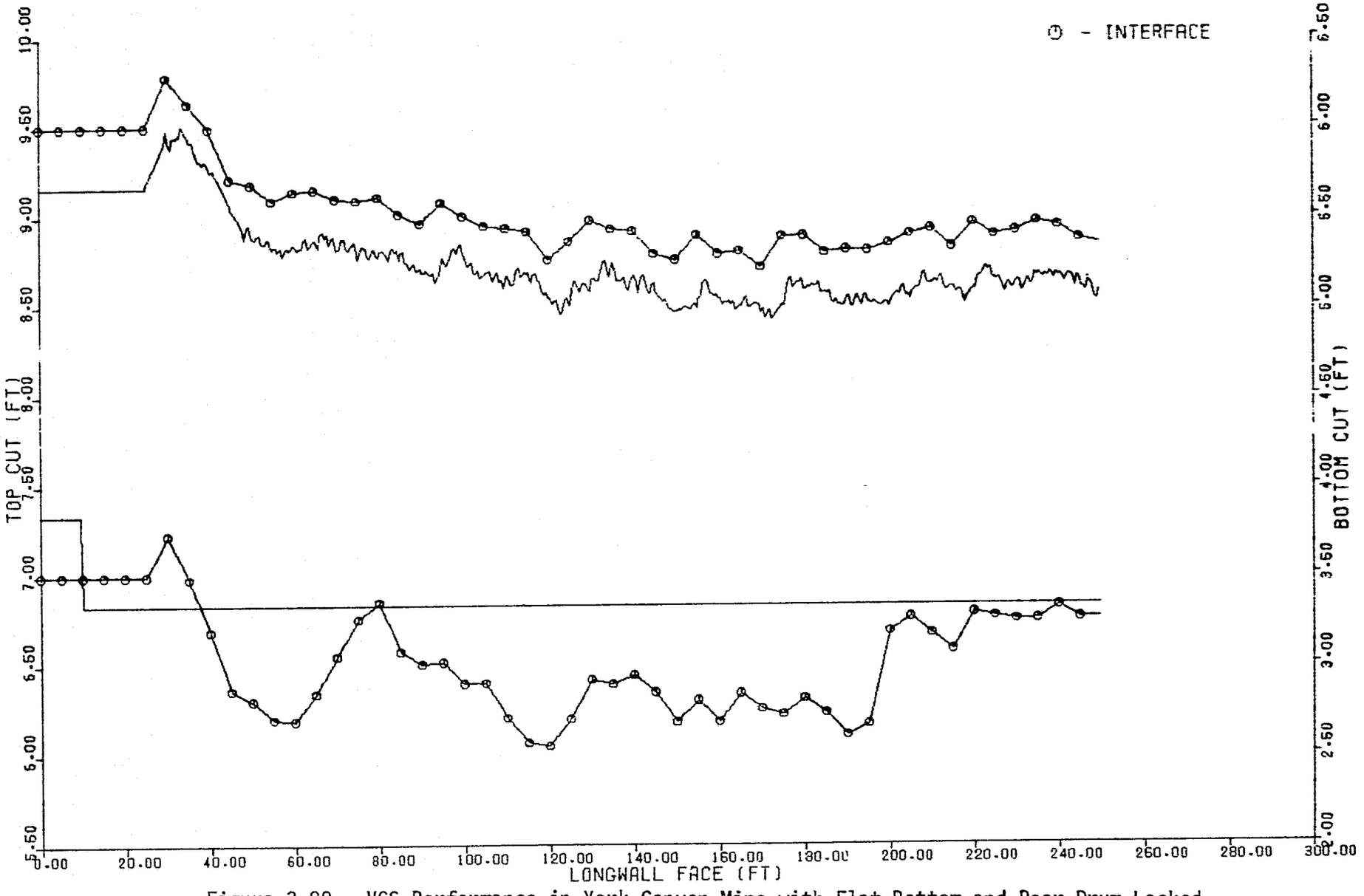

Figure 3-88. VCS Performance in York Canyon Mine with Flat Bottom and Rear Drum Locked

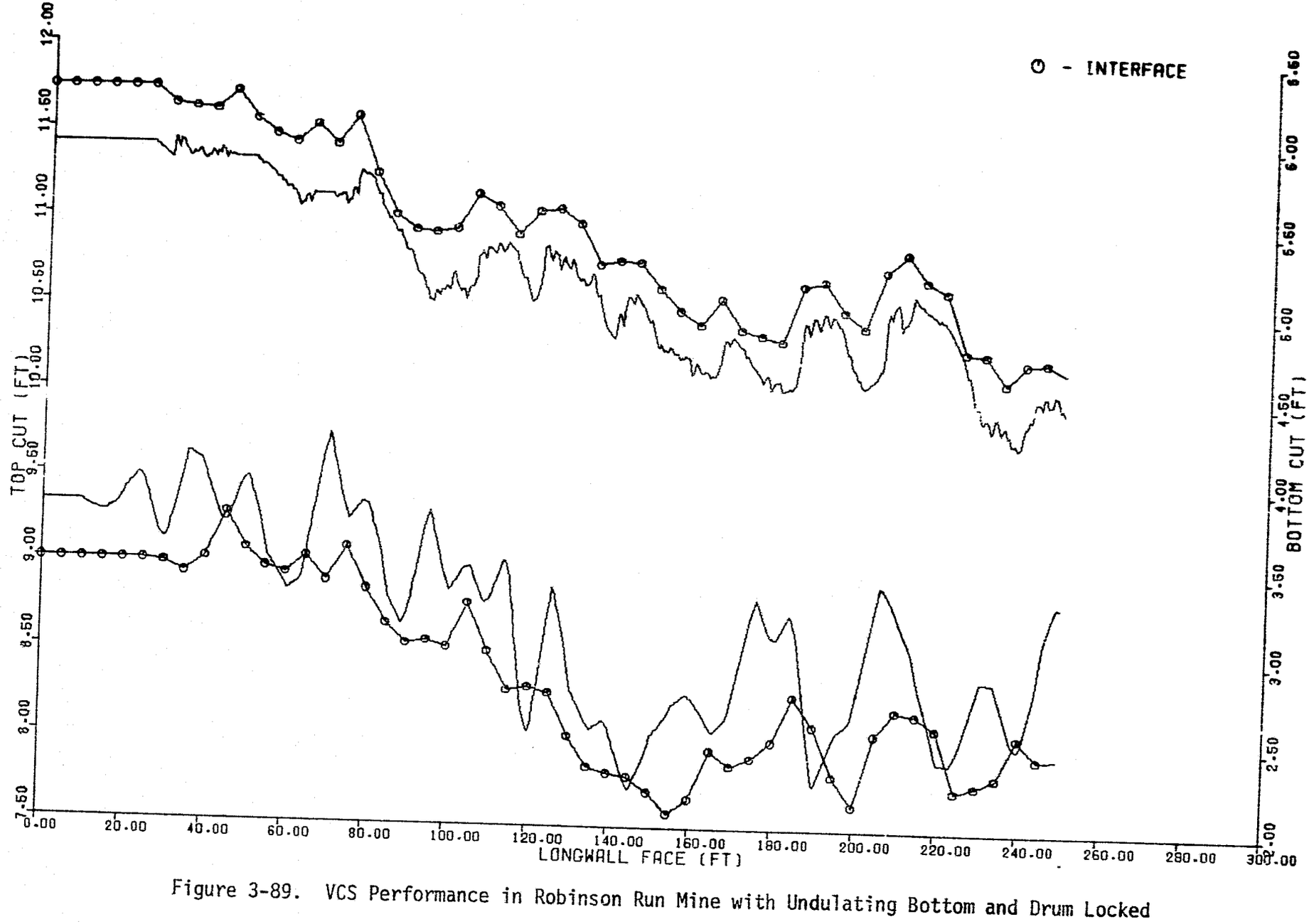

Figure 3-89. VCS Performance in Robinson Run Mine with Undulating Bottom and Drum Locked

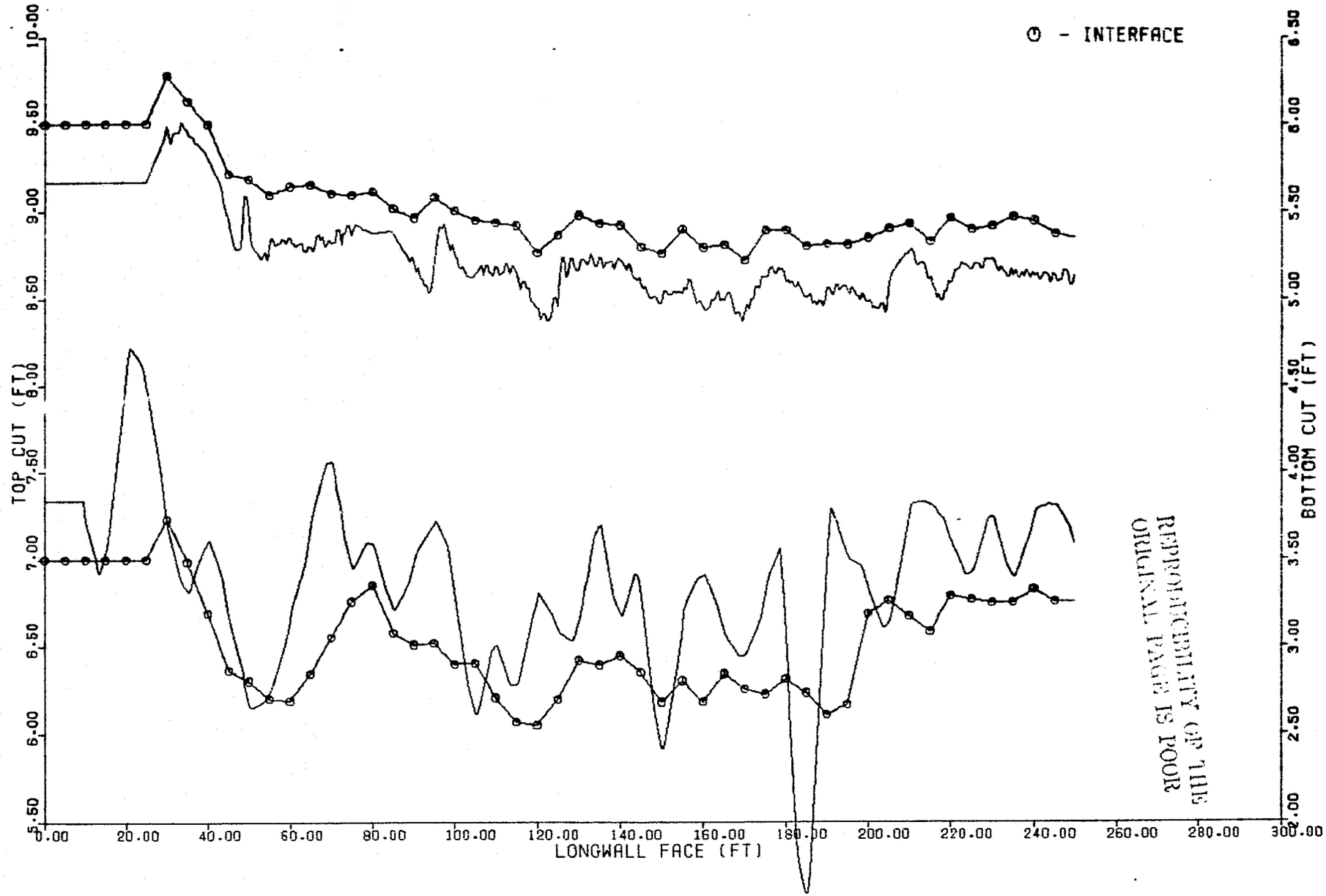

Figure 3-90. VCS Performance in York Canyon Mine with Undulating Bottom and Drum Locked

Slaving yields worse performance than locking because it tends to accentuate floor undulations. If the shearer chassis pitches up for instance, the drum cuts into the top. The VCS corrects for this by lowering the drum. The slaving will then lower the rear drum to maintain a constant height, but the pitching motion has already caused the rear drum to cut into the bottom, and this is now exagerated by the slaving. As a result, this type of slaving yields poor results. Figures 3-91 and 3-92 show slaving with an undulating bottom for the two mines.

3.7.4 Performance with Bottom Drum Delayed Slaving

The delayed slaving procedure uses height measurements which were made earlier by the front drum to control the rear drum. This has the effect of reducing the problems caused by floor undulations. With the flat bottom, the delayed slaving yields very good results with both mines, performing better in the Robinson Run mine because of the correlation of top and bottom. With the regular bottom, delayed slaving is better than simple slaving, but still does not perform as well as locking. The delayed slaving still accentuates the effects of bottom undulations. Time histories of delayed slaving with bottom undulations are shown in Figures 3-93 and 3-94.

3.7.5 Performance With Rear Drum Top Follower

Of the systems shown in Table 3-16, the top follower provides the best slaving performance. The average seam heights cut in the

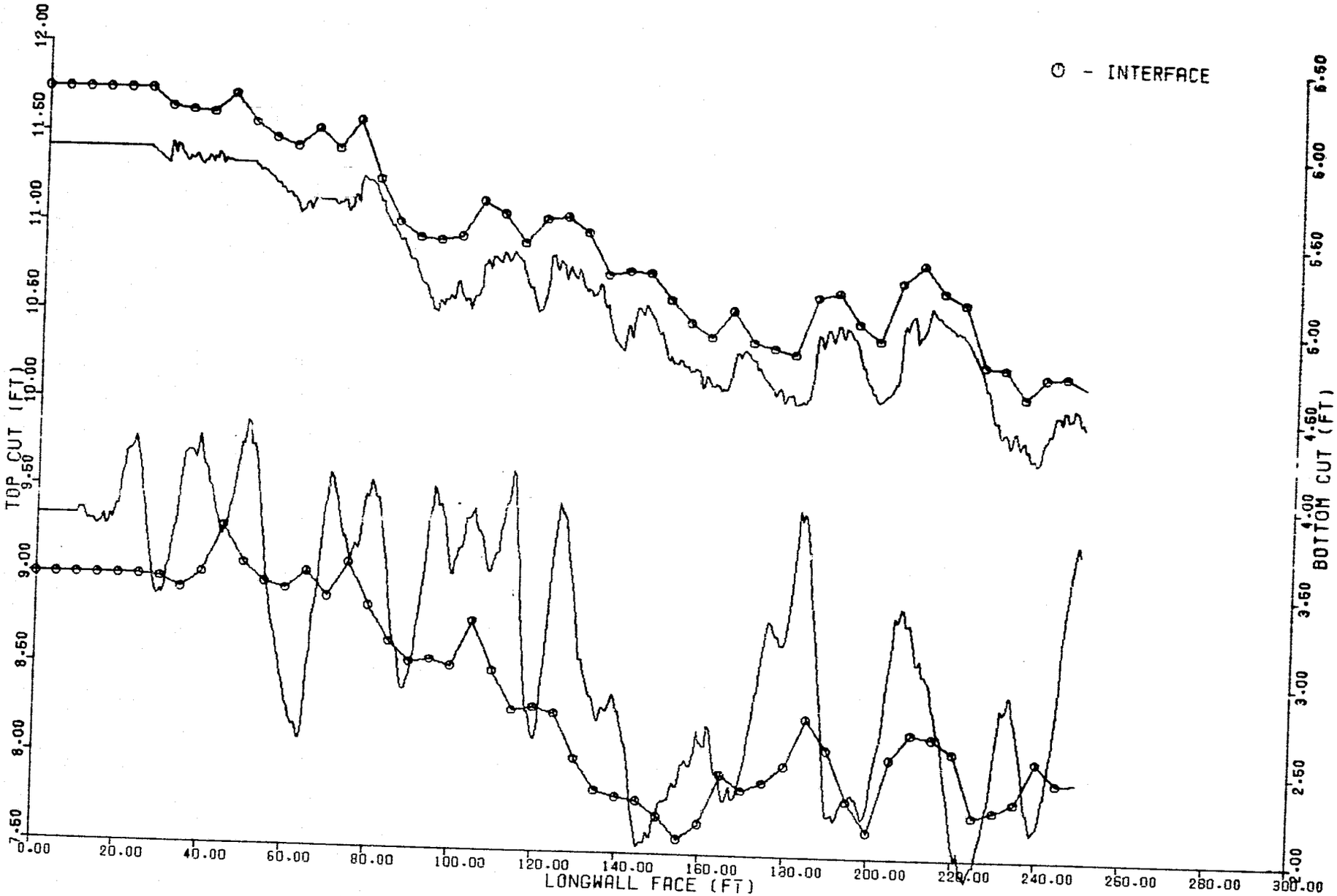

Figure 3-91. VCS Performance in Robinson Run Mine with Drum Slaving

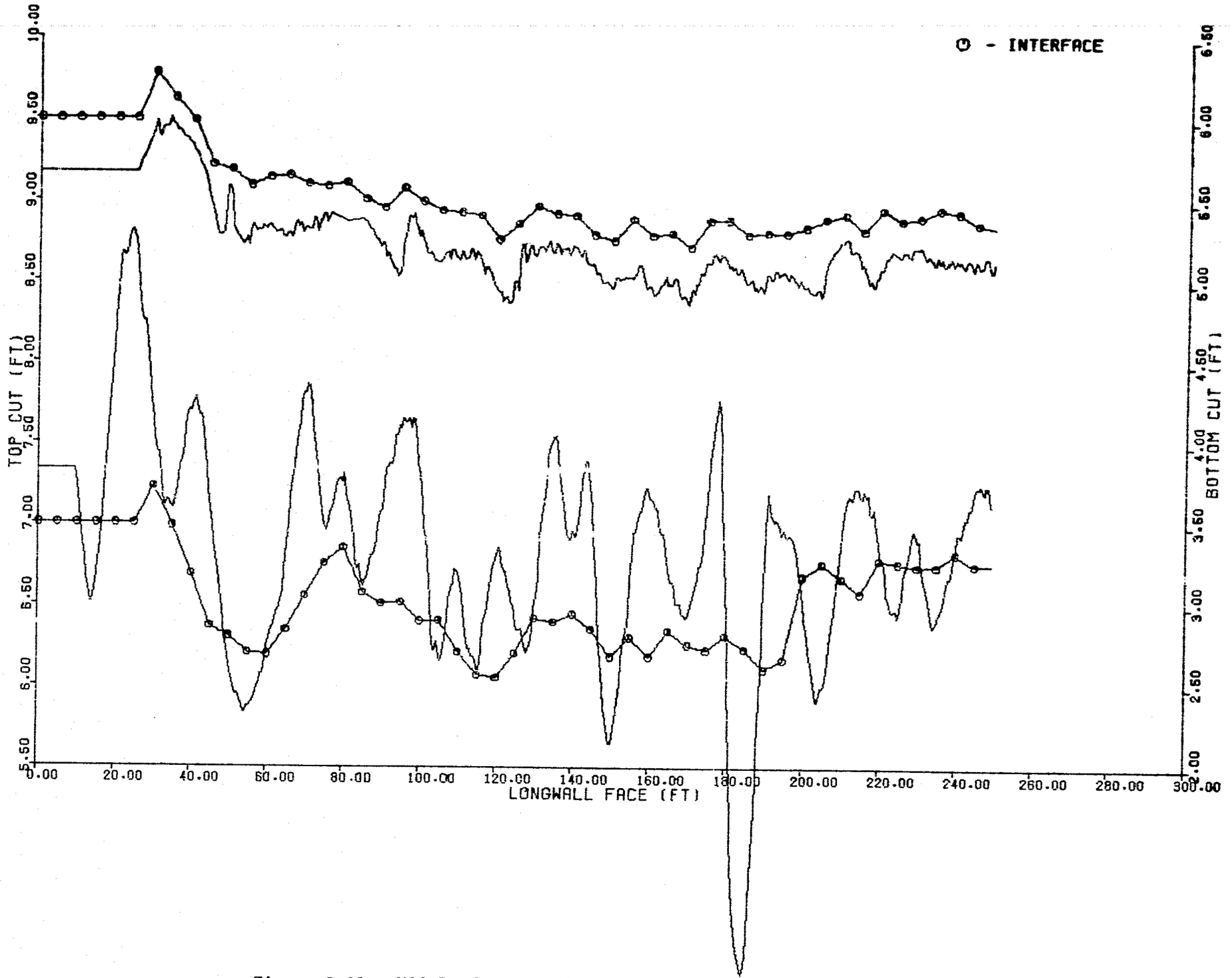

Figure 3-92. VCS Performance in York Canyon Mine with Drum Slaving

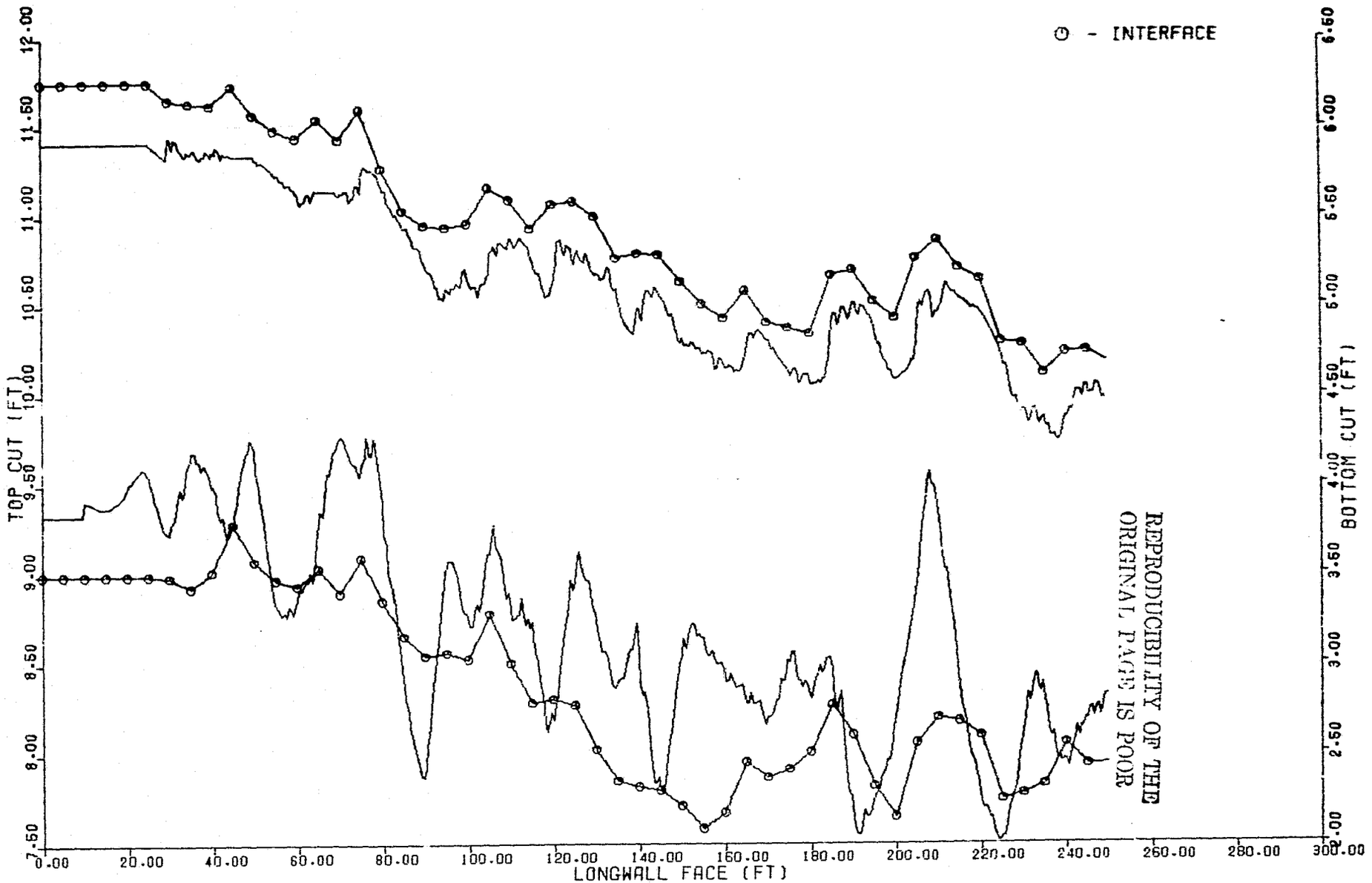

Figure 3-93. VCS Performance in Robinson Run Mine with Delayed Slaving and Floor Undulations

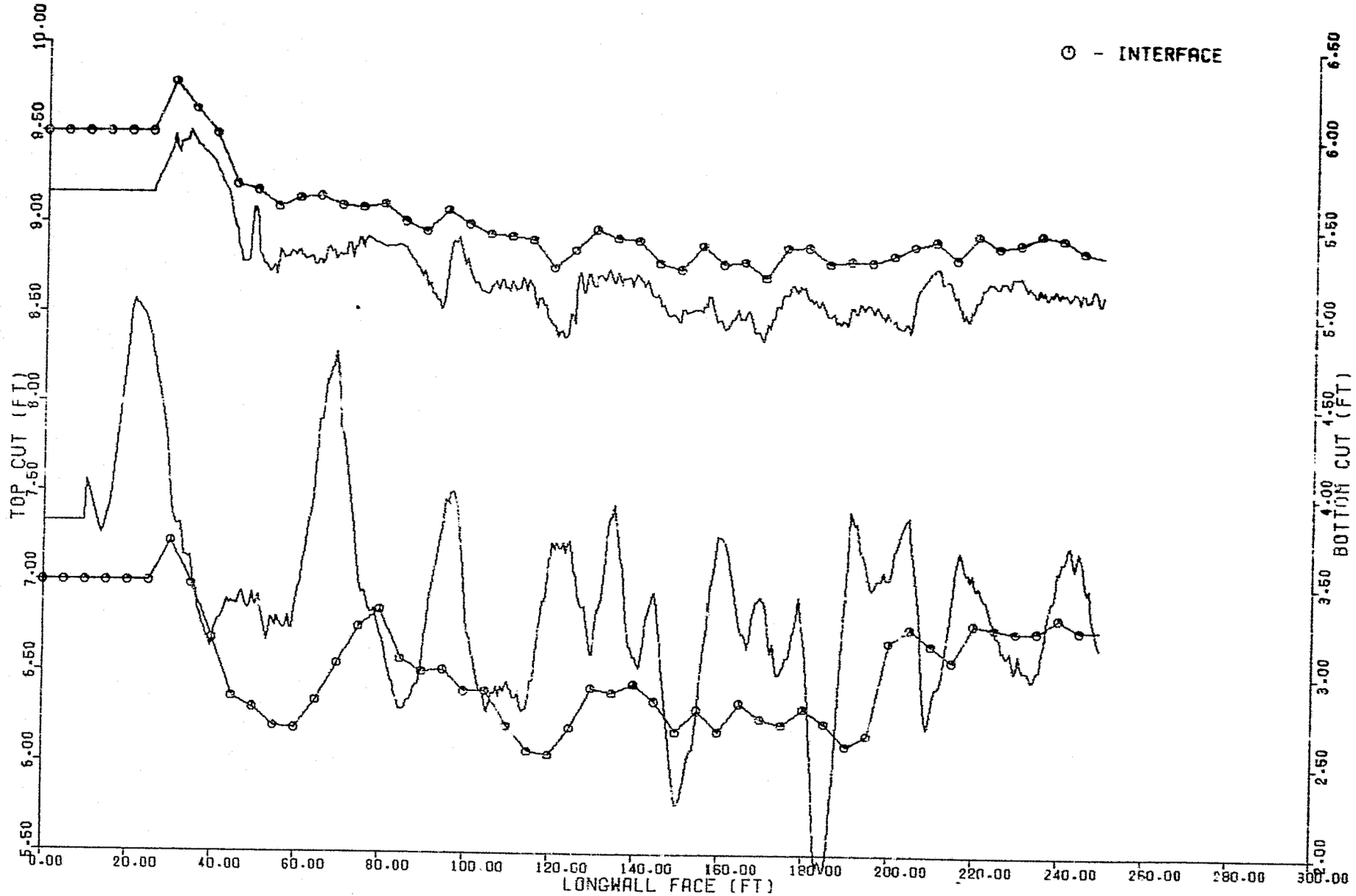

Figure 3-94. VCS Performance in York Canyon Mine with Delayed Slaving and Floor Undulations

two mines were the desired heights with standard deviations of 0.25 in. Performance is better in the Robinson Run mine because of the correlation between the top and bottom. The reason for the good performance with this sytem is that the top follower provides a measure of the effects of chassis undulation. By directly sensing the drum position relative to the mine top, and the errors due to undulation are largely eliminated. Figures 3-95 and 3-96 show performance with the top follower in the Robinson Run and York Canyon Mines, respectively.

3.7.6 Performance with Slaving and Sensitized Pick

Table 3-17 shows the results of various other slaving techniques discussed in Section 3.7.1. In all of these schemes, the rear drum was instrumented with a sensitized pick. The table shows that slaving to the top LCF does not yield good performance. This procedure was intended to provide a means of limiting the change in height from cut to cut on the bottom, but it suffers from the same problem as the other slaving procedures.

Performance with the middle LCF appears somewhat better. The use of a chassis mounted sensor was studied as a possible means of eliminating the LCF on each drum. While slaving performance was adequate, performance of the top drum cut was degraded from 1.12 in. RMS to 3.26 in. RMS. This degradation is due to the fact that the LCF sensor has the highest control authority, and therefore errors introduced by displacing the sensor to the center of the chassis have a pronounced

PERFORMANCE EVALUATION PASS 1

TOTAL COAL TAKEN = 4089.008 CU. FT.

AVERAGE CUT HIGHT = 7.418 FT.

CUT STANDARD DEVIATION = 0.015 FT.

FLOOR

RMS ERROR = 2.693 IN.

AVERAGE ABSOLUTE ERROR = 2.163 IN.

VOLUME EXCESS COAL LEFT = 63.632 CU. FT. (1.56%)

VOLUME EXCESS COAL TAKEN = 34.267 CU. FT. (0.84%)

VOLUME ROCK TAKEN = 1.484 CU. FT. (0.04%)

TIME IN ROCK = 4.08%

ROOF

RMS ERROR = 1.401 IN.

AVERAGE ABSOLUTE ERROR = 1.156 IN.

VOLUME EXCESS COAL LEFT = 10.074 CU. FT. (0.25%)

VOLUME EXCESS COAL TAKEN = 43.042 CU. FT. (1.05%)

VOLUME ROCK TAKEN = 0.000 CU. FT. (0.00%)

TIME IN ROCK = 0.00%

Figure 3-95. VCS Performance with Top Follower in Robinson Run Mine

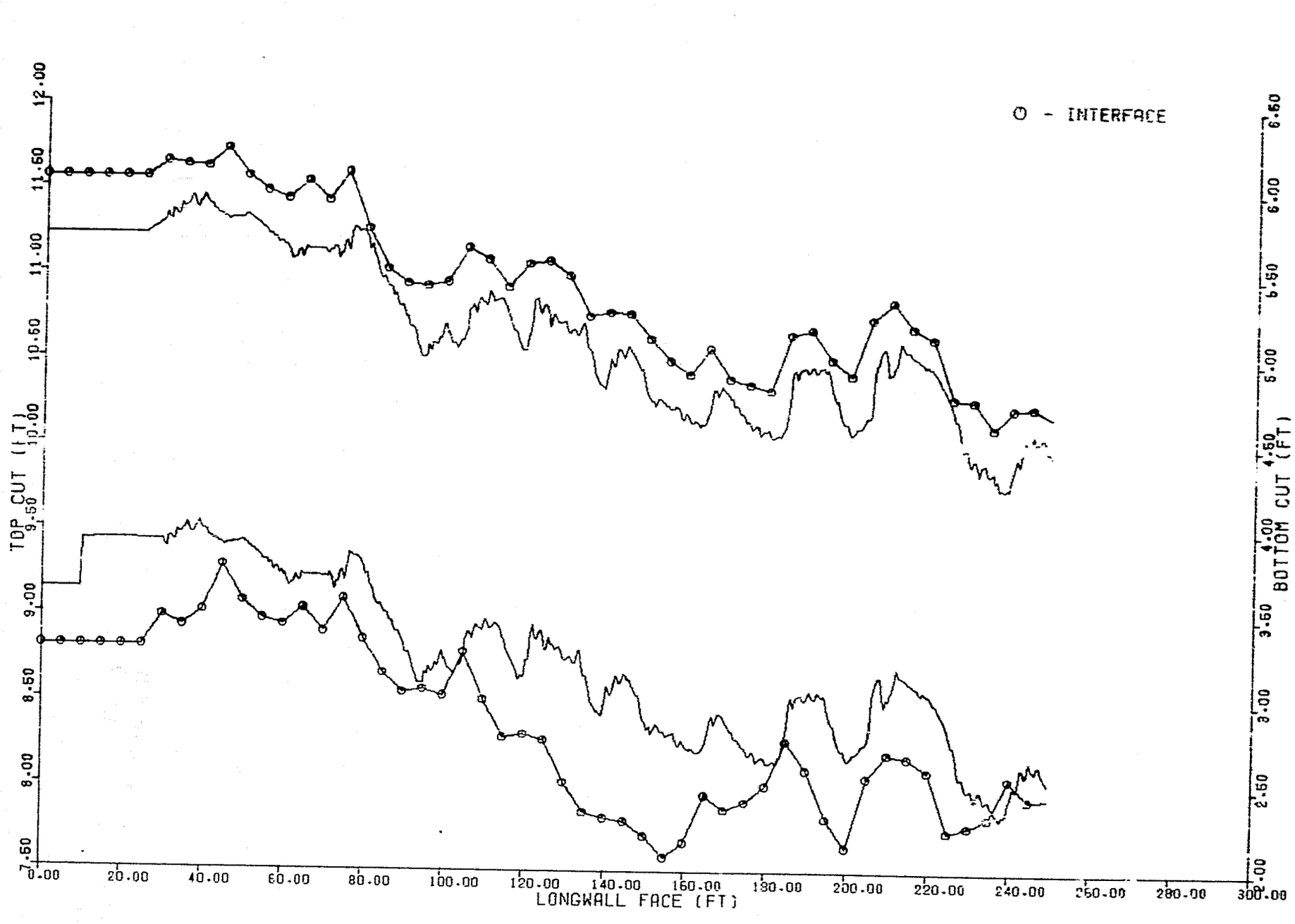

Figure 3-95. VCS Performance with Top Follower in Robinson Run Mine (Concluded)

PERFORMANCE EVALUATION PASS 1

TOTAL COAL TAKEN = 2924.378 CU. FT.

AVERAGE CUT HIGHT = 5.305 FT.

CUT STANDARD DEVIATION = 0.016 FT.

FLOOR

RMS ERROR = 3.034 IN.

AVERAGE ABSOLUTE ERROR = 2.600 IN.

VOLUME EXCESS COAL LEFT = 86.126 CU. FT. (2.95%)

VOLUME EXCESS COAL TAKEN = 32.290 CU. FT. (1.10%)

VOLUME ROCK TAKEN = 1.001 CU. FT. (0.03%)

TIME IN ROCK = 3.40%

ROOF

RMS ERROR = 1.129 IN.

AVERAGE ABSOLUTE ERROR = 0.939 IN

VOLUME EXCESS COAL LEFT = 4.893 CU. FT. (0.17%)

VOLUME EXCESS COAL TAKEN = 38.262 CU. FT. (1.31%)

VOLUME ROCK TAKEN = 0.000 CU. FT (0.00%)

TIME IN ROCK = 0.00%

Figure 3-96. VCS Performance with Top Follower in York Canyon Mine

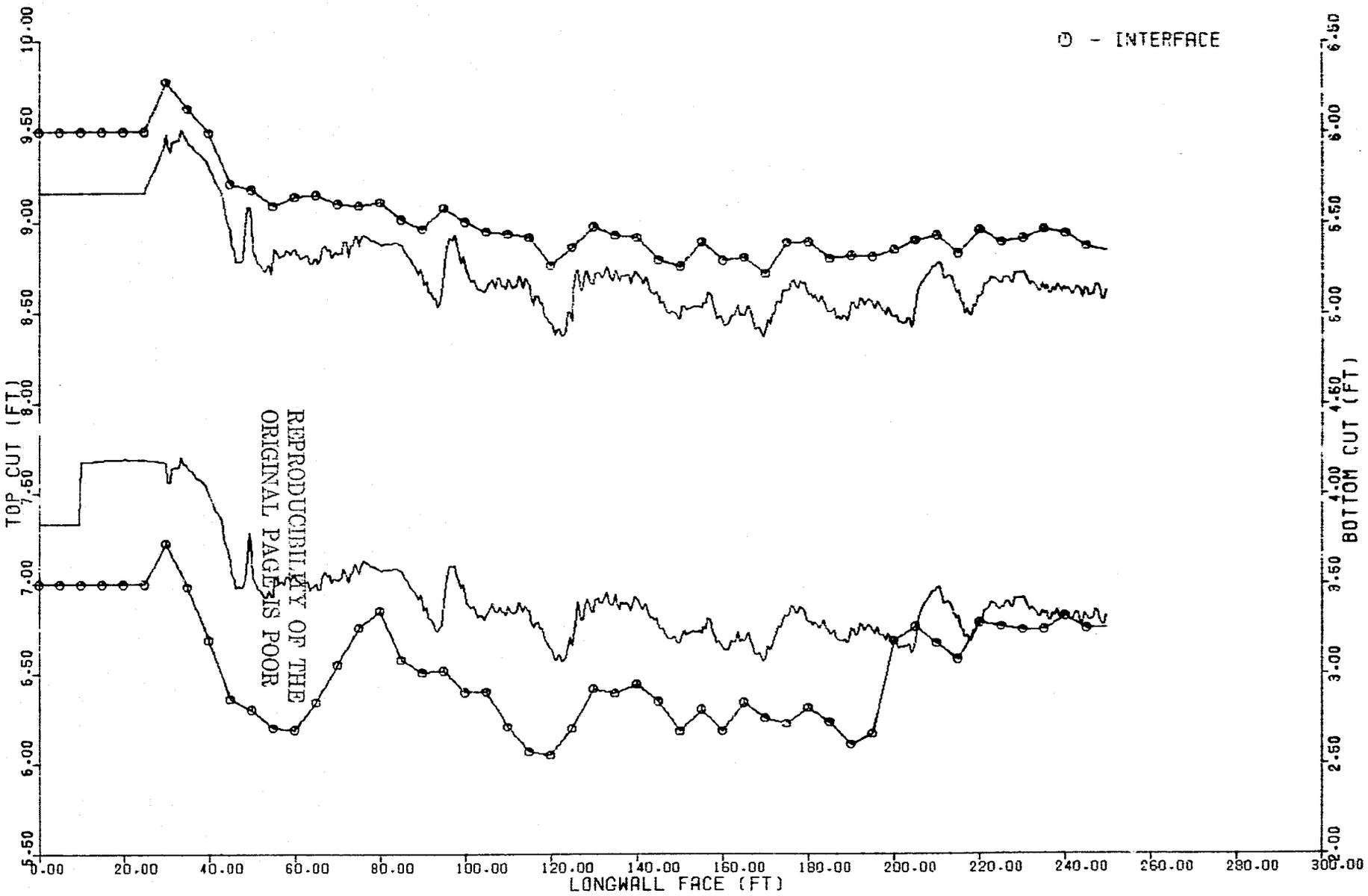

Figure 3-96. VCS Performance with Top Follower in York Canyon Mine (Concluded)

Table 3-17. VCS Performance with Drum Slaving and Sensitized Pick

CONDITIONS	YORK CANYON MINE				ROBINSON RUN MINE			
	RMS (IN.)	% TIR	MEAN HEIGHT (FT)	σ (FT)	RMS (IN.)	% TIR	MEAN HEIGHT (FT)	σ (FT)
REGULAR TRACK DELAYED SLAVED TO FRONT LCF	5.28	20.2	5.32	0.42	4.17	17.9	7.43	0.35
REGULAR TRACK SLAVED TO MIDDLE LCF	3.38	10.4	5.38	0.34	3.34	15.4	7.48	0.34
REGULAR TRACK REAR DRUM TOP FOLLOWER	3.02	3.9	5.37	0.03	2.66	3.4	7.42	0.03

(A) PICK 100% CORRECT

(B) σ IS CUT HEIGHT STANDARD DEVIATION.

effect. Finally, the rear drum top follower control was used with a pick on the bottom drum. It can be seen that use of the pick produces only a slight change in performance. Figures 3-97 and 3-98 show the results with the front LCF and middle LCF slaving.

3.8 CONCLUSIONS AND RECOMMENDATIONS

3.8.1 Recommended Sensor Configurations

Based on the previous performance studies, a recommended set of sensors can be configured. Table 3-18 lists the sensors and their characteristics that, from a performance standpoint, should be used in the VCS. For a given mining application, it may not be necessary to use all of these sensors. Preferred combinations of these sensors will be given in Section 3.8.2.

Recommended sensors for the top drum are the nucleonic CID, LCF, and sensitized pick. The nucleonic CID output interval was chosen to be 0.25 s because this represents the minimum error point and also minimized the effects of cutting speed variations. The CID should be located as close as possible to the shearing drum, indicated here as 2.5 ft. The LCF is assumed to be a continuous sensor with a range greater than the last cut distance to be maintained. Finally, two picks yield good performance, with at least 80 to 90% accuracy. The bottom drum sensors include the sensitized pick, and the rear drum top follower for slaving. This sensor should also have a continuous output.

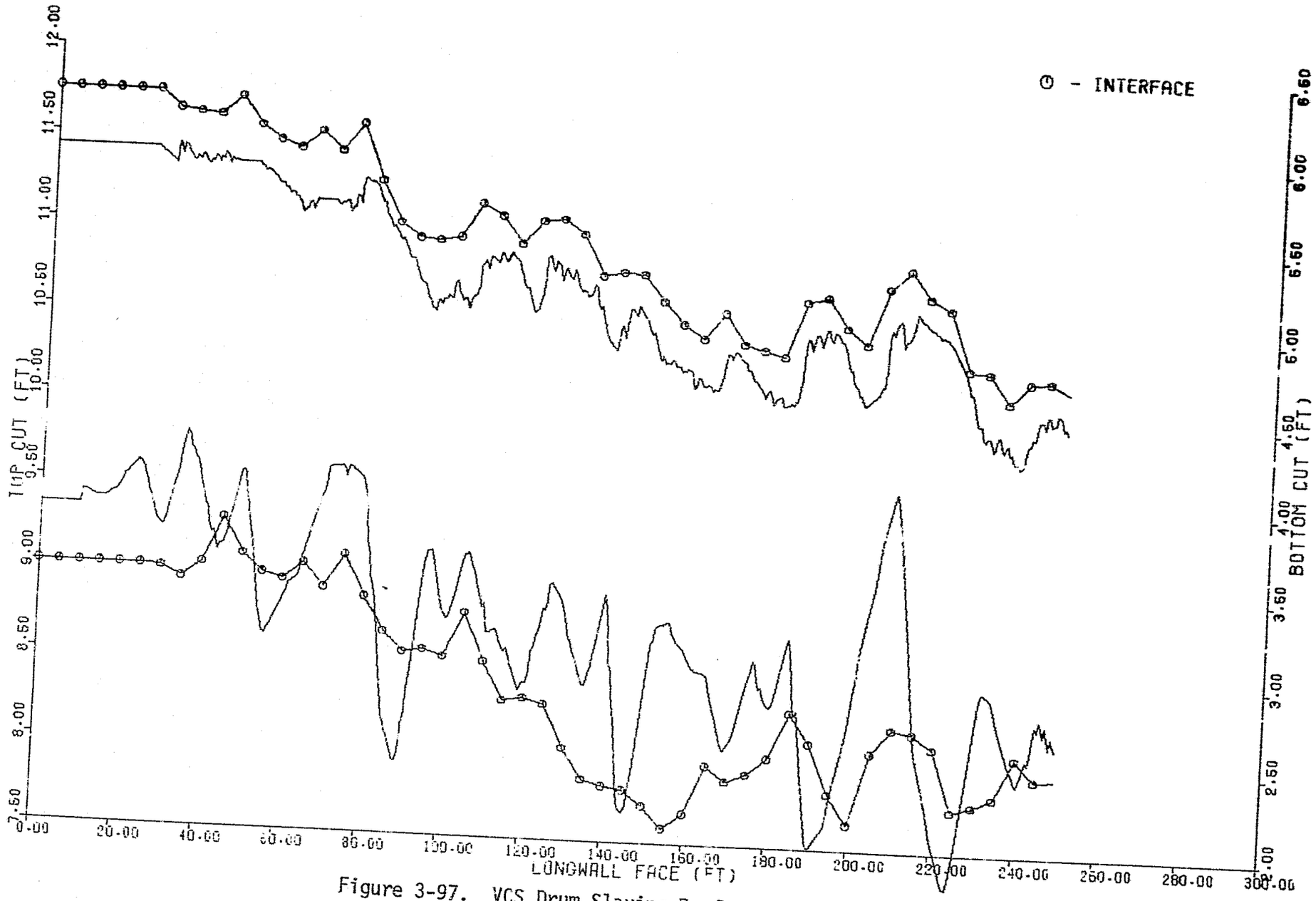

Figure 3-97. VCS Drum Slaving Performance with Front LCF

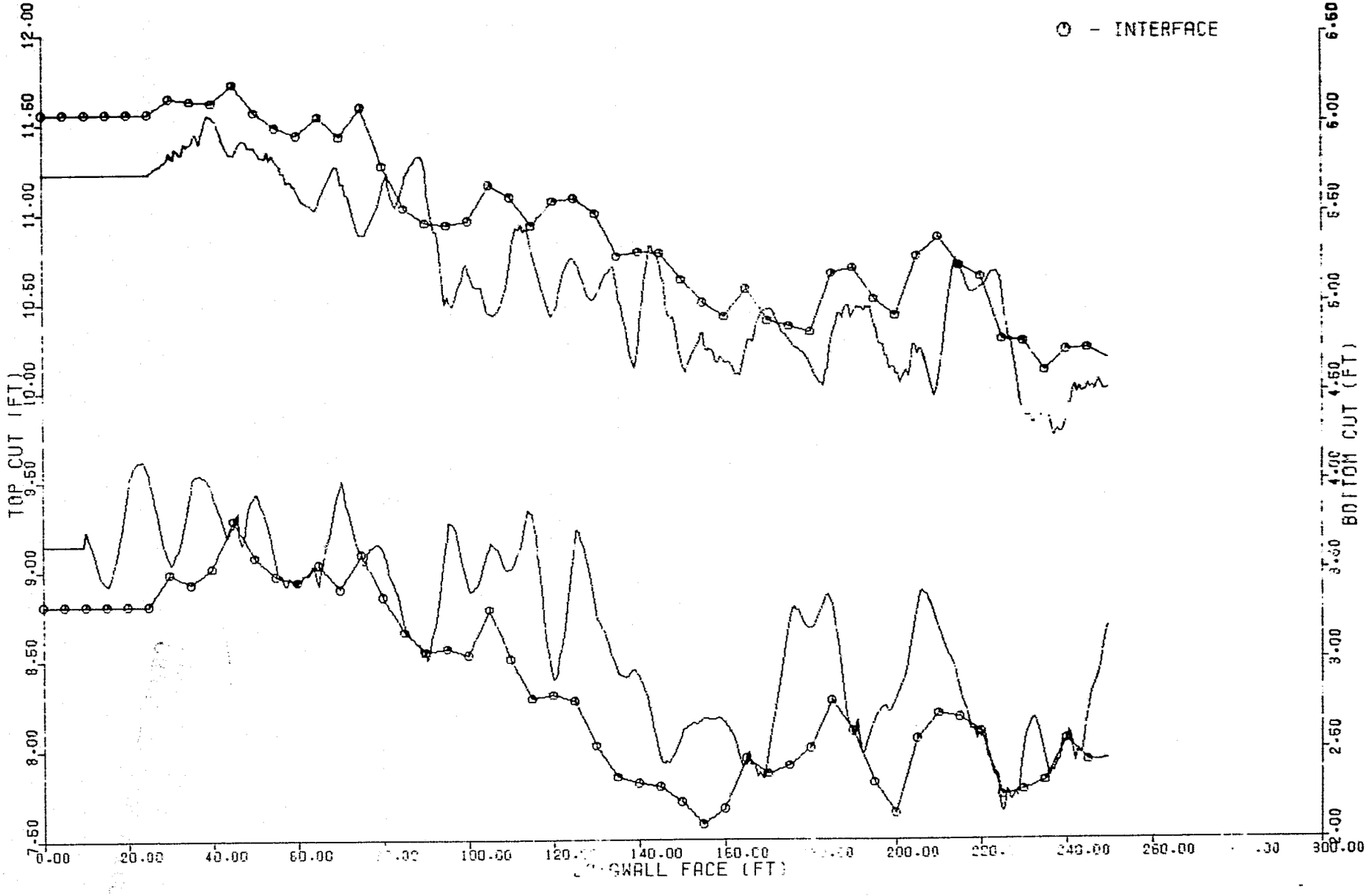

Figure 3-98. VCS Drum Slaving Performance with Middle LCF

Table 3-18. Recommended VCS Sensor Configuration

- TOP DRUM
  - NUCLEONIC CID
    - 2.5 FT BEHIND DRUM
    - 0.25 s OUTPUT INTERVAL
  - LAST CUT FOLLOWER
    - OUTPUT CONTINUOUS
    - RANGE GREATER THAN ±2 IN.
  - SENSITIZED PICK
    - 2 PICKS 180 DEG APART (LATENCY OF 0.6-0.7 s)
    - AT LEAST 80-90% ACCURATE
- BOTTOM DRUM
  - SENSITIZED PICK (AS ABOVE)
  - TOP FOLLOWER FOR SLAVING
    - CONTINUOUS OUTPUT
    - RANGE SUFFICIENT TO FOLLOW TOP

Table 3-19 shows results with a sensor configuration selected from Table 3-18. The sensor configuration was a CID, LCF, and pick on the top and bottom slaving with the rear drum top follower. These represent results from the second pass of a two-pass simulation run. These runs are representative of typical system performance in an actual mine. Figures 3-99 and 3-100 show performance with the CID sensors on top and bottom, cutting a 4 in. bias.

3.8.2 Recommended VCS Systems For Various Mine Applications

The configuration of sensors recommended for various combinations of top and bottom mining requirements is shown in Table 3-20. These configurations allow the system to be tailored to the individual mine in which it will operate.

Table 3-19. Results with Recommended VCS Sensor Configuration

CONDITIONS	TOP		BOTTOM (CID)		BOTTOM (SLAVING)	
	RMS (IN.)	% TIR	RMS (IN.)	% TIR	RMS (IN.)	% TIR
ROBINSON RUN 4 IN. BIAS	1.39	0.0	1.43	0.45	2.66	3.4
YORK CANYON 4 IN. BIAS	1.37	0.0	1.65	3.2	3.02	3.9

(A) CID, LCF, 90% PICK

(B) CID OUTPUT INTERVAL 0.25 s

(C) RESULTS FOR SECOND PASS

(D) WITH ACTUATORS

PERFORMANCE EVALUATION PASS 1

TOTAL COAL TAKEN = 4163.926 CU. FT.

FLOOR

RMS ERROR = 1.428 IN.

AVERAGE ABSOLUTE ERROR = 1.081 IN.

VOLUME EXCESS COAL LEFT = 4.192 CU. FT. (0.10%)

VOLUME EXCESS COAL TAKEN = 45.386 CU. FT. (1.09%)

VOLUME ROCK TAKEN = 0.070 CU. FT. (0.00%)

TIME IN ROCK = 0 45%

ROOF

RMS ERROR = 1.385 IN.

AVERAGE ABSOLUTE ERROR = 1.085 IN.

VOLUME EXCESS COAL LEFT = 5.523 CU. FT. (0 13%)

VOLUME EXCESS COAL TAKEN = 44.300 CU. FT. (1.06%)

VOLUME ROCK TAKEN = 0 000 CU. FT. (0.00%)

TIME IN ROCK = 0.00%

Figure 3-99. VCS Performance in Robinson Run Mine with Recommended CID, Pick and LCF Configuration Leaving a 4 In. Bias

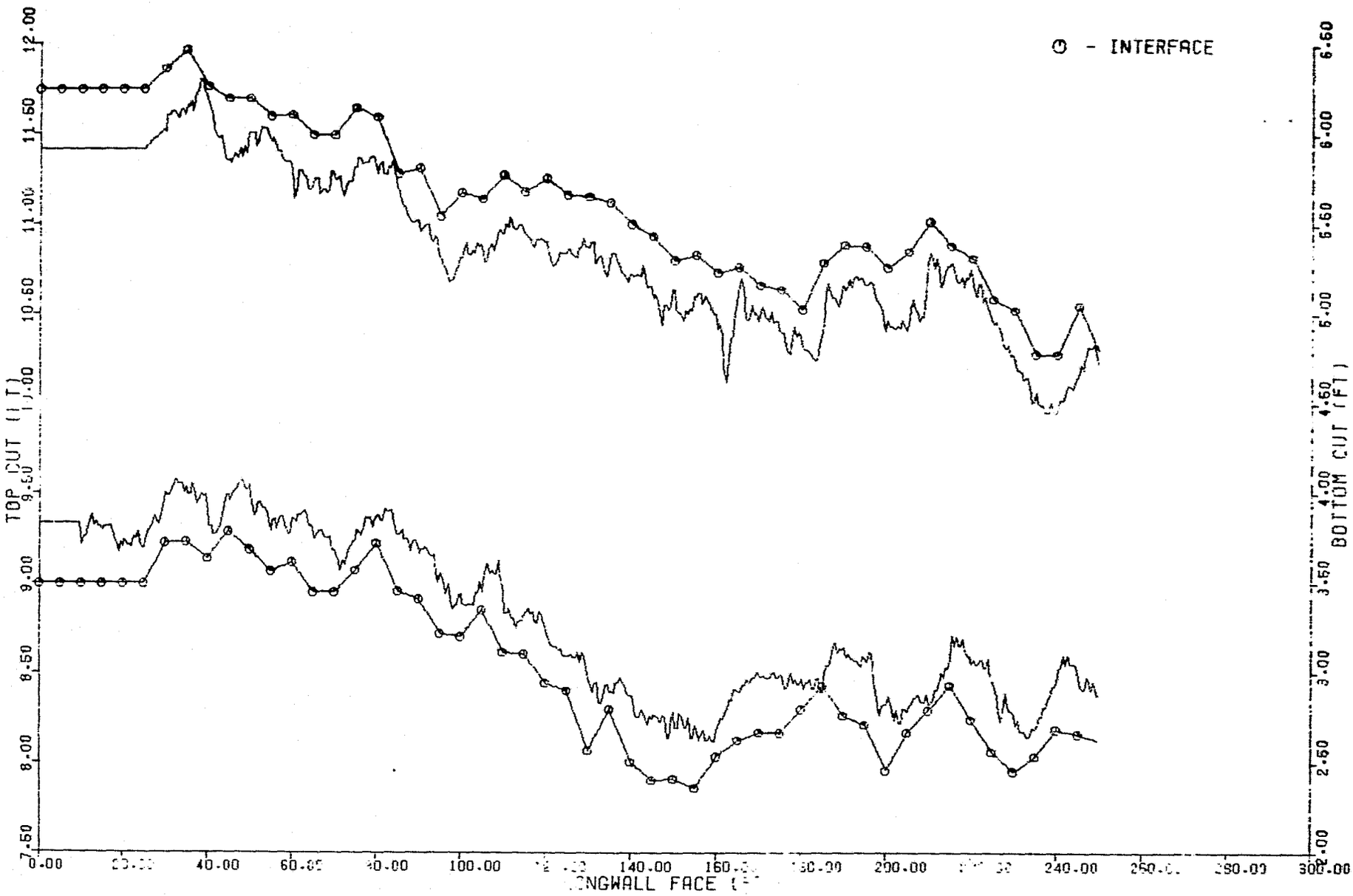

Figure 3-99. VCS Performance In Robinson Run Mine with Recommended CID, Pick and LCF Configuration Leaving a 4 In. Bias (Continued)

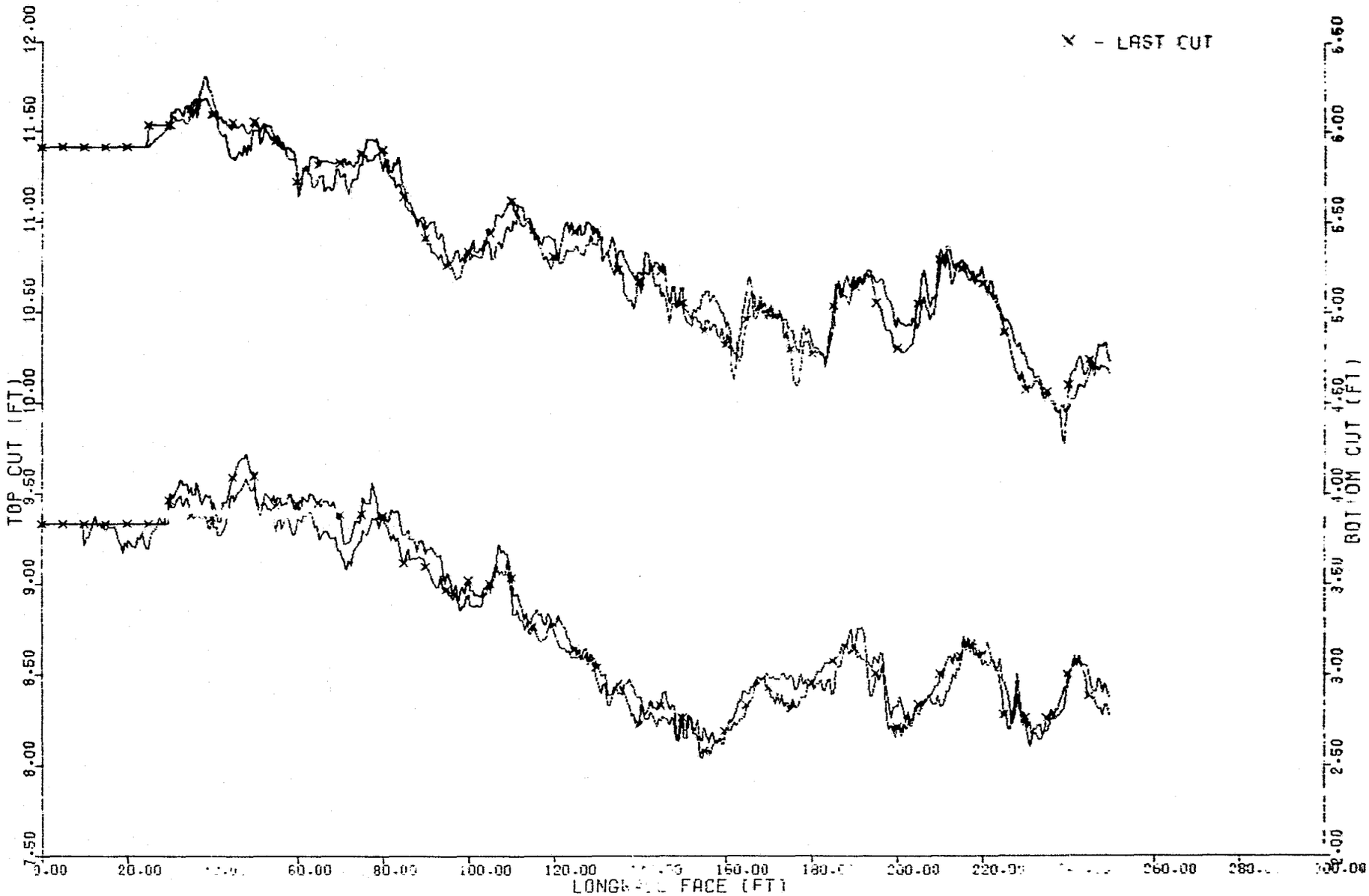

Figure 3-99. VCS Performance In Robinson Run Mine with Recommended CID, Pick and LCF Configuration Leaving a 4 In. Bias (Continued)

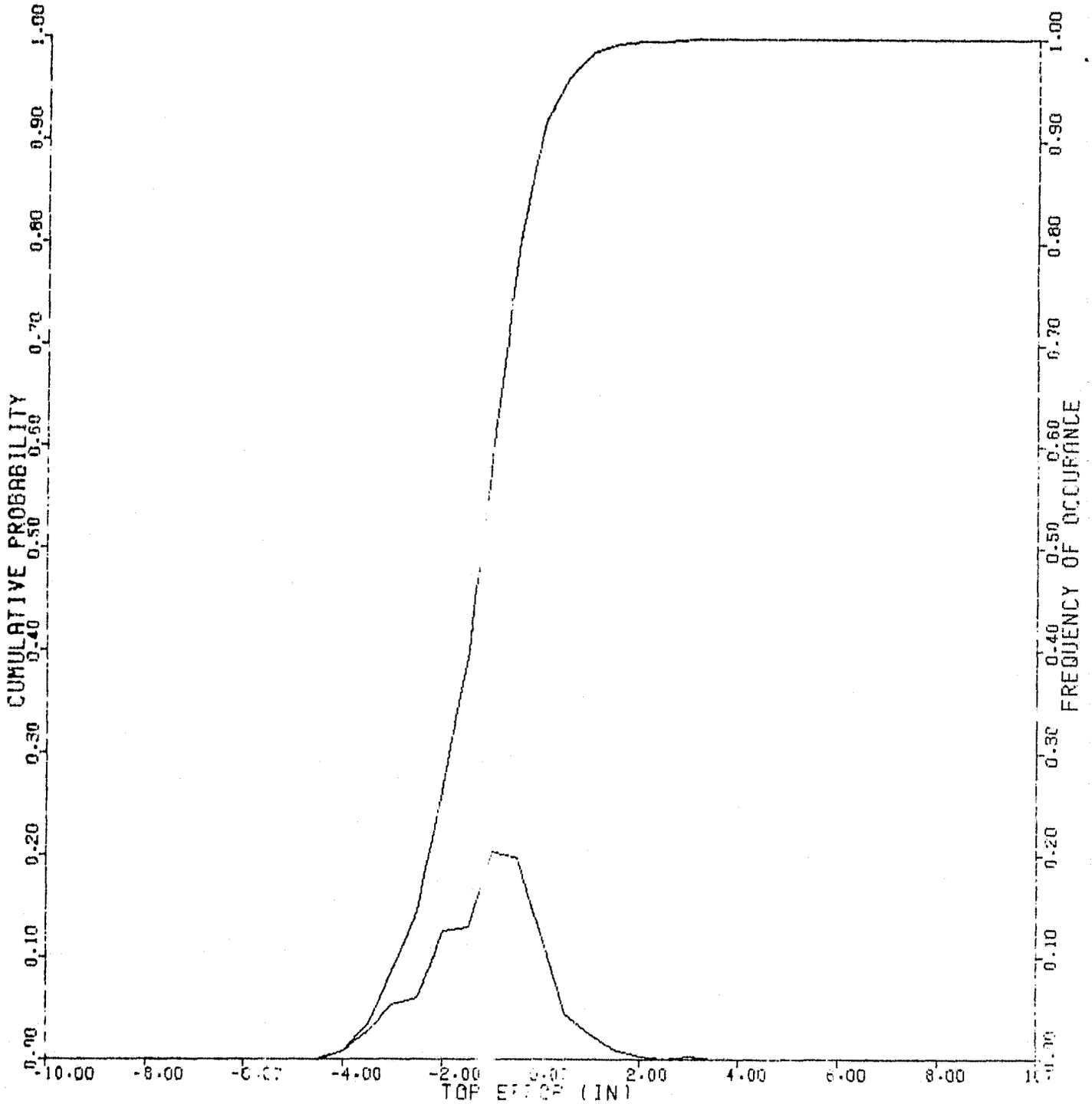

Figure 3-99. VCS Performance in Robinson Run Mine with Recommended CID, Pick and LCF Configuration Leaving a 4 In. Bias (Continued)

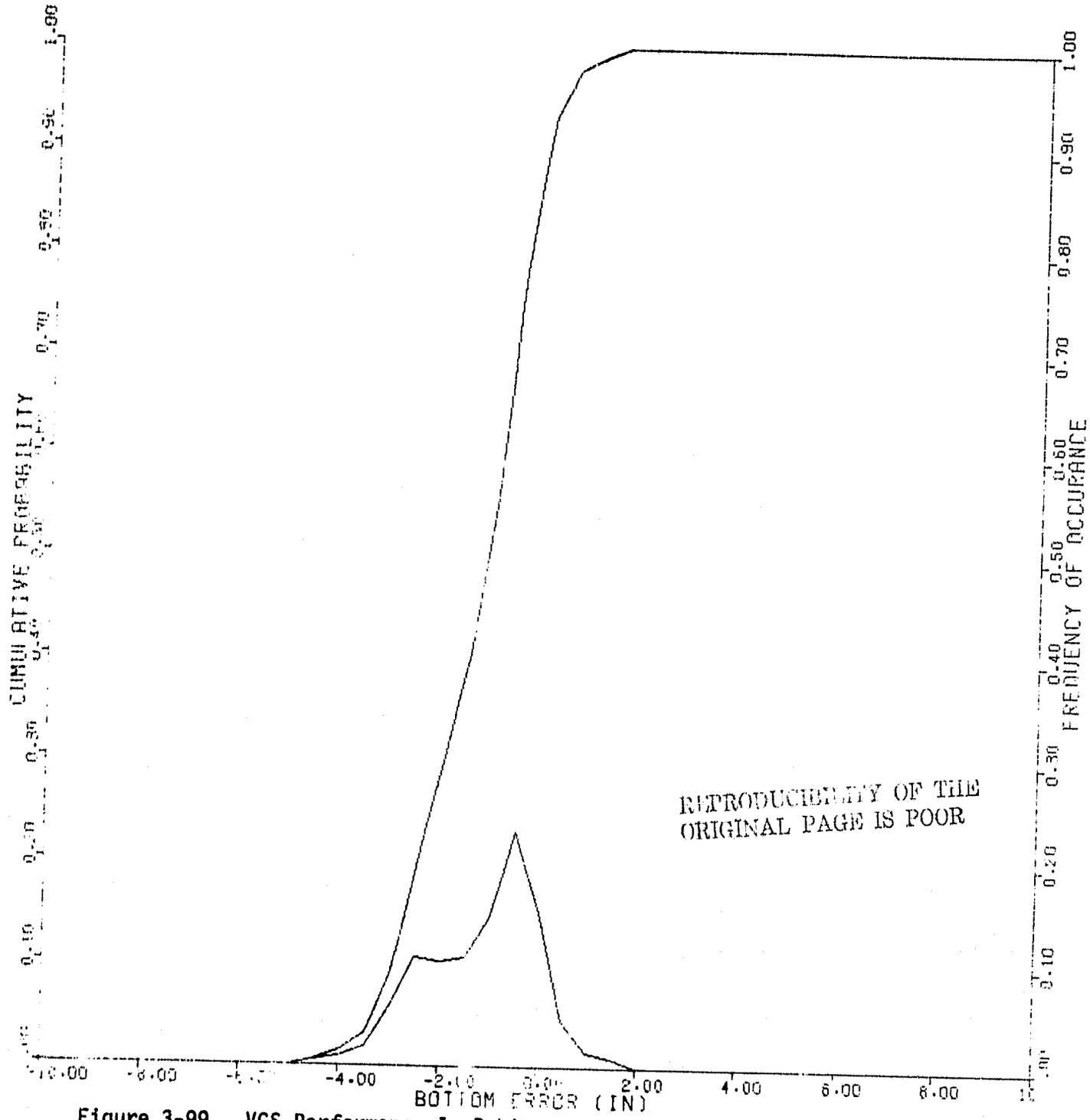

Figure 3-99. VCS Performance In Robinson Run Mine with Recommended CID, Pick and LCF Configuration Leaving 4 In. Bias (Concluded)

PERFORMANCE EVALUATION PASS 1

TOTAL COAL TAKEN = 3024.765 CU.FT

FLOOR

RMS ERROR = 1.651 IN.

AVERAGE ABSOLUTE ERROR = 1.248 IN

VOLUME EXCESS COAL LEFT = 7.414 CU.FT. (0.25%)

VOLUME EXCESS COAL TAKEN = 48.344 CU.FT. (1.60%)

VOLUME ROCK TAKEN = 1.557 CU.FT. (0.05%)

TIME IN ROCK = 3.17%

ROOF

RMS ERROR = 1.370 IN.

AVERAGE ABSOLUTE ERROR = 1.123 IN.

VOLUME EXCESS COAL LEFT = 5.647 CU.FT. (0.19%)

VOLUME EXCESS COAL TAKEN = 45.949 CU.FT. (1.52%)

VOLUME ROCK TAKEN = 0.000 CU.FT. (0.00%)

TIME IN ROCK = 0.00%

Figure 3-100. VCS Performance In York Canyon Mine with Recommended CID, Pick and LCF Configuration Leaving a 4 In. Bias

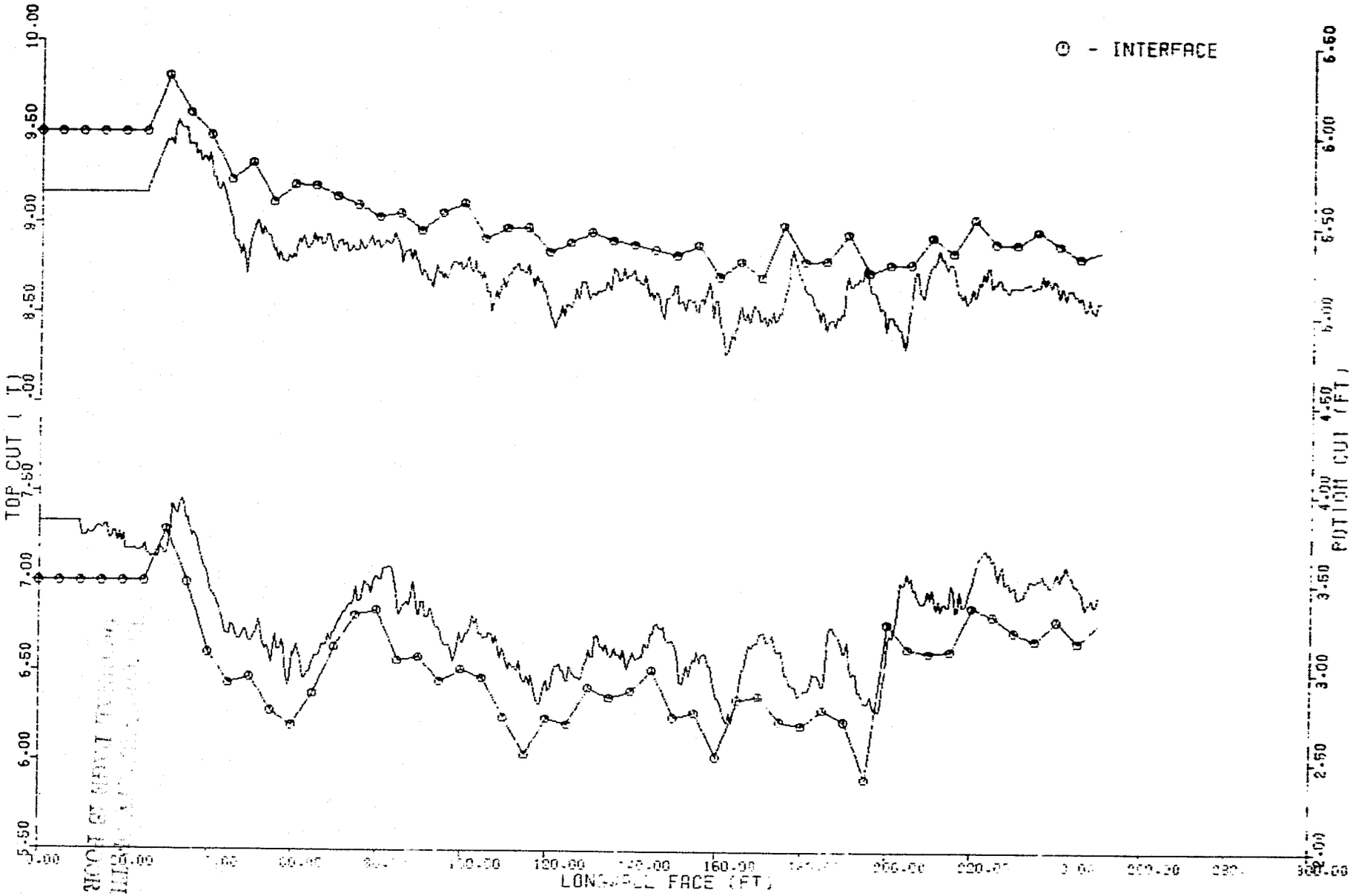

Figure 3-100. VCS Performance In York Canyon Mine with Recommended CID, Pick and LCF Configuration Leaving a 4 In. Bias (Continued)

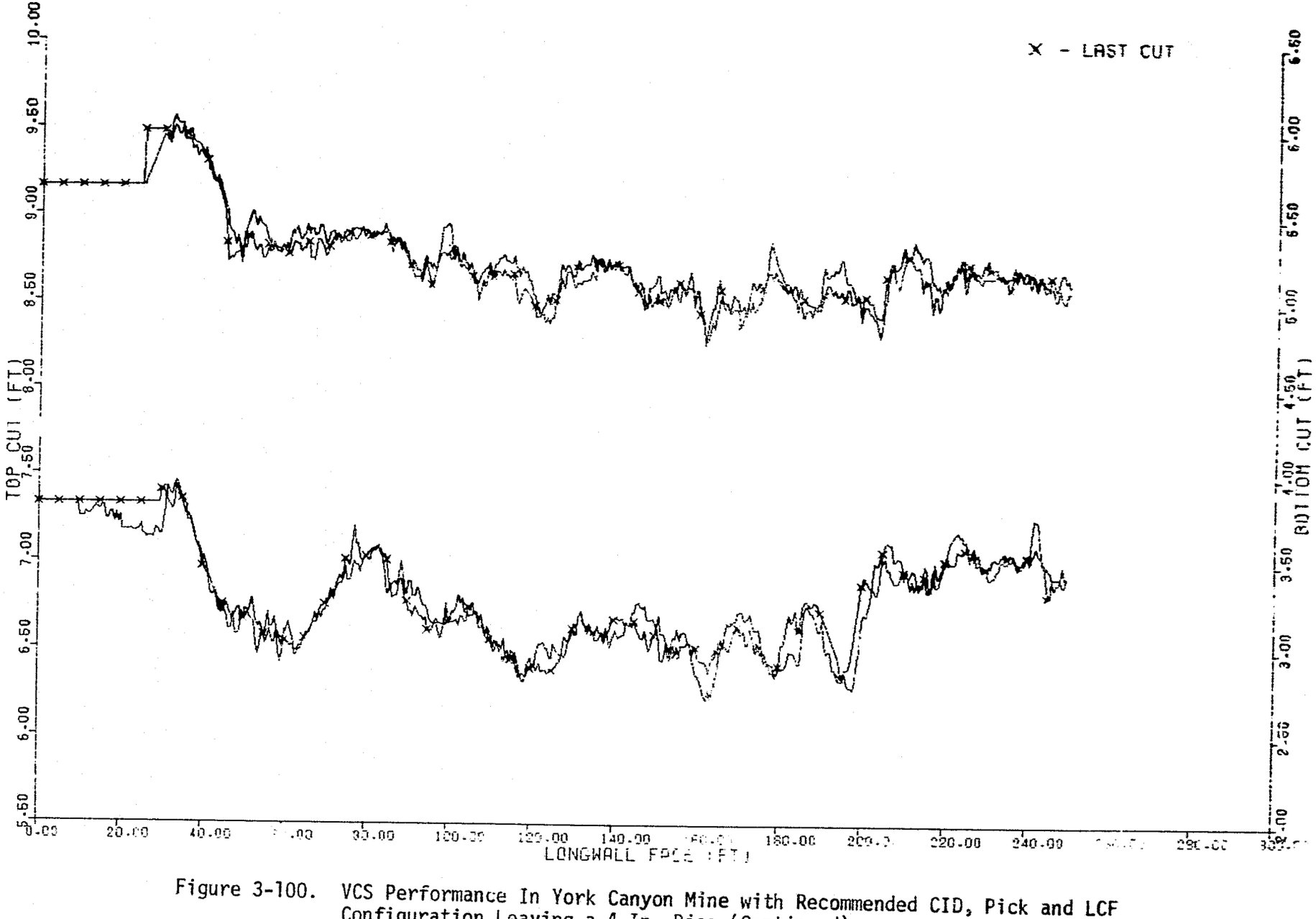

Figure 3-100. VCS Performance In York Canyon Mine with Recommended CID, Pick and LCF Configuration Leaving a 4 In. Bias (Continued)

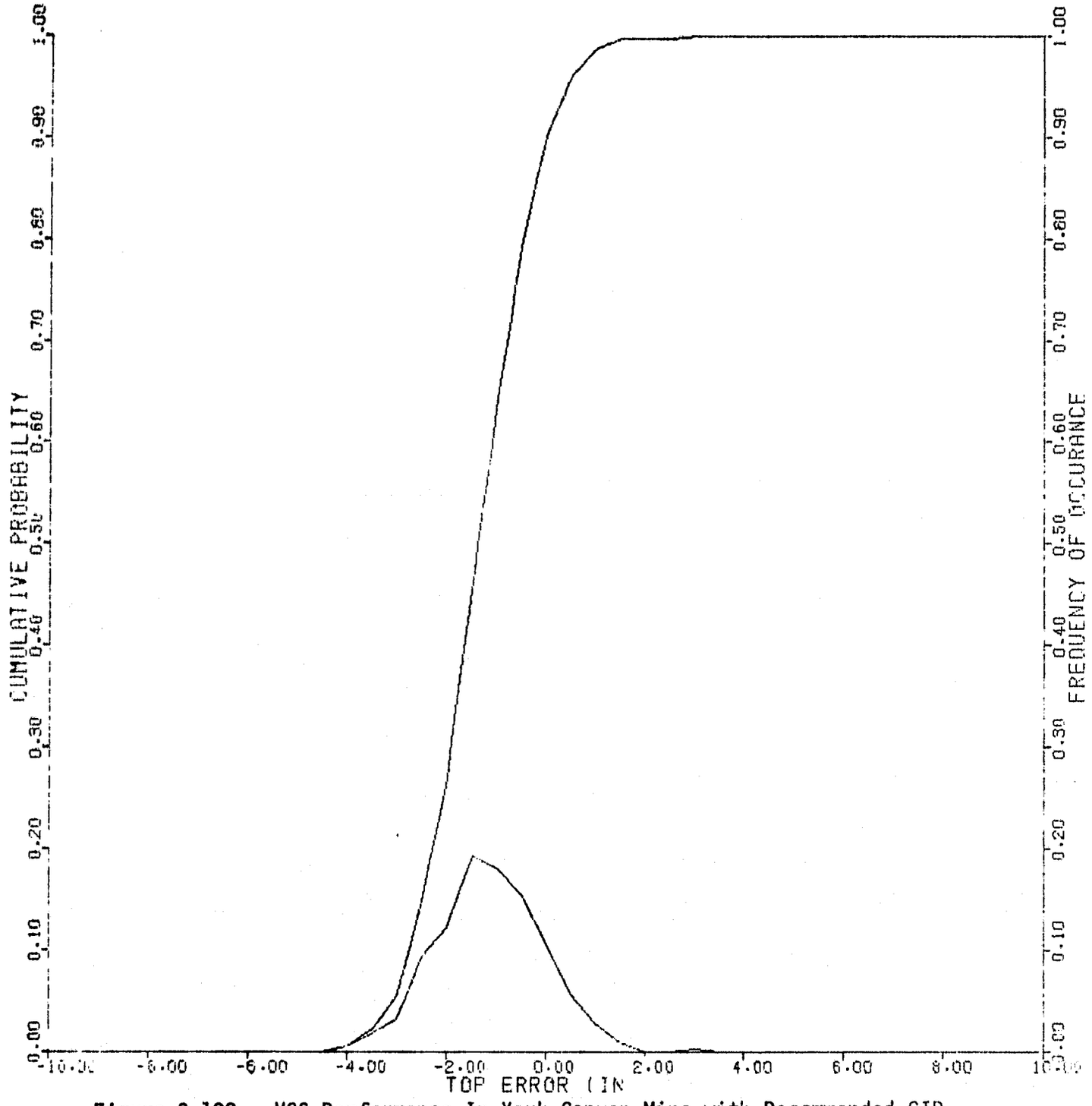

Figure 3-100. VCS Performance In York Canyon Mine with Recommended CID, Pick and LCF Configuration Leaving a 4 In. Bias (Continued)

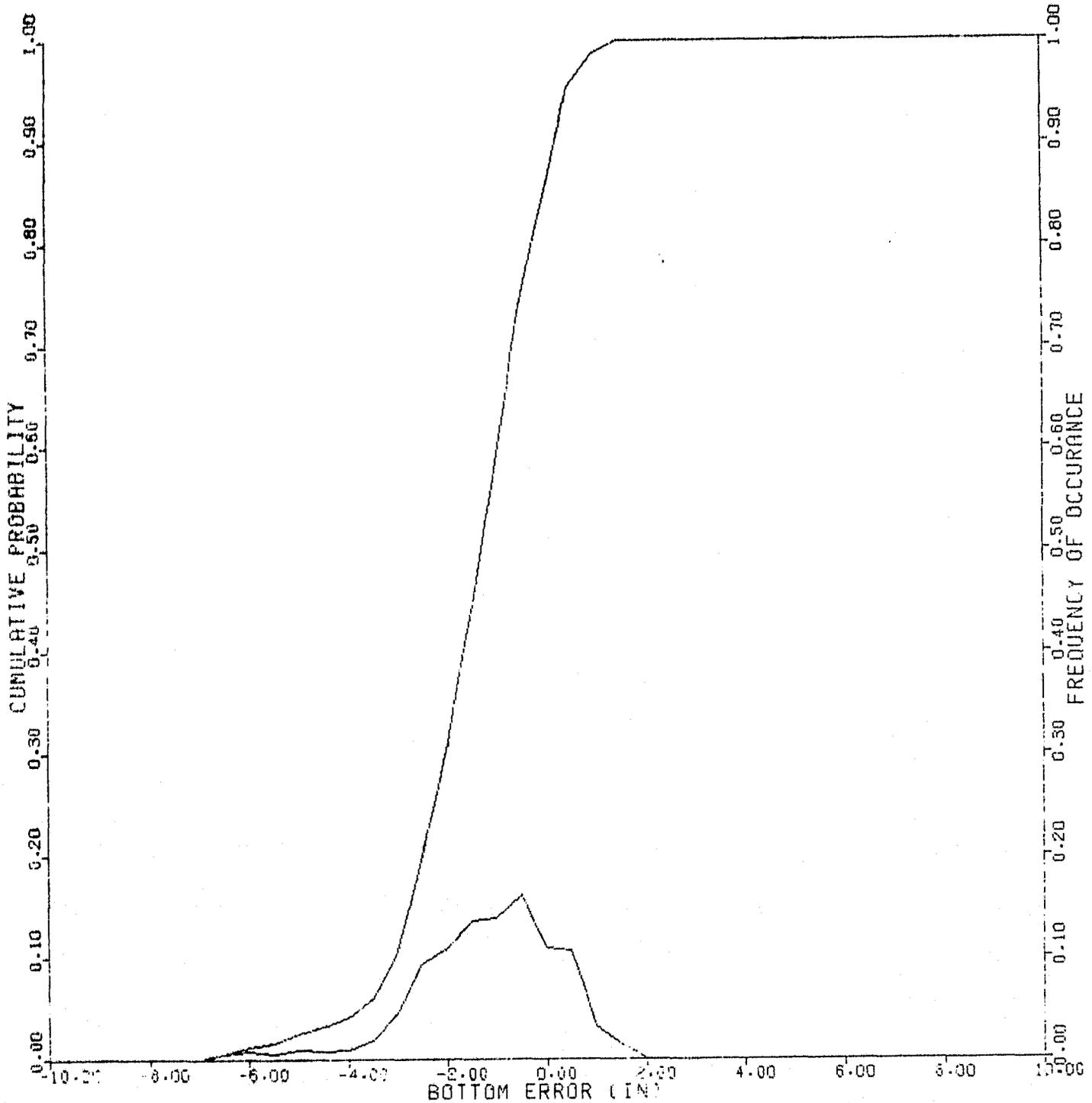

Figure 3-100. VCS Performance In York Canyon Mine with Recommended CID, Pick and LCF Configuration Leaving a 4 In. Bias (Concluded)

Table 3-20. Recommended Sensor Configuration for Various Applications

		TOP	
		TAKE ALL COAL	LEAVE COAL BIAS
BOTTOM	TAKE ALL COAL	TOP: PICKS BOTTOM: PICKS	TOP: NUCLEONIC-CID PICKS LCF BOTTOM: PICKS
	LEAVE COAL BIAS	TOP: PICKS BOTTOM: TOP FOLLOWER	TOP: NUCLEONIC-CID PICKS LCF BOTTOM: TOP FOLLOWER

4. YAW ALIGNMENT SYSTEM

4.1 FUNCTIONAL DESCRIPTION

In longwall mining after coal is cut along the face, the conveyer is pushed forward in preparation for the next cut by the roof support system. A typical sequence of operations is shown in Figures 4-1 through 4-4. In Figure 4-1 the conveyer is straight, the roof support shields have been pulled up and the shearer is at the headgate. The tailgate end of the conveyer is then advanced in preparation for the next cut as shown in Figure 4-2. Figure 4-3 shows the shearer at the tailgate end of the conveyer after it has cut the coal face. Finally, in Figure 4-4 the headgate end of the conveyer is pushed forward and the roof supports have been advanced along the tailgate end of the conveyer. The shearer can now travel from the tailgate to the headgate making a cleanup cut at the tailgate end of the conveyer and completing the cut at the headgate end. After the cut, the remaining roof supports are advanced. In this position the conveyer, shearer and roof supports are back in their original positions ready for another cycle of operation.

In the manual mode of operation, the miners push the conveyer a full stroke and then after cutting, advance the roof supports. Care must be taken to straighten the conveyer after the roof supports advance. This is accomplished by the miners sighting down the conveyer and alternately adjusting the conveyer and roof supports so they are straight. If care is not taken, the conveyer will rapidly get out of alignment resulting in the roof supports being unable to advance properly.

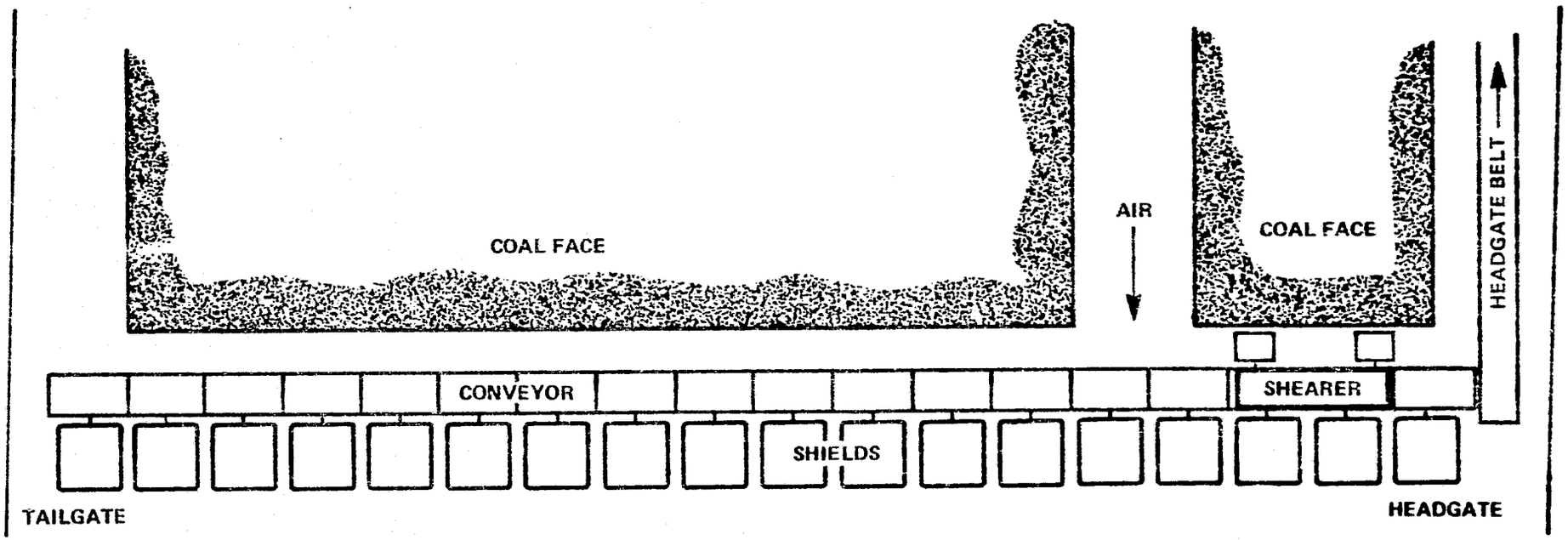

Figure 4-1. Conveyor Advance-Sequence of Operations 4

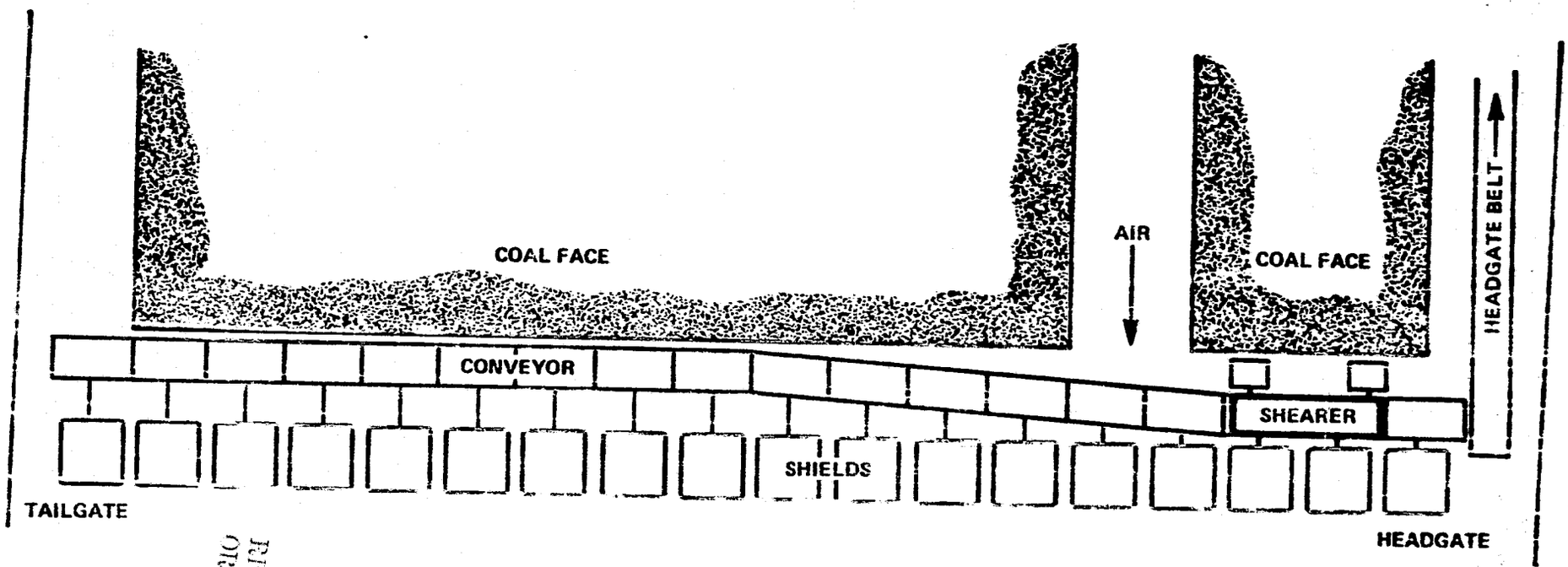

Figure 4-2. Conveyor Advance-Sequence of Operations 3

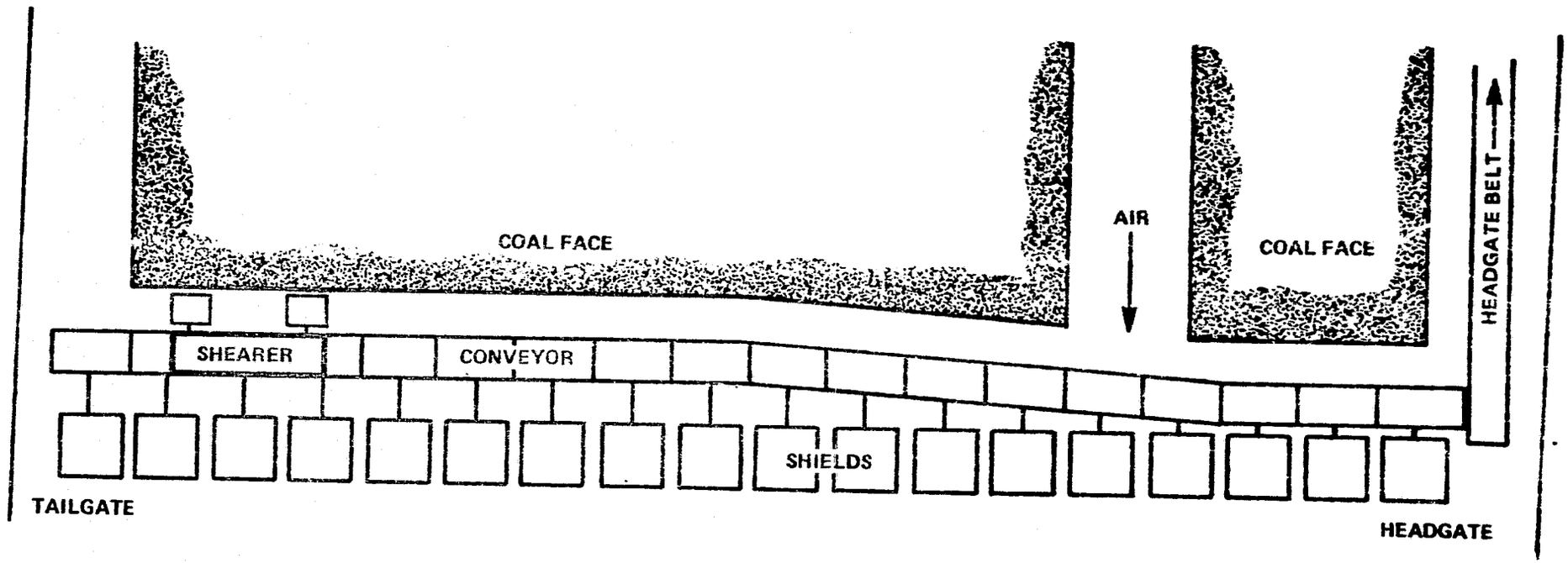

Figure 4-3. Conveyor Advance-Sequence of Operations 2

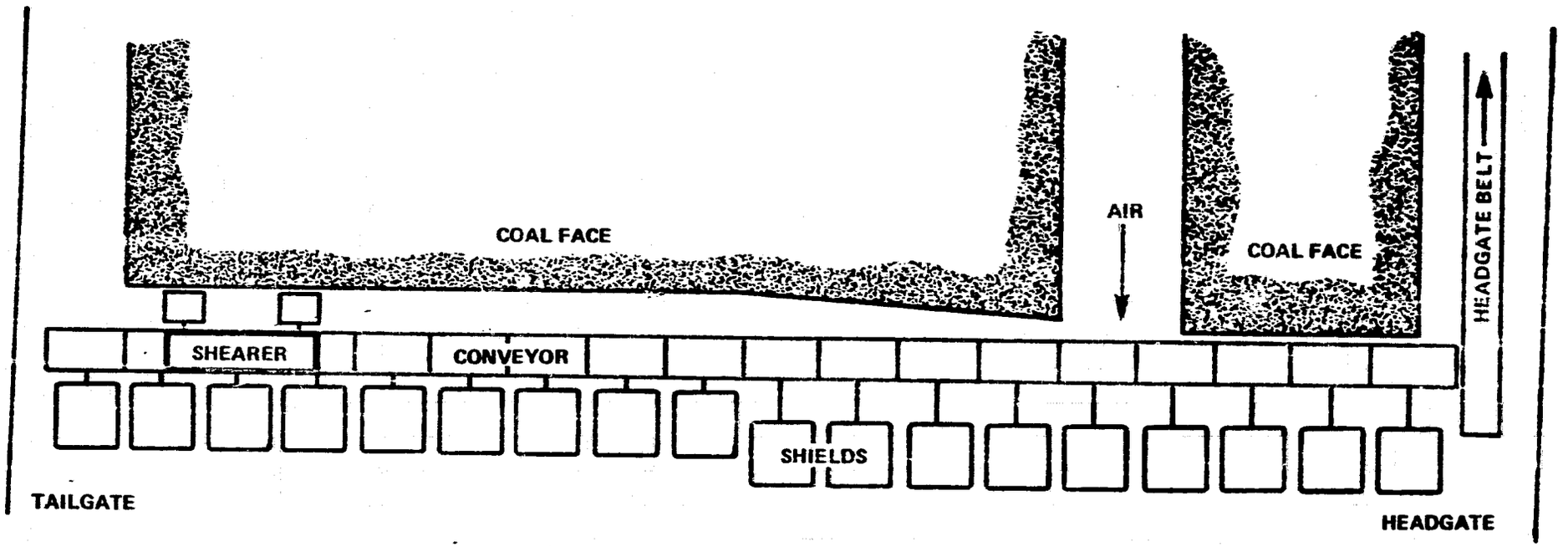

Figure 4-4. Conveyor Advance-Sequence of Operations 1

In an automatic system, measurements are made to determine the conveyer yaw alignment. Any misalignment is corrected by pushing the conveyer different amounts along the face.

The measurements can be taken when the system is in the sequence of operations as shown in Figure 4-4. The conveyer is relatively straight at this time and measurements can be made as the shearer travels from the tailgate to the headgate.

Two types of measurement devices are proposed. One is an angle cart system that measures the relative angle between two conveyer sections. The other is a directional gyro which measures the angular orientation of a conveyer section with respect to a directional reference.

Detailed descriptions of these measurement systems along with their performance evaluations are presented in the following sections.

4.2 DESCRIPTION OF THE ANGLE CART MEASUREMENT SYSTEM

The angle cart measurement device consists basically of two resolvers as shown in Figure 4-5. One resolver is lined up with one conveyer section while the other is lined up with an adjacent section. The sum of the resolver angles θ_A and θ_B gives the angle between the conveyer sections. As the angle cart moves along two conveyer sections, many measurements (200) can be made and then averaged. Hence

$$\theta = \frac{1}{200} \sum_{j=1}^{200} (\theta_{Aj} + \theta_{Bj})$$

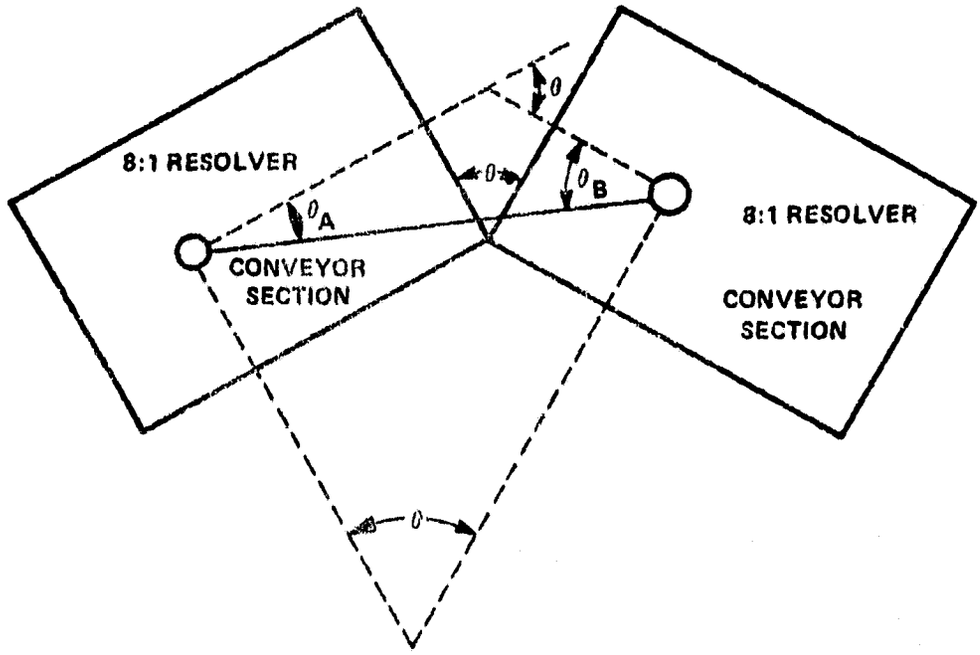

Figure 4-5. Angle Cart Measurement Device

If the standard deviation of the error in each resolver measurement is σ_r, then the standard deviation of the angle θ is

$$\sigma_m = \sqrt{\frac{2}{200}}\,\sigma_r = 0.1\,\sigma_r$$

The bias b in the angle cart measurements can be determined and removed from the measurements by computing θ when the angle cart is on a single conveyer section. Hence, if there are N conveyer sections, the bias is computed by

$$b = \frac{1}{N}\sum_{k=1}^{N} \theta_k$$

where θ_k is the angle cart output when it is on the k^{th} conveyer section. This bias is removed by

$$\hat{\theta} = \theta - b$$

where $\hat{\theta}$ is the corrected angle between the conveyor sections. The standard deviation of the error in b is given by

$$\sigma_b = \frac{1}{\sqrt{N}}\,\sigma_m$$

4.2.1 Basic Angle Cart Measurement System

The angle cart measures the angle θ between two conveyer sections. Knowing all the θ angles, the location of the conveyer end

points, and the length L of each conveyer section allows one to determine the YAW profile of the conveyer. From the geometry shown in Figure 4.6 the angle cart measures the angles θ_2 through θ_N (assuming N con veyer sections). The location of Y_o and Y_N can be measured with respect to surveyor stakes. The computed Y coordinates $\hat{Y}_i$ of the end points of each conveyer section are found as follows

$$\hat{Y}_1 = L \sin \hat{\theta}_1 + Y_o$$

$$\hat{Y}_2 = \hat{Y}_1 + L \sin (\hat{\theta}_1 + \hat{\theta}_2)$$

$$\vdots$$

$$\hat{Y}_n = \hat{Y}_{n-1} + L \sin \sum_{i=1}^{n} \hat{\theta}_i$$

$$\vdots$$

$$\hat{Y}_N = \hat{Y}_{N-1} + L \sin \sum_{i=1}^{N} \hat{\theta}_i$$

where $\hat{\theta}_i$ are the measured angles. Since all the angles are measured except θ_1, it must be determined in another manner. The last equation above can be written

$$\hat{Y}_N = L \sum_{i=1}^{N} \left(\sum_{j=1}^{i} \hat{\theta}_j \right) + Y_o$$

Note:

$$\gamma_i = \sum_{j=1}^{i} \theta_j$$

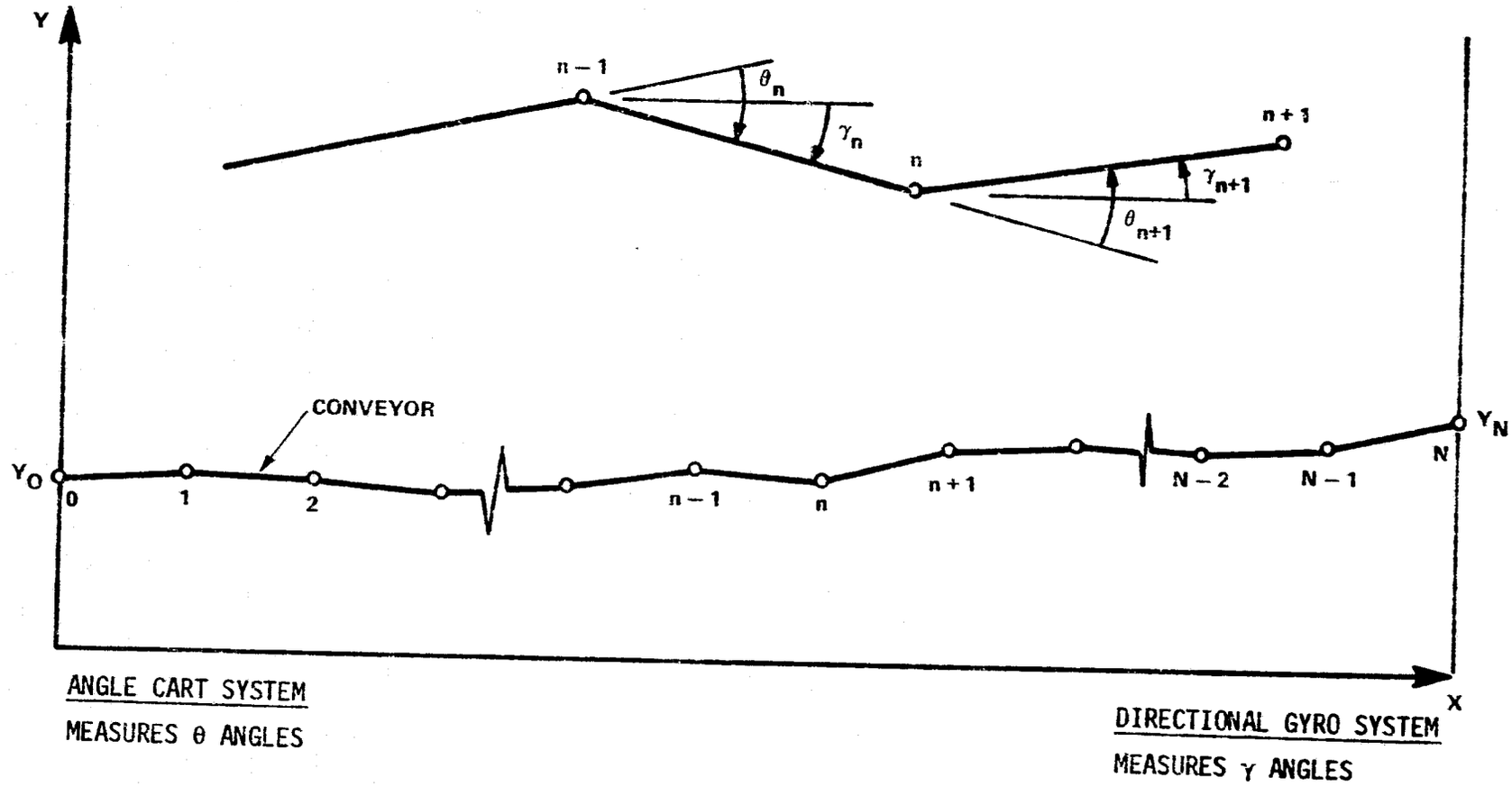

Figure 4-6. Conveyor Geometry

where γ_i is the angular orientation of the i^{th} conveyer section with respect to the horizontal. Assuming small angles

$$Y_N = Y_o + L\gamma_1 + L\gamma_2 + \ldots + L\gamma_N = Y_o + L\sum_{i=1}^{N}\gamma_i = L\sum_{i=1}^{N}\left(\sum_{j=1}^{i}\theta_j\right) + Y_o$$

Assuming that $\theta_1 = 0$ yields

$$\hat{Y}_N = L\sum_{i=2}^{N}\left(\sum_{j=2}^{i}\hat{\theta}_J\right) + Y_0$$

The value of θ_1 can then be computed by

$$\hat{\theta}_1 = -\frac{\hat{Y}_N - Y_N}{NL}$$

As a result, the yaw profile is determined by

$$\hat{Y}_n = L\sum_{i=1}^{n}\left(\sum_{j=1}^{i}\hat{\theta}_j\right) + Y_o \quad n = 1,2,3,\ldots,N$$

4.2.2 Derivation of Weighting and Bias Estimation System

If the angles θ_1 and θ_{N+1} can be measured, then a method of weighting and bias estimation can be used to determine the yaw profile. The equations are derived as follows:

Using Y_o and the angle θ_1 plus the angles θ_2 through θ_N, the Y coordinate of the N^{th} point is computed by

$$\hat{Y}_N = L \sum_{i=1}^{N} \left(\sum_{j=1}^{i} \hat{\theta}_j \right) + Y_o$$

With angle measurement errors $\hat{Y}_N$ will not equal Y_N. Therefore a bias $\hat{b}^+$ on all the angle measurements is computed so the end points match up.

$$\hat{b}^+ = \frac{2}{N(N+1)} \frac{\hat{Y}_N - Y_N}{L}$$

The corrected angle measurements are found by

$$\hat{\theta}_i^+ = \hat{\theta}_i - \hat{b}^+$$

and the yaw profile is computed using these angles.

$$\hat{Y}_n^+ = L \sum_{i=1}^{n} \left(\sum_{j=1}^{i} \hat{\theta}_j^+ \right) + Y_o$$

Using Y_N and the angle θ_{N+1} plus the other angles θ_2 through θ_N, the Y-coordinate of the 0^{th} point is computed.

$$\hat{Y}_o = L \sum_{i=1}^{N} \left(\sum_{j=N-i+2}^{N+1} \hat{\theta}_j \right) + Y_N$$

Again a bias $\hat{b}^-$ is computed

$$\hat{b}^- = \frac{2}{N(N+1)} \frac{\hat{Y}_o - Y_o}{L}$$

Also, the corrected angle measurements are found by

$$\hat{\theta}_i^- = \hat{\theta}_i - \hat{b}^-$$

and the yaw profile by

$$\hat{Y}_n^- = L \sum_{i=1}^{N-n} \left(\sum_{j=N-i+2}^{N+1} \hat{\theta}_j^- \right) + Y_N$$

As a result, there are two Y-coordinate values for each point depending on which end of the conveyer was the reference. A weighted combination of the two gives a good estimate of the yaw profile. Hence

$$\hat{Y}_n = a_n \hat{Y}_n^+ + (1 - a_n) \hat{Y}_n^-$$

where a_n is the weighting function. It is derived as follows:

The one-sided estimates can be written

$$\hat{Y}_n^+ = Y_o + L \sum_{i=1}^{n} \sum_{j=1}^{i} (\theta_j + \epsilon_j)$$

$$= Y_n + L \sum_{i=1}^{n} \sum_{j=1}^{i} \epsilon_j$$

$$= Y_n + L \sum_{j=1}^{n} (n-j+1)\, \epsilon_j$$

$$= Y_n + X_1$$

and

$$\hat{\bar{Y}}_n = Y_N + L \sum_{i=1}^{N-n} \sum_{j=N-i+2}^{N+1} (\theta_j + \epsilon_j)$$

$$= Y_n + L \sum_{i=1}^{N-n} \sum_{j=N-i+2}^{N+1} \epsilon_j$$

$$= Y_n + X_2$$

where

$$Y_n = Y_o + L \sum_{i=1}^{n} \sum_{j=1}^{i} \theta_j = Y_N + L \sum_{i=1}^{N-n} \sum_{j=N-i+2}^{N+1} \theta_j$$

is the true ordinate and

$$X_1 = L \sum_{j=1}^{n} (n-j+1)\, \epsilon_j$$

and

$$X_2 = L \sum_{j=n+2}^{N+1} (j-n-1)\, \epsilon_j$$

are the errors in $\hat{Y}_n^+$ and $\hat{Y}_n^-$, respectively.

It is assumed that the angle measurement errors $\epsilon_1, \epsilon_2, \ldots, \epsilon_N, \epsilon_{N+1}$ are pairwise uncorrelated random variables with zero means and common variance σ_m^2. It follows that X_1 and X_2 are uncorrelated and have zero means and respective variances:

$$v_1 = L^2 \sum_{j=1}^{n} (n-j+1)^2\, \sigma_m^2$$

$$= L^2\, \sigma_m^2 \sum_{k=1}^{n} k^2 = L^2\, \sigma_m^2\, \frac{n(n+1)(2n+1)}{6}$$

and

$$v_2 = L^2 \sum_{j=n+2}^{N+1} (j-n-1)^2\, \sigma_m^2$$

$$= L^2\, \sigma_m^2 \sum_{k=1}^{N-n} k^2 = L^2\, \sigma_m^2\, \frac{(N-n)(N-n+1)(2N-2n+1)}{6}$$

For any value of a_n, $\hat{Y}_n$ is an unbiased estimate of Y_n, i.e., $E(\hat{Y}_n) = Y_n$. This is true because

$$E(\hat{Y}_n) = a_n\, E(\hat{Y}_n^{+}) + (1 - a_n)\, E(\hat{Y}_n^{-}),$$

$$E(\hat{Y}_n^{+}) = Y_n + E(X_1) = Y_n + 0$$

and

$$E(\hat{Y}_n^{-}) = Y_n + E(X_2) = Y_n + 0$$

The chosen value of a_n is that which minimizes the variance of $\hat{Y}_n$. Differentiating the variance of $\hat{Y}_n$ with respect to a_n, setting the derivative equal to zero and solving for a_n gives

$$a_n = \frac{v_2}{v_1+v_2} = \frac{(N-n)(N-n+1)(2N-2n+1)}{n(n+1)(2n+1) + (N-n)(N-n+1)(2N-2n+1)}$$

4.2.3 Derivation of Angle Cart Measurement Algorithm Assuming that a Number of End Conveyer Sections Cannot be Measured

Since the shearer is approximately 30 feet long and it rides on the conveyer sections, it is possible that not all the angles between the conveyer sections can be measured. If this is the case, the control algorithm will simply assume that these angles are zero, i.e., that the conveyer is straight at the ends.

4.3 DESCRIPTION OF THE MONTE CARLO TECHNIQUE TO DETERMINE THE EFFECT OF ANGLE CART MEASUREMENT ERRORS

A Monte Carlo simulation was developed to determine the effect of angle cart measurement errors (see Figure 4.7). This was accomplished

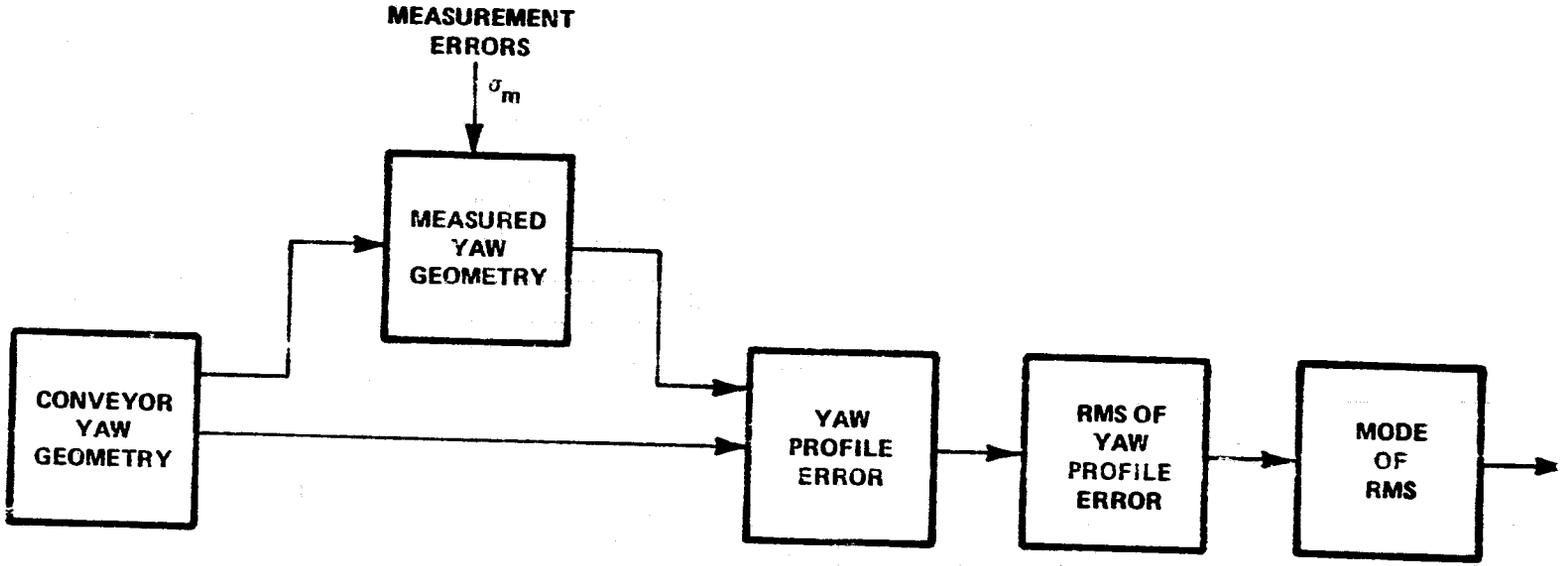

Figure 4-7. Monte Carlo Simulation

by developing a conveyer yaw geometry consisting of the true conveyer angles θ_n and the Y-coordinates Y_n. The true conveyer angles were sampled from a normal distribution with zero mean and standard deviation σ_T, i.e.,

$$\theta_i = \text{normal } (0, \sigma_T^2)$$

where $\sigma_T = 1$ degree

The Y-coordinates are then computed by

$$Y_n = L \sum_{i=1}^{n} \sum_{j=1}^{i} \theta_j$$

Measurement errors were then added to the conveyer angles and using the measurement algorithms described in Sections 4.2.1, 4.2.2 and 4.2.3 the computed Y-coordinates $\hat{Y}_n$ were determined. (It was assumed that Y_0 and Y_N were measured without error.) Next, the yaw profile error $\Delta_n = \hat{Y}_n - Y_n$ and the RMS of the yaw profile error

$$\text{RMS} = \sqrt{\frac{1}{N} \sum_{i=1}^{N} \Delta_i^2}$$

were computed. The RMS computation was made 500 times--each time using different noise measurement errors.

A statistical average of these 500 RMS values is needed for an evaluation criterion. The statistical average used is the Mode of the RMS and is computed by

$$M_R = \sqrt{\frac{\sum_{k=1}^{N_s} (RMS)_k^2}{2N_s}}$$

where $N_s = 500$.

4.3.1 Basic Measurement System

The basic measurement system is simulated by assuming the measured conveyer angles $\hat{\theta}_i$ are given by

$$\hat{\theta}_i = \theta_i + \epsilon_i + b$$

where

θ_i is the true geometric conveyer angle

ϵ_i = the random error in each measurement

and, b = the bias error in the measurement device.

These errors are simulated by sampling from normal distributions, i.e.,

$$\epsilon_i = \text{normal } (0, \sigma_m^2)$$

$$b = \text{normal } \left[0, \left(\frac{\sigma_m}{\sqrt{N}} \right)^2 \right]$$

The results of the Monte Carlo simulation are shown in Figure 4-8. As the standard deviation of the measurement error (σ_m) increases, the mode of the RMS (M_R) increases linearily.

It will be shown later that the maximum allowable value of M_R (with no other system errors) is approximately 0.2 feet. It can be

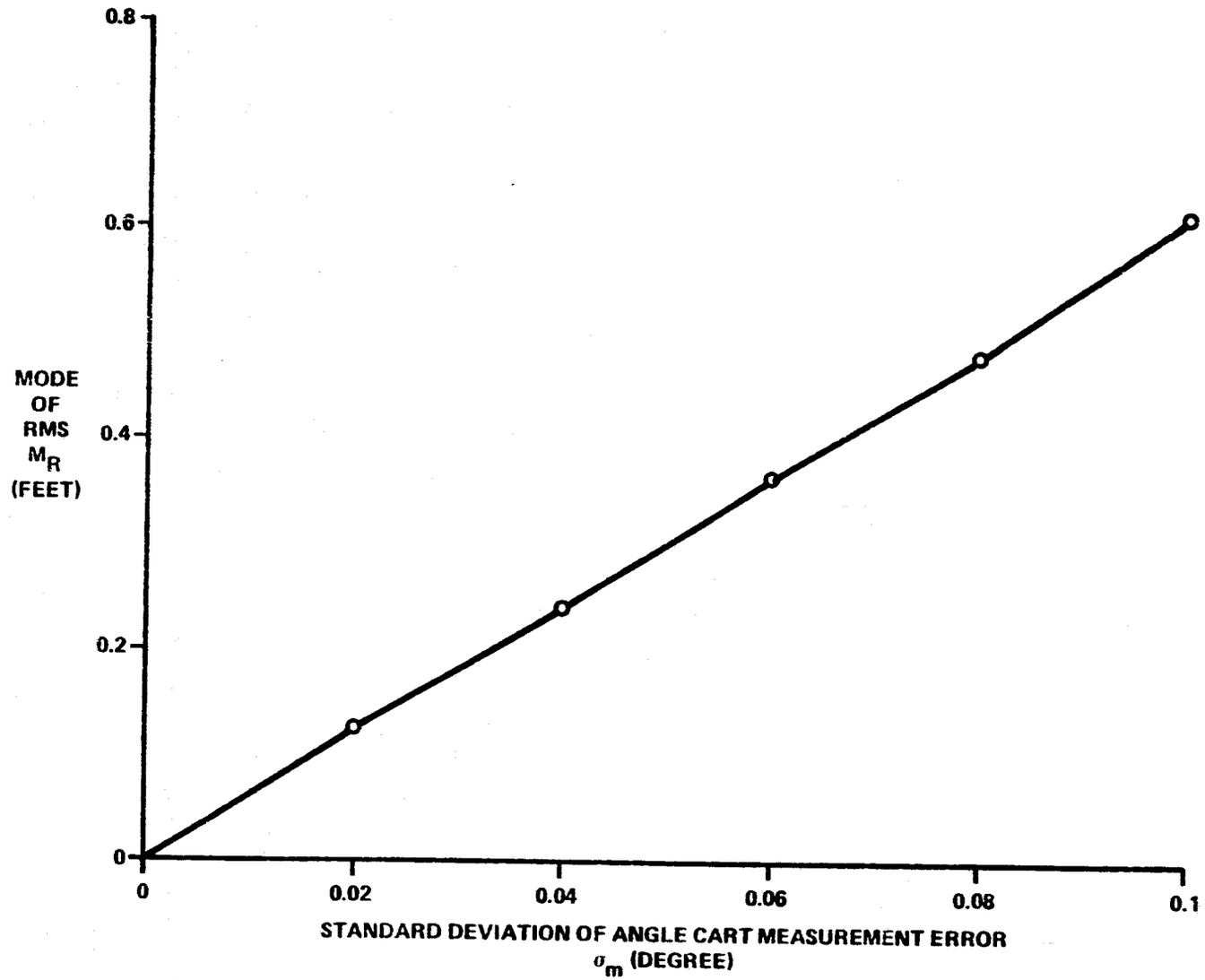

Figure 4-8. Basic Angle Cart System - Monte Carlo Results

seen, therefore, that the maximum allowable σ_m is approximately 0.04 degrees.

4.3.2 Performance of Weighting and Bias Estimation System

The weighting and bias estimation system uses two angle measurements ($\hat{\theta}_1$ and $\hat{\theta}_{N+1}$) that are not used in the basic system. These measurements have an additional error--the directional reference error for the first and n^{th} conveyor sections. The measured angles are simulated by

$$\hat{\theta}_1 = \theta_1 + \epsilon_1 + b + \epsilon_{\theta 1}$$

$$\hat{\theta}_{N+1} = \theta_{N+1} + \epsilon_{N+1} + b + \epsilon_{\theta (N+1)}$$

where

$$\epsilon_{\theta 1} = \text{normal } (0, \sigma_\theta^2)$$

$$\epsilon_{\theta (N+1)} = \text{normal } (0, \sigma_\theta^2)$$

The errors in the other angles are the same as in the basic measurement system, i.e.,

$$\epsilon_i = \text{normal } (0, \sigma_m^2)$$

$$b = \text{normal } \left[0, \left(\frac{\sigma_m}{\sqrt{N}} \right)^2 \right]$$

The results of the Monte Carlo simulation are shown in Figure 4.9. In this figure M_R is plotted versus σ_m for various values of σ_θ. It can be seen that using the criterion that the maximum allowable M_R is 0.2 feet, the maximum allowable σ_θ is 0.3 degrees. If σ_θ =

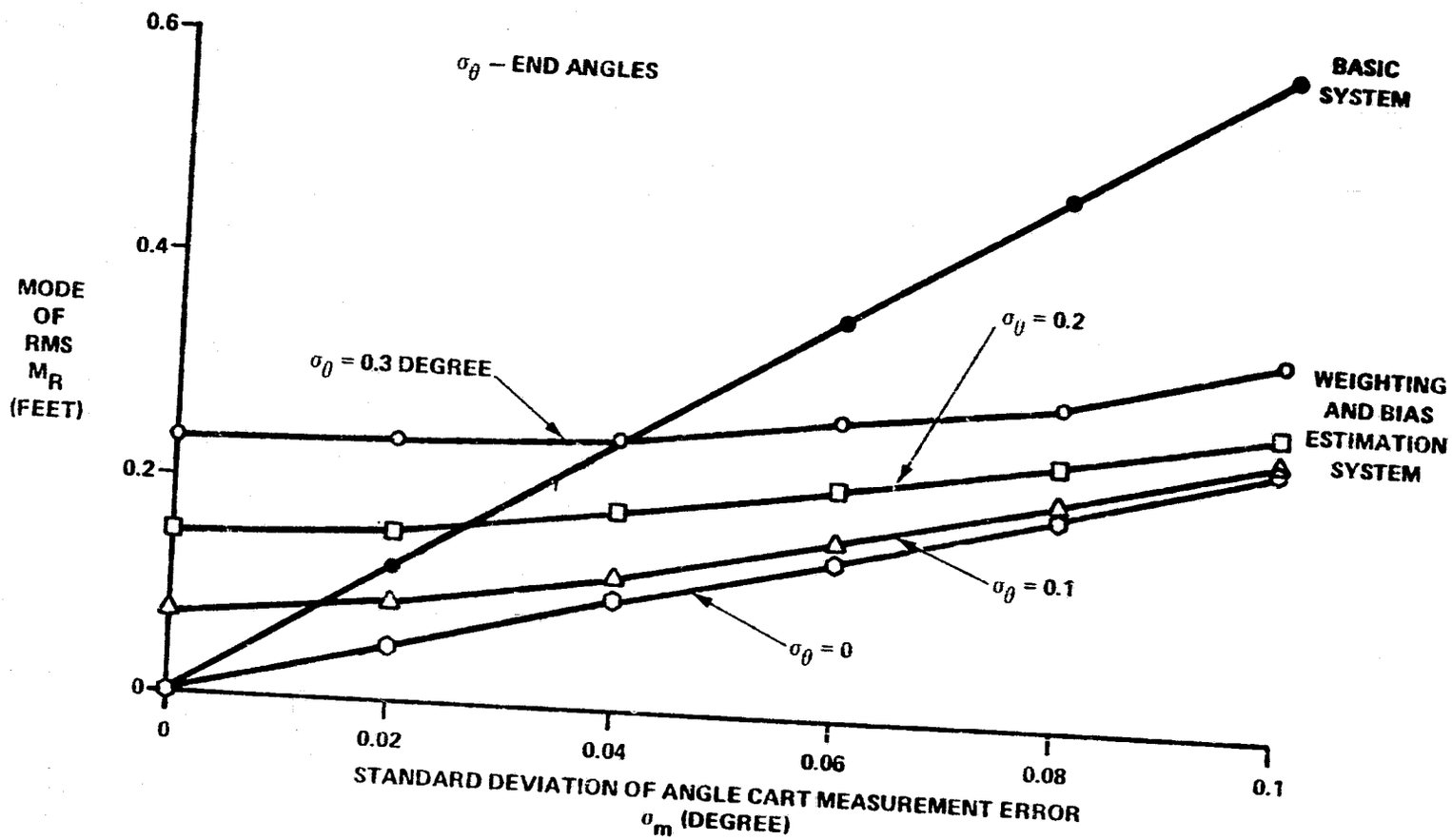

Figure 4-9. Angle Cart Systems - Monte Carlo Results

0, then a larger σ_m can be tolerated than in the basic measurement system.

It is concluded that the weighting and bias estimation algorithm is a viable system and superior to the basic system if the angle cart measurement inaccuracies are greater than 0.04 degrees but less than approximately 0.1 degrees. In that case the basic angle cart system does not provide sufficient accuracy. However, the error in the directional reference must be less than 0.2 degrees.

4.3.3 Performance of Basic Measurement System When a Number of Conveyer Sections Cannot Be Measured

The basic measurement system measures the angles θ_2 through θ_N and then computes the angle θ_1. If some of the angles at the conveyer ends cannot be measured because the shearer is in the way, then these angles will be assumed zero. In order to check the effect of this condition the Monte Carlo simulation was exercised with a number of conveyer angle measurements at each end of the conveyer arbitrarily set to zero.

The results are shown in Figures 4-10 and 4-11 where the Mode of RMS is plotted versus the number of conveyer angles at each end of the conveyer that cannot be measured. Figure 4-10 was obtained using σ_T = 0.5 degrees while Figure 4-11 is for σ_T = 1.0 degrees. The conveyer profile was simulated by sampling the angles between the conveyer sections from a normal distribution with standard deviation σ_T. Therefore, for σ_T = 1.0 degree the conveyer is more crooked (the angles between sections are larger) than for σ_T = 0.5 degree. By assuming that some of the angles at the ends of the conveyer are zero, larger errors

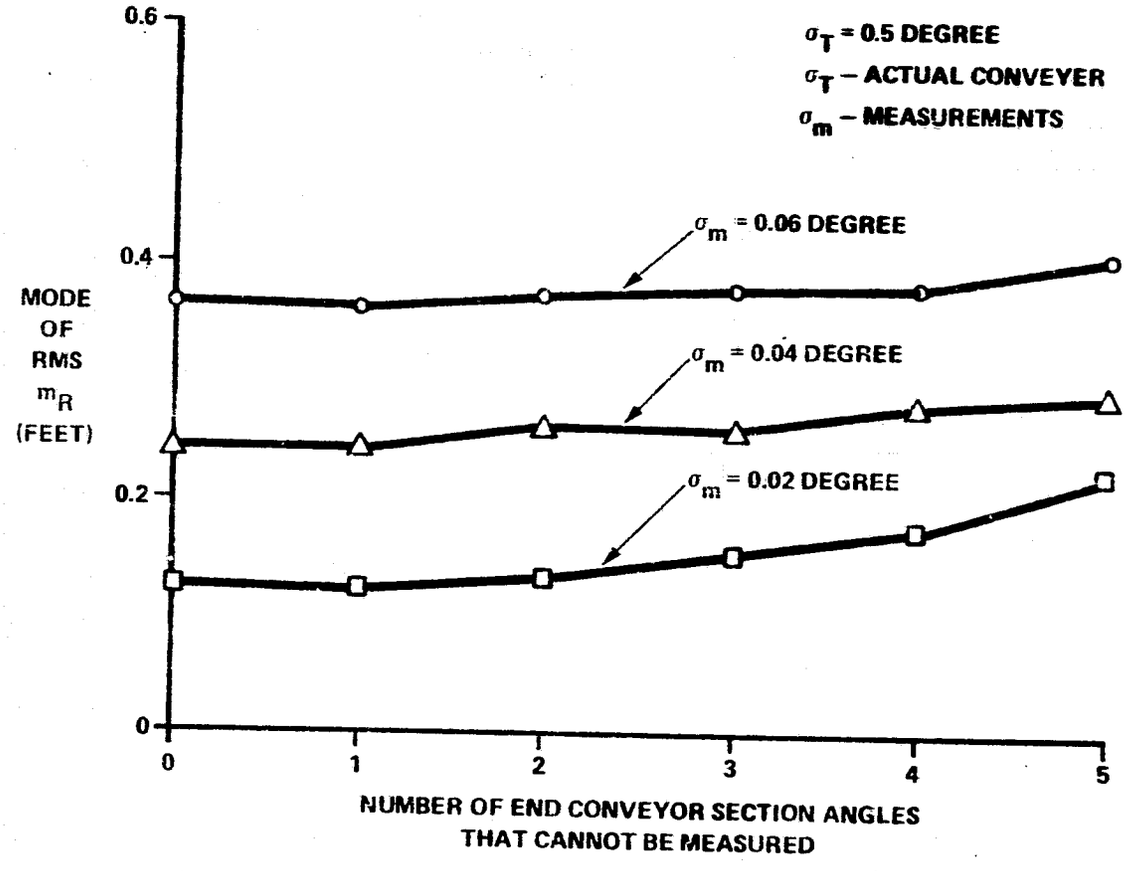

Figure 4-10. Basic Angle Cart System - Monte Carlo Results

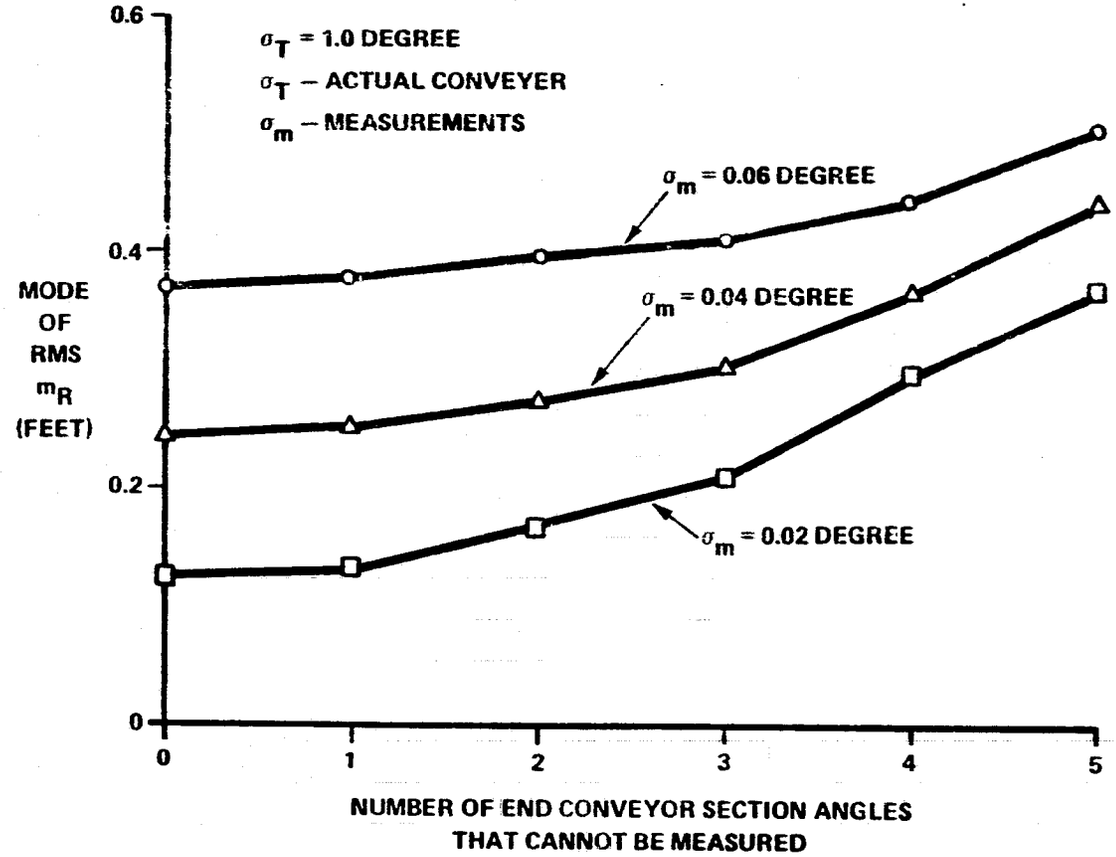

Figure 4-11. Basic Angle Cart System - Monte Carlo Results

in the computed yaw profile are expected. For σ_T = 0.5 degrees little affect on M_R is indicated for one or two angles that cannot be measured at each end of the conveyer. For σ_T = 1.0 degrees the effect on M_R is small only when one angle at each end of the conveyer is not measured. Since the magnitude of σ_T depends on operational errors such as the roof support pullup errors, the effect of not measuring some of the end conveyer angles must be studied with the yaw advancement simulation. The results of this study are described in Section 4.4.1.

4.4 DESCRIPTION OF THE YAW ADVANCEMENT SYSTEM SIMULATION USING THE ANGLE CART

As described in Section 4-1, the yaw advancement system consists of pushing the conveyer forward, pulling the roof supports up, measuring the yaw profile and then pushing the conveyer forward again. This same sequence of operations is modeled in the yaw advancement simulation (see Figure 4-12).

Conveyer Placement

Each section of the conveyer is pushed forward an amount given by the placement command ΔY_{pn} plus a placement error ϵ_{pn}, i.e.,

$$\Delta Y_n = \Delta Y_{pn} + \epsilon_{pn}$$

where ϵ_{pn} is sampled from a normal distribution $(0, \sigma_p^2)$. The amount the conveyer is pushed forward ΔY_r is limited between zero and the full ram stroke Y_A. The equations are

Figure 4-12. Yaw Advancement Simulation

If $\Delta Y_n > Y_A$, $\Delta Y_n = Y_A$

If $\Delta Y_n < 0$, $\Delta Y_n = 0$

The conveyer sections are pushed from their midpoints. Defining Y_{mn} as the Y-coordinate of the midpoint of the n^{th} conveyer section, then the Y-coordinate after pushing is given by

$$Y_{mn}^{k} = Y_{mn}^{k-1} + \Delta Y_n$$

where the superscripts define the sequence before and after pushing.

In the simulation conveyer section 1 is placed first. Its orientation is sampled from a normal distribution $(0, \sigma_1)$. Then its end points are located:

$$Y_o = Y_{m1} - \frac{L}{2} \sin \theta_1$$

$$Y_1 = Y_{m1} + \frac{L}{2} \sin \theta_1$$

Again, the advance is limited to Y_A, i.e.,

$$\text{If } Y_o^{k} > Y_o^{k-1} + Y_A,\ Y_o^{k} = Y_o^{k-1} + Y_A \text{ and } Y_1^{k} = 2Y_{m1}^{k} - Y_o^{k}$$

$$\text{If } Y_1^{k} > Y_1^{k-1} + Y_A,\ Y_1^{k} = Y_1^{k-1} + Y_A \text{ and } Y_o^{k} = 2Y_{m1}^{k} - Y_1^{k}$$

The angle θ_1 is recomputed

$$\theta_1 = \sin^{-1} \frac{Y_1 - Y_o}{L}$$

Also

$$\gamma_1 = \theta_1$$

All the other sections are then located in sequence by the following equations:

$$Y_n = 2Y_{mn} - Y_{n-1}$$

$$\text{If } Y_n^k > Y_n^{k-1} + Y_A,\ Y_n^k = Y_n^{k-1} + Y_A$$

$$\gamma_n = \sin^{-1} \frac{Y_n - Y_{n-1}}{L}$$

$$\theta_n = \gamma_n - \gamma_{n-1}$$

If after computing any θ_n

$$\theta_n > \theta_{max} \quad (\theta_{max} = 4 \text{ degrees})$$

or

$$\theta_n < -\theta_{max},$$

then θ_n is restricted to its maximum value, i.e.,

$$\theta_n = \theta_{max}$$

or

$$\theta_n = -\theta_{max}$$

and

$$\gamma_n = \gamma_{n-1} + \theta_n$$

$$Y_n = Y_{n-1} + L \sin \gamma_n$$

$$Y_{mn} = 1/2\ (Y_n + Y_{n-1})$$

Roof Support Pullup

After the conveyer has been pushed forward, the shearer will move along the conveyer making its cut. This operation, however, does not affect the conveyer yaw profile. The roof supports are then pulled up. This operation affects the conveyer profile by pulling the conveyer back as the roof supports are pulled forward. This operation is simulated by subtracting a pullup error from the Y-coordinate of the midpoint of each conveyer section, i.e.,

$$Y_{mn}^{k} = Y_{mn}^{k-1} - |\epsilon_{sn}|$$

where ϵ_{sn} is sampled from a normal distribution $(0, \sigma_s^2)$.

A yaw profile after this pul up error is computed again in the same manner as for the conveyer placement.

Measure YAW Profile

For the basic angle cart measurement system the conveyer angles θ_2 through θ_N are measured. Therefore, for all those angles errors are added, i.e.,

$$\hat{\theta}_i = \theta_i + \epsilon_i + b$$

The yaw profile is then computed as described in Section 4.2.1. The equations are

$$\hat{Y}_N = L \sum_{i=2}^{N} \left(\sum_{j=2}^{i} \hat{\theta}_j \right) + Y_o$$

$$\hat{\theta}_1 = - \frac{\hat{Y}_N - Y_N}{NL}$$

$$\hat{Y}_n = L \sum_{i=1}^{n} \left(\sum_{j=1}^{i} \hat{\theta}_j \right) + Y_o$$

For the weighting and bias estimation system, two additional angles are measured. They are θ_1 and θ_{N+1}. Errors in measuring these angles are the same as for the other angles except that they have an additional error. The additional error is in the reference direction. It is simulated by

$$\hat{\theta}_1 = \theta_1 + \varepsilon_1 + b + \varepsilon_{\theta 1}$$

$$\hat{\theta}_{N+1} = \theta_{N+1} + \varepsilon_{N+1} + b + \varepsilon_{\theta(N+1)}$$

where

$\varepsilon_{\theta 1}$ and $\varepsilon_{\theta(N+1)}$

are sampled from a normal distribution $(0, \sigma_\theta^2)$.

The remaining equations are:

$$\hat{Y}_N = L \sum_{i=1}^{N} \left(\sum_{j=1}^{i} \hat{\theta}_j \right) + Y_o$$

$$\hat{b}^+ = \frac{2}{N(N+1)} \frac{\hat{Y}_N - Y_N}{L}$$

$$\hat{\theta}_i^+ = \hat{\theta}_i - \hat{b}^+$$

$$\hat{Y}_n^+ = L \sum_{i=1}^{n} \left(\sum_{j=1}^{i} \hat{\theta}_j^+ \right) + Y_o$$

$$\hat{Y}_o = L \sum_{i=1}^{N} \left(\sum_{j=N-i+2}^{N+1} \hat{\theta}_j \right) + Y_N$$

$$\hat{b}^- = \frac{2}{N(N+1)} \frac{\hat{Y}_o - Y_o}{L}$$

$$\hat{\theta}_i^- = \hat{\theta}_i - \hat{b}^-$$

$$\hat{Y}_n^- = L \sum_{i=1}^{N-n} \sum_{j=N-i+2}^{N+1} \hat{\theta}_j^- + Y_N$$

$$a_n = \frac{(N-n)(N-n+1)(2N-2n+1)}{n(n+1)(2n+1) + (N-n)(N-n+1)(2N-2n+1)}$$

$$\hat{Y}_n = a_n \hat{Y}_n^+ + (1-a_n) \hat{Y}_n^-$$

Conveyer Placement Commands

The conveyer placement commands ΔY_{pn} are computed using the conveyer Y-coordinates $\hat{Y}_n$. It is desired to advance the conveyer as far as possible and at the same time straighten it. This is accomplished by determining the minimum Y-coordinate, advancing that section a distance $\hat{Y}_A$ and all the others an appropriate amount so that it is straight. The conveyer placement commands that will accomplish that task are derived from geometry shown in Figure 4.13

$$\Delta Y_{pn} = Y_A + \hat{Y}_{min} - 0.5\ (\hat{Y}_n + \hat{Y}_{n-1})$$

where $\hat{Y}_{min}$ is the minimum value of $\hat{Y}_n$.

4.4.1 Overall System Performance Using the Angle Cart

The overall system performance using the angle cart measuring device was determined by exercising the yaw advancement simulation.

The conveyer initial position was a straight line. Then the conveyer was pushed forward (with placement errors, σ_p) and the roof supports were pulled up (with pullup errors, σ_s). Measurements were then made (with measurement errors, σ_m) and the yaw profile computed. Next, conveyer placement commands were computed in preparation for the next advancement. Twenty consecutive advancements were made.

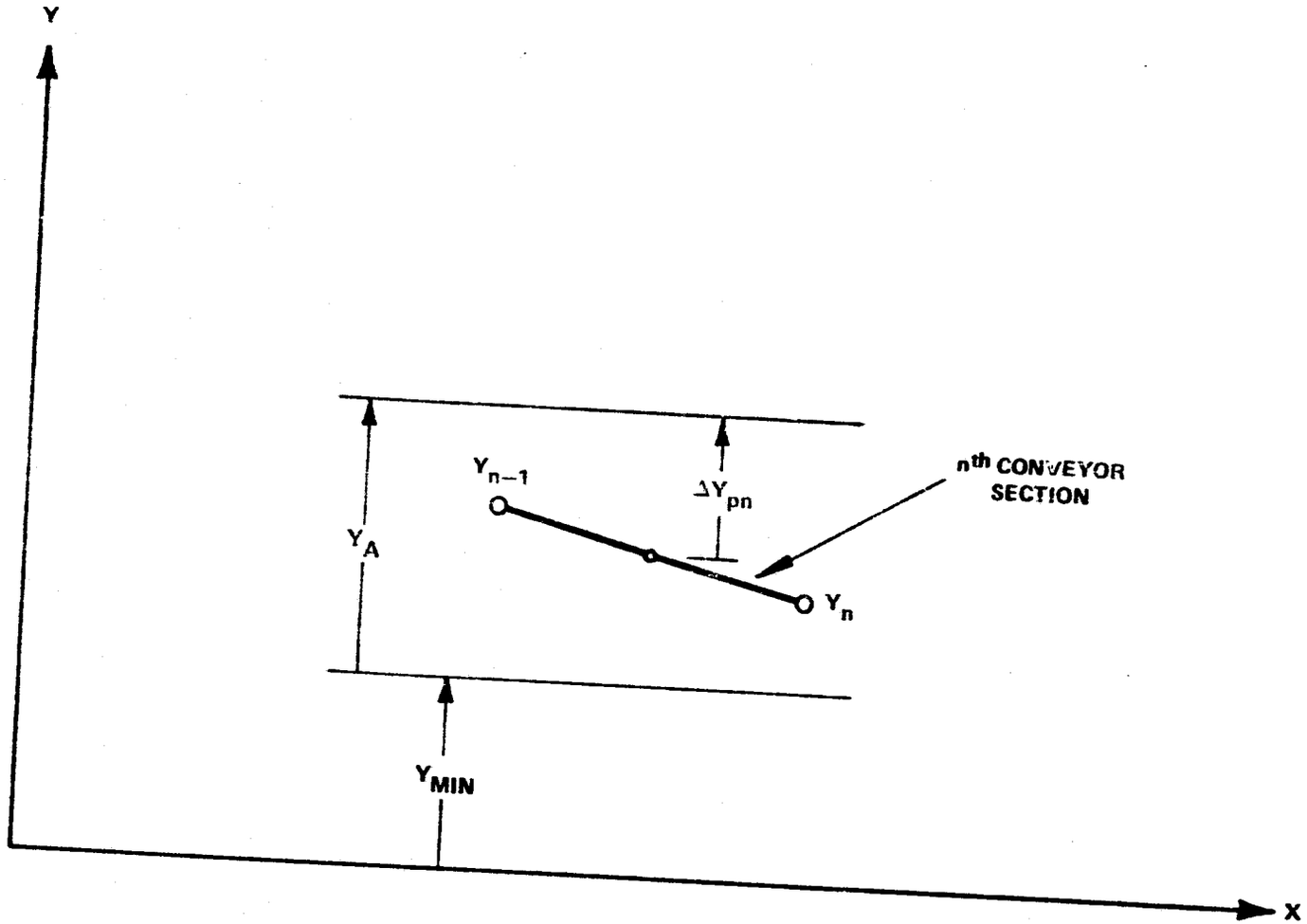

Figure 4-13. Geometry for Defining Placement Commands

In order to determine tolerable measurement errors, a placement error σ_p and a pullup error σ_s were selected and then twenty advances were made with $\sigma_m = 0$. The measurement error was then increased in 0.005 degree steps each time advancing the conveyer twenty times. As the measurement error was increased, the conveyer became more and more crooked so that for some value of σ_m the conveyer cannot advance twenty times without commanding a negative placement of the conveyer. Such a command would require the conveyer to be pulled back which is impossible. As a result, the next lower value of σ_m was deemed the maximum tolerable measurement error. Three σ_m maximums were determined for each placement and pullup error and then averaged. The results are plotted in Figures 4-14 through 4-17.

Figure 4-14 shows the maximum tolerable measurement error versus the pullup error for the basic angle cart measurement system. Two values of the placement error were considered, $\sigma_p = 0$ and 0.05 feet. The region below the curve is considered stable; above the curve the region is considered unstable.

Figures 4-15 through 4-17 show the results for the basic angle cart measurement system where it is assumed that some of the conveyer angles at each end of the conveyer cannot be measured (J defines the number at each end that cannot be measured). It can be seen that for J = 1, system performance is degraded only slightly. For J = 2, however, system performance is degraded by a considerable amount. The reason for this large effect on performance is that the conveyer pullup errors cause the conveyer angles to be large. Since they are assumed zero in the yaw profile computations when they cannot be measured, the pullup errors cause a large effect.

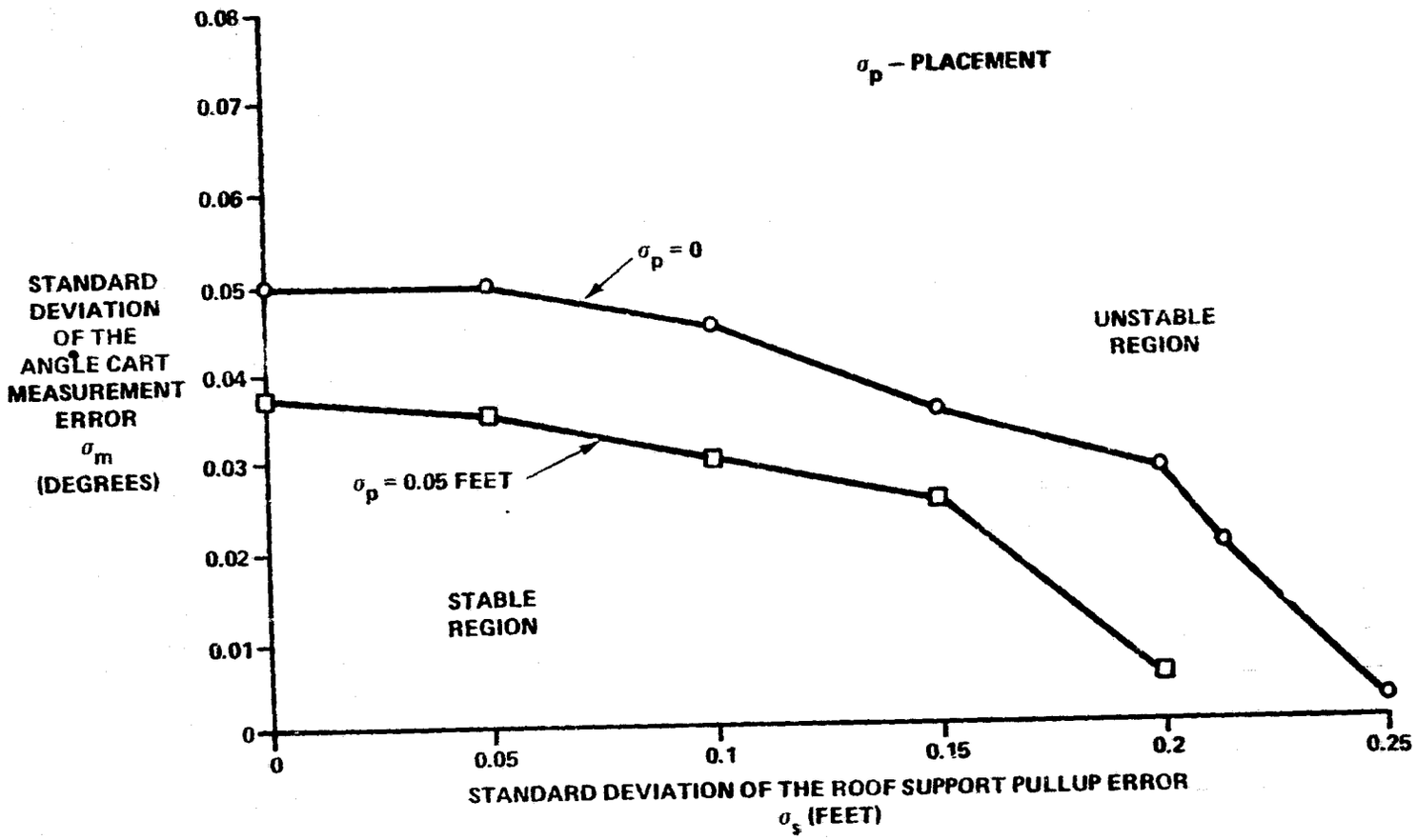

Figure 4-14. Basic Angle Cart System - Yaw Advancement Simulation Results

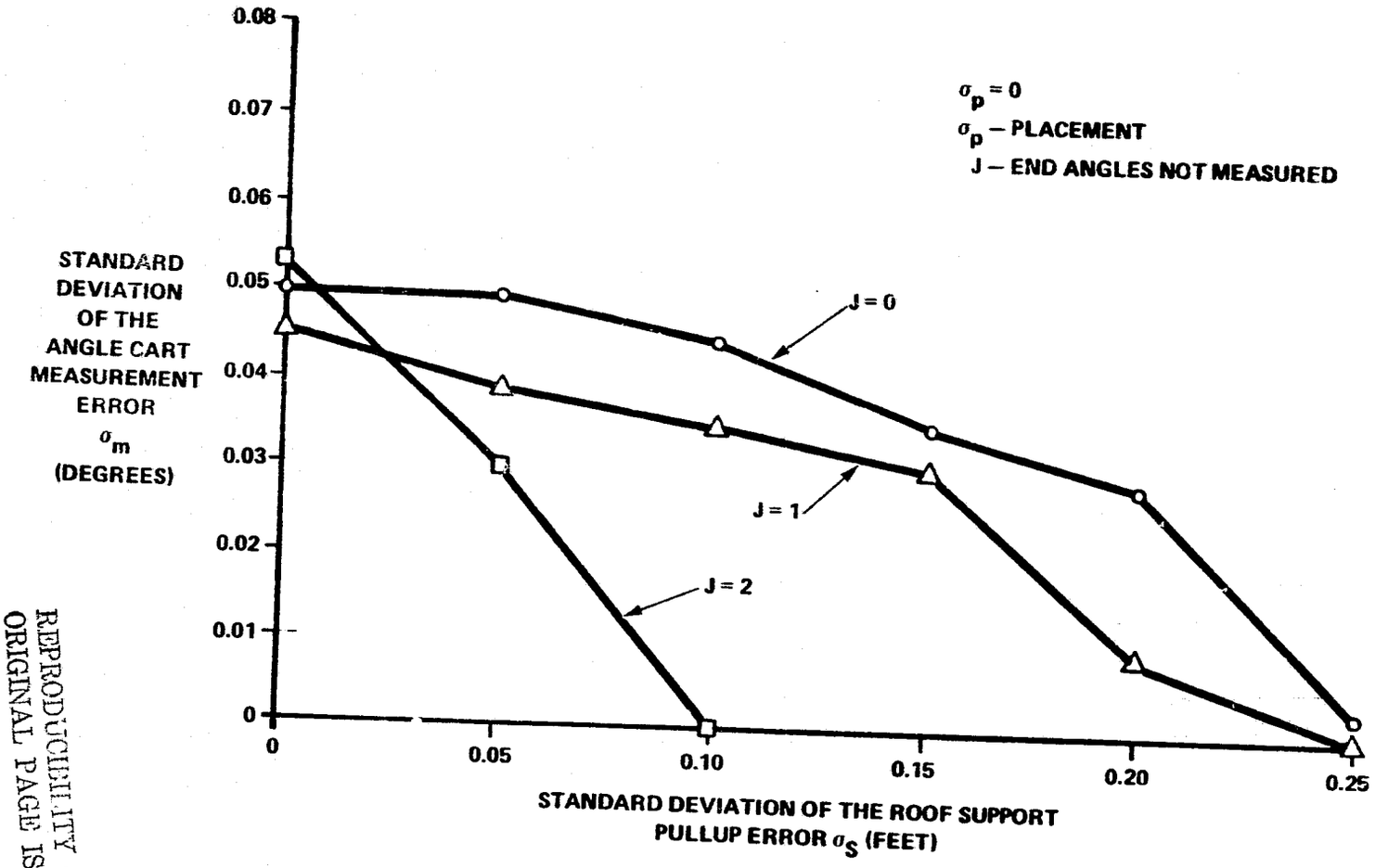

Figure 4-15. Basic Angle Cart System - Yaw Advancement Simulation Results

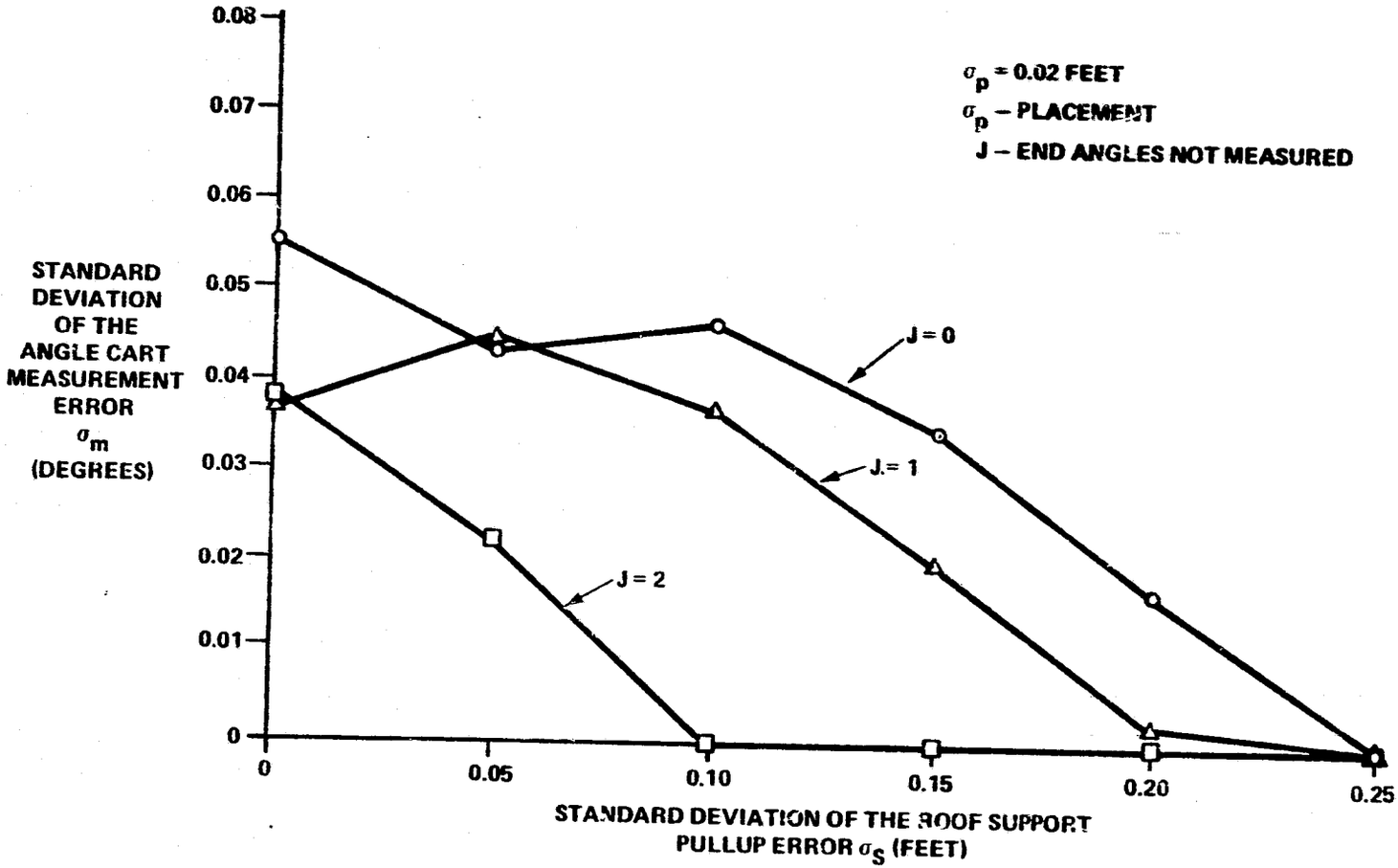

Figure 4-16. Basic Angle Cart System - Yaw Advancement Simulation Results

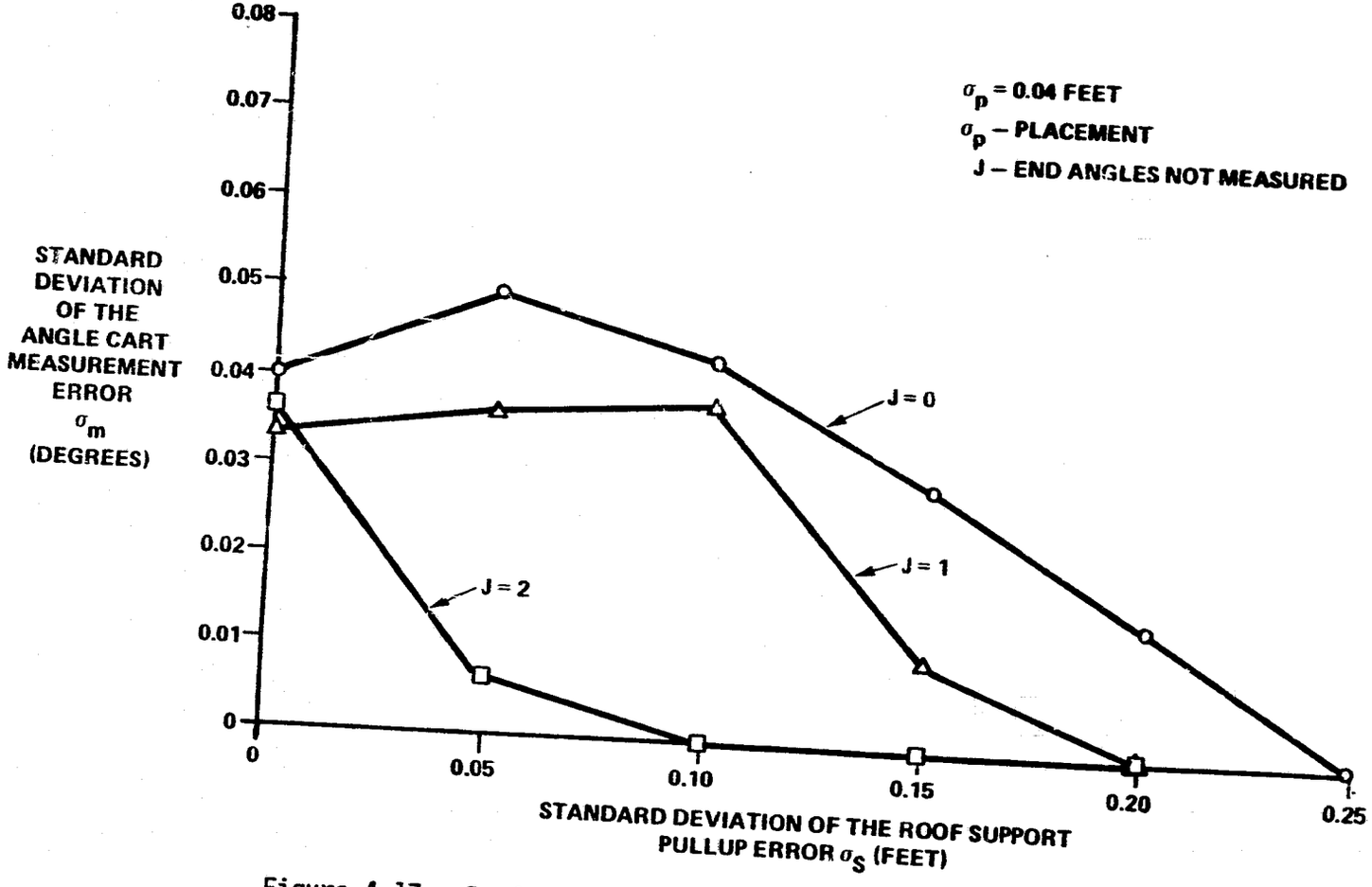

Figure 4-17. Basic Angle Cart System - Yaw Advancement Simulation Results

In Figures 4-18 and 4-19, the performance of the weighting and bias estimation system is shown. Figure 4-18 shows the performance for $\sigma_p = 0$ and Figure 4-19 shows the performance for $\sigma_p = 0.05$ feet. These figures show that the reference error σ_θ (the error in determining the reference direction of the end conveyer sections) has a large effect on the maximum tolerable measurement error σ_m. For example, the maximum allowable error in the standard deviation of the reference error is 0.2 degree. However, if the reference error can be determined more accurately than 0.2 degree, the weighting and bias estimation system gives a better performance than the basic angle cart measurement system.

4.4.2 Recommended Measurement Algorithm for the Angle Cart

The recommended measurement algorithm for the angle cart is the Basic Measurement System. This system uses the measured location of the conveyer end points and the angles between all the conveyer sections to compute the yaw profile--the Y-coordinates of the ends of the conveyer sections. From the yaw profile, conveyer placement commands are generated. The advantage of this system over the weighting and bias estimation system is that a reference direction is not needed. The basic system is therefore simpler and reference direction errors are of no concern.

The angle cart eight speed resolvers have a basic accuracy of 2 arc minutes or 1/30 degrees. Averaging 200 measurements gives the angle cart measurements an accuracy of 0.0033 degrees. This accuracy is an order of magnitude better than the requirement.

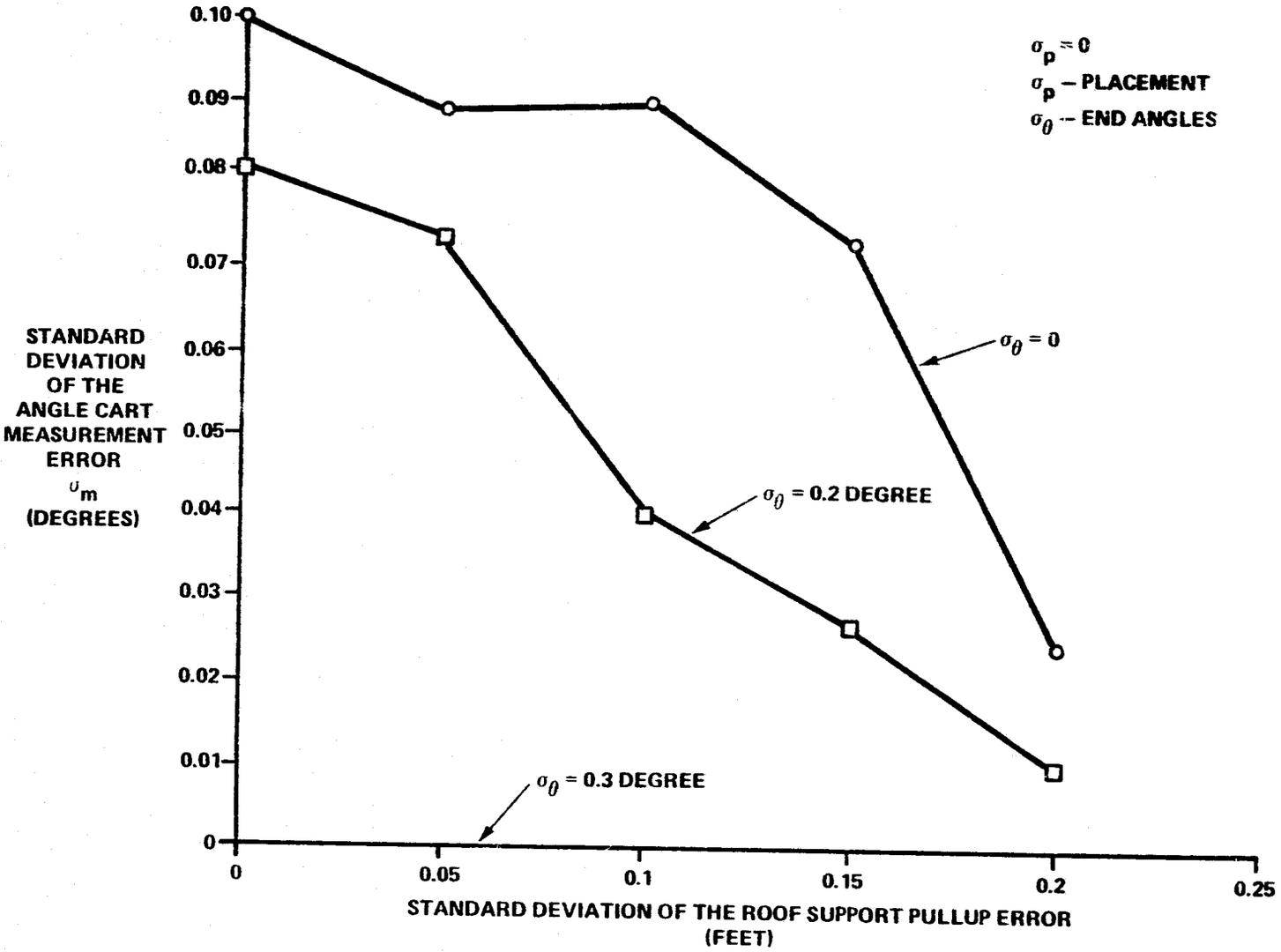

Figure 4-18. Weighting and Bias Estimation System - Yaw Advancement Simulation Results

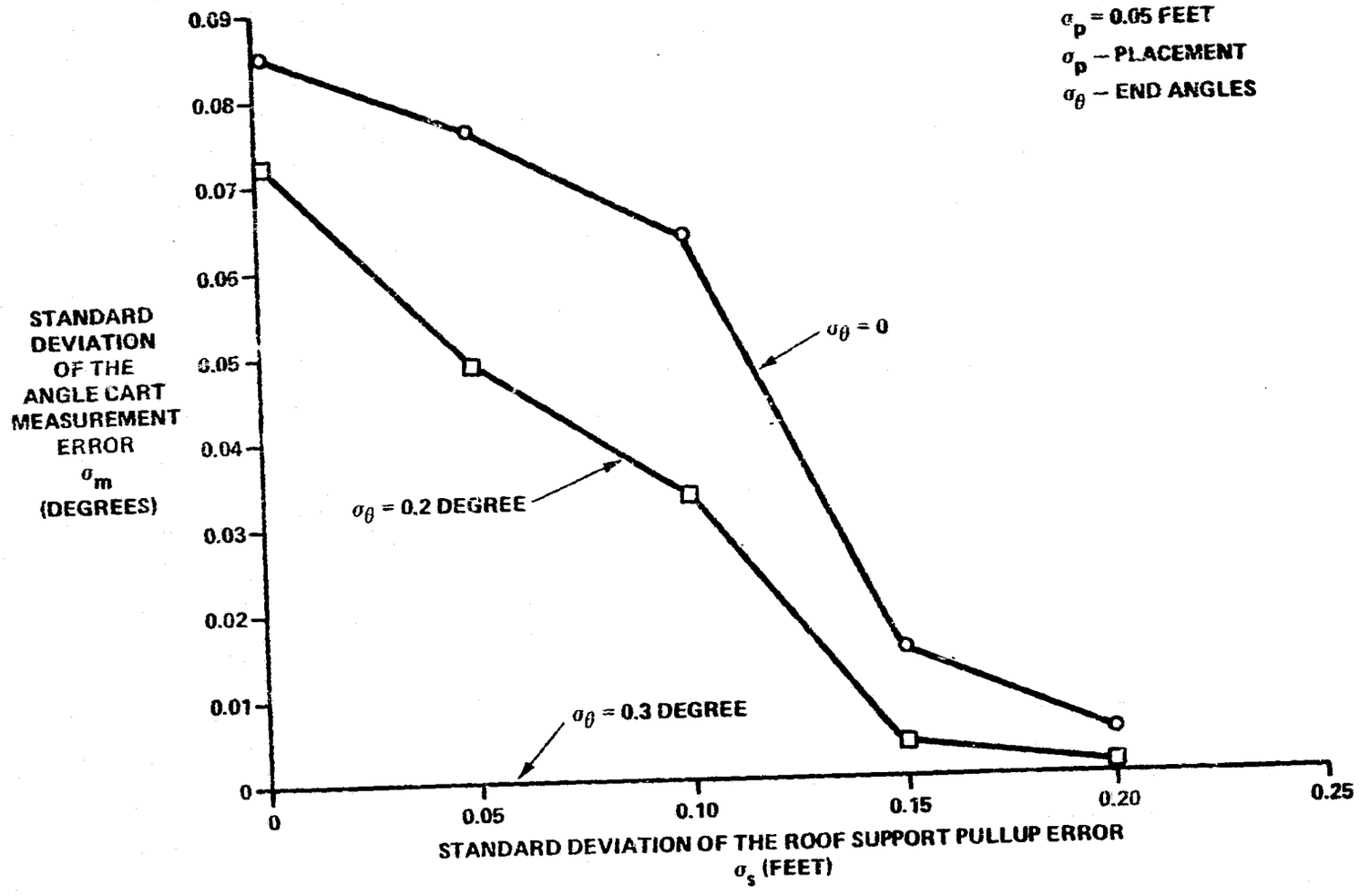

Figure 4-19. Weighting and Bias Estimation System - Yaw Advancement Simulation Results

Using the yaw advancement simulation, ten advances of the basic measurement system were simulated and the yaw profile plotted after each advance. An example of these plots is shown in Figure 4-20 where σ_p = 0.05 feet, σ_s = 0.1 feet and σ_m = 0.03 degree. It can be seen that after ten advances, approximately 14 feet of coal was cut. Without errors 20 feet of coal would have been cut. Therefore, the system efficiency is

$$\frac{14}{20} = 0.7$$

Figures 4-21 and 4-22 show the efficiency of the basic angle cart measurement system as a function of the system errors.

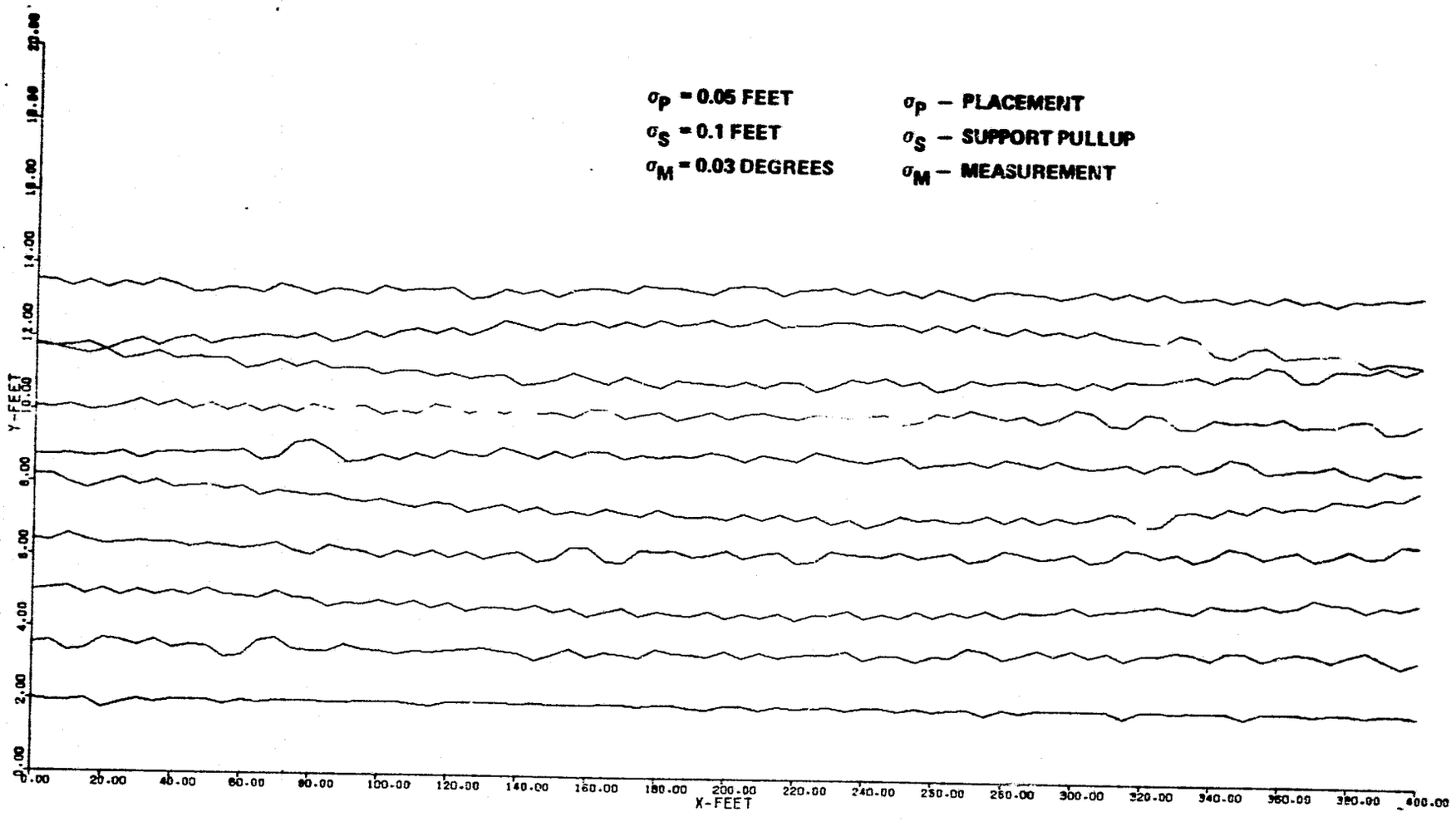

Figure 4-20. Yaw Profiles - Basic Angle Cart System

Figure 4-21. Efficiency of Basic Angle Cart System

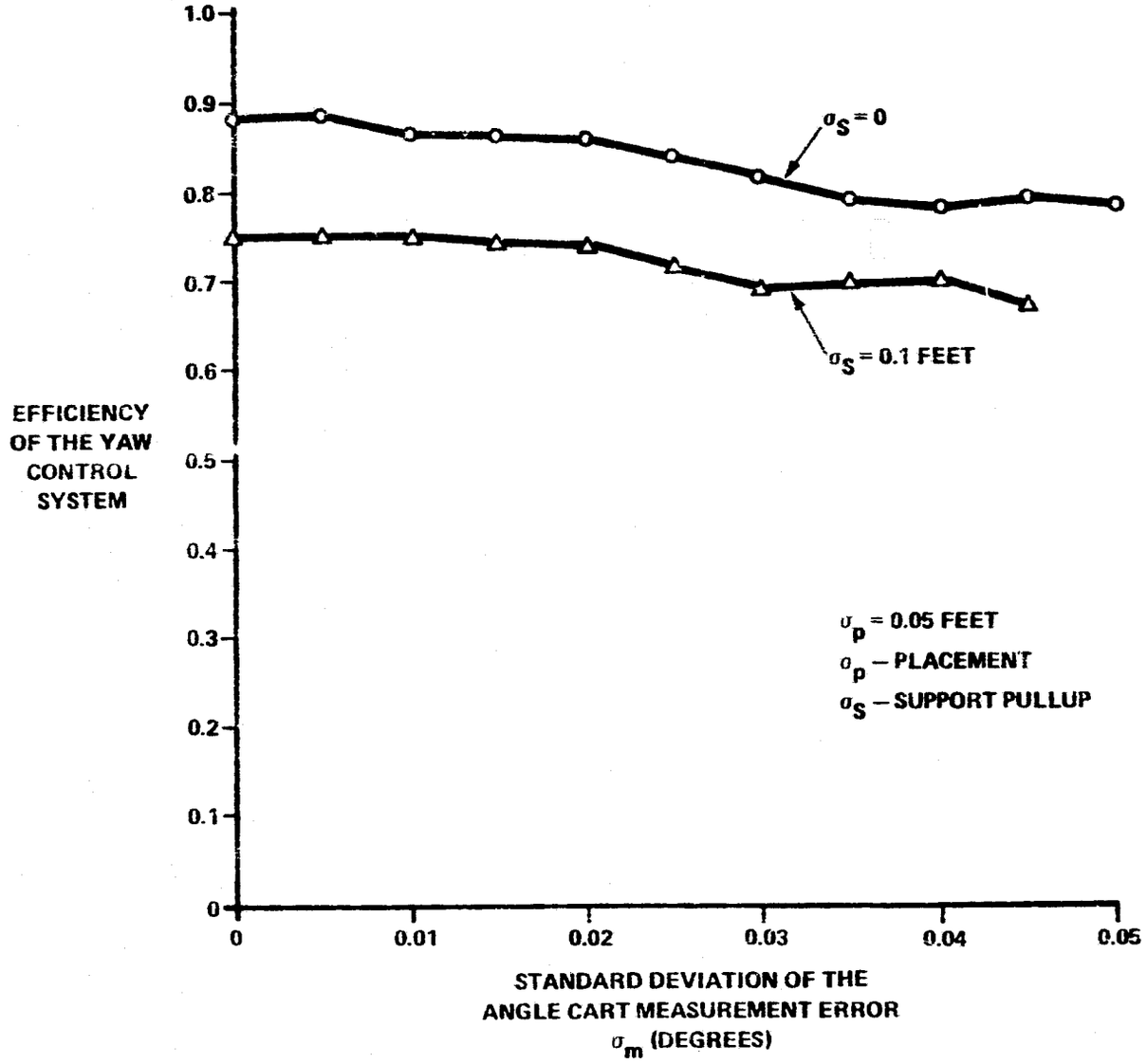

Figure 4-22. Efficiency of Basic Angle Cart System

4.5 DESCRIPTION OF THE DIRECTIONAL GYRO MEASUREMENT SYSTEM

A directional gyro mounted on the shearer or on a conveyor cart can be used to measure (with respect to a fixed directional reference) the angular orientation of each individual conveyor section. Knowing the location of the ends of the conveyor along with the conveyor angles γ_i allows the computation of the conveyor yaw profile.

Four different directional gyro measurement algorithms have been devised. The advantage of each depends partly on the relative magnitude of the gyro errors.

A description of the gyro error model and the four measurement algorithms is presented in the following sections.

4.5.1 Mathematical Model of Directional Gyro Error

The directional gyro is used to measure the orientation angle of the cart with respect to a fixed reference direction. The gyro measurement error $\varepsilon(t)$ at time t is assumed to be additive, i.e., the gyro measured angle at time t is equal to the true angle plus $\varepsilon(t)$. The dynamic mathematical model for $\varepsilon(t)$ is illustrated in the system block diagram of Figure 4-23.

The input u(t) is assumed to be a Gaussian white noise stochastic process with spectral intensity K, i.e., the u(t) are independent, zero mean Gaussian random variables such that

$$E[u(t_1)\ u(t_2)] = K\ \delta(t_1 - t_2)$$

for any t_1 and t_2, where δ denotes the Dirac delta function.

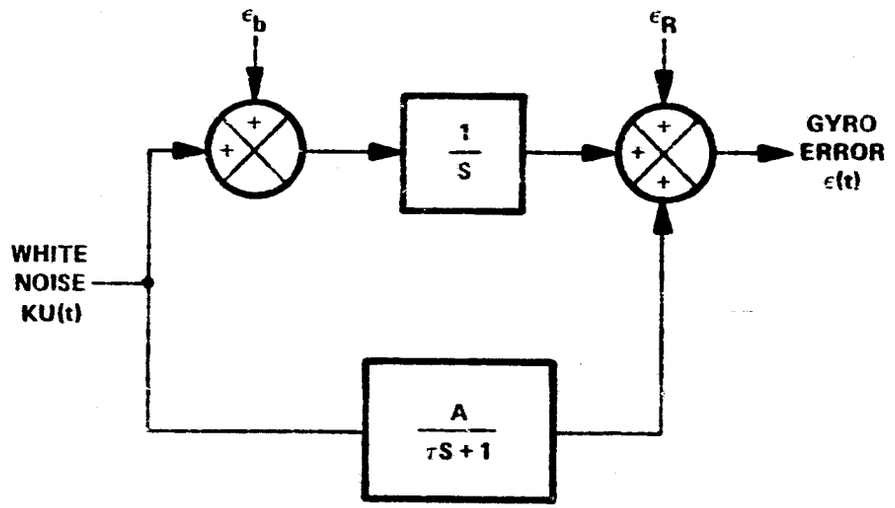

Figure 4-23. Directional Gyro Noise Model

It is seen from Figure 4-23 that $\varepsilon(t)$ is represented as the sum of four effects:

(1) An integrated white noise, i.e., "random walk" process

(2) A stationary process obtained by passing white noise through a linear first order lag filter with gain A and time constant τ.

(3) A drifting bias error $\varepsilon_b t$ where ε_b is the bias rate, assumed to be a Gaussian random variable with mean zero and variance σ_b^2

(4) A random constant bias error ε_R, representing a fixed error in the directional reference, and also assumed Gaussian with mean zero and variance σ_R^2.

The random variables $u(t)$, $t \geq 0$, ε_b and ε_R are taken to be statistically independent. From Figure 4-23, $\varepsilon(t)$ can be expressed as

$$\varepsilon(t) = \int_0^t \left(1 + \frac{A}{\tau} e^{-\frac{t-r}{\tau}}\right) u(r)dr + \varepsilon_b t + \varepsilon_R$$

For proper mathematical interpretation, the integral above should be understood to be a Wiener stochastic integral, with the term $u(r)\,dr$ replaced by $dw(r)$, where $w(r)$ denotes a Brownian motion stochastic process with variance parameter K. The covariance function of $\varepsilon(t)$ is given by

$$E[\varepsilon(t_1)\varepsilon(t_2)] = K\int_0^{t_1} \left(1 + \frac{A}{\tau} e^{-\frac{t_1-r}{\tau}}\right)\left(1 + \frac{A}{\tau} e^{-\frac{t_2-r}{\tau}} \quad dr\right)$$

$$+ \sigma_b^2 t_1 t_2 + \sigma_R^2$$

$$= K\left[t_1 + A\left(1 - e^{-\frac{t_1}{\tau}} - e^{-\frac{t_2}{\tau}}\right) + A\left(1 + \frac{A}{2\tau}\right) e^{-\frac{t_2 - t_1}{\tau}} - \frac{A^2}{2\tau}\, e^{-\frac{t_1 + t_2}{\tau}}\right]$$

$$+ \sigma_b^2\, t_1\, t_2 + \sigma_R^2$$

for $0 \leq t_1 \leq t_2$. If $t_1 > t_2$, then t_1 and t_2 must be interchanged in the above formula.

4.5.2 Derivation of the Directional Gyro Measurement Algorithm Without Averaging

The directional gyro measurement algorithm without averaging uses only a single directional gyro measurement of each conveyor section. Those measurements $\hat{\gamma}_n$ are combined with the Y coordinates of the conveyor end points to compute the yaw profile.

$$\hat{Y}_n^{+} = L \sum_{k=1}^{n} \hat{\gamma}_k + Y_o$$

$$\hat{Y}_n = \hat{Y}_n^{+} - \beta_n \left(\hat{Y}_N^{+} - Y_N\right)$$

where β_n is a weighting function derived to minimize the error in $\hat{Y}_n$. The derivation of β_n follows.

Let T denote the time for the cart to traverse a conveyor segment. The gyro measurement angle $\hat{\gamma}_k = \gamma_k + \varepsilon_k$, where γ_k is the true

angle, and the error $\epsilon_k = \epsilon((k-1)T)$ for $k = 1, \ldots, N$, since the gyro measurement is made at the beginning of the segment to obtain the smallest error variance. Thus,

$$Y_n^+ = L \sum_{k=1}^{n} (\gamma_k + \epsilon_k) + Y_o = Y_n + X_1$$

$$Y_N^+ = Y_N + X_2$$

where Y_n and Y_N are the true Y coordinates at points n and N, respectively, and

$$X_1 = L \sum_{k=1}^{n} \epsilon_k$$

$$X_2 = L \sum_{k=1}^{N} \epsilon_k$$

Hence,

$$\hat{Y}_n = Y_n + X_1 - \beta_n X_2$$

The value of β_n is chosen to minimize the variance of $\hat{Y}_n$, and is obtained by setting the derivative of this variance with respect to β_n equal to zero and solving for β_n

$$\beta_n = \frac{E(X_1X_2)}{E(X_2^2)}$$

$$= \frac{KA\left(N + 1 + \frac{A}{2\tau}\right) n + \frac{KT}{6} n\,(n-1)(3N - n - 1) + \frac{\sigma_b^2 T^2 N(N-1)}{4} n(n-1) + nN\sigma_R^2}{KA\left(N + 1 + \frac{A}{2\tau}\right) N + \frac{KT}{6} N\,(N-1)(2N-1) + \frac{\sigma_b^2 T^2}{4} N^2\,(N-1)^2 + N^2\sigma_R^2}$$

The quantities $E(X_1X_2)$ and $E(X_2^2)$ were computed by summing the appropriate covariances given by the error covariance function in Section 4.5.1 and then neglecting small terms.

4.5.3 Derivation of the Directional Gyro Measurement Algorithm with Averaging

The directional gyro measurement algorithm with averaging uses approximately 200 directional gyro measurements of each conveyor section. An average of the 200 measurements is computed and then used as a single measurement to compute the yaw profile. The equations are:

$$\hat{\gamma}_{An} = \frac{1}{N} \sum_{i=1}^{200} \hat{\gamma}_{mi}$$

where $\hat{\gamma}_{mi}$ are the individual measurements and $\hat{\gamma}_{An}$ is the average measured angle of the n^{th} conveyor section. Then

$$\hat{Y}_n^+ = L \sum_{k=1}^{n} \hat{Y}_{Ak} + Y_o$$

$$\hat{Y}_n = \hat{Y}_n^+ - \beta_n (\hat{Y}_N^+ - Y_N)$$

where β_n is the weighting function derived to minimize the yaw profile error for this condition. Its derivation follows:

Proceeding as in Section 4.5.2, the error ϵ_k is now given by

$$\epsilon_k = \frac{1}{T} \int_{(k-1)T}^{kT} \epsilon(t)dt \qquad (k = 1, \ldots, N)$$

where the discrete average has been replaced by an integral for computational simplicity. Hence,

$$X_1 = \frac{L}{T} \int_o^{nT} \epsilon(t)dt$$

$$X_2 = \frac{L}{T} \int_o^{NT} \epsilon(t)dt$$

$$\beta_n = \frac{\int_o^{NT} \int_o^{nT} E[\epsilon(t_1)\, \epsilon(t_2)]\, dt_1\, dt_2}{\int_o^{NT} \int_o^{NT} E[\epsilon(t_1)\, \epsilon(t_2)]\, dt_1\, dt_2}$$

Again, using the error covariance function in Section 4.5.1, performing the integrations above and neglecting small terms, it can be shown that

$$\beta_n = \frac{P}{Q}$$

where

$$P = K\left[-\frac{T}{6}\, n^3 + \frac{T}{2} N n^2 + AN n + \frac{A(A+2\tau)}{T} n - \frac{A(\frac{A}{2}+\tau)\tau}{T^2} - \frac{A\tau}{T}\left(N + \frac{A}{2T} + n\right)\right] + \frac{T^2 \sigma_b^2 N^2}{4}\, n^2 + N n \sigma_R^2$$

$$Q = K\left[\frac{N^3 T}{3} + AN^2 + A\left(\frac{A+2\tau}{T}\right) N - \frac{A\tau}{T^2}(A+2\tau) - \frac{A\tau}{T}\left(2N + \frac{A}{2T}\right)\right]$$

$$\frac{T^2 \sigma_b^2}{4}\, N^4 + N^2 \sigma_R^2$$

4.5.4 Derivation of the Directional Gyro Algorithm with Drifting Bias Compensation

The directional gyro algorithm with drifting bias compensation is derived by assuming that the main gyro error is the drifting bias. The directional gyro at the beginning of a sequence of measurements is nulled with respect to a fixed directional reference. As the gyro proceeds at a constant velocity along the conveyor taking measurements, it drifts at a constant rate. Hence, the error in $\gamma_1 = \Delta\gamma$; the error in $\gamma_2 = 2\Delta\gamma$; and the error in $\gamma_n = n\Delta\gamma$. As a result, $\Delta\gamma$ can be computed using the measured and computed end points, i.e.,

$$\Delta\gamma = \frac{2}{N(N+1)} \frac{\hat{Y}_N^+ - Y_N}{L}$$

where

$$\hat{Y}_N^+ = L \sum_{k=1}^{N} \hat{\gamma}_k + Y_o$$

The directional gyro measurements are then corrected by

$$\hat{\gamma}_n = \hat{\gamma}_n - n\Delta\gamma$$

and the yaw profile is computed by

$$\hat{Y}_n = L \sum_{k=1}^{n} \hat{\gamma}_k + Y_o$$

4.5.5 Derivation of the Directional Gyro Algorithm With Constant Bias Compensation

The derivation of the constant bias algorithm is similar to the drifting bias algorithm except it is assumed that the constant bias (error in the directional reference ϵ_R) is the most significant. In this case, each gyro mesurement is in error by $\Delta\gamma$. Therefore, the error in $\gamma_n = \Delta\gamma$ and it can be computed by

$$\Delta\gamma = \frac{1}{N} \frac{\hat{\gamma}_N^+ - \gamma_N}{L}$$

where

$$\hat{\gamma}_N = L \sum_{k=1}^{N} \hat{\gamma}_k + \gamma_o$$

The gyro measurements are corrected by

$$\hat{\gamma}_n = \hat{\gamma}_n - \Delta\gamma$$

and the yaw profile is computed by

$$\hat{\gamma}_n = L \sum_{k=1}^{n} \hat{\gamma}_k + \gamma_o$$

4.6 DESCRIPTION OF THE MONTE CARLO TECHNIQUE TO DETERMINE THE MEASUREMENT ACCURACY OF THE DIRECTIONAL GYRO

The Monte Carlo simulation used to evaluate the directional gyro measurement algorithms is the same as that used for the angle cart system. Only the measurement systems are changed. The simulation of the various measurement systems is described in the following sections.

4.6.1 Directional Gyro Without Averaging

The directional gyro measurement algorithm without averaging (making only a single measurement of each conveyor section) is simulated on the digital computer as follows.

The noise model defined in Section 4.5.1 is simulated on the digital computer assuming only a single measurement is taken on each conveyor segment. The equations required are:

$$C_1 = \sqrt{K\Delta}$$

$$C_2 = A \sqrt{\frac{K}{\Delta}} \left(1 - e^{-\frac{\Delta}{\tau}}\right)$$

$$C_3 = A \sqrt{\frac{K}{2\tau} \left(1 - e^{-\frac{2\Delta}{\tau}}\right) \left(1 - \frac{2\tau}{\Delta} \frac{1 - e^{-\Delta/\tau}}{1 + e^{-\Delta/\tau}}\right)}$$

$x_o = y_o = z_o = 0$ (initial conditions)

ϵ_b = normal $(0, \sigma_b^2)$

u_n = normal $(0, 1)$
v_n = normal $(0, 1)$ } independent

$a_n = C_1 u_n$

$b_n = C_2 u_n + C_3 v_n$

$$x_n = x_{n-1} + a_n$$

$$y_n = e^{-\Delta/\tau} y_{n-1} + b_n$$

$$\epsilon_R = \text{normal } (0, \sigma_R^2)$$

$$\epsilon_n = x_n + y_n + \epsilon_b^n \Delta + \epsilon_R$$

where

V = velocity at which the directional gyro traverses the conveyor in feet/second

T = time for directional gyro to traverse one conveyor segment.

Δ = sampling inverval in seconds

K = noise spectral intensity in $(rad/s)^2/(rad/s)$

A = filter gain in second

τ = filter time constant

$$\Delta = T = \frac{L}{V}$$

The directional gyro noise error at the n-1 conveyor section (ϵ_{n-1}) is added to the true conveyor angle at the n^{th} section to give the measured angle:

$$\gamma_n = \gamma_n + \epsilon_{n-1}$$

The yaw profile measurement algorithm is

$$\hat{Y}_n^+ = L \sum_{k=1}^{n} \hat{Y}_k + Y_o$$

$$\beta_n = \frac{KA(N + 1 + \frac{A}{2\tau})\, n + \frac{KT}{6}\, n\,(n-1)(3N-n-1) + \frac{\sigma_b^2 T^2\, N(N-1)}{4}\, n(n-1) + nN\sigma_R^2}{KA(N + 1 + \frac{A}{2\tau})N + \frac{KT}{6}\, N(N-1)(2N-1) + \frac{\sigma_b^2 T^2}{4}\, N^2(N-1)^2 + N^2\, \sigma_R^2}$$

$$\hat{Y}_n = \hat{Y}_n^+ - \beta_n\, (\hat{Y}_N^+ - Y_N)$$

The Monte Carlo simulation results for the directional gyro-single measurement algorithm are shown in Figures 4-24 through 4-28. In Figure 4-24 the mode of the RMS (M_R) is plotted versus the gyro noise spectral intensity K for various values of velocity V. It can be seen that traversing the face at 30 feet/minute (V = 0.5 ft/sec) requires a noise spectral intensity of 1.0×10^{-7} rad/sec to produce an M_R = 0.2 feet. This value of K corresponds to a random walk error of approximately 0.6 degrees/hour. Gyros with such a random walk error are good quality and relatively expensive.

The effect of the filter gain and filter time constant are shown in Figures 4-25 and 4-26. It can be seen that they have little effect for values much larger than their nominal values.

Figure 4-27 shows that the effect of a drifting bias σ_b has been removed by the optimum weighting measurement algorithm.

The effect of the reference error σ_R is shown in Figure 4-28. The results show that the amount of reference error that can be tolerated depends on the gyro noise spectral intensity. The yaw advancement simulation was used to study the tolerable limits of these parameters as reported in Section 4.7.1.

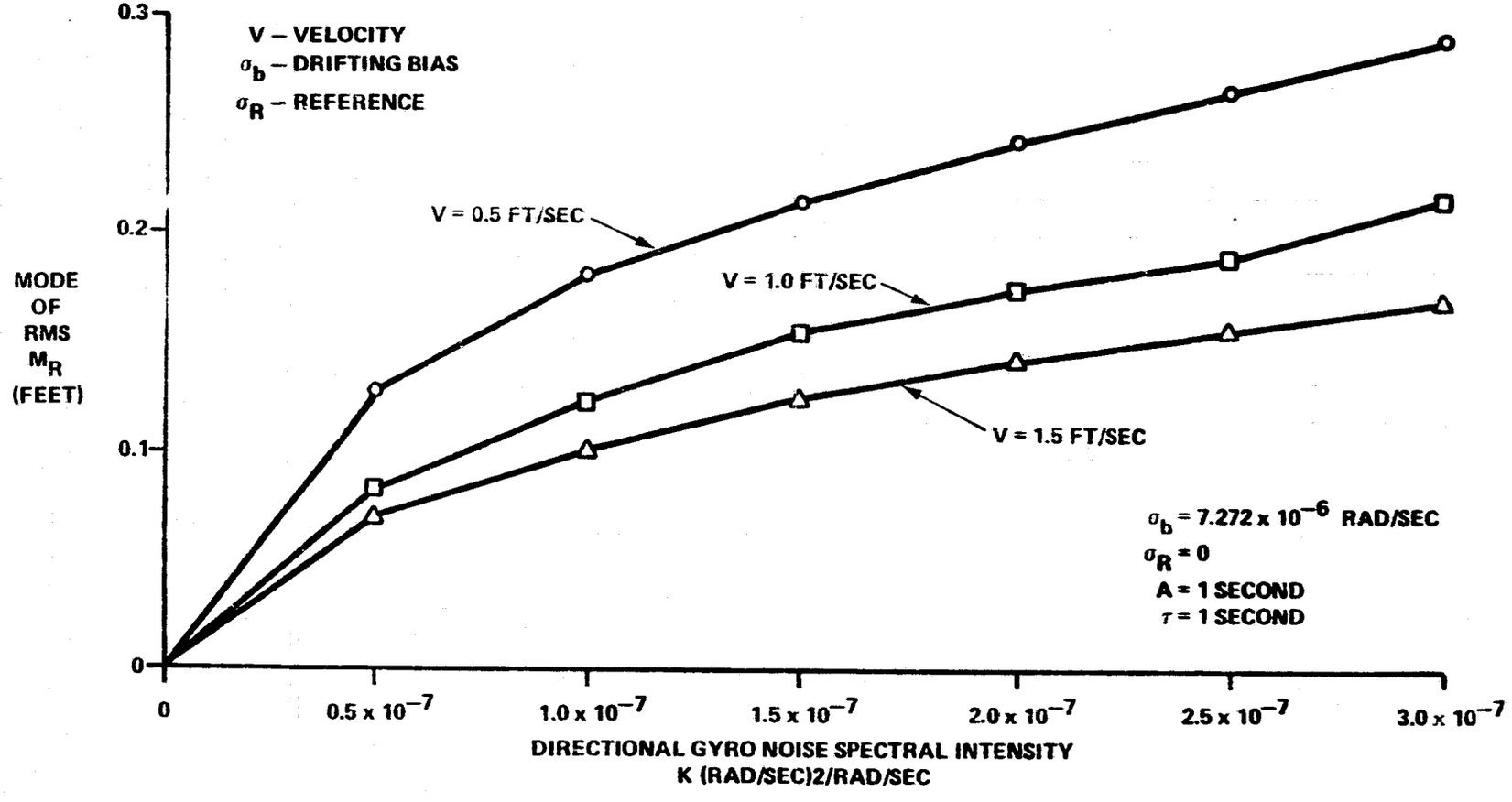

Figure 4-24. Directional Gyro - Single Measurement - Monte Carlo Results

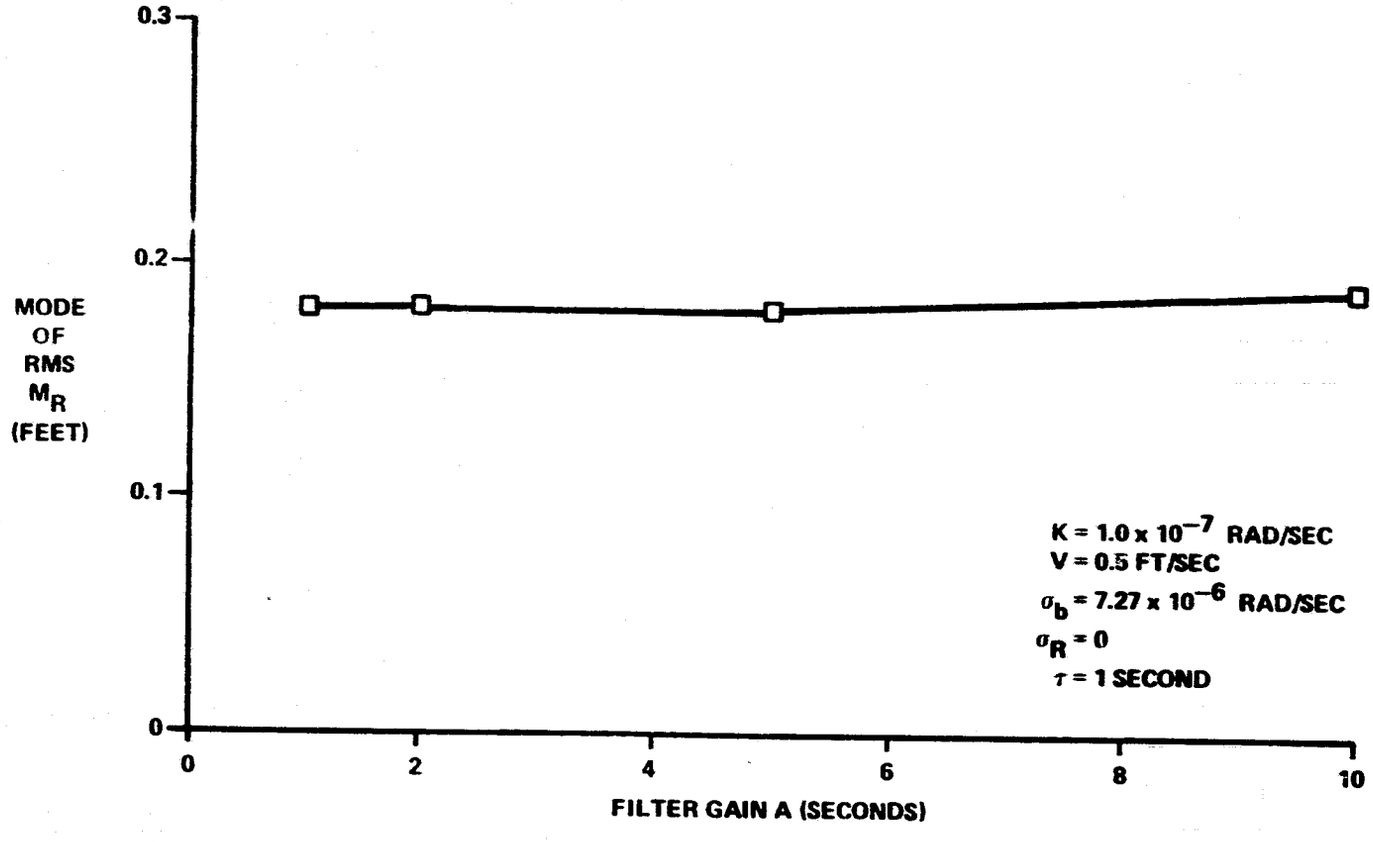

Figure 4-25. Directional Gyro - Single Measurement - Monte Carlo Results

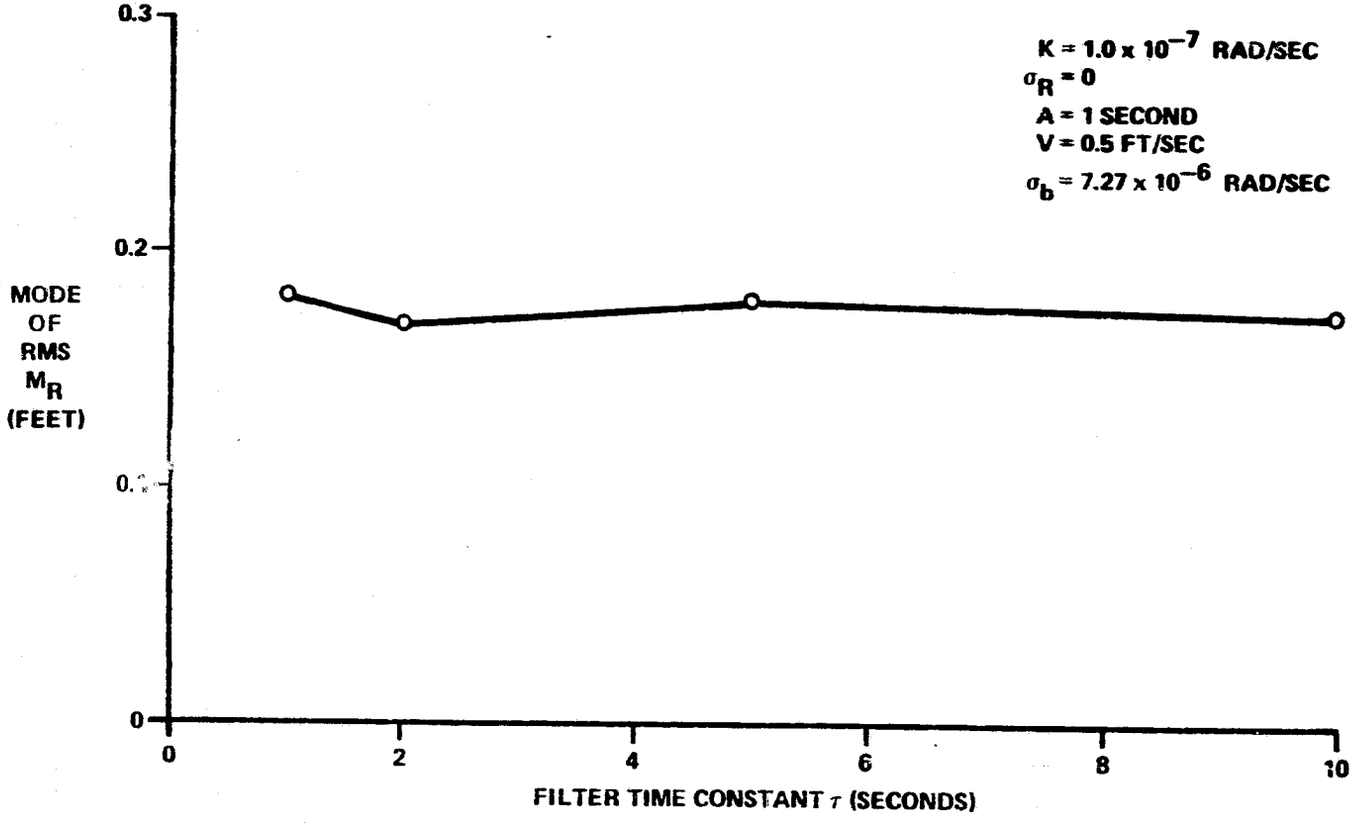

Figure 4-26. Directional Gyro - Single Measurement - Monte Carlo Results

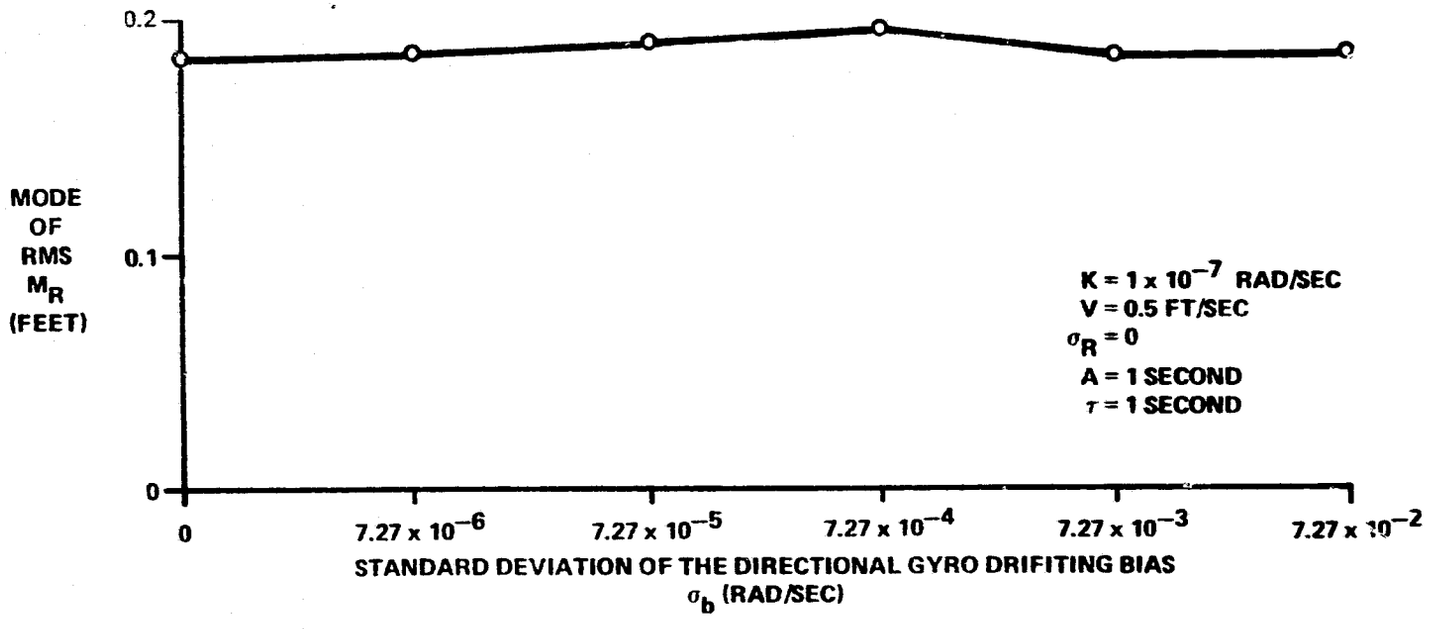

Figure 4-27. Directional Gyro - Single Measurement - Monte Carlo Results

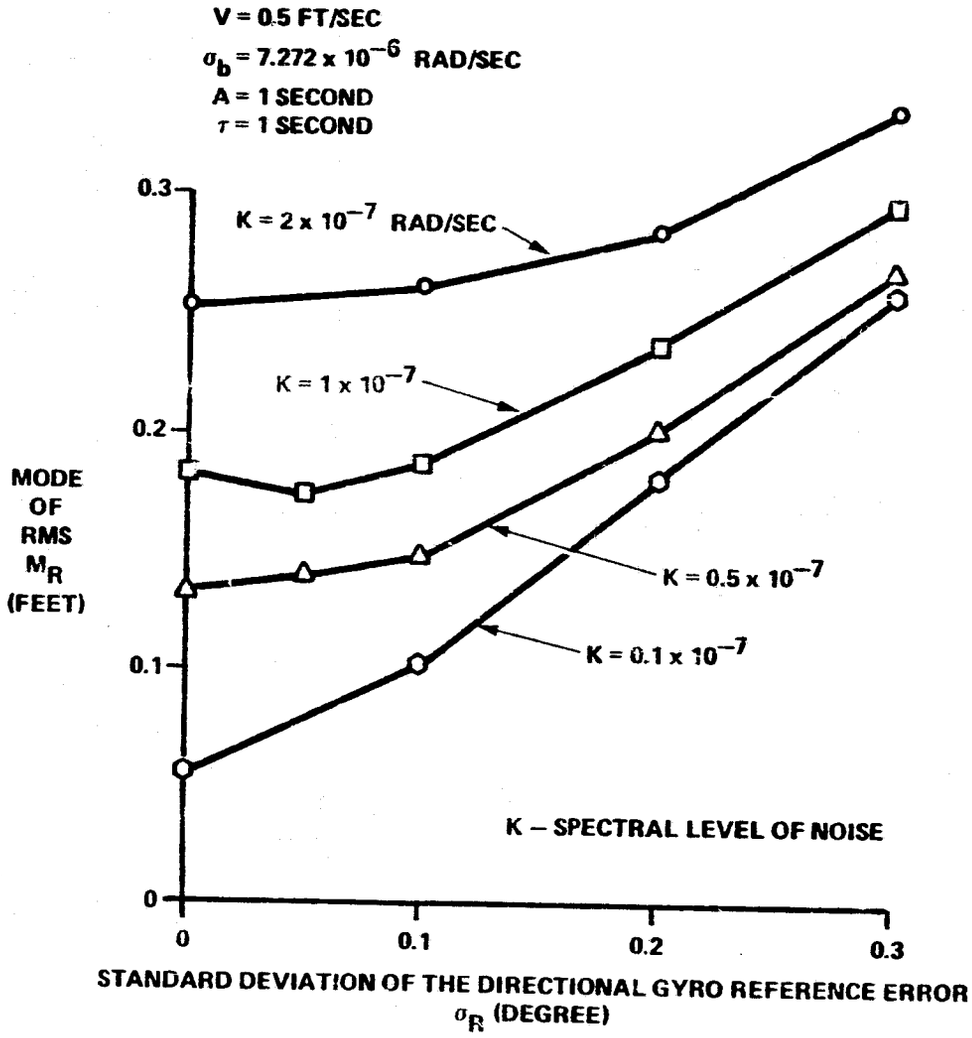

Figure 4-28. Directional Gyro - Single Measurement - Monte Carlo Results

4.6.2 Directional Gyro With Averaging

The directional gyro measurement algorithm with averaging is simulated on the digital computer as follows.

The directional gyro noise (assuming that many measurements of each section are taken and averaged) is simulated by the following equations:

$$v_1 = KT$$

$$v_2 = \frac{KA^2}{2\tau}\left(1 - e^{-\frac{2T}{\tau}}\right)$$

$$v_3 = K\left[\frac{T^3}{3} + AT^2 + A^2 T + 2AT\,\tau e^{-\frac{T}{\tau}} - 2A\tau(A + \tau)\left(1 - e^{-\frac{T}{\tau}}\right) + \frac{A^2\tau}{2}\left(1 - e^{-\frac{2T}{\tau}}\right)\right]$$

$$c_{12} = KA\left(1 - e^{-\frac{T}{\tau}}\right)$$

$$c_{13} = K\left[\frac{T^2}{2} + AT - A\tau\left(1 - e^{-\frac{T}{\tau}}\right)\right]$$

$$c_{23} = \frac{KA}{\tau}\left[(\tau^2 + A\tau)\left(1 - e^{-\frac{T}{\tau}}\right) - T\tau e^{-\frac{T}{\tau}} + \frac{A\tau}{2}\left(1 - e^{-\frac{2T}{\tau}}\right)\right]$$

$$G = v_1 v_2 - c_{12}^2$$

$$F_1 = \sqrt{v_1}$$

$$F_2 = \frac{c_{12}}{\sqrt{v_1}}$$

$$F_3 = \sqrt{\frac{G}{v_1}}$$

$$F_4 = \frac{\sqrt{v_1}\,(c_{13}\,v_2 - c_{12}\,c_{23}) + \frac{c_{12}}{\sqrt{v_1}}\,(c_{23}\,v_1 - c_{12}\,c_{13})}{G}$$

$$F_5 = \frac{c_{23}\,v_1 - c_{12}\,c_{13}}{\sqrt{v_1\,G}}$$

$$F_6 = \sqrt{v_3 - \frac{c_{13}^2\,v_2 + c_{23}^2\,v_1 - 2\,c_{12}\,c_{13}\,c_{23}}{G}}$$

$x_o = y_o = z_o = \epsilon_o = 0$ (initial conditions)

ϵ_b = normal $(0, \sigma_b^2)$

ϵ_R = normal $(0, \sigma_R^2)$

u_n = normal $(0, 1)$
v_n = normal $(0, 1)$
w_n = normal $(0, 1)$
} independent

$$a_n = F_1 u_n$$

$$b_n = F_2 u_n + F_3 v_n$$

$$c_n = F_4 u_n + F_5 v_n + F_6 w_n$$

$$x_n = x_{n-1} + a_n$$

$$y_n = e^{-\frac{T}{\tau}} y_{n-1} + b_n$$

$$z_n = T x_{n-1} + \tau (1 - e^{-\frac{T}{\tau}}) y_{n-1} + z_{n-1} + c_n$$

$$\varepsilon_n = \frac{z_n - z_{n-1}}{T} + (n - \tfrac{1}{2}) T\varepsilon_b + \varepsilon_R$$

The quantity ε_n is the averaged gyro noise on the n^{th} conveyor section and is added in the simulation to the true angle γ_n to obtain the averaged measured angle $\hat{\gamma}_n$.

$$\hat{\gamma}_n = \gamma_n + \varepsilon_n$$

The yaw profile measurement algorithm is given by the following equations.

$$\hat{Y}_n = L \sum_{k=1}^{n} \hat{\gamma}_k + Y_o$$

$$P = K\left[-\frac{T}{6}n^3 + \frac{T}{2}Nn^2 + AN\,n + \frac{A(A+2\tau)}{T}\,n - \frac{A(\frac{A}{2}+\tau)\tau}{T^2} - \frac{A\tau}{T}\left(N + \frac{A}{2T} + n\right)\right]$$

$$+ \frac{T^2\,\sigma_b{}^2\,N^2}{4}\,n^2 + Nn\,\sigma_R{}^2$$

$$Q = K\left[\frac{N^3T}{3} + AN^2 + A\left(\frac{A+2\tau}{T}\right)N - \frac{A\tau}{T^2}(A+2\tau) - \frac{A\tau}{T}\left(2N + \frac{A}{2T}\right)\right]$$

$$+ \frac{T^2\,\sigma_b{}^2}{4}\,N^4 + N^2\,\sigma_R{}^2$$

$$\beta_n = \frac{P}{Q}$$

$$\hat{Y}_n = \hat{Y}_n{}^+ - \beta_n\left(\hat{Y}_N{}^+ - Y_N\right)$$

The Monte Carlo simulation results for the directional gyro averaging system are shown in Figure 4-29. These results are almost identical to the single measurement system. Hence taking a large number of measurements and averaging does not improve the performance over taking a single measurement.

4.6.3 Directional Gyro with Drifting Bias Compensation

The directional gyro measurement algorithm with drifting bias compensation is simulated using the same equations for the gyro error as for the model with no averaging. Hence, the gyro measurements are given by

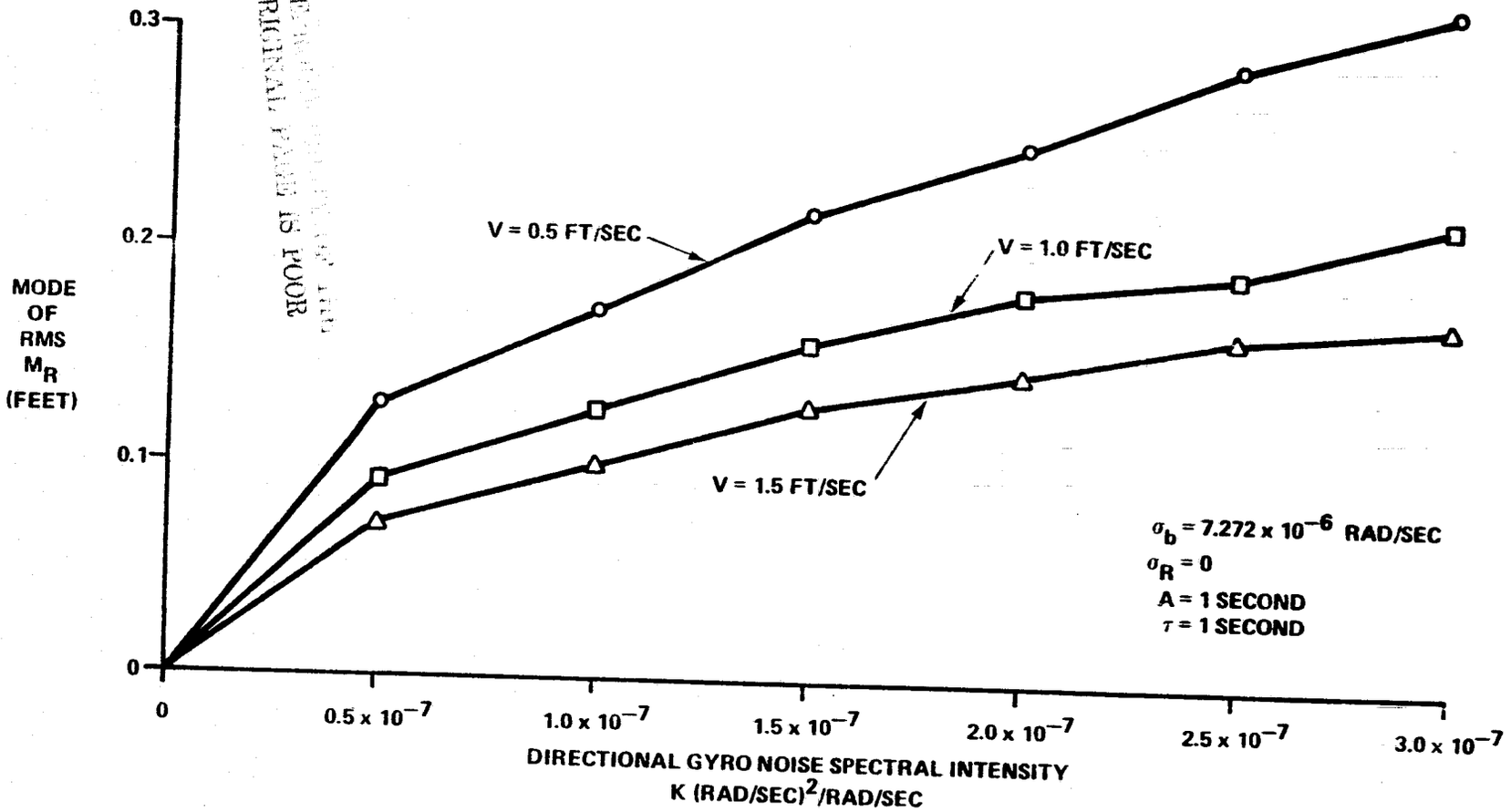

Figure 4-29. Directional Gyro - Averaging - Monte Carlo Results

$$\hat{\gamma}_n = \gamma_n + \epsilon_n$$

where ϵ_n is given by the equations in Section 4.6.1. The remaining equations are

$$\hat{Y}_N^+ = L \sum_{k=1}^{N} \hat{\gamma}_k + Y_o$$

$$\Delta\gamma = \frac{2}{N(N+1)} \frac{\hat{Y}_N^+ - Y_N}{L}$$

$$\hat{\gamma}_n = \hat{\gamma}_n - n\Delta\gamma$$

$$\hat{Y}_n = L \sum_{k=1}^{n} \hat{\gamma}_k + Y_o$$

The Monte Carlo simulation results of the directional gyro system with the drifting bias compensation are shown in Figure 4-30. This figure shows that for the same conditions the mode of RMS is slightly larger than the directional gyro system with single measurements and optimum weighting. Since the drifting bias compensation algorithm is much simpler to instrument, this system would be preferred if the size of the computer, on which the algorithm is implemented, is a factor.

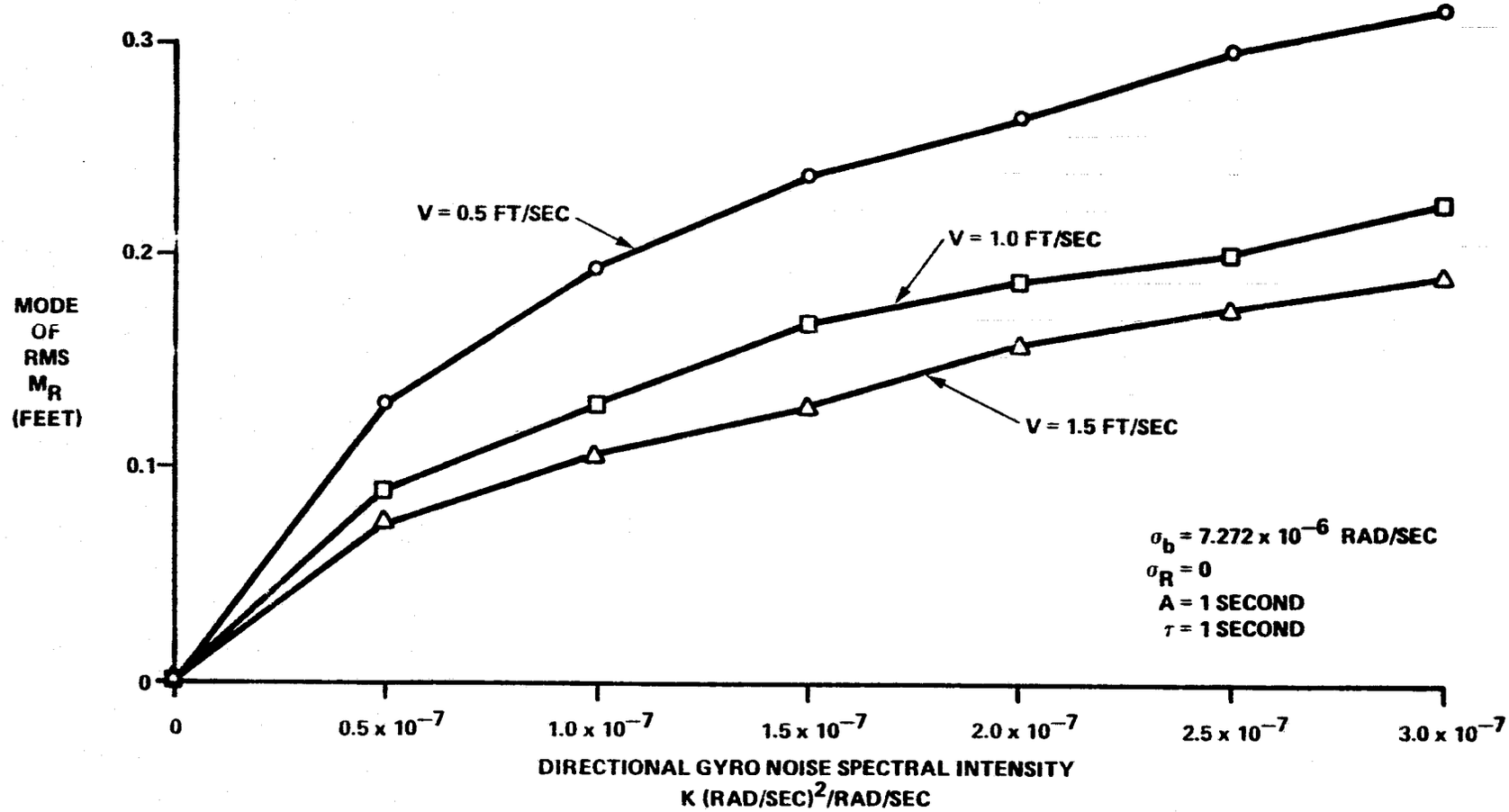

Figure 4-30. Directional Gyro - Drifting Bias Compensation - Monte Carlo Results

4.6.4 Directional Gyro With Constant Bias Compensation

The directional gyro with constant bias compensation is also simulated the same as the model without averaging except for the following equations

$$\hat{\gamma}_n = \gamma_n + \epsilon_n$$

where ϵ_n is the gyro error which is simulated by the equations given in Section 4.6.1. The remaining equations are given by

$$\hat{\gamma}_N^+ = L \sum_{k=1}^{N} \hat{\gamma}_k + \gamma_o$$

$$\Delta\gamma = \frac{1}{N} \frac{\hat{\gamma}_N^+ - \gamma_N}{L}$$

$$\hat{\gamma}_n = \hat{\gamma}_n - \Delta\gamma$$

$$\hat{\gamma}_n = L \sum_{k=1}^{n} \gamma_k + \hat{\gamma}_o$$

The Monte Carlo simulation results of the constant bias compensation system are shown in Figures 4-31 and 4-32. Figure 4-31 shows that for this system a directional reference error (constant bias) has little effect on the mode of the RMS. However, now a smaller level

Figure 4-31. Directional Gyro - Constant Bias Compensation - Monte Carlo Results

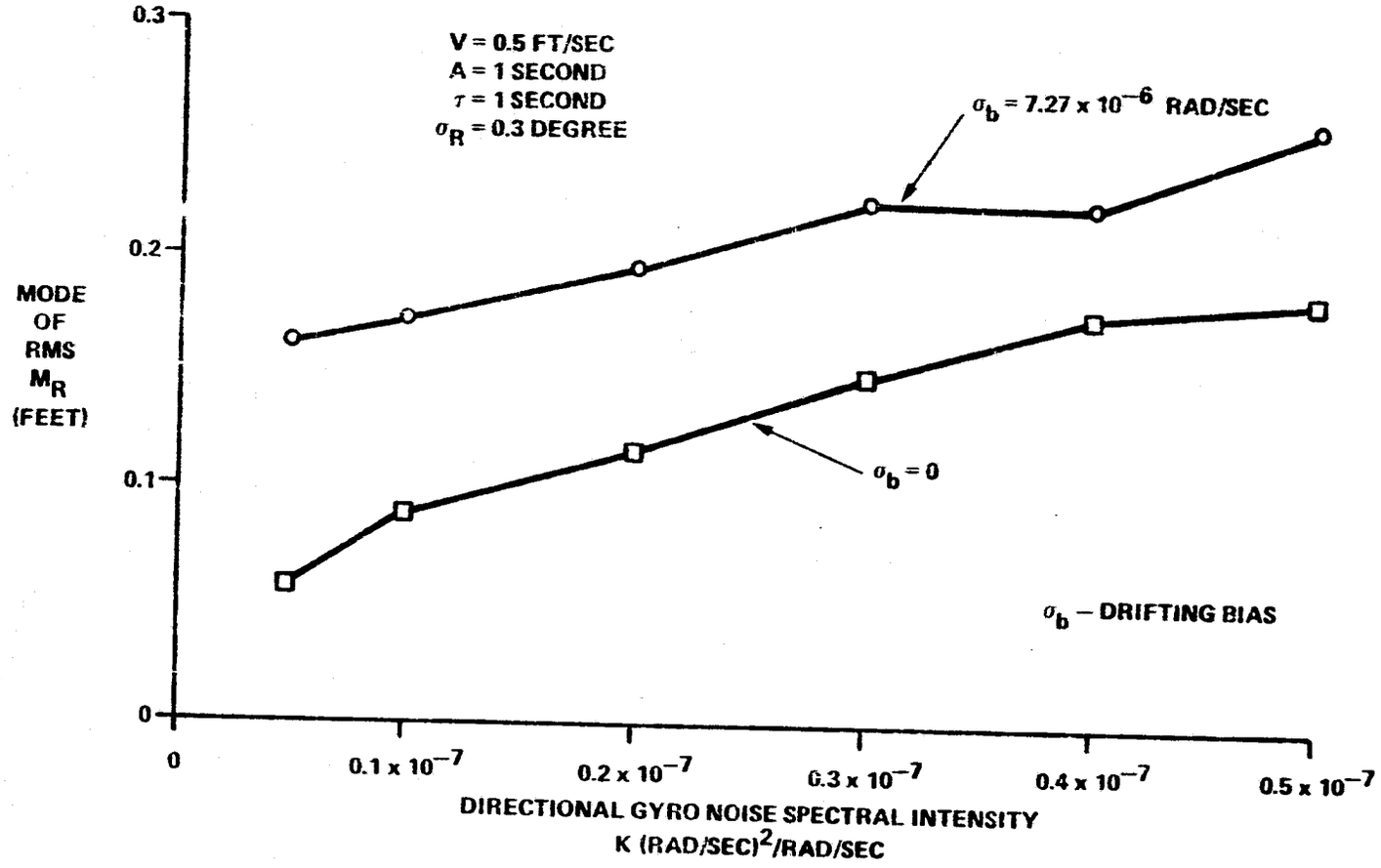

Figure 4-32. Directional Gyro - Constant Bias Compensation - Monte Carlo Results

of spectral noise intensity can be tolerated. In addition, as shown in Figure 4-32, a drifting bias affects the system performance. Selection of the directional gyro algorithm (between the single measurement system and the constant bias system) must consider the relative magnitude of the spectral noise intensity, the drifting bias, and the directional reference error.

4.7 DESCRIPTION OF THE YAW ADVANCEMENT SYSTEM SIMULATION USING THE DIRECTIONAL GYRO

This simulation is identical to that described in Section 4.4 except that the directional gyro is used for the angle measurements rather than the angle cart. The sequence of operations simulated are: (1) the conveyer is pushed forward, (2) the roof supports are pulled up, (3) the angle measurements are made, and (4) the yaw profile and conveyer placement commands are computed in preparation for pushing the conveyer forward again.

Two yaw profile measurement algorithms are simulated: the single measurement (nonaveraging) algorithm, and the constant bias compensation algorithm. The Monte Carlo simulation performance of the other two algorithms (averaging and drifting bias compensation) were very similar to the single measurement algorithm. Therefore, they are not evaluated with the yaw advancement simulation.

The yaw profile measurement algorithm for the single measurement system is simulated by

$$\hat{\gamma}_i = \gamma_i + \epsilon_i$$

where ϵ_i is the gyro error and is a function of K, the noise spectral intensity, the standard deviation of the drifting bias σ_b, and the standard deviation of the gyro reference error σ_R.

$$\hat{Y}_n^+ = L \sum_{k=1}^{n} \hat{\gamma}_k + Y_0$$

$$\beta_n = \frac{KA(N+1+\frac{A}{2\tau})n + \frac{KT}{6} n\,(n-1)(3N-n-1) + \frac{\sigma_b^2 T^2 N(N-1)}{4}\, n(n-1) + nN\sigma_R^2}{KA(N+1+\frac{A}{2\tau})N + \frac{KT}{6} N\,(N-1)(2N-1) + \frac{\sigma_b^2 T^2}{4} N^2\,(N-1)^2 + N^2\,\sigma_R^2}$$

$$\hat{Y}_n = \hat{Y}_n^+ - \beta_n\,(\hat{Y}_N^+ - Y_N)$$

The yaw profile measurement algorithm for the constant bias compensation system is simulated by

$$\hat{\gamma}_i = \gamma_i + \varepsilon_i$$

$$\hat{Y}_N^+ = L \sum_{k=1}^{N} \hat{\gamma}_k + Y_o$$

$$\Delta\gamma = \frac{1}{N}\,\frac{\hat{Y}_N^+ - Y_N}{L}$$

$$\hat{\gamma}_n = \hat{\gamma}_n - \Delta\gamma$$

$$\hat{Y}_n = L \sum_{k=1}^{n} \hat{\gamma}_k + Y_o$$

4.7.1 Overall System Performance Using the Directional Gyro

The overall system performance using the directional gyro was determined by exercising the yaw advancement simulation.

The conveyer initial position was a straight line. Then the conveyer was pushed forward (with placement errors σ_p) and the roof supports were pulled up (with pullup errors σ_s). Measurements were then made (with noise error K) and the yaw profile computed. Next, conveyer placement commands were computed in preparation for the next advancement. Twenty consecutive advancements were made.

In order to determine tolerable noise errors, a placement error σ_p and a pullup error σ_s were selected, and then 20 advances were made with K = 0. The noise was then increased in 0.2×10^{-7} rad/s steps, each time advancing the conveyer 20 times. As the noise was increased, the conveyer became more crooked so that for some value of K the conveyer could not advance 20 times without commanding a negative placement of the conveyer. Such a command would require the conveyer to be pulled back which is impossible. As a result, the next lower value of K was deemed the maximum tolerable noise error. Three K maximums were determined for each placement and pullup error, and then averaged. The results are plotted in Figures 4-33 and 4-34.

Figure 4-33 shows the maximum tolerable noise error versus the pullup error for the single measurement (no averaging) system. It can be seen that gyro reference errors (σ_R) as large as 0.2 deg have little effect on the maximum tolerable spectral noise intensity. Also, a value of $K = 1 \times 10^{-7}$ rad/s for the noise can be tolerated. This amount of noise is equivalent to a random walk standard deviation of 0.6 deg/h. Such a gyro is of good quality and will be relatively expensive.

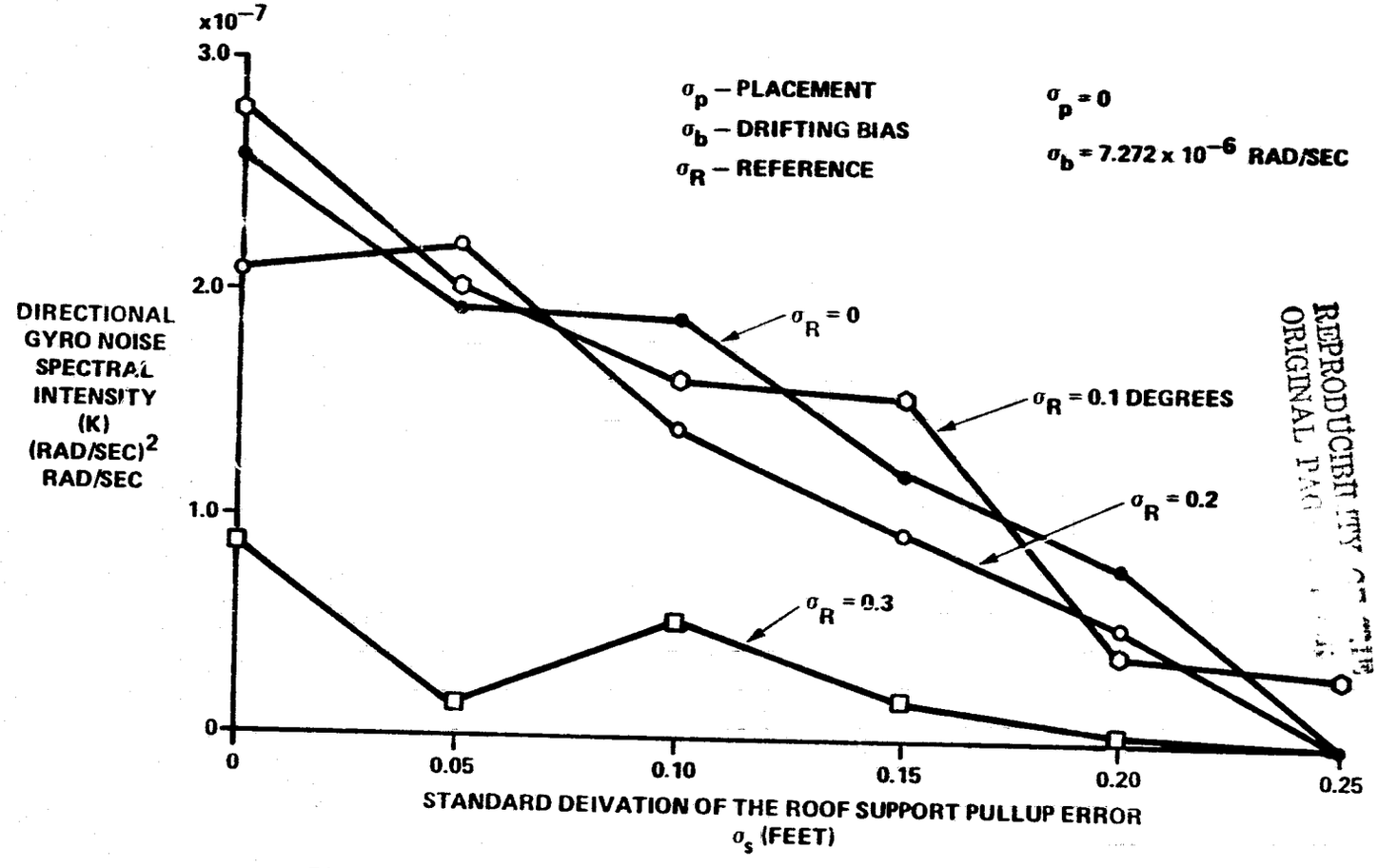

Figure 4-33. Directional Gyro - Single Measurement - Yaw Advancement Simulation Results

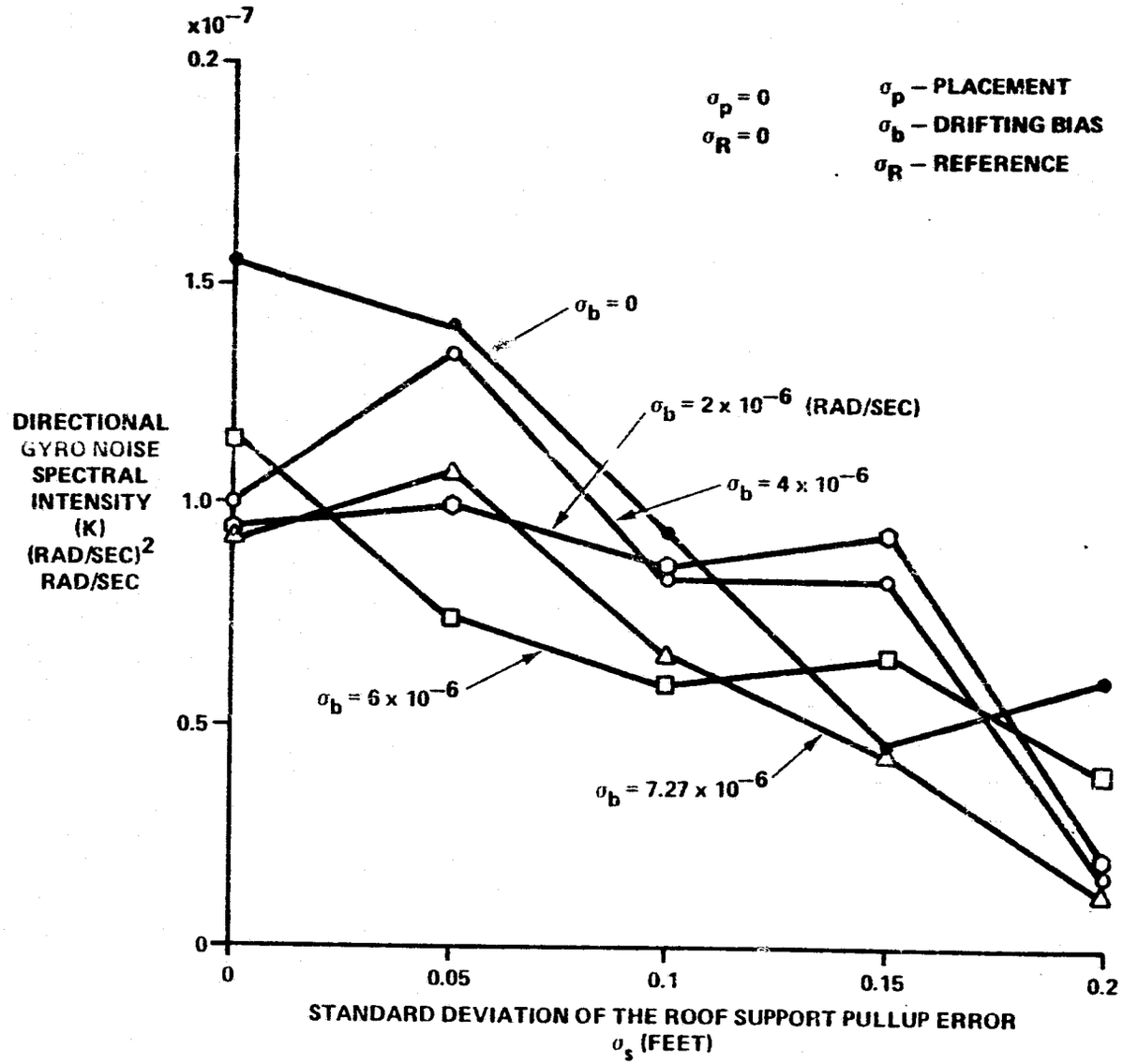

Figure 4-34. Directional Gyro - Constant Bias Compensation - Yaw Advancement Simulation Results

Figure 4-34 shows the maximum tolerable noise error versus the pullup error for the constant bias compensation system. It can be seen that the drifting bias σ_b causes a slight decrease in the tolerable noise level K. A value of $K = 0.5 \times 10^{-7}$ rad/s can be tolerated for the nominal bias of $\sigma_b = 7.27 \times 10^{-6}$ rad/s. This value is equivalent to a drift rate of 1.5 deg/h and represents a good quality gyro.

4.7.2 Recommended Measurement Algorithm for Directional Gyro

The recommended measurement algorithm for the directional gyro is the single measurement (no averaging) system. This system uses the measured location of the conveyer end points and the angular orientation of all the conveyer sections to compute the yaw profile. Only a single measurement of each conveyer section is made. An optimum weighting technique is used to minimize the yaw profile errors.

The single measurement system performance is comparable to the averaging system but does not need the large number of measurements for averaging. The drifting bias compensation system has a slightly inferior performance. The constant bias compensation system requires the noise spectral intensity to be half that of the single measurement system.

Using the yaw advancement simulation, ten advances of the directional gyro-single measurement system were simulated. The ratio of the amount of coal cut compared to that which could be cut without errors is the efficiency of the system. Figures 4-35 and 4-36 show the

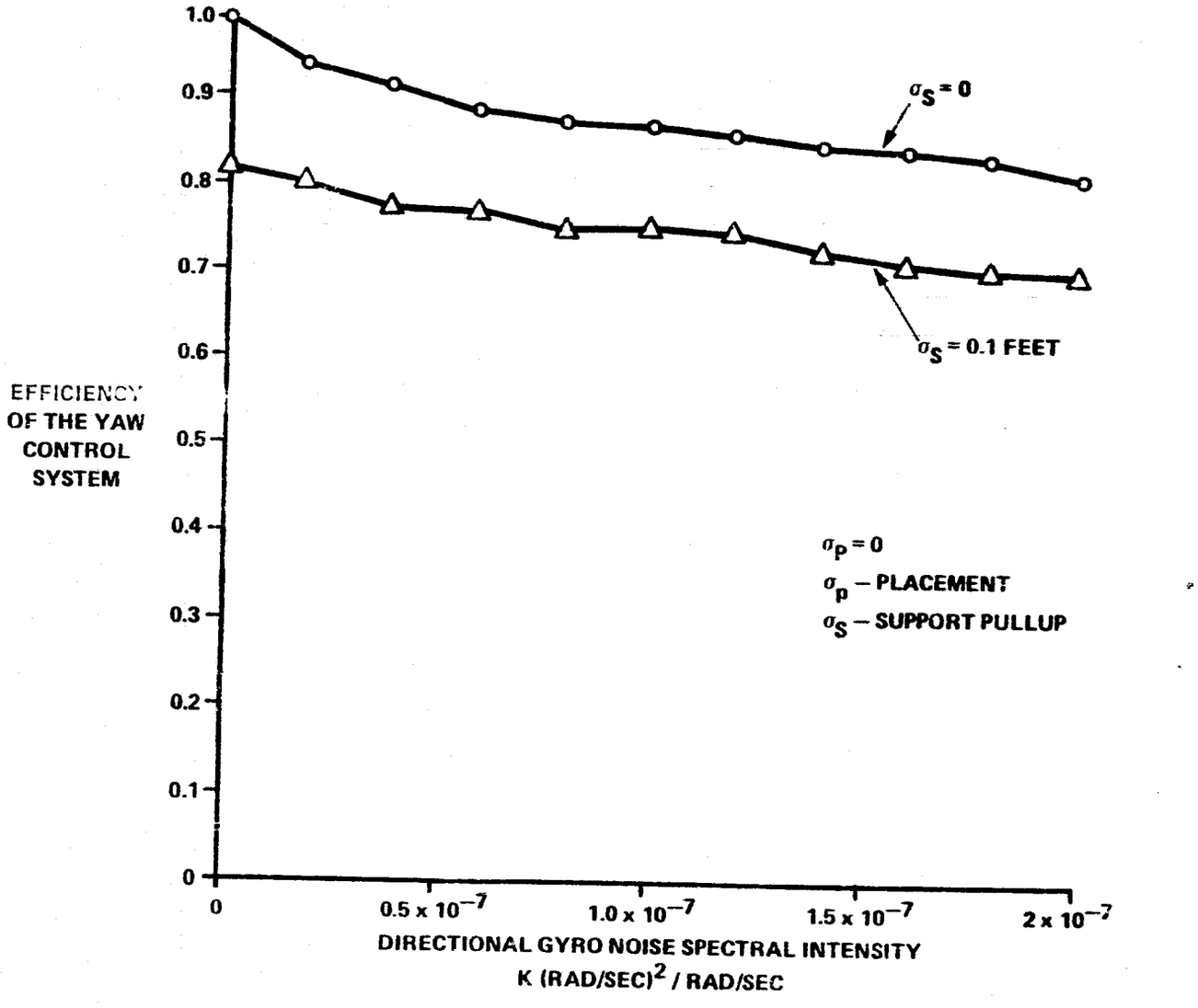

Figure 4-35. Efficiency of the Directional Gyro - Single Measurement System

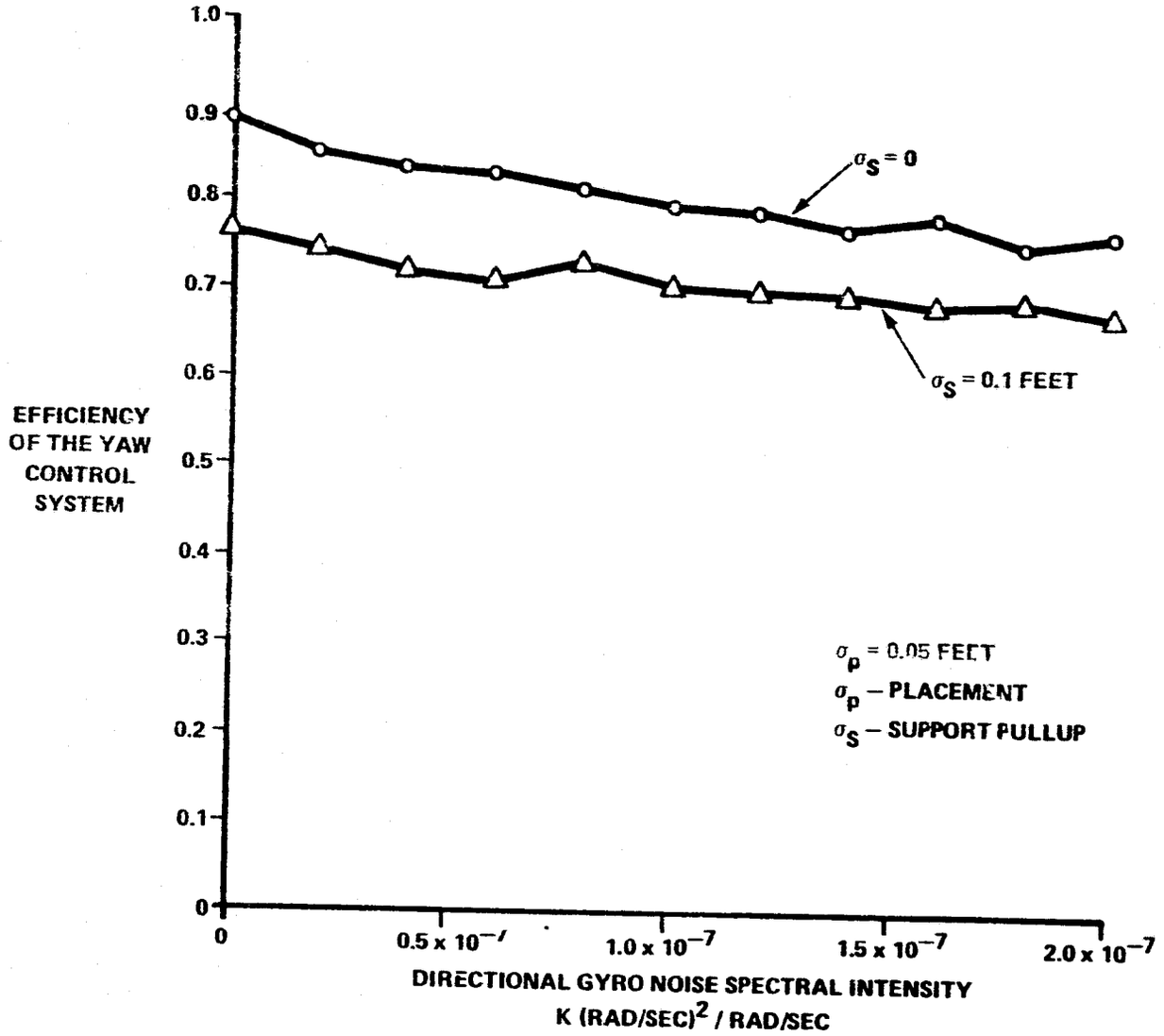

Figure 4-36. Efficiency of the Directional Gyro - Single Measurement System

efficiency of the directional gyro-single measurement system for various system errors.

4.8 CONCLUSIONS AND RECOMMENDATIONS

The yaw alignment system has been developed to automatically advance the conveyer and the pullup of the roof supports, keeping the coal face relatively straight. Angular measurements of the conveyer sections are made so that the conveyer shape (profile) can be computed. Conveyer placement commands are then computed to realign the conveyer.

Studies to evaluate this system indicate that either an angle cart or directional gyro can be used to measure the conveyer angles. The angle cart measures the relative angle between two adjacent conveyer sections while the directional gyro measures the angular orientation of a conveyer section with respect to a fixed reference.

The studies also indicate that the accuracies required of the directional gyro dictate that a relatively expensive gyro is required. In addition to this accuracy requirement, there can be some operational problems. If the gyro is mounted on the shearer, and measurements are made as the shearer is cutting coal, any delay in traversing the face will result in gyro errors continuing to build up. Another measurement pass with the shearer must then be made. If the directional gyro is not mounted on the shearer to avoid delays and to speed up the measurements, then a separate cart is needed, increasing the system cost.

As a result, the basic angle cart system is recommended. This system requires no reference angle measurements--only the angle cart measurements and the location of the two conveyer end points. Simulation results indicate that the measurement accuracies are an order of magnitude better than the requirements.

Roof support pullup errors of 0.1 ft can be tolerated. Estimates of the pullup errors indicate they are within this requirement. It is recommended, however, that study on an operating long wall miner be conducted to determine more accurately the roof support pullup errors. In addition, it is recommended that a dynamically accurate conveyer-roof support simulation be designed to study the roof support pullup errors since the present results are overly conservative.

5. ROLL CONTROL SYSTEM

5.1 FUNCTIONAL DESCRIPTION

The function of the roll control system is to provide an additional degree of control for the shearer. The shearer is equipped with hydraulic actuators which allow it to be rotated about its longitudinal axis, thus tilting both of the shearing drums relative to the coal seam. The purpose of roll control is to provide the capability to correct for twists and undulations in the conveyer. These twists can occur when coal or other debris becomes lodged under the conveyer.

The roll control system uses a roll sensor to measure the roll angle of the shearer relative to the local vertical. This signal may be biased to allow for operation in coal seams which are not level. The hydraulic actuators are commanded by the roll error angle at sensor output, through the necessary compensation. This control system is intended to be active, that is, to provide continuous control along the face during the shearing operation. The additional degree of freedom offered by roll control can be beneficial in maintaining the shearer within the coal seam.

5.2 ACTIVE ROLL CONTROL SYSTEM IMPLEMENTATION

Two alternative configurations were considered for the implementation of active roll control. These systems differ in the treatment of the roll sensor and actuator in the control loop. Figure 5-1 illustrates the two loop configurations used in this study. Here, the roll sensor is an inclinometer. The system at the top of this figure is referred to as the open actuator loop, and the system at the bottom is referred to as the closed actuator loop. This nomenclature refers to the treatment of the hydraulic actuator relative to the control loop.

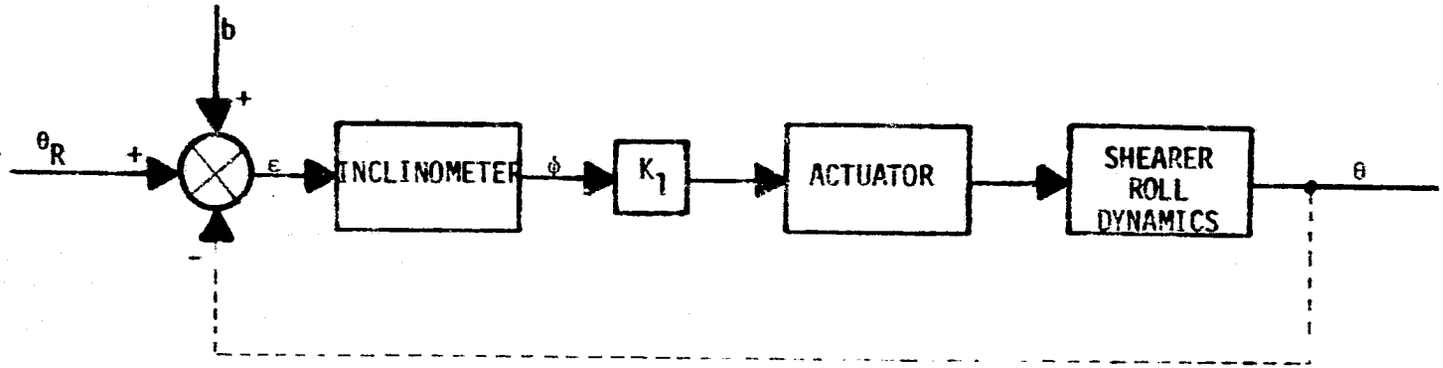

OPEN ACTUATOR LOOP

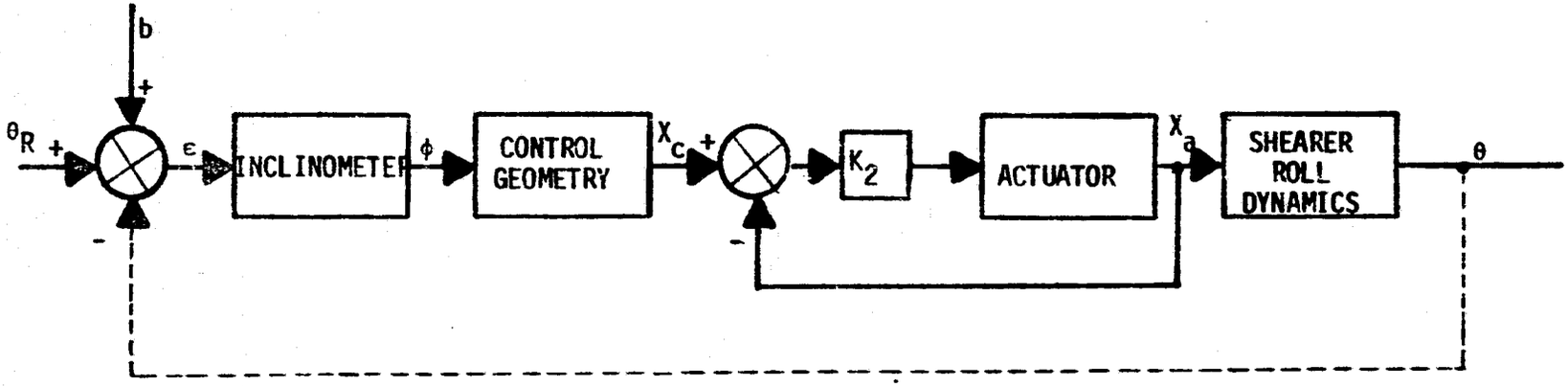

CLOSED ACTUATOR LOOP

Figure 5-1. Active Roll System Control Loop Implementations

Since the system is intended to be active during shearing operations, it will be subject to vibrational distrubances which will affect its performance. The inclinometer used as a roll sensor relies on gravitational acceleration to detect roll angles and therefore, any vibrational accelerations along the sensitive axis of this device are interpreted as roll signals and thus represent noise in the system. This problem was addressed in design and specification of the control loops.

The open actuator loop system uses the inclinomenter to sense the difference between the roll of the conveyor θ_R and the roll of the shearer θ. This signal drives the actuators through the compensation K_1, which is discussed in Section 5.4. With this system, the inclinometer is actively within the control loop and, therefore any filtering required to reduce noise levels will potentially affect loop stability. The closed actuator loop system is an alternative solution intended to provide a means of filtering inclinometer data without affecting the control loop stability. A position loop was closed around the actuator as was done for the VCS system. The inclinometer is outside of this primary loop, and therefore, acts as a reference to update the actuator loop. These two control configurations were modeled and analyzed to determine their performance.

5.3 DETAILED MATHEMATICAL MODEL FOR ROLL CONTROL SYSTEM

5.3.1 Inclinometer Sensor Model

The sensor modeled was a Moog model 86-121 inclinometer. This device uses the displacement of a sliding mass to detect inclination relative to the local vertical. The device can be viewed as a mass free to slide but subject to damping and restoring forces. When the surface on which the mass slides is tilted with respect to horizontal,

gravitational acceleration moves the mass from its null position. External acceleration in the direction of motion of the mass also causes motion. Given the following definitions:

x = mass displacement

M = mass

D = damping force constant

K = restoring force constant

g = acceleration due to gravity

a = disturabnce acceleration

the equation of the mass motion is:

$$M\ddot{x} = -D\dot{x} - Kx + Mg \sin \theta + Ma$$

The angle θ is the inclination of the mass relative to horizontal, and is the quantity to be sensed. Since inclination angles are small, $\sin \theta$ may be replaced by θ. Figure 5-2 shows a block diagram of the solution for this equation.

The Moog sensor has a natural frequency of 2.4 Hz and a damping ratio of 0.6. The unforced version of the above equation is:

$$\ddot{x} + \frac{D}{M}\dot{x} + \frac{K}{M}x = 0$$

with

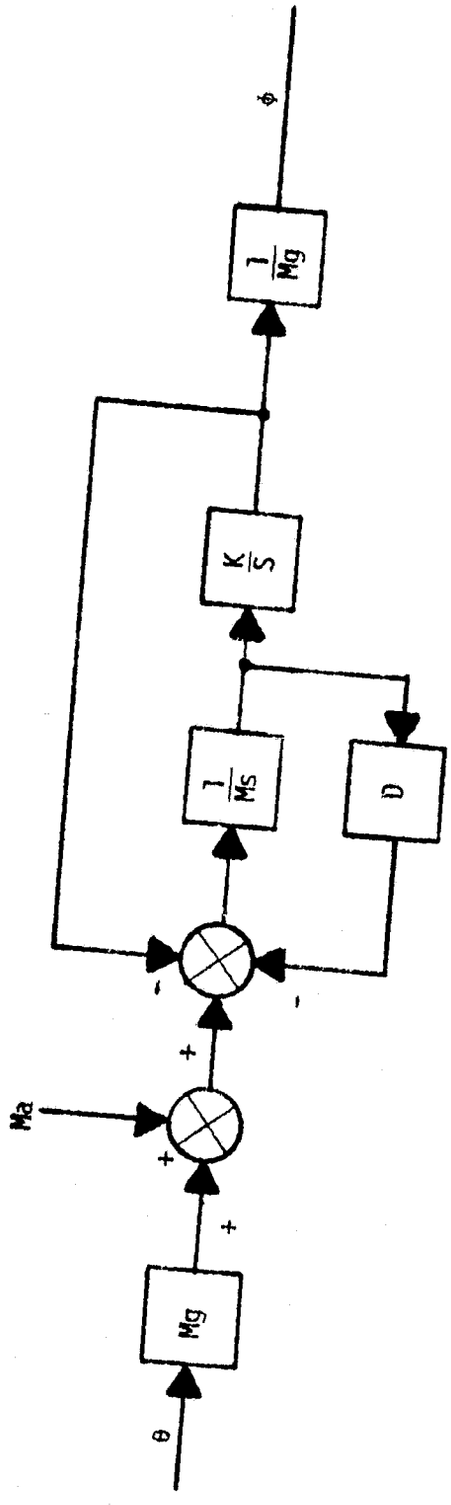

Figure 5-2. Inclinometer Model Block Diagram

$$\omega = 2.4 \text{ Hz} = 15.08 \text{ rad/s}$$

$$\omega_N^2 = \frac{K}{M} = 227.396$$

and

$$2\zeta\omega_n = \frac{D}{M} = 18.095$$

The inclinometer equation can now be rewriten as:

$$\ddot{X} = -18.095\dot{X} - 227.396X + 32.2\theta + a$$

As shown in Figure 5-2, the output of the sensor is the displacement divided by Mg to yield an angular equivalent.

5.3.2 Vibration Environment

The inclinometer must be mounted on the shearer with its sensitive axis normal to the face, if it is to sense the desired roll angle. As a result of this orientation, the inclinometer will also sense cross-axis accelerations normal to the face resulting from coal shearing. The precise nature of these cross-axis disturbances was not known, so a bandlimited white noise process was used to simulate this noise. The simulated noise was a zero mean process with an exponential correlation, i.e. white noise through a first order low pass linear filter. The first order filter was set to a 100 Hz bandwidth in these studies.

Throughout the results which follow, the cross-axis disturbances will be specified as RMS g levels. The square of this, the signal variance, represents the total g^2 in the 100 Hz bandwidth, or the area under the noise spectrum. The spectral level of the white

noise passed through the low pass filter is found by dividing the variance by the bandwidth.

5.3.3 Actuator - Shearer Model

The hydraulic actuation of the roll system is performed by two hydraulic cylinders operated in parallel. These cylinders are 22.25 in. long when retracted, and have a ram extension of 8 in. The actuators are mounted such that a 4 in. extension gives zero roll angle relative to the skid plane. Therefore, within the range of the ram extension, a roll of ± 5 deg is possible. Figure 5-3 shows the shearer geometry. The distance from the shearer pivot to actuator is 47 in. When the actuator is at its nominal extension of 4 in., $\theta_0 = 29.2$ deg. The roll of the shearer θ is the change in roll relative to θ_0. The equations for the shearer roll angle in term of actuator displacement are given as:

$$\theta = \cos^{-1}\left(\frac{D_1^2 + D_2^2 - (X_0 + X_a)^2}{2D_1 D_2}\right) - \theta_0$$

This is the same relationship used in the VCS, to determine ranging arm angles.

The model used for the shearer-actuator system is the same as the VCS actuator system shown in Figure 3-16. For this simulation, however, the lengths D and W are replaced by lengths D_1 and D_2 respectively. The simulation was also modified such that its range of roll was ± 5 deg. The model assumes that the pair of actuators can be treated as one actuator, and that the roll system has the same dynamic response and nonlinearities as the VCS system. Finally, the second order loop simulating arm flexibility in the VCS model was not used in the roll studies.

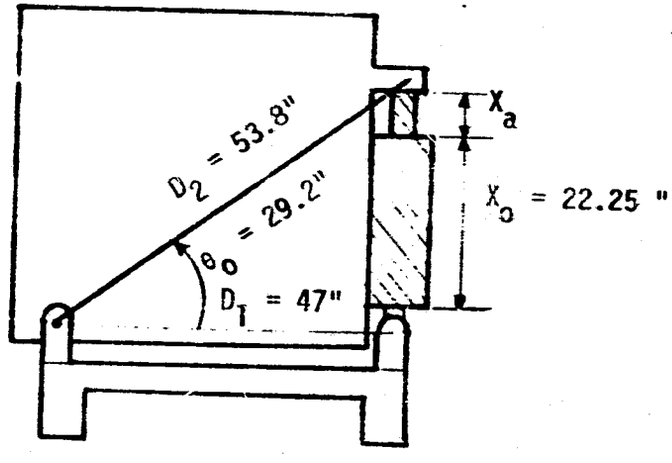

Figure 5-3. Shearer Geometry for Roll Control

5.4 ROLL LOOP DESIGN

5.4.1 Open Actuator Loop Design

The system diagram in Figure 5-1 shows a compensation K_1. This was chosen to be a simple gain so that a roll angle sensed by the inclinometer would drive the actuator control valve through this gain. The value of K_1 was selected by simulation, because of the nonlinear nature of the actuator system. The loop response varies as a function of both input amplitude and frequency, so to measure loop performance, sinusoidal inputs ranging from 1.25 to 5 deg peak were used at frequencies from 0.025 to 0.2 Hz. The performance measure used was the rms of the loop error designated as ε in Figure 5-1. Figures 5-4 through 5-6 show the loop error versus frequency for several amplitudes. Values of K_1 used were 275, 1375, and 2750 for the Figures 5-4 through 5-6, respectively.

It can be seen that the low frequency error is reduced by increasing K_1, but higher frequency error is essentially the same. This is due to the rate limited nature of the hydraulic system. At low frequencies, below 0.03 Hz, or at higher frequencies at the lower amplitudes, the actuator rates required to follow the input are less than maximum actuator rate, and resulting errors are determined largely by K_1. The larger amplitude inputs such as 5 deg, and higher frequencies above 0.05 Hz, require actuator rates beyond its capacity and cause the actuator to limit at its maximum rate introducing errors.

The maximum input frequency to be expected depends on the chassis velocity and amount of twist in the conveyor sections. If a shearer velocity of 30 ft/min is assumed, and letting every 5 ft conveyor section be alternately twisted, the resultant roll frequency would be 0.05 Hz. It was, therefore, decided that the roll loop should perform well up to this frequency. Since it is unlikely that a 5 deg

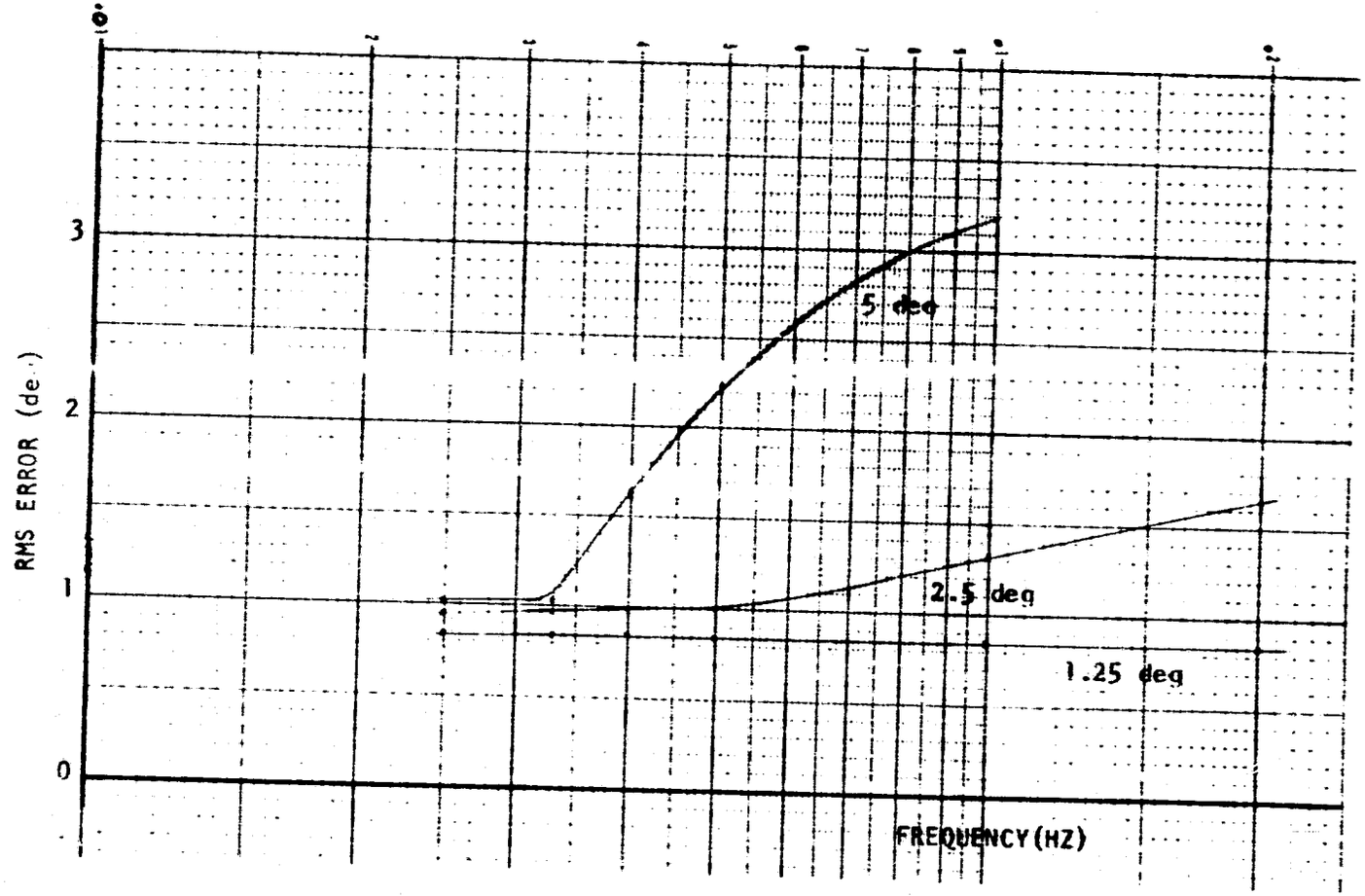

Figure 5-4. Open Actuator Loop Performance

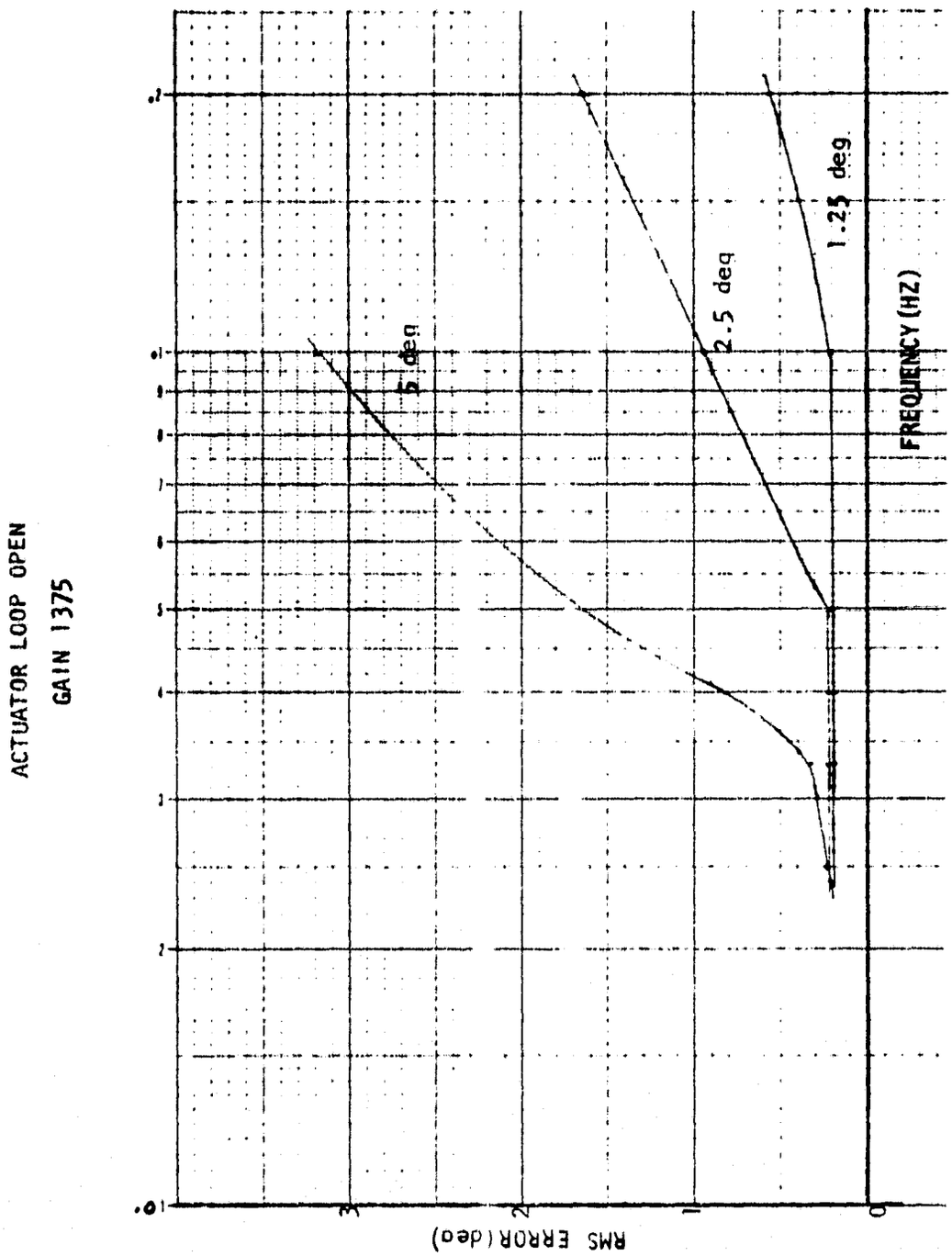

Figure 5-5. Open Actuator Loop Performance

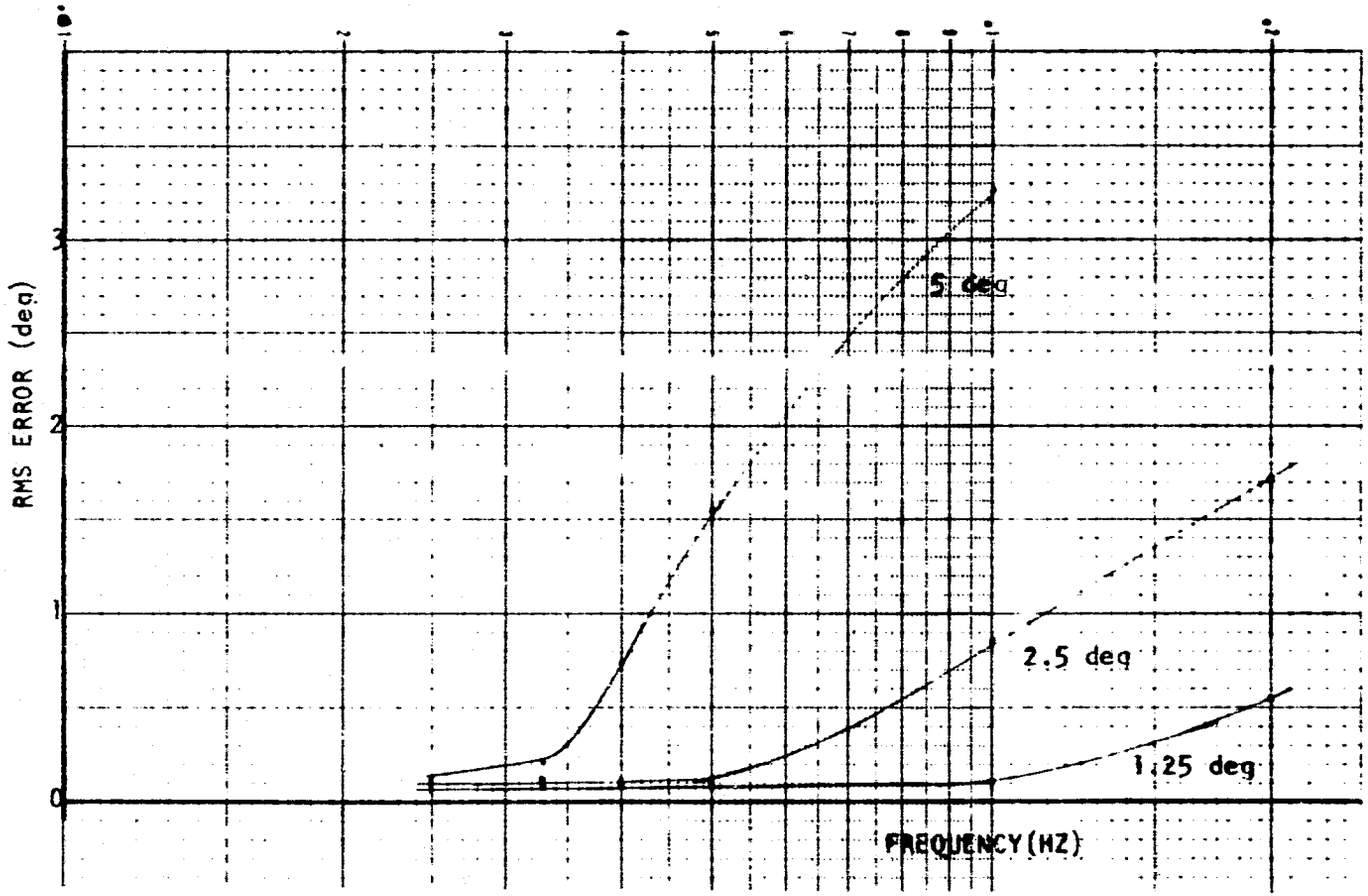

Figure 5-6. Open Actuator Loop Performance

error will occur regularly, an intermediate amplitude was selected as a reference. Figures 5-4 through 5-6 illustrate that at a 2.5 deg peak input amplitude, all values of K_1 yielded essentially a constant error up to 0.05Hz. A gain of 2750 was chosen because of minimum error. A roll error of 0.05 deg is sufficient to generate a 2.4 V signal and exceed the control valve input threshold with this gain. Figure 5-7 shows a time history of the roll angle for the system in response to a 0.05 Hz input of 2.5 deg peak amplitude.

5.4.2 Closed Actuator Loop Design

In this system, the actuator is position commanded as in the VCS system. An actuator position feedback is compared with the command and applied to the acutator control valve through the gain K_2. This gain was also selected by simulation to yield a response similar to the open actuator loop system. The calculations necessary to determine the desired actuator displacement follow those used in the VCS. The present shearer roll angle θ' is computed from the current X_a as:

$$\theta' = \cos^{-1}\left(\frac{D_1^2 + D_2^2 - (X_o + X_a)^2}{2\,D_1\,D_2}\right)$$

The desired value of roll is then $\theta' + \phi$ and the necessary X_a to achieve this is:

$$X_a = \sqrt{D_1^2 + D_2^2 - 2D_1\,D_2 \cos(\phi + \theta')} - X_o$$

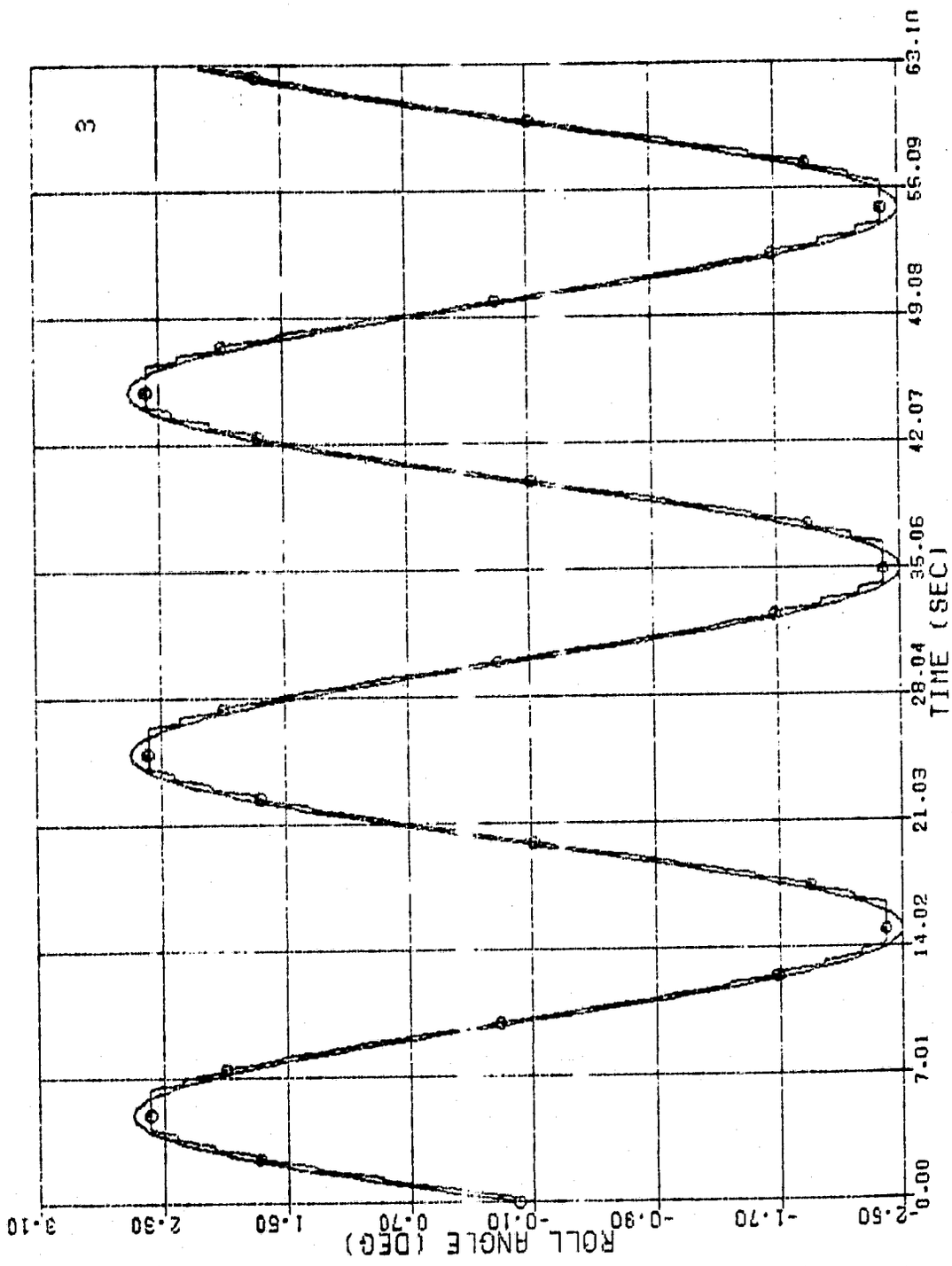

Figure 5-7. Open Actuator Loop Time History with No Noise

Figures 5-8 through 5-10 show error versus frequency plots for the closed actuator loop system with K_2 equal to 85, 170, and 340 respectively. These plots are very similar to Figures 5-4 through 5-6 except that the low frequency error is lower and less affected by gain changes. Again, at 2.5 deg input amplitude, the error response is good to approximately 0.05 Hz. The value of K_2 chosen was 170, the same gain as in the VCS system. This gain yields good performance without excessive limit cycles. Time response of the closed actuator loop system is shown in Figure 5-11. It is seen that this system is slightly more accurate than the open loop system in a noiseless environment. This is also shown in the frequency response diagrams of the two systems.

5.5. ROLL SYSTEM PERFORMANCE WITH CROSS-AXIS ACCELERATION

5.5.1 Performance with Open Actuator Loop

System performance is shown in Table 5-1, as a function of the RMS cross-axis acceleration level, which was parameterized from 0.01 to 1.0 g's. The data in this table shows RMS loop error for a sinusoidal input at a frequency of 0.05 Hz (1/20 Hz) and an amplitude of 2.5 deg peak. These results were also at maximum flow rate. Row 1 of Table 5-1 indicates the response of the nominal open loop system to cross-axis disturbances. It can be seen that even small accelerations introduce errors. The input signal has an RMS value of 1.77 deg, which would be the RMS error if no control was applied. Accelerations of 0.05 g produce errors approximately 45 percent of this value, and with noise above 0.1 g the errors are essentially as great as with no control.

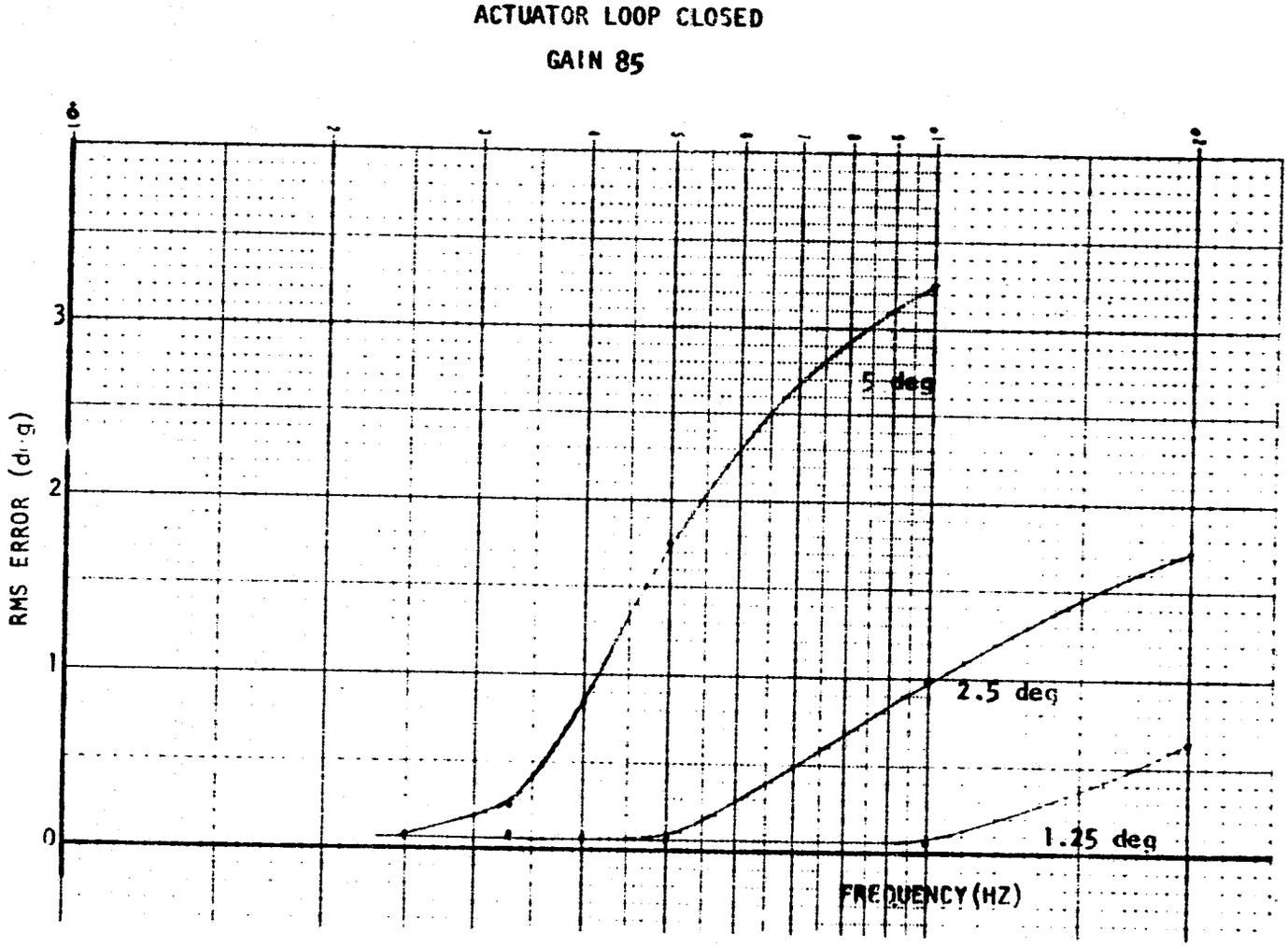

Figure 5-8. Closed Actuator Loop Performance

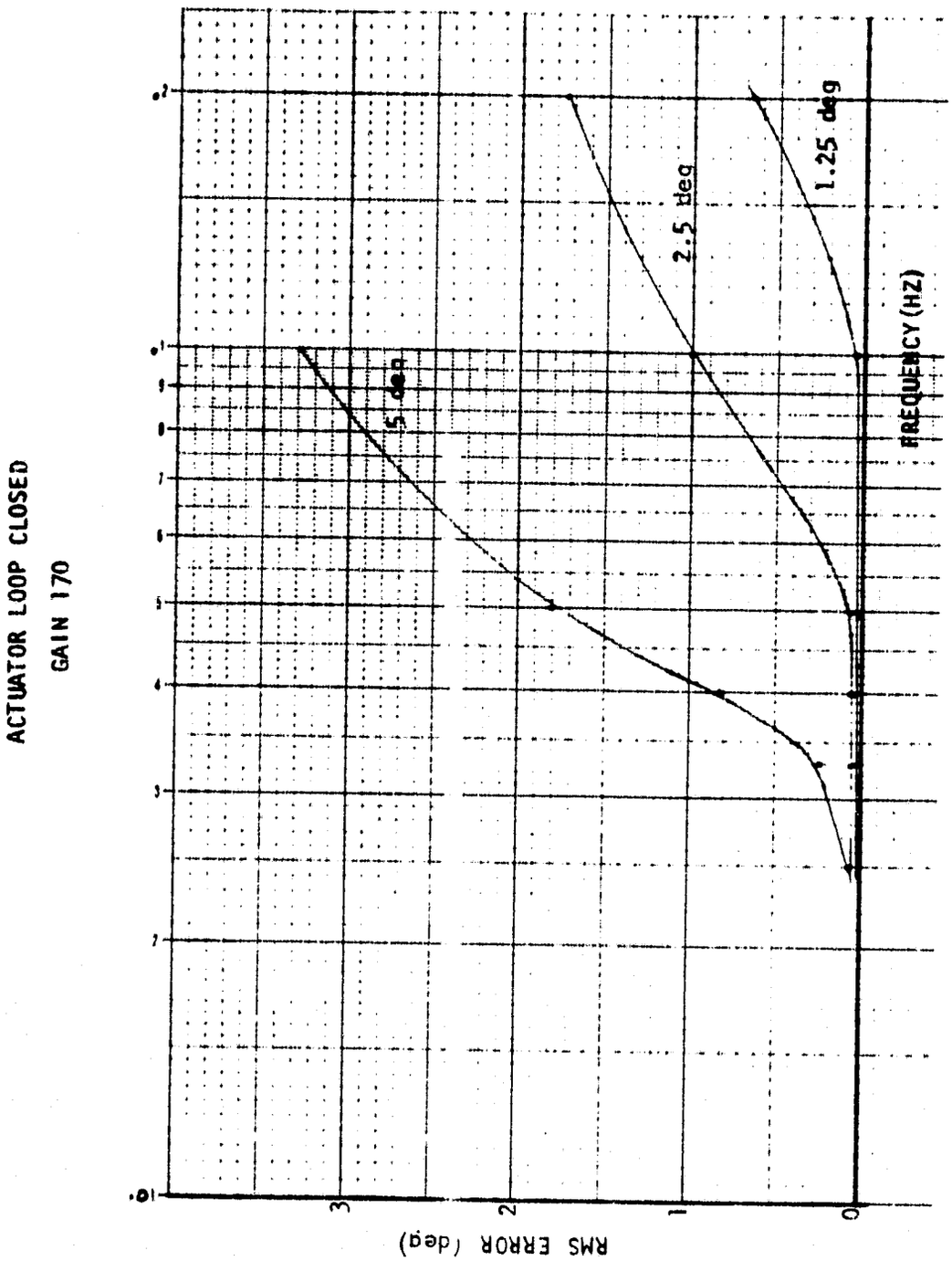

Figure 5-9. Closed Actuator Loop Performance

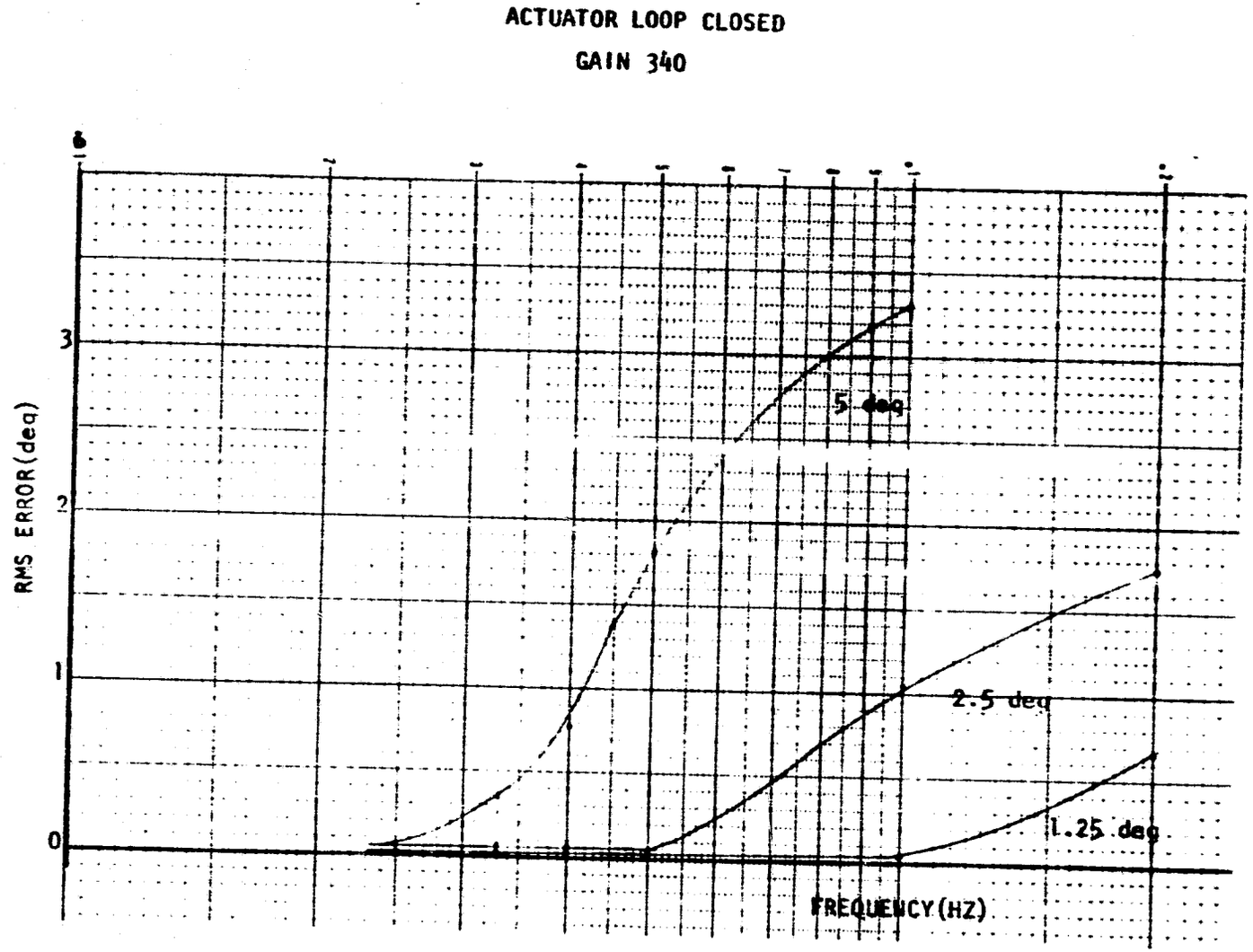

Figure 5-10. Closed Actuator Loop Performance

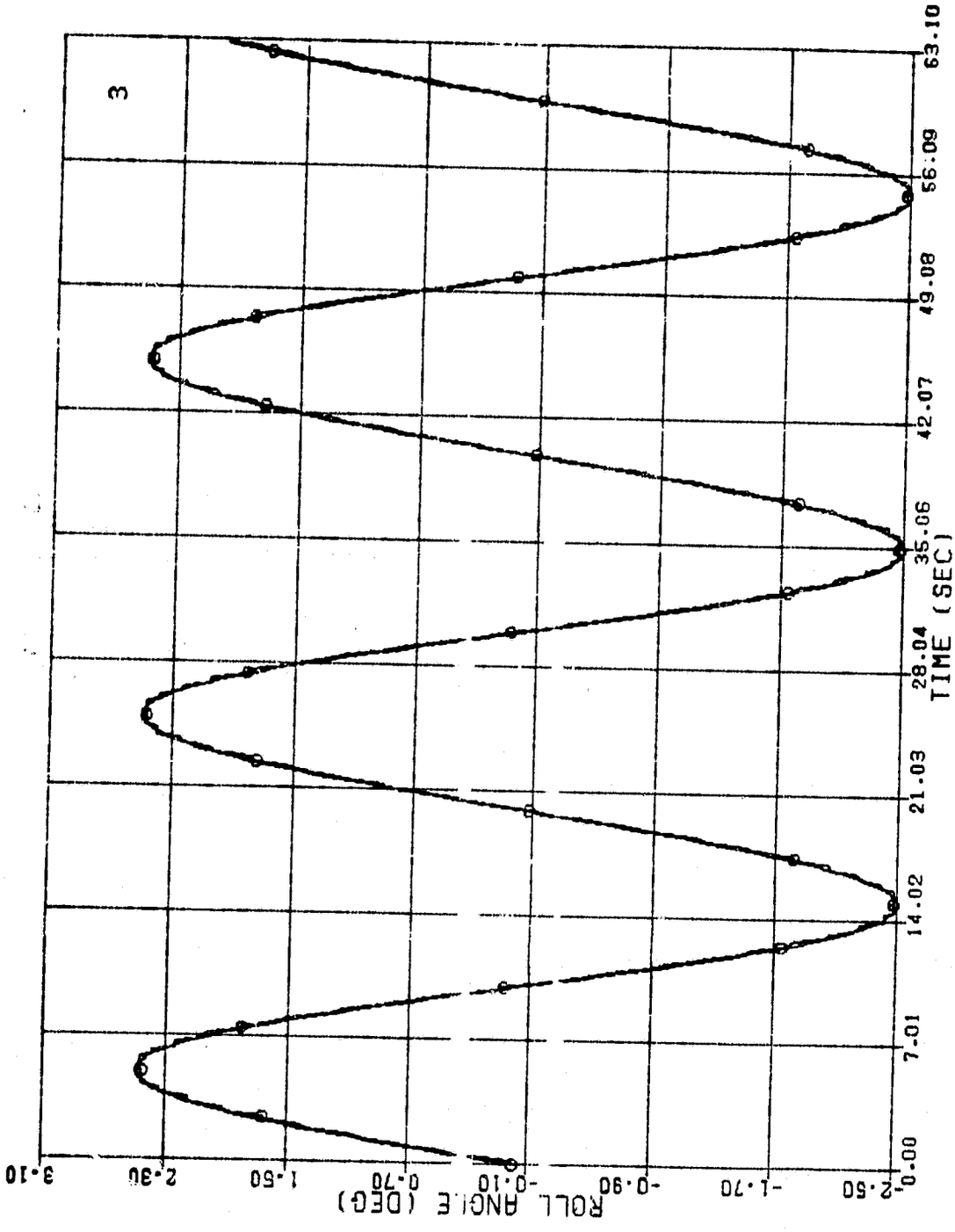

Figure 5-11. Closed Actuator Loop Time History with No Noise

Table 5-1. Performance with Cross-Axis Disturbances, 0.05 Hz Input and 8 GPM Flow Rate

SYSTEM / CROSS AXIS ACCELERATION RMS g's	RMS LOOP ERROR (DEG)					
	0.01	0.05	0.1	0.2	0.5	1.0
ACTUATOR LOOP OPEN INCLINOMETER: 2.4 Hz	0.253	0.734	1.160	1.639	1.853	2.025
ACTUATOR LOOP CLOSED INCLINOMETER: 2.4 Hz	0.225	0.712	1.164	1.642	1.852	2.006
ACTUATOR LOOP OPEN INCLINOMETER: 0.24 Hz	0.586	0.781	0.967	1.508	2.067	2.272
ACTUATOR LOOP CLOSED INCLINOMETER: 0.24 Hz	0.774	0.903	1.041	1.509	2.101	2.261

(A) INPUT: 1/20 Hz
2.5 DEG PEAK

(B) 8 GPM FLOW RATE

Row 3 of Table 5-1 shows the results of the open loop with the bandwidth of the inclinometer artificially reduced by a factor of 10 to simulate additional filtering in the loop. Performance at lower g levels degrades compared with the higher bandwidth, but improves slightly in the 0.1 to 0.2 g range. The principal reason for the change is the basic change in system accuracy resulting from the lower bandwidth. Figure 5-12 illustrates the frequency response of the reduced bandwidth loop. It can be seen that loop errors are higher over the entire frequency range. No instabilities resulted from this additional filtering. Figures 5-13 and 5-14 show the time responses of the open loop system at both inclinometer bandwidths with a 0.05 g noise input level.

System performance at a lower input frequency of 0.025 Hz (1/40 Hz) is demonstrated in Table 5-2. Rows 1 and 3 of this table show the open loop results, which indicate that performance is improved over that obtained with the 0.05 Hz input This is commensurate with the frequency response data which also showed better performance at lower frequency. Essentially, with the slower input, the system has more capacity left to follow the input and deal with the noise. At this input frequency, it takes a 0.5 g disturbance to yield errors approximately the same as with no control. Figures 5-15 and 5-16 show open loop performance at both inclinometer bandwidths with 0.1 g noise and a 0.025 Hz input frequency.

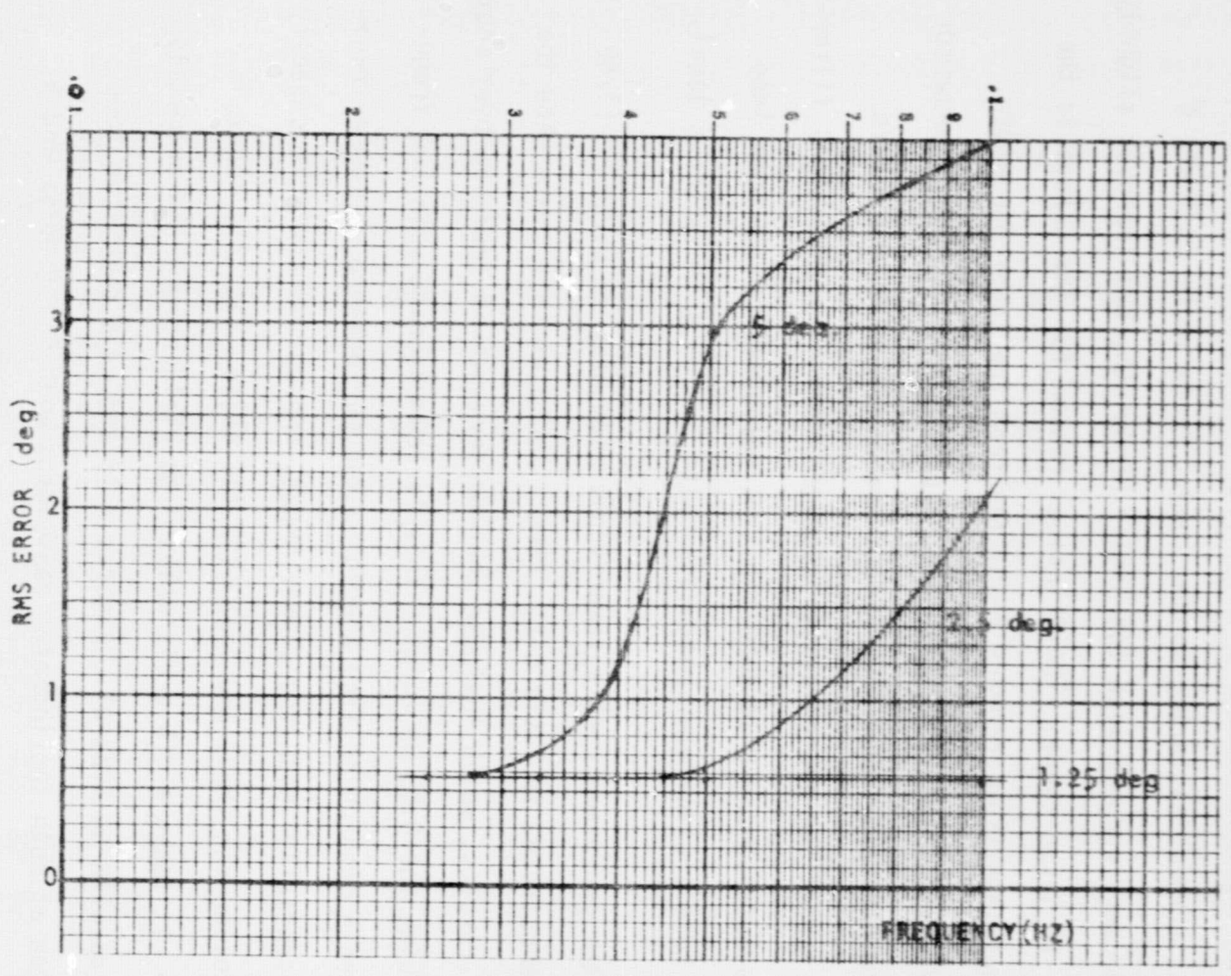

Figure 5-12. Open Actuator Loop Response with 0.24 Hz Bandwidth

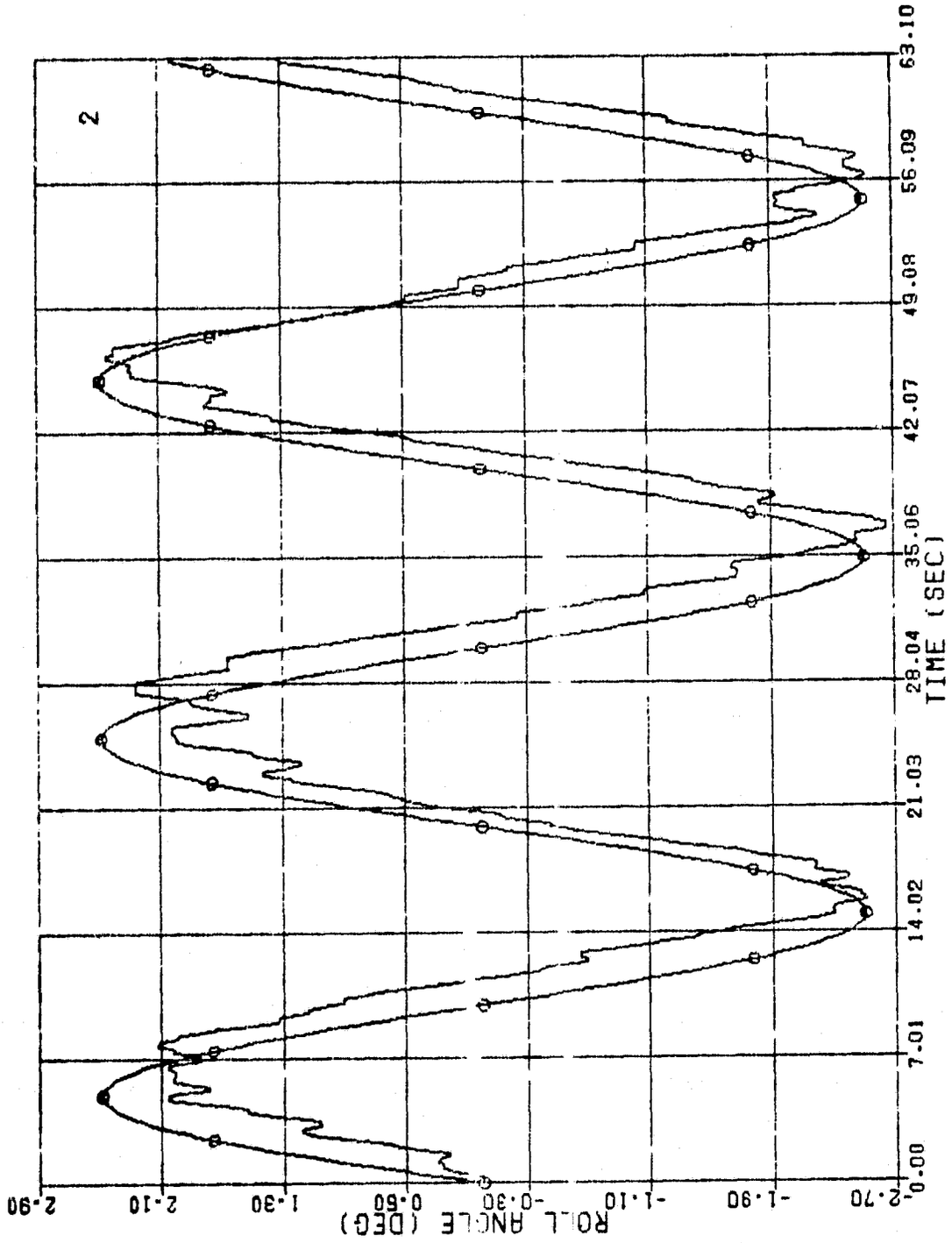

Figure 5-13. Open Actuator Loop Time History with 2.4 Hz Inclinometer Bandwidth, 0.05 g Cross-Axis Acceleration and 0.05 Hz Input

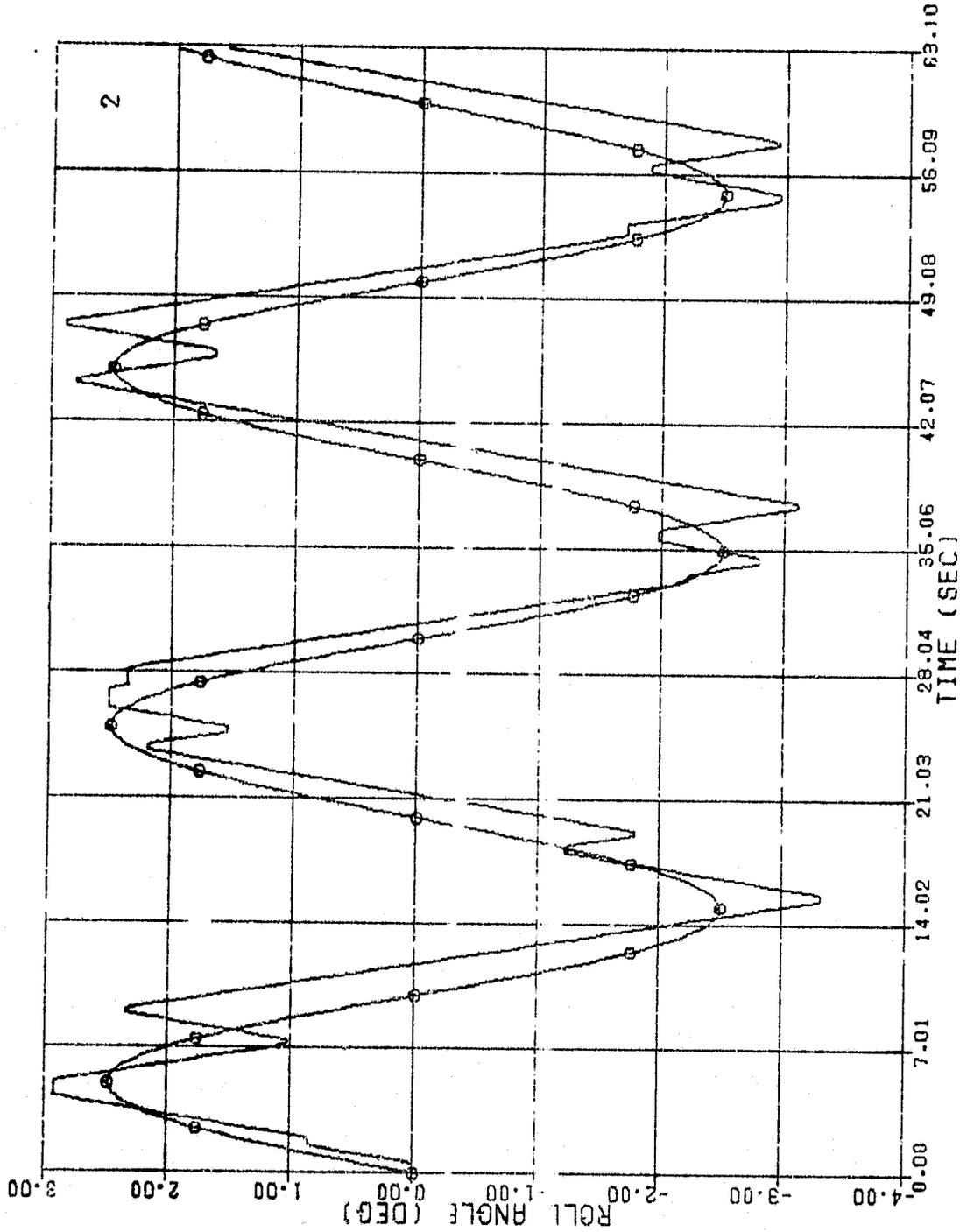

Figure 5-14. Open Actuator Loop Time History with 0.24 Hz Inclinometer Bandwidth, 0.05 g Cross-Axis Acceleration and 0.05 Hz Input

Table 5-2. Performance with Cross-Axis Disturbances, 0.025 Hz Input and 8 GPM Flow Rate

SYSTEM	CROSS AXIS ACCELERATION RMS g's	RMS LOOP ERROR (DEG)					
		0.01	0.05	0.1	0.2	0.5	1.0
ACTUATOR LOOP OPEN INCLINOMETER: 2.4 Hz		0.161	0.430	0.680	1.033	1.657	2.230
ACTUATOR LOOP CLOSED INCLINOMETER: 2.4 Hz		0.181	0.427	0.695	1.029	1.637	2.220
ACTUATOR LOOP OPEN INCLINOMETER: 0.24 Hz		0.585	0.659	0.788	0.990	1.540	2.012
ACTUATOR LOOP CLOSED INCLINOMETER: 0.24 Hz		0.659	0.708	0.815	0.998	1.535	2.010

(A) INPUT: 1/40 Hz
2.5 DEG PEAK

(B) 8 GPM FLOW RATE

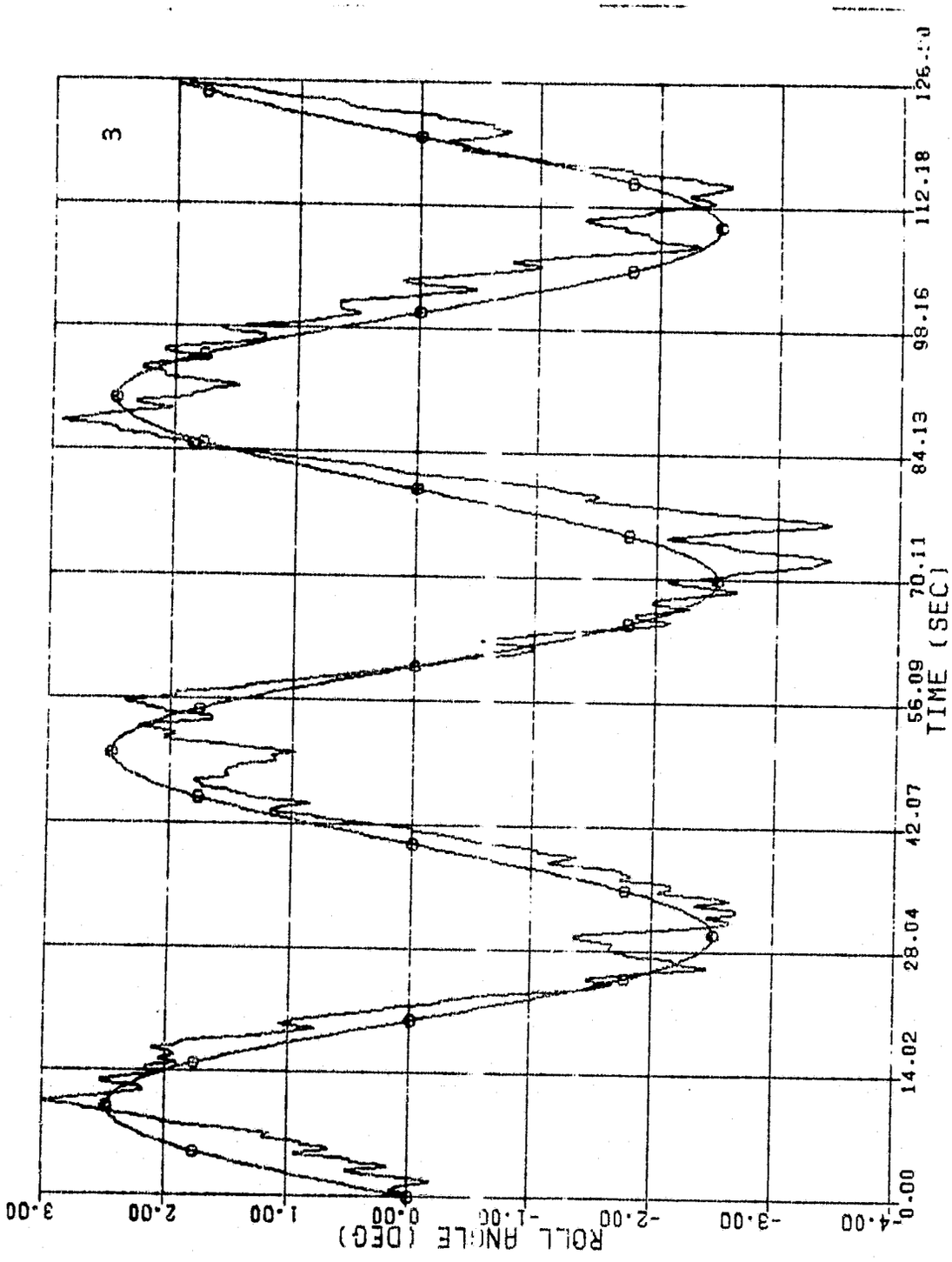

Figure 5-15. Open Actuator Loop Time History with 2.4 Hz Inclinometer Bandwidth, 0.1 g Cross-Axis Acceleration and 0.025 Hz Input

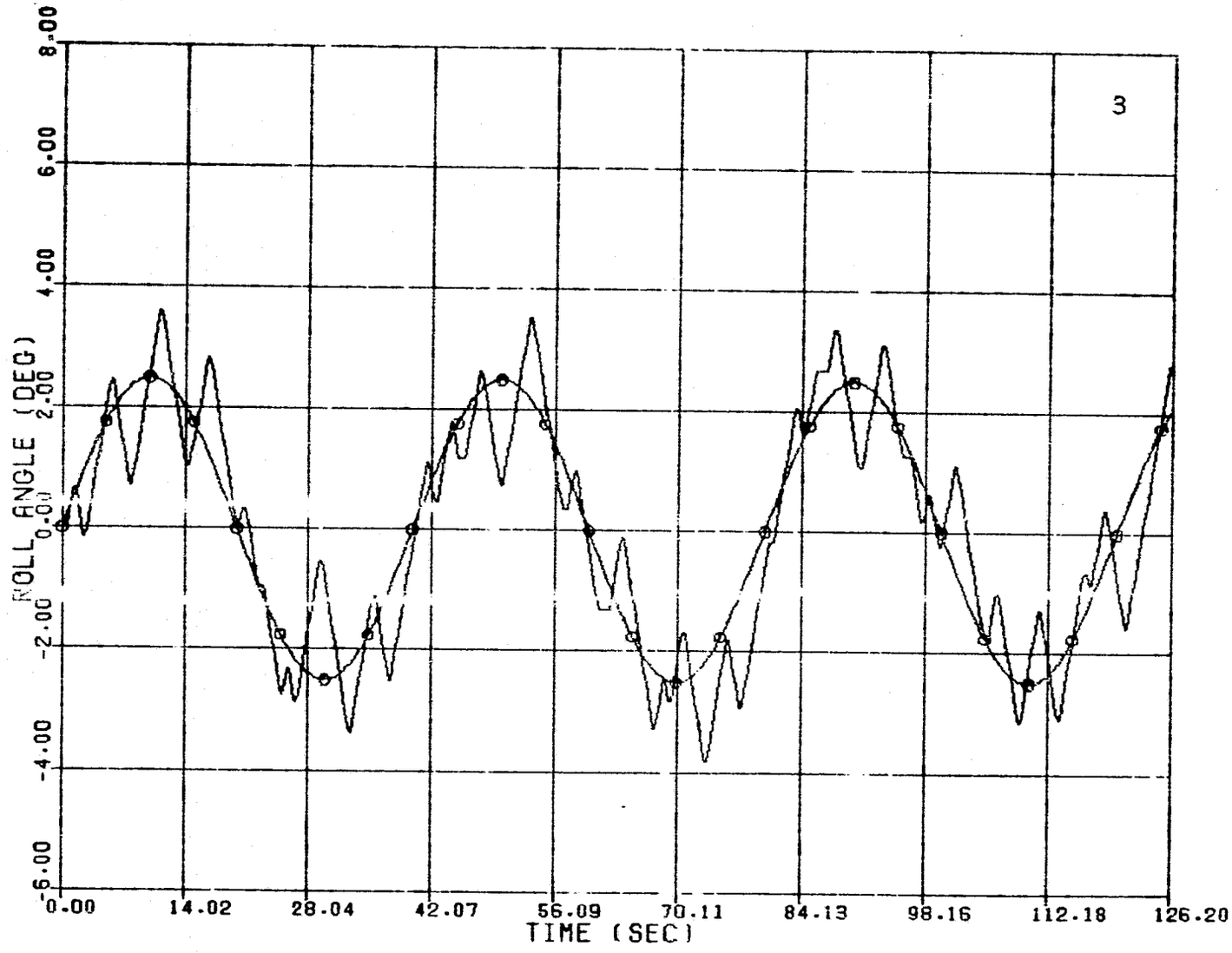

Figure 5-16. Open Actuator Loop Time History with 0.24 Hz Inclinometer Bandwidth, 0.1 g Cross-Axis Acceleration and 0.025 Hz Input

5.5.2 Performance with Closed Actuator Loop

Rows 2 and 4 of Tables 5-1 and 5-2 also show the results of the closed loop system with cross-axis disturbances. Table 5-1 shows the results with the 0.05 Hz input. The closed loop responses are essentially the same as the open loop responses at the nominal 2.4 Hz inclinometer bandwidth. At the 0.24 Hz inclinometer bandwidth, the closed loop and open loop systems perform the same at noise levels above 0.2 g, but the closed loop is worse below this point. The two systems also behave similarly at the 0.025 Hz input frequency. While errors are generally smaller than with the 0.05 Hz input, the relative relationships of the loop performance is as described above. It should be emphasized that this loop is therefore equally as sensitive to small disturbances as was the open loop. Figures 5-17 through 5-20 show time responses of the closed actuator loop with various input frequencies and noise levels.

5.5.3 Effects of Reduced Flow Rate

The hydraulic system on the shearer is shared between the roll and VCS control systems. Therefore, the 8 gpm nominally available can be shared between the 2 VCS cylinders and the roll cylinders. The flow rate is, therefore, variable depending on the activities of these systems. When flow must be shared with the VCS, there is clearly less flow available for roll actuation, and the maximum actuator extension rate is proportionately lower. This has a pronounced effect on performance. Figures 5-21 and 5-22 show that performance at higher input

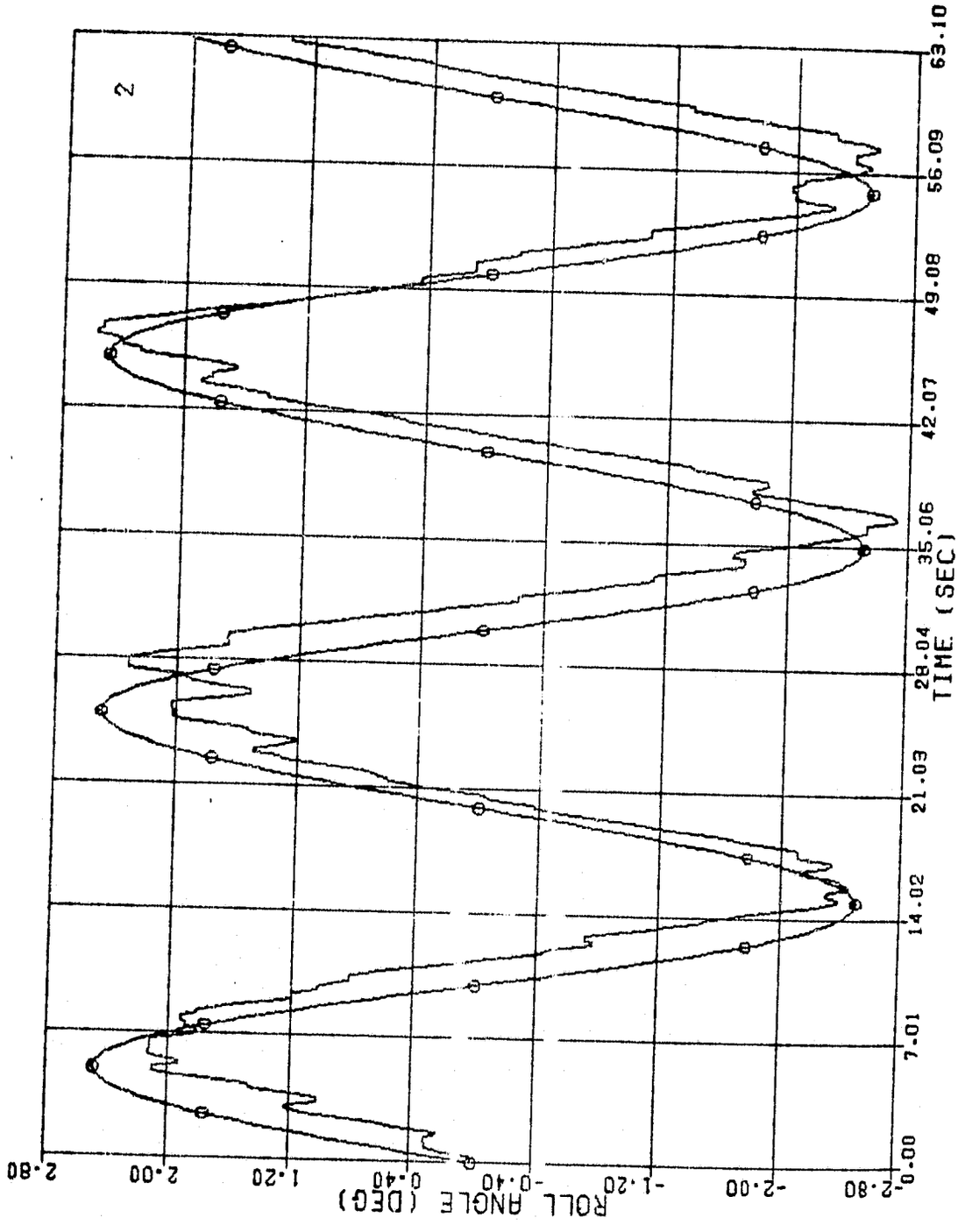

Figure 5-17. Closed Actuator Time History with 2.4 Hz Inclinometer Bandwidth, 0.05 g Cross-Axis Acceleration and 0.05 Hz Input

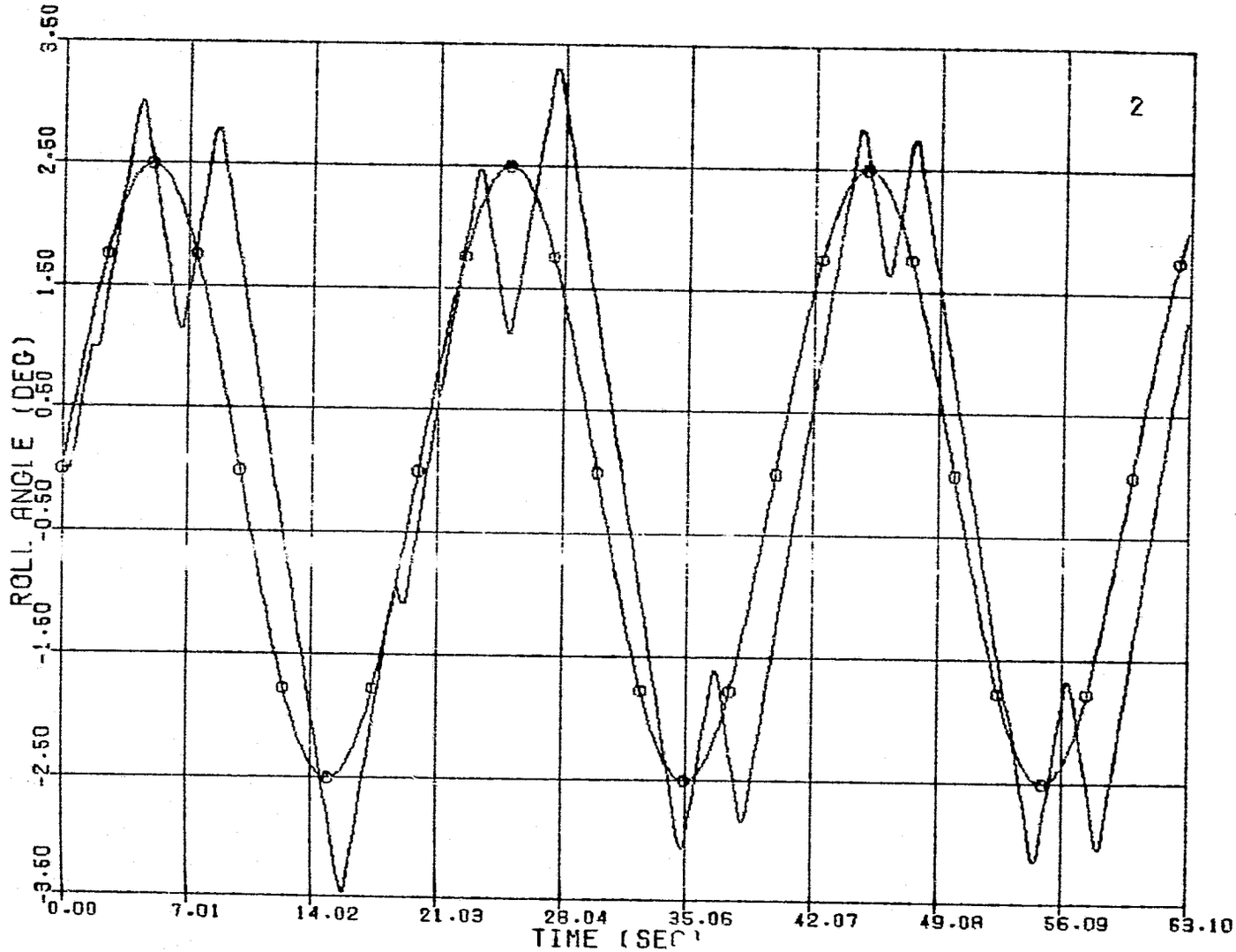

Figure 5-18. Closed Actuator Time History with 0.24 Hz Inclinometer Bandwidth, 0.05 g Cross-Axis Acceleration and 0.05 Hz Input

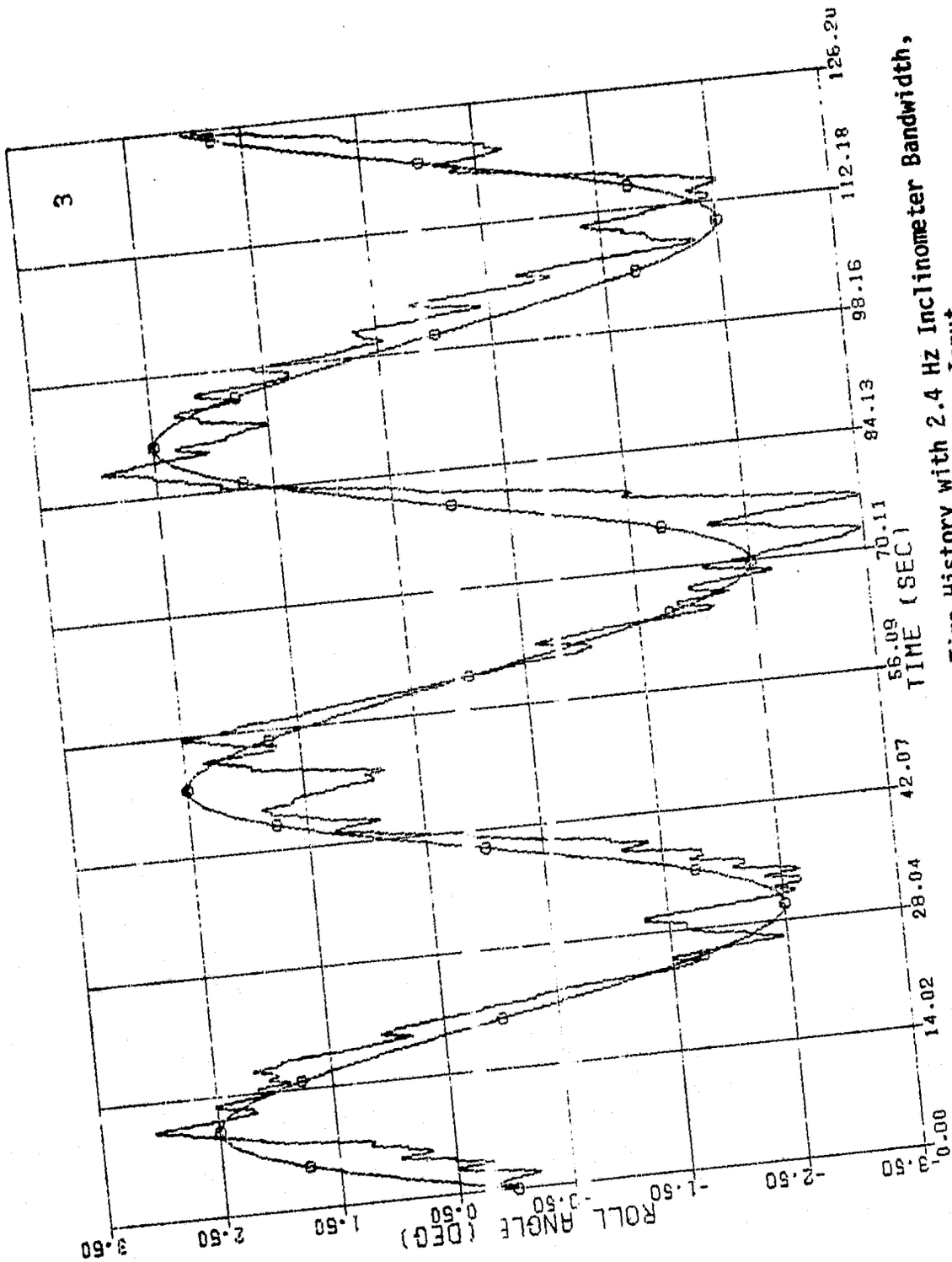

Figure 5-19. Closed Actuator Loop Time History with 2.4 Hz Inclinometer Bandwidth, 0.1 g Cross-Axis Acceleration and 0.025 Hz Input

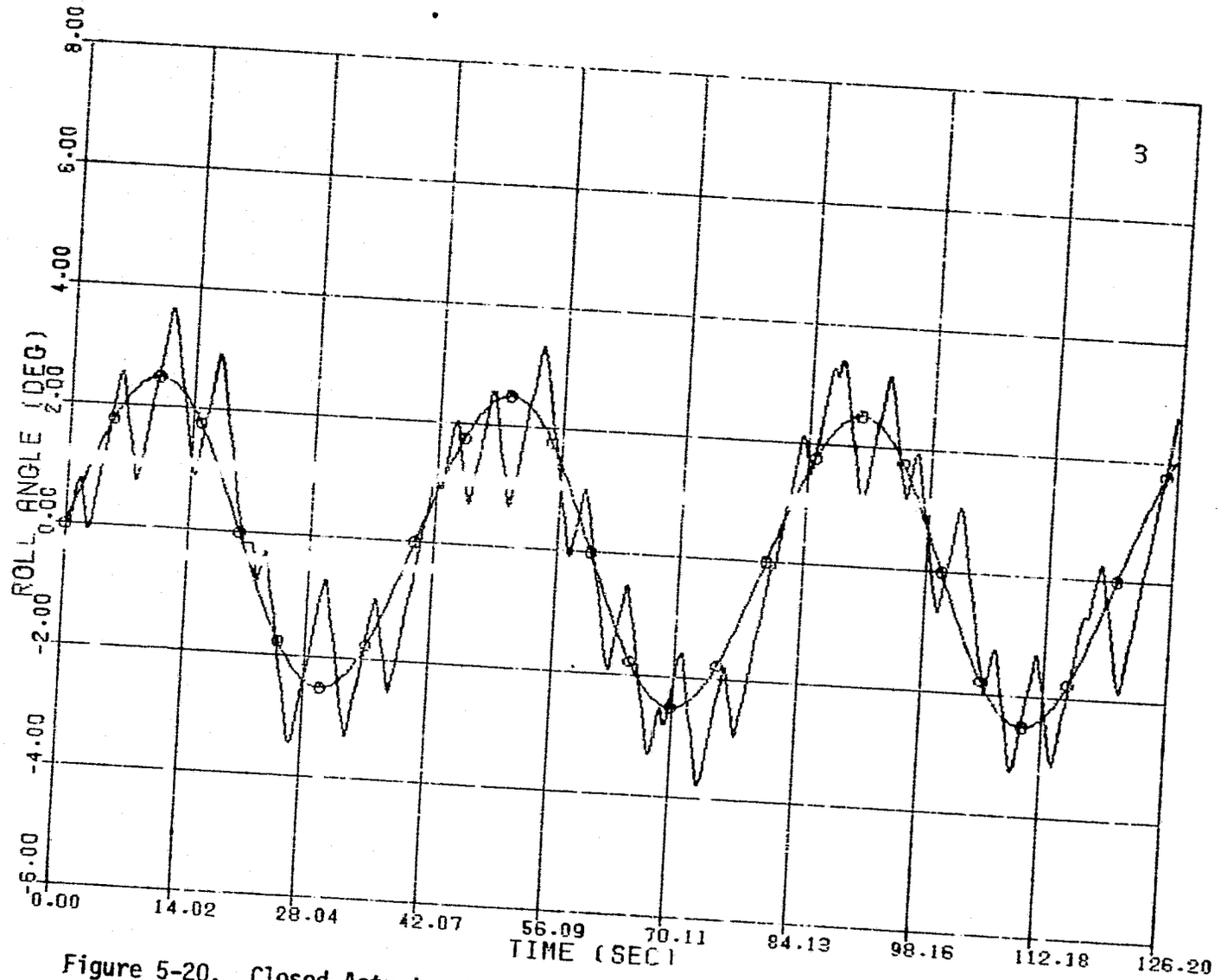

Figure 5-20. Closed Actuator Loop Time History with 0.24 Hz Inclinometer Bandwidth, 0.1 g Cross-Axis Acceleration and 0.025 Hz Input

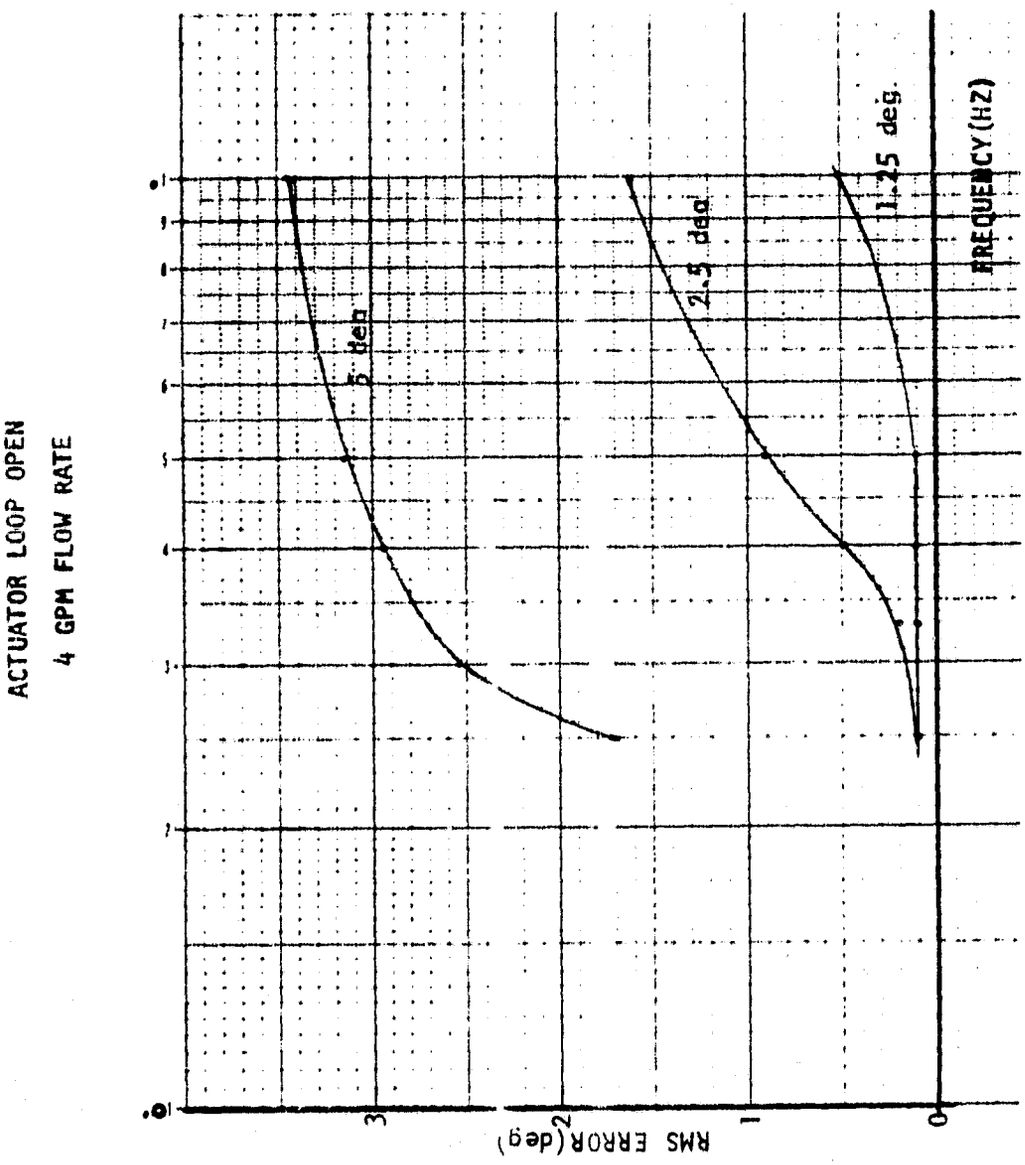

Figure 5-21. Open Actuator Loop Performance

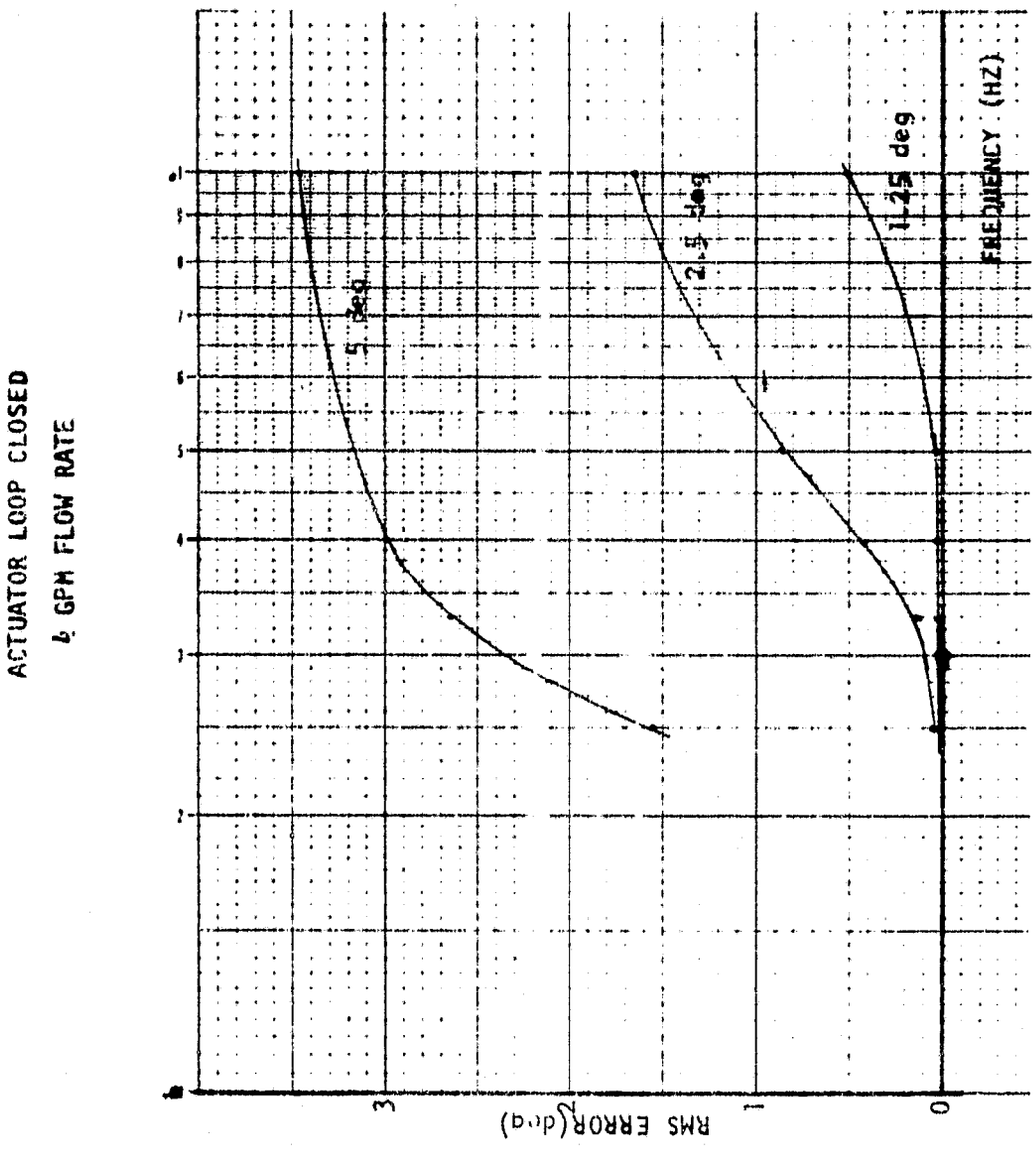

Figure 5-22. Closed Actuator Loop Performance

frequencies has degraded with both loops when the flow rate is cut in half to 4 gpm. Performance with the 2.5 deg input degrades above 0.025 Hz, thus the effective loop bandwidth has halved because the maximum flow rate halved. It is, therefore, expected that noise performance should degrade in the same manner as was seen by varying input frequency.

Table 5-3 shows the noise responses of both loops and both inclinometer bandwidths. These results were obtained with a 0.025 Hz input, and they resemble the results obtained with a 0.025 Hz input at full flow. Results with 0.24 Hz inclinometer bandwidth is somewhat better than the higher flow conditions. Figures 5-23 through 5-26 show the time histories with reduced flow rate; Figures 5-23 and 5-24 are for the open loop and 5-25 and 5-26 are for the closed loop system.

5.6 CONCLUSIONS AND RECOMMENDATIONS

While the closed actuator loop is more accurate under no-noise conditions, both loops perform similarly with cross-axis acceleration disturbances. The signal input level considered in these studies was 1.77 deg RMS. The nominal closed loop system with an input frequency of 0.05 Hz yields an error of 43 percent of the input with a 0.05 g noise level. The open loop system error is 45 percent under the same conditions. Reducing the inclinometer bandwidth or equivalently introducing additional filtering has little effect on noise performance. The major conclusion of this study is that while the closed actuator loop is slightly better than the open loop, both exhibit appreciable error in the presence of small g noise levels.

Table 5-3. Performance with Cross-Axis Disturbances, 0.025 Hz Input and 4 GPM Flow Rate

SYSTEM / CROSS AXIS ACCELERATION RMS g's	RMS LOOP ERROR (DEG)					
	0.01	0.05	0.1	0.2	0.5	1.0
ACTUATOR LOOP OPEN INCLINOMETER: 2.4 HZ	0.225	0.698	1.038	1.334	1.779	2.003
ACTUATOR LOOP CLOSED INCLINOMETER: 2.4 HZ	0.188	0.657	1.029	1.350	1.776	2.023
ACTUATOR LOOP OPEN INCLINOMETER: 0.24 HZ	0.284	0.525	0.732	1.016	1.581	1.998
ACTUATOR LOOP CLOSED INCLINOMETER: 0.24 HZ	0.299	0.596	0.763	1.020	1.591	1.995

(A) INPUT: 1/40 HZ
2.5 DEG PEAK

(B) 4 GMP FLOW RATE

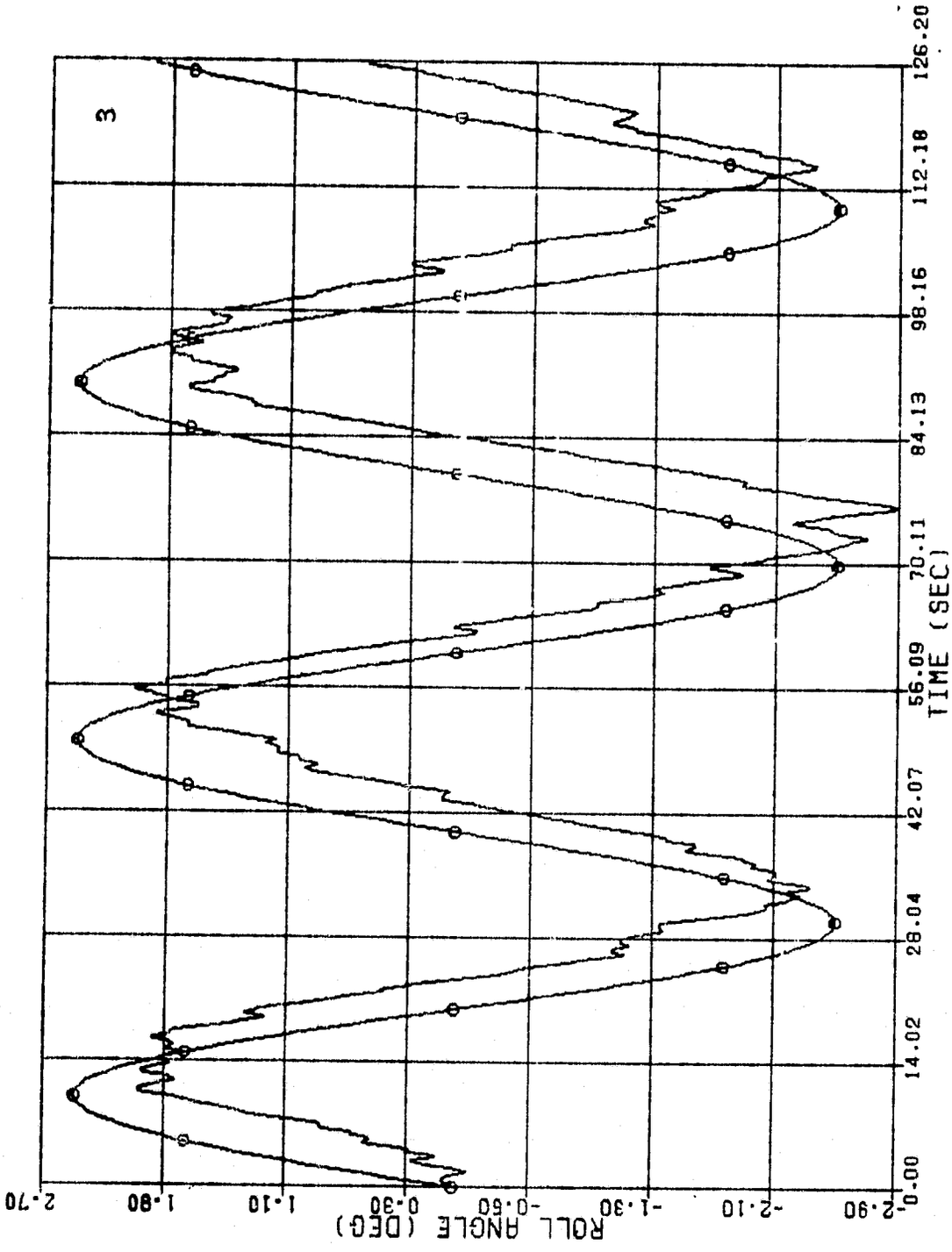

Figure 5-23. Open Actuator Loop Time History with 2.4 Hz Inclinometer Bandwidth, 0.1 g Cross-Axis Acceleration, 4 GPM Flow Rate

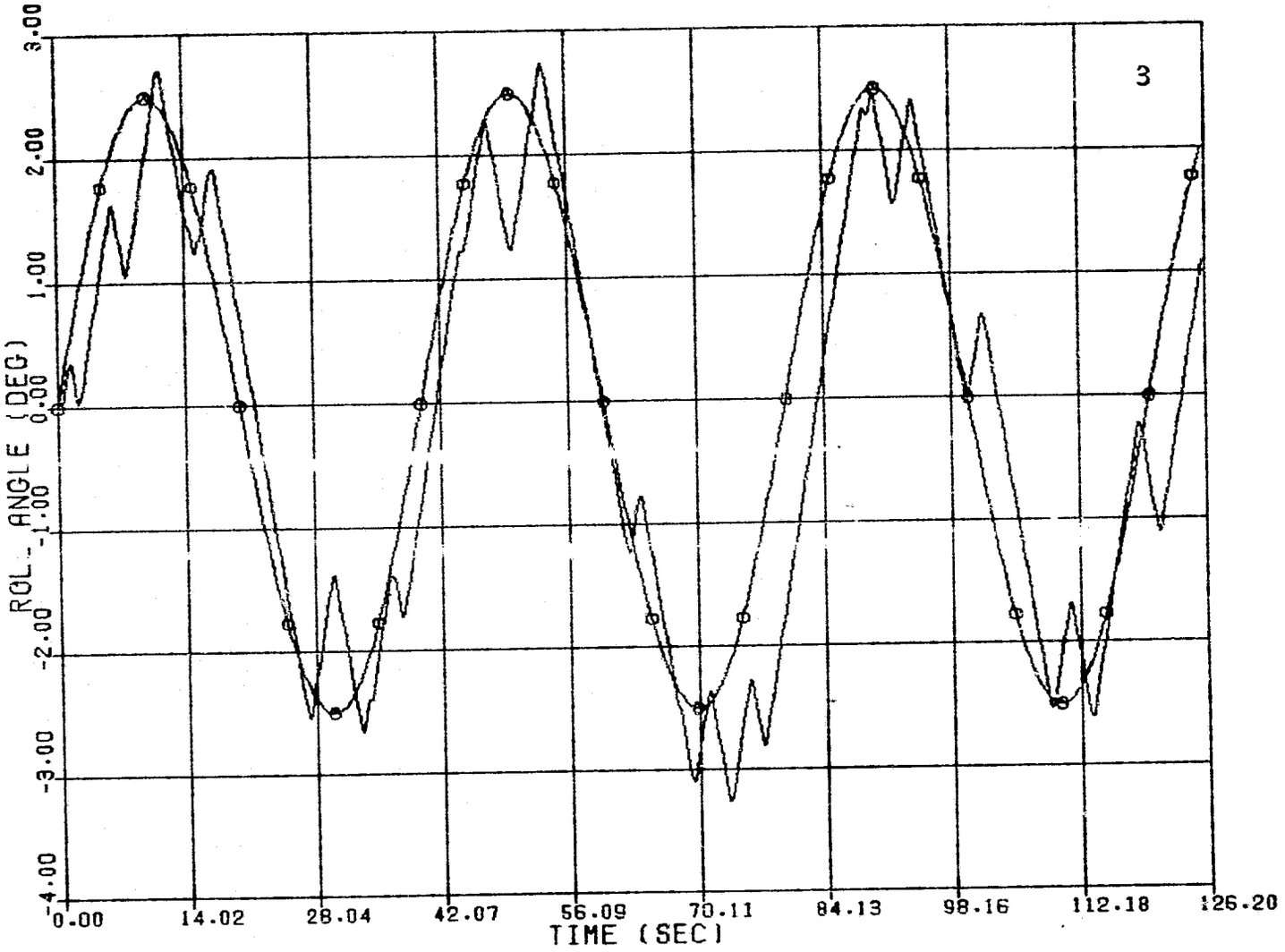

Figure 5-24. Open Actuator Loop Time History with 0.24 Hz Inclinometer Bandwidth, 0.1 g Cross-Axis Acceleration, 4 GPM Flow Rate

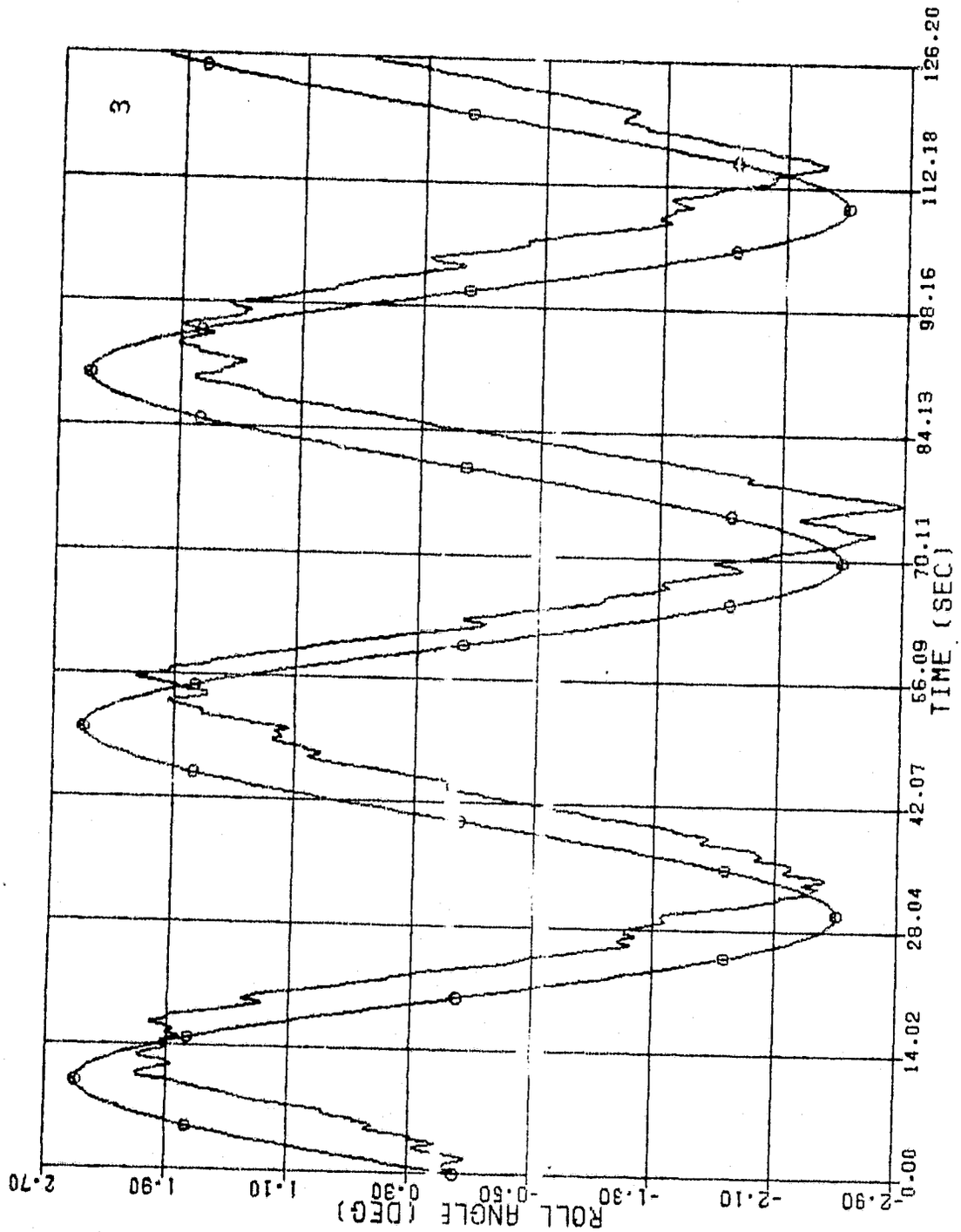

Figure 5-25. Closed Actuator Loop Time History with 2.4 Hz Inclinometer Bandwidth, 0.1 g Cross-Axis Acceleration, 4 GPM Flow Rate

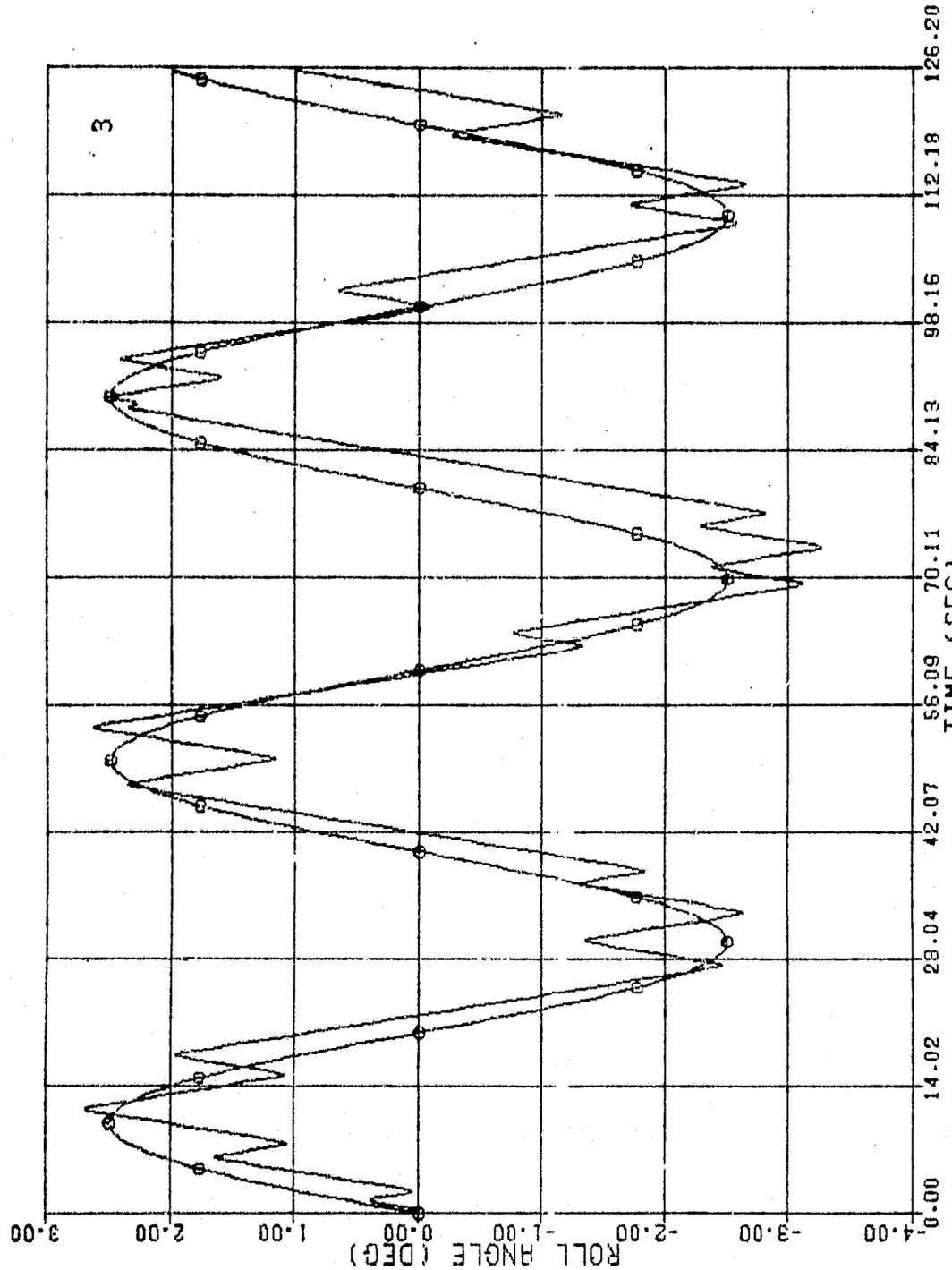

Figure 5-26. Closed Actuator Loop Time History with 0.24 Hz Inclinometer Bandwidth, 0.1 g Cross-Axis Acceleration, 4 GPM Flow Rate

6. PRELIMINARY DEFINITION OF CONTROLS AND DISPLAYS

6.1 Control & Display Philosophy for Longwall - Automated guidance and control of the longwall system does not eliminate the need for controls and displays. It does, in fact, greatly increase these requirements. Currently, the typical longwall C&D system consists of two small control panels on the shearer and a few lever controls located on the individual chocks. Figure 6-1 presents the control panel of the Joy LW300 shearer. Two of these identical panels are located on the shearer, one on each boom, and are used by the shearer operator to control boom height, haulage speed and direction, cowl position, and to start and stop the motors. No displays are needed since the operator is located in direct proximity with the equipment he is controlling and can visually observe the consequences of his actions.

With the introduction of an automated control system, it becomes necessary to monitor the automatically performed functions. It is also necessary to provide the capability for the operator to intervene in the automated process and take command of the control system. He would then function in a semi-automatic, remote control mode to control the shearer and chocks from a remote location. Additionally, it is desirable for this remote operator to be able to interrogate the automatic control system with regard to sensed data and operating parameters in the event of malfunction or degraded performance. Finally, it is necessary to maintain the capability for manual control of the system as a back-up mode of operation and for certain activities more conducive to manual control, such as turn around.

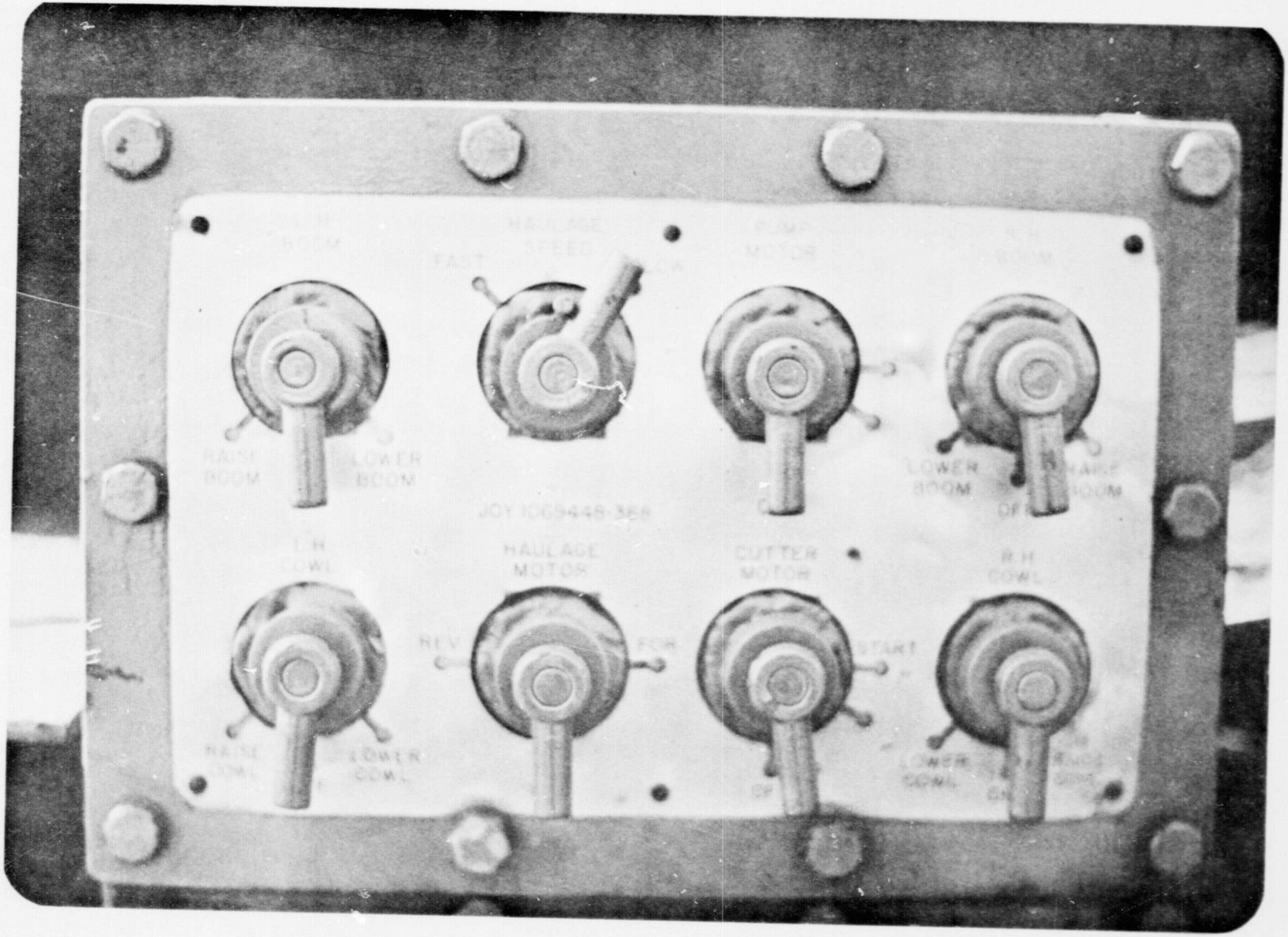

Figure 6-1. Joy LW300 Shearer Control Panel

6.1.1 Control & Display Location - The principal locations considered appropriate for control and display mounting in a longwall system are the headgate, the tailgate, the shearer, and the chocks. Of these, the headgate would appear to be the most logical location for the main control console due to its importance in the overall operation of the longwall system. The tailgate control station is some what redundant with the headgate panel and would be considered most useful if a remote control method of turn around/sump were employed. A control panel on the shearer itself is mandatory. Such a panel is needed for manual control whenever the automatic or remote control systems are not usable. Also, some controls are still necessary on the chock themselves so that they too can be manually advanced whenever necessary.

6.1.2 Communications & Interlocks - Since operation of the shearer and chock support machinery will be possible from two or more locations a system of built-in interlocks and means of communication must be provided to the operators. If the shearer is being operated in the manual or local mode, it must be impossible for the shearer to also be controlled under these circumstances from the Main Control Console, and system interlocks must prevent this possibility. Likewise, a miner working among the chocks must have the capability of isolating one or all of the chocks from the automatic sequencer to prevent sudden and unexpected movement of a chock during a maintenance or inspection activity.

Additionally, to coordinate activities between control stations, communication will be required between all personnel involved. During this preliminary analysis communications were determined necessary between the headgate, tailgate (if implemented) and shearer. It is also felt that a communications package be installed on every 5th chock. The package would consist of PA type receiver and a transmitter. This would mean that a miner working along the row of chocks would never be more than 12½ ft from a communication link. Additionally, each chock should have a control valve to isolate it, or all chocks from the processor to allow manual operations to be performed.

6.2 Control and Display Definition - A functional requirements analysis was conducted on a subsystem by subsystem basis to establish control and display requirements for the longwall system. The results of the analysis is presented in Table 6-1. By subsystem, functions to be commanded and functions to be monitored are noted. For each of these functions a preferred location is given from which to control or monitor the function and an indication as to whether this function should be controlled or monitored from a dedicated or shared C&D. The importance of the function and the necessity of seeing the data in "real time" determines whether a dedicated display is warranted. The type of control or display which can be used to satisfy the requirements is also given.

It must be emphasized that this functional requirements analysis is preliminary and it is expected that as the subsystems become better defined the control and display requirements will also become better defined. It appears at this stage that the majority of those functional requirements listed in Table 6-1 are accurate and will remain unchanged.

Table 6-1. C & D Functional Requirements

SUBSYSTEM	FUNCTION TO BE COMMANDED	FUNCTION TO BE MONITORED	PREFERRED LOCATION	DEDICATED/ SHARED	TYPE OF CONTROL/DISPLAY	REMARKS
GENERAL	Remote/Auto Mode Select		Headgate	D	Toggle Switch	Interlocked so that switch is non-functional unless shearer mounted "Auto/Local" control is in "Auto".
	Auto/Local Mode Select		Shearer	D	Toggle Switch	Interlocked so that local manual control is possible only from shearer, unless auto mode has been selected.
		Remote/Local/Auto Status Display	Headgate Tailgate Shearer	D	Rear Illuminated Status Readout	
	Speed Select		Headgate Tailgate Shearer	D	Push Button & Control Valve	Momentary pushbuttons required at headgate and tailgate. Control valve @ shearer.
		Speed Display	Headgate Tailgate	D	Rear Illuminated Status Readout	
	Pump Motor On/Off Select		Headgate Tailgate Sheared	D	Toggle and Control Valve	Momentary toggle required @ headgate & tailgage. Control valve @ shearer.
		Pump Motor Status	Headgate Tailgate	D	Rear Illuminated Status Readout	

Table 6-1. C & D Functional Requirements (Continued)

SUBSYSTEM	FUNCTION TO BE COMMANDED	FUNCTION TO BE MONITORED	PREFERRED LOCATION	DEDICATED/ SHARED	TYPE OF CONTROL/DISPLAY	REMARKS
GENERAL						
	Cutter Motor On/Off Select		Headgate Tailgate Shearer	D	Toggle and Control Valve	Momentary Toggle required at headgate & tailgate. Control valve @ shearer.
		Cutter Motor Status	Headgate Tailgate	D	Rear Illuminated Status Readout	
	Shearer Direction Select		Headgate Tailgate Shearer	D	Toggle and Control Valve	Momentary toggle required @ headgate & tailgate. Control valve @ shearer.
		Shearer Direction Status	Headgate Tailgate	D	Rear Illuminated Status Readout	
VCS						
	L.H. Boom Raise/Lower		Headgate Shearer	D	Toggle & Control Valve	Momentary toggle required @ headgate. Control valve @ shearer.
		L.H. Cutter Drum Height	Headgate Tailgate	D	Digital R.O.	
	R.H. Boom Raise/Lower		Headgate Shearer	D	Toggle & Control Valve	Momentary toggle required @ headgate. Control valve @ Shearer.
		R.H. Cutter Drum Height	Headgate Tailgate	D	Digital R.O	

Table 6-1. C & D Functional Requirements (Continued)

SUBSYSTEM	FUNCTION TO BE COMMANDED	FUNCTION TO BE MONITORED	PREFERRED LOCATION	DEDICATED/ SHARED	TYPE OF CONTROL/DISPLAY	REMARKS
VCS (Con't)	L.H. Cowl Raise/Lower		Shearer	D	Valve	
		L.H. Cowl Position	Headgate	D	Rear Illuminated Status Readout	
	R.H. Cowl Raise/Lower		Shearer	D	Valve	
		R.H. Cowl Position	Headgate	D	Rear Illuminated Status Readout	
	CID Thickness Setting		Headgate	D	Thumbwheel	
		CID (Coal) Thickness	Headgate Tailgate	D	Digital R.O	
	Sensitized Pick Output Level		Headgate	D	Thumbwheel	
		Sensitized Pick Output Level	Headgate	D	Digital R.O.	
		Sensitized Pick Coal/Shale Status	Headgate Tailgate	D	Rear Illuminated Status Readout	
		Lead Cutting Drum Command	Headgate Tailgate	D	Digital R.O.	
		Last Cut Follower	Headgate Tailgate	D	Digital R.O.	Readout gives difference between LCF & CID positions of lead cutting drum command.

Table 6-1. C & D Functional Requirements (Continued)

SUBSYSTEM	FUNCTION TO BE COMMANDED	FUNCTION TO BE MONITORED	PREFERRED LOCATION	DEDICATED/ SHARED	TYPE OF CONTROL/DISPLAY	REMARKS
VCS (Con't)		CID - Drum Position	Headgate	S	Digital R.O & Keyboard	Difference, if any, between where CID senses drum should be and where drum is
		L.H. Boom Hydraulic Pressure	Headgate	S	Digital R.O. & Keyboard	
		R.H. Boom Hydraulic Pressure	Headgate	S	Digital R.O. & Keyboard	
		Power Supply Voltage	Headgate	S	Digital R.O. & Keyboard	
		Power Supply Current	Headgate	S	Digital R.O. & Keyboard	
		Line Voltage	Headgate	S	Digital R.O. & Keyboard	
		Line Current	Headgate	S	Digital R.O. & Keyboard	
		Hydraulic Pressure	Headgate	S	Digital R.O. & Keyboard	
		Control Law Commanded Output	Headgate	S	Digital R.O. & Keyboard	
	LCF Threshold Level Adjust		Headgate	S	Keyboard	

Table 6-1. C & D Functional Requirements (Continued)

SUBSYSTEM	FUNCTION TO BE COMMANDED	FUNCTION TO BE MONITORED	PREFERRED LOCATION	DEDICATED/ SHARED	TYPE OF CONTROL/DISPLAY	REMARKS
VCS (Con't)						
		LCF Signal Level Output	Headgate	S	Digital R.O. & Keyboard	
		Distance of Shearer from Headgate/Tailgate	Headgate Tailgate	D	Pictorial Display & Digital R.O.	
		Drum Separation	Headgate Tailgate	D	Digital R.O.	
YAS						
		Chock Loaded Against Roof - Retracted	Headgate	S	Digital R.O. Plus Rear Illuminated Status Readout	Indication required for each chock
		Chock Ram Extended/ Retracted	Headgate	S	Digital R.O. Plus Rear Illuminated Status Readout	Indication required for each chock
	Emergency Shutdown of Chock		Headgate	S	Keyboard Control	Capability required to isolate chock from electronic control & thus place off-line.
		Face Alignment	Headgate	S	Digital R.O. Possibly Pictorial Display	
		Face Alignment Sensor Status	Headgate Tailgate	D	Rear Illuminated Status Readout	
	Access to Chock Command Logic		Headgate	S	Keyboard Control	

Table 6-1. C & D Functional Requirements (Continued)

SUBSYSTEM	FUNCTION TO BE COMMANDED	FUNCTION TO BE MONITORED	PREFERRED LOCATION	DEDICATED/ SHARED	TYPE OF CONTROL/DISPLAY	REMARKS
YAS (Con't)	Chock Auto/Disable		Individual Chock	D	Selector Switch	Capability required to disable individual chock or all chocks from a chock position.
		Chock Enable/Disable Status	Headgate	S	Digital R.O. & Keyboard Access	
RCS		Roll Sensor Status	Headgate Tailgate	D	Digital R.O.	
		Roll Actuator Status	Headgate Tailgate	D	Rear Illuminated Status Display	
	Command Roll Sensor Gain Change		Headgate	S	Digital R.O. & Keyboard Access	
C & W		Methane Monitor	Headgate Tailgate Shearer	D	Enunciator	
		CID Radiation Monitor	Headgate Tailgate Shearer	D	Enunciator	
		CID Status Monitor	Headgate	D	Enunciator	
		Sensitized Pick Status Monitor	Headgate	D	Enunciator	
		LCU Status Monitor	Headgate	D	Enunciator	
		Roll Sensor Status Monitor	Headgate	D	Enunciator	

Table 6-1. C & D Functional Requirements (Concluded)

SUBSYSTEM	FUNCTION TO BE COMMANDED	FUNCTION TO BE MONITORED	PREFERRED LOCATION	DEDICATED/ SHARED	TYPE OF CONTROL/DISPLAY	REMARKS
C & W (Con't)		Power Supply Status Monitor	Headgate	D	Enunciator	
		Hydraulic System Status Monitor	Headgate	D	Enunciator	
COMMUNICATION	Communication Channel Select		Headgate Tailgate Shearer	D	Selector Switch	
	Transmit Communications		Headgate Tailgate Shearer	D	Microphone/Transmitter	Communications stations (Loundspeaker & microphone) will be located on chocks 50' apart across the entire face.
		Receive Communications	Headgate Tailgate Shearer	D	Speaker/Receiver	
TROUBLESHOOTING		Subsystem Failure Indication	Headgate	D	Enunciators	Specific subsystem failure analysis logic to be determined
		Troubleshooting Aids	Shearer	D	Test Points	

However, additional requirements will most likely be generated to complement those already defined.

6.2.1 Processor Accessed Displays - Of all the display requirements, the processor accessed displays are probably least known at this time. The ability to interrogate the engineering proto-type system is very desirable. Once the system has been proved out, these display requirements may no longer exist. However, during the initial experimental system development a great number of system parameters and "nice-to-know" information can be visualized as being logically displayed, on command, by the processor. A very preliminary list of displays which may be necessary is shown in Table 6-2. This list is expected to grow extensively as the processor design develops.

6.2.2 Processor Accessed Commands - As in the case of the processor accessed displays, the commands too are ill-defined at this point in the system development. Those commands that have been identified include the following: the ability to adjust the threshold triggering level from $\pm$ 2" to some other figure should it be demonstrated that the acceptable variation between the last cut follower and the CID should be more or less stringent than the proposed $\pm$ 2"; the ability to bias the roll sensor in order to accommodate seam conditions inclined to the local vertical; access to the chock command logic in order to modify the control algorithm; the ability to shut down an individual chock and remove it from automatic control should some malfunction degrade its performance.

Table 6-2. Preliminary List of Processor Accessed Displays

C1D - DRUM POSITION

L.H. & R.H. BOOM HYDRAULIC PRESSURE

POWER SUPPLY OUTPUT VOLTAGE & CURRENT

LINE VOLTAGE & CURRENT

HYDRAULIC PRESSURE

OUTPUT OF CONTROL LAW COMMAND

ROLL SENSOR SIGNAL OUTPUT

SENITIZED PICK SIGNAL OUTPUT

INCLINOMETER SIGNAL OUTPUT

LAST CUT FOLLOWER SIGNAL OUTPUT

FACE MISALIGNMENT AT VARIOUS MEASUREMENT POINTS

CHOCKS INDIVIDUALLY CALLED UP BY NUMBER

- CHOCK ENABLE/DISABLE STATUS
- RAM EXTENDED/RETRACTED
- LOADED AGAINST ROOF/UNLOADED

MALFUNCTION ISOLATION & TROUBLESHOOTING

6.3 Preliminary Control and Display Concepts

6.3.1 Headgate Control Station Panel Layout - The preliminary headgate control station panel layout is shown in Figure 6-2. The control panel measures 19 1/4" by 11 1/4" and provides for an approximate 15% growth factor. It is felt, however, that should the growth of the C&D exceed 15% a somewhat larger panel should not pose any particular problem. Although actual C&D components have not yet been selected, representative components have been used in the panel layout to insure adequate spacing both in front and behind the panel. Controls and displays are functionally grouped by subsystem, machine component, and control functions. Each of the functional groups will be described separately.

a. Operating Mode - Two toggle switches are used. One to control system power on/off and one to select the operating mode. Only the remote or automatic mode can be selected from this panel. Should the "local" (or manual) mode be selected at the shearer, all command functions of the headgate control station are interlocked inoperable. Which ever of the three operation modes are being used would be indicated by the illumination of that display indicator.

b. Caution and Warning - The caution and warning enunciators are LED's with incorporated lens covers such as the Shelly/Datatron "Brite-Eyes". These enunciators would give positive indication of satisfactory operation-green, cautionary condition-amber, or malfunction-red. Should the methane concentration

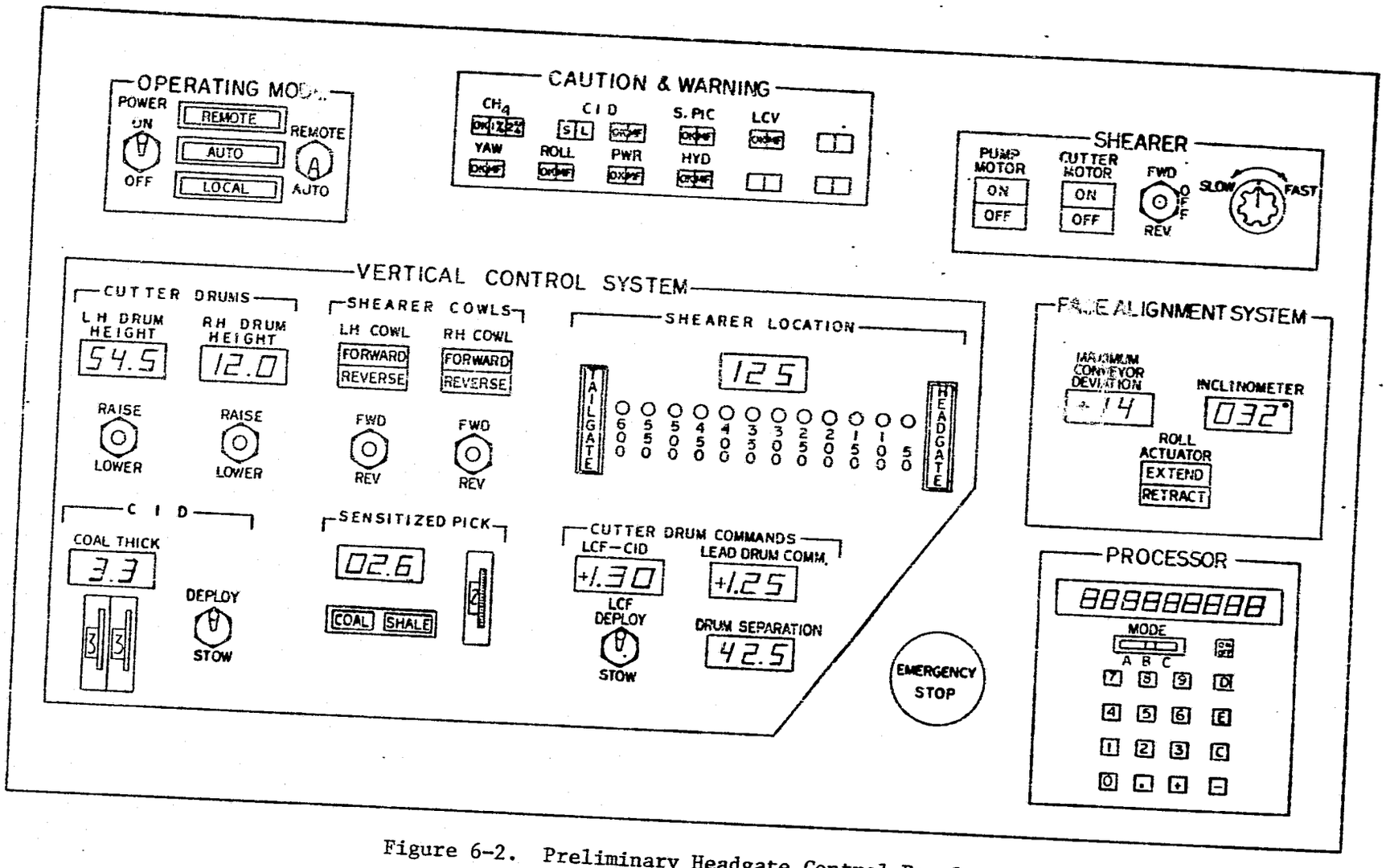

Figure 6-2. Preliminary Headgate Control Panel

rise to 2% or should a malfunction occur in an important component threatening personnel safety, the system would be automatically shut down with the enunciator indicating the reason.

c. Shearer - The shearer controls consist of two double-acting switch-lights to turn the pump motor and cutter motor on and off, a three position toggle to select desired course of the shearer, and a selector switch to select shearer speed. Although shearer speed is infinitely variable from slow to fast, a selector switch of approximately 8 position is used here rather than a potentiometer, since this would essentially yield continuous control and is a simpler and more reliable implementation particularly if multiplexing is to be employed.

d. Vertical Control System - The cutter drums are raised and lowered by means of two center-off momentary toggles. LED digital readouts are used to display drum height above the skid plane in inches.

Shearer cowls are changed from the forward to reverse position by means of two center-off momentary toggles. Rear illuminated displays indicate the cowl position. While the cowl is in transition between points, both lights would be off.

Shearer location is an LED display system to indicate where the shearer is with respect to the headgate and tailgate. If the shearer is at the headgate or tailgate, that rear illuminated display will so indicate. As the shearer begins to move from the headgate the first LED will flash until the leading edge of the shearer arrives at the 50 foot mark. At this time the

first LED will burn steady and the second will flash until the shearer reaches the 100 foot mark. The actual distance from the headgate will be displayed above the row of light on a LED digital readout.

The CID is deployed or stowed by use of a two position toggle. The desired coal thickness to be left uncut is set in with thumb wheels with the sensed coal thickness shown via a LED digital readout in inches and tenth of inches.

The Sensitized Pick displays whether it is into coal or shale by the illumination of one side of the rear illuminated display. The LED digital readout represents a RMS level readout from the sensor and the thumbwheel control allows a change in output level to be commanded.

The cutter drum commands indicate the following using LED digital readouts: 1) the difference between the last cut follower measurement and the CID measurement, 2) the control law command to the lead drum, and 3) separation between the two drum. All readouts are in inches. A two position toggle is used to deploy or stow the last cut follower.

e. Face Alignment System - Two LED digital readouts are used. The first one indicates the maximum deviation of the conveyor in inches from a true path or measure along some pre selected points. The second indicates the output of the inclinometer in degrees. The third display in this group is a rear illuminated indicator which will show whether the roll actuator is fully extended or retracted.

f. Processor - The processor input and call up control consists of a keyboard and a numeric readout. This keyboard would require a code book to allow call up of functions to be displayed and to input commands. A mode switch is shown which could be used to simplify the coding operation. Viz; with mode "C" (for chocks) selected, any of the 125 chocks could be called up simply by inputing its number.

As long as the number of functions to be called up are kept to a minimum this system would provide a simple method of processor interface. However, should the number of processor accessed displays and command grow significantly it might be desirable to utilize a full computer input keyboard and an alpha-numeric readout. Such a concept is shown in Figure 6-3.

6.3.2 Headgate Control Station Console Configuration - Should the preliminary control panel shown in Figure 6-2 be large enough to accomodate all the necessary controls and displays, a lightweight, easily portable control console should be possible. Such a concept is shown in figure 6-4. The console would be intrinsically safe and contain no power supply. Conditioned power would be supplied either from the shearer or from a separate power supply located near by at the headgate. Should the control panel grow significantly in size or should the more complex computer keyboard be required, a mobile chassis mount might be necessary. The concept shown in Figure 6-5 uses large pneumatic tires for ease of movement over

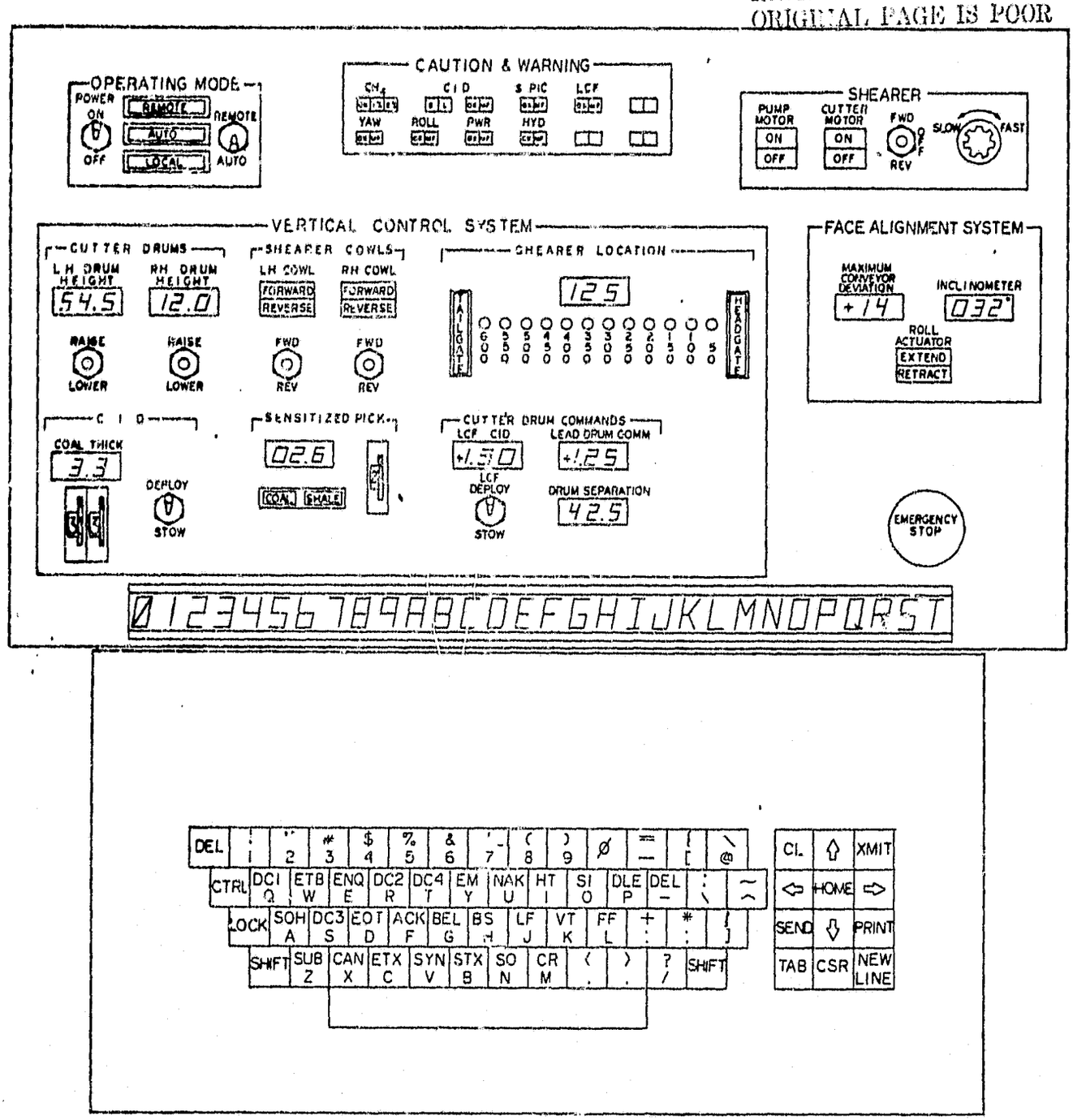

Figure 6-3. Headgate Control Panel with Alpha-Numeric Keyboard

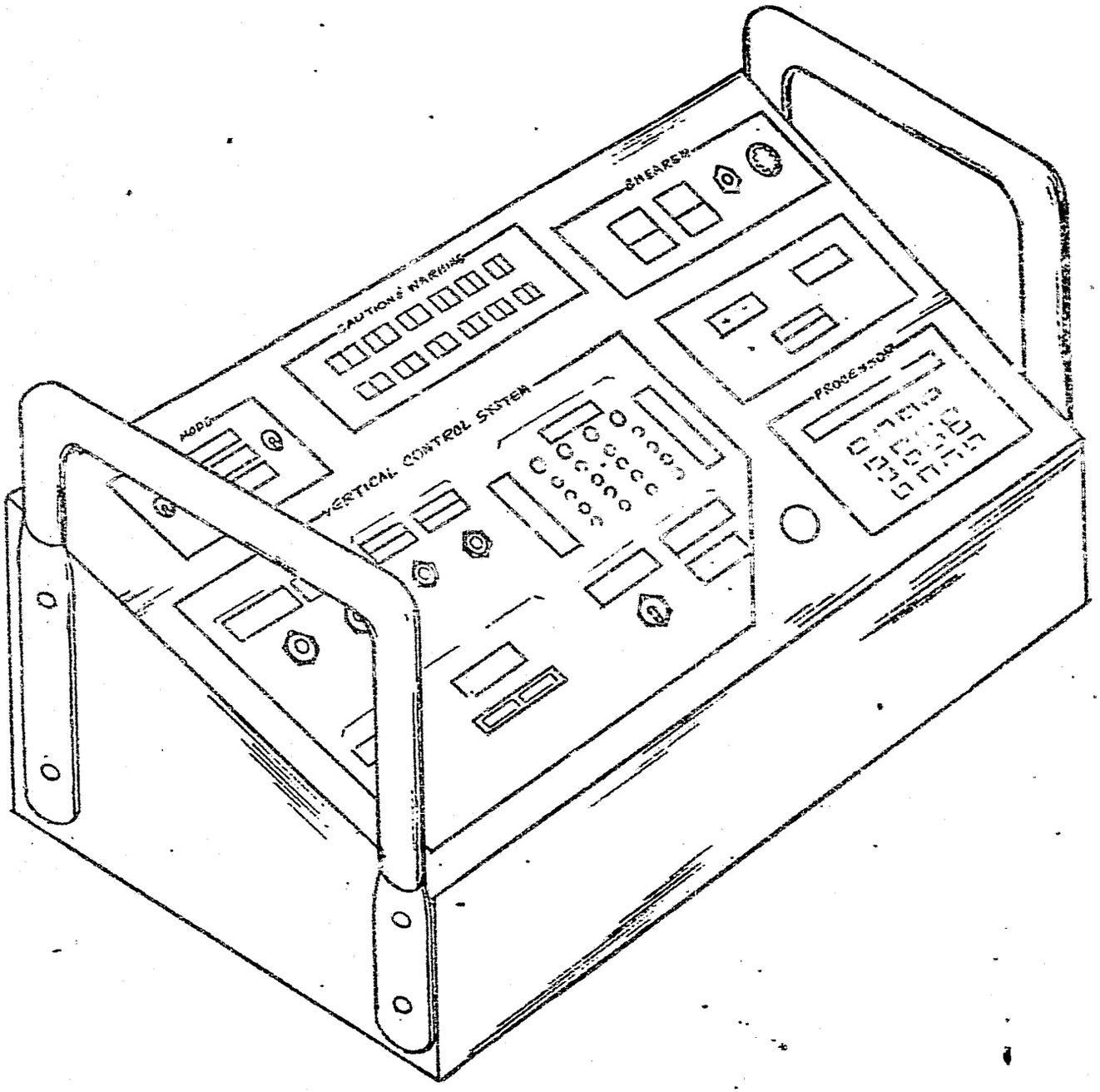

Figure 6-4. Portable Panel Concept

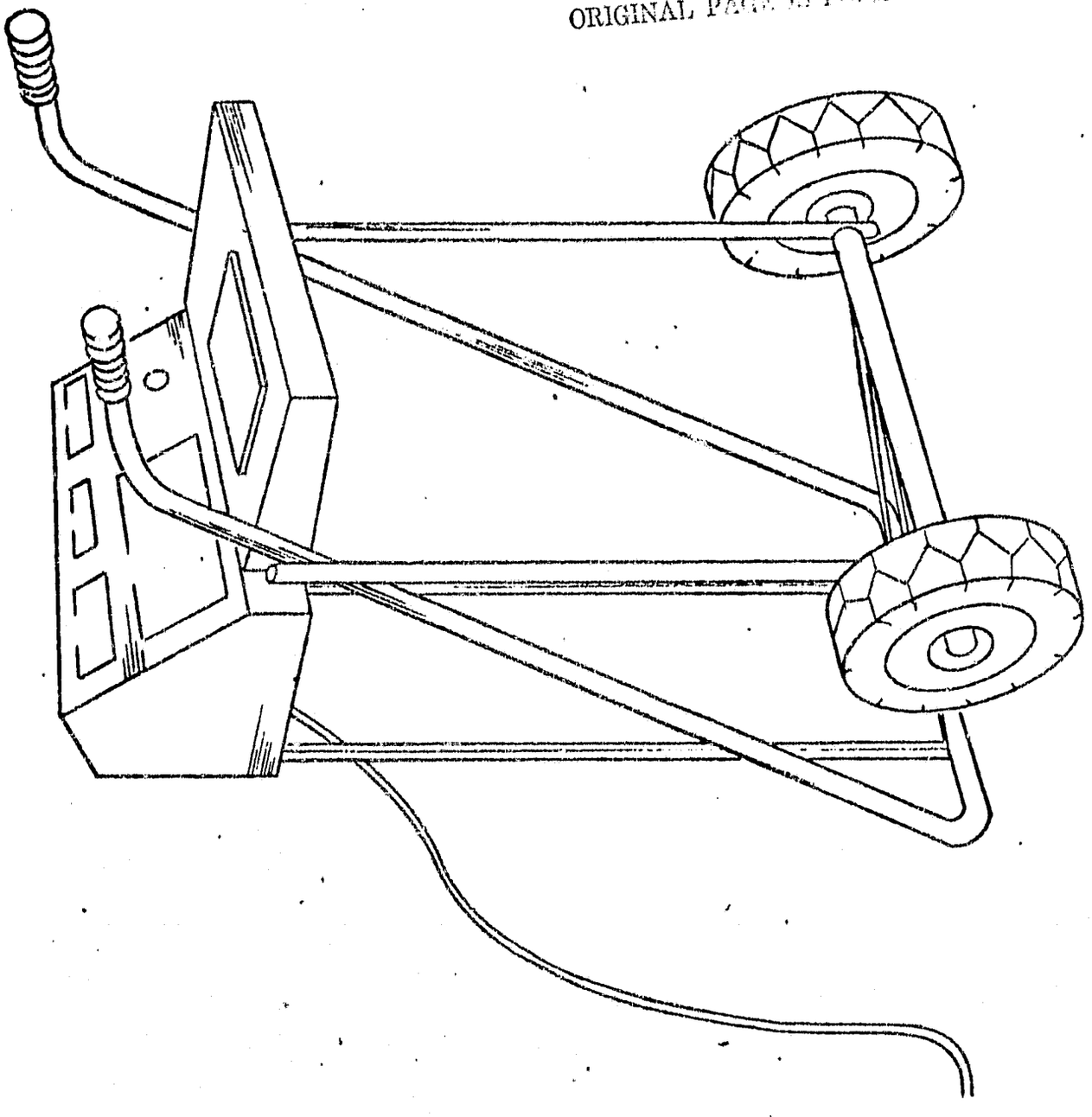

Figure 6-5. Mobile Panel Concept

rough surfaces. The console could be constructed as either a "sit-down" or "stand-up" station. Although every effort would be made to keep this console intrinsically safe, such a mobile chassis mount could accommodate a permissable unit or could possibly house a permissable power supply package in addition to the intrinsically safe console.

6.3.3 Shearer Control Panel - The preliminary concept of the shearer control panel is shown in Figure 6-6. The panel consists of the present Joy control panel with the addition of the operating mode controls & displays and the caution and warning enunciators. Further consideration will be given to this control panel during phase II.

6.3.4. Tailgate Control Station - As a result of the phase I study, no firm requirement can be seen for a tailgate control station. However, it is not felt that the concept should be definitely eliminated at this time and it is proposed that it be carried over into phase II as an open item.

6.3.5 Chock Control Panel - Each chock would maintain the control levels supplied by the manufacturer. In addition a switch or a series of switches would be provided to disable that particular chock from automatic control. Possibly the chock on either side might also be disabled from this same position, and/or all of the chocks on line might be disabled as a group.

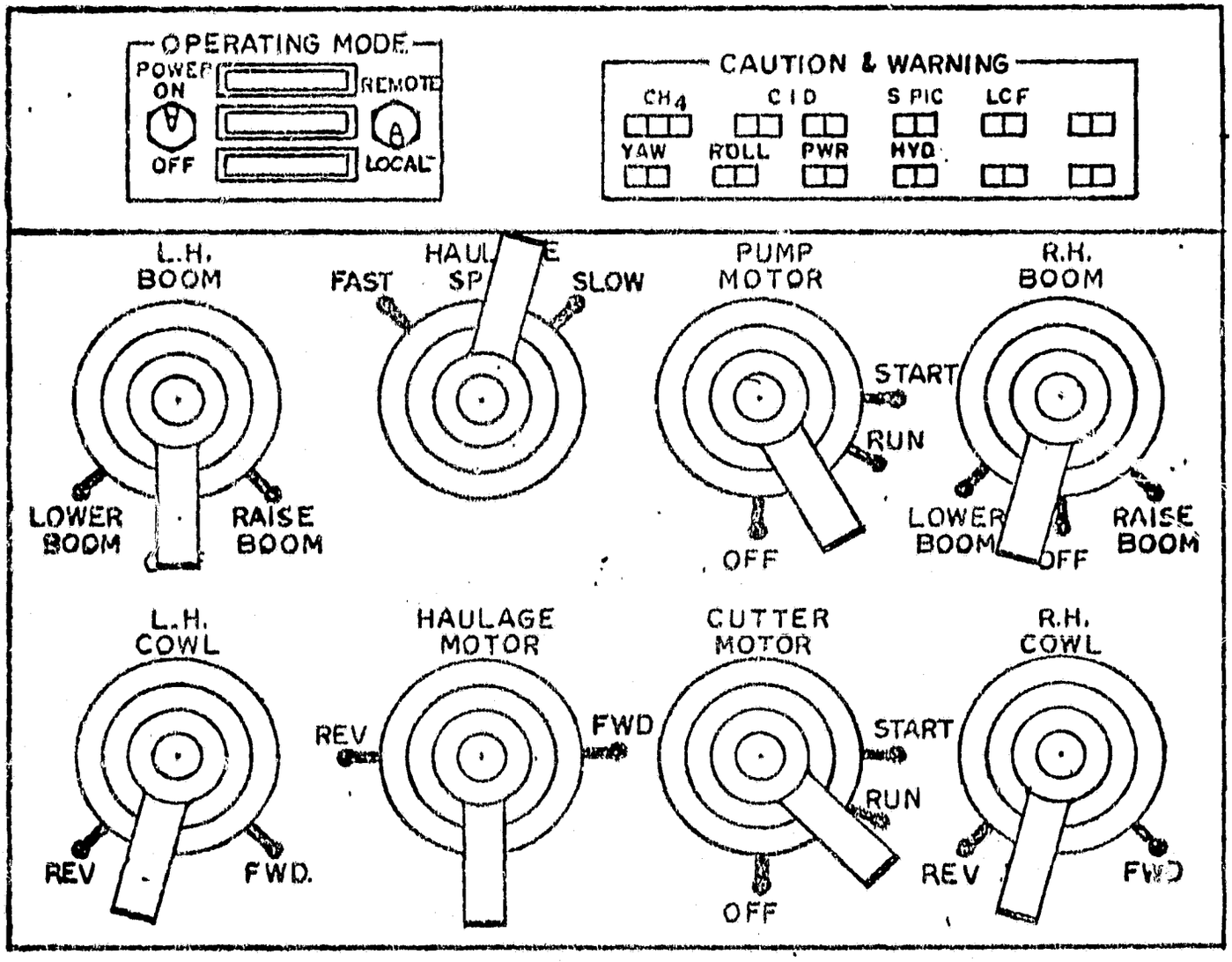

Figure 6-6. Shearer Control Panel - Preliminary Concept

6.3.6 Control and Display Component Selection - As mentioned earlier, components were investigated during this phase although component selections have not yet been made. Some decisions were reached about component selection and recommendations made. These include the following.

a. Utilization of LED readouts and displays should be made whereever possible since they are low power self-illuminating devices and meet intrinsic safety requirements.

b. It is not felt necessary to hermetically seal the control panel, but oil tight switches will be used, all connections potted, and silicone gasket material will be used on every panel opening.

c. When required, rear illuminated displays will be used in preference to non-illuminated displays which would require external illumination.

6.4 Proposed Phase II Trade Studies - During phase II a preliminary design of the longwall control and display system will be completed. Interfaces will be defined with the communications subsystem, power conditioning and distribution, and i/o assemblies. The functional requirements will be updated and panel layout modified. Component selection will be made and various analyses conducted to insure that system safety, reliability, maintainability, and human engineering requirements are met.

Additionally a number of trade studies will be conducted during phase II. These will include:

a. Panel Lighting - A review of the benefits, cost, power requirements, and human factor aspects of various panel lighting schemes. Comparisons will be made of area lighting, electroluminescence and exterior lighting.

b. Processor Keyboard - A trade study will be made of an alphanumeric vs an all numeric system of processor addressing. Consideration will be given to the use of a code book and the added volume resulting from an alphanumeric keyboard.

c. Power Supply Location - A trade study will be conducted to determine whether the C&D power supply should be located in the console itself, in the shearer, or as a separate unit.

d. Tailgate Control/Monitor Station - The usefulness of a tailgate C&D will be reviewed and a determination of its need will be specified.

7. OVERALL LONGWALL SYSTEM REQUIREMENTS

The following paragraphs outline the requirements of the recommended longwall system design by major subsystems.

7.1 Vertical Control System

Shearer Traverse Velocity - 30 ft/min nominal

Operational Modes

Take all coal on top and bottom.

Leave a prescribed amount of coal on top and take all coal on bottom.

Take all coal on top and leave a prescribed amount of coal on bottom.

Leave a prescribed amount of coal on top and bottom

Manual turn around at headgate and tailgate

Manual Operation of VCS

Maintain present cut to within a prescribed amount of previous cut.

Bottom and top drum interchangeable depending on cutting direction.

Sensor complement for taking all coal on top and bottom.

Top Drum Control

Sensitized Pick - At least two mounted 180 deg. apart in cutting drum

Last Cut Follower - Range greater than 2 in.

Bottom Drum Control

Sensitized Pick - At least two mounted 180 deg. apart on cutting drum

Last Cut Follower - Required when drums are interchanged

Sensor complement for leaving a prescribed amount of coal on top and taking all coal on bottom.

Top Drum Control

Active Nucleonic CID mounted 2.5 ft behind cutting drum

Sensitized Pick - At least two mounted 180 deg. apart on cutting drum

Last Cut Follower - Range greater than 2 in.

Bottom Drum Control

Sensitized Pick - At least two mounted 180 deg. apart on cutting drum

Active Nucleonic CID - Required when drums are interchanged

Last Cut Follower - Required when drums are interchanged.

Sensor complement when taking all the coal on top and leaving a prescribed amount of coal on bottom

Top Drum Control

Sensitized Pick - At least two mounted 180 deg. apart on cutting drum

Last Cut Follower - Range greater than 2 in.

Present Cut Follower - Required when interchanging drums

Bottom Drum Control (Drum Slaving)

Sensitized Pick - At least two mounted 180 deg. apart on cutting drum

Present Cut Follower - Range compatible with seam height

Last Cut Follower - Required when interchanging drums

Sensor complement when leaving a prescribed amount of coal on top and bottom

Top Drum Control

Active Nucleonic CID mounted 2.5 ft behind cutting drum

Sensitized Pick - At least two mounted 180 deg. apart on cutting drum

Last Cut Follower - Range greater than 2 in.

Present Cut Follower - Required when cutting drums are interchanged

Bottom Drum Control (Drum Slaving)

Sensitized Pick - At least two mounted 180 deg. apart on cutting drum

Present Cut Follower - Range compatible with seam height

Last Cut Follower - Required when cutting drums are interchanged.

Active Nucleonic CID - Required when cutting drums are interchanged.

Active Nucleonic CID

Mounted 2.5 ft behind cutting drum

Twenty inch separation between source and detector.

CSI crystal detector

Source - 30 mCi CS-137

Averaging time (Output Internal) - 0.25 sec.

Sensitized Pick - 80 to 90 percent accurate. Discrete indication whether coal or shale.

Natural Radiation CID

Used if shown to be advantageous during Phase II

Mounted 2.5 ft behind cutting drum

5 in. detection crystal

Averaging time (Output Internal) - 1 sec.

7.2 Roll Control Loop

Control Loop Bandwidth - 0.05 Hz at 2.5 deg. peak sinusoidal input

Inclinometer mounted on shearer

Inclinometer characteristics

Bandwidth - between .5 and 2.4 Hz

Damping ratio - between 0.4 to 0.8

Second Order Dynamics

Noise within control loop bandwidth - No greater than 10^{-3} g RMS

Roll Actuation Range - $\pm$ 5 in.

Roll Actuation Rate - Greater than 1 deg/sec

7.3 Yaw Alignment System

Automatic Face Advance

Manual Face Advance

Each roof support individually commanded to advance conveyor.

Angle cart system implementation with basic measurement algorithm (See Section 4.0).

Angle cart integrated with shearer

Required angle measurement accuracy - 0.03 deg one sigma

Required resolver measurement accuracy - 2 min one sigma

Sample size of resolver measurements - 200

Allowable ram placement error - 0.02 ft one sigma

Allowable roof support roll up error - 0.1 ft (1.2 in) one sigma

7.4 Controls and Displays

Main control and display station in headgate.

Control and displays on shearer for manual operation

Computer access through digital address keyboard on headgate control and display panel.

No present requirement for control and displays at tailgate.

Control and display panel inoperative when shearer is under manual control.

Critical functions have dedicated display and controls in headgate panel (See Section 6, Figure 6-2).

Utilization of LED readouts whereever possible

Use oil tight switches, all connections potted, and silicone gasket material used on every panel opening.

Rear illuminated displays used as much as possible.